UNIVERSITÀ DEGLI STUDI DI TRIESTE

UNIVERSITÀ DEGLI STUDI DI TRIESTE

XVIII CICLO DEL DOTTORATO DI RICERCA IN FISICA

Finanziato dall'Unione europea - NextGenerationEU
Funded by the European Union - NextGenerationEU

Massive Black Hole dynamics and evolution in cosmological simulations

Settore scientifico-disciplinare: **PHYS/05**

DOTTORANDA
Alice Damiano

COORDINATORE
PROF. Angelo Bassi

SUPERVISORE DI TESI
PROF. Stefano Borgani

CO-SUPERVISORE DI TESI
DOTT. Milena Valentini

ANNO ACCADEMICO 2024/2025

Finanziato dall'Unione europea NextGenerationEU | Ministero dell'Università e della Ricerca | Italiadomani | UNIVERSITÀ DEGLI STUDI DI TRIESTE

- Lei, per esempio, non teme la punizione di Dio?
- Ma che te devo dì, finché stavamo ar Medioevo, finché stavamo ancor cor sistema tolemaico, ce potevi pure crede alla punizione di Dio. C'era solo 'a tera, er sole, tre pianetini, le stelle erano dei buchetti su un telo nero, pe fa passa la luce, l'Universo era tutto lì, era l'unico giocarello che c'aveva. E allora, magari ce potevi crede che lui se poteva divertì a spiacce, a fa le pulci, a guardà dal buco de la seratura, a mannà la gente all'inferno... Ma oggi, ammesso pure che esiste, no? Che io poi sò de mentalità aperta... ma te hai visto 'a robba che c'è là fori? Mijardi e mijardi de galassie, mijardi de stelle, de pianeti, buchi neri, quasar, pulsar, oceani di materia oscura, de fasci de neutrini, di antimateria... Ma ammesso pure che esiste, no? Ma tu pensi che uno che ha fatto tutta sta robba gliene può fregà quarcosa se su sto sercio de periferia noi rubbamo, sparamo, tradimo 'e mogli, se ingroppamo fra de noi? Ma tu pensi veramente che 'a morale nostra po esse 'a questione centrale dell'Universo?
Corrado Guzzanti, Don Florestano Pizzarro

Abstract

Massive Black Holes (MBHs, with masses $> 10^6\,M_\odot$) residing at the centers of massive galaxies profoundly influence the evolution of their hosts. Accretion onto MBHs, together with the subsequent release of energy through feedback processes, powers Active Galactic Nuclei (AGN), whose signatures are observable across the entire electromagnetic spectrum, from radio jets and bubbles to X-ray coronal emission. The orbital evolution of MBHs is primarily governed by dynamical friction, the gravitational drag exerted by the surrounding matter distribution, which anchors MBHs at the centers of their hosts and drives the orbital decay of MBH pairs down to parsec-scale separations following galaxy mergers.

Since MBH accretion and the ensuing AGN feedback are strongly influenced by the local properties of the surrounding medium, an accurate description of MBH orbits is essential to capture their impact on galaxy evolution.

Cosmological hydrodynamical simulations provide a unique framework to investigate the coupled evolutionary histories of massive galaxies and their MBHs, as well as the processes governing MBH dynamics. However, the limited resolution of large-scale cosmological simulations demands sub-resolution models to capture MBH dynamics, accretion and feedback processes.

This thesis aims to improve the description of the MBH lifecycle in cosmological hydrodynamical simulations carried out with the N-body Smoothed Particle Hydrodynamics OpenGADGET3 code, focusing in particular on a novel approach to accurately track their dynamics and a critical assessment of recent advances in MBH evolution modelling.

As a first step, a novel sub-resolution prescription for dynamical friction, based on the first-order diffusion coefficient of the Fokker-Planck equation, is developed and implemented. The performance of this physically based, novel method is compared to commonly adopted techniques, such as the boosting of the BH gravitational mass and continuously repositioning the BH on the local potential minimum, across different environments: a galaxy group, a galaxy cluster and a cosmological box. This novel approach is shown to significantly improve the description of MBH orbits, reduce the population of spurious wandering MBHs, and yield a more realistic description of orbital decay and BH-BH mergers.

To further assess the capabilities of the proposed dynamical friction correction, controlled simulations of a MBH infalling into a dark matter halo, optionally including a central stellar bulge, are presented. This setup enables a direct validation of the simulated sinking timescales and analytical predictions from the OTIS code, an open-source Python library introduced for this purpose. Simulations incorporating the dynamical friction correction converge toward the analytical expectations across different resolution levels, thereby confirming the robustness and reliability of the proposed approach.

Building on these results, as a second step this thesis systematically explores the impact of dif-

ferent sub-resolution prescriptions for MBH accretion and feedback. To this purpose, a number of simulations of a galaxy group are carried out, by varying the numerical description that regulates cold gas availability and the efficiency of AGN feedback. Such extensive test simulations demonstrate how seemingly minor modeling choices can lead to substantial differences in MBH growth histories, thermodynamical properties of the intra-group plasma, and star formation activity of the brightest group galaxy.

These results provide the foundation for the realization and analysis of an extended set of zoom-in simulations of galaxy clusters and groups, carried out at high resolution: about 300 clusters and groups, each set including systems with masses in the range $(0.15-40)\times10^{14}\,M_{\odot}$. A distinguishing feature of this suite of simulations is the sampling of the parameter space describing the feeding of MBHs and the effect of the ensuing feedback on the surrounding gas. In addition to zoom-in initial conditions, we also carried out simulations of a 49 Mpc cosmological box, which provide a more typical "field" environment where the MBH-galaxy coevolution can be studied.

The results presented in this thesis highlight the central role of cold gas in shaping MBH demographics. In fact, at $z > 2$, cold gas-driven accretion fuels an extended phase of rapid MBH growth, leading to an overabundance of high-mass ($> 10^8\,M_{\odot}$) BHs at lower redshifts. At $z < 2$, the dynamical activity of galaxy clusters triggers episodic accretion driven by infalling cold gas clumps, ultimately producing overmassive BHs by $z = 0$.

This thesis makes two principal contributions. Firstly, it proposes a novel and robust model to describe the effect of dynamical friction on MBH dynamics, demonstrating its effectiveness across a variety of tests and environments. Secondly, it assesses the strengths and limitations of the currently adopted models in OpenGADGET3 in shaping MBH evolution. This highlights the need for more refined prescriptions which include the effect of AGN kinetic feedback, turbulence-driven gas accretion onto MBHs, and radiative efficiency depending on MBH properties (e.g. spin) and on the local characteristics of the surrounding gas.

Contents

Abstract 3

List of Abbreviations 9

Publication list 11

1 Introduction 13

I Observational background 19

2 The role of Massive Black Holes in our Universe 21

2.1 Multi-wavelength signatures of Active Galactic Nuclei . . . 21

2.1.1 Radio . . . 22

2.1.2 Submillimeter and Infrared . . . 23

2.1.3 Optical . . . 24

2.1.4 X-ray . . . 24

2.2 MBH–Galaxy Co-evolution: Scaling Relations . . . 25

2.2.1 $M_{\rm BH}$ versus galaxy properties . . . 25

2.2.2 The fundamental plane . . . 31

2.3 Demography of MBHs . . . 31

2.3.1 The Soltan argument . . . 32

2.3.2 The continuity equation . . . 34

3 MBHs and AGN in galaxy clusters 37

3.0.1 The overcooling problem . . . 37

3.1 AGN feeding and feedback cycle . . . 38

3.1.1 Feeding . . . 40

3.1.2 Feedback . . . 40

3.2 The ICM diversity: CC/NCC clusters . . . 43

3.2.1 Classification of CC/NCC . . . 44

3.2.2 Dynamical evolution of CC clusters . . . 44

4 Dynamical evolution of MBHs 47

4.1 From galaxy mergers to the parsec scale . . . 48

4.1.1 Introduction to the dynamical friction force . . . 48

4.1.2 Observational evidence for dual AGN . . . 54
4.2 From parsec scale to the BH coalescence . . . 57
4.2.1 Theoretical predictions . . . 58
4.2.2 Observational implications for binary MBHs . . . 61
4.3 Off-center AGN: predictions and observations . . . 63
4.4 Conclusions . . . 64

II Methodology 67

5 Numerical methods for cosmological simulations 69
5.1 Collisionless dynamics . . . 70
5.1.1 Direct N-body method . . . 73
5.1.2 The PM method . . . 76
5.1.3 Tree method . . . 78
5.1.4 Hybrid TreePM method . . . 79
5.2 Hydrodynamics . . . 79
5.2.1 Smoothed Particle Hydrodynamics . . . 80
5.3 Sub-resolution models for cooling and star formation . . . 83
5.3.1 Radiative cooling . . . 84
5.3.2 Star formation . . . 85
5.4 Sub-resolution prescriptions for BH evolution and AGN feedback . . . 89
5.4.1 Seeding . . . 91
5.4.2 Gas accretion . . . 92
5.4.3 Mergers . . . 93
5.4.4 Feedback . . . 95
5.5 Summary . . . 95

6 A new model for dynamical friction in OpenGADGET3 97
6.1 Numerical approaches to follow for BH dynamics . . . 98
6.1.1 Repositioning . . . 98
6.1.2 Boosted dynamical mass . . . 100
6.2 Sub-resolution models for DF . . . 101
6.2.1 A novel implementation for DF in OpenGADGET3 . . . 101
6.2.2 The model of Damiano et al. (2024) . . . 102
6.2.3 Comparison with other models . . . 104

III Results 107

7 Unresolved dynamical friction and MBH evolution: results from cosmological simulations 109
7.1 Set of simulations . . . 109
7.2 Statistical analysis of the BH population . . . 111
7.2.1 Centring the BHs within host galaxies . . . 111

7.2.2 The population of spurious wandering BHs . . . 112
7.2.3 Merger events and multiple BH systems . . . 117
7.2.4 The M_*–M_{BH} relation . . . 120
7.3 Analysis of individual events . . . 123
7.3.1 Event 1 . . . 127
7.3.2 Event 2 . . . 129
7.3.3 Event 3 . . . 129
7.3.4 The effect of the merging conditions . . . 130
7.4 Conclusions . . . 133

8 DF and MBH orbits: analytical predictions and numerical solutions 137
8.1 Analytical framework . . . 138
8.1.1 Infalling BH on a circular orbit in an NFW halo . . . 138
8.1.2 Elliptical orbits . . . 140
8.1.3 Adding a stellar bulge . . . 141
8.1.4 Numerical integration: the Orbital TImescale for Sinking library . . . 141
8.2 Numerical simulations . . . 144
8.2.1 Numerical DF correction . . . 144
8.2.2 Simulations set up . . . 146
8.2.3 List of simulations . . . 146
8.3 Results . . . 149
8.3.1 Infalling BH in a DM halo . . . 149
8.3.2 Infalling BH in a composite DM and stellar bulge system . . . 154
8.4 Discussion . . . 161
8.5 Conclusions . . . 163

9 Techniques for AGN feeding and feedback in OpenGADGET3 165
9.1 The set of simulations . . . 165
9.2 Results . . . 167
9.2.1 The BH lifecycle . . . 167
9.2.2 Accretion . . . 168
9.2.3 Feedback . . . 172
9.3 Summary and conclusions . . . 175

10 The Dianoga galaxy clusters: MBH demography and evolution 177
10.1 Set of simulations . . . 178
10.2 The $M_{BH} - M_*$ relation at $z = 0$ . . . 182
10.2.1 Results for M1 and M2 models . . . 182
10.2.2 The origin of the overmassive BHs . . . 184
10.2.3 The $M_{BH} - M_*$ relation for different models . . . 187
10.3 Mass and luminosity functions of BHs . . . 188
10.3.1 The BH luminosity function . . . 188
10.3.2 The BH mass function . . . 191

10.4 Multi-BH systems . . . 194
10.5 Conclusions . . . 199

11 Conclusions **201**
11.1 Summary of the results . . . 202
11.1.1 Chapter 7 . . . 202
11.1.2 Chapter 8 . . . 202
11.1.3 Chapter 10 . . . 203
11.2 Future Prospects . . . 204
11.2.1 Improving the dynamical evolution of MBHs . . . 204
11.2.2 Toward an improved modelling of BH feeding and feedback cycle . . . 205

Appendices **209**

A Simulation parameters **211**

B On the phase-space distribution function surrounding the BHs **213**

C OTIS optimization **217**

D Infalling of a BH on an orbit with initial eccentricity **221**

E The evolution of the BHLF: impact of the evaporation model **223**

Bibliography **291**

List of Abbreviations

GR	General Relativity
BH	Black Hole
MBH	Massive Black Hole
SMBH	Supermassive Black Hole
AGN	Active Galactic Nucleus
BCG	Brightest Cluster Galaxy
JWST	James Webb Space Telescope
ΛCDM	Λ Cold Dark Matter
DM	Dark Matter
BLR	Broad Line Region
NLR	Narrow Line Region
FWHM	Full Width Half Maximum
IR	Infrared
NIR	Near-Infrared
MIR	Mid-Infrared
UV	Ultraviolet
SF	Star Formation
BHLF	Black Hole Luminosity Function
BHMF	Black Hole Mass Function
XLF	X-ray Luminosity Function
SZE	Sunyaev–Zeldovich Effect
CC	Cool Core
NCC	Non-Cool Core
SFR	Star Formation Rate
DF	Dynamical Friction
GW	Gravitational Wave
IFS	Integral Field Spectroscopy
ULIRG	Ultra-Luminous Infrared Galaxy
LIRG	Luminous Infrared Galaxy
PTA	Pulsar Timing Array
NFW	Navarro Frank White
PP	Particle-Particle
PM	Particle Mesh
FFT	Fast Fourier Transform
SPH	Smoothed Particle Hydrodynamics

SN	Supernovae
ISM	Interstellar Medium
IMF	Initial Mass Function
SSP	Single Stellar Population
PBH	Primordial Black Hole
PDF	Probability Density Function
WBH	Wandering Black Hole
BGG	Brightest Group Galaxy
IC	Initial Conditions

Publication list

The work presented in this dissertation is based on the following papers submitted and published in refereed journals and two papers in preparation:

- **Damiano Alice**, Valentini Milena, Borgani Stefano, Tornatore Luca, Murante Giuseppe, Ragagnin Antonio, Ragone-Figueroa Cinthia, Dolag Klaus, *Dynamical friction and the evolution of black holes in cosmological simulations: A new implementation in OpenGADGET3*, 2024, A&A, Volume 692, A81

- **Damiano Alice**, Borgani Stefano , Valentini Milena, Murante Giuseppe, Tornatore Luca, Strakos Petr, Jaros Milan, *"Dynamical friction and massive black hole orbits: Analytical predictions and numerical solutions"*, 2025, A&A, Volume 704, A83

- **Damiano Alice**, Borgani Stefano , Murante Giuseppe, Valentini Milena, Tornatore Luca, Strakos Petr, Jaros Milan, *"Numerical solutions for black hole feeding and feedback in cosmological simulations with OpenGADGET3"*, submitted to Astronomy and Computing, under review.

- **Damiano Alice**, Borgani Stefano, Esposito Michela, Rasia Elena, Marini Ilaria, Murante Giuseppe, Valentini Milena, Biffi Veronica, *"The DIANOGA galaxy clusters: Massive Black Holes demography and evolution"*, in preparation.

- Borgani Stefano, **Damiano Alice**, Esposito Michela, Marini Ilaria, Rasia Elena, Valentini Milena, Dolag Klaus, Murante Giuseppe, Biffi Veronica, *DIANOGA simulations of galaxy clusters: properties of the baryonic components*, in preparation.

Chapter 1

Introduction

Early after the formulation of Einstein's General Relativity (GR), exact solutions to the field equations revealed the theoretical possibility of objects whose gravity is so extreme that nothing – not even light – can escape. The first of these solutions was derived by Karl Schwarzschild (Schwarzschild, 1916), who obtained an exact vacuum solution describing the space-time geometry surrounding a non-rotating, spherically symmetric mass. This solution predicts the existence of a characteristic radius, now known as the Schwarzschild radius, defining a boundary at which the escape velocity reaches the speed of light. This boundary marks the event horizon of an object whose emitted radiation cannot reach an external observer, giving rise to the concept of a black hole (BH). Subsequently, the Reissner–Nordström solution of the GR field equations (Reissner, 1916) generalized Schwarzschild's result to include electric charge, while lately the Kerr solution (Kerr, 1963) described the spacetime structure outside a rotating BH. Together, these solutions established the theoretical foundations for BHs as compact objects fully characterized – within classical GR – by mass, charge, and spin, confined by an event horizon hiding a spacetime singularity in its center.

In the early 1960s, the discovery of powerful radio sources and, shortly thereafter, of quasi-stellar objects (the so-called quasars) marked a turning point in the astrophysical interest in BHs. Objects such as 3C48 and 3C273 displayed stellar-like morphologies while exhibiting extreme redshifts, rapid variability, and extraordinary bolometric luminosities, reaching $L_{\rm bol} = 10^{46}\,{\rm erg\,s^{-1}}$ (Schmidt, 1963a; Ulrich, 1981; Matthews and Sandage, 1963; Schmidt, 1963b; Sandage, 1964; Greenstein and Matthews, 1963). These properties could not be reconciled with stellar emission but implied energy production within a compact region. Accretion onto a central, massive compact object – with typical masses $\sim 10^8\,M_\odot$ – emerged as the most likely viable physical mechanism capable of release such extreme power output (e.g. Blandford and Rees, 1978; Begelman et al., 1984). These observations provided the first compelling astrophysical evidence for the existence of massive BHs (MBHs), transforming them from merely theoretical predictions into central actors in the study of many sectors of physics, from galaxy evolution to high-energy astrophysics. Over the subsequent decades, MBHs have emerged as fundamental components of galaxy formation and evolution.

Observations have revealed imprints of BH activity and tight empirical correlations between BH mass and host galaxy properties–such as stellar velocity dispersion, bulge luminosity, and stellar mass (Kormendy and Richstone, 1992; Magorrian et al., 1998; Ferrarese and Merritt, 2000)–

suggesting that the growth of MBHs and of their host galaxies is deeply interconnected. These relations hold across a wide range of galaxy types and masses, implying that MBHs are not merely passive tracers but active characters of galaxy evolution. The physical mechanism mediating this connection is widely attributed to the energetic output produced by mass accretion onto MBHs, observed in the Active Galactic Nuclei (AGN), the so-called AGN feedback. AGN are among the most luminous and compact sources in the Universe, shedding light across the entire electromagnetic spectrum.

One of the most impressive manifestations of AGN feedback occurs in galaxy clusters, the largest gravitationally bound systems in the Universe. Energetic activity in the brightest central galaxy (BCG) can inflate vast radio-emitting bubbles that carve cavities in the surrounding X-ray–bright Intra-Cluster medium (ICM; Gitti et al. 2012; McNamara and Nulsen 2007, 2012). Through this interaction, energy is redistributed over hundreds of kiloparsecs, profoundly shaping the thermodynamical state and long-term evolution of the cluster environment. Recently, the interest on BHs has further intensified with the advent of gravitational-wave astronomy. The LIGO–Virgo–KAGRA collaboration (Abbott et al., 2018; Kagra Collaboration et al., 2019) has detected compact-object mergers with masses up to hundreds of solar masses, while the Pulsar Timing Array has reported evidence for a stochastic gravitational-wave background, possibly originating from a population of merging supermassive BH binaries (Antoniadis et al., 2023). Looking ahead, the LISA mission (Amaro-Seoane et al., 2023; Colpi et al., 2024) will directly probe the inspiral and coalescence of MBHs in the cosmic dawn, out to $z \sim 6$. These future observations would open an entirely new window onto the dynamical evolution of BHs, directly linking their growth and interactions to hierarchical structure formation.

In fact, within the standard ΛCold Dark Matter (ΛCDM) cosmological paradigm, structure formation proceeds hierarchically through mergers of dark matter (DM) haloes and their embedded galaxies. As galaxies merge, their central MBHs are brought together. Initially, dynamical friction exerted by the surrounding matter drives the MBHs toward the center of the galaxy merger remnant. At smaller separations, additional interactions with stars and gas extract angular momentum, eventually bringing the system to the milliparsec scales, where gravitational-wave emission dominates and leads to final coalescence. At the same time, recent observations from ALMA and the James Webb Space Telescope (JWST) are revealing massive galaxies and rapidly growing BHs already in place within the first billion years of cosmic history (e.g. Hodge et al., 2019; Santini et al., 2019; Carilli et al., 2008; Pavesi et al., 2016; Maiolino et al., 2015; Adamo et al., 2025; Roberts-Borsani et al., 2016; Carnall et al., 2024; Jeon and Bromm, 2019). These discoveries challenge current theoretical models and underscore the need for a robust, physically grounded description of MBH formation, growth, and dynamics (e.g. Volonteri et al., 2023; Silk et al., 2024).

Driven by advances in both hardware and software architectures, modern theoretical astrophysics resorts to detailed numerical methods to meet the challenges posed by observations. In this context, cosmological hydrodynamical simulations provide a powerful numerical laboratory to investigate the nonlinear evolution of DM, gas, stars, and BHs across cosmic times (e.g. Kravtsov and Borgani, 2012; Dolag et al., 2008; Vogelsberger et al., 2020; Springel, 2010; Teyssier, 2025;

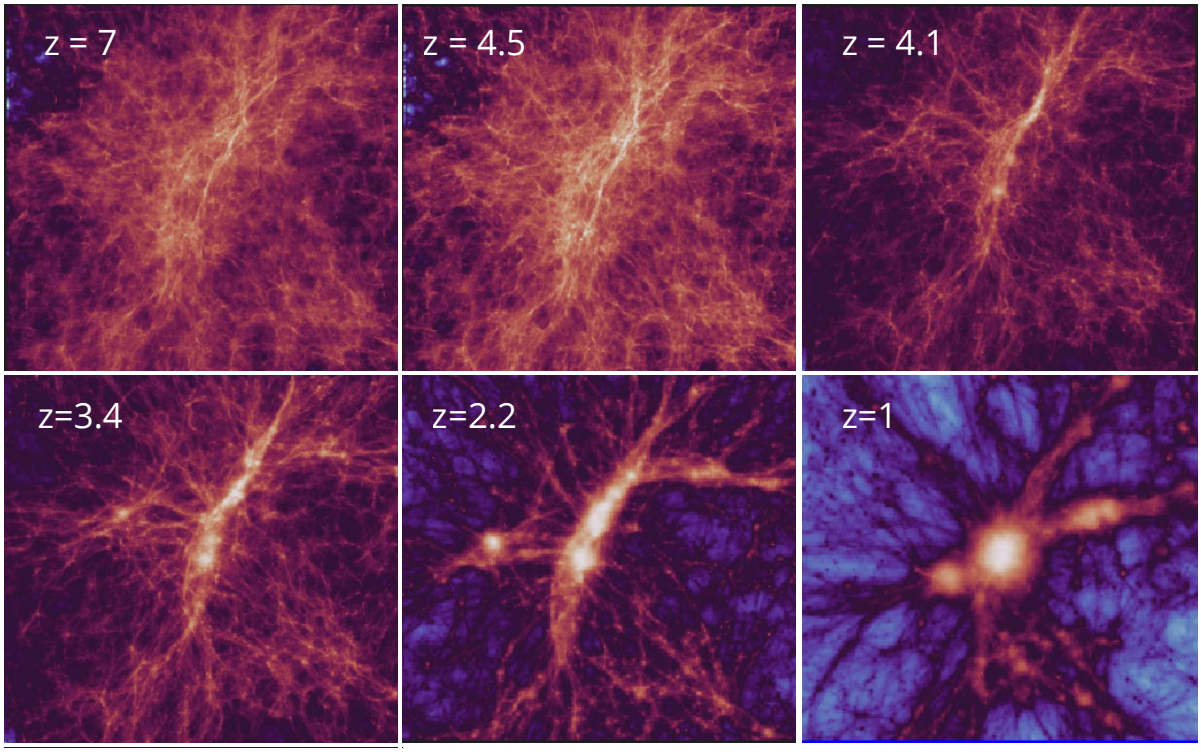

Figure 1.1: *Formation of a galaxy cluster in the* DIANOGA *cosmological simulations. The panels show projected surface density maps of gas within a* 25 Mpc *region centered on the main halo, illustrating its assembly from redshift* $z = 7$ *to* $z = 1$.

Feldmann and Bieri, 2025; Valentini and Dolag, 2025).

Within the context of cosmological hydrodynamical simulations, the fluids describing DM, stars and gas are discretized by resolution elements – either particles or mesh. The evolution of the fluid emerges from the collective behavior of these elements and the motion of single tracers has little physical meaning. This coarse-grained representation is well suited to describe the large-scale evolution of the system, but it introduces a mass and spatial threshold below which many physical processes governing galaxy evolution cannot be captured. Star formation, for instance, is regulated by cooling, turbulence, and feedback processes operating within dense molecular clouds on parsec and sub-parsec scales, yet it ultimately contributes in shaping the global baryonic content and structural evolution of galaxies. Similarly, BH accretion originates in the sub-parsec scale region around the BH, but the ensuing AGN feedback can influence the surrounding interstellar, circumgalactic, and even intergalactic and intracluster media over scales of hundreds of kiloparsecs. Capturing the combined effect of these multi-scale phenomena is unfeasible with current computational architectures and therefore requires sub-resolution prescriptions capable of embedding small-scale physics into large-scale cosmological environments. Addressing these limitations constitutes the first central goal of this Thesis, which tackles several aspects of sub-resolution modeling in the BH sector of cosmological simulations.

In the first place, the goal is to recover an improved description of the BH dynamics in the presence of finite numerical resolution. The coarse-grained *fluid* representation of gas and DM components, in fact, does not hold for BHs, which are introduced as single particles, and are

therefore intrinsically different in nature from the surrounding resolution elements. Stars, while discrete objects in reality, are far more numerous and are modeled as simple stellar populations rather than as individually resolved entities.

This discrepancy poses significant challenges for accurately tracking the BH motion.

Limited resolution not only hindes an accurate reconstruction of the gravitational interactions below the spatial resolution scale, but also imply that the surrounding particles can be significantly more massive than the physical constituents with which a BH would realistically interact. The primary consequence is that the dynamical friction force is in general poorly described. This intrinsic limitation of N-body gravity solvers in cosmological simulations was recognized early by Di Matteo et al. (2008); Springel et al. (2005), and various numerical techniques were introduced to mitigate spurious dynamical effects – sometimes severe enough to cause BHs to drift away from the centers of their host galaxies. In line with recent efforts to improve the modeling of massive BH dynamics (Hirschmann et al., 2014; Tremmel et al., 2015; Pfister et al., 2019; Chen et al., 2022; Ma et al., 2023; Genina et al., 2024), this Thesis proposes a novel sub-resolution model to account for unresolved dynamical friction, based on the inclusion of a corrective term within the N-body code OpenGADGET3 (Dolag et al., in preparation). A key objective of this Thesis is to provide a comprehensive assessment of the impact of this new model across different environments and resolution regimes. This includes a systematic comparison with previously adopted prescriptions – to evaluate whether and under which conditions the new model represents an improvement – as well as detailed tests against analytical predictions in controlled and idealized setups.

After evaluating the performance of the novel dynamical friction model, it is applied to pursue the second main objective of this Thesis: the investigation of how different sub-resolution prescriptions affect accretion and feedback in OpenGADGET3. The analysis presented in this work explores variations in the prescriptions regulating the amount of cold gas available for BH accretion and feedback, the spatial region over which AGN feedback energy is deposited, and the numerical treatment of gas accretion in the vicinity of BH particles. These effects are first studied through multiple re-simulations of a galaxy group, isolating the impact of each variation. The study is then extended to the full sample of zoom-in initial conditions of the Dianoga galaxy cluster simulations (Bonafede et al., 2011; Bassini et al., 2020; Esposito et al., 2025). The Dianoga simulation suite consists of a set of 28 galaxy cluster simulations based on *zoom-in* initial conditions, which provide increased resolution in a selected overdense region that later evolve into a galaxy cluster at $z = 0$. Figure 1.1 shows projected gas surface density maps illustrating the formation of one of the 28 clusters in the suite, from $z = 7$ (upper left) to $z = 1$ (lower right). A distinctive feature of the most recent set of simulations (Borgani et al., in prep.), presented here for the first time, is the availability of multiple realizations of subsets of the full simulation suite, obtained by varying the parameters that regulate the properties and availability of the gas reservoir governing the BH lifecycle. Within the scope of this Thesis, the resulting BH population is analysed to assess how different sub-resolution prescriptions influence the BH demography. In this context, the Thesis is structured in a *cyclic* manner. It begins by discussing the role of massive BHs based on observations and semi-empirical models, with particular attention to galaxy cluster environments. Then, it presents novel theoretical and numerical methods developed to improve the modeling of BH dynamics and growth. Finally, these methods are applied in cosmological

simulations to study BH populations as tracers of galaxy formation and large-scale structure evolution, allowing a direct comparison with the observational framework introduced in the opening chapters.

The Thesis is structured into three main parts. Chapters 2–4 provide the scientific motivation and theoretical background; Chapters 5 and 6 focus on methodology; Chapters 7–10 present the core results. More specifically, the content of the Thesis can be summarised as follows:

- **Chapter 2** presents an overview of the current understanding of the role of massive BHs in the Universe. It begins by outlining the primary observational signatures of AGN, highlighting their importance as powerful tracers of BH activity. This chapter also outlines key scaling relations between properties of the MBH population and of their host galaxies that suggest a co-evolution scenario. Finally, the chapter reviews foundational studies on semi-empirical modelling of massive BH demography across cosmic times.

- **Chapter 3** explores the impact of AGN in galaxy cluster environment, focusing on the interplay between AGN feeding and feedback in governing the thermodynamical properties of the ICM together with the dynamical evolution of the cluster.

- **Chapter 4** presents the theoretical understanding and observational constraints on the dynamical evolution of massive BHs. This chapter also offers a detailed derivation of the dynamical friction formula arising in collisional astrophysical systems.

- **Chapter 5** introduces the numerical framework of the simulations adopted in this Thesis, focusing in particular on the modelling of the collisionless dynamics, which govern the evolution of stars and BHs. The sub-resolution prescriptions for star formation, stellar evolution, BH seeding, feeding and feedback adopted in the simulations presented in the Thesis are here described.

- **Chapter 6** discusses the numerical treatment of BH dynamics in cosmological simulations. After critically assessing the strengths and limitations of different ad–hoc techniques usually adopted in the literature to account for unresolved dynamical friction, it introduces the novel dynamical friction-driven corrective approach developed in this Thesis.

- **Chapter 7** presents the performance of the proposed dynamical friction correction against standard numerical schemes in cosmological hydrodynamical simulations performed with the OpenGADGET3 code, adopted throughout the Thesis. Different environments are considered – including a galaxy cluster, a galaxy group, and a cosmological box – to assess the performance of the novel method in limiting any numerical-induced displacements from the center of the host galaxies, and in following their dynamical evolution during galaxy mergers.

- **Chapter 8** presents controlled numerical experiments designed to isolate the orbital decay of BHs in the idealized conditions in which a BH inspirals in an isolated, spherically symmetric and smooth DM halo. In these idealized setups, numerical results can be directly compared with analytical predictions, allowing a quantitative assessment of how the

inclusion of dynamical friction alters sinking timescales and assesses the reliability of the model.

- **Chapter 9** is dedicated to a detailed assessment of BH feeding and feedback models in OpenGADGET3, highlighting the role of sub-resolution descriptions and calibration parameters. By comparing multiple simulations of the same galaxy group with slightly different prescriptions, the chapter performs a systematic exploration of the sensitivity of BH – and surrounding Intra-group medium – evolution to sub-resolution modelling choices.

- **Chapter 10** presents the first results from the Dianoga suite of galaxy cluster simulations. After introducing the whole simulation set and the different models adopted for specific subset re-simulations, the Chapter analyses the properties of the emerging BH population in the local Universe. Extending the framework presented in the previous Chapter, it quantifies how different sub-resolution models shape the properties of the ICM and that of the BH populations. The improved treatment of dynamical friction further allows one to carry out a preliminary analysis of BH spatial distributions and multi–BH systems.

- **Chapter 11** summarises the main findings of the Thesis and outlines future perspectives.

Throughout the manuscript, topics that are not central to the focus of the Thesis but require deeper discussion are presented in dedicated Boxes.

Part I

Observational background

Chapter 2

The role of Massive Black Holes in our Universe

In the local Universe, the majority of the total BH mass is locked in MBHs (with mass $M_{\rm BH} > 10^6\,{\rm M}_\odot$) residing at the centers of massive galaxies. Although their existence is supported by a wealth of both theoretical and observational studies, their origins and evolutionary paths continue to reveal new and often unexpected features. This complexity arises largely from the diversity in their formation and growth histories, which challenges the development of a universal model. The vast majority of those BHs live in a *dormant* phase, but fewer than 1% (King 2003) show luminous emission across multiple wavelengths, revealing the presence of an AGN. Observations of AGN provide strong evidence for the existence of MBHs in the Universe. Moreover, the MBHs we observe today are thought to be the outcome of past episodes of rapid accretion and, importantly, their growth appears to be tightly connected to the formation and evolutionary history of their host galaxies. This chapter overviews the observational evidence for the existence and properties of MBHs. Section 2.1 introduces the main observational signatures of AGN across the electromagnetic spectrum. Section 2.2 discusses the correlations between MBH properties, their luminosity, and the correlation with the characteristics of their host galaxies. Finally, Section 2.3 presents observationally driven models for the demography and evolution of MBHs.

2.1 Multi-wavelength signatures of Active Galactic Nuclei

In what follows, we define an AGN as a system in which a significant fraction of the energy output originates not from galactic components—such as stars, dust, or interstellar gas—but from accretion processes occurring in the immediate vicinity of the galactic nucleus. AGN feature a bolometric luminosity reaching $L_{\rm bol} > 10^{45}\,{\rm erg\,s^{-1}}$ that outshines the galaxy host, and their emission is panchromatic, covering the full range of the electromagnetic spectrum. According to the unification scheme (Antonucci, 1993; Urry and Padovani, 1995), AGN share the same underlying structure, while their observed differences arise primarily from the orientation of the line of sight. Before discussing the characteristics of AGN across different wavelength ranges, it is useful to first present a schematic view of the AGN structure, shown in Fig. 2.1 [1].

[1] Figure created with Canva.

The innermost region of the AGN in the immediate vicinity of the central BH, on sub-parsec scales, hosts the accretion disk, which can be either optically thin or thick. Optically thick disks are radiatively efficient, while optically thin disks are radiatively inefficient, with energy primarily carried inward by advection of the gas flow. At parsec scales, a dust-free region composed of rapidly rotating gas clouds, the broad-line region (BLR), features Doppler-broadened spectral lines. A dust-rich axisymmetric region, the dusty torus, encloses the accretion disk and the BLR and extends up to tens of parsecs. Along the polar openings of the torus, ionization cones emerge, characterized by low-density, ionized gas that can extend from hundreds to thousands of parsecs, the narrow line region (NLR).

Figure 2.1: *Schematic representation of the AGN model.*

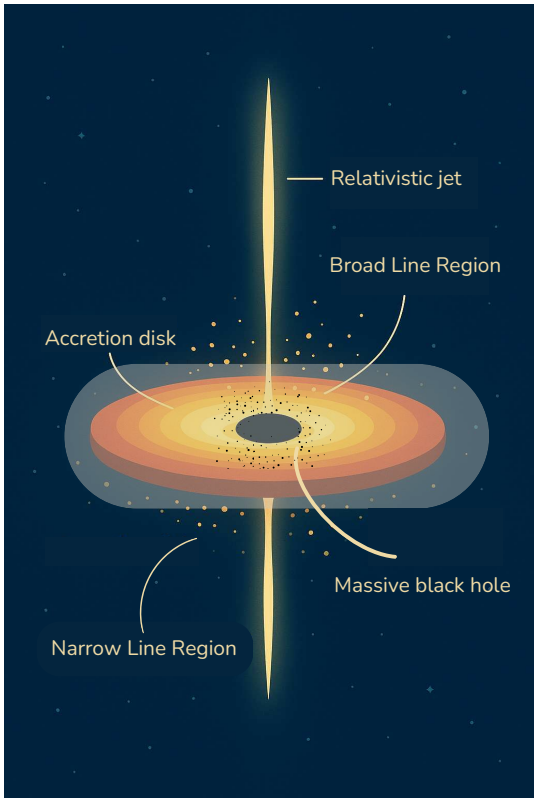

In many AGN, relativistic outflows known as radio jets are observed, with collimated structures extending from the central regions out to hundreds of parsecs or more. In the following section, we will describe how each of these components contributes to the AGN emission across different wavelengths.

According to the unification scheme, when the relativistic jet (or the symmetry axis of the accretion disk) is oriented within $\sim 45°$ of the observer's line of sight, the inner regions are directly visible. In this case, broad emission lines (with FWHM $\gtrsim 10^3\,\mathrm{km\,s^{-1}}$) produced in the BLR can be detected. At larger inclination angles, the dusty torus obscures the BLR and accretion disk, preventing direct observation of the broad lines. Instead, only narrow emission lines from the more extended NLR are seen. This orientation-driven dichotomy accounts for the classification of AGN into Type 1 (broad- and narrow-line emission visible) and Type 2 (only narrow-line emission visible).

The emission from AGN spans the entire electromagnetic spectrum, from low-frequency radio waves to hard X-rays and γ-rays, reflecting the interplay between accretion physics, relativistic jets, reprocessing structures, and the host galaxy environment. In the following, a brief overview of the emission properties across the radio, submillimeter, infrared, optical, and X-ray wavelength ranges will be provided.

2.1.1 Radio

In the late 1970s, Blandford and Rees (1978) proposed that a continuously replenished central energy source, operating over timescales of 10^6–10^7 years and producing a power output of $\sim 10^{46}$ erg s^{-1}, could explain the observed radio lobes (the "hot spots"; Hargrave and Ryle 1974) and collimated jets detected in sources such as M87 and 3C273 (Turland, 1975; Rees, 1978). This framework established the modern view that radio emission originates from synchrotron

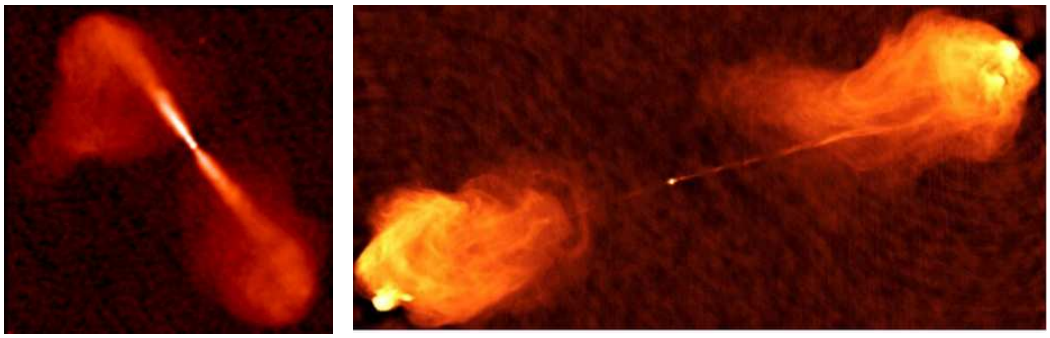

Figure 2.2: *Prototypical examples of FRI and FRII sources.* Left*: VLA 1.45 GHz image of 3C296, from Leahy and Perley (1991).* Right*: VLA 5GHz image of CygnusA from Perley et al. (1984).*

radiation, produced by ultrarelativistic electrons spiraling in strong magnetic fields. A central, spinning, and stable MBH can act as a gyroscopic anchor, stabilizing the magnetic fields that collimate and sustain relativistic jets. Today, a wide diversity of radio-loud and radio-quiet AGN has been identified. Radio-loud AGN, defined by a radio (5 GHz)-to-optical (B band) flux ratio $F_R/F_B > 10$ (Kellermann et al., 1989; Urry and Padovani, 1995), exhibit powerful extended jets that often extend far beyond the host galaxy. They are broadly categorized into Fanaroff–Riley type I (FRI) and type II (FRII) sources, characterized by symmetric but fading jets, versus high-luminosity collimated jets terminating in bright radio "bubbles" (Fanaroff and Riley, 1974). Figure 2.2 shows two classical examples of FRI (left) and FRII (right) sources. Radio-loud AGN predominantly emit non-thermal radiation, in contrast to their radio-quiet counterparts, and they often trace regions of large-scale matter overdensities, serving as valuable probes of proto-cluster environments at high redshift (Pentericci et al., 2000; Miley and De Breuck, 2008; Uchiyama et al., 2022).

2.1.2 Submillimeter and Infrared

The dusty torus reprocesses the emission of the accretion disk, absorbing ultraviolet (UV) photons from the central engine and reradiating them in the infrared (IR), with the emission typically peaking at near-IR (NIR) and mid-IR (MIR) wavelengths around $1-35$ μm (Sanders et al. 1989). Therefore, the IR and submillimeter emissions provide information about the thickness, the shape, and the dust distribution within the parsec scale surrounding the BH. The spectral decomposition suggests that the MIR component corresponds to the emission from the torus, whereas the NIR peak is associated with hot dust in the inner NLR, although several studies revealed a consistent (more than $\sim 50\%$ of the total emission) MIR polar-extended component over a few parsecs (e.g., Asmus et al. 2016; López-Gonzaga et al. 2016; Lopez-Rodriguez et al. 2025) at least in a fraction of nearby AGN. The exact distribution of dust in the torus is still a matter of debate, whether it composes a diffuse medium (Krolik and Begelman 1988; Efstathiou et al. 2013, 2022; Tristram et al. 2007), clumpy optically thick clouds (Nenkova et al. 2008; Hönig and Kishimoto 2010) or a combination of the two (Assef et al. 2013; Reyes-Amador et al. 2025). Dust emission from star formation (SF) can rival in luminosity the AGN but with typically much

cooler temperatures, reaching $T \sim 40$K. Significant SF activity is commonly present in the host galaxies of many AGN, and it often dominates the far-infrared (FIR) emission (Hatziminaoglou et al. 2010). Indeed, progress in the sub-mm and IR regime has historically been slowed by atmospheric obscuration and by contamination from both galactic (e.g., young stellar object) and extragalactic sources (e.g., star-forming galaxies and massive galaxies at high redshift; Donley et al. 2007).

The field has been revolutionized by the advent of ALMA, whose high-resolution (reaching up to 0.03" spatial resolution at wavelengths $\lambda \sim 450$ μm, Pasetto et al. 2019) submillimeter observations provide crucial insights into the morphology, column density, and dynamics of obscuring material in AGN (e.g., Carilli et al., 2008; Endsley et al., 2023; García-Burillo et al., 2014; Hodge et al., 2019; Jones et al., 2023; Kakkad et al., 2017; Maiolino et al., 2015; Pasetto et al., 2019; Pavesi et al., 2016; Ruffa et al., 2019; Santini et al., 2019; Wang et al., 2013; Stanley et al., 2018).

2.1.3 Optical

The physical mechanism powering the X-ray to optical luminosity of AGN is gas accretion onto the central region. Optical spectroscopy reveals emission lines originating from the BLR and NLR, therefore providing information on the gas distribution up to a few hundred parsecs above and below the dust plane. Although the optical range suffers from stellar contamination—which limits the completeness of optical surveys (e.g., Richards et al. 2002)—and is generally insensitive to obscured sources (e.g., Vignali et al. 2004; but see Bianchi et al. 2012 for a comprehensive review), it nevertheless provides highly informative diagnostics. For instance, spectroscopic information from broad emission lines provides a powerful probe of the innermost, sub-parsec regions around the central engine, where the dynamics are dominated by the gravitational influence of the MBH. This enables estimates of BH masses in AGN, either through direct *reverberation mapping* (see Box 2.1) or via mass-scaling relations calibrated against it (Vestergaard and Peterson 2006).

2.1.4 X-ray

AGN dominate both the source number counts and the integrated background in the X–ray band (Giacconi et al., 2002). The X-ray emission primarily arises from Compton scattering in the hot "corona" located above the accretion disk in the immediate vicinity of the central engine, with possible additional contributions from direct accretion-disk emission at softer X-ray energies (Reynolds 2003; Laurenti et al. 2022; Turner and Miller 2009). In addition, powerful X-ray continuum emission is often associated with relativistic jets (Harris and Krawczynski 2006). The detection and analysis of AGN in the X-ray band presents several advantages, extensively listed in Brandt and Alexander (2015): the X-ray emission is traceable in all AGN sources identified at other wavelengths; X-ray photons have a high penetrative power for hydrogen column densities $N_H = 10^{21} - 10^{24.5}$ that enshroud the vast majority of AGN; the contamination from starlight is relatively poor, since AGN reach much higher X-to-optical flux ratios, thus enhancing the purity of the samples. However, corrections and complementary wavelength observations are needed in the case of heavily Compton-thick absorption-obscured sources, characterized by a column density of neutral hydrogen $N_H \gg 10^{24}$.

2.2 MBH–Galaxy Co-evolution: Scaling Relations

The evolution of MBHs appears to be tightly linked to that of their host galaxies. As such, MBHs play a key role in determining the observational properties of cosmic structures at different scales. This close connection highlights their fundamental role in theories of galaxy formation and evolution and shows that by studying MBHs it is possible to gain insights into the properties of their host galaxies. The relationship is most clearly manifested in the scaling relations observed between BHs and the properties of their host galaxies. However, the physical origin of these relations, as well as the causes of possible deviations, remains not fully understood. In this section, these correlation properties will be discussed.

2.2.1 $M_{\rm BH}$ versus galaxy properties

It has been two decades now that the correlations between BH mass and host galaxy bulge mass, velocity dispersion, or luminosity have been established (Magorrian et al. 1998; Ferrarese and Merritt 2000; Gebhardt et al. 2000; Kormendy and Richstone 1995; Marconi and Hunt 2003; Kormendy and Ho 2013), showing roughly the same intrinsic scatter around 0.3 dex.

The determination of McConnell and Ma (2013) based on early-type galaxies provided with a dynamical determination of BH mass gives:

$$\log_{10}(M_{\rm BH}) = 8.32 + 5.64 \log_{10}\left(\frac{\sigma_*}{200\ \mathrm{km/s}}\right) \tag{2.1}$$

$$\log_{10}(M_{\rm BH}) = 8.46 + 1.05 \log_{10}\left(\frac{M_{\rm bulge}}{10^{11}\ M_\odot}\right). \tag{2.2}$$

where $M_{\rm bulge}$ is the galaxy bulge mass and σ_* is the bulge velocity dispersion. Within the context of this work, Eq. (2.2) will be adopted to calibrate the model parameter for BH physics in the simulations (see Chapter 5). The work by McConnell and Ma (2013) also highlights how different selection effects yield different correlations. For instance, when distinguishing between early- and late-type galaxies, they found the same slope but a different intercept, with the early-type galaxies intercept being a factor of 2 higher than the late-type galaxies at a given σ_*. Similar differences also arise when distinguishing the subsamples according to the inner surface brightness (based on the Sèrsic index, see Sahu et al. 2019) of the galaxy, the presence of an AGN (Bennert et al. 2021), or pseudobulges (Greene et al. 2008).

As for elliptical galaxies, the tightest correlation is found for those galaxies having a Sèrsic photometric profile (Sahu et al. 2019; Savorgnan et al. 2013), which are believed to be the products of *wet* (i.e., gas-rich) mergers (Greene et al. 2008; Trujillo et al. 2004; Kormendy et al. 2009; Ferrarese et al. 2006), triggering periods of sustained merger-driven SF and AGN activity. The ensuing feedback effects on the post-merged galaxy make it possible to couple the growth of the central engine to the host spheroid mass: the feedback process sweeps galaxies clear of gas, quenching both SF and BH growth, ultimately accounting for the relation between BH mass and host galaxy properties (e.g., Zubovas and King 2012). Some galaxy disks exhibit peculiar bulges, namely the pseudobulges, recognizable as cold, rotation-supported disky structures. These objects have been attributed to secular internal evolution of the galaxy disk rather than being

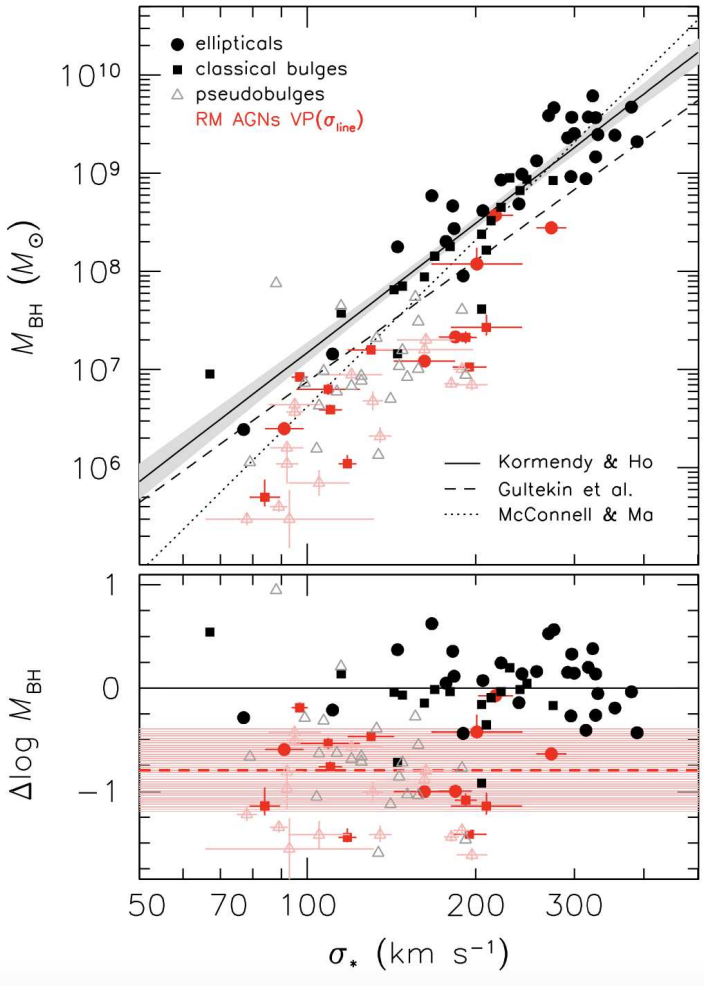

Figure 2.3: *Relation between BH mass ($M_{\rm BH}$) and velocity dispersion of the host galaxy (σ_*) from Ho and Kim (2014). The upper panel shows data from inactive (black) ellipticals (dots), classical bulges (squares), pseudobulges (triangles), and reverberation-mapped AGN (labeled as RM AGN, in red). The solid, dashed, and dotted lines correspond to the relation from Kormendy and Ho (2013); Gültekin et al. (2009); McConnell and Ma (2013), with the shading representing the* 1σ *scatter to the Kormendy and Ho (2013) relation. The bottom panel shows the residuals of the data point to the Kormendy and Ho (2013) fit, with the red shaded area indicating the median and standard deviation obtained from the reverberation-mapped AGN hosted by ellipticals and classical bulges.*

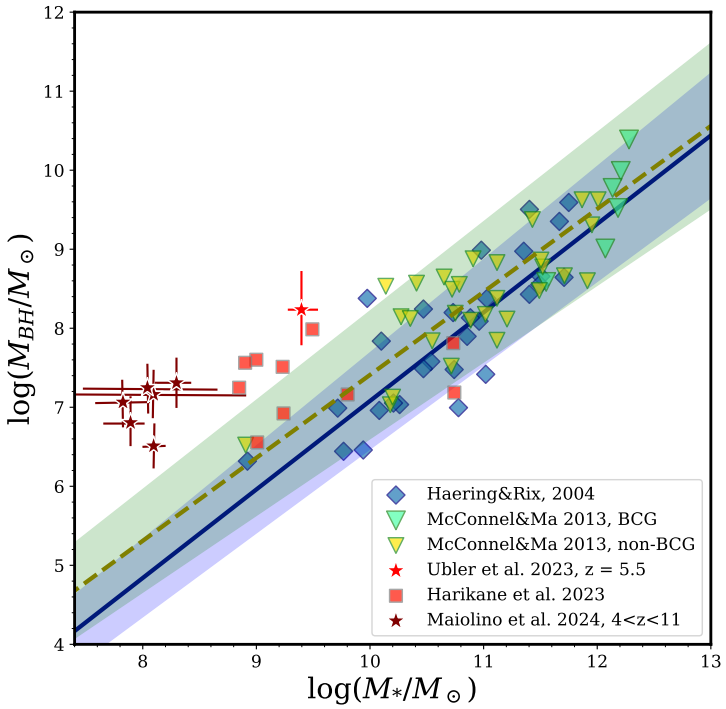

Figure 2.4: *Comparison between the* $M_{\rm BH} - M_{*,\rm bulge}$ *relations obtained by Häring and Rix (2004), McConnell and Ma (2013) and high-z observations from Übler et al. (2023); Harikane et al. (2023); Maiolino et al. (2024). Data from Häring and Rix (2004) are identified with blue squares, with the black solid line representing their best fit and the shaded blue region the standard deviation. Data from McConnell and Ma (2013) are shown in green, with lighter green corresponding to their BCG. The best fit from McConnell and Ma (2013) and the corresponding standard deviation are identified with a dashed grey line and the green shaded area. Red points represent the high-z observations from Maiolino et al. (2024) (dark red stars), Harikane et al. (2023) (squares), and Übler et al. (2023) (light red star).*

Box 2.1: Determination of BH mass

For early-type spheroids or general systems in dynamical equilibrium, dynamical measurements of BH masses rely on resolved stellar kinematics combined with detailed photometric profiles. The BH mass is inferred by modeling the stellar orbits that best match a gravitational potential composed of both the central BH and the stellar mass distribution (Schwarzschild 1979; Bender and Nieto 1990; Cappellari et al. 2002). More advanced techniques involve fitting the full line-of-sight velocity distribution, incorporating contributions from a DM halo and triaxiality (van den Bosch et al. 2008; Vasiliev and Valluri 2020). The spatial resolution achieved by ALMA significantly enhances the reliability of dynamical mass estimates. By resolving the cold molecular gas kinematics on sub-parsec scales, ALMA can probe the cold gas disk motion within the dynamical sphere of influence of a BH (Boizelle et al. 2019) revealing a velocity field is often rotation-dominated, allowing precise modeling of the enclosed mass (Tan et al. 2019; Feruglio et al. 2014; Brusa et al. 2015; Zhang et al. 2025). In weakly or mildly accreting systems, stellar dynamical modelling is generally only applicable to unobscured sources, since dust obscuration affects the AGN spectra making it difficult to recover the stellar kinematics, particularly close to the nucleus. A reliable probe of the innermost region of AGN can be the detection of water emission lines (typical of *masers*) that trace molecular gas in nearly Keplerian circumnuclear disks (see Lo 2005 for a review). The high spatial resolution of the GRAVITY instrument enables BH mass measurements using a spectro-astrometric approach. By tracking the photocenter shift of broad emission lines as a function of velocity, GRAVITY can spatially resolve the rotation of the line-emitting gas on sub-milliarcsecond scales (e.g., Amorim et al. 2021; Winkel et al. 2025), providing a direct measurement of the BLR geometry. Another highly reliable method to estimate the BH mass in Type 1 AGN is *reverberation mapping*. Reverberation mapping exploits the time delay between variability in the ionizing continuum from the accretion disk and the corresponding response of broad emission lines in the BLR. This delay reflects the light-travel time τ, giving a characteristic BLR size $R_{\rm BLR} \approx c\tau$, where c is the speed of light. Combined with the velocity width of the lines, the BH mass can then be inferred via the virial relation: (e.g., Kaspi et al. 2000):

$$M_{\rm BH} = f\frac{r_{\rm BLR}\ \sigma^2_{\rm BLR}}{G} \tag{2.3}$$

where $\sigma_{\rm BLR}, r_{\rm BLR}$ denote the velocity dispersion and spatial extension of the BLR, G is the gravitational constant, and f is the so-called "form factor" and depends on the geometry of the BLR. In the absence of reverberation mapping, the BLR size is typically inferred from scaling relations—either through the empirical correlation between BLR size and AGN luminosity (the so-called "single epoch" method). Both approaches introduce additional uncertainties, due to source-to-source variability and the fact that these relations may not hold universally, particularly at high redshift. Furthermore, the assumptions underlying the virial theorem may break down when significant inflows or outflows of gas are present within $r_{\rm BLR}$ (Richards et al. 2011; Coatman et al. 2018; Fries et al. 2023).

merger-built (Kormendy and Fisher 2008). Pseudobulge galaxies are recognized to be offset in the $M_{\rm BH} - M_{\rm bulge}$ relation when compared to classical bulges (Saglia et al. 2016), so that pseudobulges

hardly correlate with BHs at all, or exhibit significantly lower BH mass at a given bulge mass (Hu 2008; Greene et al. 2008; Kormendy and Bender 2011).
Whether the galaxies hosting an AGN follow the same relations as the quiescent ones is still a matter of debate. AGN have, in general, lower mass-to-light ratios compared to inactive galaxies, showing a significant offset in the $M_{\rm BH}$-$L_{\rm bulge}$ relation (Nelson et al. 2004; Bennert et al. 2021; see also next Section). This might indicate the presence of a young stellar population in the galaxy core (Kim and Ho 2019).

As for the $M_{\rm BH} - M_{\rm bulge}$ and $M_{\rm BH} - \sigma_*$ correlations, the results are not conclusive due to the uncertainties in the determination of both BH mass (often inferred through the single epoch method; see Box 2.1), bulge and velocity dispersions. Caglar et al. (2020); Bennert et al. (2021) find consistent results with the scaling relations holding for inactive galaxies, although previous studies (e.g. Ho and Kim 2014) found a different slope for the $M_{\rm BH} - \sigma_*$ reverberation-mapped AGN. Figure 2.3 shows their results, comparing the $M_{\rm BH} - \sigma_*$ relation for ellipticals, inactive galaxies hosting classical and pseudobulges, and reverberation-mapped AGN (in red, labeled as RM AGN). In the top panel, they also show the relations obtained by Kormendy and Ho (2013); Gültekin et al. (2009); McConnell and Ma (2013) as solid, dashed, and dotted lines, respectively. The bottom panel shows the residuals of the data points with respect to the fit by Kormendy and Ho (2013) for ellipticals and classical bulges. The red dashed line and associated shaded pink band mark the average offset and standard deviation for the reverberation-mapped AGN hosted by ellipticals and classical bulges. Galaxies hosting pseudobulges are visibly offset compared to elliptical and classical bulges, showing lower BH masses, as previously discussed.

Redshift evolution of the scaling relations

The redshift evolution of BH–host galaxy scaling relations has gained renewed importance with the advent of JWST. Earlier studies (e.g., Salviander et al. 2007) found no significant deviation from local scaling relations between BH mass and host bulge mass up to $z \simeq 0.5$, while for $z > 0.5$ the BHs already seem to have masses too high for their bulge hosts compared to the local relation, suggesting a more rapid BH growth at early cosmic times (Merloni et al. 2010).

One important caveat when dealing with high-redshift observations is that morphological decomposition of galaxies is extremely challenging due to limited spatial resolution. As a consequence, several studies have focused on the correlation between BH mass and the *total* stellar mass, rather than the canonical $M_{\rm BH}$–$M_{*,\rm bulge}$ relation. In particular, Reines and Volonteri (2015) and Volonteri and Reines (2016) investigated the relation between BH mass and total stellar mass (see also Bennert et al. 2014 for analyses involving total velocity dispersion on AGN). They found that active galaxies follow a relation distinct from that of early-type galaxies: while the slope is comparable, the normalization is more than an order of magnitude lower. They argued that this offset may arise from both nuclear activity and differences in host galaxy morphology. In the more recent follow-up work, Sturm and Reines (2024) showed that when a bulge-disk decomposition is performed, the $M_{\rm BH}$–$M_{*,\rm bulge}$ relation for active galaxies lies systematically below the canonical scaling relation defined by inactive early-type systems (i.e., Kormendy and Ho 2013). The morphological properties of the galaxies when deriving the scaling relations influence not only the slope and normalization of the local scaling relations, but also their inferred redshift evolution.

Several works (e.g., Woo et al. 2006; Bennert et al. 2011; Treu et al. 2007) reported positive evolution in $M_{\rm BH}$, particularly in samples where high-quality data allow reliable isolation of the bulge or spheroidal stellar component. In contrast, Ding et al. (2020), analyzing *HST* imaging of 32 AGN at $1.2 < z < 1.7$, found only very mild evolution, consistent with no significant redshift dependence. When focusing specifically on the bulge component, they showed that high-z AGN hosts tend to have significantly lower bulge masses, suggesting that BHs at these epochs reside in less massive (or less luminous) spheroids than their local counterparts (see also Park et al. 2015).

Additional studies have reported little to no evolution in the $M_{\rm BH}$–host galaxy relations up to $z \sim 3$ (e.g., Cisternas et al. 2011; Salviander et al. 2015; Suh et al. 2020). Suh et al. (2020) concluded that the apparent non-evolution of the $M_{\rm BH}$–M_* relation may imply that the bulk of BH and stellar mass growth occurred at earlier cosmic times (e.g., $z \sim 3$), such that much of the stellar mass was already in place by that epoch.

Nevertheless, evolution in the $M_{\rm BH}$–$M_{\rm bulge}$ relation remains plausible if bulge growth occurs through internal mass redistribution at later times. Processes such as disk instabilities or AGN-driven positive feedback (e.g., Elbaz et al. 2018) may promote bulge formation, thereby modifying the final BH–spheroid mass ratio without requiring substantial additional BH growth.

As originally pointed out by Volonteri and Reines (2016), these considerations are particularly important in the context of hydrodynamical simulations (see later Chapter 5), being often calibrated on the $M_{\rm BH} - M_{*,\rm bulge}$ relation despite lacking the spatial resolution necessary to properly model the bulge component.

Recent high-resolution observations have confirmed elevated $M_{\rm BH}/M_*$ ratios in galaxies at $2 < z < 7$, significantly above the local scaling relations, as revealed by ALMA (Pensabene et al. 2020; Feruglio et al. 2018; Trakhtenbrot et al. 2017; Bischetti et al. 2021) and JWST (Mezcua and Domínguez Sánchez 2024; Pacucci et al. 2023; Juodžbalis et al. 2024; Maiolino et al. 2024). In particular, JWST's near- and mid-infrared capabilities allow rest-frame optical spectroscopy of high-redshift sources, enabling BH mass estimates in obscured or previously inaccessible systems, revealing extreme outliers with overmassive BH in the early Universe. Figure 2.4 shows the comparison between the local relation from Häring and Rix (2004) (blue solid lines) and McConnell and Ma (2013) (green dashed line) and the JWST data from Harikane et al. (2023); Übler et al. (2023); Maiolino et al. (2024), clearly displaying the offset toward high masses of the high-redshift BH mass estimates.

If selection effects are considered to be negligible, the emerging scenario where the entire population of high-redshift BHs is systematically overmassive relative to the local $M_{\rm BH} - M_{\rm bulge}$ relation would have profound implications for theories of BH formation. It would challenge light seed models (e.g., Population III remnants) and strongly favor the formation of heavy seeds through direct collapse (see also Box 5.2). Moreover, this also poses a challenge to accretion models, as it implies that prolonged super-Eddington phases must have occurred in the early Universe.

However, some works also pointed out weaknesses in the determination of BH masses that should eventually be taken into account. Lauer et al. (2007) argued that because of intrinsic scatter and the steep decline of massive galaxies, selecting high-z black holes via AGN luminosity preferentially picks overmassive outliers, artificially making BHs appear too massive for their hosts. Similarly, Salviander et al. 2007 outlined the potential Malmquist bias affecting quasars up

to $z = 1.2$. The work by Li et al. (2024) suggests that the extreme outliers in the $M_{\rm BH} - M_{*,\rm bulge}$ relation at high redshift may be largely attributable to selection arising from finite detection limits. Their analysis shows that such biases can fully account for the apparent overmassiveness of black holes, and they caution that even in deep JWST surveys, a significant population of low-mass ($\log M_{\rm BH}/M_\odot < 5$) BHs may remain undetected. Moreover, the determination of BH masses should also account for the accretion rates of the BHs (e.g., Lupi et al. 2024). In fact, King (2024) pointed out that for high redshift and super-Eddington accreting AGN, the velocity widths are dominated by beamed outflows rather than virialized bound motion around the sources. Neglecting this beaming effect would result in significantly overestimated mass values. Accordingly, Martínez–Aldama et al. (2020) found that the size-luminosity relation, used to constrain the BH masses (Box 2.1), is mainly driven by the accretion rate intensity.

2.2.2 The fundamental plane

By investigating the properties of AGN that exhibit both a radio (5 GHz) and X-ray (in 2-10 keV band) counterpart, Merloni et al. (2003) found that the BH mass also correlates with X-ray and radio luminosity, defining a *fundamental plane of BH activity* given by

$$\log L_X = \xi_R \log L_R + \xi_M \log M_{\rm BH} + B\,, \tag{2.4}$$

where ξ_R, ξ_M are the so-called fundamental plane coefficients, L_R and L_X are the radio and X-ray luminosities, and B is a constant.

This X-ray–radio luminosity correlation indicates that accretion onto BH and the launching of relativistic outflows are intimately connected, both arising from physical processes in the innermost regions of the accretion flow where X-ray emission and jet formation originate. The relation, holding across the entire MBH mass scale from $\sim 10\,M_\odot$ to $10^6 - 10^{10}\,M_\odot$, is a strong evidence of unification of the physical processes governing the accretion onto BHs (Plotkin et al. 2012; Dong et al. 2014). Ultimately, the existence of such a suggests that gas accretion and jet production are scale-invariant phenomena. Any spatial dependence of key physical quantities—such as magnetic field strength or jet power—can be naturally scaled to the BH's gravitational radius:

$$r_{\rm BH} = GM_{BH}/c^2. \tag{2.5}$$

Moreover, the fundamental plane provides another approach to estimate BH mass directly through radio and X-ray luminosity (Merloni et al. 2003; Gültekin et al. 2019). Despite its generality, several studies have shown that applying selection criteria to distinguish between radio-quiet and radio-loud sources reveals different realizations of the fundamental plane (e.g., Bariuan et al. 2022; Wang et al. 2024).

2.3 Demography of MBHs

In the attempt to understand the origins and evolution of MBHs in our Universe, constraints have been set by matching the statistics of local MBHs to the emissivity, number density, and clustering properties of AGN at different cosmic epochs. This section is devoted to the study

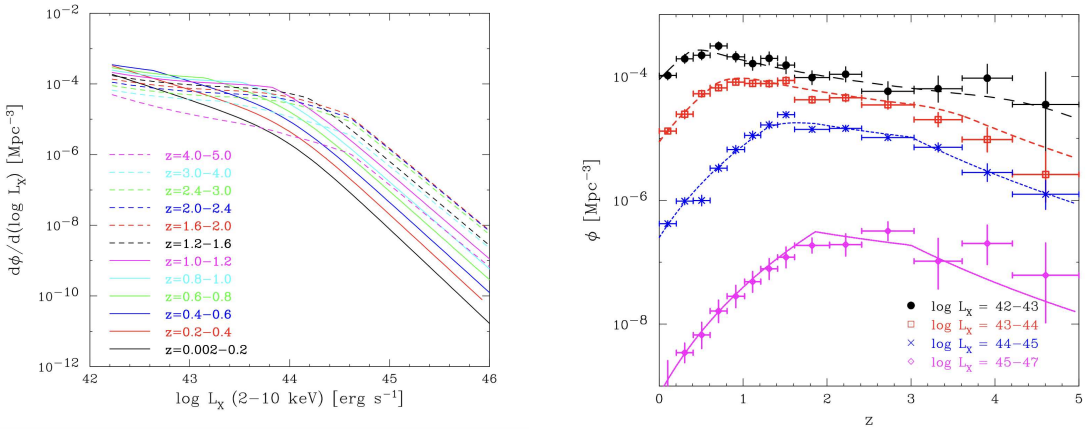

Figure 2.5: Left*: comparison of best-fit XLF at different redshift selecting only Compton-thin AGN from Ueda et al. (2014).* Right*: comoving number density of Compton-thin AGN plotted against redshift in different luminosity bins from Ueda et al. (2014). The curves are the best-fit model, and data points are calculated from either the soft or hard band sample.*

of the semi-empirical models that, starting from observational constraints such as the luminosity function of AGN or the local BH mass function (BHMF), provide insights for the evolution of BHs from first principles. The analysis developed in this section will be revisited in Chapter 10, when studying the outcomes of the simulations presented in this Thesis on the BH demography.

2.3.1 The Soltan argument

The Soltan argument (Soltan, 1982) provides a fundamental consistency test between the integrated luminosity output of accreting BHs over cosmic history and the present-day mass density locked into relic BHs. In practice, the Soltan argument states that if BHs primarily grow through radiatively efficient accretion, then the cumulative energy radiated by AGN must trace the mass density of supermassive BHs observed today. This argument links two independent observables: the AGN luminosity function and the BHMF. The AGN luminosity function Φ_L describes the number density of AGN as a function of luminosity and redshift:

$$\Phi_L = \frac{d^3N}{dV dL dz}. \tag{2.6}$$

where V is the comoving volume, N is the number of AGN and L is their luminosity. Since Φ_L depends on the intrinsic luminosity of the BH, recovering the bolometric luminosity function requires converting the observed luminosities into bolometric ones. This involves applying appropriate bolometric corrections (e.g., Marconi et al. 2004; Elvis et al. 1994) and accounting for the effects of obscuration. Several works hence adopted the hard X-ray band to trace the AGN luminosity function (XLF), since it is less affected by obscuration (e.g., Ueda et al. 2003; Silverman et al. 2008; Sazonov et al. 2007; Aird et al. 2015; La Franca et al. 2005; Georgakakis et al. 2015) although corrections from Compton-thick sources need to be applied.

Selecting AGN samples in different redshift bins allow us to trace the evolution of the AGN luminosity function. Figure 2.5 shows the luminosity function of Compton-thin hard X-ray–selected AGN in various redshift intervals from Ueda et al. (2014). The results clearly demonstrate strong

cosmic evolution of the AGN population, with a suppression of the bright end of the luminosity function at low redshift and a flattening of the faint end at high redshift. The right panel presents the integrated XLF from Ueda et al. (2014) as a function of redshift in different luminosity ranges (color-coded as indicated in the legend). In all luminosity intervals, the integrated luminosity rises to a peak before undergoing a sharp decline. The peak occurs at later times for fainter objects, suggesting an anti-hierarchical evolution: fainter AGN reach their peak activity later in cosmic history ($z \sim 1$) and exhibit a more gradual decline (Hasinger et al., 2004). These observational patterns have motivated the adoption of a luminosity-dependent density evolution parametrization to describe the evolution of the AGN XLF (e.g. Ueda et al. 2003; Miyaji et al. 2015). In this framework, the XLF evolves through different degrees of density evolution that depend on both luminosity and redshift, producing an XLF whose shape changes across cosmic time.

The Soltan argument also requires the knowledge of the BHMF, $\Phi_{M_{\rm BH}}$, which provides the number density of BHs as a function of mass and redshift:

$$\Phi_{M_{\rm BH}} = \frac{d^3N}{dV\ dM_{\rm BH}\ dz}. \tag{2.7}$$

Assuming that all galaxies host a central BH (see Sect. 2.2.1), the BHMF can be inferred from galaxy number counts combined with empirical scaling relations between BH mass and galaxy properties (e.g., Salucci et al. 1999; Marconi and Salvati 2001; Yu and Tremaine 2002). Starting from the galaxy distribution Φ_y—measured as a function of a given observable y (bulge mass or velocity dispersion)—one can derive the BHMF via an empirical scaling relation

$$M_{\rm BH} = a + by, \tag{2.8}$$

which in general is characterized by an intrinsic Gaussian scatter with r.m.s. η. The conversion from Φ_y to the BHMF is then given by (Graham et al., 2007; Tremaine et al., 2002; Marconi et al., 2004):

$$\Phi_{\rm MBH} = \int \Phi_y \frac{1}{\sqrt{2\pi\eta^2}} \exp\left\{-\frac{[M_{\rm BH} - (a+by)]^2}{2\eta^2}\right\} dy. \tag{2.9}$$

The integration of the BHMF over BH mass then yields the total comoving BH mass density at $z = 0$, $\rho_{\rm BH}$.

Provided with two independent ways to measure the AGN luminosity function and the BHMF, the Soltan argument can now be applied to recover the radiative efficiency. If MBHs grow mainly in radiatively efficient phases, the redshift evolution of the AGN luminosity function must reflect the cumulative gas accretion history of today's relic BHs.
Denoting as $\dot{M}_{\rm acc}$ the mass accretion rate onto the BH, i.e., the rate at which mass is supplied to the accretion disk, we introduce the parameter η_r as the average radiative efficiency, representing the fraction of the rest-mass energy of the accreted matter converted into radiation:

$$\eta_r = \frac{L}{\dot{M}_{\rm acc}c^2}. \tag{2.10}$$

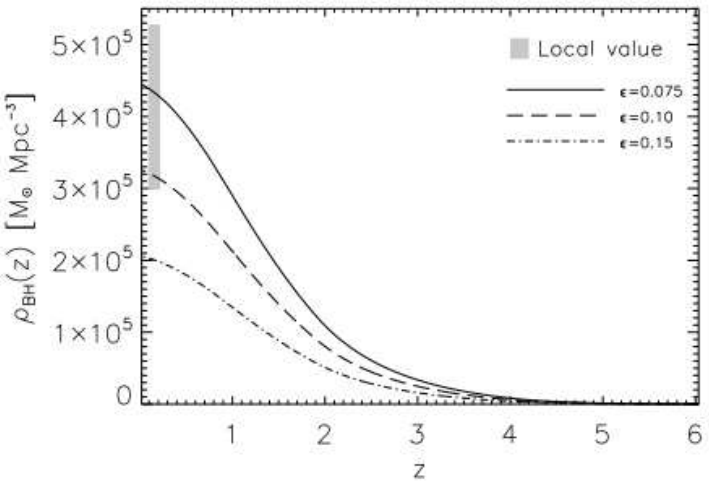

Figure 2.6: *Integrated accreted BH mass density as a function of redshift, computed from Eq. 2.12 for different radiative efficiencies ϵ, as indicated in the legend, from Shankar (2009). The grey shaded region at $z \sim 0$ represents systematic uncertainties in the local BHMF (e.g., Shankar et al. 2009).*

The actual BH mass growth rate is:

$$\dot{M}_{\rm BH} = (1 - \eta_r)\, \dot{M}_{\rm acc}, \tag{2.11}$$

where the factor $(1 - \eta_r)$ accounts for the fraction of accreted mass radiated away (Yu and Tremaine, 2002). Combining Eqs. (2.10) and (2.11), and integrating the AGN luminosity function Φ_L over luminosity and time, yields the comoving BH mass density:

$$\rho_{\rm BH} = \frac{1 - \eta_r}{\eta_r c^2} \int dt \frac{dz}{dt} \int_0^\infty \Phi_L\, L\; d\log L. \tag{2.12}$$

Finally, comparing the integrated BH mass density obtained from the accretion history (Eq. 2.12) with the locally observed mass density derived from the BHMF (Eq. 2.9) proves the Soltan argument. The agreement between these two quantities supports the hypothesis that most BH growth occurs during radiatively efficient AGN phases and sets constraints on the value of the radiative efficiency η_r.

Figure 2.6 shows the integrated accreted BH mass as a function of redshift following Eq. 2.12, for different values of the radiative efficiency (here denoted as ϵ, as labeled) from Shankar (2009). The grey shaded area at $z \sim 0$ encapsulates the systematic uncertainties in determining the local BHMF (e.g. Shankar et al. 2009, see also the discussion in 10.3.2). The match between the local and accreted mass density constrains the mean radiative efficiency to be $\lesssim 0.1$.

2.3.2 The continuity equation

Further interesting insights into the statistical population of BHs can also be gained by comparing the shape of the BHMF inferred directly at $z = 0$, as discussed in the previous section, with that obtained for AGN relics: BHs that underwent an active accretion phase in the past. The BHMF of relic AGN can be reconstructed using the continuity equation as follows.

If $\Phi_{M_{\rm BH}}$ denotes the number density of AGN relics with masses in the interval $M, M+dM$ at cosmic time t, and if no sources or sinks of BHs are present (i.e., neglecting BH formation and mergers), then the continuity equation applies:

$$\frac{\partial \Phi_{\rm M_{BH}}(M,t)}{\partial t} + M\frac{\partial}{\partial M}\left[\frac{\Phi_{\rm M_{BH}}(M,t)\,\langle \dot{M}(M,t)\rangle}{M}\right] = 0, \tag{2.13}$$

where $\langle \dot{M}(M,t)\rangle$ is the mean accretion rate for BHs of mass M at time t, and the dependence of the BHMF on mass and time has been made explicit. To solve Eq. (2.13) and obtain the distribution of BHs in mass and time, one needs to specify the average accretion history for each BH mass bin and cosmic epoch. Under the assumption that BHs mostly accrete during AGN phases, the BH growth follows Eq. (2.11), that combined with Eq. (2.10) gives:

$$\dot{M}_{\rm BH} = \frac{1-\epsilon}{\epsilon c^2} L. \tag{2.14}$$

We then introduce two more quantities: the Eddington ratio λ, defined as the ratio between the BH bolometric luminosity and the Eddington luminosity:

$$\lambda = \frac{L}{L_{\rm Edd}}, \tag{2.15}$$

and the BH *duty cycle* $U(M,t)$ defined as the number of active BHs with mass M at time t bridging the AGN mass function $\Phi_{\rm AGN}(M,t)$ to the total BHMF:

$$\Phi_{\rm AGN}(M,t) = U(M,t)\Phi_{\rm M_{BH}}(M,t). \tag{2.16}$$

Using these two definitions, together with Eq. (2.14), the average BH growth appearing in Eq. (2.13) reads:

$$\langle \dot{M}(M,t)\rangle = \frac{1-\eta_r}{\eta_r c^2} L_{\rm Edd} U(M,t) \langle \lambda(M,t)\rangle. \tag{2.17}$$

Usually, it is assumed that the Eddington rates follow a probability distribution $p(\lambda|M,t)$ defined as the normalized probability for a BH of mass M at time t to accrete at the Eddington ratio λ per unit $\log\lambda$. Therefore, the average appearing on the left term of Eq. (2.17) is:

$$\langle \lambda(M,t)\rangle = \int d\log\lambda\, \lambda\; p(\lambda|M,t). \tag{2.18}$$

Using Eq. (2.17) for the mean growth rate of BHs into Eq. (2.13) we get:

$$\frac{\partial \Phi_{M_{\rm BH}}}{\partial z} = \frac{L_{\rm Edd}}{c^2 M \ln 10}\frac{dz}{dt}\frac{\partial}{\partial \log M}\left[\frac{(1-\eta_r)}{\eta_r}\langle\lambda(M,t)\rangle \Phi_{\rm AGN}\right]. \tag{2.19}$$

Finally, the AGN mass function appearing in the former equation can be related to the bolometric luminosity function by:

$$\Phi_L(L,z) = \int d\log\lambda p(\lambda|M,z)\Phi_{\rm AGN}(M,z). \tag{2.20}$$

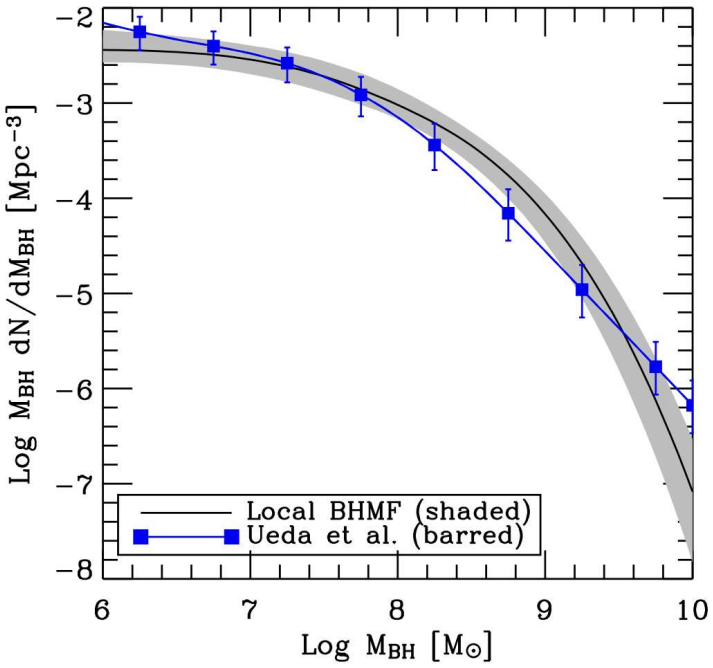

Figure 2.7: *Comparison between the local BHMF (solid black line) and the AGN relic mass function derived via the continuity equation using the AGN luminosity function of Marconi et al. (2004), integrated from* $z_s = 3$ *with an assumed radiative efficiency* $\epsilon = 0.01$.

From a given redshift z_s and assuming an Eddington ratio distribution, along with the duty cycle and the luminosity function, the continuity equation can be solved iteratively and compared with the BHMF at $z = 0$. Figure 2.7 shows the agreement between the local BHMF (solid black line) and the AGN relic mass function obtained via the continuity equation given the AGN luminosity function computed by Marconi et al. (2004). They start integrating the continuity equation given the luminosity function from Ueda et al. (2003) at $z_s = 3$, assuming a radiative efficiency $\epsilon = 0.01$ and a constant value of $\lambda = 1$ for each mass and time. In general, the good agreement between the local BHMF and the mass function of AGN relics provides strong support for the Soltan argument, reinforcing the hypothesis that local SMBHs underwent phases of luminous accretion in the past. Remarkably, this agreement also suggests that BH mergers have only a minor impact on the overall growth of the BH population, at least below $z_s = 3$. Indeed, simple models that include a merger term in Eq. 2.13 show negligible effects even for relatively high merger probabilities (Shankar et al., 2009). Analytical models by Yoo et al. (2007) demonstrate that mergers can amplify the growth of the most massive BHs within high-mass halos ($\sim 10^{15}\, M_\odot$), extending the high-mass tail of the BHMF. However, the most profound impact of BH mergers may be indirect, exerted through the evolution of BH spins and the resulting changes in radiative efficiency (e.g., Volonteri et al. 2005).

Chapter 3

MBHs and AGN in galaxy clusters

Galaxy clusters sit at the top of the hierarchy of cosmic structures. Located at the nodes of the Cosmic Web, they not only trace the growth of large-scale structure, but also host some of the most energetic processes in the Universe. Most of their baryonic content resides in a hot atmosphere ($\sim 10^7$ K) permeating the cluster, the ICM, observable in the X-ray and through the Sunyaev–Zeldovich effect (SZE) (Sunyaev and Zeldovich 1970, 1972) produced by CMB photons scattering off hot electrons. The baryonic content of a cluster is also shaped by the non-gravitational processes enhanced in such an extreme environment, foremost among them the activity of the AGN. X-ray probes pioneered by XMM and Chandra have revealed compelling evidence that AGN inject substantial amounts of energy into the ICM, decreasing radiative cooling rates and quenching SF.

Within the framework of this thesis, galaxy clusters provide a uniquely rich laboratory to investigate the evolution of MBHs and to assess how their feedback imprints itself on the thermodynamic properties of the surrounding medium. For this reason, we devote this Chapter to the observational evidence for the presence and influence of MBHs in galaxy clusters.

We begin by examining the emergence of heating mechanisms that prevent the overcooling of galaxy clusters (Sect. 3.0.1). In Sect. 3.1, we then discuss the impact of AGN on the ICM, highlighting how the feeding and feedback cycle regulates the thermodynamical properties of observed clusters. Finally, Sect. 3.2 addresses the dichotomy between clusters with cool cores and those without, presenting the classification of these two populations (Sect. 3.2.1) as well as the evolutionary transitions between them (Sect. 3.2.2).

3.0.1 The overcooling problem

The radiative cooling time of the gas in the central part of rich galaxy clusters is given by:

$$t_{\rm cool} = \frac{p}{(\gamma - 1) n_e n_H \Lambda(T)}, \tag{3.1}$$

where p, T are the pressure and temperature of the ICM, respectively, n_e and n_H are the electron and hydrogen number density, γ is the adiabatic index of the gas and $\Lambda(T)$ is the radiative cooling function of gas (Lea and De Young 1976; Cowie and Binney 1977; Fabian and Nulsen 1977; Sarazin 1986; Peterson and Fabian 2006).

Considering a gaseous atmosphere trapped in the gravitational potential well of a galaxy

cluster, the *cooling radius* $r_{\rm cool}$ is defined as the radius where the cooling time is less than the age of the system, say $t_{\rm Hubble}$: $t_{\rm cool} \sim t_{\rm Hubble}$. The gas pressure at $r_{\rm cool}$ is determined by the weight of the overlying gas, in which gas cooling is neglected. Within $r_{\rm cool}$, cooling reduces the gas temperature and the gas density must rise in order to maintain the pressure at $r_{\rm cool}$. The only way for the density to rise is for the gas to flow inward, thus originating a *cooling flow* (see Fabian 1994 and references therein). As the gas temperature drops below the virial temperature, the adiabatic compression under the action of gravitational force counterbalances the heat loss and can sustain, or even heat, the gas in the core. However, if the gravitational potential flattens in the center, the gas temperature can eventually drop catastrophically (Fabian 1994).

With the advent of high-sensitivity X-ray observations provided by the Chandra and XMM-Newton satellites, the cooling flow model started to be challenged. David et al. (2001) showed that the spectral mass deposition rate (the rate of inflow of cooling gas mass, see Eq. 3.6), was significantly lower than expected. Moreover, by analyzing soft X-ray XMM spectra, Peterson et al. (2003) found a severe deficit of emission in comparison to the predictions of the isobaric cooling-flow model at low temperatures, reaching temperatures no cooler than $T_0/3$, where T_0 denotes the temperature of the ambient medium. Furthermore, the cooling flows should give rise to centrally peaked SF rates (SFR), unless one finds a mechanism to suitably "hide" cooled gas. On the other hand, although in many cases BCGs reveal blue light indicative of an excess of on-going star formation, this rarely exceeds 10 $\rm M_\odot\ yr^{-1}$ (Fraser-McKelvie et al. 2014; McDonald et al. 2018), which is a factor 10-100 times lower than the X-ray deduced mass cooling rate (Fabian 2002). The failure of the classical cooling flow model brought, on the one hand, to the development of models accounting for a replenishing source of hot gas that could prevent the catastrophic cooling, on the other to the systematic phenomenological study of the dichotomy between clusters characterized by a central temperature drop, the *cool core* (CC) clusters, and those that do not show this feature, the non CC (NCC) clusters.

3.1 AGN feeding and feedback cycle

The heating mechanism responsible for the suppression of cooling flows should act from group to cluster scales (Thomas et al. 1986). Furthermore, it has to be self-regulated to reproduce the SFR down to predicted value, without causing overheating. Therefore, some form of feedback is required to prevent all of the gas from being heated up. The most promising candidate mechanism to reproduce this, is feedback from AGN hosted in the BCG. The radiative heating from nearly Eddington accreting MBH could release up to $10^{47}\rm erg\,s^{-1}$ and efficiently reheat the central cluster regions. However, BCGs rarely host AGN (Fabian and Rees 1995; Fabian et al. 2011). Mechanical power (Pedlar et al. 1990; Tabor and Binney 1993) might have a strong impact on the state of the gas thermodynamics in the central region. This was confirmed by a number of observations mostly in the radio and X-ray bands, which find evidence of AGN/ICM interactions in a large fraction of relaxed clusters (Boehringer 1993; Dunn and Fabian 2006; Rafferty et al. 2006b; Birzan et al. 2012). Figure 3.1 outlines the imprint of the central SMBH on the ICM for M87, the X-ray brightest elliptical galaxy in the nearby Virgo cluster. The image presents different observations of M87 from different probes at increasing resolution zooming on the central region, down to the Event Horizon Telescope image of the SMBH in the core (Event Horizon Telescope Collaboration

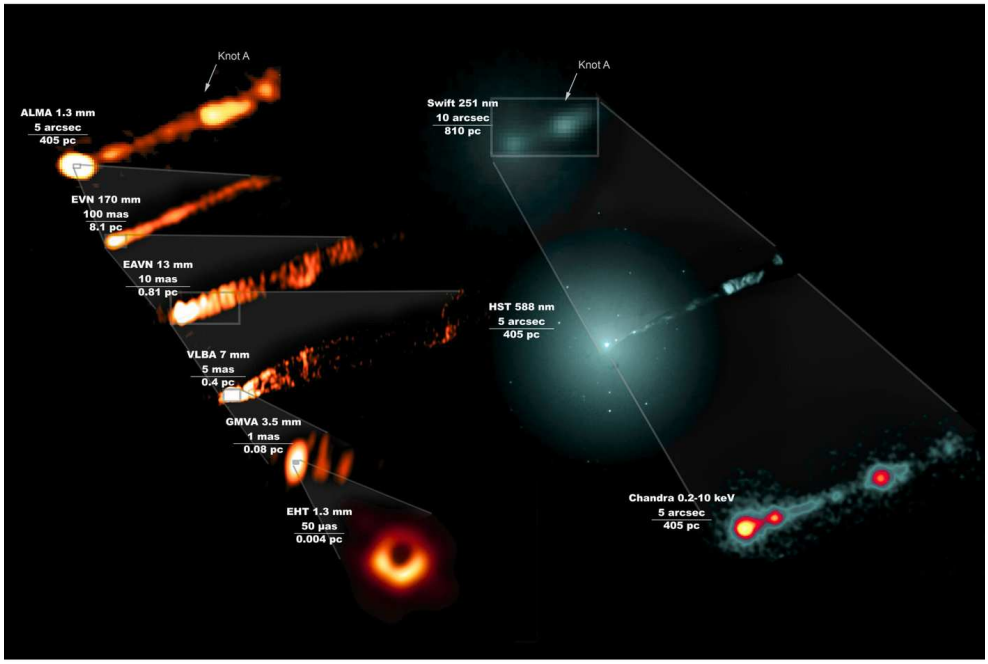

Figure 3.1: *Multiwavelength observations of the core region of M87. Image credits: The EHT Multiwavelength Science Working Group; the EHT collaboration; ALMA (ESO/NAOJ/NRAO); the EVN; the EAVN collaboration; VLBA (NRAO); the GMVA; HST; the Neil Grehrels Swift Observatory; the Chandra X-ray Observatory.*

et al. 2019). The radio data (left column) display extended radio jets, spatially coincident with the bottom left X-ray observation from Chandra. The excellent angular resolution of the Chandra X-ray observatory revealed that the central regions of many CC clusters are not relaxed, and their ICM is highly dynamic and not uniformly distributed, as there are signs of bubbles (or "cavities") on scales often approximately coincident with lobes of extended radio emission. In addition to that, observations also reveal highly disturbed structures in the cores of many clusters, such as shocks, ripples and sharp discontinuities (e.g., for reviews McNamara and Nulsen 2007, 2012 see also Gitti et al. 2012; Gaspari et al. 2020; Eckert et al. 2021; Donahue and Voit 2022). Figure 3.2 reports the image of the brightest object in the X-ray sky, the Perseus cluster, from Reynolds et al. (2020). The image displays two large cavities surrounding the inner core (shown in the bottom right inset). In turn, X-ray cavities are surrounded by rims and concentric fluctuations in surface brightness associated to pressure fluctuations due to the cavities' inflation (Fabian et al. 2003, 2006) Powerful radio jets launched by central AGN can inflate bubbles of relativistic plasma, driving weak shocks and displacing the surrounding hot intracluster gas producing visible depressions in the X-ray emission, therefore inducing gas circulation and energy deposition on scales spanning several hundreds of parsecs. Figure 3.3 shows the X-ray (left) and corresponding radio VLA (right) observations of Hydra A. The powerful radio jets propagate outward from the galaxy to the surrounding ICM. As they displace the hot plasma, hot X-ray cavities are carved out. Moreover, there has been growing evidence of filamentary warm and cold gas surrounding the BCG, potentially reaching the innermost parsecs and fuelling the central galactic engine (e.g., Edge 2001; Olivares et al. 2019; McDonald et al. 2010; Rose et al. 2019). Piecing together all

such observational results, a coherent picture emerges that cluster-central AGN can prompt a deposition of energy in the ICM, preventing over-cooling of the same gas that fuels their SMBHs. This finely tuned balance is usually referred to as the "AGN feeding and feedback cycle".

3.1.1 Feeding

While evidence of MBH feedback are observed on scales of tens to possibly hundreds of kiloparsecs, the feeding mechanism originates in the immediate surroundings of the BH, where the gas is more likely to be cold and condensed. If this cold phase results from the cooling of the surrounding hot gas, a physical link is naturally established between the central engine and the large-scale atmosphere (Gaspari et al. 2020). Russell et al. (2013) and Allen et al. (2006) showed that the nuclear X-ray luminosity correlates with the average accretion rate inferred from X-ray cavities under the assumption of Bondi accretion from the hot intra-cluster atmosphere. This supports the idea that nuclear X-ray emission traces ongoing accretion. However, Rafferty et al. (2006b); Hardcastle et al. (2007); McNamara et al. (2010) argued that galaxies hosting jets with powers exceeding 10^{45} erg s^{-1} would struggle to sustain them through hot gas accretion alone. The assumption of a hot and diffuse ICM powering the MBH through Bondi accretion is at variance with the presence of significant amounts of cold gas in BCGs (Edge 2001; Edge et al. 2010; Donahue et al. 2011; Morganti and Oosterloo 2018; Veilleux et al. 2020). With the advent of ALMA, high-resolution observations have enabled detailed studies of MBH accretion by probing the neutral and molecular gas phases in the innermost regions of BCGs. ALMA measurements reveal a rich variety of molecular gas morphologies—from disk-dominated configurations to filamentary structures—consistent with inflows along streamlines. Uplifted gas, after stalling, can fall back toward the galaxy in a circumgalactic circulation, corresponding to the episodic activity of the AGN (Russell et al. 2019; Rose et al. 2023; Brusa et al. 2015; Oosterloo et al. 2017; Audibert et al. 2023).

Thus, the simplistic picture of pure hot-mode accretion has left the stage to a multiphase feeding scenario, in which cold gas also contributes to fueling activity. Within this framework, the onset of the feeding–feedback cycle should also link the cold gas content to the power of AGN jets. Indeed, Russell et al. (2019) reported a correlation between the circumnuclear gas mass, as measured with ALMA, and the jet power inferred from the innermost radio bubbles. Although some uncertainties persist, these results strongly support the view that cold gas plays a fundamental role in sustaining accretion and triggering the feedback cycle, implying that SMBH activity is closely regulated by the average density of circumnuclear gas. Complementary observations with the JVLBA and VLBA (e.g. Morganti et al. 2023) of the 3C84 source within the Perseus clusters have detected broad (FWHM $\sim$ 500 km s^{-1}) neutral hydrogen absorption lines within the inner ($<$300 pc) region around the SMBH, providing evidence for rapidly and relatively cold rotating gas in a circumnuclear disk.

3.1.2 Feedback

Imprints of AGN feedback energy in galaxy clusters are ubiquitous. Based on a sample of 55 clusters from Dunn and Fabian (2006), Fabian (2012) found that 95% of the systems show evidence of X-ray emitting bubbles. This implies that the duty cycle of AGN activity — during which radio

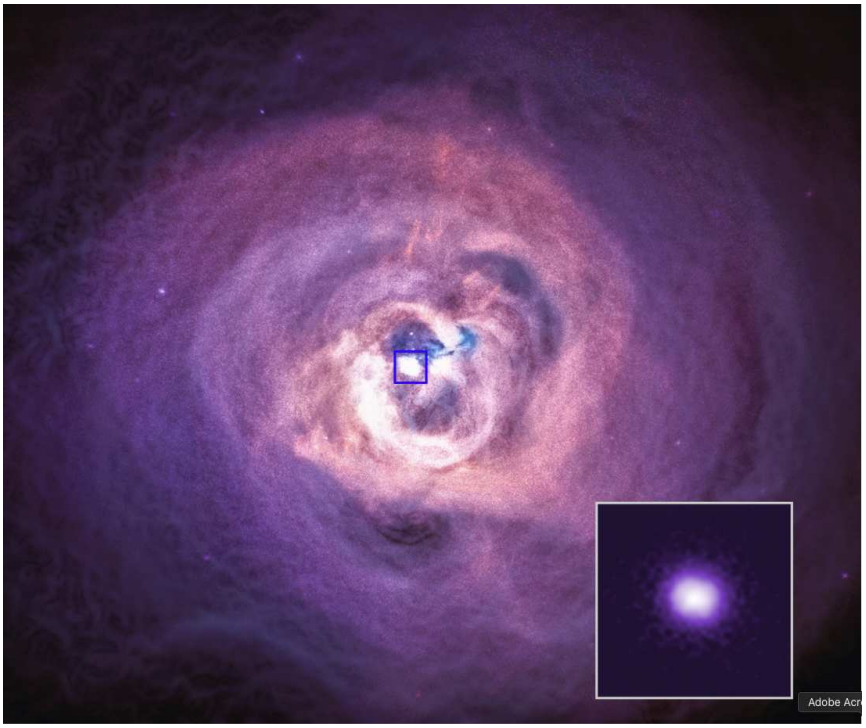

Figure 3.2: *Chandra image of Perseus cluster. The main image is* ~ 8 *arcmin. The inset on the bottom right panel presents an X-ray close up in the core region, hosting the central SMBH. Image credits: NASA/CXC/Univ. of Cambridge/Reynolds et al. (2020)*

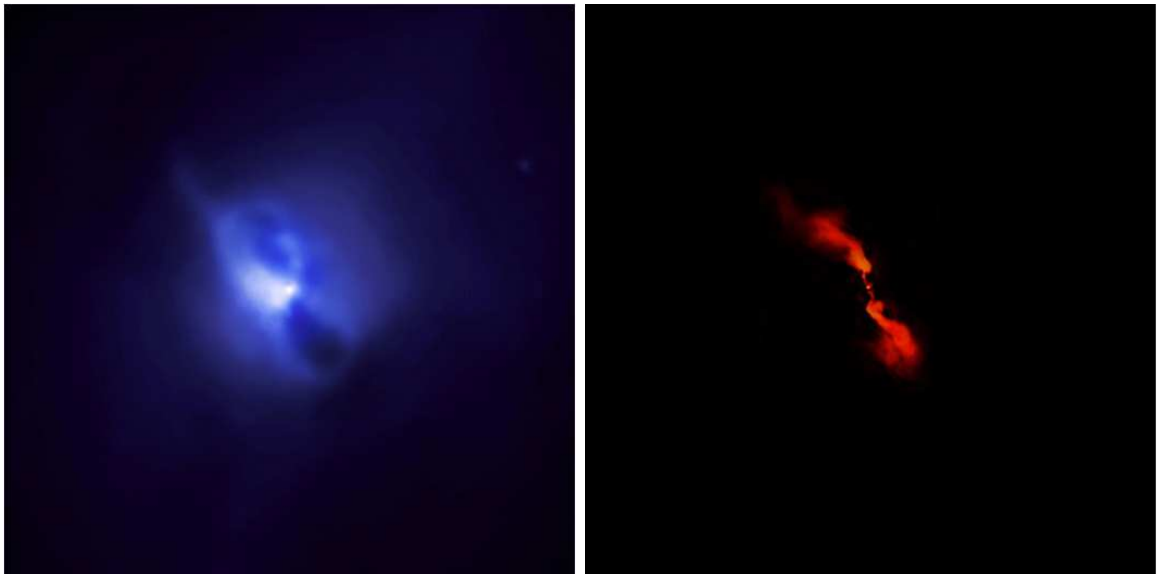

Figure 3.3: *Hydra A as seen by Chandra (left) and VLA (right). Image credits: X-ray: NASA/CXC/U.Waterloo/ Kirkpatrick et al. (2009); Radio: NSF/NRAO/VLA; Optical: Canada-France-Hawaii-Telescope/DSS.*

jets are launched and X-ray cavities are inflated — is very long in galaxy clusters. Cavities are often found in opposite pairs and appear as approximately elliptical depressions in the X-ray surface brightness, typically 20–40% fainter than the surrounding gas. Their diameters range from less than 1 kpc to nearly 200 kpc. The energy associated with an X-ray cavity provides important insights into the mechanical energy budget of the AGN as cavities can be indeed used as *calorimeters*. In particular, the energy and power of an X-ray cavity can be inferred from the sum of the internal energy of the bubble and the PdV work done by the expanding gas. Assuming pressure equilibrium with the ICM, the total enthalpy of the cavity is given by Churazov et al. (2002):

Figure 3.4: *Schematic of a bubble rising in a stratified medium, from Zhang et al. (2018). The bubble rises at its terminal velocity when the buoyancy force is balanced by the drag force.*

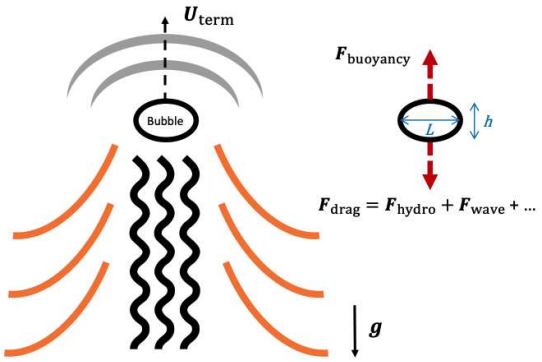

$$H = \frac{\gamma}{\gamma - 1} PV, \tag{3.2}$$

where γ is the adiabatic index of the cavity plasma, depending on whether the plasma is relativistic ($\gamma = 4/3$) or non-relativistic ($\gamma = 5/3$), and P is the surrounding gas pressure. Figure 3.4 illustrates the rise of an X-ray bubble, which reaches a terminal velocity when the buoyancy force F_{buoyancy} is balanced by the drag force exerted by the surrounding medium. For a bubble of volume V_b and cross-sectional area A_b, and given the drag coefficient C_d of the ICM, this balance implies (Zhang et al. 2018):

$$F_{\text{buoyancy}} = \rho g V_b = F_{\text{drag}} = \frac{1}{2} C_d \rho A_b U_{\text{term}}^2, \tag{3.3}$$

where ρ is the ambient gas density and g the local gravitational acceleration. Therefore, the terminal velocity is

$$U_{\text{term}} = \sqrt{\frac{2 g V_b}{A_b C_d}}. \tag{3.4}$$

If R is the distance from the cluster center (or AGN) to the middle of the cavity, the buoyant rise time — i.e. the time required for the bubble to reach its observed position — can be estimated as

$$t_{\text{buoyant}} = \frac{R}{U_{\text{term}}} = R \sqrt{\frac{A_b C_d}{2 g V_b}}, \tag{3.5}$$

which provides an estimate of the X-ray cavity age. An important observational result is that AGN feedback appears to inject, on average, the amount of energy required to offset radiative cooling in the ICM. Indeed, a correlation exists between the power needed to inflate the cavities and the X-ray luminosity, demonstrating a fine balance between cooling and heating in clusters, regulated by AGN feedback. Furthermore, by heating the intragroup and intracluster gas, AGN feedback contributes significantly to the SF quenching in cluster environments, particularly in central galaxies (e.g. Bongiorno et al. 2016). Current theoretical models invoke AGN feedback as

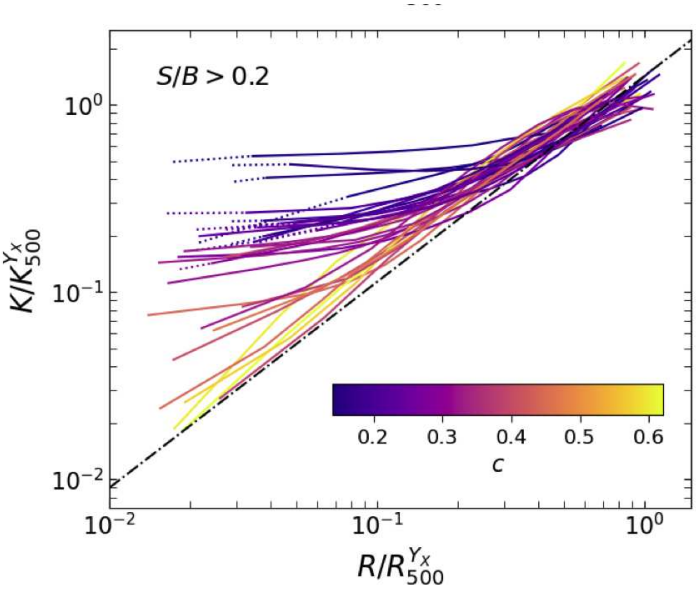

Figure 3.5: *Gas entropy of the CHEX MATE sample from Riva et al. (2024). The profiles are color coded with the concentration parameter from Campitiello et al. (2022).*

the primary mechanism responsible for this quenching (e.g. Piotrowska et al. 2022; Goubert et al. 2025; Xie et al. 2024; Combes 2017; Donnari et al. 2021; Planelles et al. 2014).

3.2 The ICM diversity: CC/NCC clusters

However, the heating mechanism preventing overcooling should not erase the CC, which is ubiquitous among clusters and groups (Vikhlinin et al. 2005, 2006; Sun 2009; Rossetti et al. 2017). CC clusters are observationally characterized by a pronounced central surface brightness peak, accompanied by a temperature decline in the innermost regions. They are typically regarded as relaxed systems (Rossetti et al. 2017), thus linking their thermodynamical properties with the dynamical evolution. Selecting 20 X-ray clusters from Chandra, Sanderson et al. (2009) found a clear dichotomy between clusters showing a low central temperature, steeply decreasing gas entropy and increasing gas density in the core with those showing a higher central temperature and gas entropy and density flattening at the core (identified as non cool cores, NCC). However, recent analysis pointed toward a more complex scenario, highlighting the strong dependence on the morphological properties of the clusters. If relaxed systems have generally a CC, disturbed ones show a higher core entropy (Pratt et al. 2010; Hudson et al. 2010; Ng and Ueda 2024; Molendi et al. 2023; Bauer et al. 2005; Burns et al. 2006; Burns et al. 2008). Figure 3.5 shows the entropy profiles in the CHEX MATE sample (Riva et al. 2024), consisting of 32 galaxy clusters with very high mass ($M_{500} > 7.75 \cdot 10^{14} M_\odot$). Initially selected with Planck SZ, the entropy profiles shown are obtained with XMM-Newton and are color-coded according to the concentration parameter by Campitiello et al. (2022). Notably, there is a strong dependence on the concentration, with lower core entropy corresponding to higher concentrations, and therefore more relaxed systems. Therefore, the dispersion present in the central region reflects the morphological variety of the cluster in the sample.

3.2.1 Classification of CC/NCC

The CC term was proposed by Molendi and Pizzolato (2001) to indicate a phenomenon of smaller entity than the extreme cooling flow, reflecting the observational evidence that the mass deposition and mass flows are much smaller than those expected for a cooling flow. In literature, the definition of CC/NCC relies, however, on several different metrics:

- **Thermodynamical properties**: a central temperature drop (Sanderson et al. 2009; Burns et al. 2008) and in general thermodynamical steep decreasing profiles of gas entropy at the core (Ghirardini et al. 2019) and central increasing gas density (Cavagnolo et al. 2008);

- **Cooling time**: clusters having shorter central cooling times (Eq. 3.1) are classified as CCs. Bauer et al. (2005) distinguishes as strong CCs those having central $t_{\rm cool} < 2$ Gyr, while NCC object have $t_{\rm cool} > 10$ Gyr (see also O'Hara et al. 2006; McDonald et al. 2013; Bharadwaj et al. 2014);

- **Mass deposition rate**: the mass deposition rate regulates the condensation of inflowing gas to the cluster core and it is defined from the gas mass at a radius r from the cluster central and the cooling times $t_{\rm cool}$ (Hudson et al. 2010):

$$\dot{M}(< r) = \frac{M_{\rm gas}(r)}{t_{\rm cool}(r) - t_{\rm cool}(0)}. \tag{3.6}$$

  Chen et al. (2007) identify CCs as those having the higher ($\dot{M}(r_{\rm cool})/M_{500} > 10^{-13}$ yr^{-1}) mass deposition rates.

- **Hα line emission**: clusters hosting multiphase gas, characterized by a cool central core and low central entropy ($\lesssim 30$ keV, cm^2), typically also display strong Hα emission-line luminosities, tracing filaments of gas cooling onto their BCG (e.g., Cavagnolo et al. 2008; Gaspari et al. 2018; Bauer et al. 2005). Therefore, the strong Hα line emission can also be used to discriminate CCs (Medezinski et al. 2019).

- **X-ray concentration parameter**: being the X-ray emissivity proportional to the gas density, the CC clusters are expected to show more X-ray bright cores. Therefore, it is possible to define an X-ray emission concentration parameter (Santos et al. 2008; Maughan et al. 2012; Rossetti et al. 2017) to distinguish CC from NCC structures.

Although these definitions lead to consistent classifications in the case of objects with marked CC/NCC traits, conversely intermediate or transitional objects can sometimes end up being classified differently by different authors.

3.2.2 Dynamical evolution of CC clusters

Several lines of evidence support the idea that the degree of cool-coreness can be interpreted within an evolutionary scenario, in which mergers and dynamical activity drive the transition from CC to NCC states. According to this hypothesis, the presence of a CC should be taken as an indicator of a relaxed cluster.

A first clue on the connection between dynamical evolution and CC properties comes from the observation that giant radio halos—commonly associated with recent mergers (Buote 2001; Cassano et al. 2010, 2013; Cuciti et al. 2015; Rickel et al. 2025; see also Ferrari et al. 2008 for a review) or dynamically disturbed systems—are absent in CC clusters. For example, Leccardi et al. (2010) analyzed a sample of XMM-Newton clusters, classifying them as merging when they exhibited radio lobes or relics, multi-peaked velocity distributions from optical spectroscopy, multiple peaks in lensing analyses, or significant morphological irregularities in the X-ray photometry. Out of 59 clusters in their sample, only two displayed both a low-entropy core and signs of ongoing merging activity. In both cases, the clusters show evidence of merger activity whose effects have not yet propagated to the core of the main structure. Based on this, the authors concluded that mergers can transform low-entropy clusters into high-entropy ones. This is consistent with Rossetti and Molendi (2010), who found that some NCC clusters still retain signatures of a CC origin, such as moderately low-entropy gas (though not as low as in CC systems).

The availability of SZ-selected cluster samples has been crucial in establishing the CC fraction (Rossetti et al. 2016, 2017; Sommer and Basu 2013; McDonald et al. 2013; Wen and Han 2013; Andrade-Santos et al. 2017), overcoming the strong bias of X-ray surveys toward CC systems, which are easier to detect in the X-ray due to their steep surface brightness profiles (Eckert et al. 2011). Moreover, SZ surface brightness is independent of redshift, enabling the detection of clusters above a given signal-to-noise threshold across cosmic time and the construction of nearly mass-limited samples out to $z \sim 1.5$. Interestingly, SZE-selected cluster samples show that the CC fraction does not evolve significantly with redshift (Ruppin et al. 2021; McDonald et al. 2017; McDonald et al. 2019). This implies that CC disruption through mergers must be counterbalanced by CC restoration mechanisms operating on timescales shorter than the Hubble time, thereby maintaining the observed relative numerosity between CC and NCC populations (Rossetti et al. 2011; Ruppin et al. 2021; Molendi et al. 2023). Consistent with this idea, Rossetti et al. (2011) emphasize that the CC/NCC transition can proceed in both directions: CCs may be disrupted by mergers, while NCCs can revert to a CC state within $\lesssim 10$ Gyr, enabling a cyclical evolution between the two states.

Chapter 4

Dynamical evolution of MBHs

The growing interest in the dynamics of MBHs in recent years is motivated by several factors. Firstly, as discussed in the previous chapters, BH activity is intimately connected to the environment they inhabit. This correlation spans several orders of magnitude in spatial scale, ranging from the innermost region where AGN fuelling takes place, to hundreds of kpc scales where the effects of AGN feedback are still observable. Consequently, localizing the precise location where the BH resides is crucial for identifying its imprint and its co-evolution with the surrounding medium.

Secondly, the increasing resolution of multi-wavelength observations over the last decade has provided compelling evidence for the dynamical evolution of MBHs, recording substantial displacements from their host galaxies, the presence of dual AGN, and binary BH systems. Finally, the advent of gravitational-wave (GW) astronomy has opened a new observational window, attracting significant attention and calling for deeper theoretical insights.

MBHs reside at the centres of massive galaxies, where they should remain anchored as a consequence of the collisional drag exerted by the dynamical friction (DF) force. When the host galaxies merge, the dynamical evolution of the MBHs is classically described in terms of three fundamental stages originally outlined in the seminal work of Begelman et al. (1980): *i*) DF-driven infall, *ii*) Hardening via stellar or gas interactions, and *iii*) GW-driven inspiralling. Depending on the properties of the binary system and of the surrounding medium, the MBHs will form a binary bound system and further lose angular momentum, subsequently reaching the GW-dominated regime leading to the final coalescence.

As the central theme of this Thesis, this chapter outlines the theoretical framework and reviews the observational evidence for the dynamical evolution of MBHs, with a particular focus on the first two evolutionary stages mentioned above. Given that the simulations presented throughout this work resolve spatial scales down to a few tenths of a parsec, special emphasis is placed on the DF-dominated regime, which is especially relevant at these scales.

Section 4.1 introduces the concept of DF force and provides a detailed derivation, which is crucial for the topics addressed in this Thesis. Section 4.1.2 explores the observational signatures of MBH systems at separations down to the parsec scale. The sub-parsec regime is discussed in Section 4.2, including a brief theoretical overview in Section 4.2.1 and a review of the observational evidences for binary MBHs in Section 4.2.2. An intriguing consequence of these dynamical processes is the potential for MBHs to become spatially offset from the centers of their host galaxies.

Such off-center BHs may result from incomplete DF-driven sinking in low-mass systems, gravitational wave recoil following MBH mergers, or three-body scattering interactions. These scenarios and their observational implications are explored in Section 4.3.

4.1 From galaxy mergers to the parsec scale

In this section, we introduce the derivation of DF from first principles. We begin with the collisional correction term to the Boltzmann equation that arises from discrete particle interactions, and then we show how this naturally leads to the Fokker–Planck equation. The theoretical foundations of this approach trace back to the seminal work of Landau (1958); Chandrasekhar (1943b). Then, additional assumptions yielding the classical DF formula from Binney and Tremaine (1987) will be presented, as this equation has become the baseline prescription for implementing DF corrections in many cosmological simulations, explored in Chapter 6. Finally, we discuss observational signatures of the DF effect, focusing on systems hosting dual AGN, where the orbital decay of massive black holes provides a direct and measurable probe of DF in galactic environments.

4.1.1 Introduction to the dynamical friction force

The Fokker-Plank approximation

Let us consider a stellar system described by the phase-space distribution function $f(\vec{x}, \vec{v}, t)$, where $\vec{x}$ and $\vec{v}$ denote the spatial and velocity vectors of the stars composing the system. Under the influence of an external force $\vec{F}$, and assuming all stars have the same mass m, the Boltzmann equation reads:

$$\frac{df}{dt} = \frac{\partial f}{\partial t} + v^j \frac{\partial f}{\partial x^j} + \frac{F^j}{m} \frac{\partial f}{\partial v^j} = \left(\frac{\partial f}{\partial t} \right)_{\text{coll}} . \tag{4.1}$$

Here, the index j runs over the velocity components (i.e. $j = 1, 2, 3$) and the collision term on the right-hand side accounts for changes in the distribution function due to stellar encounters. This term is neglected under the assumption that all stars feel a smooth potential, so that the Boltzmann equation becomes a continuity equation in phase space, the *collisionless Boltzmann equation*. However, in a discretized system of gravitationally interacting particles, collisions among pairs of particles are added on top of the action of the smooth potential. When a massive body moves through a sea of particles, the cumulative interactions between the body and the surrounding particles generate a *density wake*, resulting in the DF drag.

Under the assumption that the rate of change induced by these encounters is typically much smaller than that caused by the external force, it can be assumed that within a phase-space volume element $\Delta\vec{w} = (\Delta\vec{x}, \Delta\vec{v})$ and over a short time Δt, the external field remains constant. Let $\vec{w} = (\vec{x}, \vec{v})$ be the phase-space coordinate of a star at time t. Also, let us define the quantity $\psi(\vec{w}, \Delta\vec{w})$ so that $\psi(\vec{w}, \Delta\vec{w})\, d^6(\Delta\vec{w})\Delta t$ is the probability that a star with coordinates $\vec{w}$ is scattered within the time interval Δt to the coordinate $\vec{w} + \Delta\vec{w}$ as a result of an encounter. The phase-space distribution function within this volume then changes due to particles that are scattered either *inside* or *outside* the 6D volume element $\Delta\vec{w}$. The loss term (contribution from particles scattered

out) is:

$$\frac{\partial f}{\partial t} = -f(\vec{w}) \int d^6\Delta\vec{w}\, \psi(\vec{w}, \Delta\vec{w}), \tag{4.2}$$

while the gain term (contribution from particles scattered in) is:

$$\frac{\partial f}{\partial t} = \int d^6\Delta\vec{w}\, \psi(\vec{w} - \Delta\vec{w}, \Delta\vec{w}) f(\vec{w} - \Delta\vec{w}). \tag{4.3}$$

Combining the two terms above, the collisional term in Eq.(4.1) can be cast in the form:

$$\frac{df}{dt} = \int d^6\Delta\vec{w} \left[\psi(\vec{w} - \Delta\vec{w}, \Delta\vec{w}) f(\vec{w} - \Delta\vec{w}) - \psi(\vec{w}, \Delta\vec{w}) f(\vec{w})\right]. \tag{4.4}$$

According to the Fokker-Plank approximation, particle-particle encounters are assumed to be *weak*, meaning that $|\Delta\vec{w}|$ is small, so the first term in the square brackets of Eq.(4.4) can be expanded in a Taylor series up to the second order:

$$\begin{aligned}\psi(\vec{w} - \Delta\vec{w}) f(\vec{w} - \Delta\vec{w}) = \psi(\vec{w}, \Delta\vec{w}) f(\vec{w}) \\ - \sum_{\mu=1}^{6} \frac{\partial}{\partial w_\mu} \left[\psi(\vec{w}, \Delta\vec{w}) f(\vec{w})\right] \Delta w_\mu \\ + \frac{1}{2} \sum_{\mu,\nu=1}^{6} \frac{\partial^2}{\partial w_\mu \partial w_\nu} \left[\psi(\vec{w}, \Delta\vec{w}) f(\vec{w})\right] \Delta w_\mu \Delta w_\nu\end{aligned} \tag{4.5}$$

where the indices μ and ν run over the phase-space components, i.e. both spatial and velocity coordinates. Substituting this into Eq.(4.4) gives

$$\frac{df}{dt} = -\sum_{\mu=1}^{6} \frac{\partial}{\partial w_\mu} \left[D[\Delta w_\mu] f(\vec{w})\right] + \frac{1}{2} \sum_{\mu,\nu=1}^{6} \frac{\partial^2}{\partial w_\mu \partial w_\nu} \left[D[\Delta w_\mu \Delta w_\nu] f(\vec{w})\right], \tag{4.6}$$

where we have introduced the following quantities:

$$D[\Delta w_\mu] = \int d^6\Delta\vec{w}\, \psi(\vec{w}, \Delta\vec{w}) \Delta w_\mu, \tag{4.7}$$

$$D[\Delta w_\mu \Delta w_\nu] = \int d^6\Delta\vec{w}\, \psi(\vec{w}, \Delta\vec{w}) \Delta w_\mu \Delta w_\nu. \tag{4.8}$$

Eq. (4.7), (4.8) are often referred to as the first- and second-order diffusion coefficients. Hereafter, the assumption is made that the encounters are not only weak, but also local. In this case, the dominant contribution to the phase-space shift of a particle arises from interactions with nearby particles. If the encounters are local, the diffusion coefficients can be expressed purely as a function of the velocity shift $\Delta\vec{v}$, as in Binney and Tremaine (2011):

$$D[\Delta v_i] = \int d^6\Delta\vec{v}\, \psi(\vec{v}, \Delta\vec{v}) \Delta v_i, \tag{4.9}$$

$$D[\Delta v_i \Delta v_j] = \int d^6\Delta\vec{v}\, \psi(\vec{v}, \Delta\vec{v}) \Delta v_i \Delta v_j. \tag{4.10}$$

The focus is henceforth placed on the first-order diffusion coefficient of Eq. (4.9) which is the average change in velocity due to the encounters per unit time. This term captures the drift of the particle in velocity space and is related to the DF correction we applied. The second-order diffusion coefficient, on the other hand, describes the random scattering of the particle's velocity, representing the diffusive spread caused by these interactions. This second-order term is not considered in the present study, and its inclusion would represent an interesting avenue for future work (see Chapter 11).
Before showing how the first-order coefficient relate to the DF acceleration, a few basic results of two-body scattering need to be introduced.

Two-body scattering

Consider a scenario where two particles of mass m and M are scattering with impact parameter b and initial relative velocity $\vec{v}_0$. The particle of mass M, because of the interaction with m, experiences a deflection of its trajectory by an angle θ which is related to the impact parameter b by the following expression (Binney and Tremaine 2011):

$$\tan\left(\frac{\theta}{2}\right) = \frac{G(M+m)}{v_0^2\, b}. \tag{4.11}$$

Therefore, the impact parameter corresponding to a 90° deflection is

$$b_{90} = \frac{G(M+m)}{v_0^2}. \tag{4.12}$$

The initial velocity $\vec{v}_0$ of particle M changes as a consequence of the encounter. The change in velocity $\Delta\vec{v}$ can be decomposed in a parallel and an orthogonal component to the initial relative velocity $\vec{v}_0$, namely $\Delta\vec{v}_{\parallel}$ and $\Delta\vec{v}_{\perp}$. Again, following Binney and Tremaine (2011), such components can be written as:

$$|\Delta v_{\perp}| = v_0 \frac{m}{m+M}\sin\theta = \frac{2mv_0}{M+m}\frac{b/b_{90}}{1+b^2/b_{90}^2} \tag{4.13}$$

$$|\Delta v_{\parallel}| = v_0 \frac{m}{m+M}(1-\cos\theta) = \frac{2mv_0}{M+m}\frac{1}{1+b^2/b_{90}^2}. \tag{4.14}$$

When extending the analysis to a system populated by many particles, the differential scattering cross section for the encounters can be derived. Particles scattering from an annular region of area $d\sigma = 2\pi b db$ are deflected into an angular annulus of area $2\pi R\sin(\theta)Rd\theta$ within the solid angle $d\Omega = 2\pi\sin\theta d\theta$. Therefore, the differential scattering cross section $d\sigma/d\Omega$, using Eq. (4.11), can be written as follows:

$$\frac{d\sigma}{d\Omega} = \frac{b}{\sin\theta}\frac{db}{d\theta} = \frac{G(M+m)b}{2\sin\theta\, v_0^2\sin^2(\theta/2)}. \tag{4.15}$$

Using now Eq.(4.11) for b and $\sin(\theta) = 2\sin(\theta/2)\cos(\theta/2)$ we obtain:

$$\frac{d\sigma}{d\Omega} = \left[\frac{G(M+m)}{2v_0^2\sin^2(\theta/2)}\right]^2 = \left[\frac{b_{90}}{2\sin^2(\theta/2)}\right]^2, \tag{4.16}$$

where b_{90} is defined in Eq.(4.12).

Based on the formalism introduced in this paragraph, in the next paragraph the DF accel-

eration term will be derived from the first-order diffusion coefficient of eq. (4.9) based on the calculations on Rosenbluth et al. (1957); Ipser (1977); Binney and Tremaine (2011).

DF correction from the first order diffusion coefficient

Let us consider different populations of particles with masses m, each described by a corresponding phase-space distribution function $f_m(\vec{v})$. The mean rate of change of velocity for a particle of mass M moving at velocity $\vec{V}$, denoted as $D[\Delta V_i]$, is given by the cumulative effect of encounters with all m-mass particles. Following the formalism of Rosenbluth et al. (1957), Eq.(4.9) can be rewritten using the differential scattering cross section as:

$$D[\Delta V_i] = \sum_m \int d^3v' \, f_m(\vec{v}') \int d\Omega \frac{d\sigma(v_0, \theta)}{d\Omega} v_0 \Delta v_i, \tag{4.17}$$

where $\vec{v}_0 = \vec{v} - \vec{V}$ is the relative velocity between the background particle m and the test particle M, and $d\Omega = 2\pi \sin\theta d\theta$ is the solid angle element. Rosenbluth et al. (1957) solved the integral over the angular coordinate in Eq.(4.17) by selecting a convenient reference frame. They defined an orthonormal basis $(\hat{e}'_1, \hat{e}'_2, \hat{e}'_3)$ such that $\vec{v}_0$ lies along $\hat{e}'_1$, i.e., $\vec{v}_0 \cdot \hat{e}'_1 = |\vec{v}_0| \equiv v_0$. Starting from any fixed orthonormal basis $(\hat{e}_1, \hat{e}_2, \hat{e}_3)$ we have then:

$$\hat{e}_i \cdot \hat{e}'_1 = v_{0,i}/v_0. \tag{4.18}$$

where $v_{0,i}$ is the i-th component of $\vec{v}_0$ in the basis $(\hat{e}_1, \hat{e}_2, \hat{e}_3)$.

Denoting with ϕ the angle between the orbital plane and the versor $\hat{e}'_2$, and following the sign convention of Binney and Tremaine (1987) to ensure that the velocity change is positive when the force between the particles is attractive, as in the case of the gravitational force, we can express the change in velocity in the $(\hat{e}'_1, \hat{e}'_2, \hat{e}'_3)$ reference frame as:

$$\Delta\vec{v} = \Delta v_\parallel \hat{e'}_1 + \Delta v_\perp \cos(\phi)\hat{e'}_2 - \Delta v_\perp \sin(\phi)\hat{e'}_3, \tag{4.19}$$

where $\Delta v_\parallel$ and $\Delta v_\perp$ are the parallel and perpendicular components of the velocity change relative to $\vec{v}_0$ (and hence to $\hat{e'}_1$), as introduced in Eq. (4.14) and Eq.(4.13). Furthermore, in the generic reference frame with basis vectors $(\hat{e}_1, \hat{e}_2, \hat{e}_3)$, the components Δv_i can be expressed as:

$$\Delta v_i = (\Delta\vec{v} \cdot \hat{e}'_k)(\hat{e}_i \cdot \hat{e}'_k). \tag{4.20}$$

Assuming that the m-populations are isotropically distributed in space, we can average over the angle ϕ. Since the second and the third terms in Eq. (4.19) vanish upon averaging, combining Eqs. (4.19) and (4.20):

$$\Delta v_i = \Delta v_\parallel (\hat{e}_i \cdot \hat{e}'_1), \tag{4.21}$$

so that Eq. (4.17) becomes

$$D[\Delta V_i] = \sum_m \int dv' f_m(v') \int d\Omega \frac{d\sigma(v_0, \theta)}{d\Omega} v_0 \Delta v_\parallel (\hat{e}_i \cdot \hat{e'}_1) \, . \tag{4.22}$$

Using then Eq. (4.16) and (4.18), the diffusion coefficient can be written as:

$$D[\Delta V_i] = 2\pi \sum_m \int d^3v' f_m(v') \left[\frac{b_{90}}{2}\right]^2 v_0 v_{0_i} \times \int_{\theta_{min}}^{\theta_{max}} \frac{\sin\theta}{\sin^4(\theta/2)}(1-\cos\theta)d\theta. \tag{4.23}$$

In principle, the integration should run over the total solid angle. However, for finite systems we introduced the integration limits $\theta_{min}, \theta_{max}$ that, according to Eq. (4.11) correspond fixing the scattering angle from a maximum and a minimum impact parameter over which the DF has to be evaluated. As for the integral over the angular coordinate, it can be easily solved noting that $\sin^4(\theta/2) = (1-\cos\theta)^2/4$, so that

$$\begin{aligned} \int_{\theta_{min}}^{\theta_{max}} \frac{\sin\theta}{\sin^4(\theta/2)}(1-\cos\theta)d\theta &= \int_{\theta_{min}}^{\theta_{max}} \frac{4\sin\theta}{1-\cos(\theta)}d\theta \\ &= 4\ln(1-\cos\theta)\Big|_{\theta_{min}}^{\theta_{max}} \end{aligned} \tag{4.24}$$

Moreover, from Eq.(4.14):

$$1-\cos\theta = \frac{2}{1+b^2/b_{90}^2} \tag{4.25}$$

Using the results of Eqs. (4.24) and (4.25) and the minimum impact parameter as $b_{min} = b_{90}$ defined in Eq. (4.12):

$$D[\Delta V_i] = 2\pi \sum_m \int d^3v' f_m(v') \frac{G^2(M+m)m}{v_0^3} \ln\left(1+\frac{b_{\max}^2}{b_{90}^2}\right) v_{0_i}. \tag{4.26}$$

Equation (4.26) holds for particle populations of different mass and with different velocity distribution, with no restrictions on the relative mass ratio M/m. Therefore, in Chapter 6 this equation will be adopted as the starting point to derive an additional DF term to be included in simulations, whose gravity solver can not fully account for this effect due to limited resolution.

To understand more clearly the effect of DF force, it is useful to see its impact when some simplifying assumptions are applied. The first hypothesis is that the body of mass M is surrounded by particles having all the same mass, m'. Their velocities v' are distributed according to $f(v')$. In this case, Eq. (4.26) becomes:

$$D[\Delta V_i] = 2\pi G^2(M+m')m' \int d^3v' f_{m'}(v') \frac{1}{v_0^3} \ln\left(1+\frac{b_{\max}^2}{b_{90}^2}\right) v_{0_i}. \tag{4.27}$$

Furthermore, the 90-deflection parameter b_{90} in principle depends on the particle velocity according to Eq. (4.12). However, typically one chooses to associate to the encounters a *typical velocity* of the encounters v_{typ}. For example, a reasonable choice would be to identify the square of the typical velocity of the encounters with the square of velocity dispersion σ^2. Defining Λ as the fraction between the maximum and minimum impact parameters, we then obtain:

$$\Lambda = \frac{b_{\max}}{b_{\min}} = \frac{b_{max}\sigma^2}{G(M+m')}. \tag{4.28}$$

Under this assumption, the logarithmic term appearing in Eq.(4.29) can be put outside the integral:

$$D[\Delta V_i] = 2\pi G^2 (M + m')m' \ln\left(1 + \frac{b_{\max}^2}{b_{90}^2}\right) \int d^3v' f_{m'}(\vec{v'}) \frac{1}{v_0^3} v_{0_i}. \tag{4.29}$$

We further note that:

$$\frac{\partial}{\partial V_i}\frac{1}{v_0} = \frac{v_{0_i}}{v_0^3}\,, \tag{4.30}$$

so that Eq. (4.29) can be rewritten in a more compact form:

$$D[\Delta V_i] = -2\pi G^2 (M + m')m' \ln\left(1 + \Lambda^2\right) \frac{\partial}{\partial V_i} h(\vec{V})\,. \tag{4.31}$$

In the above equation, we have introduced the *Rosenbluth potential*, that takes the expression (Rosenbluth et al. 1957):

$$h(\vec{V}) = \int \frac{f_{m'}(\vec{v'})}{|\vec{V} - \vec{v'}|} d^3\vec{v'}\,. \tag{4.32}$$

In terms of the Legendre polynomials the denominator in the integral in Eq. (4.32) can be cast in the form (Binney and Tremaine 2011, Appendix L):

$$\frac{1}{|\vec{V} - \vec{v'}|} = \sum_{l=0}^{+\infty} P_l(\cos\gamma) \frac{v_<^l}{v_>^{l+1}}\,, \tag{4.33}$$

where γ is the angle between $\vec{V}$ and $\vec{v'}$ while $v_<$ and $v_>$ denote the minimum and maximum value between $|\vec{V}|$ and $|\vec{v'}|$, respectively. Under the additional assumption that the velocity distribution function is isotropic and using Eq. (4.33), the Rosenbluth potential of Eq. (4.32) becomes:

$$h(V) = 2\pi \sum_{l=0}^{+\infty} \int dv' f_{m'}(v') \frac{v_<^l v'^2}{v_>^{l+1}} \int_0^\pi d\gamma P_l(\cos\gamma) \sin\gamma, \tag{4.34}$$

where $h(V)$ depends only on the magnitude of $\vec{V}$. This equation can be further simplified using the following property of the Legendre polynomials:

$$\int_{-1}^{1} dx\ P_l(x) = 2\delta_{0l}\,, \tag{4.35}$$

where δ denotes the Dirac delta function. By adopting this property in the integral over the angle coordinate in Eq. (4.34), one obtains:

$$h(V) = 4\pi \left[\frac{1}{V}\int_0^V dv'\, v'^2 f_{m'}(v') + \int_V^\infty dv'\, v' f_{m'}(v')\right]. \tag{4.36}$$

Finally, noticing that $\partial V/\partial V_i = V_i/V$, then:

$$D[V_i] = \frac{V_i}{V} D[\Delta V_\parallel] \tag{4.37}$$

where $D[\Delta V_\parallel]$ is the average change in velocity acting *parallel* to the initial velocity of the particle M. Then, substituting Eqs. (4.36) and (4.37) in Eq. (4.31) the following expression for the drift

diffusion term is obtained:

$$D[\Delta V_{\parallel}] = -\frac{8\pi^2 G^2 (M+m')m' \ln(1+\Lambda^2)}{v_0^2} \int_0^V dv' v'^2 f_{m'}(v'). \tag{4.38}$$

Therefore, under the assumptions made so far, the first–order diffusion coefficient depends only on the field particles moving *slower* than the test particle M. As pointed out by Binney and Tremaine (2011), this is indeed expected. The Rosenbluth potential $h(\vec{V})$ can be interpreted as the velocity–space analog of the gravitational potential at a position $\vec{x}$ generated by a mass distribution $\rho(\vec{x'})$:

$$\Phi(\vec{x}) = G \int d^3\vec{x}' \, \frac{\rho(\vec{x'})}{|\vec{x} - \vec{x}'|}. \tag{4.39}$$

In this analogy, the velocity distribution function of the field particles, $f_{m'}(\vec{v'})$, plays the role of the mass density $\rho(\vec{x'})$. Furthermore, in the case of a spherically symmetric system, Newton's shell theorem applies. Equation (4.38) should thus be understood as the velocity–space counterpart of Newton's theorem (Binney and Tremaine 2011). Moreover, being the gradient of a potential in velocity space (see Eq. 4.31) the first order diffusion-coefficient can be interpreted simply as an acceleration in velocity space.

This acceleration always acts opposite to the initial velocity of particle M, thereby continuously decelerating it.

When the particle is placed on a circular orbit in a simple system characterized by a deep central potential well, the consequence of this deceleration is a loss of angular momentum. Under these conditions, the orbit shrinks over time, eventually leading to the sinking of the particle toward the center of the gravitational potential. This mechanism constitutes the foundation of the results presented in Chapter 8.

4.1.2 Observational evidence for dual AGN

Much like for the detection of single AGN, also the hunt for dual AGN requires a multiwavelength approach (e.g. Li et al. 2024) to correctly identify and characterize dual AGN candidates. The source selection relies on two complementary methodology: follow-up higher-resolution observation of dual candidates identified in wide-surveys or directly using the data from survey fields (e.g., SDSS in optical, GOALS in mid-IR, COSMOS and Chandra Deep Field-North and South in X-rays). In the optical band, photometric identification of sources—already strongly limited by resolution—must often be followed up with spectroscopic observations, typically searching for double-peaked emission lines ([OIII],Hα, Hβ [SII]) from the NLR (Hennawi et al. 2006; Comerford et al. 2013; del Moral-Castro et al. 2025; Severgnini et al. 2021a; Zheng et al. 2024; Comerford et al. 2018).

Even the spectroscopic identifications suffer from strong limitations in terms of both purity and completeness of the resulting source catalogs. This is because double-peaked features can also arise from bi-conical outflows from a single NLR or rotating disks, demonstrating that this technique is ineffective at finding closely separated dual AGN (Rosario et al. 2011; McGurk et al. 2015; Komossa et al. 2008; XueGuang 2025; Maschmann et al. 2023). Integral field spectroscopy (IFS) combines imaging and spectroscopy by recording a full spectrum at each spatial element within

the field of view, providing both spatially resolved and high-resolution spectral information. This allows one to distinguish between genuine dual AGN (where the double-peaked lines trace orbital motion around two nuclei) and single AGN mimicking this signature (McGurk et al. 2015). Still, optical selection alone can be inconclusive, as it is sensitive to dust attenuation and one of the two AGN may lack an optical counterpart altogether. For this reason, X-ray follow-up observations are often invoked to overcome these limitations.

X-ray observations offer deeper insight into nuclear activity, as extinction and dilution from SF significantly limit the detection of MBH accretion-related signatures in the optical band. Once again, the search for dual AGN candidates is limited by spatial resolution. Even with the exquisite angular resolution of Chandra, on-axis observations translate into ~ 20 pc spatial resolution for sources at redshift $z = 0.001$, ~ 1.8 kpc at $z = 0.1$ and ~ 8 kpc at $z = 1$. XMM has ~ 6 times worse resolution, but acquires larger photon statistics due to its wider effective area (De Rosa et al. 2018). X-ray studies at low redshift have revealed that the dual AGN frequency (Koss et al. 2012) and luminosity increases with decreasing separation (Hou et al. 2020; Satyapal et al. 2014b; Koss et al. 2012; Kocevski et al. 2012) suggesting that mergers can trigger MBH activity.

Moreover, several studies (De Rosa et al. 2018; Ricci et al. 2017; De Rosa et al. 2022) have shown that AGN pairs are often heavily dust-enshrouded, with strong evidence that galaxy mergers can funnel gas and dust into the central regions. This supports the need to explore the IR band when searching for accreting MBHs, especially in merging systems. For instance, Koss et al. (2018) conducted high-resolution IR follow-up observations of X-ray-selected AGN from the Swift/BAT sample. Their study revealed that heavily obscured, luminous AGN ($L_{\rm bol} > 10^{44}$ erg s^{-1}) exhibit a significant excess of late-stage nuclear mergers (with BH separations < 3 kpc) compared to unobscured AGN.

The IR selection turns out to be crucial for the selection of dual AGN candidates: within the IRAS catalogue, the majority of ultraluminous infrared galaxies (ULIRGs) and a significant fraction of luminous infrared galaxies are triggered by galaxy interactions (Sanders et al. 1989; Sanders and Mirabel 1996), with the fraction of ULIRGs and LIRGs hosting an AGN being higher compared to non-AGN systems. Mateos et al. (2017), Satyapal et al. (2014a), and Barrows et al. (2023) demonstrated that the number of AGN identified via IR selection exceeds that found in optical and X-ray matched catalogs, particularly for IR-bright sources. Additionally, Satyapal et al. (2014c) showed that the AGN fraction in merging galaxies increases with decreasing projected separation, again underscoring the importance of IR observations in identifying dual AGN during mergers.

The advent of JWST increased the sensitivity of follow-ups of dual AGN candidates (Ceci et al. 2025; Muñoz et al. 2025) and helped unveil the population at higher redshift (Ishikawa et al. 2025; Perna et al. 2025; Li et al. 2025). Using JWST Near-Infrared Spectrograph Perna et al. (2025) hunted for dual AGN within a sample of 16 pre-identified AGN with X-ray emission $L_{2-10\rm keV} > 10^{44}$erg s^{-1} within $2 < z < 6$. They report the presence of a triple AGN system and four dual AGN having separation within $3 - 28$ kpc, more than doubling the previous number of candidates in the sample and suggesting that there could be more dual AGN than previously expected. The work by Li et al. (2025) further confirms these results, looking at 59 objects and also profiling a fraction of moderate luminosity $L_{\rm bol} \sim 10^{43} - 10^{46}$ obscured AGN, that are two orders of magnitude higher than expected from the X-ray catalog.

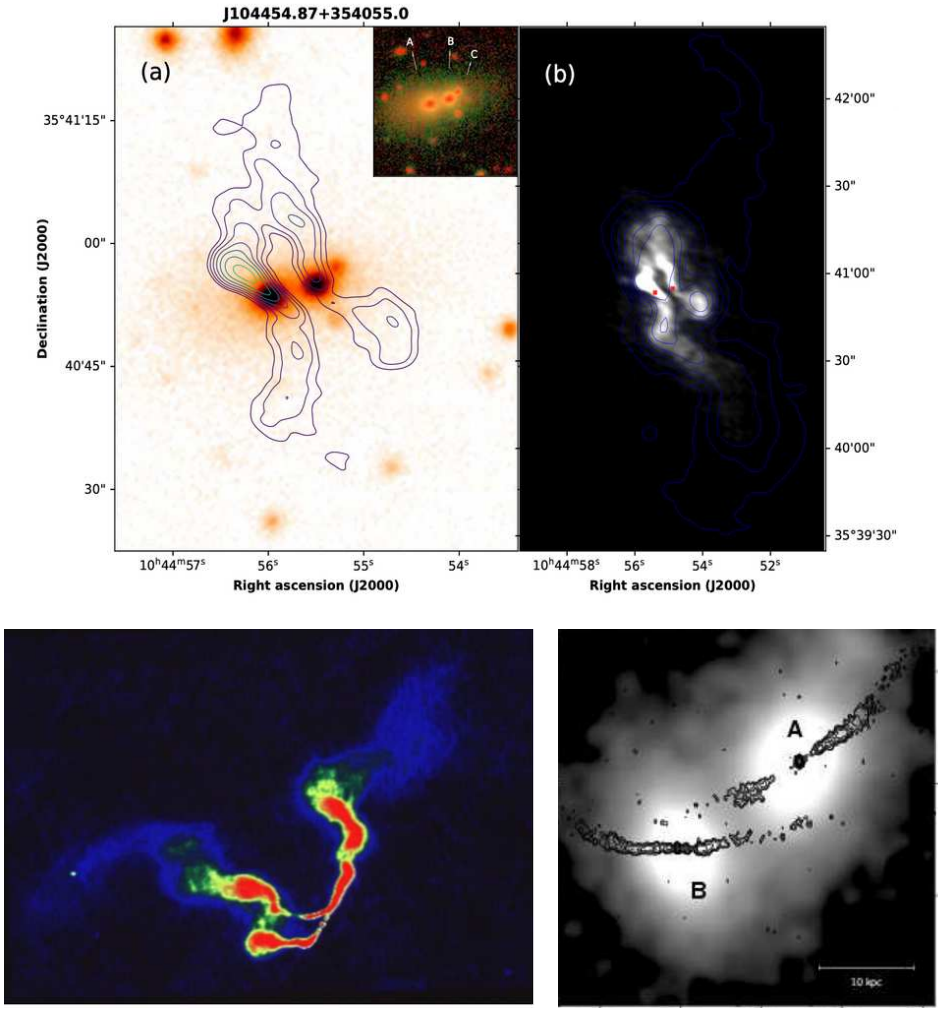

Figure 4.1: *Three different detections of twin radio galaxies. Central top panel displays the detection of a twin radio galaxy by Gopal-Krishna et al. 2022. The central image features an optical (r band)-radio (1.4 GHz, solid contours) overlay of the galaxy pair, with an inset on the right showing the g, r, z band colour-composite image. Bottom left panel displays the first detection of a jet-pair ejection in 3C 75 (Abell 400), as reported by Owen et al. (1985). The bottom right panel highlights the twin jets of* PKS2149 − 158*, showing optical data superimposed with VLA 6 cm radio contours (black), a composite image from Guidetti et al. (2008).*

Even though radio emission is not affected by dust obscuration and can reach relatively high-resolution to resolve pairs with linear separation as small as about 1 pc in the local Universe, the population of radio-emittering dual AGN is quite sparse ($< 10\%$, Ivezić et al. 2002). Moreover, the narrow field of view of radio observations limits their use for the *blind* detection of dual sources. As a result, radio emission is typically investigated only after candidates have been identified at other wavelengths. For instance, Balmaverde et al. (2018) detected a double knot in the [OIII] (MUSE) emission of 3C459 FRII radio galaxy. The center of one knot coincides with the radio core, while the second knot seems to be a second heavily obscured AGN which is undetected in the IR and Chandra observations, but visible by MUSE. The detection of two radio galaxies with kiloparsec-scale jets (so-called "Twin Radio Galaxies") is extremely rare and only few examples of those objects have been observed. The top central panel of Fig.4.1 displays the recent detection of a twin radio galaxy by Gopal-Krishna et al. (2022) with an optical (r band)-radio (1.4 GHz, solid contours) overlay of the galaxy pairs on the left side, and an inset showing the $g-, r-, z-$ band colour-composite image on the right side. The left side shows the corresponding 144 GHz image. Bottom left plot shows the first detection of a jet-pair ejection in 3C75 from Owen et al. (1985), associated with the binary nucleus of Abell400. Bottom right panel shows the twin jets emitted by PKS 2149-158, displaying the superposition of optical and radio VLA 6 cm (black contours) observations (Parma et al. 1991; Guidetti et al. 2008) from Guidetti et al. (2008).

Finally, an original recent method for the detection of dual AGN candidates is the identification of their *astrometric variability*. This technique involves the detection of astrometric shift of the photocenter of an AGN measured at different epochs, leveraging the positional accuracy of the *Gaia* satellite (Liu 2015) and has now led to the identification of thousands of quasar pair candidates (Chen et al. 2025) to be confirmed with spectroscopic or multi-wavelength follow-ups. The radio follow-up with VLA performed by Schwartzman et al. (2024) confirmed almost half of the previous vastrometric selected sample as dual AGN, assessing the strong potential of this method. Moreover, another emerging successful technique for the detection of dual AGN and even AGN at sub-parsec separation is the *Gaia Multi-Peak* (GMP, Mannucci et al. 2022) technique, consisting in the detection of multi-peaked object in the *Gaia* data relases (**?**Wu et al. 2024).

4.2 From parsec scale to the BH coalescence

As the MBH binary system approaches the sub-parsec separation, the surrounding stellar density typically becomes too low to sustain efficient angular momentum loss via DF. At this stage, other mechanisms must take over to further shrink the binary down to milli-parsec scales, where GW emission becomes the dominant driver of orbital decay, ultimately leading to coalescence. The efficiency of this binary shrinkage phase depends sensitively on the structural properties of the merger remnant nucleus—such as its density profile and geometry—as well as on the abundance and thermodynamical state of the gas. In this section, we review the theoretical pathways that can lead MBH binaries from parsec to milli-parsec separations and discuss their observable implications. We first consider gas-poor galactic nuclei, where binary evolution is governed primarily by stellar dynamical processes. We then turn to gas-rich environments, where interactions with circumnuclear discs and gaseous inflows can strongly influence the orbital evolution of the binary. Finally, we discuss the current observational electromagnetic signatures of MBH binaries

across different evolutionary stages.

4.2.1 Theoretical predictions

Gas-poor mergers

Following a galaxy merger, the DF force efficiently brings the two MBH together until they form a gravitationally bound pair. This occurs when the when the semi-major axis shrinks to a value $a_{\rm hard}$ (Quinlan 1996; Yu 2002; Milosavljević and Merritt 2001; Colpi 2014; Makino and Funato 2004; Mikkola and Valtonen 1992), given by the *hard binary separation*:

$$a_{\rm hard} \sim \frac{G\mu}{3\sigma_*^2}\,. \tag{4.40}$$

Here μ is the reduced mass of the binary and σ_* is the stellar velocity dispersion. For two BHs of equal mass of $10^7\ M_\odot$, $a_{\rm hard}$ is about one parsec. At this separation, stars that impinge on the binary's orbit can be expelled with velocities comparable to the binary's orbital velocity. The loss of angular momentum will continue via interactions with and ejection of nearby stars, in a process called stellar hardening. In these collisions, stars are ejected with average velocity v_* comparable to the binary orbital velocity:

$$v_* = \sqrt{\frac{G(M_1+M_2)}{a}} \gg \sigma_*. \tag{4.41}$$

These stellar interactions transfer orbital energy from the binary to the stars, causing the binary's orbit to decay (Colpi 2014). The efficiency of the binary hardening in gas-poor nuclei depends on the host nucleus geometry and density profile. Early numerical simulations by Milosavljević and Merritt (2001) show that after a rapid initial depletion of the *loss cone*–the region of phase space corresponding to orbits with sufficiently low angular momentum to undergo strong interactions with the binary–the binary shrinks typically only by a factor of a few (~ 5) $a_{\rm hard}$ (Milosavljević and Merritt 2003). Because the remaining stellar mass available for interaction is $\lesssim \mu$, once this supply is exhausted the binary may still be more than an order of magnitude wider than the separation required for gravitational-wave–driven coalescence within a Hubble time. In such cases, the binary's evolution can stall, leading to the so-called "final parsec problem" (Milosavljević and Merritt 2003; Quinlan and Hernquist 1997; Roos 1981; Valtonen 1996; Gould and Rix 2000; Yu 2002). However, recent high-resolution simulations and the consideration of non-spherical galactic geometries suggest that this 'bottleneck' may be more numerical than physical. The key issue is whether stars can be continuously supplied to the loss cone. Any mechanism that efficiently replenishes this reservoir enhances the stellar scattering rate and sustains binary hardening. In gas-poor galaxies, loss-cone refilling proceeds through two conceptually distinct channels: collisional and collisionless processes. In spherical systems, refilling proceeds via the collisional two-body relaxation (see later Box 5.1). Stellar encounters gradually diffuse angular momentum, scattering stars onto low-angular-momentum orbits that intersect the binary. However, for most galactic nuclei the relaxation time exceeds the Hubble time and therefore in spherical system the collisional loss-cone refilling is inefficient and a long-term stalling is expected. In N-body simulations (see Sect. 5.6) the collisionless fluid is sampled by discrete N particles, the relaxation time scales as $N/\log N$, leading to a *spurious* numerical refilling of the loss cone if the systems are described by

less star particles than the true number of stars (Milosavljević and Merritt 2001; Milosavljević and Merritt 2003; Gualandris and Merritt 2007). In non-spherical galaxies, the collisionless refilling of the loss cone is significantly more efficient due to the torque exerted by the non-spherical potential. Since angular momentum is not conserved, in axisymmetric systems particles can reach much smaller radii, while in triaxial systems they can be placed on centrophilic orbits that naturally bring them close to the center (Yu 2002; Merritt and Poon 2004; Holley-Bockelmann et al. 2002). As a result, a substantially larger fraction of stars contributes to the replenishment of the loss cone (Gualandris et al. 2017). The first simulations following the binary shrinking from the merger of the host galaxies showed that the merger remnant showed significant triaxiality (e.g. Barnes and Hernquist 1992; Berczik et al. 2006; Khan et al. 2011; Preto et al. 2011; Khan et al. 2012; Gualandris and Merritt 2011), with a rate of binary evolution weakly dependent on the number of particles sampling the system, suggesting that the collisionless loss-cone refilling due to asymmetric potential can naturally solve the final parsec problem. Carrying out direct N-body integrations of binary evolution in spherical, axisymmetric and triaxial galaxies sampled with $N \leq 10^6$ particles, Vasiliev et al. (2015) showed not only that the binary hardening rate was dependent on N, but the contribution of nonspherical torques to the rate of loss-cone repopulation was found to be below or comparable to the contribution from collisional effects. This is at odds with the work by Khan et al. (2013), and the subsequent work by Vasiliev et al. (2015) who developed a Monte Carlo galaxy model where stars move in a smooth gravitational potential and two-body relaxation can be tuned—or even turned off entirely—to isolate purely collisionless dynamics. They found that in the collisionless limit, triaxial galaxies naturally keep feeding stars into the binary's loss cone so the BHs merge within a Hubble time. The high-resolution reached by the N-body simulations implying direct summation of Gualandris et al. (2017) showed that in spherical galaxies the binary hardening rate strongly depends on particle number N, as expected if collisional relaxation drives the evolution, while in triaxial galaxies the hardening rate becomes independent of N above about five million particles—indicating a collisionless mechanism. Even mildly triaxial systems efficiently refill the loss cone and push binaries into the gravitational-wave regime, leading them to conclude that there is no final-parsec problem in gas-free galaxies because triaxiality alone sustains binary evolution.

Another proposed mechanism for the binary to lose angular momentum is the arrival of a third intruder MBH, which forms a hierarchical triple system. Gravitational "slingshot" effects involving the intruder modify the binary's binding energy and can lead to the recoil of the binary itself (Volonteri et al. 2003). Through extensive simulations of triple system orbital parameters, Bonetti et al. (2018) determined that $20 - 30\%$ of MBH binaries that would otherwise stall can be driven to coalescence by the influence of a third MBH. Interestingly, Hoffman and Loeb (2007) found that the lightest BH in the triplet may be ejected from the system, potentially wandering into the galactic halo or being expelled entirely. This mechanism is crucial as it predicts the formation of a population of wandering BHs off-centered from the galactic core, a topic particularly relevant for this Thesis and detailed further in a dedicated Section (Sect. 4.3).

Gas-rich mergers

Wet galaxy mergers are expected to channel large amounts of gas toward the center of the merger remnant. As gas flows down to parsec scales, it can settle into a circumbinary disc surrounding the MBH binary (e.g. Mihos and Hernquist 1995; Barnes and Hernquist 1996; Escala et al. 2004; Mayer et al. 2007). Once formed, the disc interacts with the binary via gravitational torques — primarily mediated by outer Lindblad resonances — driving an exchange of angular momentum between the binary and the surrounding gas (Goldreich and Tremaine 1979; Papaloizou and Pringle 1977; Artymowicz and Lubow 1994, 1996; Begelman et al. 1980). The efficiency of this exchange depends sensitively on the physical properties of the disc, including its viscosity, thickness, and thermodynamic structure.

If the resonant torques are sufficiently strong, they can overcome viscous inflow and truncate the inner disc, ultimately carving out a hollow around the binary (Lin and Papaloizou 1979; Milosavljević and Phinney 2005; MacFadyen and Milosavljević 2008) having a typical inner edge of a few times the binary separation for nearly equal-mass systems (Artymowicz and Lubow, 1996). The subsequent evolution of the binary is then governed by how efficiently angular momentum is transported between the binary and the outer disc.

Early analytical studies found that resonant torques at the inner edge of the disc lead to a net transfer of angular momentum from the binary to the disc, causing the binary to shrink (Papaloizou and Pringle 1977; Goldreich and Tremaine 1979; Armitage and Natarajan 2002; Liu et al. 2003). However, later numerical simulations outlined a more complex picture. Even in the presence of a cavity, gas can stream across the gap and accrete onto the BHs (Artymowicz and Lubow 1996; Escala et al. 2005; Cuadra et al. 2009; Roedig et al. 2011; Shi et al. 2012; D'Orazio et al. 2013; Farris et al. 2014; Günther and Kley 2002), implying that disc truncation does not necessarily halt mass inflow.

To characterize the relative importance of tidal torques over viscous transport, Nixon and Pringle 2021 introduced the parameter f, defined as the ratio of the outward viscous angular momentum flux at the disc inner edge to the inward advected flux there. When $f \gg 1$, resonant torques dominate and the disc is efficiently truncated. If viscous and resonant torques are comparable, a non-axisymmetric cavity forms and the binary is fed by time-dependent accretion streams (Artymowicz and Lubow 1996). In contrast, for sufficiently high viscosity — corresponding to thicker discs — resonances may fail to halt accretion, allowing gas to flow inward relatively unimpeded ($f \ll 1$).

The long-term orbital evolution of the binary depends critically on these disc properties. Two-dimensional simulations have suggested that the net angular momentum transferred from the disc to the binary per unit mass accreted can be positive, potentially driving binary expansion (Muñoz et al. 2019, 2020; Duffell et al. 2020; Moody et al. 2019). Tiede et al. (2020) and Heath and Nixon (2020) detailed how the binary shrinkage is sensitive to the disk thickness. Including additional physical effects in the context of three-dimensional hydrodynamical simulations further enriches the picture. For instance, Franchini et al. (2021) demonstrated that sufficiently massive, self-gravitating circumbinary discs can induce binary shrinkage, consistent with earlier studies (e.g., Cuadra et al. 2009; Roedig et al. 2011). Colder and thinner discs tend to suppress gas inflow into the cavity more efficiently, enhancing binary hardening. Binary shrinkage has also been reported

in simulations of eccentric systems and in models incorporating non-isothermal thermodynamics, radiation pressure effects, binary eccentricity and different alignments between the binary and the disk (e.g. Dittmann et al. 2024; Chen et al. 2026; Cocchiararo et al. 2025). An important consequence of the disc-binary interactions is the possible time-dependent modulation of gas inflow that may produce characteristic electromagnetic variability (e.g., Franchini et al. 2024), providing a potential observational signature of MBH binaries. This brings us to the next section, where the observational signatures of MBH binaries within sub-pc scales are reviewed.

4.2.2 Observational implications for binary MBHs

Reaching the high spatial sensitivity requested to resolve SMBH at sub-parsec separation is only feasible with radio observations. However, photometric and spectroscopic techniques have also been used to infer the presence of a binary BH system, mostly aiming to detect any time-dependent variability. Indeed, If one of the two companion BHs is active, time-dependent velocity shift of the BLR emission during multi-epoch spectroscopic observations can be an indicator of the orbital motion of the BH in a binary system (e.g. Tsalmantza et al. 2011; Decarli et al. 2013; Guo et al. 2019). If both BHs involved in a binary system are active, their presence may be indicated by double-peaked emission lines from the NLR (e.g. Severgnini et al. 2021b) or by velocity-shifted features in the emission lines originating from each BH (Zheng et al. 2024; Chen et al. 2025). However, such distinct double-peaked profiles typically emerge only during a specific phase of binary evolution–when the BHs are close enough that their relative line-of-sight orbital velocity exceeds the FWHM of the individual broad emission components–yet their BLR remain largely separate.

At earlier stages, the orbital velocity difference is too small to clearly distinguish the emission from each BLR, generally resulting in asymmetric broad-line profiles. As the binary evolves further and the two BLRs begin to merge, the emission-line profiles become increasingly complex, and any observed peak splitting no longer reliably traces the binary's orbital motion (Shen and Loeb 2010). Moreover, both double-peaked emission lines and their variability can also be explained by alternative scenarios, such as emission from gas in the outer regions of a single accretion disk (Gezari et al. 2007; XueGuang 2025; Ridley et al. 2024; Ward et al. 2024).

Galaxy mergers can funnel gas into the central region of the post-merger galaxies hosting the MBH binary (e.g. Casey-Clyde et al. 2025). Therefore, the net accretion rate onto the MBHs is significant and can fuel quasar-like luminosity. Photometric observations can capture periodic modulation of the luminosity originating either from fluctuations in the accretion flows (Graham et al. 2015) and relativistic Doppler-boost from highly compact binaries having orbital velocity reaching few percent of the light speed (D'Orazio et al. 2015). Ground-based surveys [1] can now provide light curves spanning over ~ 20 years and more than one thousand photometric measurement per object. Huijse et al. (2025) recently leveraged the astrometric variability with Gaia mentioned in Sect. 4.1.2 to select over ~ 180 binary BH candidates.

Also periodic X-ray variability can serve as a method to identify MBH binary candidates

[1] Such as the Catarina Time Transient Survey (Djorgovski et al. 2011), the Palomar Transient Factory (Law et al. 2009), the Panoramic Survey Telescope and Rapid Response System (Bolden and Kervin 2010) and the Zwicky Transient Facility (Bellm et al. 2019)

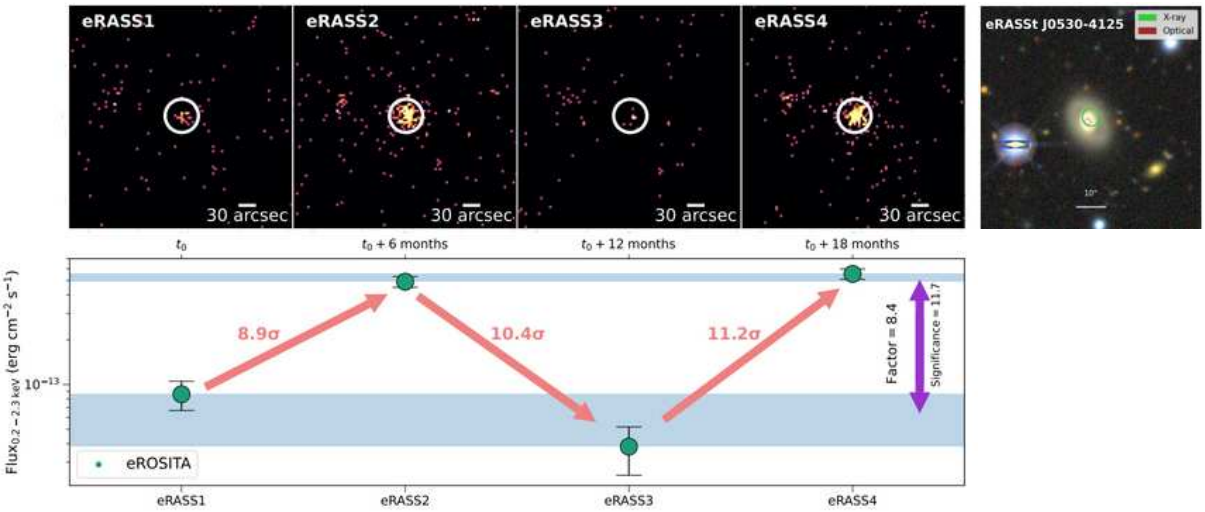

Figure 4.2: *Visualization of a SMBH candidate (J0530-4125) from Tubín-Arenas et al. (2025). Top panels: number counts for each eRosita scan at the location of the source. The rightmost panel shows the optical Legacy Survey Viewer (Dey et al. 2019) image of the source. The red diamond and the green circle represents the optical (Gaia) and X-ray (eRosita) selected centers. Bottom panel: flux variability of the source in the X-ray band over 18 months of observation.*

with periodically modulated accretion. Their X-ray and UV light curves are expected to vary regularly with periods comparable to that of the binary (Bowen et al. 2018, 2019). Although hard X-ray systematic searches for periodic variability performed with the Swift/BAT survey led to inconclusive results (Serafinelli et al. 2020; Liu et al. 2020), recently Tubín-Arenas et al. 2025 selected 16 suitable SMBH binary candidates with the Spectrum-Roetgen-Gamma (Sunyaev et al. 2021)/eRosita all sky survey (Predehl et al. 2021) combined with optical spectroscopy. Figure 4.2 shows the variability and optical counterpart of J0530-4125, one of the selected SMBH candidates by Tubín-Arenas et al. (2025). The top panel presents the observed X-ray photon counts from the eROSITA survey across four consecutive 6-month observation periods. The rightmost panel panel overlays the optical image from the Legacy Survey Viewer (Dey et al. 2019). The red diamond marks the optical center as identified by Gaia, while the green circle indicates the location of the X-ray emission detected by eROSITA. The bottom panel displays the flux variability of the source, corresponding to the number counts shown in the top panel.

As mentioned at the beginning of this section, radio observations through VLBI is the only method offering the milli-arcsecond resolution required for the imaging of sub-parsec separated MBH binaries. For instance, Khan et al. (2013) reported the detection of two compact radio components separated by 0.35 pc in the luminous infrared galaxy NCG7674.

The most extensively studied and arguably one of the strongest candidates for hosting a SMBH binary is OJ 287 (see Komossa et al. 2021; Dey et al. 2019 for reviews). This system exemplifies the power of multi-wavelength synergy in the identification of SMBH binary candidates. Its optical light curve exhibits periodic outbursts approximately every 12 years (Kidger et al. 1992; Shi and Liu 2007), and successful modeling of the system dynamics suggests the presence of two SMBHs with masses of $1.8 \cdot 10^{10} M_\odot$ and $1.5 \cdot 10^{8} M_\odot$ (Valtonen et al. 2012) whose orbits has a semi-major

axis of 0.45 pc. OJ 287 is also known for its extreme activity across multiple wavelengths, showing optical, X-ray, and UV outbursts on various timescales (Sillanpaa et al. 1996; Kidger et al. 1992; Prince et al. 2021; Zhang et al. 2025; Fan et al. 2010; Wang et al. 2025). According to the widely accepted model proposed by Lehto and Valtonen (1996)–though alternative interpretations have been suggested (e.g., Zwick and Mayer 2023)–these outbursts are caused by the secondary, less massive BH periodically impacting the accretion disk of the primary during its orbit.

4.3 Off-center AGN: predictions and observations

One of the consequences of the dynamical processes described in this section is the possibility for some BHs to remain displaced from the centers of their host galaxies. The offset may originate from different mechanism, such as GW recoil and three-body interactions. In fact, following a SMBH merger, the asymmetric emission of GW during coalescence imparts momentum to the merged BH, eventually ejecting it from the central potential well and causing it to wander in the galaxy halo (i.e Gualandris and Merritt 2007; Volonteri 2007; Campanelli et al. 2007; Loeb 2007). Furthermore, during a multi-body interaction between BHs, gravitational slingshot effects can eject one of the BHs or displace it from the center.

As the BH is displaced by several kiloparsecs, the timescale required for it to sink back to the galactic core depends on the DF force. The DF-driven sinking timescale varies with the BH mass and the shape of the galaxy's potential. DF can be highly inefficient in clumpy, disturbed, or shallow potentials, such as those typical of dwarf galaxies.

Recent observational works provide evidence for the existence of off-nuclear BHs in dwarf galaxies. Among them, Reines et al. (2020) identified spatially offset radio sources in ~ 40 dwarf galaxies using VLA observations. These galaxies also show signatures of recent interactions or mergers. This sample was significantly expanded by Barrows et al. (2025), who reported 328 VLA radio sources offset from the optical centers of SDSS host galaxies. After excluding sources likely associated with radio jets (which may appear offset but still originate from a central BH), they found that such offsets are more common in galaxy cluster environments, possibly due to the higher rates of mergers and interactions. These interactions typically involve the central galaxy and one of the satellites, rather than satellite–satellite encounters, because the relative velocities between satellites are generally too high to allow efficient interactions (see also the discussion in Section 10.4).

Using integral field spectroscopy from the SDSS–MaNGA survey, Mezcua and Domínguez Sánchez (2020) found that a large fraction of AGN-related emission in dwarf galaxies is spatially offset from the optical core. Their follow-up work (Mezcua and Domínguez Sánchez 2024) confirmed and extended these results, reporting spatially offset BHs in $\sim 62\%$ of their expanded dwarf galaxy sample.

At higher redshift, Spingola and Barnacka (2020) reported a candidate off-nuclear BH at $z = 1.4$ in a strongly lensed merging galaxy system. The BH was identified through a combination of VLBI and HST imaging.

In the context of recoiling BHs and those displaced via three-body interactions, several studies have reported positional offsets between AGN emission and the optical centers of galaxies, interpreted as evidence for off-center BHs (Kim et al. 2018, 2022; Jadhav et al. 2021; Hogg et al. 2021;

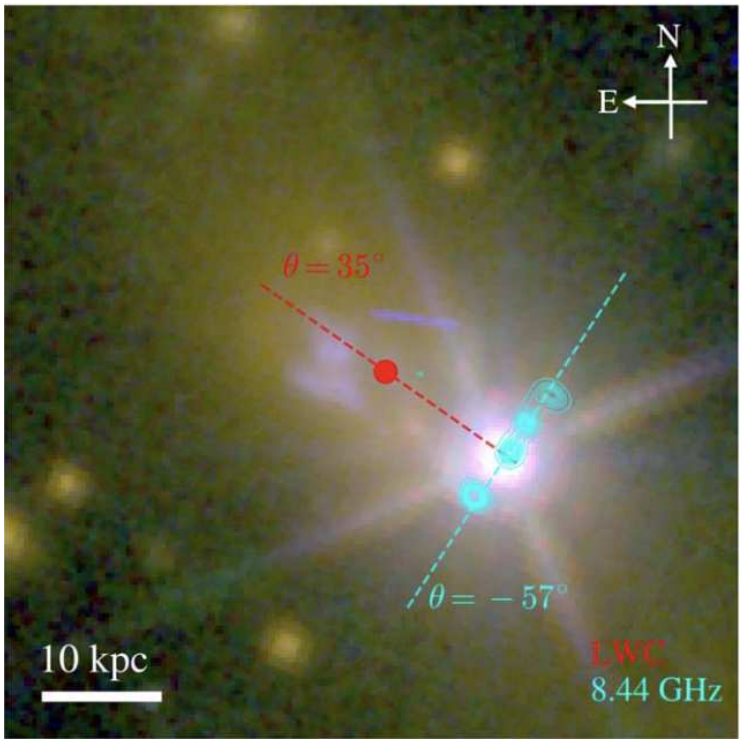

Figure 4.3: *3C186 HST image from Morishita et al. (2022). The light-weighted center is overlaid as a red dot and 8.44 GHz radio emission from VLA data are marked via cyan contours. Dashed lines indicate the directions of the inferred spatial offset (red) and radio jet (cyan).*

Ward et al. 2021). Notably, Kim et al. (2018) and Ward et al. (2021) observed velocity shifts and oscillatory patterns in AGN, suggestive of BHs orbiting within the galaxy potential after being displaced.

A particularly compelling case is 3C186, a promising recoiling SMBH candidate located in a galaxy cluster at $z = 1.0685$ (Chiaberge et al. 2018; Boschini et al. 2024; Morishita et al. 2022). Chiaberge et al. (2018) reported a spatial offset of ~ 11 kpc between the quasar and the host galaxy center, along with a significant velocity offset of $\sim 2140\,\mathrm{km\,s^{-1}}$ in the broad emission lines compared to the NLR, consistent with predictions for a gravitationally recoiling SMBH. Figure 4.3, from Morishita et al. (2022), illustrates the spatial offset and radio jet orientation of 3C 186. The light-weighted center of the host galaxy is marked with a red dot, along with the 8.44 GHz radio emission in cyan, highlighting the positional displacement between the AGN and the stellar component.

4.4 Conclusions

In this Chapter, the theoretical background and observational evidences for the mechanism driving the dynamical evolution of MBH and AGN, spanning spatial scales ranging from tenths of kiloparsec down to the sub-parsec, have been presented. These systems probe different physical regimes: at large separations, orbital decay is governed by galaxy interactions, DF, and the global potential of the host, while at sub-kpc scales the dynamics become increasingly sensitive to local gas inflows, stellar scattering, and the structure of the nuclear environment. Observations of

spatially offset AGN, wandering BHs, and dual AGN candidates are increasingly offering valuable constraints on the strength and variability of DF in real galactic environments.

These findings naturally highlight the urgency of properly modelling DF in cosmological simulations. In the next chapters, the numerical framework of simulations will be presented, discussing the technical challenges arising from limited resolution. When the resolution is insufficient to resolve the physical scales on which DF operates, the description of BH dynamics can be incorrect altering significantly the demographics of dual and binary AGN. This will motivate the introduction of an improvement of the sub-resolution prescriptions adopted to correct for the unresolved DF in large-scale cosmological simulations.

Part II

Methodology

Chapter 5

Numerical methods for cosmological simulations

Cosmological simulations serve as cosmic laboratories where the highly non-linear processes driving galaxy formation and evolution can be experimented with. From the very first inclusion of BHs in such simulations (Springel et al. 2005; Di Matteo et al. 2008; Somerville 2008), it became evident that AGN could act as "cosmic regulators", shaping the SF history, dynamical state, and structural evolution of galaxies. Since then, significant computational effort has been devoted to refining BH modeling both in idealized galaxy-scale simulations (e.g., Hopkins et al. 2005; Capelo et al. 2015; DeBuhr et al. 2011; Johansson et al. 2009; Callegari et al. 2009, 2011; Colpi et al. 2009; Park et al. 2017, see also Vogelsberger et al. 2020 for a review) and large-scale cosmological simulations aiming to constrain the statistical properties and evolution of the BH population (Sijacki et al. 2007; Hirschmann et al. 2014; Dubois et al. 2016; Micic et al. 2007; Booth and Schaye 2009; Steinborn et al. 2015; Volonteri et al. 2016a, see Talbot et al. 2024; Sala et al. 2024; Kao et al. 2025 for more recent works).

As discussed in the previous chapters, the BH accretion and the ensuing feedback processes take place in the immediate vicinity of the BH, on sub-parsec scales. However, their effects can propagate over hundreds of kiloparsecs, influencing the large-scale structure of galaxies and their environments. Capturing such a vast dynamic range in spatial scales remains computationally unfeasible with current resources. Therefore, processes occurring below the resolution limit – such as AGN accretion and feedback, as well as star formation and stellar evolution – are modeled through *sub-resolution* prescriptions, phenomenological models used to mimic the effects of unresolved processes on the resolved scales.

The numerical modeling of BHs in cosmological simulations and their role in structure evolution constitutes the core of this Thesis, as new models–particularly focused on BH dynamics–will be introduced, along with an analysis of their interplay with other physical processes in shaping the statistical properties of galaxies, galaxy groups, and clusters. These developments are implemented within the OpenGADGET3 code (Dolag et al., in prep.). The aim of this chapter is to introduce the code methodology used to model the collisionless (Sect. 5.1) and collisional (Sect. 5.2) components, as well as the sub-resolution prescriptions for star formation, evolution, and feedback (Sect. 5.3), and for AGN accretion and feedback (Sect. 5.4). Given their particular relevance for this Thesis, the dynamical evolution of BHs in the simulations will be described in detail in the next chapter.

5.1 Collisionless dynamics

In cosmological simulations, the components describing DM, stars, and massive BHs are evolved under the influence of gravity alone and are treated as collisionless. This means that angular deflections arising from individual particle encounters do not significantly alter their orbits. The validity of this approximation can be assessed by estimating the two-body relaxation time of the system. As an application of the concepts introduced in Sect. 4.1.1, the two-body relaxation process is briefly discussed in Box 5.1. Subsequently, the numerical techniques employed to integrate the equations of motion will be presented, starting from direct N-body methods (Sect. 5.1.1) and then focusing on the gravity solvers implemented in OpenGADGET3 (Sect. 5.1.3, 5.1.2, and 5.1.4).

According to the ΛCDM model, the Universe is dominated by cold DM, which can be described as a collisionless non-relativistic fluid of particles of mass m under the influence of a gravitational field with collective potential Φ. In an expanding background characterized by the scale factor $a(t)$, the comoving coordinates of the particles $\vec{x}(t)$ are related to the physical ones by:

$$\vec{r}(t) = \vec{x}(t)a(t) \tag{5.1}$$

and the momentum conjugate to $\vec{x}(t)$ is defined as:

$$\vec{p} = ma^2(t)\dot{\vec{x}}(t). \tag{5.2}$$

In a collisionless fluid, the mean free path of individual particles is much larger than the characteristic size of the system, meaning that encounters between particles are so rare that their cumulative effect can be neglected. Instead, the system's dynamics can be described statistically through a distribution function $f(\vec{x}, \vec{p}, t)$ such that the number of particles dN within the phase-space volume centered in $(\vec{x}, \vec{p})$ having length $(d^3\vec{x}, d^3\vec{p})$ is:

$$dN = f(\vec{x}, \vec{p}, t)d^3\vec{x}d^3\vec{p}. \tag{5.3}$$

The evolution of the phase-space distribution function is then determined by the comoving collisionless Boltzmann equation, also known as the Vlasov equation:

$$\frac{\partial f}{\partial t} + \frac{\vec{p}}{ma^2}\vec{\nabla} f - m\vec{\nabla}\Phi \cdot \frac{\partial f}{\partial \vec{p}} = 0, \tag{5.4}$$

which corresponds to Eq. (4.1) by neglecting the collisional term. The Vlasof equation must be then coupled with the Poisson equation, describing the evolution of the potential:

$$\nabla^2\Phi(\vec{x}, t) = 4\pi G\, a^2(t)\, \delta\rho(\vec{x}, t) \tag{5.5}$$

where $\delta\rho(\vec{x}, t)$ is the *density fluctuation* describing the difference between the mass density $\rho(\vec{x}, t)$ and the background density $\bar{\rho}(t)$ obtained by averaging over a sufficiently large (representative) volume of the Universe. Eqs. (5.4) and (5.5) define a six-dimensional problem in phase-space.

Due to such a high dimensionality, a numerical approach to solve these equations, the $N-body$ technique, consists of splitting the phase-space into domains and following the orbits of these *pseudoparticles* (e.g. Yepes, 1997).

For instance, consider an initial volume V characterized by an average density $\bar{\rho}(t)$. This volume can be divided into n pseudoparticles, each assigned a mass

$$M = \bar{\rho}(t)\,\frac{V}{n},$$

which defines the *mass resolution* of the simulation. In velocity space, the Zel'dovich approximation is used to assign initial velocities to the (cold) particles, based on their displacement field. The dynamical evolution of the pseudoparticles is then determined by integrating the following equations for their comoving phase-space coordinates $(\vec{x}_i, \vec{p}_i)$:

$$\frac{d\vec{p}_i}{da} = \frac{\vec{\nabla}\Phi}{a} \quad ; \quad \frac{d\vec{x}_i}{da} = \frac{\vec{p}_i}{\dot{a}a} \tag{5.6}$$

where the index i denotes the i-th of the n pseudoparticles.

Throughout this work, we will refer to these *pseudoparticles* simply as *particles*, keeping in mind that they in fact represent a discrete sampling of a continuous collisionless fluid.

In principle, the potential $\Phi(\vec{x}_i)$ at the position of the i-th particle is generated by all other particles in the system. Once cast in a discretised form, the gravitational dynamical equation for the N-body system can be evolved using either particle-based or grid-based approaches. In particle-based methods, the equations of motion are directly integrated for each particle representing the system. The gravitational force acting on a particle can be computed either by summing the contributions from all other particles (direct N-body methods) or by employing a hierarchical decomposition of space, in which the particle distribution is recursively divided into cells of decreasing size—an approach adopted by Tree algorithms. Examples of codes adopting a pure Tree as the gravitational solver are earliest version of GADGET (Springel et al. 2001), 2HOT (Warren 2013) or ChaNGa (Menon et al. 2014). Alternatively, in grid-based methods, particles are interpolated onto a mesh, and the gravitational potential is obtained by solving the Poisson equation on the grid. This is typically done through a convolution with the Green's function in Fourier space, as in particle–mesh (PM) schemes. The adaptive mesh refinement (AMR) technique, adopted for instance in ENZO (Bryan et al. 2014) and RAMSES (Teyssier 2010) builds upon this framework by starting from a coarse PM grid and iteratively refining the cells in regions of high particle density, thereby enhancing spatial resolution where needed. These two approaches can also be combined into hybrid methods, such as TreePM codes, which use a PM scheme to compute long-range forces and a Tree algorithm to resolve short-range interactions efficiently. Within the next subsections, together with a discussion of the direct N-body method (Sect. 5.1.1), we will introduce both the Tree and PM technique, which constitute the backbone of the collisionless hybrid TreePM gravity solver in OpenGADGET3.

Box 5.1: Two-body relaxation

The importance of collisionality in a system can be estimated by comparing two quantities: the crossing time and the *relaxation time*. As the DF in simulations is a consequence of the

collisionality, it is useful to derive the expression for these time scales. For a comprehensive discussion, the reader is referred, for instance, to Binney and Tremaine (1987).

Let us consider a stellar system composed of N stars, each of mass m, and let R denote the characteristic size of the system. Then, the number density of stars is approximately $n \sim N/R^3$ while the total mass is $M = Nm$. During each two-body encounter, the stellar velocity is deflected according to Eqs.(4.14) and (4.13). Considering deflections in the perpendicular direction, if the typical impact parameter is $b \gg b_{90}$, the velocity change can be approximated as:

$$\Delta v_\perp = \frac{2Gm}{bv}\,, \tag{5.7}$$

where v is the magnitude of the initial relative velocity between the stars.

Assuming that the system is isotropic, since successive encounters are randomly oriented and uncorrelated, the velocity perturbations add in quadrature and therefore $(\Delta v_\perp)^2$ increases over time. The rate of increase of the mean square perpendicular velocity due to encounters ranging from minimum and maximum impact parameters $b_{\rm min}$ and $b_{\rm max}$, is then:

$$\frac{d}{dt}(\Delta v_\perp)^2 \sim \int_{b_{\rm min}}^{b_{\rm max}} (\delta v_\perp)_1^2\, nv\, 2\pi b\, db \sim \frac{8\pi G^2 m^2 n}{v} \ln\left(\frac{b_{\rm max}}{b_{\rm min}}\right). \tag{5.8}$$

The *two-body relaxation time* is defined as

$$t_{\rm R} = \frac{v^2}{\frac{d}{dt}(\Delta v_\perp)^2} = \frac{v^3}{8\pi G^2 m^2 n \ln(b_{\rm max}/b_{\rm min})}, \tag{5.9}$$

and measures the characteristic time over which gravitational encounters significantly perturb stellar orbits.

A simple estimate for the characteristic stellar velocity can be obtained from the virial theorem:

$$v^2 \sim \frac{GM}{R} \sim GmnR^2, \tag{5.10}$$

where $M = Nm$ is the total mass of the system and $n \sim N/R^3$ its number density. The corresponding *crossing time* is

$$t_{\rm cr} \sim \frac{R}{v} \sim \frac{1}{\sqrt{Gmn}}, \tag{5.11}$$

where Eq. (5.10) has been used in the last step.

Assuming that the maximum impact parameter is of the order of the system size, we set

$$b_{\rm max} \sim R \sim \left(\frac{N}{n}\right)^{1/3}, \tag{5.12}$$

while the minimum impact parameter is approximately the mean interparticle separation,

$$b_{\rm min} \sim n^{-1/3}. \tag{5.13}$$

With these approximations, the relaxation time becomes

$$t_{\mathrm{R}} \sim \frac{N}{8\pi \ln N}\, t_{\mathrm{cr}}. \tag{5.14}$$

This scaling highlights that two-body relaxation is suppressed in systems with large particle numbers. While higher densities shorten the crossing time, the large value of N makes the relaxation time exceed the Hubble time. Consequently, systems such as the Milky Way can be regarded as effectively collisionless.

5.1.1 Direct N-body method

In order to solve this N-body problem, one can simply sum over all the contributions from the individual particles, meaning that the gravitational potential at the position $\vec{x}_i$ is calculated as:

$$\Phi(\vec{x}_i) = -G \sum_{j \neq i} \frac{m_j}{\left(|\vec{x}_i - \vec{x}_j|^2 + \epsilon^2\right)^{1/2}} \tag{5.15}$$

where $\vec{x}_j$ and m_j are the comoving coordinates and mass of the j-th particle. The potential in Eq. (5.15) resembles a Newtonian gravitational potential leading to gravitational acceleration between particles. However, in cosmological N-body simulations the particles do not represent real stars or dark matter clumps, but they are rather tracer particles sampling an underlying collisionless mass distribution. This motivates the introduction of the *gravitational softening length* ϵ in the denominator of Eq. (5.15). First, the rate of velocity change due to two-body encounters in Eq. (5.8) increases strongly for small impact parameters, leading to short relaxation times. The softening length ϵ mitigates this by smoothing the force at small separations, suppressing spurious two-body relaxation effects (Dolag et al. 2008).

Second, without gravitational softening, the force between two particles would diverge as their separation approaches zero, resulting in arbitrarily large accelerations. Since the evolution is solved with discrete timesteps, two particles can occasionally approach each other very closely, producing unphysically large accelerations that may cause the integration scheme to diverge (e.g. Rodionov and Sotnikova, 2005). Even reducing the timesteps does not cure the problem: close encounters between particles have a little physical meaning, since the particles only trace a smooth collisionless density field. Therefore, softening is necessary to preserve the collisionless nature of the system.

Different choices for the softening length

The choice of the optimal gravitational softening length in N-body simulations is a non-trivial issue. On the one hand, the softening length must be large enough to suppress spurious two-body collisionality. On the other hand, if ϵ is too large, it biases the gravitational potential and artificially suppresses small-scale structures, imposing a strong constraint on the spatial resolution of the simulation. In other words, gravitational softening reduces the variance of the force estimate due to particle discreteness, but introduces a bias: the bias increases with ϵ, while the variance decreases (Zhan 2006). Therefore, an optimal value of ϵ must balance these two competing effects.

The optimal softening length is commonly determined via convergence studies (Navarro et al.

1996; Moore et al. 1998; Splinter et al. 1998; Power et al. 2003; Zhan 2006; Ludlow et al. 2019; Zhang et al. 2019). Power et al. (2003) performed systematic convergence tests in isolated Navarro–Frenk–White (NFW) (Navarro et al. 1997) haloes at fixed initial conditions, exploring the interplay between timestep selection, force accuracy, adaptive multistep schemes, and softening. From their empirical analysis they proposed that an optimal softening length is

$$\epsilon_{\rm P03} = 4\,\frac{r_{200}}{N_{200}^{1/3}}, \tag{5.16}$$

where r_{200} and N_{200} are, respectively, the radius and the number of particles enclosed within the region of mean density 200 times the critical density of the Universe.

More recently, Zhang et al. (2019) revisited the study from Power et al. (2003) using modern simulation codes and found that convergence could be achieved with a smaller softening, $\epsilon \simeq 0.5\,\epsilon_{\rm P03}$. However, both of these studies focus on isolated haloes, while large cosmological simulations include haloes spanning a wide range of mass and dynamical states. Ludlow et al. (2019) investigated how halo dynamical properties depend on particle number and softening length, and showed that relaxation effects are dominated by the particle number rather than softening, since cumulative perturbations arise primarily from numerous distant interactions rather than rare close encounters. They also argued that a reasonable choice for the softening length is a fixed fraction (typically $< 10\%$) of the mean inter-particle separation. Alternative approaches employ an *adaptive* softening length, allowing the softening scale to vary in space and time according to the local density of the system (e.g. Mostoghiu Paun et al. 2025). In this way, high-density regions can achieve higher force resolution, while low-density regions remain protected against spurious two-body effects. However, this comes at the cost of increased computational complexity and requires the inclusion of additional correction terms in the equations of motion to ensure conservation of the total energy (Iannuzzi and Dolag 2011).

The problem of choosing a softening length can be traced back to modelling single particles as finite-size mass distributions with a given density profile. A possible choice is to model the density profile with a *Plummer sphere*:

$$\rho(\vec{r}) = \frac{3m}{4\pi\epsilon_{\rm PL}^3}\left(1+\frac{|\vec{r}|^2}{\epsilon_{\rm PL}^2}\right)^{-5/2}, \tag{5.17}$$

where m is the mass of the particle and $\vec{r}$ the radial coordinate. Note that the density profile in Eq.(5.17) decreases at large distances and for $|\vec{r}| = 0$ is that of a homogeneous sphere of mass m and radius $\epsilon_{\rm PL}$. The potential solution of the Poisson using the density in eq.(5.17) is:

$$\Phi(r) = -\frac{Gm}{\sqrt{(\vec{r}^2+\epsilon_{\rm PL}^2)}}. \tag{5.18}$$

This expression coincides with the individual particle contributions in Eq. (5.15), thus demonstrating that in N-body simulations the interactions are modelled as that of a single point particles represented by Plummer sphere and the softening length coincides with the radius of the sphere. However, a limitation of fixed gravitational softening is that it modifies the force law at all spatial scales. To alleviate this, OpenGADGET3 employs a kernel-based, spline softening scheme

(Dehnen 2001; Barnes 2012; Springel et al. 2001) where the mass distribution is smoothed on a kernel $W(r,h)$ and takes the form:

$$\rho(\vec{r}) = mW(r,h), \tag{5.19}$$

where r is the magnitude of $\vec{r}$ and the kernel is defined on a compact support $[0;h]$ using a cubic spline kernel (Monaghan and Lattanzio, 1985):

$$W(r,\epsilon) = \frac{8}{\pi\epsilon^3}\begin{cases} 1-6\left(\frac{r}{\epsilon}\right)^2+6\left(\frac{r}{\epsilon}\right)^3 & \text{if } 0\le\frac{r}{\epsilon}\le\frac{1}{2} \\ 2\left(1-\frac{r}{\epsilon}\right)^3 & \text{if } \frac{1}{2}<\frac{r}{\epsilon}\le 1, \\ 0 & \text{if } \frac{r}{\epsilon}>1. \end{cases} \tag{5.20}$$

. This approach has the advantage that the force recovers the exact Newtonian form for $r > h$, whereas the Plummer–softened force converges much more slowly to the Newtonian limit.

For a given softened spline kernel, the *Plummer equivalent softening* is defined as: $\epsilon_{\rm PL} = \epsilon/2.8$. For this choice, the potential minimum at $r = 0$ has the same depth when using a cubic spline kernel or a Plummer sphere (Springel et al. 2001, Appendix A).

In cosmological hydrodynamical simulations, different particle *species* sample distinct physical components: collisionless fluids such as DM, collisional gas, or discrete objects and populations, like stars and BHs. Each species can be assigned a different gravitational softening length, reflecting the effective spatial resolution or the physical scale associated with that component.

When particles belonging to different species interact gravitationally, a prescription must be adopted to define the effective softening between particles i and j. Importantly, this prescription must be symmetric in (i,j) in order to guarantee exact momentum conservation in the N-body system. In OpenGADGET3, following the original implementation of GADGET (Springel et al., 2001), the interaction softening between particles i and j with softenings h_i and h_j is chosen as the maximum softening between the two species:

$$h_{ij} = \max(h_i, h_j). \tag{5.21}$$

Alternative symmetrization schemes have been discussed extensively in the literature and recently reviewed by Hopkins et al. (2023). Two commonly adopted choices are (e.g. Price and Monaghan 2007; Springel 2010; Hubber et al. 2018):

(i) Averaging the potentials

$$\tilde{\phi}_{ij}(r) = \frac{1}{2}\left[\phi_0(r,h_i)+\phi_0(r,h_j)\right], \tag{5.22}$$

where $\phi_0(r,h)$ is the softened potential corresponding to softening h.

(ii) Averaging the softenings

$$h_{ij} = \frac{h_i+h_j}{2}, \qquad \tilde{\phi}_{ij}(r) = \phi_0(r,h_{ij}). \tag{5.23}$$

When neighbouring particles have similar softenings ($h_i \sim h_j$), these prescriptions yield nearly indistinguishable results, and several comparison studies (e.g. Dyer and Ip, 1993; Power et al., 2003; Grudić and Hopkins, 2020; Hopkins et al., 2023) have shown that differences are typically sub-dominant compared to integration and time-stepping errors.

However, the situation changes qualitatively in the limit of strongly unequal softenings. Consider a particle a representing an extended background distribution with softening h_a, and a compact particle b with $h_b \ll h_a$ (e.g. a BH embedded in a DM background). In the limit $h_b \to 0$, particle b behaves as a point mass moving through a smooth extended potential.

Averaging the potentials gives:

$$\tilde{\phi}_{ab}(r) = \frac{1}{2}\left[\phi_0(r, h_a) + \phi_0(r, h_b)\right]. \tag{5.24}$$

Since $\phi_0(r, h_b) \to -G/r$ as $h_b \to 0$, the interaction approaches:

$$\tilde{\phi}_{ab}(r) \sim -\frac{G}{2r} \quad \text{as } r \to 0, \tag{5.25}$$

reintroducing an almost Newtonian divergence. This can lead to large-angle two-body scattering, artificial ejections, and unphysical disruption of bound systems (Hopkins et al., 2023). Averaging the softenings avoids the divergence, but yields an effective softening:

$$h_{ab} = \frac{h_a}{2} \tag{5.26}$$

in the limit $h_b \to 0$, systematically underestimating the physical interaction scale and producing forces that are too strong at small separations. For highly unequal softenings, the maximum-softening prescription:

$$h_{ab} = \max(h_a, h_b) \tag{5.27}$$

recovers the correct asymptotic behaviour and provides the most physically consistent interaction. In this limit, it becomes exact for the interaction between a point mass and an extended density distribution.

The approach described in this section, called the Particle-Particle (PP) method, adopts a direct summation over all the tracer particles in Eq. (5.15). This can be computationally expensive as the computing time scales with N^2, where N is the number of tracer particles, thus making the computation prohibitive for very large values of N. Alternative methods, based on suitable approximations, were developed to reduce the computational costs. In what follows, two techniques, the PM and the Tree algorithm, will be introduced, as OpenGADGET3 adopts a hybrid scheme combining these methods to compute *long* and *short* range interactions, respectively.

5.1.2 The PM method

Unlike direct N-body methods, which explicitly compute the mutual gravitational interaction between individual particle pairs, PM methods calculate the gravitational force by solving the Poisson equation for a *global* gravitational potential field. Therefore, the PM method is intrinsically suited to solve the evolution of a collisionless fluid. The underlying idea is to approximate the collisionless matter distribution by interpolating particle masses onto a fixed spatial mesh,

where the Poisson equation can be efficiently solved.

The transition from a local, discrete particle-based estimate to a global, mesh-based one proceeds by sampling the mass density field on a regular grid. Since the particles are point-like tracers of the underlying continuous mass field, their mass distribution must be smoothed before being assigned to the mesh. This smoothing is achieved by introducing an interpolation kernel, effectively giving each particle a finite spatial extent or *shape* instead of representing it as a Dirac δ-function.

The interpolation kernel distributes a fraction of the mass of a particle located at position $\vec{x}_i$ to neighbouring mesh points with coordinates $\vec{x}_p$. This fraction is determined by a *weighting function* $W(\vec{x}_i - \vec{x}_p)$, which quantifies the overlap between the particle's extended mass profile and the volume of the grid cell centred at $\vec{x}_p$. The resulting density field on the mesh is then given by

$$\rho(\vec{x}_p) = \frac{1}{h^3} \sum_{i=1}^{N} m_i \, W(\vec{x}_i - \vec{x}_p), \tag{5.28}$$

where h is the mesh spacing, m_i is the mass of particle i, and the sum runs over all N particles.

In OpenGADGET3, the density assignment is performed using the *Cloud-In-Cell* (CIC) scheme. In this method, each particle is treated as a cubical mass distribution of uniform density with side length equal to the grid spacing h. As a consequence, each particle contributes mass to the eight nearest grid points, with weights determined by the relative distance from the particle to each grid node.

Once the mass density field has been assigned to the mesh, the gravitational potential is obtained by solving Poisson's equation. The PM algorithm proceeds in the following steps:

1. Compute the Fourier transform of the density contrast field on the mesh using a Fast Fourier Transform (FFT);

2. Solve Poisson's equation in Fourier space,

$$\tilde{\Phi}(\vec{k}) = -\frac{4\pi G}{k^2} \tilde{\rho}(\vec{k}), \tag{5.29}$$

   to obtain the gravitational potential in Fourier space;

3. Perform an inverse FFT to recover the gravitational potential $\Phi(\vec{x}_p)$ on the mesh in configuration space;

4. Evaluate the gravitational force on the mesh as $\vec{F} = -\vec{\nabla}\Phi$ using finite differences;

5. Interpolate the mesh-based forces back to the particle positions using the same weighting function $W(\vec{x}_i - \vec{x}_p)$ employed for density assignment, thus ensuring momentum conservation.

The computational cost of PM is dominated by the FFT performed to solve the Poisson equation on the mesh. If the number of grid cells is M, the computational cost of the FFT scales as $O(M \log M)$. Since M is typically chosen to be proportional to the number of particles N, the overall computational complexity of the PM method scales as $O(N \log N)$, which represents a significant improvement over the $O(N^2)$ scaling of direct N-body methods (Sect. 5.1.1). However, the accuracy of the force calculation strongly depends on the grid size.

5.1.3 Tree method

Another technique to reduce the computational expense of direct summation is the Tree method. This technique relies on a hierarchical grouping of particles into larger aggregate cells. The gravitational influence of each cell on a distant target particle is approximated by means of a multipole expansion, so that the collective contribution of many particles can be represented by a single multipole force term. Consequently, instead of computing $N-1$ pairwise force evaluations per particle, as required in a direct-summation N-body method, the gravitational force on a particle is obtained with substantially fewer operations, because distant particle groups are treated as effective 'macro-particles'. Only nearby particles are resolved individually, while distant ones are approximated through progressively coarser levels of the tree hierarchy, thereby reducing the number of force calculations. Figure 5.1 [1] provides a schematic representation of the OctTree (Barnes and Hut 1986) algorithm adopted in OpenGADGET3. Starting from a cubical root node encompassing the full mass distribution, this is repeatedly subdivided into a number of *daughter* nodes of half the side length each, eventually ending up with a *leaf* node containing single particles.

Forces are then obtained by 'walking' down the tree according to an *opening criterion* that determines whether the multipole expansion of the root node is considered to provide an accurate enough partial force. This criterion typically depends on the spatial extent s of the node and its distance r from the target particle, so that a node is opened and the process is iterated if:

$$\theta_c < \frac{r}{s}\,. \tag{5.30}$$

Here θ_c is a critical angle that *controls* the accuracy on the force computation.

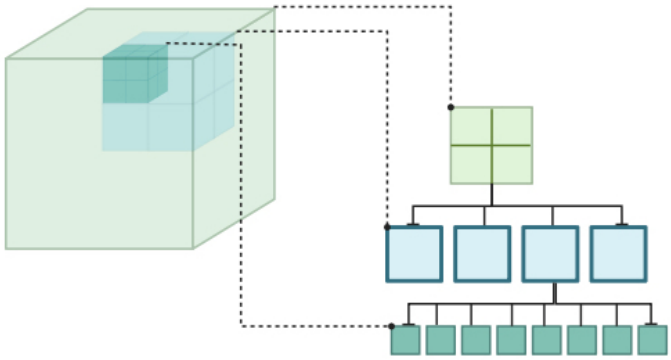

Figure 5.1: *Schematic illustration of the OctTree. The particles are first enclosed in a cube (root node). This cube is then iteratively subdivided into cubes of half the side length, until exactly one particle is left in each final cube (leaves of the tree).*

Alternatively, OpenGADGET3 employs a different opening criterion that takes also into account the total mass M contained within the node, the node side length l and the total acceleration obtained in the last time-step $|\vec{a}|$:

$$\frac{GM}{r^2}\left(\frac{l}{r}\right)^2 \leq \alpha|\vec{a}|\,. \tag{5.31}$$

In this case, the control of the force accuracy is controlled by the *tolerance parameter* α that compares a rough estimate of the truncation error (right hand-side in Eq. 5.31) with the size of the total expected force. As discussed by Springel (2005), this allows the relative force error to remain approximately constant by adapting the opening criterion to the evolving dynamical state of the system. For instance, the opening angle automatically increases at lower redshift as clustering increases. This adaptive approach yields greater force accuracy for a given computational cost

[1] Figure made with BioRender.

compared to a fixed geometrical criterion such as that defined in Eq.(5.30). Wherever a group of particles is seen by a target particle under an angle larger than the critical opening angle, the process of walking down the tree continues until the leaf node is reached.

5.1.4 Hybrid TreePM method

OpenGADGET3 employs a hybrid gravitational solver combining the hierarchical Tree algorithm with the PM approach, known as the TreePM scheme (Xu, 1995; Bode et al., 2000). In practice, the gravitational potential is decomposed in Fourier space into a *long-range* and a *short-range* contribution:

$$\Phi_{\vec{k}} = \Phi_{\vec{k}}^{\rm long} + \Phi_{\vec{k}}^{\rm short}. \tag{5.32}$$

The long-range force is computed with a PM method, solving for the potential in Fourier space given by:

$$\Phi_{\vec{k}}^{long} = \Phi_{\vec{k}} e^{-|\vec{k}|^2 r_s^2}, \tag{5.33}$$

where the length scale r_s controls the spatial scale of the force split.
The short range contribution in Eq. (5.32) is calculated in configuration space using the Tree. The short-range potential in configuration space is given by the following real-space expression:

$$\Phi^{short}(\vec{x}) = -G \sum_{i=1}^{N} \frac{m_i}{r_i} \mathrm{erfc}\left(\frac{r_i}{2r_s}\right), \tag{5.34}$$

where m_i are particle masses, $r_i = |\vec{x} - \vec{x}_i|$, and erfc denotes the complementary error function, which rapidly suppresses the contribution for particles at $r_i > r_s$. For the detailed values of the parameters regulating the transition between the Tree and the PM algorithms adopted in this Thesis the reader is referred to Appendix A.
The adoption of a hybrid method offers significant advantages in both force accuracy and computational efficiency. Notably, tree construction is required only within a localized region surrounding each particle, reducing the computational overhead. Force inaccuracies primarily emerge at the grid scale due to mesh anisotropy, yet the RMS force error remains below 2%(Springel 2005).

5.2 Hydrodynamics

The evolution of the gaseous component is dominated by frequent particle interactions, which makes it a collisional medium. In what follows we assume that the mean free path of gas particles is much smaller than the characteristic spatial scales over which macroscopic gas properties vary, the so-called fluidodynamical limit. Under this condition, the gas can be treated as a continuous fluid and described in terms of smooth fields such as density, velocity, and pressure. Assuming further that viscosity is negligible at the scales of interest, the gas behaves as an ideal (inviscid) fluid. Its evolution is then governed by the Euler equations of hydrodynamics, which in comoving

Lagrangian form read:

$$\begin{aligned} \frac{d\rho}{dt} &= -\rho\,\vec{\nabla}\cdot\vec{v} && \text{(continuity equation)} \\ \frac{d\vec{v}}{dt} &= -\frac{\vec{\nabla}P}{\rho} + \vec{F}_{\rm ext} && \text{(Euler equation)} \\ \frac{du}{dt} &= -\frac{P}{\rho}\,\vec{\nabla}\cdot\vec{v} + \dot{Q} && \text{(1st law of thermodynamics)} \end{aligned} \tag{5.35}$$

where ρ, $\vec{v}$, P and u are gas mass density, velocity, pressure and specific internal energy, respectively. $\dot{Q}$ denotes the specific heating or cooling rate, while $\vec{F}_{\rm ext}$ represents the external force per unit mass, which in OpenGADGET3 corresponds to the gravitational force computed by the N-body solver (Sect. 5.1).
To close the above system of equations, one needs to specify an equation of state, which establishes the relationship between pressure and density:

$$P = (\gamma - 1)\rho u \tag{5.36}$$

where γ is the polytropic index. The numerical integration of Eqs. (5.35) can be performed using two main approaches: grid-based (Eulerian, e.g. Laney 1998) and particle-based (Lagrangian, Monaghan and Gingold 1983; Monaghan and Lattanzio 1985) methods. In grid-based schemes–adopted, for instance, in the ENZO (Bryan et al., 2014) or RAMSES (Teyssier, 2010)codes–the fluid is discretized over a fixed or adaptive mesh, and the hydrodynamical equations are solved by computing the fluxes of mass, momentum, and energy across the boundaries of adjacent cells. In contrast, Lagrangian methods follow the motion of individual fluid elements as they move through space, naturally adapting the resolution to regions of higher density. Interesting comparisons of code performance between Eulerian and Lagrangian methods for hydrodynamics are presented, for example, in Frenk et al. (1999); O'shea et al. (2005); Bauer and Springel (2012), and—when including the full complexity of cosmological simulations including sub-resolution models for baryonic physics—in Sijacki et al. (2012); Kereš et al. (2012); Nelson et al. (2013). In the following, we focus on the Lagrangian Smoothed Particle Hydrodynamics method, which is one of the hydrodynamical schemes implemented in OpenGADGET3 and adopted in the simulations presented in this Thesis. As an alternative to standard Smoothed Particle Hydrodynamics (SPH), a Godunov-SPH scheme (Inutsuka 2002) was implemented in version of GADGET3, preliminary to OpenGADGET3, by Murante et al. (2011). More recently, Groth et al. (2023) introduced a novel hydrodynamical solver in OpenGADGET3 based on the Meshless Finite Mass (MFM) method (Hopkins, 2015). This approach is conceptually similar to SPH but differs in how it defines the fluid volume associated with each particle resorting to a Voronoi tessellation rather than a spherical smoothing kernel, thus allowing for a more accurate and adaptive representation of the fluid domain.

5.2.1 Smoothed Particle Hydrodynamics

Within the SPH approach, the fluid is represented by a finite set of particles. Each particle carries the thermodynamic properties of a fluid element, so that at a given time t the state

of the gas is described by the positions $\vec{r}_j$, velocities $\vec{v}_j$, and entropies s_j of these particles. To reconstruct continuous fluid fields (such as density or pressure) from this discrete particle distribution, SPH employs an interpolation procedure based on a *smoothing kernel* $W(\vec{x}, h)$. This kernel has dimensions of inverse volume and spreads the contribution of each particle over a finite region of space defined by the *smoothing length* h. The kernel function is required to be normalized to unity,

$$\int W(\vec{x}, h)\, d^3x = 1, \tag{5.37}$$

to be positive, symmetric and isotropic (i.e. it depends only on $|\vec{x}|$), and to have *compact support*, such that only neighbouring particles within a radius of order h contribute to the interpolation. In the limit $h \to 0$, the kernel approaches the Dirac delta distribution,

$$\lim_{h\to 0} W(\vec{x}, h) = \delta(\vec{x}), \tag{5.38}$$

recovering the exact discrete particle representation.

A continuous field $A(\vec{x})$ can be obtained from the discrete macro-particle representation through kernel interpolation as:

$$\langle A(\vec{x})\rangle = \sum_j m_j \frac{A_j}{\rho_j} W(|\vec{x} - \vec{r}_j|, h), \tag{5.39}$$

where m_j and ρ_j are the mass and density of particle j, respectively, and W is the smoothing kernel with characteristic smoothing length h.

The kernel compact support ensures that, although the sum in Eq. (5.39) should run over all the particles in the simulation, it actually encompasses only the particles lying within the kernel support. By applying Eq. (5.39) to the mass density field at the position of the i-th particle at the position $\vec{x}_i$ one obtains:

$$\rho_i = \langle \rho(\vec{x}_i)\rangle = \sum_{j=1}^{N} m_j W(\vec{x}_i - \vec{x}_j, h). \tag{5.40}$$

Using a fixed smoothing length is inadequate in systems with strong density contrasts. In overdense regions it would oversmooth the fluid properties by averaging over too many neighbouring particles, whereas in underdense regions it would lead to noisy estimates due to an insufficient number of neighbours. One way to overcome this limitation is to allow the smoothing length to vary according to the local density. In practice, an *adaptive* smoothing length h_i for the i-th particle having mass density ρ_i can be defined such that:

$$\rho_i h_i^3 = \text{const.} \tag{5.41}$$

This definition has two important consequences (Springel (2010)). First, the mass density in Eq. (5.40) becomes a function both of the particle positions and of the smoothing length h_i. At the same time, Eq. (5.41) implicitly defines the function $h_i(\vec{r_1}, ..., \vec{r_N})$ in terms of the particle coordinates.

An elegant approach to derive the set of Eqs. (5.35) within the SPH framework is to follow a

Lagrangian derivation, as initially proposed by Gingold and Monaghan (1982). The Euler equation for an inviscid fluid follow from the Lagrangian (Eckart 1963):

$$\mathcal{L} = \int \rho \left(\frac{v^2}{2} - u \right) dV \,, \tag{5.42}$$

where u, ρ and v denote the internal energy per unit mass, the density and the velocity fields of a fluid element. The discretized SPH version of the Lagrangian can be written as a function of the masses of the fluid macro-particles m_i, velocities v_i and internal energy per unit mass u_i as:

$$\mathcal{L}_{\rm SPH} = \sum_i^N \frac{1}{2} m_i v_i^2 - m_i u_i. \tag{5.43}$$

The particle pressure p_i can be expressed through an entropic function A_i:

$$p_i = A_i \rho_i^\gamma = (\gamma - 1)\rho_i u_i \tag{5.44}$$

where γ is the polytropic index of the gas. The equations of motion of the fluid will be then retrieved from Euler-Lagrange equations:

$$\frac{d}{dt} \frac{\partial \mathcal{L}_{\rm SPH}}{\partial \dot{\vec{r}}_i} - \frac{\partial \mathcal{L}_{\rm SPH}}{\partial \vec{r}_i} = 0 \,. \tag{5.45}$$

Once applied to Eq. (5.43) and using the first law of thermodynamics at constant entropy, the above equation gives:

$$m_i \frac{d\vec{v}_i}{dt} = \sum_j^N m_j \frac{p_j}{\rho_j^2} \frac{\partial \rho_j}{\partial \vec{r}_i}. \tag{5.46}$$

The r.h.s. of Eq. (5.46) involves the spatial derivatives of the mass density field. Since density depends both on spatial coordinates and the smoothing length, we have:

$$\frac{\partial \rho_j}{\partial \vec{r}_i} = \nabla_i \rho_j + \frac{\partial \rho_j}{\partial h_j} \frac{\partial h_j}{\partial \vec{r}_i}. \tag{5.47}$$

Taking the derivative of $\rho_j h_j^3 = \text{const}$ with respect to $\vec{r}_i$ (Eq. 5.41) gives:

$$\frac{d\rho_j}{dh_j} \frac{dh_j}{d\vec{r}_i} \left[1 + \frac{3\rho_j}{h_j} \left(\frac{d\rho_j}{dh_j} \right)^{-1} \right] = -\nabla_i \rho_j \tag{5.48}$$

and combining Eq. (5.47) and (5.48):

$$\frac{d\rho_j}{d\vec{r}_i} = \left(1 + \frac{h_j}{3\rho_j} \frac{\partial \rho_j}{\partial h_j} \right)^{-1} \nabla_i \rho_j \tag{5.49}$$

leading to the expression for the last term in Eq. (5.46).

Starting from the expression for the total derivative of the density with respect to the particle

position, and using the identity:

$$\vec{\nabla}_i \rho_j = m_i \vec{\nabla}_i W_{ij}(h_j) + \delta_{ij} \sum_{k=1}^{N} m_k \vec{\nabla}_i W_{ki}(h_i), \tag{5.50}$$

we finally obtain the discrete equations of motion in the SPH formulation. Substituting Eq. (5.50) into the Euler-Lagrange equation and assuming adiabatic, inviscid flow, the momentum equation becomes

$$\frac{d\vec{v}_i}{dt} = -\sum_{j=1}^{N} m_j \left[f_i \frac{P_i}{\rho_i^2} \vec{\nabla}_i W_{ij}(h_i) + f_j \frac{P_j}{\rho_j^2} \vec{\nabla}_i W_{ij}(h_j) \right], \tag{5.51}$$

where the correction factors f_i account for the spatial variation of the adaptive smoothing length and are defined as

$$f_i = \left[1 + \frac{h_i}{3\rho_i} \frac{\partial \rho_i}{\partial h_i} \right]^{-1}. \tag{5.52}$$

The SPH equations of motion given in Eq. (5.51) replace the original system of coupled partial differential equations with a system of ordinary differential equations. Mass conservation is already guaranteed by the Lagrangian nature of the method and the Lagrangian symmetries also ensure energy conservation, translational invariance (momentum conservation) and rotational symmetry (angular momentum conservation).

So far, the SPH equations have been derived under the assumption of entropy conservation. However, the Euler equations are nonlinear and can naturally develop discontinuities even when evolving from perfectly smooth initial conditions (Springel, 2010). These discontinuities manifest as shocks and contact discontinuities. At a shock front, the specific entropy of the gas must increase according to the second law of thermodynamics, implying that the flow is no longer inviscid in the shock layer and the ideal Euler equations must be modified to include dissipation. To capture shocks correctly, a dissipative mechanism must therefore be introduced. In SPH, this is achieved through an artificial viscosity term, originally introduced by Monaghan and Gingold (1983). To improve the treatment of shocks and reduce unwanted viscous effects in shear flows, OpenGADGET3 employs artificial viscosity term by Monaghan (1997) provided with a limiter (Balsara, 1995) which suppresses artificial viscosity in regions dominated by shear velocity curls and vorticity. In addition, an adaptive treatment of artificial conduction is also included to promote thermal energy transport across contact discontinuities. A detailed description of the artificial viscosity and conduction schemes implemented in OpenGADGET3 is provided by Beck et al. (2015).

5.3 Sub-resolution models for cooling and star formation

In the attempt to follow the coupled evolution of cosmic structures within cosmological hydrodynamical simulations, one has to consider that many key phenomena occur on scales far below the size of a simulation element (whether a grid cell or SPH particle), and therefore cannot be modelled directly. Among these processes are atomic and molecular cooling, the formation of molecular clouds that collapse to form stars, and the subsequent supernova (SN) explosions and stellar winds. These phenomena occur on sub-parsec scales and are far below the typical resolu-

tion scale of modern cosmological simulations. In this Section, the sub-resolution modelling of gas cooling, star formation, and stellar evolution is discussed, with particular emphasis on the specific implementation included in OpenGADGET3. These prescriptions will be adopted within the simulations presented throughout this Thesis. For completeness, the reference values of all relevant parameters entering the sub-resolution prescriptions—together with a concise explanation of their role—are reported in Appendix A and summarized in Table A.1. Given their central role in this Thesis, the sub-resolution prescriptions concerning the BH sector will be discussed separately in Sect. 5.4.

5.3.1 Radiative cooling

The efficiency of radiative gas cooling depends strongly on the temperature, density, and chemical composition of the gas. In the standard cosmological scenario of structure formation, the first gravitationally bound objects are expected to form in metal-free halos with virial temperatures $T_{\rm vir} < 10^4\,{\rm K}$, where atomic line cooling is inefficient due to the lack of electronic excitation in neutral hydrogen. In this regime, cooling is instead dominated by molecules, primarily molecular hydrogen (H_2) and hydrogen deuteride (HD), which form via gas-phase reactions and allow the temperature of primordial gas clouds to decrease to $\sim 10^2\,{\rm K}$ (Lepp and Shull, 1984; Puy and Signore, 1998). As the first stars explode, enriching the surrounding medium, metal cooling due to collisions between ions and free electrons becomes the dominant process. The total cooling can be described by a cooling function $\Lambda(T, \rho, Z)$, which quantifies radiative energy losses per unit volume depending on the gas temperature T, density ρ and metallicity Z. Figure 5.2 shows the cooling rate Λ by Maio et al. (2007) and Wiersma et al. (2009) as a function of gas temperature. In the left panel, the cooling rate is shown for different metal fractions corresponding to the different curves at fixed hydrogen number density $n_{\rm H} = 10^{-3}{\rm cm}^{-3}$. For temperature lower than 10^4 K and low metal fractions ($\sim 10^{-5} - 10^{-6}$) the dominant coolers are molecules. Around $10^4 \lesssim T \lesssim 10^5\,{\rm K}$, two characteristic cooling peaks arise from collisional excitation of hydrogen and helium. At higher metallicities, those are washed out by the contributions of different metals to the ionization processes. The right panel illustrates the individual contributions of different metal species to the total cooling rate in the temperature range $10^4 \lesssim T \lesssim 10^8\,{\rm K}$ computed using CLOUDY (Ferland et al. 1998; Ferland et al. 2023) from Wiersma et al. (2009).

At high redshift, the virial temperature $T_{\rm vir}$ can be related to the virial mass as (Greif et al., 2008):

$$T_{\rm vir} \simeq 10^4 \left(\frac{M_{\rm vir}}{5 \cdot 10^7 {\rm M}_\odot}\right)^{2/3} \left(\frac{1+z}{10}\right) \tag{5.53}$$

implying that at redshift $z \sim 9$, the halos dominated by molecular cooling have masses $< M_{\rm vir} \simeq 5 \cdot 10^7\,{\rm M}_\odot$. In the simulations presented in this Thesis, the mass resolution is comparable to this threshold, meaning that the molecular cooling phase is not fully resolved. Although molecular cooling is crucial in simulations of the early Universe (see, e.g. Maio et al. 2007 for its implementation in GADGET-2), this work focuses on the regime where atomic cooling dominates. In OpenGADGET3, radiative cooling is implemented following Wiersma et al. (2009), accounting for 13 individual metal species (C, Ca, O, N, Ne, Mg, S, Si, Fe, Na, Al, Ar, Ni). Cooling assumes ionization equilibrium above $T \geq 10^4\,{\rm K}$ and includes the effect of photoionization by an evolving,

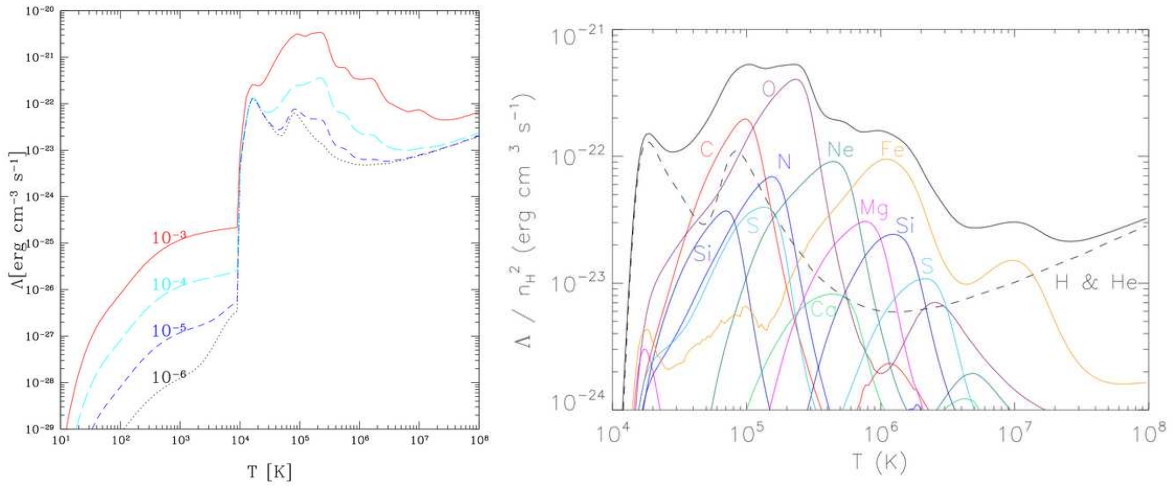

Figure 5.2: *Cooling rates by Maio et al. (2007) (left) and Wiersma et al. (2009) (right). Left: th total colling rate due to* H, He, *metals,* H_2 *and* HD *as a function of temperature. Different curves refer to different number fraction of metals from* 10^{-3} *to* 10^{-6} *as indicated in the labels. The right panel shows the different metal contributions to the total cooling rate in the temperature range* 10^4 K $<$ T $<$ 10^8K *for hydrogen number density* $n_{\rm H} = 10^{-4}{\rm cm}^{-3}$

uniform UV/X-ray background (Haardt and Madau, 1996; Madau et al., 1999; Haardt and Madau, 2001).

5.3.2 Star formation

In the Milky Way and in nearby galaxies, star formation is observed to take place within massive, cold, and dense molecular clouds. These structures typically have masses in the range $M \sim 10^4 - 10^{6.5}\,M_\odot$, temperatures of $T \sim 10 - 40\,{\rm K}$, and molecular hydrogen number densities $n_{\rm H_2} \sim 10^2 - 10^5\,{\rm cm}^{-3}$. The strongest observed correlation with star formation rates (SFRs) is with the molecular gas content or with the dust mass as a tracer of molecular gas. This empirical trend suggests that star formation is primarily driven by the dense molecular phase of the interstellar medium (ISM). High gas volume densities, together with efficient dust shielding, act to decouple the dense cores of molecular clouds from the interstellar radiation field. As a result, the gas can cool rapidly, reduce its thermal pressure support, and undergo gravitational collapse, eventually leading to the formation of stars (Tacconi et al. 2020). Within the context of hydrodynamical cosmological simulations, these processes act on scales which are far below the current resolution. Early sub-resolution star formation models described ISM as a two-phase medium, consisting of cold clouds embedded in a hot diffuse phase in pressure equilibrium (e.g. Yepes, 1997; Springel and Hernquist, 2003). In these models, star formation originates from the cold phase, while SN heating evaporates cold clouds and regulates the hot phase. More recent models link star formation directly to the molecular gas fraction. Different approaches have been proposed to estimate the abundance of molecular hydrogen (H_2) including equilibrium-based models where the H_2 fraction depends on the local metallicity or non-equilibrium chemical models that follow time-dependent H_2 formation and destruction on dust grains (Gnedin et al., 2009; Christensen et al., 2012) based on phenomenological prescriptions (Krumholz, 2013; Murante et al., 2015).

Within the simulations presented in this Thesis, we adopt the sub-resolution hybrid multiphase

model proposed by Springel and Hernquist (2003) – hereafter SH03 – along with the chemical enrichment and stellar evolution model introduced by Tornatore et al. (2007). In this model, gas particle exceeding a threshold density value are treated as two-phase medium consisting of a hot and a cold component. These two phases are assumed to be in pressure equilibrium, and the model self-regulates the formation of stars through a balance between radiative cooling, SN heating, cloud evaporation and wind injection.

Star formation in the multiphase ISM

Once the gas density exceeds a star formation threshold $\rho_{\rm th}$, the gas particles enter a multi-phase stage where their total gas density ρ can be split into a cold (ρ_c) and a hot (ρ_h) component, where

$$\rho = \rho_c + \rho_h. \tag{5.54}$$

Denoting with u_h and u_c the hot and cold gas energy per unit mass, the thermal energy per unit volume in the multi-phase regime can be expressed as:

$$\epsilon = u_h \rho_h + u_c \rho_c. \tag{5.55}$$

The mass and energy exchange between the phases is regulated by star formation, heating from SN and gas cooling. In particular, the model assumes that the conversion from cold clouds into stars happens on a timescale t_* that depends on the local gas density:

$$t_*(\rho) = t_{0_*} \left(\frac{\rho}{\rho_{th}} \right)^{-1/2}. \tag{5.56}$$

Here t_{0_*} is a model parameter (see SH03). When a given star formation episode occurs, a fraction β –depending on the specific choice of the initial mass function (IMF)– of the stars are short-lived and die instantaneously as SNII, so that the rate of star formation rate can be written as:

$$\frac{d\rho_*}{dt} = (1-\beta)\, \frac{d\rho_c}{t_*}. \tag{5.57}$$

However, the SNII instantaneous explosion also releases energy which is promptly available. As a result, the cold gas phase is heated up by this feedback energy. If e_{SN} is defined as the energy released by a single SNII, and n_{SN} as the number of stars per solar masses ending up as SNII, the average return of energy per unit solar mass exploded is $\epsilon_{SN} = e_{SN} \cdot n_{SN}$. Using Eq. (5.57), the heating rate is:

$$\frac{d(\rho_h u_h)}{dt} = \epsilon_{SN} \frac{d\rho_*}{dt} = \beta \frac{u_{SN} \rho_c}{t_*} \tag{5.58}$$

where :

$$u_{SN} = (1-\beta)\beta^{-1} \epsilon_{SN}. \tag{5.59}$$

Concurrently, radiative cooling of the hot phase increases the mass of the cold gas reservoir. This process depends on the cooling function $\Lambda(\rho_h, u_h, Z)$, which includes a dependence on metallicity Z, and yields:

$$\frac{d\rho_c}{dt} = \frac{1}{u_h - u_c} \Lambda(\rho_h, u_h, Z). \tag{5.60}$$

Combining the effects of star formation, supernova heating, and cooling, the evolution of the total thermal energy density is:

$$\frac{d}{dt}(\rho_h u_h + \rho_c u_c) = -\Lambda(\rho_h, u_h, Z) + \beta\frac{u_{\rm SN}\rho_c}{t_*} - (1-\beta)\frac{\rho_c u_c}{t_*}. \tag{5.61}$$

The coexisting processes of gas cooling, star formation and SNII feedback are expected to reach a stationary self-regulated equilibrium, where the balance of heating and cooling keeps the thermal energy content stable. In this regime, multiphase particles evolve at constant pressure, constrained to an effective adiabatic equation of state:

$$P_{\rm eff} = (\gamma - 1)(\rho_h u_h + \rho_c u_c), \tag{5.62}$$

where γ is the adiabatic index.

Evolution of the Single Stellar Population

Within the model originally introduced by Tornatore et al. (2007) and implemented in OpenGADGET3, when a gas particle is converted into a star particle, it represents a *single stellar population* (SSP), meaning a coeval set of stars formed with the same initial metallicity and distributed in mass according to an assumed initial mass function (IMF). The subsequent evolution of each SSP—including mass return and chemical enrichment of the surrounding ISM—depends on four main ingredients: the lifetimes of stars of different masses, the rates of Type Ia and Type II supernovae (SNe), the metal yields from stellar evolution, and the adopted IMF. The IMF plays a crucial role, as it sets the relative number of massive stars, intermediate-mass stars, and low-mass stars in each stellar population and the ensuing chemical enrichment from SNII and SN Ia explosions. The simulations performed in this Thesis rely on a Chabrier (Chabrier 2003) IMF. Type II SNe explosion rate is fully determined by the stellar lifetime function and the IMF, since they explode promptly after star formation. As for Type Ia SNe, they are assumed to arise from binary stars; OpenGADGET3 adopts the single-degenerate scenario of Nomoto and Hashimoto (1988), where a CO white dwarf accretes matter from a companion star until reaching the Chandrasekhar limit. The explosion rate is modelled through a delay-time distribution convolved with the SF history of each SSP. Since a star particle forms instantaneously in the simulation, its star formation history is a delta function in time, thus simplifying the computation of SN event rates. Chemical enrichment by stars is contributed by SN II explosions, assuming instantaneous recycling approximation, while SN Ia explosions and mass-loss from intermediate and low mass stars contribute with mass-dependent life-times. As for the yields, in the simulations presented in this work adopt the yields from Thielemann et al. (2003) for Type-Ia SN, the mass- and metallicity-dependent yields by Karakas (2010) for AGB stars, and the yields by Nomoto et al. (2013) for Type-II SN.

Wind particles

Within the model of SH03, wind particles are responsible for transporting mass and energy away from the star forming regions, thereby heating the surrounding gas through shocks and

regulating the cooling and the resulting star formation rate. The underlying assumption of the model is that the mass-loss rate going into winds $\dot{M}_w$ is proportional to the star formation rate:

$$\dot{M}_w = \eta_w \dot{M}_* \tag{5.63}$$

where where η_w is a model parameter, fixed by SH03 to a value of $\eta_w = 2$ based on the observational constraints by Martin (1999). Furthermore, SH03 make the assumption that winds carry a fixed fraction χ of the SN energy, therefore:

$$\frac{1}{2}\dot{M}_w v_w^2 = \chi \epsilon_{SN} \dot{M}_*, \tag{5.64}$$

which, combined with Eq. (5.63) and (5.59), gives the following expression for the wind velocity:

$$v_w = \sqrt{\frac{2\beta\chi u_{SN}}{\eta_w(1-\beta)}}. \tag{5.65}$$

In the model by SH03, χ is a model parameter set at $\chi \simeq 0.25$, giving values for the wind velocity $v_w \in [350 - 500]$ km s^{-1}. In OpenGADGET3 there is the optional choice to keep v_w as the model parameter, and in the simulations presented in this Thesis v_w is fixed at 350 km s^{-1}.

The numerical implementation of the stellar wind outflows is outlined here. Star forming gas particles are converted into wind particles according to a probability that depends, in turn, on the single particle cold content. Specifically, defining as x the fraction of cold mass of a particle, within a single time interval Δt we can define the probability p as:

$$p = x\ \Delta t / t_* \tag{5.66}$$

so that, following SH03, the amount of stars formed in this time interval can be expressed by:

$$m_* = m(1 - e^{-p})\,. \tag{5.67}$$

In analogy, the probability for a star-forming particle to be converted into a wind particle is set to:

$$P = 1 - e^{-\epsilon_w \cdot p} \tag{5.68}$$

where $\epsilon_w = \eta_w(1-\beta)$. According to SH03, we assume $\eta = 2$. If the particle is converted into a wind particle, it will be launched in the direction perpendicular to the local orbital plane (i.e. with equal probability along the versor $\hat{n}_w = \vec{v} \times \vec{a}/|\vec{v} \times \vec{a}|$ where $\vec{v}, \vec{a}$ are the initial velocity and acceleration of the particle) with initial velocity magnitude v_w. Once launched into the outflow, wind particles are temporarily decoupled from hydrodynamical interactions. This allows them to leave the dense ISM without disrupting it. At the moment they became wind particles, a "delay time" δt_w is associated to each of them. The particle will leave the wind stage if either a time interval $\Delta t > \delta t_w$ has passed, or if it reaches a density region where the density is a fraction $f_{\rm dec}$ of the density threshold for SF: $\rho < 1/2\ f_{dec}\, \rho_{th}$ where again f_{dec} is a free parameter of the model.

It is worth recalling that all parameters associated with the models introduced in this Section are reported in Table A.1, together with the default values adopted in the simulations presented

in this Thesis.

5.4 Sub-resolution prescriptions for BH evolution and AGN feedback

To capture the presence and influence of MBHs on galaxy evolution within cosmological simulations, suitable sub-resolution models are required to bridge the gap between unresolved small-scale physics and the resolved, large-scale dynamics. After introducing the theoretical framework underlying MBH formation, we will present the sub-resolution models adopted for their seeding (Sect. 5.4.1), growth through gas accretion (Sect. 5.4.2), coalescence through mergers (Sect. 5.4.3), and the feedback energy they release into the surrounding medium (Sect. 5.4.4). In each subsection, we will specify the particular implementation adopted in OpenGADGET3.

Box 5.2: Routes to MBH formation

The existence of very massive BHs ($M_{\rm BH} \simeq 10^9$ M$_\odot$) already in place within the first billion years from the Big Bang challenges the BH formation and early growth theories. Those mechanism span a wide range of hydrodynamical and pure gravitational-induced processes operating in the early Universe, extensively reviewed, among the others, by Volonteri (2010); Latif and Ferrara (2016); Volonteri et al. (2021); Inayoshi et al. (2020). Several formation channels have been proposed, often categorized into *light* and *heavy* seeds (but see Regan and Volonteri (2024) for a comprehensive discussion on this bimodality). Light seeds originate from the collapse of the first stars, while heavy seeds are attributed to different processes, as the direct collapse of massive gaseous halos, stellar collisions or BH mergers. A few details on those formation channels are given below.

- **Population III (Pop III) remnants:** The first generation of stars (Pop III) formed in minihaloes of mass $\sim 10^5$–$10^6\,M_\odot$ from the gravitational collapse of primordial gas. These structures are dominated by molecular hydrogen cooling (Sect. 5.3.1), which limits the temperature to 10^2 K, warmer than the present-day ISM. The first controlled simulations of these environments showed that these conditions disfavour the emergence of fragmentation, promoting the formation of very massive stars ($M_\star \gtrsim 100\,M_\odot$), which can collapse into BHs (e.g. Bromm et al., 1999; Abel et al., 2000; Nakamura and Umemura, 2001; Whalen et al., 2008; Alvarez et al., 2009). More recent simulations, relying on higher resolution and more detailed environmental-driven physical processes, suggest that fragmentations does act occur at these earlier times eventually leading to the formation of pre-Pop III star clusters rather than a single object. Still, those dense environments could favour stellar mergers eventually ending up as a Pop III star being a MBH seed (Prole et al. 2022; Liu et al. 2024; Clark et al. 2011; Hirano and Bromm 2017, see also Klessen and Glover 2023 for a comprehensive review);

- **Direct collapse black holes:** Another formation channel invokes the gravitational collapse of massive and dense gaseous haloes (Haehnelt and Rees 1993; Begelman et al. 2006; Loeb and Rasio 1994). In massive haloes with virial temperatures $T_{\rm vir} \gtrsim 10^4$ K,

atomic hydrogen cooling becomes efficient and can trigger gravitational collapse. However, to avoid fragmentation and prevent normal star formation, cooling by molecular hydrogen must be suppressed. Several mechanisms have been proposed to prevent fragmentation and molecular cooling as, for instance, the presence of a photodissociating UV background (e.g. Chon and Omukai 2025). The atomic-cooling clouds collapse potentially yields the formation of *supermassive stars* with masses $10^5 - 10^6\,M_\odot$ (e.g. Latif and Ferrara 2016), subsequently forming massive BHs due to the general relativistic instability. Begelman et al. (2008) have also theorized the origin of *quasi-stars*: owing to the extremely high infall rates, the central collapsing cloud is continuously compressed and heated, eventually preventing the formation of an ordinary hydrostatic star. When the core temperature reaches $T \sim 5 \times 10^8\,K$, catastrophic neutrino losses trigger the collapse of the core into a BH. The resulting structure, the quasistar, consists of a relatively low-mass BH embedded within a massive, radiation-pressure-supported envelope. The BH subsequently grows by accreting material from the envelope, until its increasing luminosity eventually disperses the surrounding gas, leaving behind a MBH seed;

- **Runaway stellar collisions in dense star clusters:** A third pathway relies on stellar dynamical processes in extremely dense star clusters. In low-metallicity environments, where radiatively driven stellar winds are weak, massive stars can undergo repeated direct collisions before they evolve off the main sequence. If the cluster core reaches sufficiently high densities, core collapse can occur on a timescale shorter than the lifetimes of massive stars, triggering a runaway sequence of mergers that forms a very massive star ($\sim 10^2$–$10^4\,M_\odot$) (Portegies Zwart et al. 2004; Devecchi and Volonteri 2009; Vergara et al. 2025). The collapse of this object then leaves an intermediate-mass black hole seed. Gas-rich environments further enhance this process by deepening the potential well and sustaining high stellar densities via gas accretion.

Also, the direct collapse of primordial density fluctuations has been proposed as a speculative formation channel for black holes, giving rise to the so-called *primordial black holes* (PBHs). Moreover, the advent of JWST has revealed a new class of compact sources commonly referred to as *Little Red Dots* (LRDs). These objects share a set of intriguing observational properties: they are detected at high redshift ($6 \lesssim z \lesssim 8$), exhibit compact morphologies, lack detectable X-ray and hot dust emission, show a pronounced V-shaped continuum in the UV–optical bands, and display broad Balmer absorption lines (Inayoshi 2025; Pérez-González et al. 2024). The nature of LRDs is still debated. Their properties may be consistent with early super-Eddington accreting AGN (e.g. Pacucci and Narayan 2024), or alternatively with the presence of supermassive stars (Nandal and Loeb 2025; Zwick et al. 2025; Begelman and Dexter 2025). Both scenarios have profound implications, as LRDs may represent the long-sought *nurseries* of MBHs in the early Universe (Akins et al. 2024) .

5.4.1 Seeding

Most of the physical processes that lead to the formation of MBHs (see Box 5.2) require extremely high resolution to be modelled self-consistently, ideally resolving the collapse of single molecular clouds at high redshift. Since these scales lie far below the resolution of modern cosmological hydrodynamical simulations, the BH formation is described in such simulations by means of sub-resolution models applied to DM halos expected to host such BHs, which are identified at run-time by a halo finder and are expected to host such BHs.

In the attempt to mimic the local conditions expected at high redshift during the collapse of very massive stars, constraints have been introduced on the halo mass and on the gas and stars already formed within such halos. These include imposing thresholds on the local gas density (typically above the star formation threshold), metallicity (preferentially metal-poor gas, $Z < 10^{-4} Z_{\odot}$), and dynamical properties, such as gravitational acceleration of the gas cell (Hopkins et al., 2022), Jeans mass (Bellovary et al., 2018), halo spin (Bhowmick et al., 2021) or velocity dispersion (Kaviraj et al. 2017), to ensure that the gas is gravitationally unstable and prone to collapse.

Taylor and Kobayashi (2014) performed a parametric study to investigate the impact of different seed masses and density thresholds in metal-free environments. They found that, at increasing resolution, lower seed masses combined with higher density thresholds lead to better agreement with key observables such as the BH–galaxy mass relation, the cosmic star formation history, and galaxy mass–size relations. Habouzit et al. (2017) attempted to reproduce light seeds originating from Pop III stars by selecting gas particles that are both metal-poor ($Z < 10^{-3.5} Z_{\odot}$) and dense (above the star formation threshold), and converting them into BH seeds. The seed mass is drawn from a logarithmically flat IMF, by estimating the fraction of stellar mass that ends up as in BHs. More recently, both light- and heavy-seed scenarios have been explored within the BRAHMA simulation suite (Bhowmick et al., 2024). In their model, heavy seeds born in dense, poorly enriched and collapsing haloes and an additional population of lower-mass BHs are seeded in resolved galaxy environment, favouring overdense regions. For the first time, Prole et al. (2025) introduced a statistical model for primordial BH seeding in cosmological simulations by converting DM particles (with mass resolution $M_{\rm DM} = 1.6 \times 10^4\,{\rm M}_{\odot}$) into BH particles to match a target PBH/DM abundance ratio in zoom-in simulations down to $z = 20$.

Despite these recent developments, most large-volume cosmological simulations still lack sufficient resolution to capture realistic seed formation, and therefore adopt the simple assumption that if a halo is sufficiently massive, a BH must already exist at its centre, without explicitly modelling its birth channel (e.g. Springel et al. 2005; Crain et al. 2015; Weinberger et al. 2018).

In OpenGADGET3, BH seeding is restricted to haloes hosting a *bona fide* galaxy. Haloes are identified using a Friends-of-Friends (FoF) algorithm with a linking length of 0.2 times the mean inter-particle separation of DM particles. To ensure that BHs are seeded only in resolved, star-forming systems, we follow Hirschmann et al. (2014) and augment the standard halo mass threshold (Springel et al., 2005) with requirements on the stellar and gas content of the halo. In detail, in the cosmological simulations presented in this work, the following seeding conditions must all be met: *(i)* the DM mass of the halo exceeds the value of 6.94×10^{10} ${\rm M}_{\odot}$; *(ii)* the stellar mass is at least 2 per cent of the total halo mass and 5 per cent the DM mass; *(iii)* the gas mass

reaches a value of 10 per cent of the stellar mass; *(iv)* the halo does not contain any other BH particle. If a halo fulfils these conditions, the most bound star particle is converted into a BH. The mass of a BH particle at seeding, $M_{\rm BH,seed}$, is not fixed, but scales with the amount of stars in the FoF group according to:

$$M_{\rm BH,seed} = M_0 \, \frac{M_{*,\rm h}}{f_* \, M_{\rm DM,seed}} \, , \tag{5.69}$$

where $M_{*,\rm h}$ is the stellar mass assigned to a FoF halo, f_* and $M_{\rm DM,seed}$ are the input parameters for the fraction of stellar mass and the minimum DM mass for a FoF halo where to seed a BH, respectively. As for M_0, it is the minimum seeding mass of a BH particle, when the seeding conditions are just met. In particular, in OpenGADGET3 we adopt $\rm M_0 = 2.7 \times 10^5 \, M_\odot$, $M_{\rm DM,seed} = 6.94 \times 10^{10}$ $\rm M_\odot$. It is important to notice that in some cosmological simulations, as the ones presented in Chapters 7 and 9, the mass of DM or the minimum mass of star particles is larger that the minimum seeding mass of BHs. This is an intrinsic limitation related to the finite resolution achieved in sampling with particles a collisionless fluid, and is different with respect to what happens in the real Universe, where the MBH hosted at the center of a galaxy is way more massive than the surrounding stars. As a consequence, despite the initial BH position at seeding is at the location of the most bound particle, two-body scattering with neighboring particles can easily cause the BH to be scattered outside its host galaxy.

5.4.2 Gas accretion

The processes regulating the onset of gas accretion onto MBHs occur in their immediate vicinity (< 1 pc) and therefore require sub-resolution models to be captured in simulations with parsec-scale or coarser spatial resolution. The most widely used prescription is based on accretion from a spherical, non-rotating, homogeneous gaseous medium surrounding the BH—namely the Bondi accretion model (Bondi, 1952). According to this model, the gas accretion rate scales with the square of the BH mass according to

$$\dot{M}_{\rm BH} = \frac{4\pi G^2 M_{\rm BH}^2 \rho}{(c_s^2 + v^2)^{3/2}} \, . \tag{5.70}$$

Here c_s and v are the local sound speed and the relative velocity of the BH with respect to the surrounding gas. In cosmological simulations, the Bondi radius is typically unresolved, implying that the gas density and sound speed entering the formula are averaged over scales much larger than the true accretion region. In addition, the accretion rate is capped at the Eddington limit:

$$\dot{M}_{\rm Edd} = \frac{4\pi G m_p M_{\rm BH}}{\eta_r \sigma_T c}, \tag{5.71}$$

where m_p is the proton mass, σ_T the Thomson scattering cross section, and η_r the radiative efficiency. The assumptions underlying the Bondi model—adiabatic, steady, spherically symmetric flow with unperturbed boundary conditions at infinity—are often violated in realistic astrophysical environments. Turbulence, radiative cooling, and heating in the hot gaseous halo can significantly alter the inflow, leading to strong deviations from the idealized Bondi picture. To address these

limitations, several alternative models have been proposed. Hopkins and Quataert (2011) introduced a torque-limited accretion model in which gravitational instabilities drive gas inflow; this approach was later implemented in the SIMBA simulations (Davé et al., 2019), applying torque-driven accretion to the cold phase and Bondi accretion to the hot phase. When applying the Bondi accretion rate, Springel et al. (2005) further add an accretion *boost factor* α to account for the unresolved ICM. Booth and Schaye (2009) explored a density-dependent, non-constant boost factor for BH accretion, emphasizing its importance for the BH self-regulation regime. Moreover, Gaspari et al. (2013) demonstrated that, within scales of a few hundred parsecs, accretion is dominated by thermally unstable cold gas, whose angular momentum is dissipated through collisions, leading to chaotic cold accretion. They found that, when cooling and turbulence are included, the accretion rate can be enhanced by a factor of ~ 100 compared to the classical Bondi rate, whereas in the adiabatic case the rate is about ten times lower. Accordingly, OpenGADGET3 implements the model of Steinborn et al. (2015), which adopts a Bondi-like accretion formula where the boost factor α varies upon the temperature of the surrounding gas:

$$\dot{M}_{\mathrm{Bondi}} = \frac{4\pi G^2 M_{\mathrm{BH}}^2 \alpha \rho}{(c_s^2 + v^2)^{3/2}} \tag{5.72}$$

with α defined as:

$$\alpha = \begin{cases} 100 & \text{for cold gas } (T < 10^5\,\mathrm{K}), \\ 10 & \text{for hot gas } (T > 10^5\,\mathrm{K}). \end{cases} \tag{5.73}$$

A constant radiative efficiency $\eta_r = 0.1$ is adopted.

In addition, each BH particle is assigned a dynamical mass, which is used for gravitational interactions and is updated in a discrete fashion through a stochastic swallowing scheme (Springel et al., 2005). In this approach, the BH swallows neighbouring gas particles probabilistically. As a result, the actual and dynamical BH masses may temporarily differ, reflecting the coarse-grained nature of accretion imposed by the finite mass resolution of the simulation. To minimize this discrepancy, OpenGADGET3 allows each gas particle to be divided into n_s "slices". During an accretion event, the BH swallows only one of these slices, so that a gas particle loses a fraction $1/n_s$ of its original mass. Higher values of n_s correspond to a finer sampling of the accretion flow and a smaller mismatch between the two BH mass definitions. In this stochastic framework, the probability that a BH swallows a gas slice during a timestep is

$$p = \frac{m_{\mathrm{gas}}}{m_{\mathrm{acc}}} \left(1 - e^{-\dot{M}_{\mathrm{BH}} \Delta t / m_{\mathrm{gas}}}\right), \tag{5.74}$$

where m_{gas} is the mass of the gas particle under consideration, and m_{acc} is the mass associated with a single slice (i.e. the initial gas-particle mass divided by n_s), and Δt is the BH timestep. In the default OpenGADGET3 implementation, only multiphase gas particles are eligible to be swallowed.

5.4.3 Mergers

The ability to follow the coalescence stage of BHs depends both on the spatial resolution of the simulation and on the sub-resolution prescriptions adopted for their dynamics, which will

be discussed in detail in the next Chapter. With gravitational softening lengths of the order of hundreds of parsecs, as in the cosmological simulations presented in this Thesis, DF is still the dominant mechanism driving the orbital decay of BH pairs. As a consequence of this limited resolution, the processes described in Sect. 4.2.1 are highly under-resolved, thus preventing the simulation from capturing the stages of binary formation, hardening and the final coalescence (see Sect. 4.2.1). In large-scale cosmological simulations, a widely used sub-resolution prescription for BH-BH merging is to assume that two BHs coalesce once their separation falls below a limiting distance $d_{\rm merg}$ — typically comparable to the resolution limit or to the gravitational softening length. In this case, the less massive (or less bound) BH is removed, and the surviving BH inherits the total mass of the pair. To avoid spurious mergers between BHs that are not gravitationally bound, an additional constraint is often imposed on their relative velocity. For example, Davé et al. (2019), Crain et al. (2015), and Dubois et al. (2016) merge BHs if their relative velocity is lower than the mutual escape velocity.

In OpenGADGET3, we adopt a limiting distance for mergers of

$$d_{\rm merg} = 5 \cdot \epsilon_{\rm BH} \tag{5.75}$$

where $\epsilon_{\rm BH}$ is the BH gravitational softening length. The adopted distance threshold depends sensitively on the accuracy of the BH dynamical reconstruction. The factor of five represents a conservative choice intended to compensate for uncertainties in the reconstructed BH orbits arising from the sub-resolution treatment of DF. When an artificial boosting of the BH dynamical mass is implemented (see Sect. 6.1.2; as in Esposito et al. 2025; Sala et al. 2024), long-lived and poorly resolved BH pairs survive and their orbital decay is not reliably captured (see Sect. 7.3). In contrast, when artificial repositioning to the local potential minimum is employed (see Sect. 6.1.1), the physical interpretation of the merger distance becomes less critical. The repositioning scheme continuously forces BHs toward the local minimum of the gravitational potential rapidly driving the pair to very close distances. As a result, mergers typically occur within only a few time steps once the BHs are embedded into the potential well of the same galaxy and the precise boosting of the softening entering in Eq. (5.75) has little dynamical relevance. The DF prescription introduced in this Thesis (see Sect. 8.2.1) provides a more accurate treatment of BH orbital evolution. This improvement will enable a more reliable modelling of BH dynamics and, in future simulation generations, allow the merger-distance threshold to be relaxed without compromising physical consistency.

To prevent artificial mergers during fly-by encounters — where two BHs may temporarily pass within $d_{\rm merg}$ at high relative velocity while remaining unbound — we additionally require that the relative velocity of the BH pair be smaller than half of the local sound speed (Di Matteo et al. 2008):

$$v_{\rm rel} < 0.5 \cdot \ c_s \tag{5.76}$$

Second, we impose that the two BHs are gravitationally bound, expressed as:

$$\frac{|\Phi_{\rm BH_1} - \Phi_{\rm BH_2}|}{a} < 0.5 \ c_s^2 - v_{\rm rel}^2 \tag{5.77}$$

where $\Phi_{\rm BH_1}$ and $\Phi_{\rm BH_2}$ are the gravitational potentials at the positions of the two BHs, c_s is the

local sound speed, $v_{\rm rel}$ is their relative velocity, and a is the cosmological scale factor, normalized to unity at redshift $z = 0$. During a merger event, the BH residing in the deeper potential well (i.e. with the lower value of Φ) is designated as the primary and accretes the secondary BH. Consequently, the remnant BH retains the position and velocity of the primary, while its mass increases by the mass of the swallowed BH.

5.4.4 Feedback

The injection of thermal and mechanical energy from AGN is extremely challenging to model, as its effects span many orders of magnitude in scale — originating at sub-parsec distances and impacting the intergalactic medium up to hundreds of kiloparsecs away. Following the early implementations by Springel et al. (2005) and Steinborn et al. (2015), in OpenGADGET3 AGN feedback is modelled as a purely thermal process. The rate of energy injection is computed as

$$\dot{E} = \eta_r \eta_f \dot{M}_{\rm BH} c^2, \tag{5.78}$$

where $\dot{M}_{\rm BH} = \min(\dot{M}_{\rm Bondi}, \dot{M}_{\rm Edd})$ is the BH accretion rate, η_r is the radiative efficiency, and η_f represents the fraction of the radiated energy that is thermally coupled to the surrounding gas. We further mimic the transition between the quasar and radio modes of AGN feedback by varying η_f, following the prescriptions of Sijacki et al. (2007) and Fabjan et al. (2010). When the accretion rate drops below one hundredth of the Eddington limit, the thermal coupling efficiency is increased by a factor of four. Unless stated differently, we adopt $\eta_f = 0.05$ in the quasar mode and $\eta_f = 0.2$ in the radio mode for the simulation presented in this work. This implementation neglects a direct mechanical energy injection, which is included in other simulations (e.g. Davé et al. 2019; Dubois et al. 2016; Trebitsch et al. 2021), typically in the form of bipolar jets launched perpendicular to the galactic disk. Moreover, the simulations presented in this work assume a constant radiative efficiency, whereas in reality η_r depends on the spin of the BH through its effect on the innermost stable circular orbit (ISCO) radius (Trebitsch et al., 2021). A model incorporating spin evolution and spin-dependent radiative efficiency has recently been implemented in OpenGADGET3 by Sala et al. (2024). This implementation is not included in the simulations presented here.

5.5 Summary

This Chapter outlined the numerical framework underlying the simulations presented in this Thesis, with particular emphasis on the modules governing BH dynamics. Special attention was devoted to the collisionless sector—describing gravitational interactions among particles—as these components directly govern the orbital evolution of BHs. In this context, Sect. 5.1 detailed the TreePM algorithm implemented in OpenGADGET3, as well as the implications of choosing the simulation resolution and gravitational softening length. These aspects are crucial for the remainder of this Thesis, as several upcoming results hinge on implementing a strategy to model a fundamentally collisional process as DF within a collisionless gravitational framework that does not inherently capture sub-resolution dynamical interactions. After describing the techniques used to compute hydrodynamic forces (Sect. 5.1 and 5.2), the extensive set of sub-resolution prescriptions for SF and evolution, metal cooling, and stellar feedback in OpenGADGET3 have

been reviewed in Sect. 5.3. A dedicated section (Sect. 5.4) was then devoted to the treatment of BH physics. This implementation provides the foundation for the parameter exploration and methodological developments presented in Chapters 9 and 10, where the BH dynamics will be investigated in detail. Once again, the reader is referred to Table A.1 for all the model parameters associated with the sub-resolution prescriptions introduced in this Chapter.

Chapter 6

A new model for dynamical friction in OpenGADGET3

The content of this Chapter is partially based on Damiano et al. (2024, 2025).

Cosmological simulations are a powerful tool for studying the nonlinear evolution of structures arising from the gravitational instability of primordial density perturbations and from the interactions between baryonic matter — gas, stars and BHs — and DM, as discussed in the previous chapter. In N-body simulations, the collisionless component is represented by macro-particles (Sect. 5.1), whose individual trajectories carry no direct physical meaning; only their ensemble properties are physically relevant. Instead, it is the ensemble properties of the particle distribution that carry the physical significance. A BH particle, on the other hand, is introduced in cosmological simulations as an individual collisionless particle (see Sect. 5.4.1), and has a specific physical meaning; its presence is capable of impacting significantly the global properties of the galaxy it belongs to. Unlike the surrounding macro-particles, BHs are not entities whose motion can be interpreted solely on a global scale. Instead, their motion mirrors the effective motion of an astrophysical object. This asymmetry between BH particles — which represent individual astrophysical objects — and the surrounding macro-particles — which represent coarse-grained phase-space elements — constitutes a fundamental conceptual inconsistency when modelling BH dynamics.

Specifically, scattering interactions between a BH and its surrounding particles can *heat* the BH orbit. A spurious, numerical displacement of a BH from the centre of the host galaxy is a major consequence of this heating, and can eventually lead to the formation of unwanted *wandering* BHs. Furthermore, this displacement also compromises the reliable tracking of BH–BH mergers, ultimately leading to an incorrect description of AGN feedback, which in turn strongly affects the resulting evolution of the host galaxy.

These issues ultimately arise because standard N-body simulations do not self-consistently recover the DF force at finite resolution. As the magnitude of the drag due to DF depends on the interactions between BHs and the surrounding particles, any limitation in reconstructing the correct gravitational interactions at the N-body resolution level results in an inaccurate representation of this effect. For this reason, cosmological simulations started to incorporate numerical "tricks" to try to control the dynamics of the BHs, such as artificially repositioning the BHs at the position of a local minimum of the gravitational potential (Springel et al., 2005; Di Matteo

et al., 2008; Davé et al., 2019; Crain et al., 2015; Weinberger et al., 2018; Sijacki et al., 2015a; Ragone-Figueroa et al., 2018; Bassini et al., 2019; Henden et al., 2018), or using a boosted dynamical mass to enhance the effect of the resolved DF (Curtis and Sijacki, 2015; Bassini et al., 2020). Other works have already suggested addressing this problem by introducing an explicit correction for the unresolved DF (Hirschmann et al., 2014; Tremmel et al., 2015; Tremmel et al., 2017; Bird et al., 2022; Chen et al., 2022; Pfister et al., 2019; Ma et al., 2023; Genina et al., 2024). After reviewing other implementations to control the BH dynamics in Sect. 6.1, this Chapter introduces a novel implementation of the DF correction based on the first diffusion coefficient of the Fokker-Planck equation (see Sect. 4.1.1) in Sect. 6.2.1 and highlights the difference with other DF sub-resolution prescriptions in Sect. 6.2.3. The implementation presented here represents a key step in the development of this Thesis, as its formulation will serve as the foundation for all subsequent tests and analyses. In particular, it will be applied in two complementary contexts: within cosmological simulations (Chapter 7), where it will be directly compared against alternative sub-resolution schemes for BH dynamics, and within idealized isolated setups (Chapter 8), designed to provide a controlled environment for validating the physical accuracy of the model and for assessing its performance across different resolution regimes.

6.1 Numerical approaches to follow for BH dynamics

Two widely adopted strategies to control the dynamics of massive BHs in cosmological simulations are the repositioning technique and the use of a boosted dynamical mass. Both approaches are implemented in OpenGADGET3, providing the opportunity for a direct comparison that will be examined in the first results Chapter of this Thesis (Chapter 7). It is therefore useful to summarise here the principles underlying each method, together with the motivations for their use and the potential limitations associated with their implementation.

6.1.1 Repositioning

A major limitation in the treatment of BH particles in N-body simulations is that they can escape from the centres of the host galaxies. One of the most widely used methods to avoid this spurious numerical effect consists of repositioning, at each time step, the BH particle at the position of the most bound particle among its neighbours. Different implementations vary in their choice of search radius and in the additional constraints imposed when selecting the target particle where to move the BH. In this way, the BH particle is generally forced to remain at the centre of its host sub-halo (see e.g. Di Matteo et al., 2008; Booth and Schaye, 2009; Ragone-Figueroa et al., 2018; Davé et al., 2019).

As pointed out by Tremmel et al. (2015), this method may have major shortcomings during mergers or high-speed close encounters between galaxies. During a close encounter between two galaxies, one of the two BHs may select as the most bound neighbour particle a particle belonging to the other galaxy. In this case, at the next time step the BH is suddenly and unphysically relocated to the neighbouring galaxy, thus leaving its original host galaxy without a central BH. In addition, a BH that has been displaced to the outer regions of its host galaxy is typically repositioned toward the centre of the new host system, where another BH may eventually be

present. In this way, BH-BH mergers will become faster and more frequent. An example of such BH *teleporting* is shown in Fig. 6.1, from one of the simulations presented in this Thesis (the `C113` galaxy group, see Chapter 7 and 9). The panels display stellar density maps during an episode of teleportation occurring between redshifts $z = 2.3$ and $z = 2.17$ in a simulation of a group-sized halo (see Sect. 7.1). The BHs involved in the event are marked with red crosses, and blue circles enclose the central BH, scaling linearly with its mass. In the left and central panels, the arrow highlights a clump of particles lacking a central BH, moving toward the central galaxy, which already hosts a central and a satellite BH in its outskirts. By the central panel, the clump has approached the system; in the right panel, the satellite BH has disappeared, while the mass of the central BH has increased, indicating that a merger has occurred between the satellite and the central BH. To highlight this mass increase, the white circle in the rightmost panel indicates the mass of the BH at the previous snapshot (i.e. referring to $z = 2.21$ in the central panel). This sequence represents a typical teleportation event, where a satellite BH identifies neighboring particles belonging to another substructure (the clump), which itself lies closer to a more massive system. This leads to a cascade of positional *jumps* of the BH and artificially accelerated mergers.

To prevent the occurrence of these spurious behaviours, different definitions of the neighbours, over which to search for the most bound particle, have been employed. The original radius was set as the SPH smoothing radius of the BH particle, or some kernel radius associated with a different hydro solver (e.g. Di Matteo et al., 2008; Vogelsberger et al., 2013; Davé et al., 2019). Other authors preferred to search the most bound particle within the BH gravitational softening or a small multiple of it (e.g. Booth and Schaye, 2009; Ragone-Figueroa et al., 2018), since the smoothing length can be much larger, thus exacerbating the problem mentioned above. A further condition usually introduced to search for the most bound particle is that its velocity relative to the BH has to be smaller than a limiting value, in the attempt to ensure that it belongs to the same galaxy. The most commonly used criterion to choose this limiting relative velocity is a fraction of the local sound speed, as originally introduced by Di Matteo et al. (2008). However, Ragone-Figueroa et al. (2018) and Bahé et al. (2022) found that this criterion is not effective. In particular, the results from Ragone-Figueroa et al. (2018) improved by imposing a maximum velocity of the order of the typical motions of particles within galaxies, namely 100-200 km/s. The choice of these values and of a smaller search radius dictated by the BH gravitational softening limited to a good degree the unphysical transfer of a BH to another galaxy in their zoom-in cluster simulations, since the typical orbital velocities of galaxies in clusters are much larger. In a dedicated study, Bahé et al. (2022) found that repositioning is a necessary prerequisite to enhance AGN accretion and the resulting feedback. This procedure promotes MBH mergers, thereby accelerating their early growth, increasing the local gas density around the BH, and reducing its relative velocity — both factors that amplify the Bondi accretion rate in Eq. (5.72). Recently, Buttigieg et al. (2025) found instead that in the FABLE simulation (Henden et al. 2018) repositioning - even when limited within the softening length - often leads to *premature mergers* of the BHs happening even before the merger of the host galaxies. Those premature mergers are a consequence of the teleporting effect as indicated in Fig. 6.1.

In the simulations presented in the following Chapter, the repositioning will be performed by selecting the most bound neighbour particle within the SPH smoothing length, provided that its relative velocity is smaller than 25% of the local sound speed. The motivation behind this choice

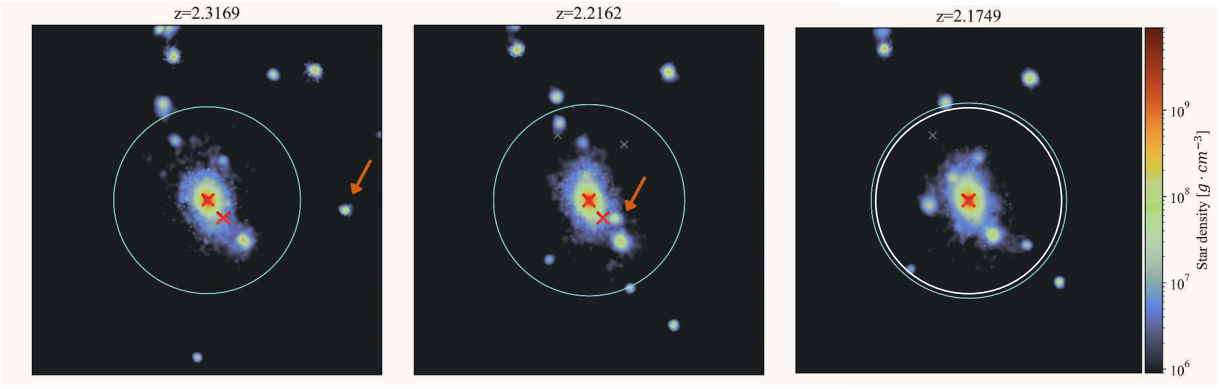

Figure 6.1: *Example of a "BH teleportation" event between $z = 2.3$ and $z = 2.17$ in a group-sized zoom in simulations (the* `Cl13` *simulation presented in Chapter 7). The panels show stellar density maps, red crosses mark the position of the two BHs involved in the merger event and the circle enclosing the central BH scales with the mass of the BH. In the rightmost panel, the former (i.e. referring to the central panel) BH mass is highlighted with a white circle, to underline the difference after the merger event. The arrow highlights a clump of particles without a central BH approaching the main galaxy.*

lies in the increased resolution of the simulation compared to those presented in Ragone-Figueroa et al. (2018), now able to provide a more complex merger dynamics, and the purpose to highlight the limitations of this commonly used repositioning technique.

6.1.2 Boosted dynamical mass

An alternative approach to account for the limited mass resolution when the mass of the BH particles is close to its seeding mass is to increase the BH dynamical mass at seeding artificially. In this approach, once seeded, two different masses are assigned to the BH: the real mass, m_r, which grows continuously by the Eddington-limited Bondi-like prescription Eq. (5.72), and the dynamical mass, m_d, which enters in the computation of gravitational force. At seeding, the latter is set at a relatively large value, typically equal to the mass of DM particles, while the former is a few orders of magnitude smaller. As long as $m_r < m_d$, the value of m_d does not increase by gas accretion, which only affects the value of m_r. Once $m_r \geq m_d$, the real mass increases in a continuous way, while the dynamical mass increases according to a stochastic prescription for the swallowing of neighbour gas particles (Springel et al. 2005, see also Sect. 5.4.2). From then on, the two masses remain similar, differing only because of the stochastic swallowing of gas particles.

This artificial boost of the BH dynamical mass at seeding is intended to amplify the effect of the numerically resolved DF, eventually preventing the BH from escaping the host halo soon after it is seeded.

Clearly, this method is also prone to spurious effects. For instance, Tremmel et al. (2015) pointed out that initialising the BH mass with a value hundreds of times higher than its real value introduces a non-negligible alteration of the local gravitational potential thus unavoidably impacting its subsequent evolution.

6.2 Sub-resolution models for DF

The numerical approaches presented so far exhibit a number of intrinsic limitations. Hence, developing a physically motivated correction for the unresolved DF acting on BH particles — rather than relying on ad hoc prescriptions — is highly desirable. In existing implementations (Hirschmann et al. 2014; Tremmel et al. 2015; Pfister et al. 2019; Ma et al. 2023; Genina et al. 2024), a correction for unresolved DF is introduced as a correction term added to the acceleration computed by the gravity solver, so that the total acceleration acting on the BH is:

$$\vec{a}_{\rm BH} = \vec{a}_{\rm grav} + \vec{a}_{\rm DF}, \tag{6.1}$$

where $\vec{a}_{\rm DF}$ represents the DF correction. Although the specific estimates of this term differ among models, they all address the same fundamental challenge, explained here below.

As discussed in Sect. 5.1, the N-body method serves to approximate a collisionless fluid, in which individual particle encounters are negligible and only collective gravitational effects matter. However, the derivation of DF (Sect. 4.1.1) originates from single scattering events and, as such, it is intrinsically a collisional process. In fact, DF arises from the diffusion coefficients, which are obtained by expanding the collisional term of the Boltzmann equation (Eq. 4.1). Thus, the core difficulty lies in embedding a *collisional* effect within a *collisionless* numerical framework. In practice, when computing the DF correction in Eq. (6.1), two main sources of uncertainty emerge:

- **Phase-space distribution function:** its local estimate can be coarse due to limited mass resolution and the chosen softening length;

- **Maximum impact parameter:** determining the spatial scale over which the DF correction should be applied is non-trivial, since part of the total DF effect may already be captured by the gravitational solver.

Differences among existing DF implementations primarily arise from their assumptions regarding these two quantities entering Eq. (4.26). In the following, we present a novel implementation of the DF correction, presented in Damiano et al. (2024) and Damiano et al. (2025), emphasizing its conceptual and practical distinctions from previous approaches.

6.2.1 A novel implementation for DF in OpenGADGET3

The novel implementation that will be introduced here starts from the first order diffusion coefficient of Eq.(4.26). To constrain the phase-space distribution function and the maximum impact parameter, the assumption is made that the BH is surrounded by a populations of "stellar" particles within a region of radius $b_{\rm max}$ around the BH. Within each population, stellar particles share the same mass m_j. Therefore, the coarse-grained phase-space distribution around the position of the BH can be expressed by the following equation:

$$\mathrm{f}(\tilde{\mathrm{x}}, \tilde{\mathrm{V}}) = \sum_{\mathrm{j}} \tilde{\mathrm{n}}_{\mathrm{j}} \delta(\tilde{\mathrm{V}} - \tilde{\mathrm{v}}_{\mathrm{j}}) \tag{6.2}$$

where $(\vec{x}, \vec{V})$ are the phase-space coordinates of the BH, the index j runs over all the particles in the population lying within $b_{\max}$ and $\tilde{n}_j$ denotes the effective spatial volume assigned to particle j (i.e. a volume weight). Equation (6.2) provides the fundamental basis of the model. The ensuing DF model has been initially developed assuming an homogeneous and isotropic density around the BH by Damiano et al. (2024). This assumption has been lately relaxed in Damiano et al. (2025) to overcome some limitations in the regime where the BH mass is lower than the surrounding macro-particle mass. In order to have a comprehensive and complete description, both the derivations are detailed below.

6.2.2 The model of Damiano et al. (2024)

Assuming a spherical, homogeneous, and isotropic distribution of particles around the BH, and under the hypothesis that the maximum impact parameter to be considered for the DF correction is the BH softening length, $\epsilon_{\rm BH}$, the spatial volume weight is equal for each particle and given by:

$$\tilde{n}_j = \frac{3}{4\pi\epsilon_{\rm BH}^3}. \tag{6.3}$$

leading to a total number density given by $N/\tilde{n}_j$, where N is the total number of particles lying below the softening length.

Equation (4.26) provides the first diffusion coefficient in the Fokker-Planck approximation for the $i-$th velocity component of the BH V_i. Using Eq.(6.2) for the phase-space distribution function together with Eq. (4.12), the number density defined by Eq. (6.3) and again setting $b_{\max} = \epsilon_{\rm BH}$, $D[\Delta V_i]$, becomes:

$$D[\Delta V_i] = \frac{3}{2\epsilon_{\rm BH}^3} \sum_j \frac{G^2(M+m_j)m_j}{|\vec{v}_j - \vec{V}|^3} \ln\left(1+\Lambda(m_j,\vec{v}_j)^2\right)(v_{i,j} - V_i), \tag{6.4}$$

where M is the mass of the BH, and the argument of the Coulomb logarithm Λ is given by:

$$\Lambda(m_j,\vec{v}_j) = \frac{(\vec{v}_j - \vec{V})^2\epsilon_{\rm BH}}{G(M+m_j)}. \tag{6.5}$$

Therefore, the total DF correction to be applied in Eq. (6.1) will be:

$$\vec{a}_{\rm DF} = D[\Delta\vec{V}] = \frac{3}{2\epsilon_{\rm BH}^3} \sum_j \frac{G^2(M+m_j)m_j}{|\vec{v}_j - \vec{V}|^3} \ln\left(1+\Lambda(m_j,\vec{v}_j)^2\right)(\vec{v}_j - \vec{V}). \tag{6.6}$$

The underlying assumption of this implementation are listed in the box below.

Assumptions underlying the DF correction

1. **Local density assumption:** The gas and stellar distributions within the BH softening length are assumed to be spherically homogeneous, as described by Eq. (6.3). This assumption will be further relaxed in Sect. 8.3.1.
2. **Maximum impact parameter:** The maximum impact parameter is set equal to the BH softening length, $\epsilon_{\rm BH}$, implying that the DF contribution on scales larger than $\epsilon_{\rm BH}$ is captured by the gravitational solver.
3. **Velocity distribution:** The velocity distribution within $\epsilon_{\rm BH}$ is assumed to follow the form given in Eq. (6.2).

The model of Damiano et al. (2025)

Starting from the general expression of the phase-space distribution function given in Eq. (6.2), the diffusion coefficient in Eq. (4.26) can be written as

$$D[\Delta V_i] = 2\pi \sum_j \tilde{n}_j \frac{G^2(M+m_j)m_j}{|\vec{v}_j - \vec{V}|^3} \ln\left[1+\Lambda(m_j,\vec{v}_j)^2\right](v_{i,j}-V_i), \tag{6.7}$$

which corresponds to Eq. (6.4) when the assumption of Eq. (6.3) is no longer imposed. Under the assumption that the DF correction $\vec{a}_{\rm DF}$ in Eq. (6.1) acts only below $\mathrm{b}_{\rm max,c}$ around a BH of mass $M_{\rm BH}$ and velocity $\vec{v}_{\rm BH}$:

$$\begin{aligned}\vec{\mathrm{a}}_{\rm DF} = D[\Delta\vec{v}_{\rm BH}] \sum_j^N & -2\pi G m_j (M_{\rm BH}+m_j)\,\tilde{n}_j \\ & \times \ln\left[1+\Lambda(m_j,\vec{v}_j)^2\right] \frac{\vec{v}_j - \vec{v}_{\rm BH}}{|v_j - v_{\rm BH}|^3}\,.\end{aligned} \tag{6.8}$$

In analogy with Eq. (6.5) for $\mathrm{b}_{\rm max,c}$, in Eq. (6.8):

$$\Lambda(m_j,\vec{v}_j) = \frac{(\vec{v}_j - \vec{V})^2 b_{\rm max,c}}{G(M_{\rm BH}+m_j)}. \tag{6.9}$$

Note that Eq.(6.8) generalizes the formulation of Eq. (6.6) for non-uniform density around a BH particle. Moreover, it does not explicitly assume the BH softening to be the maximum impact parameter, but a threshold given $\mathrm{b}_{\rm max,c}$ is fixed for the correction. As introduced in Sect. 5.1.1, the OpenGADGET3 code derives the spline-softened gravitational force by taking the force from a point mass m to be the one resulting from a density distribution $\rho(\mathrm{r}) = \mathrm{mW}(\mathrm{r},\epsilon)$ (see Springel et al. 2001, Appendix A) where $\mathrm{W}(\mathrm{r},\epsilon)$ is the cubic spline kernel of Eq. (5.20) and ϵ is the softening length. Therefore, then the *weight* of the j-th particle placed at the position $\vec{r}_j$

in Eq.(6.8) is $\tilde{n}_j = W(r_j, \epsilon)$ and it becomes:

$$\vec{a}_{\rm DF} = \sum_{j}^{N(<b_{max,c})} -2\pi G m_j (M_{\rm BH} + m_j) W(r_j, \epsilon) \times \ln(1 + \Lambda(m_j, \vec{V})^2) \frac{\vec{v}_j - \vec{V}}{|\vec{v}_j - \vec{V}|^3} \,. \tag{6.10}$$

By this way, the first assumption listed in the Box of Sect. 6.2.2 is also relaxed.

These models and the underlying assumptions will be extensively tested and justified in the following of this Thesis, by analysing a variety of numerical simulations involving different environments and resolutions. Before proceeding, it is important to stress that the DF implementation adopted in this work applies only to the stellar and DM components; the contribution from the gaseous phase (e.g. Ostriker 1999; Lescaudron et al. 2023; Dubois et al. 2016) is neglected in the simulations presented here. In their seminal work, Ostriker (1999) derived an analytic expression for the DF force exerted by a gaseous medium in the case of a uniform, stationary flow past the BH. Using very high–resolution simulations (down to ~ 0.1 pc), Chapon et al. (2013) carried out simulations of a major merger between Milky Way–like galaxies. They found that the effectiveness of the gaseous drag manifests within the 2–3 pc trailing wake behind the BH. However, the strength of the drag depends sensitively on the BH's velocity relative to the gas, the BH mass, the local gas density, and the polytropic index of the gas equation of state. In particular, they showed that the gaseous drag is most effective in the transonic regime—when the BH velocity approaches or exceeds the local sound speed—while it becomes strongly suppressed by stiffer equations of state, both because the gas is more subsonic and the density is lower. More recently, Chen et al. (2022) implemented a sub-resolution prescription based on the Ostriker (1999) formula. They found a broad correlation between the efficiency of the gaseous drag and the BH mass, with substantial scatter for $M_{\rm BH} \sim 10^5 - 10^6\,M_\odot$. Moreover, they showed that across all BH mass regimes, the drag exerted by the gas is weaker than the DF contribution from collisionless particles, which exceeds the gaseous drag by more than two orders of magnitude for $M_{\rm BH} > 10^7, M_\odot$. Given the resolution of the simulations analysed in this Thesis, the sub-pc region where gaseous drag becomes significant (as identified in Chapon et al. 2013) is far from being resolved, the assumption of ideal gas contributes to reduce the gaseous DF. For this reason, the gaseous DF contribution is neglected here. Nonetheless, implementing a gas–DF model would be relevant for future high-resolution simulations in high-redshift environments, where the gas density and thermodynamics may play a stronger dynamical role (see also Chapter 11).

6.2.3 Comparison with other models

The implementation of a correction of the DF force acting on BH particles, based on the original derivation by Chandrasekhar (1943a), has been explored in various studies since the very first implementations (e.g. Hirschmann et al. 2014, Tremmel et al. 2015). A common aspect

of all such approaches is that they start from Eq. (4.26), and implicitly assume that the BH is surrounded by a homogeneous and infinite distribution of particles all having the same mass, which is smaller than the BH particle mass. Different approaches rely on different assumptions of the physical size of the region where to correct for the unresolved DF, i.e. on the actual value of $b_{\rm max}$. For instance, in the work by Hirschmann et al. (2014), $b_{\rm max}$ is defined as the typical size of the system hosting the BH and, as such, it is set to the half-mass radius of the sub-halo[1]. On the other hand, Tremmel et al. (2015) argued that DF is correctly computed by the N-body solver at scales larger than the gravitational softening length of the BH, $\epsilon_{\rm BH}$. Accordingly, a correction term to the DF should be added only on scales smaller than $\epsilon_{\rm BH}$, so that $b_{\rm max} = \epsilon_{\rm BH}$.

Pfister et al. (2019) used the grid code RAMSES (Teyssier 2010), and included a DF correction considering the contributions from particles lying below $4\Delta x$, where Δx is the local mesh size. Finally, the DF model by Chen et al. (2022) and Bird et al. (2022) assumes a constant value of $b_{max} = 10\,h^{-1}$ckpc and 20 kpc, respectively. As for the velocity distribution function of the sea of particles around the BH, Hirschmann et al. (2014), Chen et al. (2007) and Bird et al. (2022) adopt the same standard hypothesis, originally formulated by Chandrasekhar (1943a) and Binney and Tremaine (1987), of a local Maxwellian velocity distribution. Under the further hypothesis that $M_{\rm BH} \gg m$, where m is the mass of the particles around the BH, the DF force can be cast in the form

$$\vec{F}_{\rm DF} = -4\pi\rho \left(\frac{G{\rm M}_{\rm BH}}{v_{\rm BH}}\right)^2 {\rm F}(x)\ln(\Lambda)\widehat{v}_{\rm BH}\,. \tag{6.11}$$

Here, ρ is the smoothed density at the position of the BH, contributed by stellar and DM particles, using the BH smoothing length. Furthermore, $\widehat{v}_{\rm BH}$ is the versor of the BH velocity relative to the 'sea' of surrounding particles, while

$${\rm F}(x) = {\rm erf}(x) - \frac{2x}{\sqrt{\pi}}e^{-x^2} \quad ; \quad x = \frac{v_{\rm BH}}{\sigma_v}, \tag{6.12}$$

with σ_v representing the velocity dispersion of the surrounding particles.

Rather than assuming a specific expression for the velocity distribution function of the particles around a BH, Tremmel et al. (2015) proposed to incorporate the mass m of the surrounding particles within the integral over velocities, thus moving the uncertainty on the velocity distribution function to an uncertainty on the mass density of the surrounding particles, which they calculated using 32 neighbors of the BH. Based on this approach, Bellovary et al. (2021) excluded from their analysis the BHs with masses lower than three times the mass of the DM particles, claiming that for those particles even the DF correction introduced is not efficient. This result justifies the choice made by Chen et al. (2022) to include both a DF correction and a boosted dynamical mass for BH particles.

In a recent paper, Genina et al. (2024) adopt the same functional form of the DF prescription from Tremmel et al. (2015), but assess the relative contributions of the maximum and minimum impact parameter. They also propose an additional correction term, on top of the DF correction, based on the second-order term of the Fokker-Planck approximation (Eq. 4.6 and 4.10), to account for the stochasticity of the system. Following a systematic approach, they test the DF

[1]This parametrisation required an on-the-fly execution of the `SubFind` algorithm (Dolag et al., 2009) to identify the substructures hosting the BHs and to compute their half-mass radius.

implementation in an idealized DM halo and propose an expression for the radius over which the DF should be corrected, corresponding to $\sim 0.45\,\epsilon_{\rm BH}$ for large-scale cosmological simulations. By directly comparing the sinking timescale of a BH in the simulated halos at different resolution with the ones obtained by the regularised integrator KETJU (Mannerkoski et al. 2023), they find that the combination of parameters adopted both in Tremmel et al. (2015) and Chen et al. (2022) leads to sinking timescales which are too short. Finally, a scheme that stands out from the others is the one proposed by Ma et al. (2023). In their approach, a discrete N-body correction, similar to the one proposed in Sect. 6.2.1, is taken into account, but still acting only on scales above the gravitational force resolution of simulations. Differently from such an approach, the model that we described in the previous section explicitly intends to correct for the interactions that take place below the BH softening scale which, by definition, are not correctly described by the N-body solver.

Overall, the main differences between the DF correction proposed in this Thesis and other formulations proposed in the literature lie in the relaxation of the assumptions that *(a)* the velocity distribution function is Maxwellian; *(b)* that the masses of the surrounding particles are negligible compared to that of the BH. The summation leading to DF correction proposed in Eq. (6.6) arises from single scatters between the BH and each particle within the BH softening, each contributing with its own velocity and mass. In this way, the dynamical heating of BHs as a consequence of the noisy background potential, taking place whenever their mass is comparable to or even lower than that of the surrounding particles, is reduced. This aspect is particularly important, as the BH is embedded in a sea of pseudo-particles whose masses and individual scatterings can significantly influence its motion. Moreover, it is worth noticing that, once the scaling of the softening length with resolution is defined (see Sect. 5.1.1), Eq. (6.6) does not include any free parameter that require adjustment with changing resolution. This characteristic represents a major advantage of the formulation, as it ensures that the DF correction remains physically motivated and, as a matter of fact, resolution-independent.

Part III

Results

Chapter 7

Unresolved dynamical friction and MBH evolution: results from cosmological simulations

The content of this Chapter is based on Damiano et al. (2024), with additional material and extended discussions included for completeness.

Within this Chapter, the performance of the DF implementation introduced in Sect. 6.2.1 is presented against the repositioning technique (Sect. 6.1.1) and the boosted dynamical mass (Sect. 6.1.2) within cosmological hydrodynamical simulations carried out with the OpenGADGET3 code. The goal is to assess whether the DF prescription provides an accurate description of DF force acting on BHs and how it compares with other commonly used ad-hoc numerical prescriptions in the context of cosmological hydrodynamical simulations.

To address these points, we simulate a group-sized halo and a cluster-sized halo, with initial conditions from the Dianoga set (Bonafede et al. 2011; Bassini et al. 2019, 2020; Marini et al. 2021; Esposito et al. 2025), along with a cosmological box with a comoving size of 16 Mpc per side (16 cMpc). The simulations were carried out three times, maintaining identical settings for all parameters, except for the sub-resolution prescription governing the BH dynamics: continuous repositioning on a local potential minimum, boosted dynamical mass, and the novel model to correct the unresolved DF. After presenting the characteristics of the simulations in Sect. 7.1, the analysis of the simulation results proceeds along two lines. The first one, presented in Sect. 7.2, investigates the impact of the adopted dynamical prescriptions on the overall BH population. This includes testing the effectiveness of BH centering (Sect. 7.2.1), the assessment of the population of *wandering* and multiple BHs within the same host system (Sect. 7.2.2 and Sect. 7.2.3), and the examination of the resulting scaling relation between BH and host galaxy mass (Sect. 7.2.4). The second line of analysis focuses on the detailed orbital evolution of individual BHs and their progression toward coalescence under different dynamical sub-resolution prescriptions (Sect. 7.3). Finally, the main conclusions are summarized in Sect. 7.4.

7.1 Set of simulations

To assess the performance of the novel DF correction and to compare it with other prescriptions, we carried out a set of two zoom-in simulations (a group-sized and a cluster-sized halo), and a cosmological box (with side length of 16 cMpc) with the OpenGADGET3 code, all at the

Simulation	Model	$M_{\rm vir}$ [10^{13} M$_\odot$]	$R_{\rm vir}$ [kpc]
Cl13	REPOS	1.27	610.89
	DYNMASS	1.26	609.33
	DYNFRIC	1.26	609.75
D9	REPOS	18.76	1497.17
	DYNMASS	19.02	1504.28
	DYNFRIC	18.89	1499.24
CosmoBox	REPOS	2.57	751.01
	DYNMASS	2.58	751.55
	DYNFRIC	2.65	760.15

Table 7.1: *Summary of the simulation sets. Column 1: simulation name; Column 2: method for accounting for unresolved dynamical friction (DF); Columns 3–4: virial mass and virial radius, respectively, of the most massive halo at* $z = 0$.

same resolution. This allowed us to test the new implementation in different environments. All simulations are performed assuming a flat ΛCDM cosmology with $\Omega_m = 0.24$, $\Omega_b = 0.0375$ for total matter and baryon density parameters, $h = 0.72$ for the Hubble parameter, $n_s = 0.96$ for the primordial spectral index, $\sigma_8 = 0.8$ for the power spectrum normalisation. Table 7.1 reports a description of the main characteristics of these simulations. The selected zoom-in regions belong to the DIANOGA simulation set introduced by Bonafede et al. (2011) and Bassini et al. (2020) but adopting the same resolution as the ones presented in Esposito et al. (2025), corresponding to the mass and spatial resolution reported in Table A.1. The D9 cluster has a mass $M_{200} \simeq 1.53 \times 10^{14}$ M$_\odot$ at $z = 0$, while the other region refers to a lower-mass group of M$_{200} \simeq 1.38 \times 10^{13}$ M$_\odot$, namely Cl13[1]. As for the cosmological box, namely CosmoBox, it is simulated by adopting exactly the same cosmological model, the same implementation of all physical processes as the zoom-in simulations as well as the same resolution.

This setup enables a detailed study of systems characterized by dense environments and frequent interactions — such as galaxy clusters and groups — while also allowing for a statistical analysis of the BH population within a representative cosmological volume. In detail, the simulations include the sub-resolution prescriptions for SF, stellar evolution, metal cooling, stellar winds, BH formation, accretion and AGN feedback already specified in Sect. 5.3 and 5.4. All the parameters adopted for the sub-resolution modules are briefly summarised in Appendix A and Table A.1.

Each simulation was carried out three times under identical numerical and physical conditions, differing only in the sub-resolution prescription governing BH dynamics: continuous repositioning to a local potential minimum (Sect. 6.1.1), labelled as REPOS in Table 9.1, dynamical mass boosting (Sect. 6.1.2), indicated as DYNMASS, and the novel DF correction model introduced in Sect. 6.2.2 (Sect. 6.2.1), indicated as DYNFRIC. It is worth emphasizing that the DF model adopted in this work follows the formulation defined in Eq. (6.6), which assumes the BH softening length as the

[1] M_{200} indicates the total mass contained within a sphere of radius R$_{200}$ which contains an overdensity equal to $200\rho_c(z)$, where $\rho_c(z) = 3H(z)^2/8\pi G$ is the critical cosmic density at redshift z. In Table 7.1 the 'virial radius' R$_{\rm vir}$ is defined as the radius within which the mean halo density corresponds to the prediction of spherical collapse (e.g. Eke et al., 1996). Accordingly, the 'virial mass' M$_{\rm vir}$ is the mass of a sphere enclosed within a radius R$_{\rm vir}$.

maximum impact parameter. Within this radius, the surrounding particles are considered to have a number density described by Eq. (6.3). Consequently, the assumptions underlying the DF implementation correspond to those summarized in Box in Sect. 6.2.2. Moreover, substructures sampled with a different number of particles allows for preliminary study of the effectiveness of Eq. (6.2) and Eq. (6.3) to assess the phase-space distribution function within different environments. Those tests are presented in Appendix B and demonstrate that for well-resolved sub-halos this assumption is valid.

7.2 Statistical analysis of the BH population

The primary aim of our DF model is to avoid spurious numerical effects that other methods may produce, as discussed in Sect. 6.1.1 and Sect. 6.1.2. Thus, in this section, we present an analysis of the overall properties of the population of SMBHs in our simulations, focusing on the ability of our DF model to: place and hold the BHs at the centre of the host galaxies (Sect. 7.2.1), prevent BH particles from spuriously wandering outside the host galaxies (Sect. 7.2.2), reproduce the co-evolution of BHs and host galaxies (Sect. 7.2.4).

7.2.1 Centring the BHs within host galaxies

To assess the ability of each model to correctly locate the BHs at the centre of the host sub-halos, all the main halos and sub-halos having a BH within their DM half-mass radius (hereafter R_{HMS}) have been selected. Each BH is associated to the closest (sub-)halo, as this procedure allows to assess how BHs are kept at the centre of their host or are off-centred. Sub-halos are identified by the `SubFind` algorithm (Dolag et al., 2009) and are requested to feature at least 20 particles. In the zoom-in simulations, all the halos that contain within their R_{200} at least one low-resolution DM particle spuriously scattered within the high-resolution region are excluded from this analysis. Then, the distance between the (sub-)halo centres and the closest BH is calculated. The sub-halo centres are identified with the minimum of the gravitational potential occurring among the member particles of that sub-halo. Their values are retrieved from the `SubFind` output.

Figure 7.1 shows the histogram of the probability density function (PDF) of the number of (sub-)halos having a BH within their R_{HMS}, versus the distance Δr from the associated BH. The sample of sub-halos in Fig. 7.1 is obtained by summing up all the (sub-)halos from `D9`, `Cl13` and `CosmoBox`. However, it has been verified that the individual analysis of each of these simulations keeps the overall results unchanged. Each column displays the PDF derived with the novel DF prescription (solid black line), overlaid on the corresponding PDFs obtained using the boosted dynamical mass (left column) and repositioning (right column) techniques, both shown in blue. Different rows refer to different redshifts, with results at $z = 3, 1, 0$ from top to bottom. For reference, the dashed-dot vertical line marks the value of the Plummer-equivalent softening length of BH particles (see Sect. 5.1.1). Not surprisingly, the `REPOS` prescription predicts sub-halos that host generally well-centred BHs. This is the most consistent advantage of the repositioning technique, as well as the most predictable, since it explicitly forces the BHs to be relocated at each time-step at the centre of their host substructures. As for the `DYNMASS`, it shows the

Table 7.2: *Percentages of sub-halos from each simulation that contribute to the distributions shown in Fig.7.1.*

	REPOS			DYNMASS			DYNFRIC		
	`Cl13`	`D9`	`CosmoBox`	`Cl13`	`D9`	`CosmoBox`	`Cl13`	`D9`	`CosmoBox`
$z = 3$	11	82	7	12	83	5	12	83	5
$z = 1$	10	78	12	9	80	11	10	78	12
$z = 0$	13	70	17	10	75	15	10	75	15

Table 7.3: *Percentages of sub-halos from each simulation that contribute to the distributions shown in Fig.7.1. For each implementation, the percentage of sub-halos for each simulation is indicated:* `Cl13`*,* `D9` *and* `Cosmobox`*, in the left, central and right columns, respectively. Percentages are listed for different redshifts (as in Fig.7.1):* $z = 3$*,* $z = 1$*, and* $z = 0$*.*

least pronounced tail for higher distances ($\Delta r > 1\,\mathrm{ckpc}$) at $z = 3$. In fact, at high redshift, the impact of a large dynamical mass is relatively more important given that a larger number of BHs is expected to have relatively smaller true mass and live in less resolved hosting halos. Interestingly, in this regime, the DF model performs quite well in keeping BHs at the centre of their host halos, without resorting to ad-hoc prescription. The comparable performance of the two methods is actually a nontrivial and encouraging result for the DF implementation; in fact, accurate centring of the BHs in sub-halos is obtained as a result of an implementation of the DF correction instead of an artificial increase of BH masses, which have the side effect of altering the structure of the sub-halos gravitational potential, thereby impacting on the resulting galaxy formation process (e.g. Chen et al., 2022). Table 7.3 reports the percentage of sub-halos with which each simulation contributes to the differential distribution of Fig.7.1. The `D9` simulation provides the most numerous population of centred sub-halos, with at least 70% of the total distribution.

7.2.2 The population of spurious wandering BHs

Another crucial aspect to consider when judging the reliability of a DF model is its capability of preventing BHs from escaping the host sub-halos because of two-body interactions with larger-mass particles or during merger events. In the following, the population of these numerically-induced kicked-off BHs will be denoted as *spurious wandering* BHs (sWBHs). In detail, a BH will be referred to as a sWBH whenever its distance from the closest sub-halo is larger than twice the $\mathrm{R_{HMS}}$ of the closest sub-halo. With this definition, we deliberately focus on BHs that have been expelled from their parent galaxies to a degree that is significantly larger than in the classical "wandering" population, highlighting cases where the displacement is numerically induced. Thus, they should not be confused with the 'classical' population of off-centre wandering BH as, for instance, investigated by Tremmel et al. (2018a), Ricarte et al. (2021) (but see also Sect. 4.3), which instead are expected to become wandering as a consequence of numerically resolved gravitational dynamics.

It is worth noting that our definition can misidentify sWBHs during close encounters between sub-halos, when a non-sWBH belonging to a sub-halo can temporarily become a wanderer of the closer sub-halo passing by. However, it has been verified that limiting the search only to those BHs with a distance exceeding twice the $\mathrm{R_{HMS}}$ of the closer among the *two* sub-halos, the results

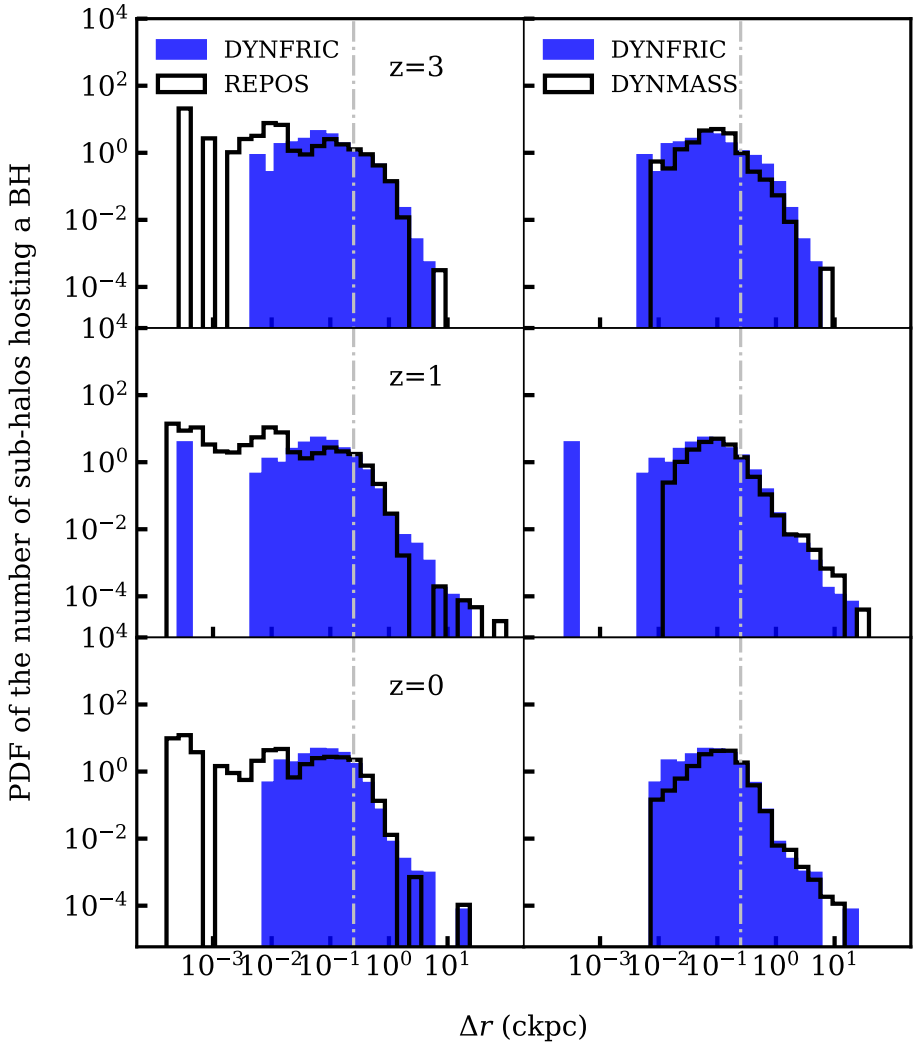

Figure 7.1: *Probability density distribution of the distances between sub-halos identified by* `SubFind` *and the closest BH particle within the* R_{HMS} *of each sub-halo of* `C113`, `D9` *regions, and* `Cosmobox`. *The rows show the results obtained at different redshifts:* $z = 3$ *(up),* $z = 1$ *(central), and* $z = 0$ *(bottom). The columns report the results comparing* `DYNFRIC` *and* `REPOS` *on the left, and* `DYNFRIC` *and* `DYNMASS` *on the right side. The dash-dotted line indicates the softening length of the BH as a reference for the spatial resolution of the simulation.*

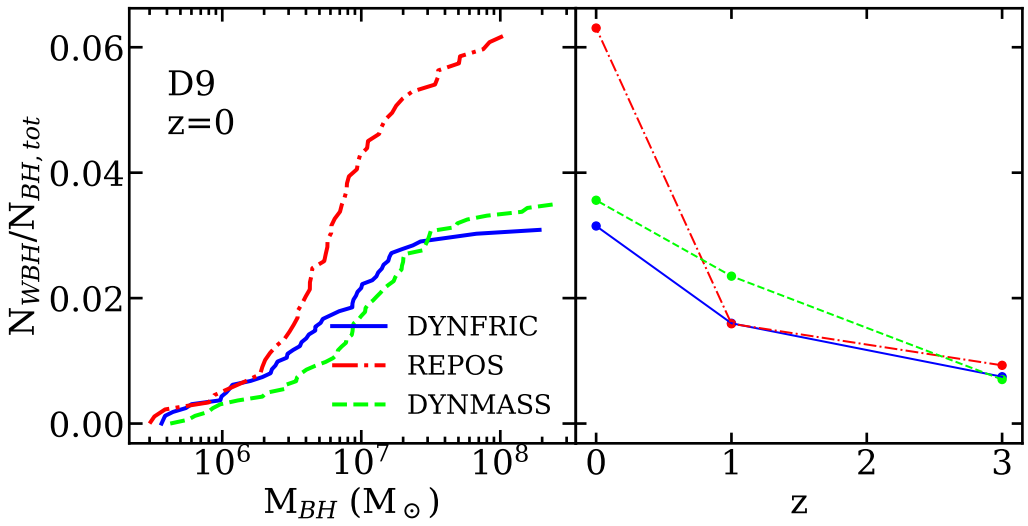

Figure 7.2: *Cumulative number of wandering BHs to the total number of BHs found in the* D9 *region as a function of the BH mass at* $z = 0$ *(left panel), and as a function of redshift for* $z = 3$, $z = 1$, *and* $z = 0$ *(right panel). In the left panel, no mass threshold is adopted to select the BHs, and hence all the BHs with mass above the seeding mass are included. In both panels, the simulation using the DF model, marked with a blue line, is compared with* REPOS *in red and* DYNMASS *in green. The wandering BHs are defined as those having a distance larger than two times the* R_{HMS} *from the closest sub-halo.*

reported below do not vary considerably.

Throughout this section, only the results from the D9 simulation are presented, as its larger population of sWBHs enables a more accurate statistical analysis.

Figure 7.2 shows the cumulative fraction of wandering BHs to the total number of BHs as a function of BH mass at $z = 0$ in the left panel, and as a function of redshift in the right panel, for all the considered sub-resolution models. In the left panel, for each BH mass on the x-axis the corresponding cumulative fraction of wandering BHs is shown on the y-axis.

Irrespective of the method employed to keep the BH centred, the ratio of the wandering BHs to the total number of BHs increases as larger BH masses are taken into account at the numerator. Each curve extends up to the value of the mass of the most massive wandering BH found in the considered simulation. The REPOS simulation, in particular, exhibits the highest fraction of wandering BHs. The percentage of wandering BHs in the simulation using the repositioning scheme rises for massive BHs ($M_{BH} > 10^7 M_\odot$). Figure 7.3 shows the number of sWBHs for each mass bin found in the D9 simulation at z = 0. For every simulations, the majority of wandering sWBHs' masses lies below 10^8. The REPOS simulations shows a double peak at $M_{BH} \sim 10^7 M_\odot$ and $10^7 < M_{BH} < 10^8$. Again, this suggests that the repositioning technique adopted in this work can produce a significant displacement or BH 'teleporting' of even massive BHs. The peak of the distribution in the DYNMASS simulation is shifted toward larger masses compared to REPOS. Moreover, DYNMASS reproduces lower sWBHs for $M_{BH} < 10^7$ compared to DYNFRIC and more for $M_{BH} > 10^7$. This is expected since on one hand, BHs in the low-mass range are boosted in mass, preventing them from escaping the surrounding sub-halo. On the other, once their mass grows up to M_{DM}, no correction acts on the dynamics of the BHs. Using the DYNFRIC technique, the

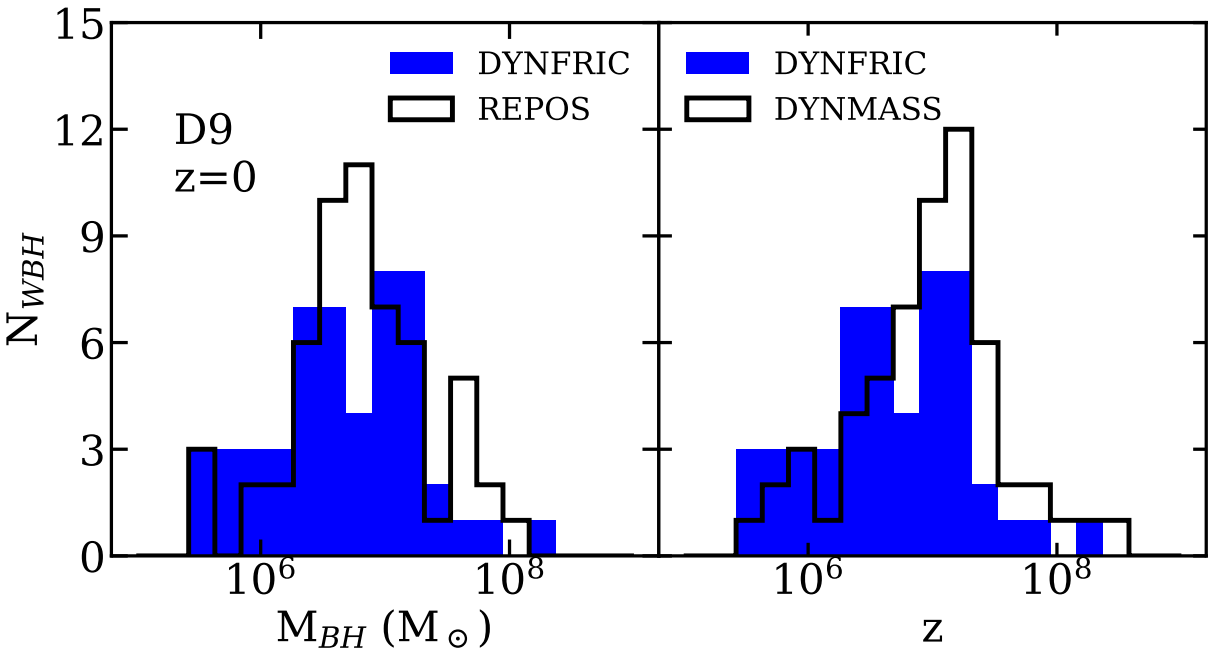

Figure 7.3: *Histogram of the number of sWBHs as a function of their mass for the* `D9` *simulation at z=0. The distribution of sWBHs is overlaid for* `DYNFRIC` *and* `REPOS` *on the left and* `DYNFRIC` *and* `DYNMASS` *on the right.*

peak of the distribution lowers down compared to the other simulations. The number of sWBHs with $M_{BH} < 10^7$ is slightly higher than for `REPOS` and `DYNMASS`, but it reduces in the high-mass end. The increase of wandering BHs when using the repositioning mechanism is surprising: these massive BHs should reside in sub-halos having a deeper potential well. Therefore, they should be less prone to wander outside their host galaxy. The origin for the excess of wandering BHs in the `REPOS` scheme can be ascribed both to close encounters between sub-structures and, at decreasing redshift, to the presence of large-scale potential gradients. To illustrate how these mechanisms work, examples of sWBHs within the `REPOS` simulation are shown in the two panels of Fig. 7.4.

Each panel of this figure shows, on the central plot, the projected stellar density around two wandering BHs, BH `2` in the top panel, and BH `4` in the bottom panel. The position of the other BHs in the field are indicated with cyan (for sWBHs) or green (for centred BHs) crosses.

Furthermore, the centres of neighboring sub-halos are denoted by shaded white dots, with circles corresponding to the sub-halo R_{HMS} enclosing them. The side plots display the gravitational potential Φ of the stars along the x-axis (on the top) and y-axis (on the right). In the top panel of Fig.7.4, BH `2` wanders due to a close encounter between two sub-halos, one having a deeper potential well. BH `2` then migrates to the location of the most bound neighbouring particles, thus moving along the gradient of the potential of the central sub-halo, and leaving its initial host sub-halo. It is worth noticing that, as defined here, a BH lying within twice the R_{HMS} of a sub-halo can be a wander: our definition classifies as not wandering only those BHs located within twice the R_{HMS} of the closest sub-halo. The bottom panel of Fig. 7.4 shows the position at $z = 0.06$ of the supermassive sWBH `4` with a mass of 10^{10} $M_\odot$. Being embedded in the large-scale potential gradient of the most massive halo, depicted in the side plots of the panel, BH `4` escaped from its original sub-halo. This demonstrates that for the repositioning scheme implemented in this

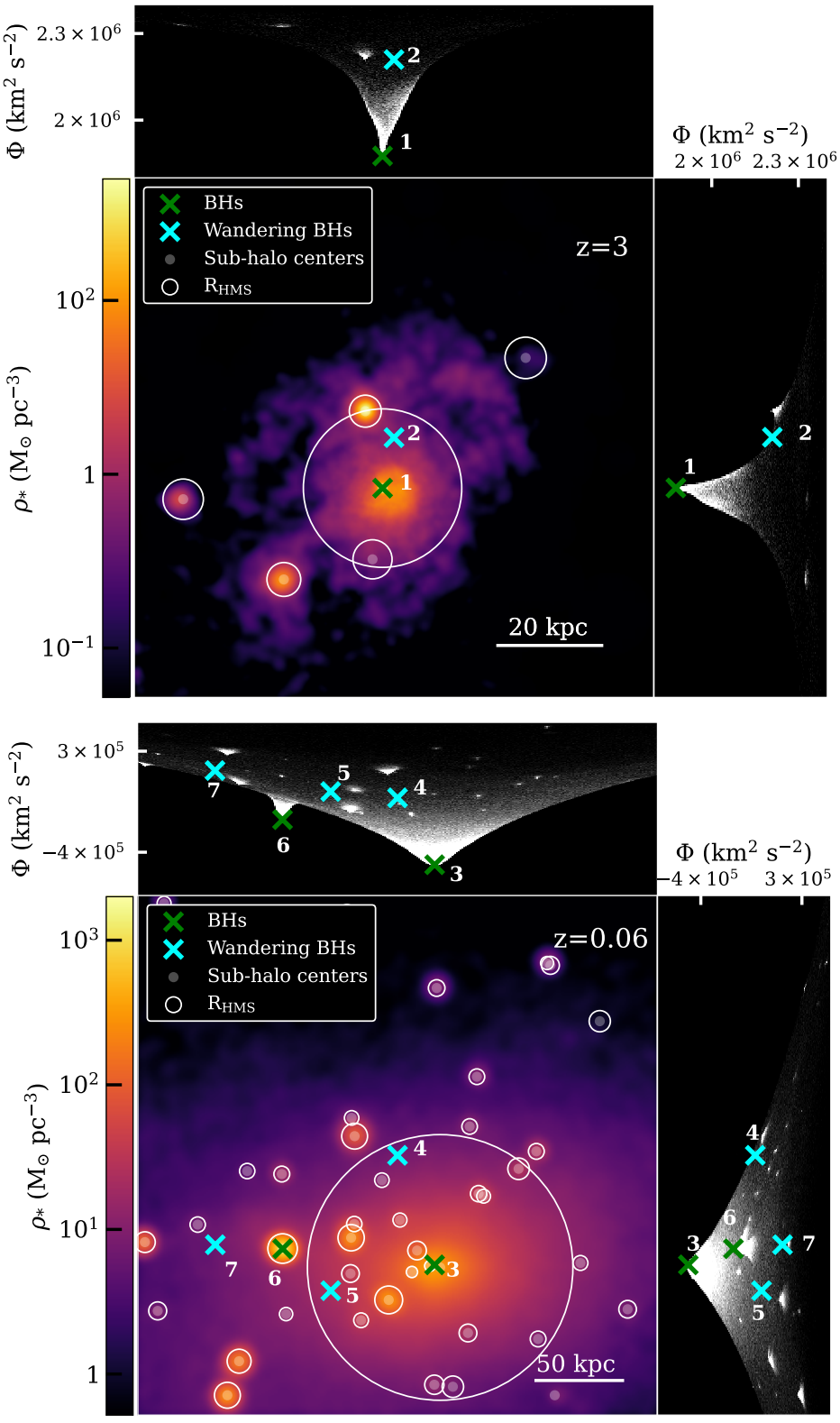

Figure 7.4: *Stellar density projection along the z-axis with depths of* 100 *kpc (top) and* 300 *kpc (bottom), centred on the position of a wandering BH at redshift* $z = 3$ *(tagged as BH 2; left panel), and of a wandering BH at* $z = 0.06$ *(tagged as BH 4; right panel) in the* `D9` *simulation using the* `REPOS` *scheme. In both panels, the cyan crosses identify the wandering BHs, while the green crosses identify the BHs centred in their host. Sub-halo centres are represented as white shaded dots, with the white circles indicating the corresponding* R_{HMS}*. On the top and on the right of each panel the gravitational potential* Φ *of all the star particles is shown as light white dots, while the one of the BHs in the field is identified with crosses, projected along the two orthogonal directions.*

work (Sect. 6.1.1), even the most massive BHs can move away from their host galaxies, thereby completely changing their gas accretion and the ensuing release of feedback energy.

In the simulations using the DF correction and `DYNMASS`, wandering BHs instead originate from two-body or even three-body scattering. When the BH is not repositioned, the dynamics during these events can be quite complex; this aspect is analysed in more detail in Sect. 7.3.

Finally, Fig. 7.5 displays the position of all the BHs in a projected stellar density map within 1 Mpc from the centre of the most massive halo in the `D9` simulation at redshift $z = 0$ for `REPOS` (top panel), `DYNMASS` (bottom left panel) and `DYNFRIC` (bottom right panel). BHs are plotted with crosses of different colours depending on their distance Δr from the closest sub-halo, comparing it to the R_{HMS} of this sub-halo. Dark-blue crosses indicate BHs with $\Delta r < R_{HMS}$, green crosses are for $R_{HMS} \leq \Delta r < 2 \times R_{HMS}$, and cyan crosses mark the wandering BHs, i.e. those with $\Delta r \geq 2 \times R_{HMS}$. Circles enclose the ten most massive sub-halos in the region, each having radius that is suitably scaled according to the value of its R_{HMS}. Each circle is centred on the sub-halo position and has a radius proportional to its R_{HMS}. The radius of the yellow circle corresponds to the actual physical value of the R_{HMS} of the BCG. For the purpose of readability, a different scaling for marking the size of the other sub-halos is adopted, as indicated in the figure legend.

Figure 7.5 shows that the `DYNFRIC` simulation exhibits a smaller population of sWBHs compared to `DYNMASS` (8 sWBHs against 13 within the main halo R_{HMS}), mainly located close to multiple BH systems. Most of the `DYNMASS` wandering BHs occupy the central region of the halo. However, crucial differences arise between `REPOS` and the outcomes of the other simulations: the overall population of BHs using the repositioning scheme, significantly decreases both in the core and in the outskirts of the halo. Most of the sub-halos, identified by stellar density peaks or with circles for the more massive ones, lack a central BH.

7.2.3 Merger events and multiple BH systems

The occurrence and timing of merger events are highly sensitive to the prescription to control the BH dynamics. In agreement with Buttigieg et al. (2025) and Bahé et al. (2022), the results presented here further confirm that the `REPOS` simulations facilitate the coalescence when two BHs approach a distance $d_{\rm merg}$ (see Sect. 5.4.3), making them merge on shorter timescales than when the other prescriptions are adopted.

Figure 7.6 displays the cumulative (upper part) and the differential (lower part) distributions of the number of merger events as a function of the redshift, for the three simulations. `DYNFRIC` and `DYNMASS` simulations predict similar results, with `DYNFRIC` showing slightly more mergers in denser regions (`Cl13` and `D9`) and fewer mergers in the `CosmoBox` simulation. By contrast, all the simulations based on `REPOS` feature a significantly higher number of mergers, more than twice the number of mergers of both `DYNFRIC` and `DYNMASS` in the zoom-in simulations and more than three times in the `CosmoBox` simulation. Interestingly, the density peak of mergers for the repositioning model occurs at $z \simeq 1.5$ in all the simulations.

Before the merging events occur, one would expect to find structures hosting systems of two or more BHs. However, the increase of mergers in the repositioning scheme is not counterbalanced by an increase of multiple systems, i.e. of structures containing two or more BHs. To demonstrate this, Figure 7.7 shows the ratio between the number of sub-halos hosting more than one BH

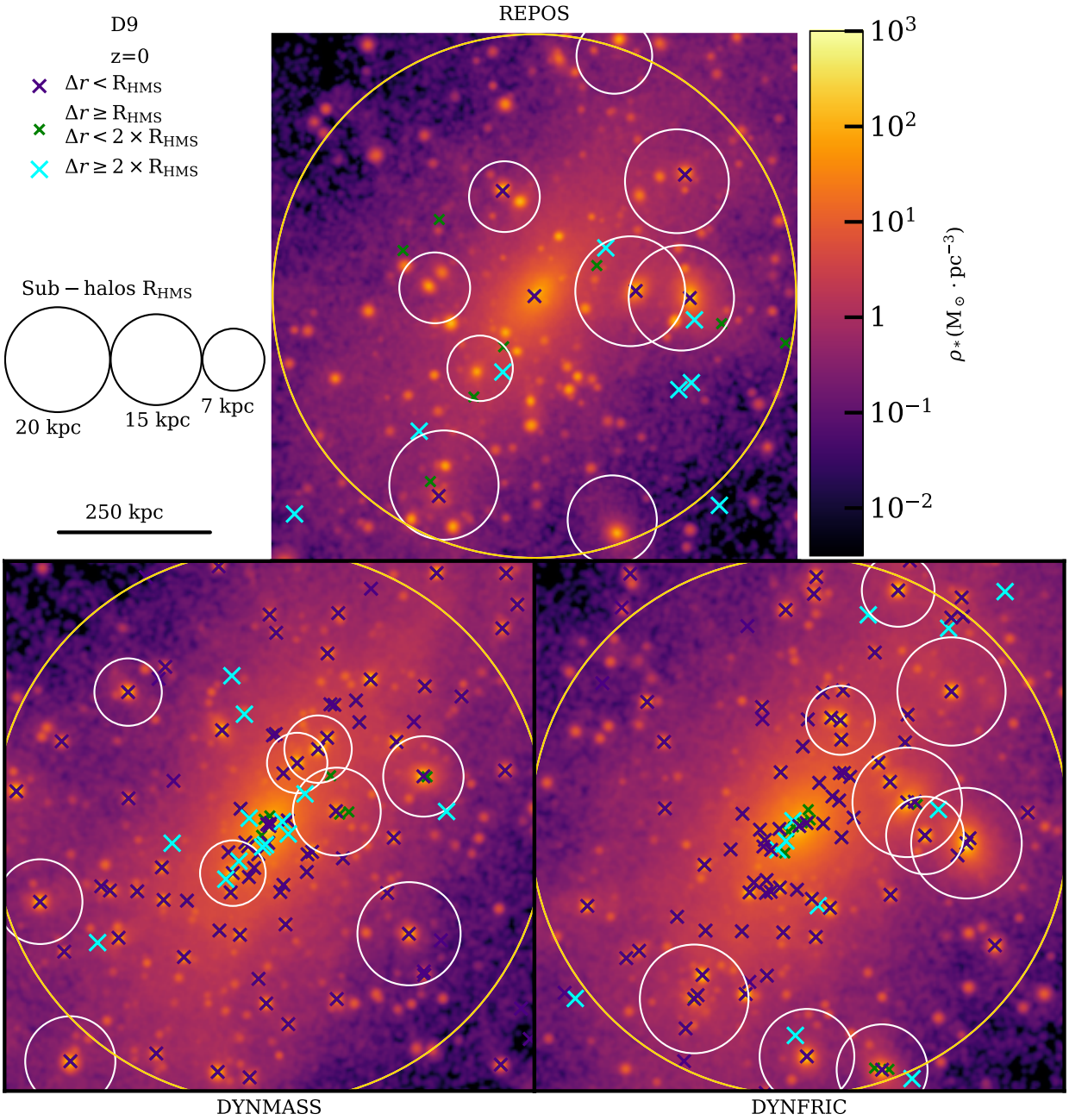

Figure 7.5: *Stellar density maps along the z-axis with a depth of* 1 *Mpc centred on the most massive halo of* D9 *at* $z = 0$ *in the* REPOS *(top),* DYNMASS *(bottom left), and* DYNFRIC *(bottom right) simulations. The panels are all 1 Mpc on a side. In each panel, dark-blue crosses identify the BHs located within the* R_{HMS} *of the associated sub-halo (the same criterion adopted in Sect. 7.2.1). BHs lying between* R_{HMS} *and* $2R_{HMS}$ *of the closest sub-halo are marked with green crosses, while wandering BHs (defined as those located beyond* $2R_{HMS}$ *of the closest sub-halo) are shown as light-blue crosses. The values of* R_{HMS} *of the ten most massive structures correspond to the radii of the circles, each centred on the position of the corresponding sub-halo. The* R_{HMS} *of the BCG, in yellow, corresponds to the physical size of the yellow circle. The legend in the upper left panel of the plot shows the scaling size of the other sub-structures in the region, marked in white.*

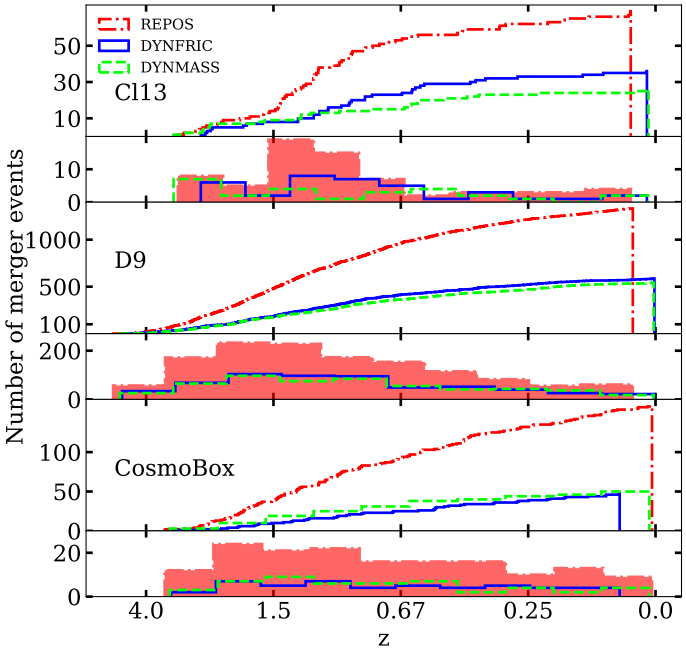

Figure 7.6: *Cumulative and differential distributions of the number of merger events as a function of redshift.* `Cl13`, `D9` *and* `CosmoBox` *are in the first, second, and third rows, respectively. The* `REPOS` *simulation results are marked with a dash-dotted red line (with a shaded area marking the differential distributions), the* `DYNFRIC` *simulations with a blue solid line and the* `DYNMASS` *simulations with a dashed green line. The curves stop at the redshift corresponding to the occurrence of last merger event.*

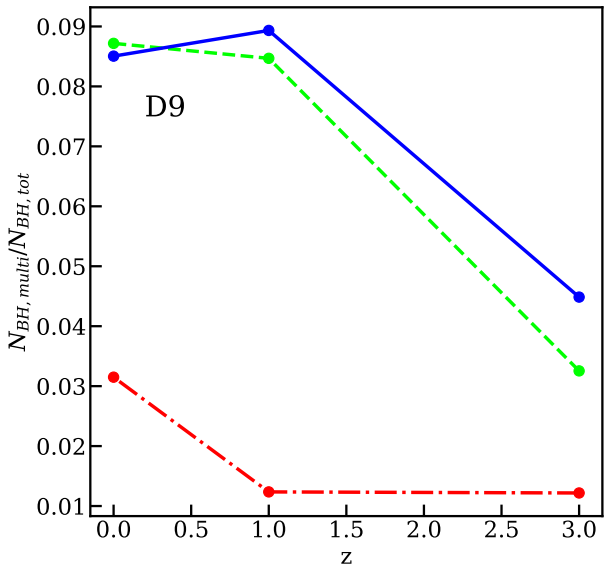

Figure 7.7: *Ratio between the number of sub-halos hosting more than one BH and the total number of sub-halos hosting at least one BH in* `D9` *simulations. We consider* `DYNMASS` *(dashed green line),* `DYNFRIC` *(solid blue line) and* `REPOS` *(dot-dashed red line) at* $z = 3, 1, 0$.

Simulation	REPOS	DYNFRIC	DYNMASS
Cl13	206	191	184
D9	2239	2206	2169
CosmoBox	328	314	323

Table 7.4: *Number of seeded BHs in each simulation for every sub-resolution prescription adopted.*

within the $R_{\rm HMS}$ to the total number of sub-halos hosting at least one BH for $z = 3, 1, 0$ in the D9 simulations. While the percentage of sub-halos hosting multiple BHs reaches more than 8% in DYNFRIC (blue) and DYNMASS (green) simulation, the REPOS shows a consistently lower percentage. The concurrence of a larger number of mergers and the near absence of multiple systems found for the REPOS simulations can be ascribed to extremely fast mergers, with multiple BHs coexisting within the same halo only for a rather short time.

However, the number of merger events is influenced both by the adopted model to trace the BH dynamics and by the specific seeding prescription adopted. In principle, a higher number of merging events may be associated with a more frequent seeding. This situation may arise when, following a merging event between BHs but not between their corresponding halos, one of the two halos remains orphan of its BH, while still matching the seeding conditions (see Sect. 5.4.1). In this case, a new BH would be seeded at the centre of the orphan halo, thereby possibly contributing to increase the BH-BH merger rate. To quantify how this 'seeding bias' affects the merging predictions of from each model, Table 7.4 reports the number of seeded BHs in each simulation.

The increase in the total number of seeded BHs in the REPOS simulations is only marginal. The absence of a proportional rise in the number of seeded BHs despite the increase in mergers in the REPOS simulations can be addressed on the concurrence of two particular seeding conditions.

On the one hand, the seeding occurs exclusively within the main halos identified by the FoF halo finder, and not within the sub-halos identified by SubFind. On the other hand, BHs are not seeded in FoF groups which already contain a BH particle. Instead, the more frequent scenario in the REPOS simulations is the merging of two BHs initially belonging to two sub-structures contained within the same FoF halo. In this case, no further seeding takes place within the sub-halo which eventually remains orphaned of its BH.

Moreover, the simulations adopting the dynamical mass implementation predict less mergers in the D9 and Cl13 simulations (Fig. 7.6) and a slightly higher fraction of multiple BH systems at z=0 (Fig. 7.7) compared to DYNFRIC, even if the latter exhibits a higher number of seeded BHs (Table 7.4). This circumstance already suggest that the dynamical mass model delays some merger events compared to DYNFRIC, something that will be explored in detail in Sect. 7.3.

7.2.4 The M_*–$M_{\rm BH}$ relation

A first diagnostic to investigate how the processes of SF and galaxy evolution are intertwined with the evolution of the population of SMBHs is to look at the relationship between SMBH masses and stellar masses of the bulges of the host galaxies (Sect. 2.2.1). Figure 7.8 shows this relation obtained by varying the implementation for the BH dynamics in all the simulations for the three initial conditions considered in our analysis. In detail, for each halo with a mass larger

	$\log_{10}(M_*/M_\odot)$	$\log_{10}(M_{BH}/M_\odot)$	Distance (kpc)
Cl13			
REPOS	11.28	9.13	0.03
DYNMASS	11.27	9.01	0.10
DYNFRIC	11.25	9.07	0.07
D9			
REPOS	11.75	10.0	0.10
DYNMASS	11.89	9.52	0.12
DYNFRIC	11.83	9.47	0.07
CosmoBox			
REPOS	11.36	9.35	1.25×10^{-3}
DYNMASS	11.39	9.16	0.16
DYNFRIC	11.47	9.4	0.08

Table 7.5: *Stellar mass, associated BH mass, and its distance from the halo centre for the most massive halo identified within each simulation.*

than a threshold value $M_{\rm thr} = 10^{10} M_\odot$, a distinction is made between the central galaxy, to be identified with BCG or Brightest Group Galaxy (BGG; marked with diamond symbols in Fig. 7.8), and the satellite galaxies, which are hosted within the substructures identified by SubFind (marked with circles). Since the SubFind algorithm does not split the diffuse stellar component of the Intra-Cluster light to the one bound to the BCG, at least for large-mass halos a fixed physical aperture is adopted, within which measuring the BCG/BGG stellar masses (see for instance Marini et al. 2020). A fixed aperture is also commonly adopted for a fair comparison with observational measurements of BCG/BGG stellar masses (Bassini et al., 2019; Ragone-Figueroa et al., 2018). For the BCGs and brightest group galaxies (BGGs), the stellar mass is computed by summing the mass of all star particles within a radius of 70 kpc from the centre. For satellite galaxies, the stellar mass corresponds to the total mass of the star particles assigned to the substructure by SubFind. The most massive BH within 70 kpc from the centre is associated with the central galaxies, while for satellite systems the closest BH within their $R_{\rm HMS}$ is considered. Symbols are colour-coded according to the distance between the centres of the galaxies and their associated BHs. For reference, each panel also reports the scaling relation from McConnell and Ma (2013) and the observational data for BCGs and BGGs presented by Gaspari et al. (2019). Overall, all simulations reproduce the observed relation reasonably well, albeit with a slightly higher normalisation. This consistency not only supports the calibration of the AGN feedback parameters but also indicates that the scaling relation is largely insensitive to the specific prescription adopted to model unresolved dynamical friction in BH dynamics. Table 7.5 presents data on stellar mass, associated BH mass, and the distance of the BH from the halo centre for the most massive halo within each simulation. The DYNFRIC simulations predict better centred BHs compared to the DYNMASS simulations, although all the distance values are below the resolution limit of the simulations.

As for Cl13, the DYNFRIC, REPOS and DYNMASS simulations all produce very similar results. In all the three cases, the stellar mass of the BGG, and the mass of the hosted SMBHs are quite similar at $z = 0$.

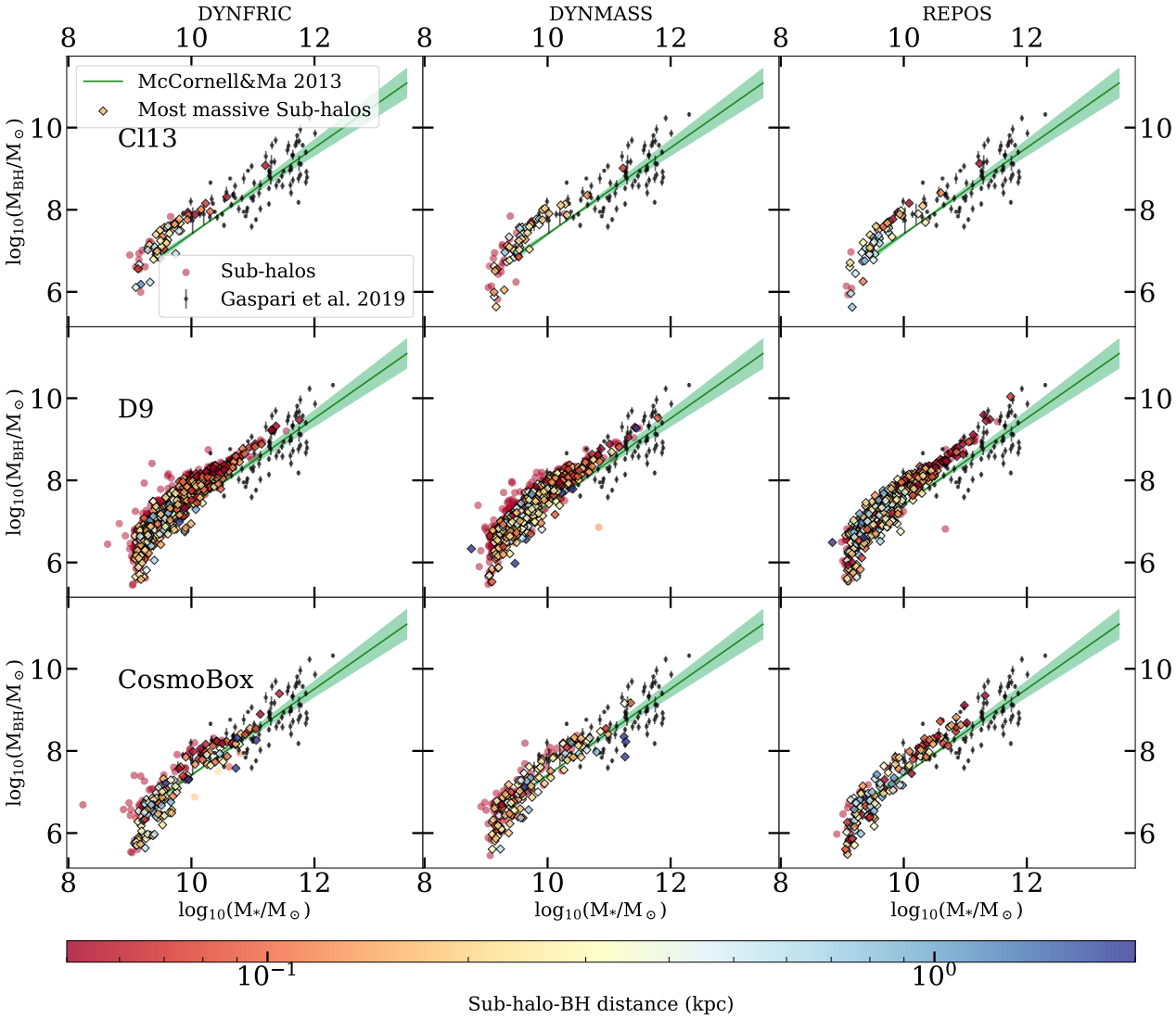

Figure 7.8: *Relationship between BH mass and stellar mass of the host galaxies in the* `Cl13` *(upper panels),* `D9` *(central panels), and* `CBox` *simulations (lower panels). Each column contains the results obtained with a different BH dynamics prescription:* `DYNFRIC` *(left),* `DYNMASS` *(central),* `REPOS` *(right). The diamonds refer to the BHs associated with the main halos while circles correspond to sub-halos belonging to halos more massive than* 10^{10} $M_\odot$*. Diamonds and circles are colour-coded according to the distance between the sub-halo centres and the associated BHs. For comparison, the black points with error bars represent the observational data from Gaspari et al. (2019), and the green line with shaded area indicates the relation derived by McConnell and Ma (2013).*

In the D9 region, the larger statistics of sub-halos helps to better understand what happens in the different scenarios. Still, the DYNFRIC and the DYNMASS simulations produce comparable results, with the DYNFRIC simulation even further reducing the offset of the most massive BHs from the centre of their host galaxies. The results for the D9 region using REPOS are in good agreement with the observational data for $M_* < 10^{11}$ $M_\odot$. However, this simulation predicts BHs that are more massive compared to the other implementations, again due to an excess of merging episodes, as already discussed. We note that the BH having the highest mass in the D9 region results from the merging between the BH 3 and the massive wandering BH 4 in Fig. 7.4 that reached the centre of the BCG from $z = 0.06$ to $z = 0$.

Finally, the CosmoBox results confirm the substantial agreement between our predictions and observations. The DF model further demonstrates its increased efficiency in centring the BHs compared to DYNMASS. Nonetheless, both simulations reveal three massive sub-halos with a stellar mass $> 10^{10.5}$ $M_\odot$, whose BHs have a significant displacement. The visual representation of these three occurrences is depicted in Fig. 7.9, which shows the projection of the stellar density centred around these pathological sub-halos. In the first row, two analogous situations are presented: a close encounter between two substructures hosting BHs of different masses. The displacement obtained in Fig. 7.8 follows from the association of the most massive BH to the central halo, marked in Fig.7.9 with a red circle. This feature, rather than being a real off-centring of the BH, is a consequence of the adopted method to associate a BH to a given structure. The third sub-halo, shown in the bottom right panel of Fig.7.9, hosts a truly off-centre BH. This is the outcome of a merger event between two substructures which took place at redshift $z = 0.19$ (see bottom left panel). Since then, the BH belonging to the merging substructure did not have the time to sink to the centre of the merged sub-halos, hence the displacement at $z = 0$ between the centre identified by SubFind and the BH.

7.3 Analysis of individual events

Besides the analysis of the properties that emerge from the population of BHs in each simulation, it is interesting to perform a detailed study of the effect of different sub-resolution prescriptions on the dynamics of single BHs and merger events. To better understand the BH dynamics, due to the different prescriptions to follow it, the following approach is adopted. The configuration of BHs and their host galaxies is frozen at two snapshots from the Cl13-DYNMASS simulation, corresponding to redshifts $z = 3$ and $z = 1.26$. These snapshots are then used as initial conditions for a new set of simulations employing four different prescriptions for BH dynamics: the DYNFRIC model introduced in Sect. 6.2.1; the DYNMASS method (Sect. 6.1.2); the REPOS method (Sect. 6.1.1); and a fourth run, NOCORR, in which no correction to the BH position is applied. Simulations initialized at $z = 3$ are evolved down to $z = 2$, while those starting at $z = 1.3$ are evolved to $z = 0.95$. In this way, the BHs begin with identical initial positions, masses, and velocities, and reside in substructures with the same physical properties. Consequently, any differences in their subsequent trajectories arise solely from the distinct sub-resolution prescriptions used to follow their dynamics. To ensure that the results were reproducible and marginally affected by the possible chaotic nature of a simulation, each simulation was carried out twice, obtaining results which show marginal differences in the timings, while leaving the general results qualitatively un-

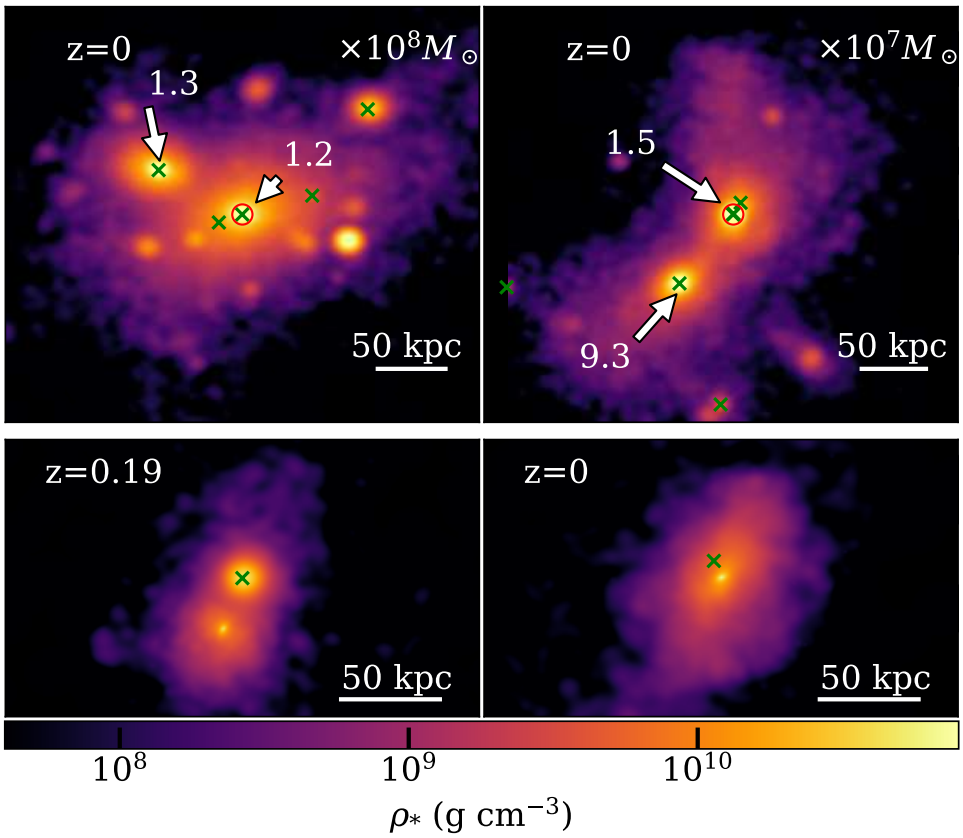

Figure 7.9: *Stellar density maps along the z-axis with depth of* 350 *kpc (upper row) and* 260 *kpc (bottom row) of the massive sub-halos having a large separation between sub-halo centre and the associated BH in the* `CosmoBox` *simulation, using the* `DYNFRIC` *model (blue diamonds in the corresponding plot in Fig.7.8, for* $\log_{10}(M_*/M_\odot) > 10$*), at redshift* $z = 0$*. BHs are marked by green crosses. Upper panels: two close encounters between structures. The halo centre is identified as a red circle. The arrows link to the values of the BH masses (in units as specified in the label). In both the left and right panels, the most massive BH belongs to the off-centre substructure. Bottom panels: a merger event between two substructures at redshift* $z = 0.19$ *(left panel) and the resulting merged halo at* $z = 0$ *(right panel). The plot on the right side captures an off-centre BH while sinking toward the halo centre.*

	$m_{\rm BH,cen}$ ($M_\odot$)		$m_{\rm BH,sat}$ ($M_\odot$)		M_{sub} ($M_\odot$)		Δr (kpc)
Event 1	3.23×10^5	×	3.63×10^5	×	6.96×10^{10}	×	4.08
Event 2	3.60×10^6	×	7.20×10^5	×	8.11×10^{10}	×	1.48
Event 3	6.39×10^8	×	2.04×10^6	×	4.50×10^{11}	×	10

Table 7.6: *Initial characteristics of merger events described in Sect.7.3. Column 1 and 2: initial true masses of the central ($m_{BH,\rm cen}$) and satellite ($m_{BH,\rm sat}$) BHs in the events described in Sect.7.3, at the initial redshifts $z = 3$ (for Events 1 and 2) and $z = 1.26$ (for Event 3). In Events 1 and 2, the BH masses of both* $\rm BH_{cen}$ *and* $\rm BH_{sat}$ *are boosted in the* `DYNMASS` *runs. On the other hand, we only boost the satellite BH mass in Event 3. Column 3: mass of the sub-halo hosting the events. Column 4: initial distance between the two BHs.*

changed. Clearly, restarting `DYNFRIC` and `REPOS` simulations from an output produced at a given intermediate redshift by the `DYNMASS` run leads to a structure evolution and dynamics that are different from those produced by using `DYNFRIC` and `REPOS` since the initial redshift, as described in the previous sections.

In particular, the analysis here below focuses on the evolution of binary BH systems, typically characterised by a massive BH located at the centre of a substructure, indicated as $\rm BH_{cen}$, and a second displaced BH, the 'satellite', labelled as $\rm BH_{sat}$. The analysis focuses on three events, each for a different value of the central-to-satellite mass ratio between the BHs, $f_{\rm m} = \rm m_{BH,cen}/m_{BH,sat}$; those events are labelled as Event 1, Event 2 and Event 3 in the following. Event 1 consists of a binary system of two BHs initially displaced by 4 kpc from each other. The initial BH mass ratio is $f_{\rm m} = 1.1$, and both BHs have a mass smaller than $m_{\rm DM}$ (see Table 7.6). For that reason, both masses are boosted in the `DYNMASS` simulation. Event 2 involves a binary system of two BHs, initially at a distance of 1.5 kpc, with a higher mass ratio ($f_{\rm m} = 50$) compared to Event 1, but at the same redshift. Still, the two masses are both increased in the `DYNMASS` run. Event 3 consists of a binary system of two BHs initially separated by 10 kpc at z = 1.26. The BHs have a large mass ratio $f_{\rm m} = 313$. This time, only $\rm BH_{sat}$, whose mass is less than $m_{\rm DM}$, undergoes the dynamical mass correction in the `DYNMASS` simulation.

The characteristics of these three events are summarised in Table 7.6. Figure 7.10 provides a graphical representation of the stellar density map at the redshift reported in the legend. The figure also includes the trajectory of the $\rm BH_{sat}$, colour-coded according to redshift, within the substructure hosting that event. Each row displays a single event, and results from the `DYNFRIC`, `DYNMASS`, `REPOS` and `NOCORR` simulations are presented from left to right in each column.

Figure 7.11 displays on the left column, for the different events in each row, the distance between $\rm BH_{cen}$ and $\rm BH_{sat}$, namely Δr, during the event. The dashed green line, the solid blue line, the dash-dotted red line and the short-dashed orange line indicate the `DYNMASS`, `DYNFRIC`, `REPOS` and `NOCORR` runs, respectively. The horizontal grey solid line represents the distance threshold which is necessary for the merger event $d_{\rm merg}$ to happen (Eq. 5.75). The right side of Fig.7.11 focuses on the results of the `DYNFRIC` runs. In particular, we plot Δr in the top panel, and the

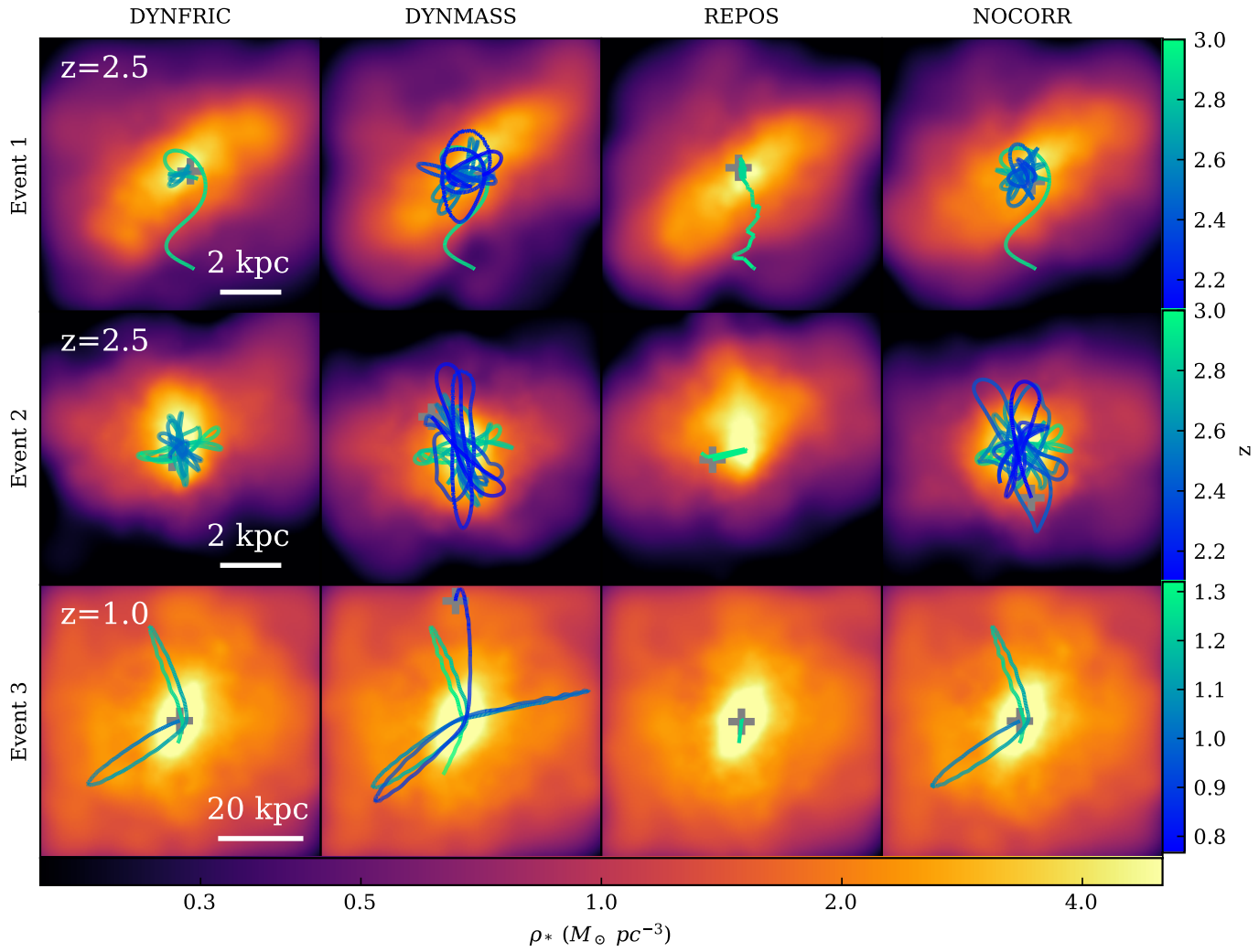

Figure 7.10: *Stellar density map along the z-axis with depth of* 10 *kpc in the top and central row and* 70 *kpc in the bottom row, centred on the central BH (*$\mathrm{BH_{cen}}$*) of Event 1 in the top row, Event 2 in the central row and Event 3 in the bottom row. The maps of stellar density refer to the redshift indicated on the left panel of each row. In each panel, the curve shows the orbit of the satellite BH (*$\mathrm{BH_{sat}}$*) involved in the merger event, colour-coded according to the redshift. The crosses indicate the last position of the satellite BH before either the merging event or the end of the simulations (see Sect. 7.3). The columns display the BH evolution using different sub-resolution prescriptions, from the left: using DF (first column), using a boosted dynamical mass (second), adopting the repositioning scheme (third) and finally without any correction for BH dynamics (fourth).*

ratio between the DF force and the gravitational force (including the contribution of the DF correction), both for BH_{cen} (light-blue) and BH_{sat} (light green) in the bottom panel. In the following subsections, each event will be analysed separately.

7.3.1 Event 1

Looking at the upper row of Fig. 7.11, the simulation adopting the `DYNFRIC` model exhibits oscillations with gradually decreasing amplitude and gently drives the two BHs toward the merger. In the `DYNMASS` simulation, instead, the distance between the BHs exhibits persistent oscillations, which do not decrease in amplitude. Rather than driving the BHs to form a close pair, the enhanced dynamical mass intensifies their mutual gravitational attraction, causing collisions resulting in sustained relative distance fluctuations. The simulation that does not employ any correction shows, after an initial gradual decrease of the distance, a second phase during which the two BHs keep oscillating with respect to each other, with a nearly constant amplitude. The merger between the two BHs, which occurs right after $z \sim 2.5$, is preceded by a sudden decrease in distance. The inset in the upper right side zooms on the results of the `REPOS` simulation. The merger event occurs very rapidly, with the distance between the two BHs decreasing through discrete 'jumps' as large as almost 1 kpc.

The figure shows that the two BHs can be closer than d_{merg}, yet without merging. However, this represents a necessary, but not sufficient condition for the merger to happen. Indeed, merging requires the BHs to fulfill also the binding criteria (Eqs. 5.77, 5.76). Whenever they are closer than d_{merg}, they merge if their relative velocity is less than half of their surrounding sound speed and if the gravitational binding criterion defined in (5.77) is also satisfied. From the visual representation of Fig.7.10 we can infer that `DYNFRIC`, `DYNMASS` and `NOCORR` show similar paths for BH_{sat} until it first crosses the denser region of the sub-halo. Then, `DYNFRIC` and `NOCORR` simulations bound BH_{sat} in the core of the host. Besides, `DYNMASS` reproduces constant oscillation at rather fixed apocentric distances. A detailed analysis of the reason why the merger does not occur in the `DYNMASS` simulation shows that the merger failure is due to the enhanced relative velocity and to the difference in the gravitational potential between BH_{sat} and BH_{cen}. While crossing the distance threshold imposed by the merging criteria at the pericentre, the higher relative velocity and the larger potential difference compared to `DYNFRIC` prevent both merging conditions from being satisfied. The sound speed surrounding the BHs remains comparable in the two simulations. These considerations are still valid to explain why the `DYNMASS` simulation fails to reproduce the merger in Event 2 and Event 3.

On the other hand, the path of BH_{sat} in the `REPOS` simulation is discontinuous and short compared to the others: through successive repositioning steps, the BH drops at the centre of the sub-halo. The right panel of the plot highlights the features arising from the application of the DF correction in the `DYNFRIC` model. In this case, the DF force responds to a local increase of stellar density. The ratio between the gravitational and the DF forces oscillates for both BHs with oscillation of comparable amplitude, indicating that they are orbiting around a central denser zone. Indeed, looking at the upper row of Fig. 7.10 it can be observed that the final merger will take place in the central, denser region on the substructure.

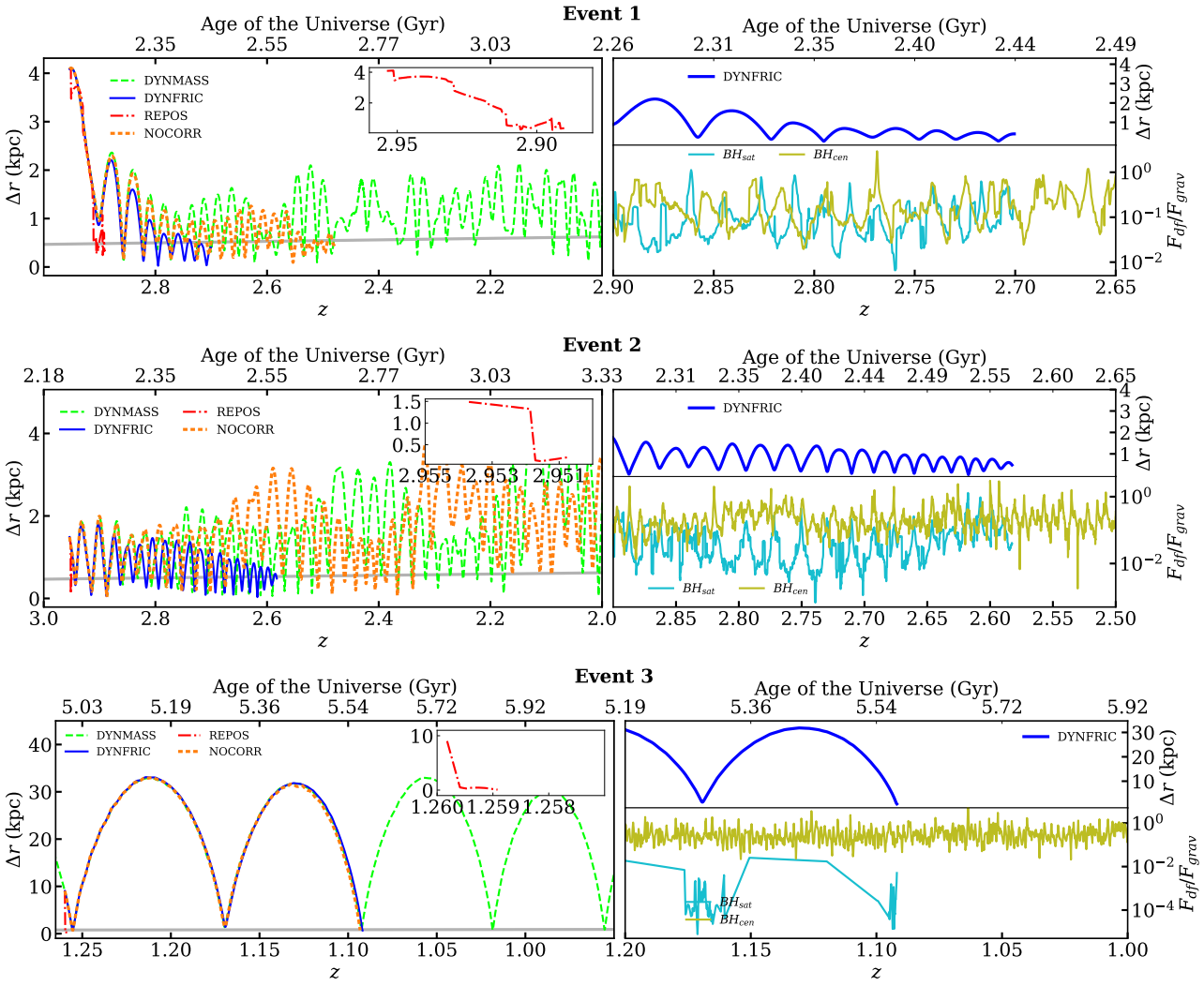

Figure 7.11: *Left column: evolution of the distance between the central and the satellite BH in Event 1 (top), Event 2 (central), Event 3 (bottom). The dashed green line displays the evolution using the dynamical mass scheme (*`DYNMASS`*), the blue solid line is for the DF scheme (*`DYNFRIC`*), the dash-dotted red line for the repositioning (*`REPOS`*), and the densely dashed orange line is for the case without any sub-resolution prescription (*`NOCORR`*). The horizontal grey solid line represents the distance threshold which is necessary for the merger event d_{merg} to happen. Right column: evolution of the distance between the BHs for the* `DYNFRIC` *case (top panel) and ratio between the DF and gravitational forces during each event.*

7.3.2 Event 2

The second rows of Fig. 7.10 and of Fig.7.11 show the evolution of the distances during Event 2. Again, throughout the event, `REPOS` and `DYNFRIC` lead to immediate and gradual BH coalescences of the BHs, respectively.

`DYNMASS` and `NOCORR` do not produce any merger, thus leaving BH_{sat} swing around the central one. Thus, neither an ad hoc increase of the BH mass nor the N-body gravity solver without any correction is sufficient to damp the oscillations of the smaller BH. Furthermore, the visual representation in Fig.7.10 demonstrates that `DYNFRIC`, `DYNMASS` and `NOCORR` simulations all produce an initial tilt of the orbit of BH_{sat} in the direction of the elongated denser region of the sub-halo. Then, in the `DYNFRIC` simulation, the contribution of DF leads the BH toward the centre. The right panel in Fig.7.11 illustrates the F_{df}/F_{grav} trend, showing that for this Event 2 the peaks of the contribution of the DF on BH_{sat} usually take place in correspondence with the minimum distance between the two BHs: as BH_{sat} approaches BH_{cen}, it crosses the central region where the density of stellar particles is higher, thus leading to an increase of the DF acting on it. On the other hand, the DF acting on BH_{cen} is relatively stronger during all the duration of the event, consistent with the more central position that it occupies.

7.3.3 Event 3

Finally, the bottom rows of Fig. 7.10 and of Fig. 7.11 show the evolution during Event 3. In this case, at the lower redshift reached by restarting the simulations at $z = 1.26$ to $z = 0.96$, the mass of BH_{cen} is more than 300 times higher than that of BH_{sat}. The latter is initially revolving around the central BH with large oscillations of approximately 30 kpc in amplitude. Once again, `REPOS` allows the two BHs, initially displaced by 10 kpc, to merge nearly instantaneously, with a 'long-range teleporting' of BH_{sat} from the outskirt to the centre of the substructure, reported in the top-right inset in the bottom left panel of Fig. 7.10. Numerical details of the repositioning scheme can affect the amplitude of the jump: its size could be smaller should different or additional constraints be taken into account (e.g. Ragone-Figueroa et al. 2018, as also discussed in Sect. 6.1.1).

Distance oscillation in `DYNFRIC`, `DYNMASS`, and `NOCORR` nearly coincide with each other. However, while `DYNFRIC` and `NOCORR` enable the merger to occur after a short time, this does not happen for `DYNMASS`. The reason for this lies in the different ways in which these simulations match the merging conditions: the distance threshold criterion is satisfied by all three simulations, but the other merging conditions remain unsatisfied for the `DYNMASS` simulation. BH_{sat}, having its dynamical mass boosted, keeps revolving around BH_{cen} performing wide oscillations of 30 kpc in amplitude. In any case, the similarity of the oscillations described by `DYNFRIC` and `NOCORR` suggests that the DF correction in the former should be subdominant in this case. The orbits of BH_{sat} further demonstrate that `DYNFRIC`, `DYNMASS` and `NOCORR` produce almost identical results until $z \simeq 1.1$. In the `DYNMASS` simulation, the subsequent oscillations of the BH seem to be result of 'kicks' that BH_{sat} receives while crossing the denser core of the sub-halo. In the right panel, it can be noticed that F_{df}/F_{grav} for BH_{sat} oscillates in phase with the distance between the BHs. Further analysis, illustrated in the next section, showed that this feature is driven by wide oscillations of the gravitational force, which increases when approaching the galactic core

where $\mathrm{BH_{cen}}$ resides. Moreover, the value of $F_{\rm df}/F_{\rm grav}$ for $\mathrm{BH_{cen}}$ is significantly higher than for $\mathrm{BH_{sat}}$. This happens both because of the higher mass of the central BH and due to the strong DF correction due to the concentration of stellar particles in the central sub-halo region.

In summary, these three events highlight the importance of adding a correction to the gravitational force on BHs contributed by the unresolved DF, as demonstrated in Sect. 7.3. Furthermore, the description of such examples of merging events also reveals the significant limitations in correctly describing the dynamics of a system of two BHs of both the `REPOS` (in the worst-case scenario considered here) and the `DYNMASS` schemes. Indeed, simulations based on `REPOS` generate 'jumps' of the BHs, while `DYNMASS`, by artificially boosting the BH mass, produces two-body scattering effects, preventing the formation of a bound system. Lastly, using an additional constraint on the relative velocity between the BH and the selected neighbor particles in the `REPOS` model (see Sect.6.1.1) does not sensibly change merging and sinking timescales when the two BHs are located within the same sub-halo, as in Event 1 and Event 2.

7.3.4 The effect of the merging conditions

In all the three events described above, the `DYNMASS` simulation fails to reproduce the merger event, although the apocenter distance of the merging BH falls several times below the minimum threshold distance for merging, $d_{\rm merg}$. To investigate further the origin of this behaviour, Fig. 7.12 and Fig. 7.13 show the comparison between some relevant quantities during the merger Event 1 for the `DYNFRIC` (blue) and the `DYNMASS` (green) simulations. To generate the scatter plots, whenever a BH meets any of the three merger criteria in Eqs. (5.77), (5.76), and (5.75)—but does not satisfy all of them simultaneously—we record the corresponding quantities appearing in these equations, namely the BH distance Δr, their relative velocity to the surrounding particle $\mathrm{v_{rel}}$, the local sound speed c_s and the difference between the potential Φ of the central and the satellite BHs.

From the top to the bottom panel, this figure shows: the relative distance Δr between the merging BHs, their relative velocity v_{rel}, the surrounding sound speed (computed with gas particles within the smoothing length), the quantity $2\,v_{rel}/c_s$ and the ratio

$$f_b = \frac{|\Phi_{BH_{cen}} - \Phi_{BH_{sat}}| + v_{rel}^2}{0.5\ c_s^2}\,, \tag{7.1}$$

where $\Phi_{BH_{cen}}$ and $\Phi_{BH_{sat}}$ are the gravitational potentials of the central and satellite BHs. The merging criteria in Eqs. (5.75), (5.77) and (5.76), require that:

1. $\mathrm{\Delta r} = 5 \cdot \epsilon_{\rm BH}$;
2. $2\mathrm{v_{rel}}/\mathrm{c_s} < 1$;
3. $f_b < 1$,

respectively. To simplify the interpretation of the plot, horizontal lines indicate whenever the merger conditions are met: the grey line marks the condition 1, the sky blue horizontal line marks the condition 2 and the dashed grey line marks the condition 3. Vertical blue and dashed grey

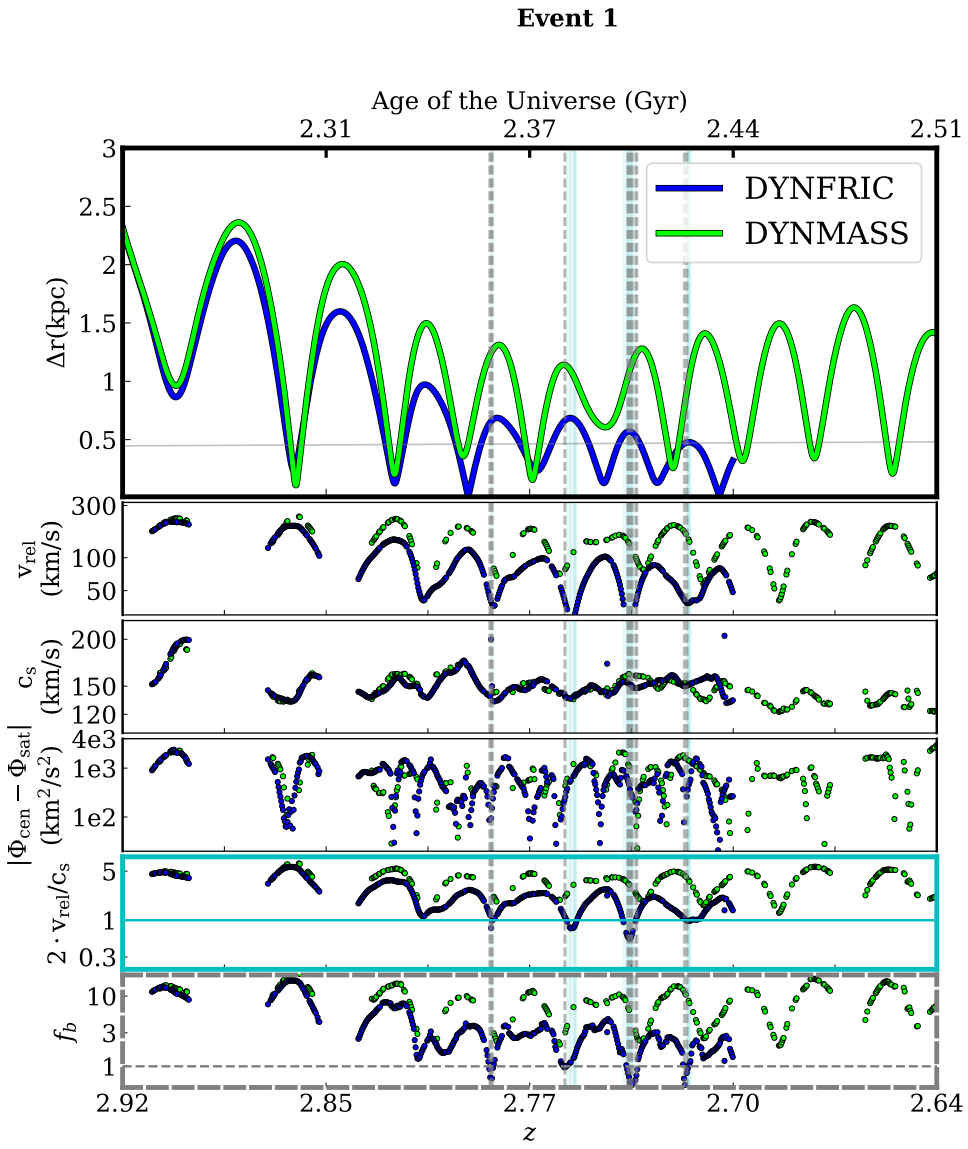

Figure 7.12: *Relevant quantities contributing to the mergers in Event 1. From top to bottom we plot: relative distance between the BHs, their relative velocity, surrounding sound speed, absolute value of their potentials difference,* $2\mathrm{v_{rel}}/\mathrm{c_s}$ *,* f_b *defined in Eq. 7.1. The grey line of the top plot corresponds to* $\Delta r = 5{\cdot}\epsilon_{BH}$*, while the light blue and dashed grey horizontal lines of the bottom plots correspond to* $2\mathrm{v_{rel}}/\mathrm{c_s} = 1$ *and* $\mathrm{f_b} = 1$*. The vertical lines indicate times when either* $2\mathrm{v_{rel}}/\mathrm{c_s} < 1$ *(light-blue vertical line) or* $\mathrm{f_b} < 1$*.*

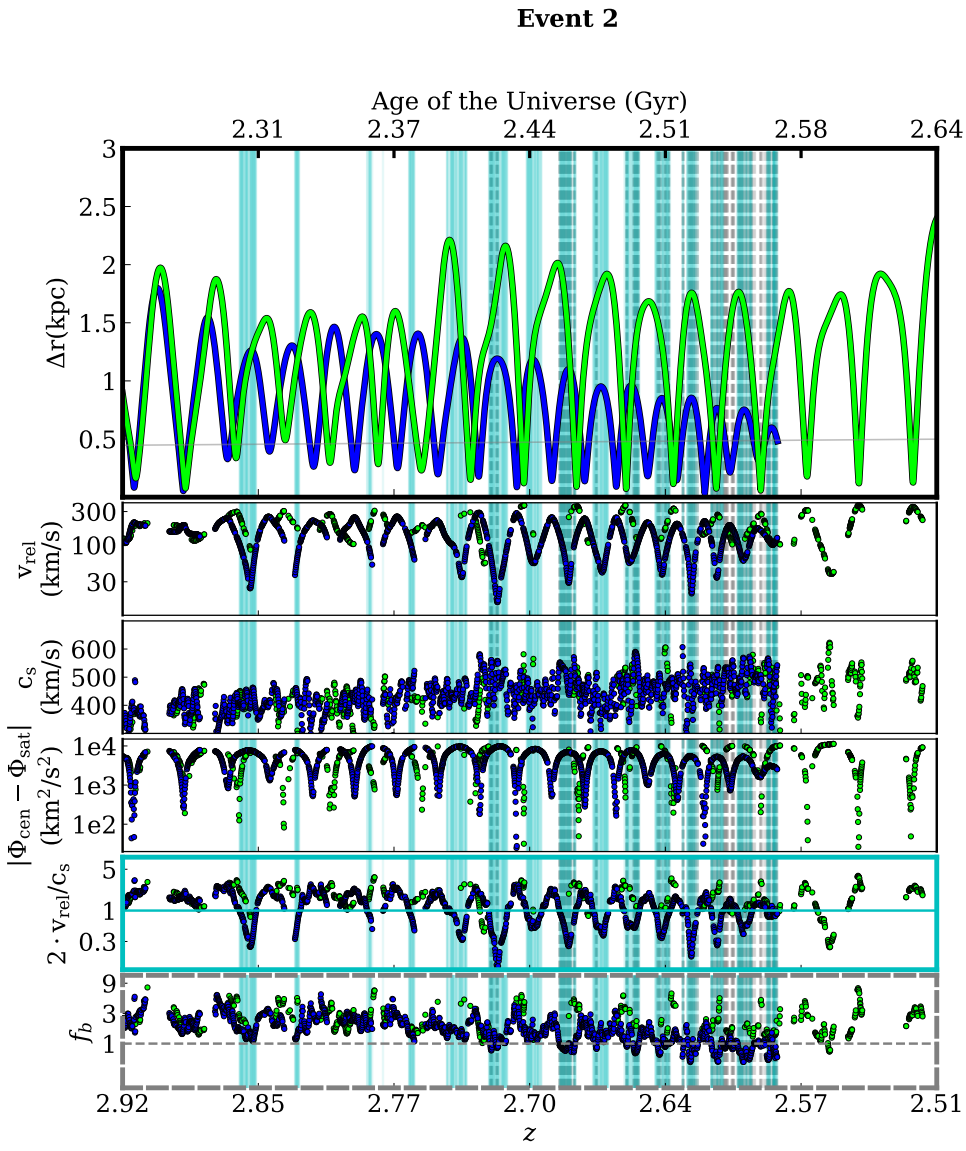

Figure 7.13: *Same as Fig. 7.12 but for Event 2.*

lines mark the epochs when, in the DYNFRIC simulation, the conditions $2v_{rel}/c_s < 1$ and $f_b < 1$ are met, respectively.

Oscillations during each orbit place the relative distance and relative velocity out of phase: minima in distance coincide with maxima in velocity, and vice versa. For small variations of the sound speed, the merging criteria effectively require that both the apocentric distance and the maximum relative velocity decrease from one orbit to the next. This simultaneous trend is what drives merger Event 1 in the DYNFRIC simulation. In contrast, when the BH masses are boosted, the relative velocity between the two BHs does not steadily decline. In this case, the gravitational bonding criterion is satisfied mainly because (*i*) the difference in gravitational potential between the two BH positions becomes smaller and (*ii*) the relative velocity decreases. Both effects reduce the numerator in Eq. 7.1, while the sound speed remains nearly unchanged between the two simulations. During Event 2 (Fig. 7.13), the relative velocity reaches deeper minima in the DYNFRIC simulation, making criteria 2 and 3 more easily satisfied. As in Event 1, the BH separation gradually shrinks, so the merger occurs once the apocentric distance falls below the prescribed threshold.

7.4 Conclusions

Within this Chapter, the performance of the novel technique to capture DF in simulations introduced in Sect. 6.2.1 have been tested in the context of cosmological hydrodynamical simulations in different astrophysical environments. Specifically, simulations of a group-sized and a cluster-sized, among with a cosmological volume with a box size of (16 comoving Mpc)^3 halo have been carried out using the OpenGADGET3 code. The performance of the new model was evaluated against two alternative approaches: the repositioning scheme and the adoption of an enhanced dynamical mass to reinforce the unresolved contribution of dynamical friction. To this end, each simulation was repeated three times, varying only the sub-resolution prescription for BH dynamics among these three techniques, while keeping all other parameters identical. The main conclusions can be summarised as follows.

- **Offset**: The simulations using the continuous repositioning of BH particles on the local potential minimum (REPOS scheme) exhibit the smallest offset between the BH and the centre of the host sub-halo. Our model to correct unresolved DF (DYNFRIC scheme) provides an accurate centring, even outperforming, at $z < 1$, the scheme based on boosting the dynamical mass of BH particles at seeding (DYNMASS scheme). See Sect.7.2.1 and Fig.7.1.

- **Wandering BHs**: The DYNFRIC simulations produce the smallest population of wandering BHs, which are predominantly found in multiple BH systems. The REPOS prescription features the most numerous and massive set of wandering BHs, as close encounters between galaxies and large-scale potential environments favour the spurious repositioning of BHs outside their host sub-halos. See Sect.7.2.2, Fig.7.2, Fig.7.4, and Fig.7.5.

- **Mergers**: The overestimate of merger events in the REPOS simulations in denser environment leads to an excess of galaxies deprived of a central BH, an effect that is more pronounced in the denser environment of a massive galaxy cluster. See Sect. 7.2.3, Fig. 7.6, and Fig. 7.5.

- **$M_* - M_{BH}$ relation**: The good agreement with the observational data, that is, the ability of all the simulations to reproduce the observed $M_* - M_{BH}$ scaling relation, demonstrates a relative insensitivity of this diagnostic to the particular prescription adopted, while it is sensitive to the choice of the parameters regulating BH accretion and the ensuing AGN feedback efficiency. See Sect. 7.2.4 and Fig. 7.8.

To delve deeper into the details of how different prescriptions affect the orbits of BH particles, Sect. 7.3 focuses on specific BH–BH interaction events. To disentangle the possible diversity in the substructure evolution between different simulations, those are restarted from two snapshots of the group-sized halo at $z = 3$ and at $z = 1.26$ to explore how BHs respond to different methodologies governing their dynamics in the same environment. This section also contain a simulation that does not include any sub-resolution prescription to correct the orbits of BH particles. The results of this further analysis, introduced in Sect. 7.3, Fig. 7.10, and Fig. 7.11, can be summarised as follows:

- **DF**: The novel model, adding the DF correction, predicts damped orbits of the satellite BHs, which gradually approach the centre of a host galaxy, and eventually form a close BH–BH pair.

- **Dynamical mass**: The large BH dynamical masses in the `DYNMASS` scheme can lead to spuriously strong interactions between BHs, which could delay or even prevent merger events. Moreover, such interactions eventually inhibit the BHs from satisfying the gravitational boundedness criteria for merging. The overall results, in terms of the quality of the description of orbital decay in BH pairs, can be worse than those obtained without any prescription to correct BH dynamics for unresolved DF.

- **Repositioning**: The `REPOS` method in the flavour presented in these simulations (Sect. 6.1.1) enables extremely rapid mergers preceded by large and sudden movements of the satellite BH, which promptly reaches the central region of the sub-halo with a few 'jumps' eventually spanning several kiloparsecs.

In summary, an extensive analysis of the BH population arising in different simulations demonstrates that the novel implementation of the correction for DF force acting on BH particles introduced in Sect. 6.2.1 provides a robust and reliable description of the DF exerted on BHs by their surroundings. This model achieves at least the same performance as other ad hoc numerical prescriptions in terms of centring BHs in their host halos, while significantly reducing the population of wandering BHs, and overcoming the limitations of these prescriptions in terms of their ability to describe BH-BH merger events. Although these results are encouraging, showing its good performance when compared to ad hoc prescriptions, already introduced in the literature, is not sufficient to fully demonstrate the reliability and correctness of the proposed DF model. A comprehensive validation requires a dedicated resolution study to determine the range of numerical resolutions over which the model remains accurate. Moreover, since the model is designed to partially recover the DF acting on BHs, it should also be able to reproduce DF-driven timescales (Sect. 4.1) — as, for instance, the sinking of a satellite BH into the potential well of a central galaxy following a galactic merger, prior to the final BH coalescence. However, such an analysis

requires defining a "true" sinking timescale for comparison. This reference value should be obtained by a priori knowledge of the exact DF acting on the BH (Eq. 4.26), which in turn demands that the phase-space distribution function be fully constrained. This can only be achieved in controlled, isolated simulations, where the complexity inherent to a cosmological environment — such as interactions, gas inflows, and outflows — is removed. These simulations will be presented and systematically analysed in the next Chapter.

Chapter 8

DF and MBH orbits: analytical predictions and numerical solutions

The content of this Chapter is based on Damiano et al. (2025), with additional material and extended discussions included for completeness.

As illustrated in the previous Chapters, DF not only anchors MBHs to the galactic center but also facilitates their gradual loss of angular momentum, driving their inspiralling orbits toward the galactic core (e.g. Antonini and Merritt, 2011; Li et al., 2020; Vecchio et al., 1994; Taffoni et al., 2003; Volonteri et al., 2015). Determining the timescale for MBH sinking and coalescence remains a complex issue stemming from the complex dynamical environment in which MBHs evolve — a regime that deviates significantly from idealized analytical descriptions and demands both high numerical precision and spatial resolution in simulations to be properly captured. Analytically, the DF force assumes a simple form (Binney and Tremaine 1987, Eq. 6.11) only under rather stringent hypotheses: the surrounding particles are negligible in mass compared to the perturber, are distributed in a uniform and homogeneous medium, and obey a well-defined a priori known velocity. However, it is unlikely that the BH experiences the passage through such a homogeneous and isotropic medium when infalling to the galactic core. Furthermore, the maximum radius within which to account for the DF is a free parameter whose choice has a significant impact on the resulting timescale for sinking.

While the analytical solution derived from the DF formula can be inaccurate, searching for a numerical solution is equally challenging (e.g. Taffoni et al. 2003). The primary difficulty lies in the large spatial range required to properly simulate the infall of a MBH toward the galactic center, alongside the high spatial and mass resolution necessary to accurately capture gravitational interactions, including both DF and large-scale galactic torques (e.g. Bortolas et al. 2020). In the context of cosmological N-body simulations, both coarse mass resolution and too aggressive gravitational force softening (see Sect. 5.1.1) can introduce numerical heating into the BH's motion, as was shown in the previous Chapter. Due to the uncertainties described above, validating any DF correction against analytical predictions requires idealized environments in which the phase-space distribution of particles is known a priori and well represented by the numerical N-body technique.

To this end, this Chapter presents a systematic study of the infall of a BH within a DM halo, with and without the inclusion of a stellar bulge, to assess the performance of the DF correction

event in the regime in which the BH mass is smaller than that of the surrounding particles. To this end, the refined DF prescription introduced in Sect. 6.2.2 will here be tested. Additionally, the Orbital TImescale for Sinking (OTIS) library — a new open-source Python package — is presented. OTIS solves the equations of motion for a BH sinking within a NFW DM halo (Navarro et al., 1997; Navarro et al., 1996), optionally including a stellar bulge following a Hernquist (1990) density profile. This tool enables fast and flexible comparison between numerical results and theoretical expectations. Using these methods, BH sinking timescales are systematically compared to analytical predictions across varying resolutions, both with and without the DF correction. The analytical framework upon which OTIS is built, is introduced in Sect. 8.1, along with the description of the numerical technique employed in the Python library (Sect. 8.1.4). Then, the numerical set up is described in Sect. 8.2. The overall results of the simulations performed are illustrated separately for a pure DM halo (Sect. 8.3.1) and when adding also a central stellar component (Sect. 8.3.2). Finally, Sect. 8.4 and 8.5 discuss and summarise the main findings.

We highlight that 3D visualizations produced with BLENDER for several simulations presented in this Chapter are publicly available here.

8.1 Analytical framework

In this section, the steps required to derive the analytical solution for the sinking timescale of a BH moving within an NFW potential, eventually coupled with a central stellar bulge, are presented (Sect. 8.1.1, 8.1.2). Then, Sect. 8.1.4 introduces the Python library that has been developed to integrate the equations of motion of the BH in these scenarios.

8.1.1 Infalling BH on a circular orbit in an NFW halo

The NFW halo density profile $\rho_{\rm H}$ can be expressed as a function of the halo-centric distance r as (Navarro et al. 1996, 1997):

$$\rho_{\rm H}(\mathrm{r}) = \frac{\rho_{\rm s}}{\frac{\mathrm{r}}{\mathrm{r_s}}\left(1+\frac{\mathrm{r}}{\mathrm{r_s}}\right)^2} \tag{8.1}$$

where $\mathrm{r_s}$ is the scale radius, defined by the virial radius $\mathrm{r_{vir}}$ [1] and the concentration parameter c such that $\mathrm{r_s} = \mathrm{r_{vir}/c}$, and $\rho_{\rm s}$ is the mass density at $\mathrm{r_{vir}}$. By integrating Eq.(8.1), the expression for the halo mass enclosed within a radius r can be obtained:

$$\mathrm{M_H(r)} = 4\pi\rho_{\rm s}\mathrm{r_s^3}\left[\ln\left(1+\frac{\mathrm{r}}{\mathrm{r_s}}\right) - \frac{\mathrm{r}}{(\mathrm{r_s}+\mathrm{r})}\right]. \tag{8.2}$$

Assuming a BH to be placed at a given distance r from the center of the halo on a circular orbit, its initial circular velocity will be

$$\mathrm{v_c(r)} = \sqrt{\frac{\mathrm{GM_H(r)}}{\mathrm{r}}}, \tag{8.3}$$

[1] Using the same formalism as Springel and White (1999), we define the virial radius as the radius within which the mean halo density corresponds to an overdensity δ_c= 200 times the critical cosmic density at redshift z, i.e. $\rho_{\rm c}(\mathrm{z}) = 3\mathrm{H(z)}/8\pi\mathrm{G}$.

whereas the gravitational potential at the BH position is obtained through the Poisson equation:

$$\Phi_{\rm BH}(\mathrm{r}) = -4\pi \mathrm{G}\rho_{\rm s}\frac{\mathrm{r_s^3}}{\mathrm{r}}\ln\left(1+\frac{\mathrm{r}}{\mathrm{r_s}}\right). \tag{8.4}$$

Therefore, the radial acceleration felt by the BH takes the expression:

$$\tilde{\mathrm{a}}_{\rm BH}(\tilde{\mathrm{r}}) = -\tilde{\nabla}\Phi_{\rm BH} = \mathrm{G}\frac{\mathrm{M_{vir}}}{\ln(1+\mathrm{c})-\frac{\mathrm{c}}{1+\mathrm{c}}}\frac{1}{\mathrm{r}^2}\left[\frac{\mathrm{r}}{\mathrm{r_s}+\mathrm{r}}-\ln\left(1+\frac{\mathrm{r}}{\mathrm{r_s}}\right)\right]\hat{\mathrm{r}}, \tag{8.5}$$

where $\mathrm{M_{vir}}$ is the halo mass within $\mathrm{r} = \mathrm{r_{vir}}$ obtained from Eq.(8.2) and the "hat" indicates a unit vector. When the halo is sampled with a finite number of particles of mass $\mathrm{m_p}$, they exert a friction on the BH travelling through them. This force causes a gradual loss in the angular momentum of the BH and from simple dynamical arguments the path of the infalling BH as it moves inwards toward the center can be extracted. Rodriguez et al. (2018) derived the equation for the orbital evolution of the BH for circular orbits around the center of the halo, following a Hernquist (1990) profile. In the following calculations, the same methodology is applied to a halo characterized by an NFW density profile, with the BH initially placed on a circular orbit around the halo center In Sect. 8.1.2 the latter assumption will be relaxed, by considering the possibility of an initial ellipticity of the BH orbit. The magnitude of the torque acting on the infalling BH of mass $\mathrm{m_{BH}}$ when orbiting toward the center takes the general form:

$$\frac{\mathrm{dL}}{\mathrm{dt}} = \mathrm{m_{BH}}\left(\mathrm{v_c}+\mathrm{r}\frac{\mathrm{dv_c(r)}}{\mathrm{dr}}\right)\frac{\mathrm{dr}}{\mathrm{dt}} \tag{8.6}$$

$$= \mathrm{m_{BH}}\frac{\mathrm{v_c(r)}}{2}\left(1+\frac{\mathrm{d}\log \mathrm{M_H(r)}}{\mathrm{d}\log\ \mathrm{r}}\right)\frac{\mathrm{dr}}{\mathrm{dt}}. \tag{8.7}$$

By replacing the NFW mass profile defined in Eq.(8.2) and its derivative in the previous equation, one obtains:

$$\frac{\mathrm{dL}}{\mathrm{dt}} = \mathrm{m_{BH}}\frac{\mathrm{v_c(r)}}{2}\left\{1+\frac{\mathrm{r}^2}{\mathrm{r_s^2}\left(1+\frac{\mathrm{r}}{\mathrm{r_s}}\right)^2\left[\ln\left(1+\frac{\mathrm{r}}{\mathrm{r_s}}\right)-\frac{\mathrm{r}}{\mathrm{r_s}+\mathrm{r}}\right]}\right\}\frac{\mathrm{dr}}{\mathrm{dt}} \tag{8.8}$$

$$= \mathrm{m_{BH}}\mathcal{F}(\mathrm{v_c},\mathrm{r_s},\mathrm{r})\frac{\mathrm{dr}}{\mathrm{dt}}, \tag{8.9}$$

where $\mathcal{F}(v_c, r_s, r)$ is defined as:

$$\mathcal{F}(\mathrm{v_c},\mathrm{r_s},\mathrm{r}) = \frac{\mathrm{v_c(r)}}{2}\left\{1+\frac{\mathrm{r}^2}{\mathrm{r_s^2}\left(1+\frac{\mathrm{r}}{\mathrm{r_s}}\right)^2\left[\ln\left(1+\frac{\mathrm{r}}{\mathrm{r_s}}\right)-\frac{\mathrm{r}}{\mathrm{r_s}+\mathrm{r}}\right]}\right\}. \tag{8.10}$$

The angular momentum torque on a BH moving on a circular orbit is caused by the DF force, which is perpendicular to the radial direction. Therefore, the torque magnitude can be expressed as (Rodriguez et al., 2018):

$$\frac{\mathrm{dL}}{\mathrm{dt}} = \mathrm{m_{BH}}\mathrm{a_{DF}}\mathrm{r}, \tag{8.11}$$

where the DF acceleration a_{DF} acting on the BH has been introduced. Under specific assumptions – i.e., (*i*) the surrounding particle distribution must be infinite, isotropic and homogeneous (thus ensuring that the perpendicular component of the velocity change during two-body scattering is negligible), (*ii*) self-interactions among the surrounding particles are negligible and (*iii*) the mass of these particles is much smaller than the BH mass, i.e. $m_p \ll m_{BH}$ – this acceleration is given by (Binney and Tremaine 1987):

$$\tilde{a}_{DF}(r) = -8\pi^2 \log(1+\Lambda^2)\, G^2 m_p (m_{BH}+m_p) \frac{\int_0^{v_{BH}} v^2 f(v) dv}{v_{BH}^2} \hat{v}_{BH}, \tag{8.12}$$

where v_{BH} is the BH velocity, G is the gravitational constant, f(v) is the velocity distribution function of the surrounding particles and $\Lambda = b_{max}/b_{min}$ where b_{max}, b_{min} are the maximum and minimum impact parameter to account for. Assuming that the surrounding particle distribution is Maxwellian and Λ is large so that $\log(1+\Lambda^2) \sim 1/2 \log(\Lambda)$, Binney and Tremaine (1987) showed that this expression can be simplified as:

$$\tilde{a}_{DF}(r) = -\frac{4\pi \ln(\Lambda) G^2 \rho (M_{BH}+m_p)}{v_{BH}^2} \left[\mathrm{erf}(\mathcal{X}) - \frac{2\mathcal{X}}{\sqrt{\pi}} e^{-\mathcal{X}^2} \right] \hat{v}_{BH}\,. \tag{8.13}$$

Here erf is the error function, ρ is the density surrounding the BH, while $\mathcal{X}$ depends on the velocity of the BH v_{BH}, and on the velocity dispersion of the surrounding medium σ as:

$$\mathcal{X} = \frac{v_{BH}}{\sqrt{2}\sigma}. \tag{8.14}$$

Combining Eq. (8.8), (8.11) and (8.13), one obtains an expression for the radial velocity of the BH particle inspiralling into a NFW halo:

$$\frac{d\tilde{r}}{dt} = -\frac{4\pi \ln(\Lambda) G^2 \rho_H (M_{BH}+m_p)}{v_{BH}^2 \mathcal{F}(v_c, r_s, r)} \left[\mathrm{erf}(\mathcal{X}) - \frac{2\mathcal{X}}{\sqrt{\pi}} e^{-\mathcal{X}^2} \right] r \hat{v}_{BH}. \tag{8.15}$$

Lastly, the square of the velocity dispersion appearing in Eq.(8.14) from the Jeans equation takes the form:

$$\sigma_H^2(r) = \frac{1}{\rho_H(r)} \int_r^\infty \rho_H(r') \frac{G M_H(r')}{r'^2} dr' \tag{8.16}$$

and can be integrated using Eq. (8.1) and (8.2).

8.1.2 Elliptical orbits

The previous discussion related to an initially circular orbit can be extended to elliptical orbits. In this case, the assumption that the orbit remains circular while the BH is sinking is clearly no longer valid. Therefore, Eq. (8.11) does not hold. To derive an analytical expression for the sinking timescale in this more general context, the total BH acceleration can be decomposed into a first component which is instantaneously directed toward the center of the NFW halo and a second component which is always antiparallel to the BH velocity vector:

$$\vec{a}_{BH} = -a_H(r)\hat{r} - a_{DF}\hat{v}_{BH}. \tag{8.17}$$

The first term in the above equation is given by Eq. (8.5), while the second one by Eq.(8.15). In the following, the orbital eccentricity is defined according to its standard formulation:

$$e = \sqrt{1 - \frac{\mathrm{L}^2}{\mathrm{G M_H m_{BH}^2 d_a}}}\,, \tag{8.18}$$

where L is the angular momentum of the BH and $\mathrm{d_a}$ is the apocentric distance.

8.1.3 Adding a stellar bulge

Following the formalism of Springel and White (1999), the stellar bulge superimposed on the NFW DM halo is modelled as a non-rotating spheroid described by a Hernquist density profile:

$$\rho_\mathrm{b}(\mathrm{r}) = \frac{\mathrm{M_B}}{2\pi}\frac{\mathrm{r_b}}{\mathrm{r}(\mathrm{r_b}+\mathrm{r})^3} \tag{8.19}$$

where $\mathrm{M_B}$ is the total bulge mass and r_b its scale radius. Integrating over the radial coordinate, the bulge mass as a function of the radius can be obtained:

$$\mathrm{M_b}(\mathrm{r}) = \frac{\mathrm{M_B r}^2}{(\mathrm{r_b}+\mathrm{r})^2}\,. \tag{8.20}$$

The gravitational potential associated with this bulge component is given by:

$$\Phi_\mathrm{b} = -\frac{\mathrm{GM_B}}{\mathrm{r}+\mathrm{r_b}}, \tag{8.21}$$

so that the acceleration acting on a BH infalling into the bulge is:

$$\tilde{\mathrm{a}}_\mathrm{BH} = -\tilde{\nabla}\Phi_\mathrm{B} = -\frac{\mathrm{GM_B}}{(\mathrm{r}+\mathrm{r_b})^2}\hat{\mathrm{r}}. \tag{8.22}$$

Solving the Jeans equation, one can derive the velocity dispersion for the bulge component:

$$\begin{aligned}\sigma_\mathrm{b}^2(r) \;=\; & -\mathrm{GM_b\,r\,(r_b+r)^3}\left[\frac{\ln|\mathrm{r}| - \ln|\mathrm{r}+\mathrm{r_b}|}{\mathrm{r_b^5}} + \frac{1}{\mathrm{r_b^4(r+r_b)}}\right.\\ & \left. + \frac{1}{2r_\mathrm{b}^3(r+\mathrm{r_b})^2} + \frac{1}{3r_\mathrm{b}^2(r+\mathrm{r_b})^3} + \frac{1}{4r_\mathrm{b}(r+\mathrm{r_b})^4}\right].\end{aligned} \tag{8.23}$$

When adding the bulge counterpart, the resulting density and velocity distribution of the system can be expressed as the sum of the halo and the bulge components. The circular velocity at radius r of the BH in the composite system is then given by:

$$\mathrm{v_{c,BH}}(\mathrm{r}) = \sqrt{\frac{\mathrm{G}\left[\mathrm{M_H}(\mathrm{r}) + \mathrm{M_b}(\mathrm{r})\right]}{\mathrm{r}}}. \tag{8.24}$$

8.1.4 Numerical integration: the Orbital TImescale for Sinking library

To apply the analytical framework presented in the previous sections, the Orbital TImescale for Sinking (OTIS) Python library has been developed, designed to integrate the BH equations

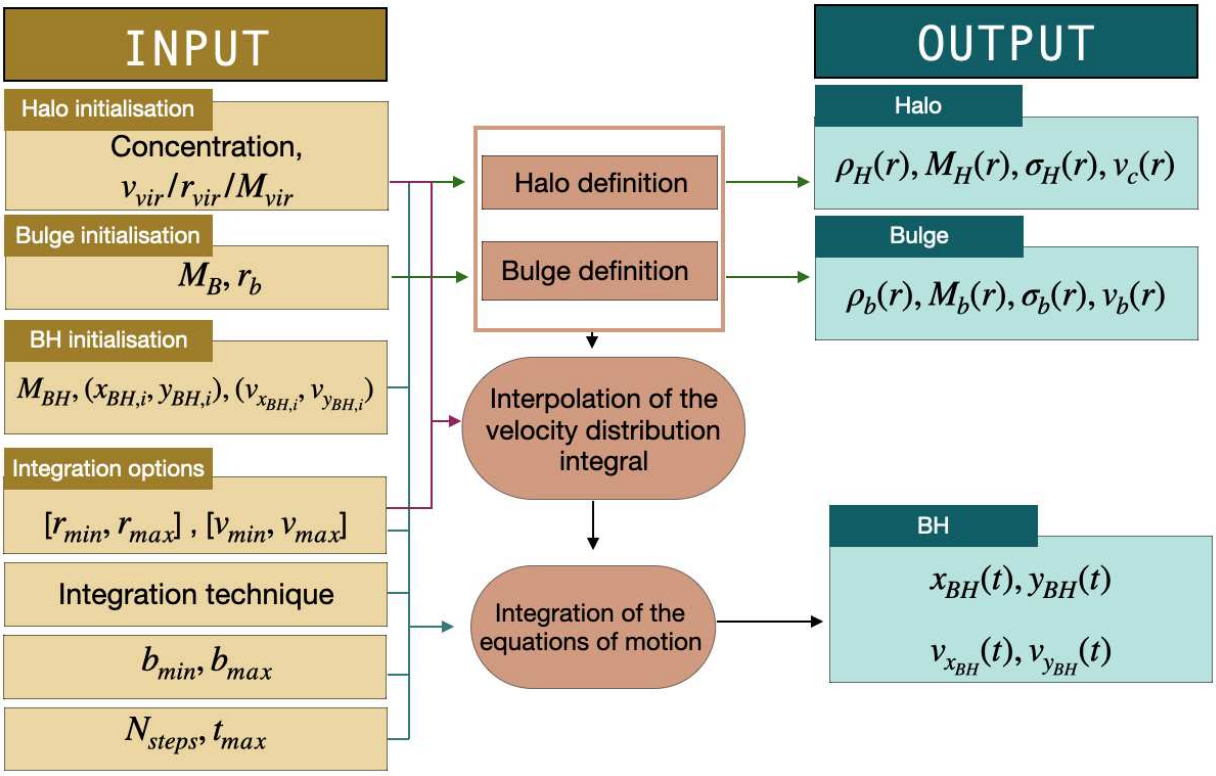

Figure 8.1: *Schematic flowchart of the OTIS library. The code workflow starts with the initialization of the DM halo parameters, including the concentration parameter and virial quantities, eventually followed by the initialization of the stellar Hernquist bulge. The density, mass, and velocity dispersion profiles of both the halo and the bulge can be hence retrieved. The BH is then initialized with its mass and phase-space coordinates. The integral of the velocity distribution function is precomputed on a phase-space grid, enabling fast interpolation during the numerical integration of the equations of motion. User-configurable options allow customization of the interpolation technique, integration method, time steps, and impact parameters.*

of motion in an NFW halo, eventually including a stellar core at its center. The code is publicly available at the OTIS GitHub repository [2]. OTIS enables the computation of the orbital sinking timescale by solving the equations of motion of the BH moving under the influence of gravitational attraction and DF. The gravitational acceleration is computed self-consistently from the NFW and bulge potential, while the DF acceleration is modelled according to Eq.(8.12). The modular structure of the code enables a flexible configuration of interpolation techniques and can account for different initial conditions for both the halo and the BH, making it well-suited for fast calculations of sinking timescales in both idealized and simple multi-component systems.

Figure 8.1 summarizes the OTIS code flow. Given the halo concentration parameter and one of the virial quantities (radius, velocity or mass), the code computes the DM density, mass, and velocity dispersion profiles, assuming an input value for the Hubble parameter. When also the bulge component is included, its initialization requires the definition of the bulge total mass and scale radius. The BH is initialized at a user-defined phase-space coordinate $(\mathrm{x_{BH,i}}, \mathrm{y_{BH,i}}, \mathrm{v_{x_{BH},i}}, \mathrm{v_{y_{BH},i}})$ with mass $\mathrm{M_{BH}}$.The trajectory of the BH is assumed to be on a plane intersecting the halo center, reducing the problem to a two-dimensional one.

[2] https://github.com/alicedamiano5/OTIS.git

As described by Eqs. (8.16) and (8.23), the velocity dispersion depends on the radial coordinate. Consequently, the integral entering Eq.(8.12) itself depends on the radius. To optimize performance, OTIS precomputes this integral on a user-configurable phase-space grid, which is then used during the integration of the equations of motion. The library provides various user-configurable options, including the integration method (from the predefined SciPy techniques, Virtanen et al. 2020), the number of time steps at which to output the solution, the integration time limit, and the values of the minimum and maximum impact parameters b_{min} and b_{max}. Due to the adaptive timesteps adopted by the integrators, the final solutions can differ significantly when using different integration methods. To overcome this, a default maximum timestep size of 0.01 Gyr is set by default. However, to ensure maximum flexibility for different applications, this parameter is also user-configurable. The outcomes of different tests for different integrators and timestep sizes are summarized in Appendix C and can be found in the code GitHub documentation. Within this Chapter, the `Radau` integration technique is adopted.

In line with Genina et al. (2024) and following the work by Just et al. (2010), the following expression for the minimum impact parameter is assumed:

$$b_{min} = \frac{GM_{BH}}{v_{BH}^2 + 2/3\sigma^2}\,, \tag{8.25}$$

corresponding to the minimum impact parameter for a 90-deflection two-body encounter occurring at a typical velocity $v_{typ}^2 = v^2 + 2/3\sigma^2$ for a Maxwellian velocity distribution function.

Figure 8.2 shows the outcome of the OTIS code for a BH embedded in an NFW DM halo (first three columns from the left) as well as in a configuration that includes a central stellar bulge having a Hernquist profile (fourth column). The NFW has total mass $M = 10^{13}$ $M_\odot$ and concentration $c = 4.38$, while the bulge mass is 10^{11} $M_\odot$ and its scale radius is $r_s = 7.2$ kpc. Starting from a BH located in (20 kpc ,0), from left to right the panels show the trajectory of a BH when embedded in an NFW halo and provided with an initial ellipticity $e = 0$, $e = 0.5$, $e = 0.8$, while the fourth column shows the results adding a central bulge and assuming an initial ellipticity $e = 0$.

Panels in the first row display BH orbits in a static potential generated by the system, without accounting for any interactions between particles. In this case, the BH acceleration is determined solely by Eq. (8.5) and Eq.(8.22). Panels in the second row assume that the potential arises from a system of discrete particles and includes interactions by adding a DF force, as described by Eq.(8.13). The third row presents the BH radial distance from the halo center as a function of time, comparing three cases: when the DF is absent (green line), the infall when the BH is placed in the DM halo on initial circular orbit ($e = 0$, purple line) and the specific orbital configuration shown in the second row (orange line). When DF is included, the BH progressively spirals toward the halo center, whereas in its absence, it remains on a stable circular orbit. For eccentric orbits, the apoapsis-periapsis distance is not constant; instead, DF gradually circularizes the orbit, a well-known effect due to DF (e.g., Bonetti et al. 2020; Gualandris et al. 2022). The inclusion of the bulge component slightly reduces the sinking timescale, shortening it by approximately 200 Myr. Interestingly, OTIS also predicts minor oscillations also in the $e = 0$ case shown in the first row. It has been verified that these oscillations persist even when increasing the numerical accuracy of both the integrator and the interpolation grid, but are removed when directly integrating eq.

(8.15), which implies orbital circularity by construction. Based on these tests, the appearance of small orbital eccentricities is a physical consequence of the dynamical friction acceleration acting on the BH. Indeed, the angular momentum loss causing the mild inspiralling of the BH toward the halo center develops small eccentricities, even when it is initially placed on a perfectly circular orbit.

8.2 Numerical simulations

We carried out several simulations with the aim to assess the performance of DF correction at different resolutions, both with and without DF prescriptions. In this section, we describe the specific model we follow to correct for unresolved DF (Sect. 8.2.1) and the general simulation setup we adopt in this work (Sect. 8.2.2). We finally introduce the list of simulations in Sect. 8.2.3 whose results will be presented in Sect. 8.3.

8.2.1 Numerical DF correction

Throughout this Chapter, the outcome of the numerical DF correction introduced in Sect.6.2.1 is further tested and compared to simulations that do not include any DF correction at different resolution. In detail, to avoid double-counting the DF contribution already captured by the gravitational solver, the DF correction is applied only at distances smaller than a chosen maximum impact parameter, denoted as $b_{max,c}$. Within Sect.6.2.1 and in the simulations presented in Chapter 7, $b_{max,c} = \epsilon_{BH}$, where ϵ_{BH} is the gravitational softening length of the BH particle. However, in this Chapter this assumption is adopted only when the BH mass exceeds that of the surrounding DM particles. As the BH becomes less massive, alternative values for $b_{max,c}$ will be explored, to assess their impact (see Sect. 8.3.1).

Moreover, the assumption that the normalized number density of particles surrounding the BH can be expressed as in Eq. (6.3) is here relaxed. Starting from the general expression of the phase-space distribution function given in Eq. (6.2) and assuming that the DF correction in Eq. (6.1) acts only below $b_{max,c}$ around a BH of mass M_{BH} and velocity $\vec{v}_{BH}$, we rewrite Eq. (6.8):

$$\tilde{a}_{DF} = D[\Delta\tilde{v}_{BH}] \sum_{j}^{N} -2\pi G m_j (M_{BH} + m_j)\, \tilde{n}_j \times \ln\left[1 + \Lambda(m_j, \tilde{v}_j)^2\right] \frac{\tilde{v}_j - \tilde{v}_{BH}}{|v_j - v_{BH}|^3}, \tag{8.26}$$

where m_j, $\vec{v}_j$ are the mass and velocity of the j-th particle, $\tilde{n}_j$ is the normalized local number density and the summation runs over all the N particles that are found within a distance $b_{max,c}$ from the target BH particle. In analogy with Eq. (6.5) for $b_{max,c}$, $\Lambda(m_j, \vec{v}_j)$ takes the general form of Eq. (6.9).

As noticed in Sect. 6.2.2, the main update of the novel implementation is that it relaxes the assumption of uniform densities and equal masses around the BH. In this way, the first assumption listed in the Box of Sect. 6.2.2 is also relaxed. In Sect. 8.3.1, the calculation of the number density is described in detail, showing its dependence on the specific gravitational kernel adopted (Eq. 5.20).

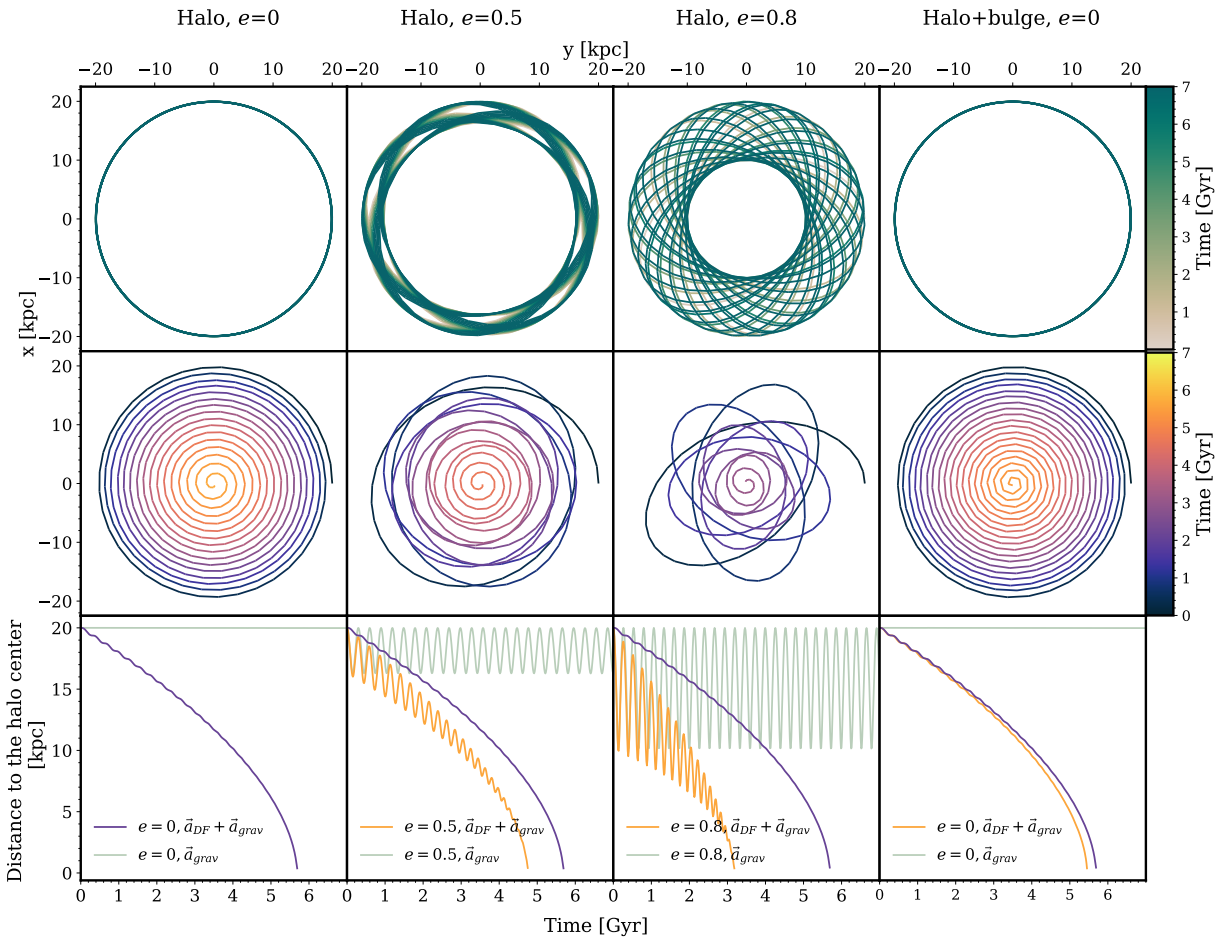

Figure 8.2: *Evolution of a BH embedded in an NFW DM halo, with and without a central stellar bulge, as simulated using the* OTIS *code. The first three columns correspond to BH trajectories in an NFW halo with initial distance of* 20 *kpc from the halo center and orbit ellipticities* $e = 0$, $e = 0.5$, $e = 0.8$, *while the fourth column includes a central bulge and shows the trajectory of the BH initially at* 20 *kpc and placed on a circular orbit. In the first and second row, the trajectory color-code refers to the time elapsed since the beginning of the simulation, as indicated by the color map. Top row: BH trajectories when it is embedded within the static gravitational potential generated by the mass distribution, thus neglecting collisional effects from two-body encounters. Middle row: BH trajectories when collisional effects are included through the analytical description of the DF force (see Eq. 8.12). Bottom row: time evolution of the BH's radial distance from the halo center. The green line shows the distance when* $\tilde{a}_{BH}$ *follows eq. (8.5) (or eq. 8.22 in the last column) mimicking the effect of a BH embedded in a collisionless medium. The purple line adds the DF contribution given by Eq. (8.12) for eccentricity* $e = 0$ *while the distance corresponding to the middle row of each panel is displayed by the orange curve.*

8.2.2 Simulations set up

We generate several simulations of an NFW halo at different resolution levels using the `MAKEGALAXY` code (Springel and White 1999), selecting an NFW DM density profile with a concentration parameter of $c = 4.38$ and virial mass $M_{200} = 10^{13}$ $M_\odot$. This choice, consistent with Genina et al. (2024), ensures that for an orbiting BH of mass 10^9 $M_\odot$ with initial halocentric distance $r = 20$ kpc $\simeq 1/4$ r_s, the significantly larger mass of the host halo minimizes perturbations to the halo density and velocity distributions, preventing artificial alterations of its structure. The halo center position is calculated using the shrinking sphere algorithm developed by Power et al. (2003).

To explore the effects of DF on the BH in a more complex system, Sect. 8.1.3 presents an additional set of simulations at varying resolutions, incorporating a central stellar bulge modeled with a Hernquist profile. The bulge is characterized by a mass of $M_b = 10^{11}$ $M_\odot$ and scale radius $r_s = 7$ kpc. All the simulations presented are carried out using the `OpenGADGET3` code, employing the hybrid TreePM method introduced in Sect. 5.1.4 to accurately resolve gravitational interactions across different spatial scales. As discussed in Sect. 5.6, when calculating the force softening between particles having different softening lengths, the code adopts the largest softening of the particles among the tree node, according to the initial implementation in GADGET of Springel et al. (2001). This detail is relevant for multi-component system and its effects will be analysed in Sect. 8.3.2.

8.2.3 List of simulations

A BH having mass $M_{BH} = 10^9$ $M_\odot$ is introduced at 20 kpc from the center within the halo configuration (eventually complemented with a central stellar bulge) described in the previous sections. Table 8.1 summarizes the full set of simulations performed. From left to right, each column reports: the specific label assigned to each simulation, the BH to DM particle mass ratio M_{BH}/M_{DM}, the BH to stellar mass ratio M_{BH}/M_* (where present), the number of particles used to sample the halo N_{Halo}, the number of stellar particles used to sample the bulge N_{Bulge}, the softening of the BH, DM and stellar particles, whether the simulations adopts the DF correction or not and finally what is the maximum impact parameter adopted in the DF correction.

These simulations are organized into four main sets (separated by horizontal lines in Table 8.1), each designed to address a specific aspect of the DF correction.

- In the first set of simulations, DM halo is sampled with progressively increasing particle numbers $(10^5, 10^6, 10^7, 5 \times 10^7)$. For each realization of the halo, the system is evolved both including and neglecting the effect of the DF correction in Eq. (6.8) (simulations labelled with $*$_DF_ or $*$_NODF_, respectively). For each simulation, two different choices for the softening length are explored, either following Power et al. 2003 (hereafter P03):

$$\epsilon_{P03} = \frac{4R_{vir}}{\sqrt{N_{vir}}}\,, \tag{8.27}$$

Label	M_{BH}/M_{DM}	M_{BH}/M_*	N_{Halo}	N_{Bulge}	ϵ_{BH} (kpc)	ϵ_{DM} (kpc)	ϵ_* (kpc)	DF correction	$b_{max,c}$
H1e5_NODF_p03	7	-	10^5	-	4.43	4.43	-	NO	-
H1e6_NODF_p03	70	-	10^6	-	1.44	1.44	-	NO	-
H1e7_NODF_p03	7×10^2	-	10^7	-	0.44	0.44	-	NO	-
H5e7_NODF_p03	3×10^3	-	5×10^7	-	0.22	0.22	-	NO	-
H1e5_NODF_z19	7	-	10^5	-	2.22	2.22	-	NO	-
H1e6_NODF_z19	70	-	10^6	-	0.72	0.72	-	NO	-
H1e7_NODF_z19	7×10^2	-	10^7	-	0.22	0.22	-	NO	-
H5e7_NODF_z19	3×10^3	-	5×10^7	-	0.11	0.11	-	NO	-
H1e5_DF_p03	7	-	10^5	-	4.43	4.43	-	YES	ϵ_{BH}
H1e6_DF_p03	70	-	10^6	-	1.44	1.44	-	YES	ϵ_{BH}
H1e7_DF_p03	7×10^2	-	10^7	-	0.44	0.44	-	YES	ϵ_{BH}
H5e7_DF_p03	3×10^3	-	5×10^7	-	0.22	0.22	-	YES	ϵ_{BH}
H1e5_DF_z19	7	-	10^5	-	2.22	2.22	-	YES	ϵ_{BH}
H1e6_DF_z19	70	-	10^6	-	0.72	0.72	-	YES	ϵ_{BH}
H1e7_DF_z19	7×10^2	-	10^7	-	0.22	0.22	-	YES	ϵ_{BH}
H5e7_DF_z19	3×10^3	-	5×10^7	-	0.11	0.11	-	YES	ϵ_{BH}
LR_H1e4_NODF	0.7	-	10^4	-	14	14	-	NO	-
LR_H1e4_DF	0.7	-	10^4	-	14	14	-	YES	ϵ_{BH}
LR_H1e4_DF_2	0.7	-	10^4	-	14	14	-	YES	$2\epsilon_{BH}$
LR_H7e3_NODF	0.5	-	7×10^3	-	19	19	-	NO	-
LR_H7e3_DF	0.5	-	7×10^3	-	16	16	-	YES	ϵ_{BH}
LR_H7e3_DF_2	0.5	-	7×10^3	-	16	16	-	YES	$2\epsilon_{BH}$
LR_H5e3_NODF	0.35	-	5×10^3	-	19	19	-	NO	-
LR_H5e3_DF	0.35	-	5×10^3	-	19	19	-	YES	ϵ_{BH}
LR_H5e3_DF_2	0.35	-	5×10^3	-	19	19	-	YES	$2\epsilon_{BH}$
B1e5_NODF_ϵ_{DM}	7	1.4×10^2	10^5	2×10^4	4.43	4.43	1.63	NO	-
B1e6_NODF_ϵ_{DM}	70	1.4×10^3	10^6	2×10^5	1.44	1.44	0.51	NO	-
B1e7_NODF_ϵ_{DM}	7×10^2	1.4×10^4	10^7	2×10^6	0.44	0.44	0.16	NO	-
B1e5_NODF_ϵ_*	7	1.4×10^2	10^5	2×10^4	1.63	4.43	1.63	NO	-
B1e6_NODF_ϵ_*	70	1.4×10^3	10^6	2×10^5	0.51	1.44	0.51	NO	-
B1e7_NODF_ϵ_*	7×10^2	1.4×10^4	10^7	2×10^6	0.16	0.44	0.16	NO	-
B1e5_DF_ϵ_{DM}	7	1.4×10^2	10^5	2×10^4	4.43	4.43	1.63	YES	ϵ_{BH}
B1e6_DF_ϵ_{DM}	70	1.4×10^3	10^6	2×10^5	1.44	1.44	0.51	YES	ϵ_{BH}
B1e7_DF_ϵ_{DM}	7×10^2	1.4×10^4	10^7	2×10^6	0.44	0.44	0.16	YES	ϵ_{BH}
B1e5_DF_ϵ_*	7	1.4×10^2	10^5	2×10^4	1.63	4.43	1.63	YES	ϵ_{BH}
B1e6_DF_ϵ_*	70	1.4×10^3	10^6	2×10^5	0.51	1.44	0.51	YES	ϵ_{BH}
B1e7_DF_ϵ_*	7×10^2	1.4×10^4	10^7	2×10^6	0.16	0.44	0.16	YES	ϵ_{BH}
LR_B1e4_NODF_-ϵ_{DM}	0.7	14	10^4	2×10^3	14	14	5.15	NO	-
LR_B1e4_NODF_ϵ_*	0.7	14	10^4	2×10^3	5.15	14	5.15	NO	-
LR_B1e4_DF_ϵ_{DM}	10^{13}	14	10^4	2×10^3	14	14	5.15	YES	ϵ_{BH}
LR_B1e4_DF_ϵ_*	0.7	14	10^4	2×10^3	5.15	14	5.15	YES	ϵ_{BH}
LR_B1e4_DF_2	0.7	14	10^4	2×10^3	5.15	14	5.15	YES	$2\epsilon_{BH}$
LR_B1e4_DF_4	0.7	14	10^4	2×10^3	5.15	14	5.15	YES	$4\epsilon_{BH}$

Table 8.1: *List of simulations. From left to right: the simulation label, the mass ratio of the BH to DM particles, the BH to stellar mass ratio, the total number of particles sampling the halo and the bulge, the softening lengths assigned to the BH, DM, and stars, whether the simulation includes the DF correction, and the maximum impact parameter considered in the DF correction.*

or following Zhan 2006 (hereafter Z19):

$$\epsilon_{Z19} = \frac{2R_{vir}}{\sqrt{N_{vir}}}\,. \tag{8.28}$$

The corresponding simulations are labelled with $*$_p03 or $*$_z19. Before initializing the BH orbit, it has been verified that adopting the smaller softening length $\epsilon_{\rm Z19}$, compared to the standard $\epsilon_{\rm P03}$, does not alter the density and velocity distributions of the system, which must remain consistent with the analytical predictions. This check is crucial to ensure that no spurious differences in the halo properties, possibly induced by different choices of the softening, affect the subsequent BH dynamics. However, the choice of the softening length not only affects the performance of the N-body gravity solver but also the DF correction. Since in this set $\rm b_{max,c} = \epsilon_{BH} = \epsilon_{DM}$, by decreasing the softening corresponds to shrinking the region within which the DF correction is calculated.

The purpose of this set of simulations is threefold: to assess the performance of the DF correction across different resolutions, to test its numerical convergence against resolution, and to study the dependence on the choice of the softening length.

- A second set of simulations is devoted to the study of the same configuration but at lower resolution (beginning with LR_) when $\rm M_{BH} < M_{DM}$. Aiming to improve the DF prescription, the outcomes of enlarging the impact parameter $\rm b_{max,c}$ to two times the BH softening will be presented.

- A third set of simulations is carried out also including a central stellar bulge. The DM halo with $10^5, 10^6, 10^7$ particles and the stellar bulge with $2\times10^4, 2\times10^5, 2\times10^6$ particles, respectively. The softening length for the star particles is scaled using the relation:

$$\epsilon_* = \epsilon_{\rm DM}\left(\frac{\rm M_*}{\rm M_{DM}}\right)^{1/3}. \tag{8.29}$$

Also in this case, the BH is initially placed at 20 kpc from the center, corresponding to approximately three times the bulge scale radius (see Sect. 8.2.2). As a result, the BH is initially embedded in a DM-dominated environment before gradually sinking into the stellar-dominated core. This raises the question of whether the optimal softening choice for the BH should follow the DM or stellar softening. To address this, two approaches will be compared: *(i)* assigning to the BH the same softening as the DM particles $\epsilon_{\rm BH} = \epsilon_{\rm DM} = \epsilon_{\rm P03}$, and *(ii)* assuming for the BH the same softening of the star particles, $\epsilon_{\rm BH} = \epsilon_*$ based on Eq.(8.29).

Both configurations are tested in simulations with and without the DF correction. In cases where DF correction is applied, the reference choice for the maximum impact parameter is $\rm b_{max,c} = \epsilon_{BH}$.

- Similarly to the second set but this time including the stellar central bulge, an additional low-resolution, fourth set of simulations is presented. Within this set, the BH mass is smaller than the typical DM particle mass (i.e. $\rm M_{BH} < M_{DM}$). In this setup both choices (Eq.s 8.27 and 8.28) of BH softening are explored, and two additional tests are performed with an increased maximum impact parameter, $b_{\rm max,c} = 2\epsilon_*$.

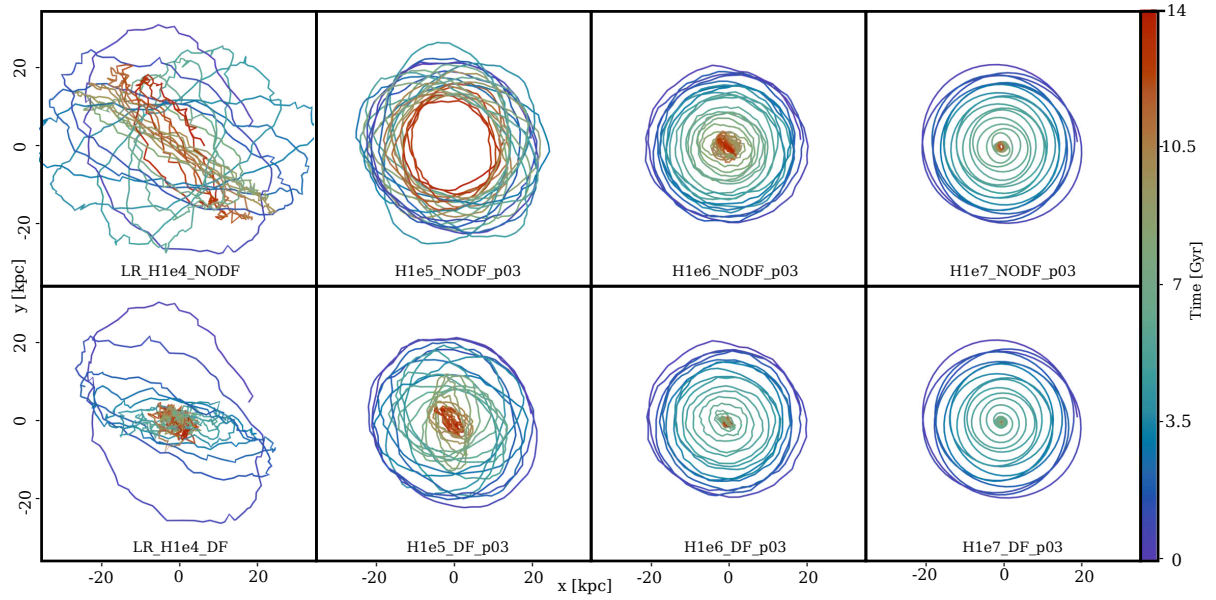

Figure 8.3: *Projected trajectory of the BH in the DM halo on the initial orbital plane, for simulations at progressively increasing resolution, from left to right, as indicated by the labels (see Tab. 8.1 for the description of the label of each simulation). Trajectories are color-coded by time, as shown by the colormap.*

It is worth noticing that, in all the simulations including the bulge, the BH has a larger mass than the stellar particles, as indicated by the third column in Tab. 8.1, even for these low-resolution tests.

8.3 Results

Throughout this section, the results of the simulations listed in Tab. 8.1 are outlined, analysing separately the outcomes of the different sets of simulations. Section 8.3.1 analyses the timescale for sinking of a BH infalling into a DM halo. Section 8.3.2 presents the same results but for a multi-component system composed of a DM halo provided with a central stellar bulge.

8.3.1 Infalling BH in a DM halo

For all the configurations described in this section, a BH of $10^9\,M_\odot$ is placed on a circular orbit at 20 kpc from the DM halo center. Figure 8.3 shows the trajectories of the BH for simulations with progressively increasing resolution, displayed from left to right, as indicated by the labels below each panel (see Tab. 8.1). The orbits are projected in the initial orbital plane and color-coded by time, as shown in the colormap. Regardless of whether the DF correction is applied, the BH develops an eccentric orbit even when initially placed on a circular orbit; the eccentricity decreases with increasing resolution. At the two lowest resolutions, the effect of DF is clearly visible: the BH orbits decays to small halo-centric radii when DF is included, whereas the orbital decay is stalling without DF. In the following subsections, this behaviour is quantified by analyzing

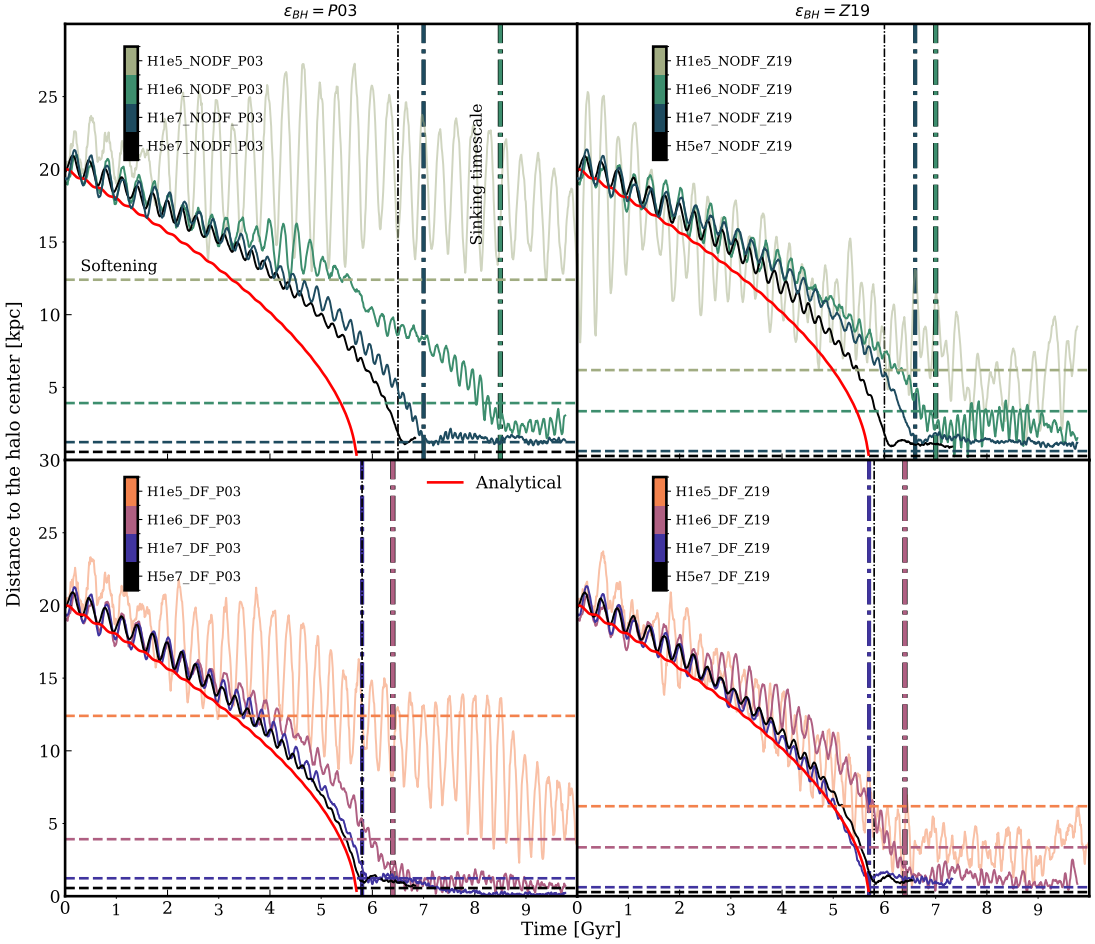

Figure 8.4: *Sinking timescales for a BH initially seeded on a circular orbits within a DM-only NFW halo at* 20 *kpc from the halo center. The left and right columns show simulations with softenings derived from Eq.(8.27) and Eq.(8.28), respectively. Top plots refer to simulations without any DF correction, while the bottom plots include the DF correction according to Damiano et al. (2024) (Sect. 6.2.2). Lines are color-coded by resolution, with lighter to darker shades indicating increasing resolution (as shown in the colormap). Horizontal dotted lines represent the softening lengths, and vertical dash-dotted lines mark the sinking timescales for the three highest resolution runs. The red line shows the analytically predicted merging timescale using* $\mathrm{b_{max}} = 20$ *kpc.*

the BH–halo center distance at different resolutions, with particular focus on the lowest-resolution cases (where $M_{\rm BH} < M_{\rm DM}$) discussed in Sect. 8.3.1. The 3D rendered movies of the simulations presented in this section are available for download here[3].

Reference resolutions

Figure 8.4 shows the time evolution of the distance of the BH from the halo center in different simulations. The left and right columns show simulations where the particle softenings follow Eq.(8.27) and Eq.(8.28), respectively. Top panels present the results of simulations without any sub-resolution prescriptions for BH dynamics, while the bottom plots show those where the BH dynamics includes the DF correction introduced in Sect. 6.2.2. Curves are color-coded according to resolution, with darker shades representing higher resolution. Horizontal, dashed lines indicate the

[3] https://sites.google.com/inaf.it/massiveblackholesinking/home-page/dowloads

values of the softenings, color-coded according to the resolution of the corresponding simulation. The sinking timescale can be visually identified as the moment when the BH trajectory transitions from a steeper descent to a shallower, flatter curve. Vertical dash-dotted lines mark the sinking timescales hence identified for the three highest resolution simulations. The red line represents the predicted orbit retrieved from OTIS (Sect. 8.1.4), using a maximum impact parameter b_{max} of 80 kpc, corresponding to the NFW halo scale radius. In the simulations using the softening $\epsilon_{BH} = \epsilon_{P03}$, at lowest resolution and without the DF correction (H1e5_NODF_P03) the BH does not sink toward the halo center in 10 Gyrs. However, when the DF correction is applied at the same resolution, the sinking process becomes faster and the BH crosses its softening scale at $\sim$ 6 Gyrs. For higher-resolution simulations, the BH gradually sinks toward the center with or without the DF correction. For H1e6_NODF_p03 the sinking timescale is 8.5 Gyr, delayed by about 2 Gyr compared to analytical predictions. At higher resolutions, for H5e7_NODF_p03, the timescale approaches 6 Gyr. Applying the DF correction, H1e6_DF_p03, H1e7_DF_p03 and H5e7_DF_p03 predict sinking timescales in good agreement with theory, with a timescale for sinking of 6.5 Gyr. Notably, H1e6_DF_p03 achieves the predicted timescale for sinking of H5e7_NODF_p03 but with a 50 times-lower resolution.

Furthermore, H1e7_DF_p03 and H5e7_DF_p03 converge to a sinking timescale of approximately 6 Gyr. For simulations using $\epsilon_{BH} = \epsilon_{Z19}$ and without the DF correction, the sinking timescale is shorter than in the corresponding simulations with $\epsilon_{BH} = \epsilon_{P03}$.

When including the DF correction, the results for the three higher resolution simulations align closely with those adopting $\epsilon_{BH} = \epsilon_{P03}$, thus indicating a weak sensitivity of our DF correction model on the softening choice at these resolutions. On the other hand, H1e5_DF_z19 shows sinking timescales which are in agreement with theoretical expectations, despite the delay shown by the same simulation based on the P03 softening. In summary, the DF correction forces the BH to sink toward the halo center in the relatively low-resolution runs, while at higher resolution simulations show good agreement with theoretical predictions and resolution convergence. The additional convergence seen when reducing the softening length in line with Z19 indicates that: considering only particles within the ϵ_{Z19} softening is sufficient to produce a DF correction that matches the analytical predictions; extending the correction region to ϵ_{P03} for the higher resolution cases (where $M_{BH}/M_{DM} > 70$) does not significantly affect the results.

Stability at lower resolutions

All the simulation setups analyzed so far involved BH having a mass larger than the surrounding particles. However, the seeding massed of BHs (see Sect. 5.4.1) within cosmological simulations can be smaller than nearby DM and star particles. This is a critical regime for tracking BH dynamics, as two-body encounters can spuriously heat the BH motion, resulting in an inaccurate representation of its trajectory. To mitigate possible shortcoming, Chen et al. 2007 coupled the DF correction to a boosted dynamical mass unless, so that the mass of the BH entering in the computation of the gravitational force is set to be at least to a value comparable or exceeding the mass of the surrounding particles. Within this section, the performance of the DF correction technique are tested in this "low resolution" regime. Before proceeding further, the DF model is here refined by relaxing the assumption of a homogeneous background density. In addition,

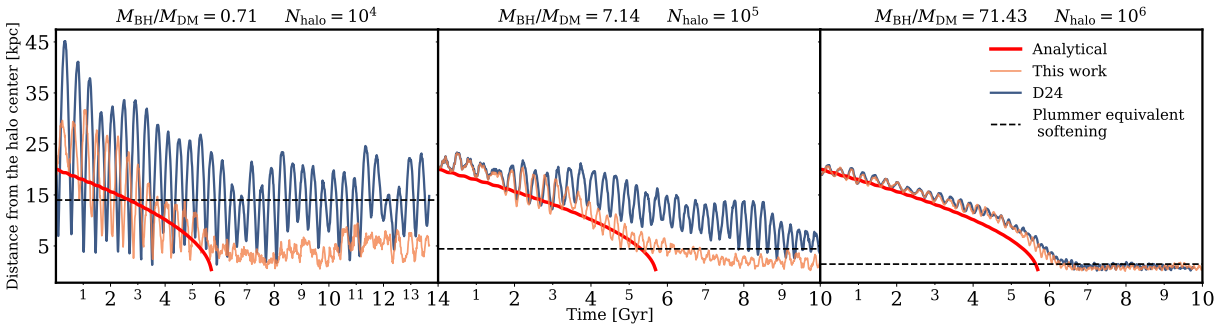

Figure 8.5: *Trajectories of a BH placed on a circular orbit at* 20 *kpc from the center of a DM halo for three different halo resolutions. From left to right, the halo is sampled with* 10^4, 10^5 *and* 10^6 *particles. The dashed black lines indicate the Plummer-equivalent softening length of each simulation. Orange lines represent the BH trajectory when the DF correction is applied according to Eq.(6.10), while the blue lines correspond to the original DF correction in Eq.(6) of D24, the red line shows the analytical prediction from OTIS (Sect. 8.1.4). The ratio of the BH mass to the surrounding DM particle mass is indicated at the top of each panel.*

the correction is tested by extending the maximum correction region beyond the softening length, i.e. adopting $b_{max,c} > \epsilon_{BH}$. The following section illustrates how these refinements improve the accuracy of the predicted sinking timescales and enhance the robustness of the method across different mass regimes, including cases where $M_{BH}/m_j < 1$.

As introduced in Sect. 5.1.1, the OpenGADGET3 code derives the spline-softened gravitational force by taking the force from a point mass m to be the one resulting from a density distribution $\rho(r) = mW(r, \epsilon)$ (see Springel et al. 2001, Appendix A) where $W(r, \epsilon)$ is the cubic spline kernel of Eq. (5.20) and ϵ is the softening length. Therefore, the local number density from the j-th particle placed at a position r_j in Eq.(8.12) is $\tilde{n}_j = W(r_j, \epsilon)$ and Eq.(8.12) becomes (see also Sect. 6.2.2, Eq. 6.10):

$$\vec{a}_{DF} = \sum_{j}^{N(<b_{max,c})} -2\pi G m_j (M_{BH} + m_j) W(r_j, \epsilon) \times \ln(1 + \Lambda(m_j)^2) \frac{v_j - v_{BH}}{|v_j - v_{BH}|^3} . \tag{8.30}$$

Figure 8.5 shows the results of the application of Eq.(6.10) instead of Eq.(6.6) adopted in Damiano et al. (2024) (hereafter, D24), when $M_{BH} < M_{DM}$ (left plot) and $M_{BH} > M_{DM}$ (central and right plots) for the usual DM halo characteristics and initial BH coordinates described in Sect. 8.2.2. The dashed black line corresponds to the Plummer-equivalent softenings $\epsilon_{BH} = \epsilon_{P03}$ equal to 14.4, 4, 44 and 1.44 kpc from the left to the right panel. The orange curve in each plot indicates the trajectory of the BH when the DF correction is applied according to Eq.(6.10). The blue curve corresponds to the original implementation of D24 (see Eq.6.6). The red line indicates the analytical prediction according to the OTIS library. The ratio of the BH mass to the mass of the surrounding DM particles is indicated at the top of each panel. In the left plot, where the BH mass becomes smaller than that of nearby particles and using the DF correction of Eq. (6.4), the BH cannot sink to the halo center but oscillates with a maximum apocenter distance to the

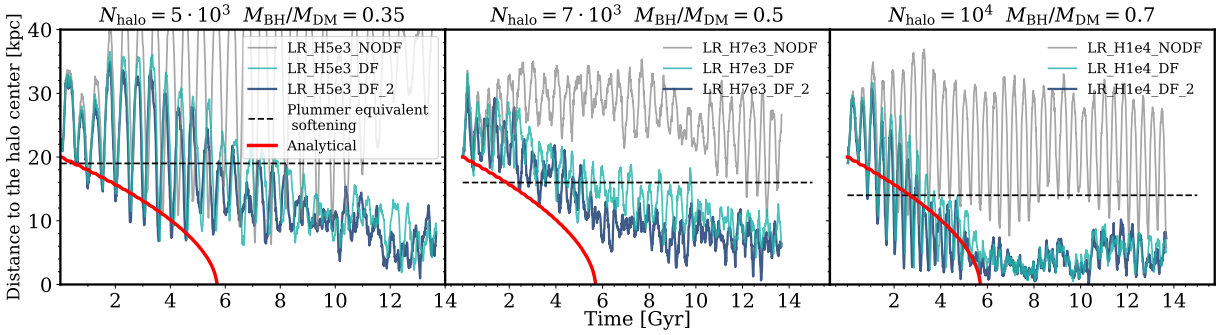

Figure 8.6: *Sinking path of a BH of mass* M_{BH} *infalling in a DM halo sampled with DM particles of mass* M_{DM} *such that* $M_{BH}/M_{DM} < 1$. *Each column refers to a different halo sampling, with increasing halo resolution from left to right. The grey curve corresponds to the simulation without the DF correction, whereas the blue curve refer to the simulation where the DF correction applied to the BH and computed according to Eq.(6.10) with* $b_{max,c} = 2\epsilon_{BH}$ *and* $b_{max,c} = \epsilon_{BH}$ *(lighter curve). The analytical estimation from OTIS is displayed in red. The Plummer-equivalent softening in each simulation is marked with the horizontal dashed line. For the details of each simulation, refer to Tab. 8.1.*

center of the halo higher than the Plummer-equivalent softening. However, at this resolution, refining the description of the surrounding spatial distribution significantly improves the results: the BH sinks well below the Plummer-equivalent softening with timescales in agreement with the analytical results. Even when $M_{BH} > M_{DM}$ the refinement shows its success: the delayed sinking process predicted by the DF correction from D24 is now reduced and once again, the improved sinking timescale is in good agreement with the analytical predictions.

Lastly, at higher resolution (right panel) the refinement has a negligible impact on the BH trajectory. The blue and orange trajectories are similar, indicating that the refinement can be applied with the same effectiveness as the original implementation in this regime.

The second refinement expands the spatial region over which the DF correction is applied. At lower resolutions, the assumption that DF effects are adequately captured at resolved scales may no longer be valid. To account for this, the impact of adopting different values for the maximum impact parameter in the DF correction is investigated here below.

Figure 8.6 presents the results of these tests. From left to right, each column displays our findings when sampling the DM halo with $5 \times 10^3, 7 \times 10^3, 10^4$ particles. In these cases, the BH is less massive than the DM particles, with corresponding mass ratios of $M_{BH}/M_{DM} = 0.35, 0.5, 0.7$. The grey curves represent results obtained without applying the DF correction, while the blue curves illustrate the trajectory of the BH when the DF correction is implemented according to Eq.(6.10), with $b_{max,c} = \epsilon_{BH}$ (lighter) or $b_{max,c} = 2\epsilon_{BH}$. The analytical solution from OTIS (Sect. 8.1.4) is shown in red, and the dashed black line indicates the softening length of each simulation.

Across all the resolutions analyzed, the DF correction plays a crucial role in confining and driving the BH toward the center of the halo. Without the DF correction, the BH does not experience any orbital decay, whereas with the correction applied, it sinks well below the softening scale. Although this orbit shrinking occurs below the resolved scales, the process is captured with a timescale that is delayed when $M_{BH}/M_{DM} = 0.35, 0.5$ but aligns with the analytical prediction when $M_{BH}/M_{DM} = 0.7$. However, it is worth highlighting that in all these low resolution tests,

the BH exhibits considerable orbital scatter, and its trajectory is not circular.

Lastly, increasing the size of the region within which the DF correction is applied does not lead to any significant improvement in the sinking timescale at any resolution. This suggests that particles located below the softening scale contribute most significantly to the DF correction. To validate this result, the corrective has been further extended region to $b_{max,c} = 4\epsilon_{BH}$ and repeated the simulations with the same set-up presented in this section obtaining the same conclusions (see also Sect. 8.3.2).

Based on the tests carried out in this section, we conclude that the DF correction introduced in D24 (see Eq.(6.4)) is not adequate for accurately modelling the evolution of BHs when their mass is smaller than the mass of the surrounding particles. However, by introducing refinements that relax some of the underlying assumptions in the formula, the results significantly improve. Specifically, incorporating a spatially dependent phase-space density (Fig. 8.5) allows for a more accurate reproduction of the sinking process of BHs, even those lighter than the surrounding DM particles.

8.3.2 Infalling BH in a composite DM and stellar bulge system

This section describes the results for the orbital evolution of a BH embedded in a composite system, composed of a DM halo hosting an inner stellar bulge. The initial position of the BH is, as in the previous sections, 20 kpc from the halo center, and its initial velocity is the circular velocity at this halo-centric distance. Being the scale radius of the bulge $r_b = 7.2$ kpc, the BH is initially placed in a DM-dominated region, with its orbit subsequently decaying into the stellar-dominated core. As anticipated in Sect. 8.2.2, the `OpenGADGET3` code uses, for the interactions between particles with different softenings, the largest softening among all the particles in each tree node. This is particularly relevant in a multi-softening system as the one presented in this section, where the BH experiences the transition from a DM-dominated to a stellar-dominated regime. To exploit the differences between different choices for ϵ_{BH}, this section presents the results from simulations where the BH gravitational softening is set to be equal to both the DM, $\epsilon_{BH} = \epsilon_{DM}$, and stellar particles one, $\epsilon_{BH} = \epsilon_*$, with ϵ_* scaling with resolution according to Eq.(8.29). All the simulations are carried out both with and without the DF correction, using Eq.(6.10) with $b_{max,c} = \epsilon_{BH}$. Section 8.3.2 presents the results obtained when using a larger DF correction region.

Reference resolutions

Fig. 8.7 presents the results of these simulations, showing the distance to the system for different runs. The left panels compare simulations with and without the DF correction, as well as with different choices for the BH softening length: for $\epsilon_{BH} = \epsilon_{DM}$ or $\epsilon_{BH} = \epsilon_*$. The meaning of each label is indicated in Tab. 8.1. Simulations at increasing resolution are shown from top to bottom. Simulations at lower resolution and without the DF correction, B1e5_NODF_ϵ_{DM} and B1e5_NODF_ϵ_*, exhibit the slowest orbital decay, crossing the BH softening length only after ~ 9 Gyr, with no significant difference for different choices of ϵ_{BH}. Increasing the number of particles sampling the halo and the bulge as for B1e6_NODF_ϵ_{DM}, the BH sinking timescale is noticeably delayed when approaching the bulge-dominated region. Interestingly, this effect is less pronounced in B1e6_NODF_ϵ_*. According to the choice for the force softening – see Sect. 8.2.2

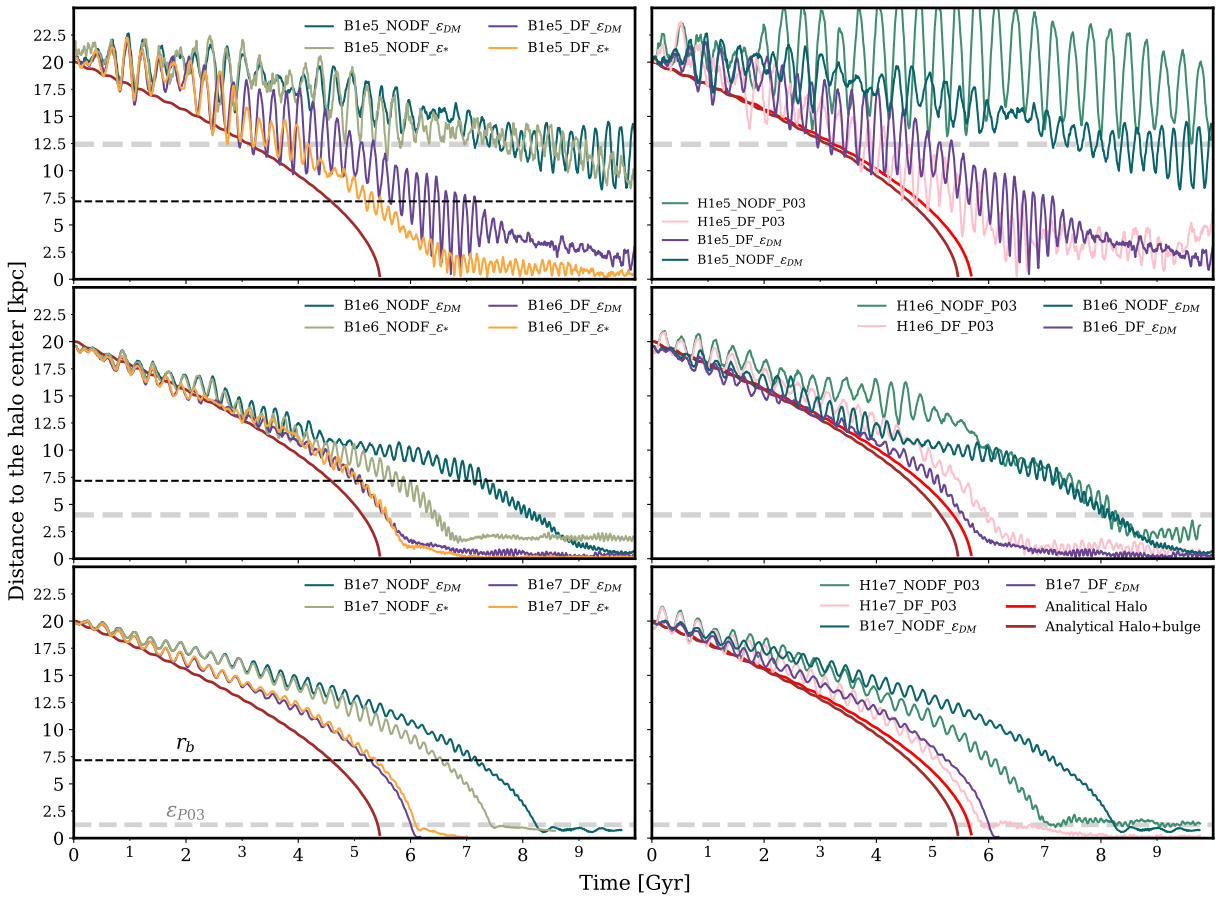

Figure 8.7: *Comparison of the evolution of BH halo-centric distances during the BH sinking for different simulation setups. The results at increasing resolutions are shown from top to bottom. Left column compares simulation using* $\epsilon_{\rm BH} = \epsilon_{\rm DM}$ *or* $\epsilon_{\rm BH} = \epsilon_*$ *for simulation with and without the DF correction. The right panels display the results for a BH embedded either in the NFW halo alone (as described in Sect. 8.2.2) or with the addition of a central stellar bulge. The red curves show the analytical predictions computed with* OTIS*, with the lighter curve corresponding to the DM-only case and the darker curve including the central bulge. Dashed horizontal lines indicate the Plummer-equivalent softenings used in the simulations, with Z19 softenings marked in black and P03 softenings in grey.*

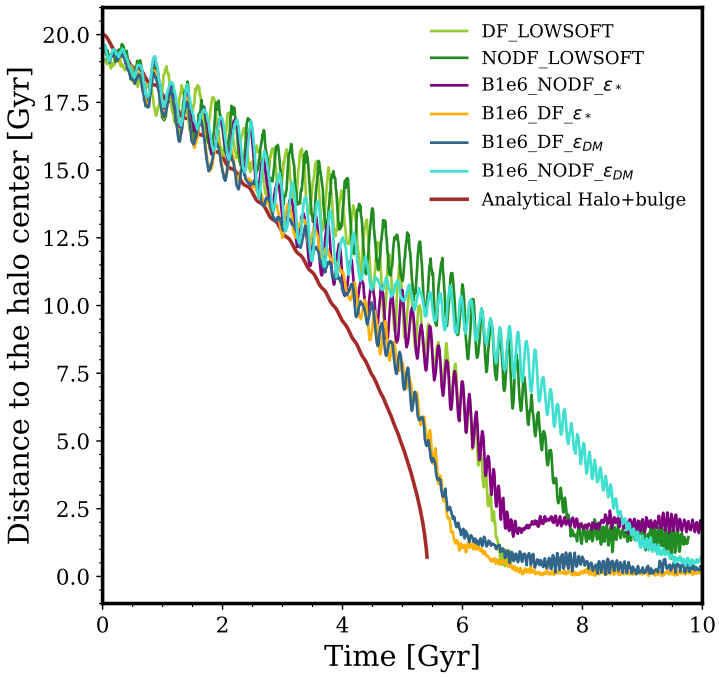

Figure 8.8: *Evolution of the BH–halo center distance for simulations with the same mass resolution as* B1e6_DF_ϵ_* *but using reduced gravitational softening lengths:* $\epsilon_{\rm DM} = 0.72$, $\epsilon_{\rm BH} = \epsilon_* = 0.25$. *The green curves show the results from these simulations, with the darker line corresponding to the run without dynamical friction (*NODF_LOWSOFT*) and the lighter green line including the DF correction (*DF_LOWSOFT*). For reference, we plot in yellow and purple the outcome of* B1e6_DF_ϵ_* *and* B1e6_NODF_ϵ_*, *while blue curves shows the results from* B1e6_NODF_$\epsilon_{\rm DM}$ *(light) and* B1e6_DF_$\epsilon_{\rm DM}$ *(dark). The red line represents the analytical predictions from* OTIS.

– in the DM-dominated region, the BH primarily interacts with the DM softening length, leading to a nearly identical trajectory for both softening choices. However, as the BH approaches the bulge scale radius, the impact of softening differences becomes evident: larger softening values lead to longer sinking timescales, consistent with the findings in Sect. 8.3.1.

Nevertheless, these differences largely vanish when comparing B1e5_DF_$\epsilon_{\rm DM}$ and B1e5_DF_ϵ_*, thus confirming that the introduction of the DF correction compensates for the different choices of softening. Simulations at higher resolution reinforce these trends, with only a mild deviation observed in B1e7_NODF_$\epsilon_{\rm DM}$ when approaching r_b. However, also in this case, the sinking timescale does not converge in simulations without the DF correction at different resolutions and different choices for the BH softening.

Since the presence of a central stellar component is expected to reduce the sinking timescale (as predicted by analytical estimates, see Fig. 8.2), it is useful to compare the numerical results with and without the central bulge. The right column of Figure 8.7 directly compares analogous simulations with and without the stellar bulge, using $\epsilon_{\rm BH} = \epsilon_{\rm DM} = \epsilon_{\rm P03}$ in both cases, also comparing the versions with and without the DF correction. Interestingly, even when sampling the halo with 10^7 particles - a configuration that successfully reproduced the results of the infall in the DM only case depicted in Fig. 8.4 - the BH exhibits a longer sinking timescale in the presence of a central stellar bulge, an effect that is less pronounced when using the DF correction.

The delay in the BH orbital decay is less pronounced when its gravitational softening length

is set equal to that of the stellar particles. This suggests that this effect may be driven by the softened nature of the gravitational interactions. In order to verify this, two additional tests were carried out further reducing the softening lengths to the values $\epsilon_{\rm DM} = \epsilon_{\rm Z19}$ and $\epsilon_{\rm BH} = \epsilon_*$, where ϵ_* follows eq. (8.29). Figure 8.8 which compares the BH–halo center distance in two simulations—one with DF, labelled as DF_LOWSOFT and one without, namely NODF_LOWSOFT—with the same resolution as B1e6_DF_ϵ_*, but using the smaller softening lengths, so that $\epsilon_{\rm DM} = 0.72$, $\epsilon_{\rm BH} = \epsilon_* = 0.25$. The results are compared both with simulations at the same mass resolution but using a larger force softening and with analytical predictions from OTIS. Again, reducing the softening causes a significant delay in the orbital decay. This result highlights that simulations involving multiple particle species are particularly sensitive to softening choices. Deviations from analytic expectations can arise either due to softened gravitational interactions (for too large softenings) or from numerical heating caused by two-body encounters (for too small softenings). In both cases, the application of the DF correction partially mitigates these effects.

Interestingly, B1e7_DF_ϵ_* delays the sinking process with respect to the lower resolution simulation B1e6_DF_ϵ_*. To investigate the possible origin for this, several tests with different softening choice and configuration of the initial conditions (ICs) have been carried out. First, the simulation B1e9_1e7_DF_ϵ_* was restarted from the same ICs, but varying the BH softening length by a factor of two—both increasing and decreasing it—resulting in $\epsilon_{\rm BH} = 0.88$ and 0.08, respectively. This tests assess the influence of the chosen softening length on the results. Additionally, an additional simulation has been carried out, identical to B1e9_1e7_DF_ϵ_* but using a different random realization of the halo, in order to explore whether the configuration of the initial conditions could affect the BH sinking timescale. This simulation is labelled as B1e9_1e7_DF_ϵ_*_NEWIC. Figure 8.9a presents the results of these tests, showing the BH distance to the halo center as a function of time. The simulations with reduced and increased BH softening are labeled LOWSOFT and BIGSOFT, shown in teal and red, respectively. The fiducial B1e9_1e7_DF_ϵ_* run is shown in yellow, while B1e9_1e7_DF_ϵ_*_NEWIC in pink. As previously discussed, we find that a smaller softening length leads to a delayed sinking timescale—here by approximately 400 Myr—compared to the fiducial run. Interestingly, the simulation with a different IC realization results in a faster sinking timescale. This is not unexpected: prior studies (e.g., Genina et al. 2024) have demonstrated that the specific details of the ICs can significantly influence BH orbits, leading to variations in the sinking time. In fact, they report that even in high-resolution runs, the IC realization can slightly change orbital decay (see their Figures 2 and 11).

Finally, we tested the effect of increasing resolution. Adding a new simulation with $N_{\rm halo} = 5 \times 10^7$ particles, labelled as B5e7_DF_ϵ_* and adopting $\epsilon_{\rm DM} = 0.2$ and $\epsilon_* = \epsilon_{\rm BH} = 0.073$. Figure 8.9b compares the BH–halo center distance over time for , B1e6_DF_ϵ_*, B5e7_DF_ϵ_*, B1e7_DF_ϵ_*_NEWIC and B1e7_DF_ϵ_*, shown in teal, red, pink, and yellow, respectively. As expected, higher resolution leads to shorter sinking timescales. Notably, the results for B1e6_DF_ϵ_* and B1e6_DF_ϵ_* are now in good agreement.

These tests reveal that slight discrepancies can eventually arise from the specific realization of the ICs that can impact the sinking timescale, with different ICs introducing stochastic variations. It is worth noting that the random seed used for the halo realization and variations in the softening length are not the only sources of divergence as chaotic behavior can also arise from differences

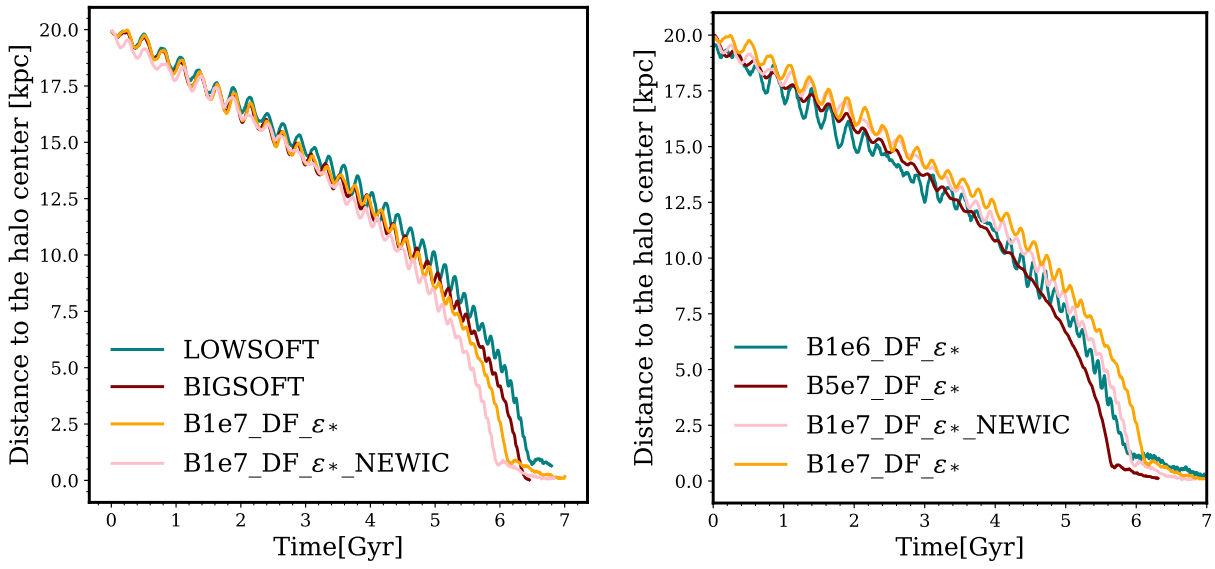

Figure 8.9: *Comparison of the BH–halo center distance for variations in softening (left) and in mass resolution (right). (a): Time evolution of the distance between the BH and the halo center for different simulations at the same resolution as* B1e7_DF_ϵ_*. *The fiducial run is shown in yellow, while simulations with reduced and increased BH softening lengths are LOWSOFT (teal) and BIGSOFT (red).* B1e7_DF_ϵ_*_NEWIC *uses the same parameters as the fiducial run but a different realization of the initial conditions. (b) Distance to the halo center as a function of time for simulations with varying resolution:* B1e6_DF_ϵ_* *(teal),* B5e7_DF_ϵ_* *(red),* B1e7_DF_ϵ_NEWIC *(pink), and* B1e7_DF_ϵ_* *(yellow).*

in machine precision and specific hardware settings, not addressed in this work.

Stability at low resolution

To extend the analysis to systems composed of particles with masses larger than the BH mass, this section presents a study the trajectory of the BH under these conditions, similar to what illustrated in Section 8.3.1. In particular, the conclusion of Sect. 8.3.1 was that refining the D24 model by incorporating a kernel-dependent number density in Eq.(6.10) successfully reproduced the sinking process, even at low resolution, but no significant improvement was found when enlarging the corrective region. Given these findings, a comparable set of tests is performed in configurations that include a stellar bulge component. The results of these simulations are shown in Figure 8.10, illustrating the evolution of the BH distance from the halo center under different simulation setups.

The figure compares cases without the DF correction either when $\epsilon_{\rm BH} = \epsilon_{\rm DM}$ or $\epsilon_{\rm BH} = \epsilon_*$ (lighter and darker green curves), to those where the DF correction is applied using different impact parameters. The outcomes of simulations where $b_{\rm max,c} = \epsilon_{\rm BH}$ are shown in purple, where the darker line corresponds to $\epsilon_{\rm BH} = \epsilon_{\rm DM}$ and the lighter one to $\epsilon_{\rm BH} = \epsilon_*$. The maximum impact parameter was then increased to $b_{\rm max,corr} = 2\epsilon_{\rm BH} = 2\epsilon_*$ (dark orange) and $b_{\rm max,corr} = 4\epsilon_{\rm BH} = 4\epsilon_*$ (light orange).

When the DF correction is not included, the BH orbit does not decay, regardless of the softening

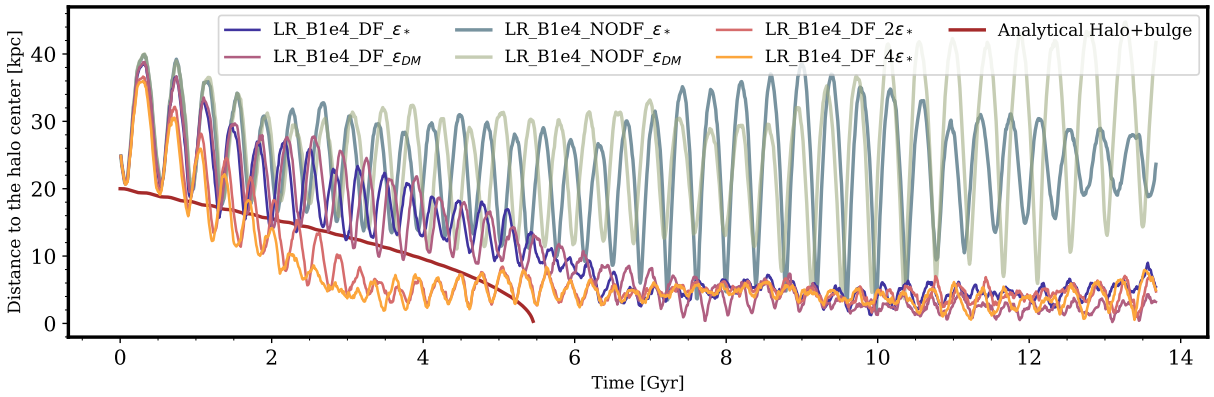

Figure 8.10: *Evolution of the BH's distance from the halo center in low-resolution simulations including both a DM halo and a stellar bulge. The figure compares different setups: no DF correction (lighter and darker lines for different softening choices), DF correction with* $b_{max,c} = \epsilon_{BH}$ *and* $\epsilon_{BH} = \epsilon_{DM}$ *or* $\epsilon_{BH} = \epsilon_*$ *(lighter and darker purple lines), and DF correction with an extended impact parameter* $b_{max,c} = 2\epsilon_{BH}, 4\epsilon_{BH}$ *(lighter and darker orange lines). The brown curve represents the analytical sinking timescale from* OTIS.

choice. However, once the correction is acting, the BH sinks to the center, again showing no dependence on the adopted BH softening. Notably, increasing the maximum impact parameter results in an accelerated sinking process. Ultimately, enlarging beyond ϵ_{BH} the region within which the DF is corrected region does not improve the performance of the model in the DM halo-only case, while leading to an overestimation of the DF in a multi-component system, eventually producing too short sinking timescales compared to analytical predictions.

Contributions to the DF acceleration

In a system composed of both DM and stellar components, it is interesting to examine the relative importance of different terms in the DF correction model and, in particular, to assess the separate contributions of stars and of DM to the overall DF force.

Figure 8.11 presents the analysis of these different components entering Eq.(8.12) for simulation LR_B1e4_DF_ϵ_*, B1e5_DF_ϵ_* and B1e6_DF_ϵ_*,B1e7_DF_ϵ_*. The first panel from the top shows the evolution of the BH distance to the halo center, followed by the relative strength of the DF acceleration compared to the gravitational acceleration (second panel). The third panel illustrates the relative contributions of stars and DM to the total DF correction, while the fourth panel shows the number of particles enclosed within ϵ_{BH} (hence contributing to the DF correction). The last two panels report the value of $\log(1+\Lambda^2)$ and the term $1/v_{rel}^3$:

$$\frac{1}{v_{rel}^3} = \sum_i^{N(<\epsilon_{BH})} \frac{1}{(v_i - v_{BH})^3}\,. \tag{8.31}$$

The horizontal dashed lines in the top panel mark the softening values color-coded according to the simulation they refer to.

As illustrated in the second row, a notable feature of these results is the enhanced DF correction at lower resolutions. With increasing resolution, DF is more accurately captured by the

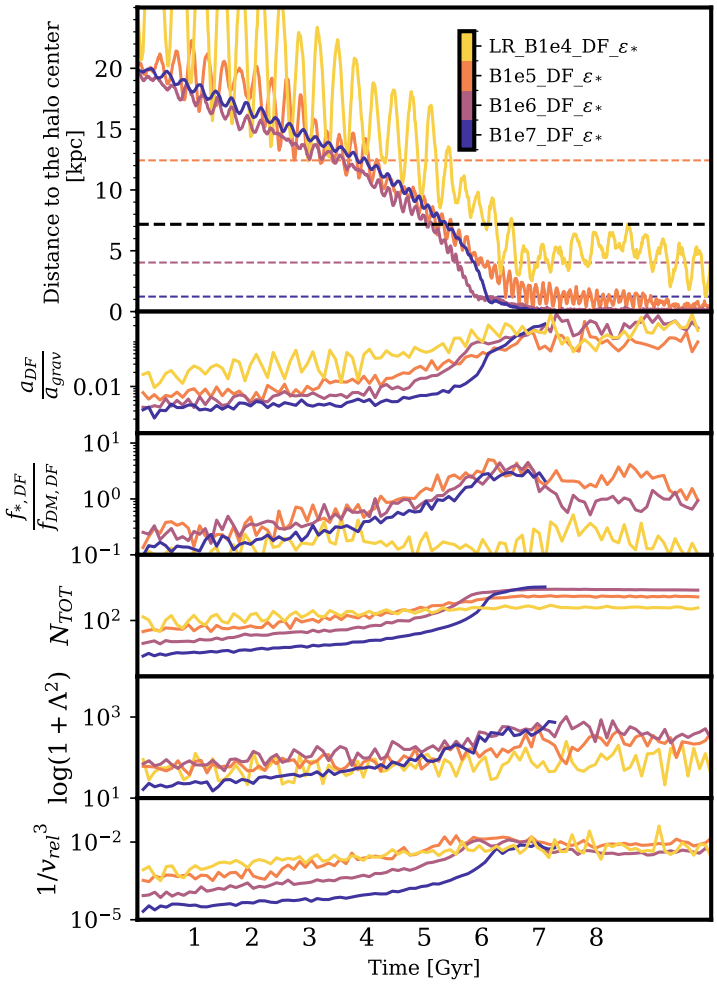

Figure 8.11: *Breakdown of the different contributions to the DF correction term in Eq.(8.12) for simulations LR_B1e4_DF_ϵ_*, B1e5_DF_ϵ_*, B1e6_DF_ϵ_*, and B1e7_DF_ϵ_*. From top to bottom, the panels show: BH distance to the halo center, ratio of DF acceleration to gravitational acceleration, ratio of stellar to DM contributions to DF, total number of particles within $\epsilon_{\rm BH}$, Coulomb logarithm term, and inverse velocity term of Eq.(8.31).*

gravitational solver, reducing the need for an explicit DF correction, which consequently becomes progressively weaker. This effect is naturally accounted for in the prescription adopted, thus demonstrating that convergence to the analytical predictions can be achieved already at relatively low resolution. The relative contribution of the stellar component to DF also increases as the BH approaches the bulge-dominated region, except in the lowest-resolution simulation, where the softening is so high to already account for the entire stellar mass enclosed within the bulge from previous times in the simulation. This effect is further reflected in the number of particles within $\epsilon_{\rm BH}$, which remains constant at the lowest resolution but increases for higher-resolution cases. Remarkably, the higher is the number of particles contributing to the DF correction, the lower is the relative velocity between the BH and the surrounding medium, leading to an increase of the velocity contribution in Eq.(6.10).

8.4 Discussion

Within this Chapter, analytical predictions (Sect. 8.1) and numerical simulations (Sect. 8.2) of the sinking timescale for a BH infalling into a DM halo have been compared, both with and without a central stellar bulge. The analytical results were computed using OTIS Python library to numerically solve the equations of motion of the BH (Sect. 8.1.4). The BH inspiral phase within the halo core was simulated using the OpenGadget3 code, exploring a wide range of resolutions and softening configurations. A refined prescription for correcting unresolved dynamical friction was applied, extending the original D24 model, and its impact on the BH dynamics was systematically evaluated.

Figure 8.12 summarizes some of our key findings of the analysis. In both panels, the sinking timescale is plotted as a function of the total number of particles in the halo, when the BH is embedded in a pure DM NFW halo (left panel) or when a stellar Hernquist bulge is also included (right panel). Symbols represent different simulation setups: circles and diamonds indicate simulations with and without DF correction, respectively. The horizontal red dashed line marks the analytical sinking timescale predicted by OTIS. In the right panel, teal-edged points correspond to simulations where the BH softening matches the DM particle softening ($\epsilon_{\rm BH} = \epsilon_{\rm DM}$), while black edges correspond to simulations where $\epsilon_{\rm BH} = \epsilon_*$. The color of each point encodes the mean eccentricity of the BH during its inspiraling. Eccentricities are calculated by identifying local maxima and minima in the BH distance to the halo center (apocenter $r_{\rm apo}$ and pericenter $r_{\rm peri}$) and computing the eccentricity for each orbit as:

$$e = \frac{r_{\rm apo} - r_{\rm peri}}{r_{\rm apo} + r_{\rm peri}}. \tag{8.32}$$

The eccentricity is then averaged over all orbits to obtain the color-coded value shown in the colorbar.

In the left panel, the absence of the DF correction results in significantly longer sinking timescales for the BH. In low-resolution runs, they often even fail to sink, as discussed in Sect. 8.3.1. Reducing the gravitational softening shortens the sinking time even without DF, but this effect remains insufficient to fully recover the analytical prediction. On the other hand, applying the DF correction produces sinking timescales that better match the analytical predictions across

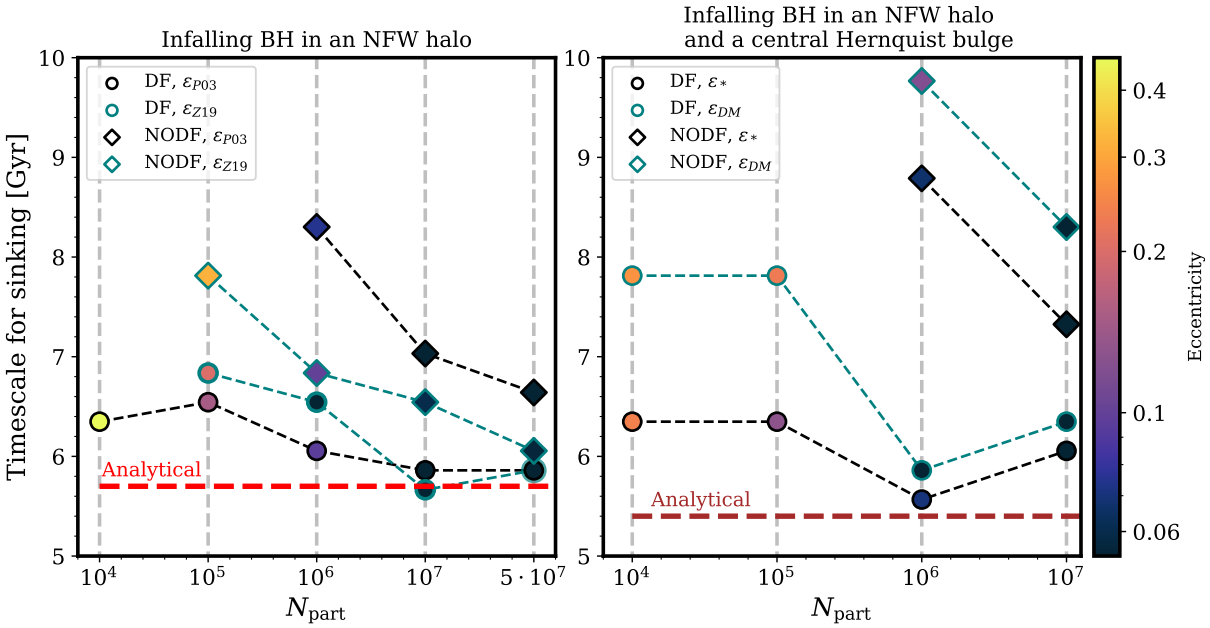

Figure 8.12: *BH sinking timescale as a function of the total number of particles in the halo, for a pure DM NFW halo (left) and for a DM halo with a central Hernquist bulge (right). Diamonds indicate simulations without DF correction, circles indicate simulations with DF correction. The horizontal red dashed line shows the analytical sinking timescale from* OTIS. *In the left panel, teal-edged points, connected by teal dashed lines, adopt softening from eq. (8.28), black-edged points connected by black dashed lines are for the softening from eq. (8.27). In the right panel, teal edges and teal dashed lines correspond to* $\epsilon_{\rm BH} = \epsilon_{\rm DM}$, *while black edges with black dashed lines correspond to* $\epsilon_{\rm BH} = \epsilon_*$. *The color of each point indicates the BH orbital eccentricity, as highlighted in the colorbar.*

all resolutions, and most importantly, reduces the sensitivity on the specific softening choice, as explained in Sect. 8.3.1.

The inclusion of a stellar bulge, as depicted in the right plot, adds complexity to the BH sinking process. In principle, the higher central density contributed by the bulge, should accelerate the BH decay. However, the simulations presented in Sect. 8.1.3 reveal that numerical heating — especially at low resolution — counteracts this effect, thereby delaying the BH infall. Simulations without DF correction show pronounced deviations from analytical predictions, particularly at low resolutions. Quite remarkably, the application of the DF correction mitigates these numerical effects. Moreover, Fig. 8.11 illustrates that the DF correction is most significant in the dense central regions, where the relative velocity between the BH and surrounding particles decreases. In these conditions, the DF correction can contribute up to $\sim 10\%$ of the total gravitational acceleration. As already pointed out by Genina et al. (2024), the dynamical heating of the BH induced by the numerical resolution not only affects the sinking timescale but also the orbital eccentricity. Figure 8.12 shows that the lower the resolution the higher is the mean orbital eccentricity. Even initially placing the BH on a circular orbit, it acquires a mean eccentricity reaching up to ~ 0.5 at lower resolution. In this case, the addition of the DF correction only slightly mitigates this effect at low resolution.

8.5 Conclusions

In this Chapter, results from a suite of controlled numerical experiments were presented to investigate the orbital decay of a BH within a DM halo, both with and without the inclusion of a central stellar bulge. The analysis aimed to quantify the impact of including an additional DF correction to the BH gravitational acceleration, to assess whether the resulting sinking timescales converge with increasing numerical resolution, and to evaluate the agreement between numerical results and analytical predictions across different resolutions. Furthermore, the role of a stellar bulge in shaping BH orbital evolution was explored, together with the ability of the DF correction to reproduce the BH sinking process even in the challenging regime where the BH mass is smaller than that of the surrounding particles. To properly address these objectives, a series of N-body simulations performed at varying resolution and compared with the outcomes of analytical models. On the analytical side, detailed in Sect. 8.1, the OTIS library (publicly available at `https://github.com/alicedamiano5/OTIS.git`) was developed to integrate the equations of motion of an inspiralling BH within an NFW halo, optionally including a stellar bulge. As for the numerical approach, the N-body TreePM code OpenGadget3 was used to simulate the sinking of a BH initially placed at 20 kpc from the center of the halo. The DF correction applied consist of a refined version of the prescription introduced in Damiano et al. (2024) and Sect. 6.2.1, by incorporating a kernel-weighted estimate of the local density surrounding the BH, described in Sect. 8.2.1 and 8.3.1. From this study, the following main conclusions can be drawn:

- Impact of the DF correction and numerical convergence: The addition of the DF correction significantly reduces the BH sinking timescale compared to the cases of uncorrected DF. The results converge at increasing resolution, thus confirming the robustness of the implementation. See Sect. 8.3.1, Fig. 8.4

- Comparison with analytical predictions: Simulations with the DF correction closely match analytical expectations. In contrast, simulations without DF correction show that the BH fails to sink at low resolution or exhibits significant delays ranging from 2 Gyr to 500 Myr depending on resolution. See Sect. 8.3.1, Fig. 8.4.

- Impact of the stellar bulge: Differently from what expected from analytical predictions, the inclusion of a stellar bulge delays the sinking process in numerical simulations due either softened interactions or numerical heating. However, the DF correction is able to mitigate this effect. We find that the stellar contribution to DF becomes significant—up to 10%—in the central stellar core. See Sect.8.3.2 Fig. 8.7 and Fig. 8.11.

- Stability at low resolution: The refined DF model allows accurate tracking the BH inspiralling orbits even when the BH mass is lower than that of surrounding particles, a challenging regime for standard N-body simulations and typical of cosmological simulations. See Sect. 8.3.1, 8.3.2, Fig. 8.5 and 8.10.

As a general conclusion, this study demonstrates that the refined DF implementation—besides having a solid theoretical foundation, see Sect. 4.1.1—yields reliable results at high resolution and, when refined according to Sect. 6.2.2, it can help to control BH dynamics even in the critical low-mass regime. This has key implications in views of its application to cosmological simulations: reliable BH tracking is essential to accurately model BH-galaxy co-evolution, since BH motion affects gas accretion, the deposition of the ensuing AGN feedback energy and hence the subsequent evolution of the host galaxy.

This part of the thesis has focused on the dynamical evolution of MBHs, with particular emphasis on the implementation and validation of a novel DF correction. By testing the performance of the model across a range of environments—spanning both controlled simulations (Chapter 8) and full cosmological setups (Chapter 7)—we have assessed its robustness against different ad hoc numerical techniques and convergence across different resolution regimes. These tests indicate that the DF correction provides a reliable description of the orbital decay of MBHs in numerical simulations. Building on this framework, the following chapters will apply this implementation within OpenGADGET3 to investigate the feeding and feedback processes of MBH, and their impact on galaxy evolution.

Chapter 9

Techniques for AGN feeding and feedback in OpenGADGET3

The content of this Chapter is based on Damiano et al. 2025 (Astronomy & Computing, submitted) "Numerical solutions for black hole feeding and feedback in cosmological simulations with OpenGADGET3", with additional material and extended discussions included for completeness.

To investigate the complex interplay of processes governing cosmic structure formation, cosmological simulations model unresolved, highly non-linear physics through sub-resolution prescriptions (see Sect. 5.3 and 5.4). As simulations reach higher resolution and probe more extreme environments—such as galaxy groups and clusters—new technical challenges arise, particularly in modelling the interaction between MBHs and the surrounding gas. In this Chapter, the influence of the choice of specific numerical implementations of AGN feeding and feedback in the OpenGADGET3 code is critically examined. In particular, the focus will be on the impact of the stochastic swallowing of gas particles during BH accretion, the implementation of a model for the evaporation of cold gas clouds, different kernel-weighting schemes used to distribute AGN feedback energy in radio mode and the complex coupling between AGN-driven feedback and SN–driven galactic winds. To this end, a galaxy group halo is re-simulated multiple times, each realization differing by a single modified implementation aspect. After introducing in Sect. 9.1 the methodology adopted for the simulations, results arising from four different choices for the sub-resolution prescriptions for BH feeding and feedback are illustrated in Sect. 9.2. The results are summarised and discussed in Sect. 9.3

9.1 The set of simulations

The simulations presented in this work are carried out using the OpenGadget3 code introduced in Chapter 5. Initial conditions correspond to the `Cl13` galaxy group described in Sect. 7.1, adopting the same cosmological parameters ($\Omega_m = 0.24$, $\Omega_b = 0.0375$, $h = 0.72$, $n_s = 0.96$, $\sigma_8 = 0.8$) and resolution (Appendix A). Therefore, the DM and gas particle masses are $m_{\rm DM} = 4.69 \times 10^7\ M_\odot$ and $m_{\rm gas} = 8.67 \times 10^6\ M_\odot$, respectively and the spatial resolution for DM particles is set to $\epsilon_{\rm DM} = 4.13$ comoving kpc (ckpc) until $z = 2$, and then fixed in physical units to $\epsilon_{\rm DM} = 1.38$ kpc for $z < 2$. For stars, BHs, and gas particles, the gravitational softenings are fixed

in physical units at $\epsilon_* = \epsilon_{\rm BH} = 0.35$ kpc and $\epsilon_{\rm gas} = 1.38$ kpc, respectively. The hydrodynamic and gravitational solvers are unchanged (SPH and TreePM methods, respectively, see Sect. 5.1.4 and 5.2), but selected sub-resolution prescriptions – introduced in Sect. 5.3 and Sect. 5.4 – are modified to assess their individual impact. In particular, the following implementations are tested:

- **Stochastic BH accretion**: Sect. 5.4.2 introduced the numerical implementation of gas accretion onto the BHs in OpenGADGET3. Along with the *continuous* gas accretion following Eq. (5.72), the code includes a stochastic *discrete* swallowing of gas particles. We remind that this stochastic swallowing was excluded in the previous lower-resolution Dianoga simulations by Bassini et al. (2019); Bassini et al. (2020); Ragone-Figueroa et al. (2018). The impact of the gas swallowing for BH accretion is here explored for higher-resolution simulations.

- **Evaporation of cold clouds**: A mechanism is implemented to allow the *evaporation of cold clouds*: an initially multiphase gas particle lying within the BH smoothing length can leave the multiphase stage whenever the AGN feedback energy it receives is sufficient to "evaporate" its cold component. In practice, assuming that the entire feedback energy is deposited into the cold phase, the specific energy of the cold gas is computed and compared to the average specific energy of the particle. If the former exceeds the latter, the particle exits the multiphase regime. Once this occurs, the particle is prevented from re-entering the multiphase stage – even if its density remains above the SF threshold – until its temperature, through radiative cooling, falls below a factor $\epsilon_{\rm evap} \gtrsim 1$ of the temperature corresponding to the adiabat defined by the SF model (see Eq. 5.62). When this condition is met, the gas particle can again become multiphase and star forming.

- **AGN feedback energy weighting in radio mode**: As described in Sect. 5.4.4, OpenGADGET3 does not currently include an explicit implementation of kinetic AGN feedback. However, at low accretion rate $\dot{M}_{\rm BH}/\dot{M}_{\rm Edd} = 1\%$ a four times higher coupling efficiency is assumed, so that the AGN feedback thermal energy injection is relatively stronger. The spatial distribution of the injected thermal energy in this regime depends on the adopted kernel-weighting scheme. When using the standard SPH-like kernel, particles located closer to the BH receive a larger fraction of the feedback energy. As an alternative, a modified top-hat weighting scheme is explored, redistributing the feedback energy more uniformly among gas particles within the BH smoothing length.

- **Coupling stellar winds with AGN feedback**: Given their role in modelling SN-driven feedback processes (see Sect. 5.3), in the galactic outflow model implemented in OpenGADGET3 wind particles are assumed to be hydrodynamically decoupled from the surrounding gas. This raises the question whether wind particles should receive AGN feedback energy while they are hydrodynamically decoupled. During the wind phase, particles may be either included or excluded from the list of BH neighbors. If excluded, they are effectively "ghost" particles: they do not contribute to the local gas density – thereby not affecting Bondi accretion – and they do not receive any AGN feedback energy. If included, they would contribute to the BH's local density and are eligible to receive AGN feedback energy.

Table 9.1: *List of simulations.*

Label	Stochastic swallow	Cold clouds evaporation	Kernel in radio mode	AGN feedback for winds
`FIDUCIAL`	ON	OFF	SPH	OFF
`C113_NOSWALLOW`	OFF	OFF	SPH	OFF
`C113_EVAP`	ON	ON	SPH	OFF
`C113_KTOPHAT`	ON	OFF	Top-hat	OFF
`C113_AGNWIND`	ON	OFF	SPH	ON

In the following, the simulation including gas swallowing, no evaporation of cold clouds, a top-hat kernel weighting scheme in radio mode, and wind particles excluded from the BH neighbour list will be referred to as the `FIDUCIAL` case. This reference simulation will be compared to four additional runs, each differing from the `FIDUCIAL` case by varying one of these parameters at a time. All the simulations performed are listed in Table 9.1, that specifies the choices for the different sub-resolution implementations explored along with their corresponding labels.

9.2 Results

9.2.1 The BH lifecycle

BH growth is strongly influenced by the dynamical history of the host galaxy—including mergers, tidal stripping, and gas inflows—which determines the timing and frequency of BH–BH mergers and leads to significant system-to-system diversity. As a result, each BH follows a distinct evolutionary path. Nonetheless, some common features can be highlighted. To isolate these common characteristics, the analysis below is restricted to BHs exhibiting quiescent dynamical evolution, remaining central within their hosts and unaffected by merger events.

Figure 9.1 shows the evolution of one of the selected BH showing, from top to bottom, the evolution of BH mass, Eddington ratio $\dot{M}_{\rm BH}/\dot{M}_{\rm Edd}$, surrounding density and released feedback energy of Eq. (5.78). In the second top panel, the dashed grey line marks the threshold value for the Eddington ratio that in our model separates the quasar and radio modes of feedback. Accordingly, in the bottom panel, the rate of feedback energy is highlighted with two different colours according to the accretion regime: purple dots correspond to phases when BH operates in quasar mode ($\eta_f = 0.05$), teal ones identify the radio mode period ($\eta_f = 0.2$). Moreover, the contributions from hot and cold gas to the total density are shown separately in the third panel, as indicated in the legend.

Right after seeding at $z \sim 5.5$, this BH grows substantially through cold gas accretion. During this stage, the BH mass increases significantly (by three orders of magnitude in this specific case) and correspondingly, the cold gas density around the BH decreases progressively due to the release of thermal feedback energy. At $z \sim 2.6$ the surrounding gas density drops to a level where the Eddington ratio falls below the threshold and triggers the transition to radio mode. As soon as the BH enters the radio mode, the AGN feedback energy that couples with the surrounding gas is enhanced by a factor of four (see Sect. 5.4.4). This increased feedback rapidly depletes the cold gas component, causing the BH accretion to become dominated by the hot gas phase.

In practice, as a consequence of our parameter choice, the radio-mode transition sets off a chain reaction loop: whenever the accretion rate drops below the radio mode threshold, the increase in feedback energy (caused by the enhanced feedback factor η_f) further heats and depletes

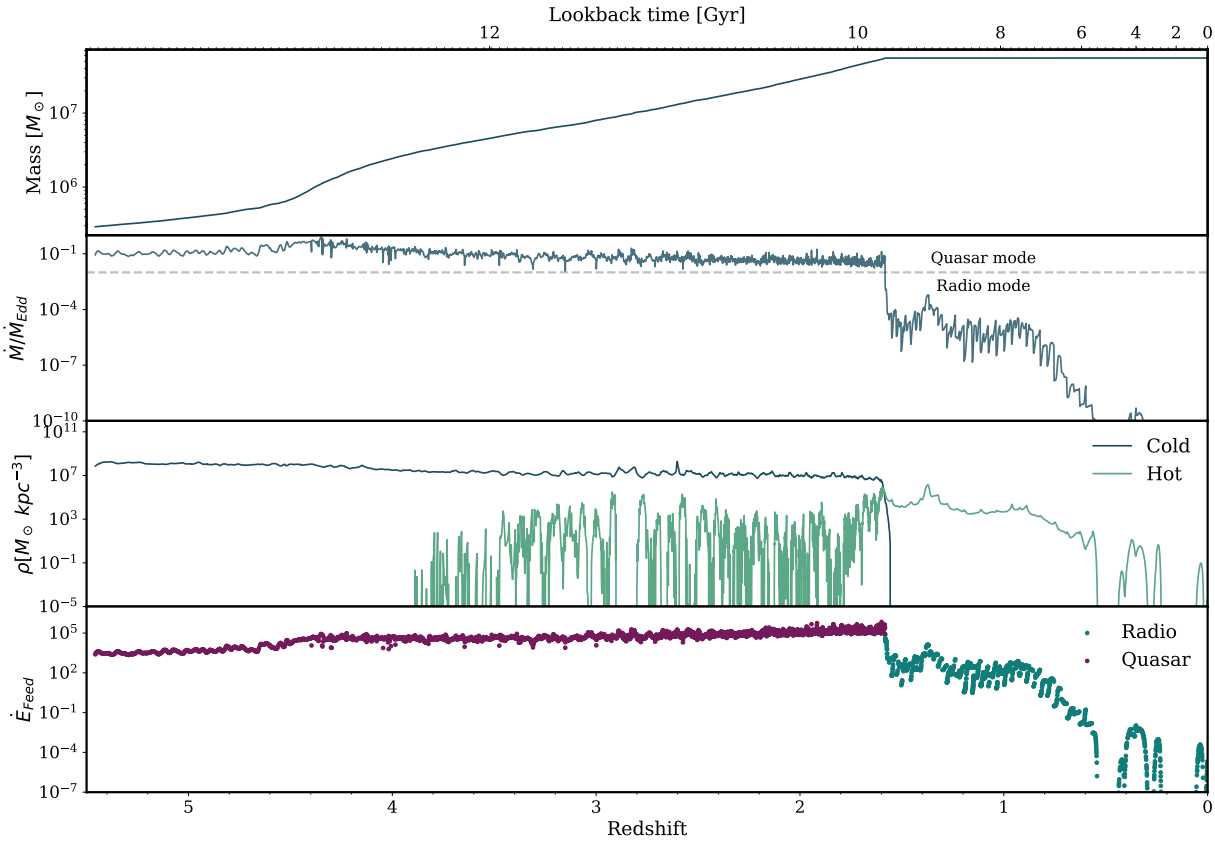

Figure 9.1: *Redshift evolution of key BH properties for a BH in the* `FIDUCIAL` *simulations (Table 9.1). From top to bottom: BH mass; Eddington ratio* $\dot{M}_{\rm BH}/\dot{M}_{\rm Edd}$ *with the grey dashed line indicating the threshold between quasar and radio modes; gas density surrounding the BH, with cold and hot gas contributions shown separately; and the rate of feedback energy released by the BH (Eq. 5.78). The dashed grey line in the second panel indicates the threshold value of the Eddington ratio triggering the quasar/radio modes transition. The last bottom panel highlights separately in purple and teal the feedback energy rate corresponding to quasar and radio mode, respectively.*

the reservoir of cold gas surrounding the BH. Conversely, as will be further discussed in Sect. 9.2.2, if cold gas is funneled back into the BH sphere of influence during the radio mode phase, since α_{cold} is 10 times larger than α_{hot}, the BH may switch back to the quasar mode, with a corresponding reduction of the feedback energy. Therefore, this energy can struggle to heat the cold gas effectively, resulting in a prolonged phase of strong cold gas accretion. Finally, the transition from quasar to radio mode is clearly reflected in the slope of the BH mass growth over time: once the BH enters radio mode, its mass growth rate becomes shallower.

9.2.2 Accretion

The role of gas swallowing

We assess the effect of stochastic gas-particle swallowing by comparing the `FIDUCIAL` simulation, that includes BH accretion from gas swallowing, with `C113_NOSWALLOW` that excludes an explicit particle swallowing.

Figure 9.2a shows, from top to bottom: the evolution of the star formation rate (SFR) of the

BGG, the central BH mass, the BH-to-Eddington accretion ratio $\dot{M}_{\rm BH}/\dot{M}_{\rm Edd}$, and the ratio of cold to hot gas density surrounding the BH. The yellow and blue lines represent the simulations with and without gas swallowing, respectively. In the bottom three panels, the dark blue line tracks the evolutionary history of a BH progenitor — the former central BH of the proto-BGG - merging with the one highlighted in light blue, as indicated in the second row. The SFR is computed from ages of those stellar particles that, at $z = 0$, lie within an aperture of 30 kpc from the halo center, as identified by SubFind (Dolag et al., 2009).

The green horizontal dashed line in the third panel marks the threshold between quasar and radio mode phases, while in the bottom plot it visually distinguishes stages of cold- or hot-dominated BH surrounding density. We first note that the evolution of this BH differs substantially from that of the relatively quiet BH discussed in Sect. 9.2.1. At variance with the lifecycle of the BH shown in Fig. 9.1, the BHs shown in Fig. 9.2a undergo multiple transitions between quasar and radio modes, and correspondingly also cold- and hot-dominated accretion phases. The differences between the `FIDUCIAL` and the `Cl13_NOSWALLOW` simulations appear both in the overall SFR of the BGG and in the individual growth of the central BH. In particular, when gas particles are not swallowed, they remain in the surroundings of the BH. They can either be heated and expelled or, if AGN feedback is insufficient, remain near the BH, increasing the local gas density and sustaining prolonged accretion episodes.

Indeed, the early growth phase of the BH – driven predominantly by cold gas – lasts longer in the `Cl13_NOSWALLOW` simulation. This persistent cold component not only influences the BH accretion history but also impacts the host galaxy: between lookback times corresponding to 10 and 8 Gyr, the SFR is noticeably higher in the run without swallowing, indicating that cold gas remains available for both SF and BH accretion. At later times, a second episode of cold-driven accretion occurs. Again, in the absence of explicit swallowing, this episode lasts longer, as cold gas is harder to deplete and continues contributing to the BH accretion over an extended period. The inset in the second panel highlights the BH mass growth during this later extended episode of cold-gas-dominated accretion in the `Cl13_NOSWALLOW` simulation, showing a distinct steepening of the mass growth, corresponding to a mass increase by a factor of ~ 5. This second phase of rapid accretion also coincides with a boost in the SFR of the BGG. However, because the BH undergoes fewer mergers in `Cl13_NOSWALLOW`, this accretion boost does not translate into a significant difference in the final BH mass. However, the effect of including an explicit swallowing of gas particles is clearly evident when examining the detailed evolutionary tracks. In the non-swallowing case, the gas accumulates near the BH, enhancing the local gas density. This effect is particularly evident for cold gas, which fuels stronger accretion episodes, potentially triggering transition to radio mode. As a result, cold-dominated accretion events last longer in the `Cl13_NOSWALLOW` simulation. At the same time, this cold reservoir leads to higher SFR in the host galaxy during those phases.

Cold gas accretion: evaporation of cold clouds

The BH histories analysed in the previous section show, after the first cold accretion initial growth phase, a second episode of cold-gas-driven accretion, eventually prolonged by non-swallowed gas particles. This episode is an example of the chain reaction mentioned at the end of

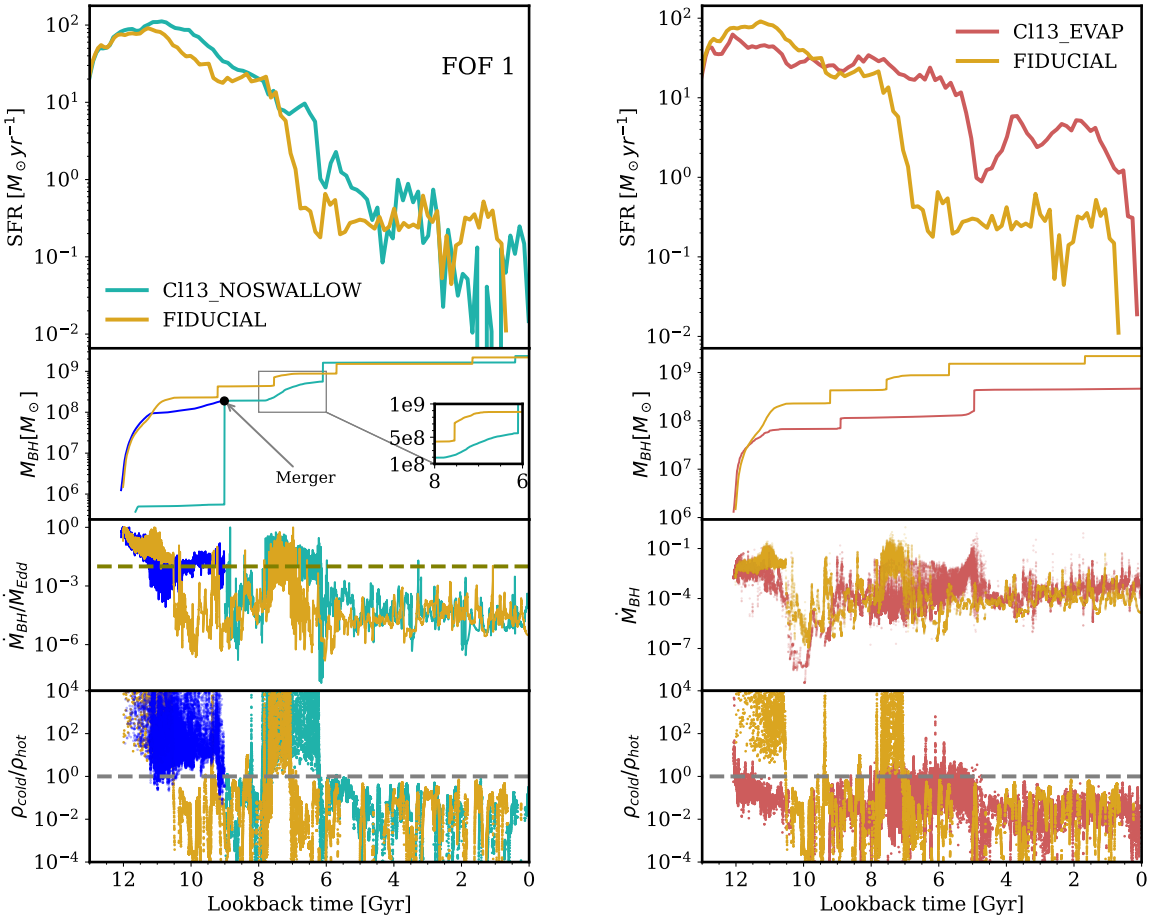

(a) (b)

Figure 9.2: *(a) Comparison of SFR and BH properties as a function of time for the* `FIDUCIAL` *(yellow) and* `Cl13_NOSWALLOW` *(blue) simulations. From top to bottom: SFR of the BGG within an aperture of* 30 *kpc, BH mass growth, Eddington ratio (with the quasar–radio mode threshold marked by a dashed line), and cold-to-hot gas density ratio (with a grey dashed line distinguishing between cold- and hot-dominated phases). (b): Same as for (a), but for simulations with and without cold clouds evaporation, namely* `Cl13_EVAP` *(red) and the* `FIDUCIAL` *(yellow). The third panel displays the BH accretion rate rather than the Eddington ratio reported in Fig. 9.2a.*

Sect. 9.2.1, where the boosted cold accretion can trigger again the transition to the low-feedback quasar-mode regime. Similar low redshift accretion-driven episodes can eventually lead to strong accretion episodes and overmassive BHs, with masses reaching values even larger than 10^{11} $M_{\odot}$ (Borgani et al. ,in preparation, Damiano et al.,in preparation). These cases will be extensively analysed in the next Chapter 10 and particularly in Sect. 10.2.2. To mitigate runaway accretion episodes, we introduce a prescription that allows the cold component of multiphase particles to evaporate. In practice, a multiphase gas particle exits this state when feedback heating evaporates its cold component and can re-enter the star-forming phase only after cooling below a threshold temperature.

Figure 9.2b shows the same quantities as Fig. 9.2a, comparing two `Cl13` simulations—one without cold gas evaporation (the `FIDUCIAL` simulation in yellow) and one with evaporation enabled (`Cl13_EVAP`, red). The simulation illustrated here adopts $\epsilon_{\rm evap} = 2$. For clarity, in the third panel reports the BH accretion rate rather than the Eddington ratio.

At early times, the BGG features a lower SFR when using the evaporation model, and clear differences appear in the evolution of the BH accretion history. The reduced abundance of cold gas in the BH vicinity (see bottom panel) suppresses the BH accretion rate. As a consequence, as the BH mass growth becomes shallower in correspondence to the transition to radio mode, the BH mass is significantly reduced – $4 \cdot 10^7$ $M_{\odot}$ in `Cl13_EVAP` versus $2 \cdot 10^8$ $M_{\odot}$ in the `FIDUCIAL` simulation. The later cold-gas-driven accretion episode is also suppressed, and the final BH mass at $z = 0$ is nearly an order of magnitude lower when evaporation is included. This result further emphasizes the central role of cold gas in driving BH growth, particularly at high redshift.

While the evaporation reduces the amount of cold gas within the BH sphere of influence, it does not quench star formation. As shown in the top panel, the global SFR is over an order of magnitude higher in the `Cl13_EVAP` simulation at later times – a trend consistent across other FoF halos in the simulation. However, the depletion of cold gas around the BH significantly suppresses BH growth at both low and high redshift. At low redshift, this mechanism effectively prevents the BH from overgrowing due to the availability of cold gas. At high redshift, it eases the rapid growth phase of BHs. On the other hand, if AGN feedback efficiently evaporates the cold gas within the BH sphere of influence – thereby suppressing its growth – the evaporation also enhances the density of the halo. Figure 9.3 shows the gas density (top panels) and temperature (bottom panels) within a 2 Mpc region centered on the main halo, comparing simulations with (right column) and without (left column) cold gas evaporation. When the evaporation model is applied, the gas density near the center increases significantly, while the temperature –especially in the outskirts – drops. Given that the BH mass in the `Cl13_EVAP` is significantly lower, both these features can be explained by a less efficient BH feedback.

The effect of BH-BH mergers

In Fig. 9.2a and 9.2b a sharp drop can be identified in the SFR of the `FIDUCIAL` model at lookback time of 8 Gyr. This decrease coincides with a rapid increase in the local cold gas density. This epoch also corresponds to a merger event, marked by a sudden vertical jump in the BH mass (see also the inset in Fig. 9.2a). Figure 9.4 shows the detailed evolution of this event. From top to bottom, the panels display: the relative distance between the two merging BHs (blue line),

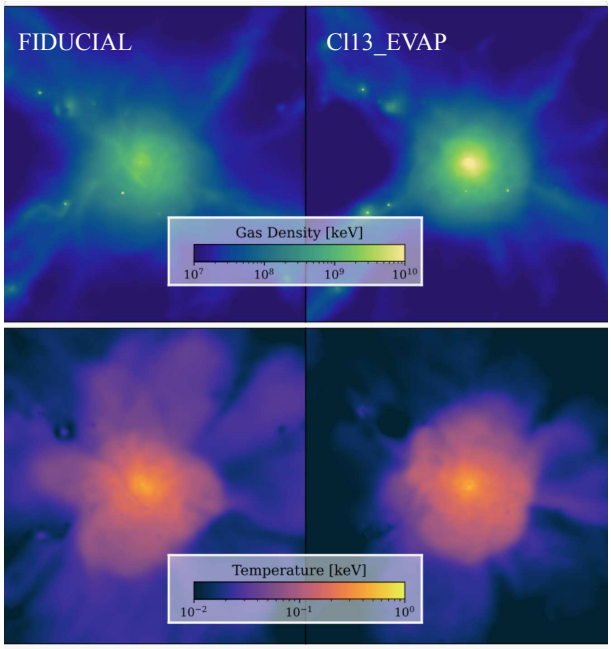

Figure 9.3: *Density (upper panels) and temperature (lower panels) of the gas in simulations with (right) and without (left) the evaporation of cold clouds. Each panel spans 2 Mpc on a side and is centered on the main halo.*

their masses, Eddington ratios, and the cold gas densities in their surroundings. In the bottom three panels, the orange lines represent the swallowing BH, while the red lines correspond to the swallowed BH. Initially, the swallowing BH is in radio mode, accreting hot gas with low efficiency. In contrast, the incoming, less massive BH is embedded in a cold-gas-rich environment, which is responsible for its rapid growth. As the two BHs approach each other, the less massive BH brings along its cold gas reservoir, which funnels gas into the sphere of influence of the more massive BH. Rapid spikes, associated with orbital pericenter passages, appear in the bottom two panels. Once their relative distance drops below ~ 10 kpc, the cold gas around the smaller BH also begins to surround the more massive one. This inflow enhances the BH accretion, triggering the transition from the radio mode back to the quasar mode. In this case, the merger acts as a catalyst for rapid gas accretion and contributes to the subsequent suppression of star formation in the host galaxy.

9.2.3 Feedback

Kernel weighting scheme

The recent work by González Villalba et al. (2025) analyses AGN feedback in the Magneticum simulations (Dolag et al., 2025). They show that simulations fail to reproduce the observed scaling between jet power and the BH sphere of influence. Specifically, observational data from Rafferty et al. (2006a) and Eckert et al. (2021) show that the radius of the BH sphere of injection increases with jet power, while simulations show the opposite trend. In the simulation setup adopted by González Villalba et al. (2025), the feedback energy — modeled as described in Sect. 5.4.4 — is distributed among the BH's neighbour gas particles within the BH smoothing length according to the standard SPH kernel weighting scheme, a Wedland C6 kernel. Within this kernel-weighting

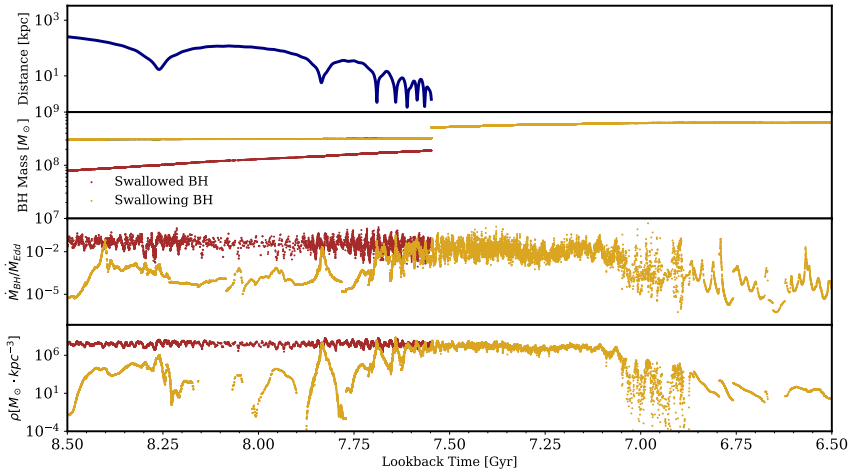

Figure 9.4: *Relative distance and relevant quantities during the merger event in the* `FIDUCIAL`*simulation shown in the inset of Fig. 9.2a. From top to bottom: the relative distance between the merging BHs (blue line), their masses, Eddington ratios, and the local cold gas densities. In the bottom three panels, orange and red lines indicate the swallowing and swallowed BHs, respectively.*

scheme, particles closer to the BH receive a larger fraction of feedback energy. This confines energy deposition to a small physical volume, amplifying the discrepancy with observations. To broaden the feedback distribution, we perform a preliminary test using a top-hat kernel that deposits feedback energy uniformly within the BH smoothing length.

Although a statistical comparison between the two kernel implementations is inconclusive, as no significant trends on the $M_{\rm BH}$–M_* relation or in the BHMF is observed, some differences emerge when analysing the single evolutionary path of individual BHs. Differences are expected to arise primarily during the radio mode. To minimize the impact of differing dynamical histories, we focus on BHs that remain in radio mode until $z = 0$. For each selected BH, the evolutionary path was traced in one simulation, and the corresponding counterpart was identified in the other run, based on the different kernel for distributing feedback energy, thus enabling a direct, mirrored comparison of their histories. Figures 9.5a and 9.5b illustrate two representative examples. In each case, results from the simulation employing an SPH-weighted AGN feedback energy distribution in radio mode (`FIDUCIAL`) are shown in teal, while those adopting a top-hat kernel-weighted distribution (`C113_KTOPHAT`) are shown in red. From top to bottom, the panels display the BH mass growth, Eddington ratio, surrounding gas density, and the respective contributions of cold and hot gas (darker and lighter curves). In both models, the transition to the radio mode rapidly depletes the cold gas component. However, the top-hat kernel weighting achieves a more efficient depletion, effectively preventing cold gas from refilling the BH sphere of influence. This leads to a lower BH Eddington ratio relative to the SPH-kernel case. Nevertheless, as discussed in Sect. 9.2.1, BH growth in the radio mode remains modest and predominantly merger-driven; hence, despite the lower Eddington ratios and gas densities, the final BH masses remain largely unaffected.

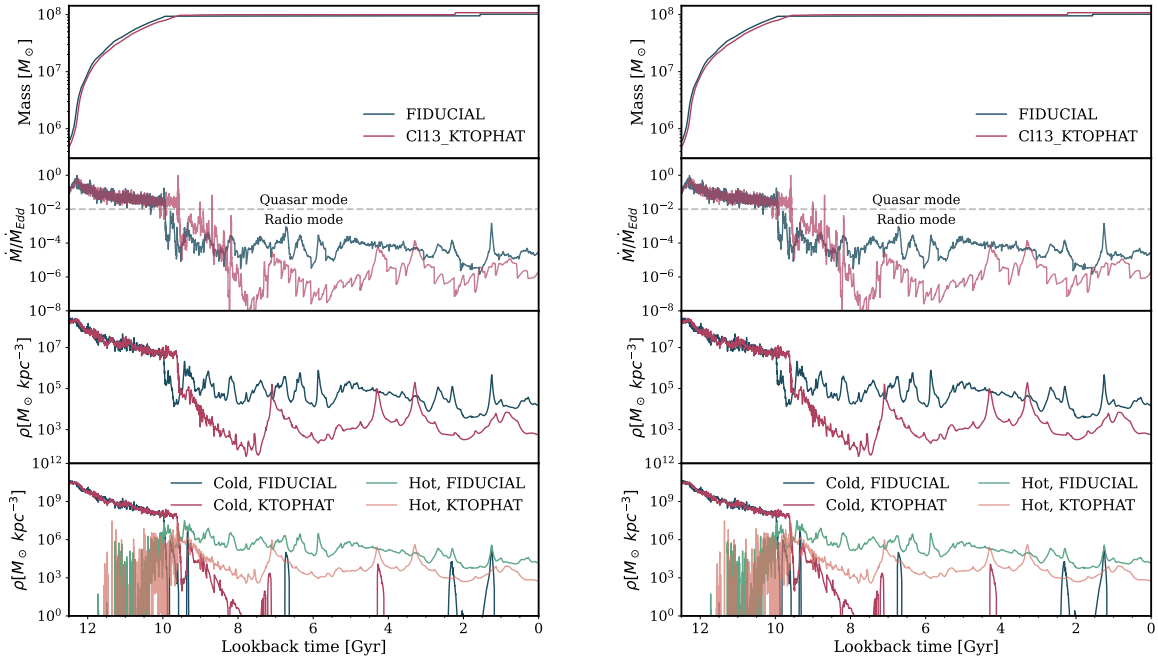

(a) (b)

Figure 9.5: *Evolution of the properties of two BHs evolving simulations adopting an SPH-kernel weighting of AGN feedback energy in radio mode (teal) or instead a top-hat weighting (red). From top to bottom panels show BH mass growth, Eddington ratio, surrounding gas density, and the cold/hot gas (marked with a darker/lighter curve) contributions to gas density as functions of time.*

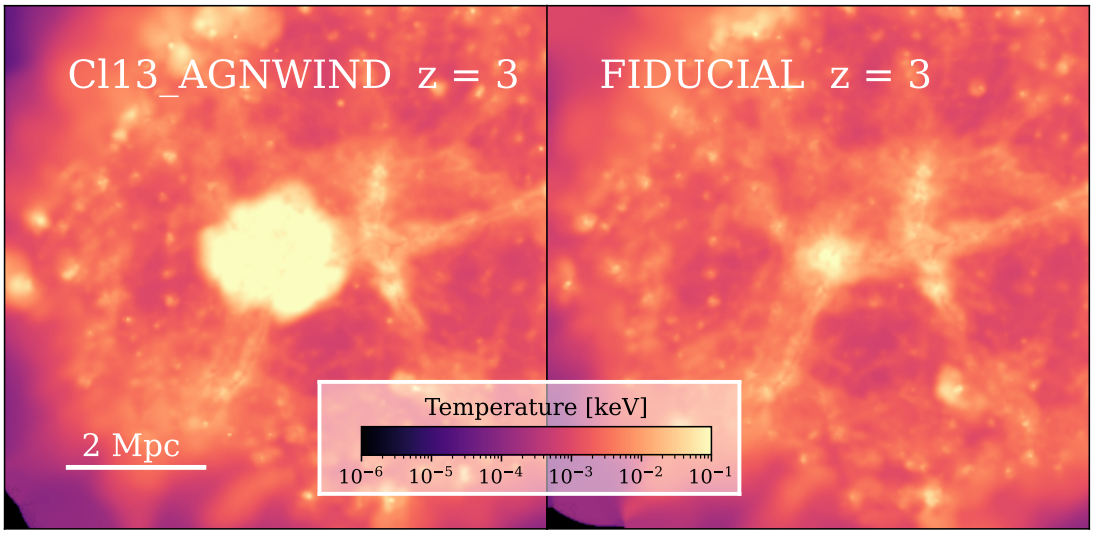

Figure 9.6: *Temperature maps from two simulations highlighting the impact of including wind particles in the AGN feedback loop. Left panel shows* `Cl13_AGNWIND` *simulation at* $z = 3$ *with wind particles participating in feedback and accretion. Right panel shows the corresponding map for the* `FIDUCIAL`*simulation at the same redshift.*

AGN feedback and wind particles

In OpenGADGET3, stellar wind particles — representing SN-driven feedback — are treated as hydrodynamically decoupled from the surrounding gas. This introduces uncertainty regarding their interaction with AGN feedback during the decoupled phase. When excluded from the BH neighbor list, these particles neither contribute to the local gas density nor receive AGN feedback energy; when included, they affect both. Because they are thermodynamically decoupled, feedback energy assigned to them is stored and released only upon recoupling, potentially at large distances from the BH, which may significantly alter the feedback outcome.

Figure 9.6 illustrates this effect by showing temperature maps from the `Cl13_AGNWIND` simulation (left) and the `FIDUCIAL` one at $z = 3$. In the left panel, wind particles are included in the accretion and feedback loop, while in the right panels they are excluded. When included, wind particles accumulate feedback energy over time and release it suddenly upon recoupling, inflating large (~ 2 Mpc across) hot bubbles at significant distances from the BH. The formation of these hot bubbles arises purely from the numerical choices adopted for the treatment of wind particles and their interplay with AGN feedback. To prevent their emergence, the simulations presented in Chapter 10 exclude winds from contributing to the BH feedback loop.

9.3 Summary and conclusions

Within this, the impact of different numerical implementations of BH feeding and feedback has been assessed. In particular, the same group-sized halo has been re-simulated with identical settings but varying, one at a time, the prescriptions for: stochastic gas swallowing, evaporation of cold clouds, kernel choices for energy redistribution in AGN radio-mode feedback, and the coupling between BH and SN-driven wind particles. From this study, the following conclusions can be drawn:

- BH lifecycle: Early BH growth is dominated by cold gas accretion, which sustains a prolonged quasar-mode phase. Once hot gas dominates within the BH smoothing length, the BH transitions to radio mode, where accretion is milder, while a higher feedback efficiency suppresses further growth. Episodes of cold gas inflow, e.g. from mergers, can trigger transitions back to quasar mode, making cold gas removal challenging. See Sect. 9.2.1 and 9.2.2.

- Stochastic swallowing: Excluding explicit gas-particle swallowing allows gas to accumulate around the BH, increasing the local density and potentially triggering runaway accretion. At low redshift, when cold gas is funneled into the smoothing length of a BH in radio mode, stochastic swallowing helps prevent prolonged episodes of BH overgrowth.

- Evaporation of cold clouds: Introducing cold-cloud evaporation suppresses BH accretion but unexpectedly enhances star formation in the BGG, increases central gas densities, and lowers temperatures in the outskirts.

- Kernel weighting scheme for radio mode: The choice of kernel in radio mode has only a minor impact. A top-hat kernel-weighted energy redistribution can more effectively deplete

local gas reservoirs, but since BH growth in radio mode is modest, the effect on global scaling relations remains negligible.

- Wind and AGN feedback coupling: Allowing wind particles to receive AGN feedback while hydrodynamically decoupled produces spurious "hot bubbles" when the stored energy is abruptly released at recoupling.

These results highlight the significant impact that numerical details of the AGN feedback implementation have on gas thermodynamics and galaxy evolution, and further emphasize the need for consistent and controlled coupling between star formation and AGN feedback models within cosmological simulations. Based on our tests, we identify a fiducial model for a more extended set of zoom-in cluster simulations (Borgani et al., in prep.), which includes stochastic gas swallowing, neglects cold cloud evaporation, adopts an SPH-weighted scheme to distribute feedback energy, and excludes wind particles from receiving AGN feedback. Nonetheless, important limitations remain, such as excessive BH growth at low redshift in the presence of cold clumps.

These more comprehensive tests, together with a deeper analysis of the resulting BH demography, will be presented in the following chapter.

Chapter 10

The DIANOGA galaxy clusters: MBH demography and evolution

The content of this Chapter is based on "The DIANOGA galaxy clusters: Massive Black Hole demography and evolution" (Damiano et al., in preparation) and "DIANOGA simulations of galaxy clusters: properties of the baryonic components", Borgani S., Damiano A., et al. (in preparation).

As a final component of this Thesis, the present Chapter brings together the results on the improved dynamical evolution of MBHs in simulations, introduced in Chapters 7 and 8, and extensive tests of the BH feeding and feedback models discussed in Chapter 9. In doing so, it addresses the challenges within the complexity offered by the extreme environment of galaxy clusters. Specifically, this Chapter analyses the present-day ($z = 0$) BH population in the DIANOGA suite of zoom-in simulations of galaxy clusters (Bonafede et al., 2011; Esposito et al., 2025; Bassini et al., 2020). A cosmological box evolved with the same numerical framework is used as a reference for a 'field' environment. Building on the tests performed in Chapter 9, subsets of the full DIANOGA sample were re-simulated adopting different prescriptions for BH accretion, feedback efficiency, and cold-gas regulation, allowing a controlled assessment of how these parameters affect BH growth in dense, highly dynamical environments. This analysis serves two main purposes. First, it quantifies how different sub-resolution models shape the thermodynamical state of galaxy clusters and, in particular, the demographics of the BH population they host. Second, by employing the improved DF correction scheme introduced by Damiano et al. (2024), it enables a detailed study of BH spatial distribution within substructures and the incidence and properties of systems hosting multiple BHs.

This Chapter is organised as follows. Section 10.1 describes the full set of simulations analysed. The statistical properties of the BH population at $z = 0$ are then examined through the $M_{\rm BH}$–M_* relation (Sect. 10.2), the bolometric luminosity function (BHLF, Sect. 10.3.1), and the BH mass function (BHMF, Sect. 10.3.2). The population of systems hosting multiple BHs and the role of DF are discussed in Sect. 10.4. Finally, Sect. 10.5 summarises the main findings and outlines future perspectives.

10.1 Set of simulations

In the following, we analyse different sets of galaxy clusters drawn from the DIANOGA simulation suite. A detailed description of the full dataset will be presented in a forthcoming paper (Borgani et al., in prep.). Here we briefly summarise the characteristics relevant for the results presented in this Chapter. The DIANOGA suite consists of 29 Lagrangian regions extracted from a parent cosmological box of side length 1 cGpc h^{-1}, originally evolved at low resolution with 1024^3 DM particles. The adopted cosmology follows a standard ΛCDM model, with parameters $\Omega_b = 0.0375$, $\Omega_\Lambda = 0.76$, Hubble parameter $h = 0.72$, primordial spectral index $n_s = 0.96$, and power spectrum normalisation $\sigma_8 = 0.8$ (Bonafede et al., 2011). High-resolution zoom-in initial conditions were generated using the ZIC technique (Tormen et al., 1997), by adding small-scale density modes while ensuring the absence of low-resolution particle contamination within at least 5 $R_{\rm vir}$ of each cluster at $z = 0$. In this way, each zoomed-in Lagrangian region is sufficiently extended to resolve not only the main cluster halo but also nearby group-sized systems. Overall, the set of 29 simulations includes 336 halos with $M_{200} \geq 1.5 \times 10^{13} M_\odot$, out of which 74 and 24 have masses larger than $10^{14} M_\odot$ and $10^{15} M_\odot$, respectively. The corresponding particle masses and gravitational softening lengths in the high-resolution regions are listed in Table A.1. In addition, to have a reference for the field, a cosmological box simulation with side length 49.26 cMpc h^{-1} was also simulated employing the same mass and spatial resolution with 576^3 particles and an initially equal number of gas particles. Within this Chapter, results for different simulations of the 28 regions are presented. All the clusters have been re-simulated with modifications to the SF and BH modules, for a total of 78 simulations. All of them share the same resolution, the baseline model for star formation and evolution presented in Sect. 5.3 with parameters listed in Table A.1. The BH accretion, merger, and feedback models follow the prescriptions presented in Sect. 5.4, with variations in selected parameter values. To describe the different simulation subsets and the corresponding modifications to the sub-resolution implementations, a reference model, M1, is first defined, and the remaining six models are then presented as variations on this baseline configuration.

Model M1

In this reference simulation, the sub-resolution prescriptions for SF, stellar evolution and the BH sector follow the prescriptions presented in Sect. 5.3, 5.4 (Table A.1) but the feedback factor entering the calculation of the of the AGN feedback is boosted to a value of $\eta_f = 0.1/0.4$ in the quasar/radio mode. This choice corresponds to a feedback efficiency twice as large as that adopted in the simulations analysed in previous Chapters. In line with the analysis presented in Chapter 9, and in order to limit the impact of cold gas accretion, stochastic gas swallowing by BHs is enabled following the prescription described in Sect. 5.4.2. The evaporation of cold gas clouds introduced in Sect. 9.1 is not included. Wind particles do not contribute to either the calculation of BH density or the BH feedback, and the SPH kernel is adopted to redistribute BH feedback energy in radio mode.

Model	η_f	(α_h, α_c)	Eddington	Evaporation	Regions
M1	0.10	(10,100)	yes	no	29
M2	**0.05**	(10,100)	yes	no	29
M3	**0.05**	**(3,30)**	yes	no	2
M4	**0.05**	(10,100)	yes	**yes**	4
M5	0.10	(10,100)	yes	**yes**	3
M6	**0.20**	(10,100)	yes	**yes**	3
M7	**0.05**	(10,100)	**no**	no	8

Table 10.1: *Description of the different models that have been simulated. Column 1: ID of the model; Column 2: BH feedback efficiency η_f in quasar mode (see Eq. 5.78; Column 3: values of the cold and hot boost factors for the Bondi accretion (see Eq. 5.72); Column 4: enforcement of the Eddington limit (see Eq. 5.71) the BH accretion rate; Column 5: implementation of the evaporation of cold clouds; Column 6: number of regions for which each model has been simulated.*

Model variants

Starting from the M1 reference configuration, additional simulation sets were produced by modifying specific aspects of the physical model:

- **M2**: Identical to the reference model, but with reduced feedback coupling efficiencies, $\eta_f =$ 0.05 and 0.2 in the quasar and radio modes, respectively.
- **M3**: Same as the reference model, but with different boost factors for cold and hot gas accretion, maintaining a fixed ratio between them: $\alpha_{\rm cold} = 30$ and $\alpha_{\rm hot} = 3$.
- **M4**: Same as the reference model, but including the evaporation prescription described in Sect. 9.1.
- **M5**: Combination of the M2 feedback efficiencies with the evaporation model.
- **M6**: Same as the reference model, but with stronger AGN feedback, $\eta_f = 0.2$ and 0.8 in the quasar and radio modes, respectively, and with the evaporation model enabled.
- **M7**: Same as the reference model, but allowing BHs to accrete at rates up to four times the Eddington limit. The evaporation model is disabled.

It is worth noting that all models adopt the DF implementation from Damiano et al. (2024). This is particularly important as it allows testing the robustness of the DF correction in a variety of complex environments. Table 10.1 summarises the key characteristics of each model, focusing on the parameters that vary among them, while Table 10.2 lists the label assigned to each region, the values of M_{200} and R_{200} for the most massive uncontaminated halo with total mass $M_{\rm tot} > 1.5 \times 10^{13}\ M_\odot$, the number N_{13} of such haloes, and the models used to simulate each cluster. Note that all 29 (the DIANOGA clusters and the cosmological box) regions have been simulated with both the M1 and M2 models. Given the larger statistical sample available for these two models, a more detailed analysis will be presented for them. Figure 10.1 shows the projected surface density within 15 Mpc/h to the main halo center within each region, displaying D1 to D29 from top right to bottom left.

Region	M_{200} $[10^{14} M_\odot]$	R_{200} [Mpc]	N_{13}	Models
D1	18.61	2.49	6	M1,M2,M7
D2	4.87	1.59	6	M1,M2,M3,M4,M5,M6,M7
D3	7.36	1.83	4	M1,M2,M7
D4	5.70	1.68	2	M1,M2,M4,M5,M6,M7
D5	1.79	1.14	3	M1,M2,M7
D6	15.19	2.33	12	M1,M2
D7	16.58	2.40	15	M1,M2
D8	18.04	2.46	14	M1,M2,M4
D9	1.44	1.06	3	M1,M2,M3,M4,M5,M6,M7
D10	16.51	2.39	10	M1,M2,M7
D11	13.17	2.22	14	M1,M2
D13	17.89	2.46	15	M1,M2
D14	20.07	2.55	7	M1,M2,M4
D15	19.65	2.54	11	M1,M2
D16	38.79	3.18	21	M1,M2
D17	17.90	2.46	4	M1,M2
D18	12.03	2.15	12	M1,M2,M7
D19	16.19	2.38	12	M1,M2
D20	19.83	2.54	12	M1,M2
D21	17.21	2.43	5	M1,M2
D22	21.92	2.63	14	M1,M2
D23	15.39	2.34	8	M1,M2
D24	14.93	2.31	4	M1,M2
D25	11.39	2.11	5	M1,M2
D26	15.97	2.37	9	M1,M2
D27	18.11	2.47	4	M1,M2
D28	22.39	2.65	20	M1,M2
D29	17.17	2.42	16	M1,M2
Box	1.76	1.13	25	M1,M2

Table 10.2: *Summary of the simulated regions. Column 1: Region label. Column 2: Virial mass M_{200} of the most massive uncontaminated halo with total mass $M_{\rm tot} > 1.5 \times 10^{13}\ M_\odot$. Column 3: Virial radius R_{200} corresponding to that halo. Column 4: Number of uncontaminated haloes with mass $M_{\rm tot} > 1.5 \times 10^{13}\ M_\odot$, denoted as N_{13}. Column 5: Simulation models applied to each cluster.*

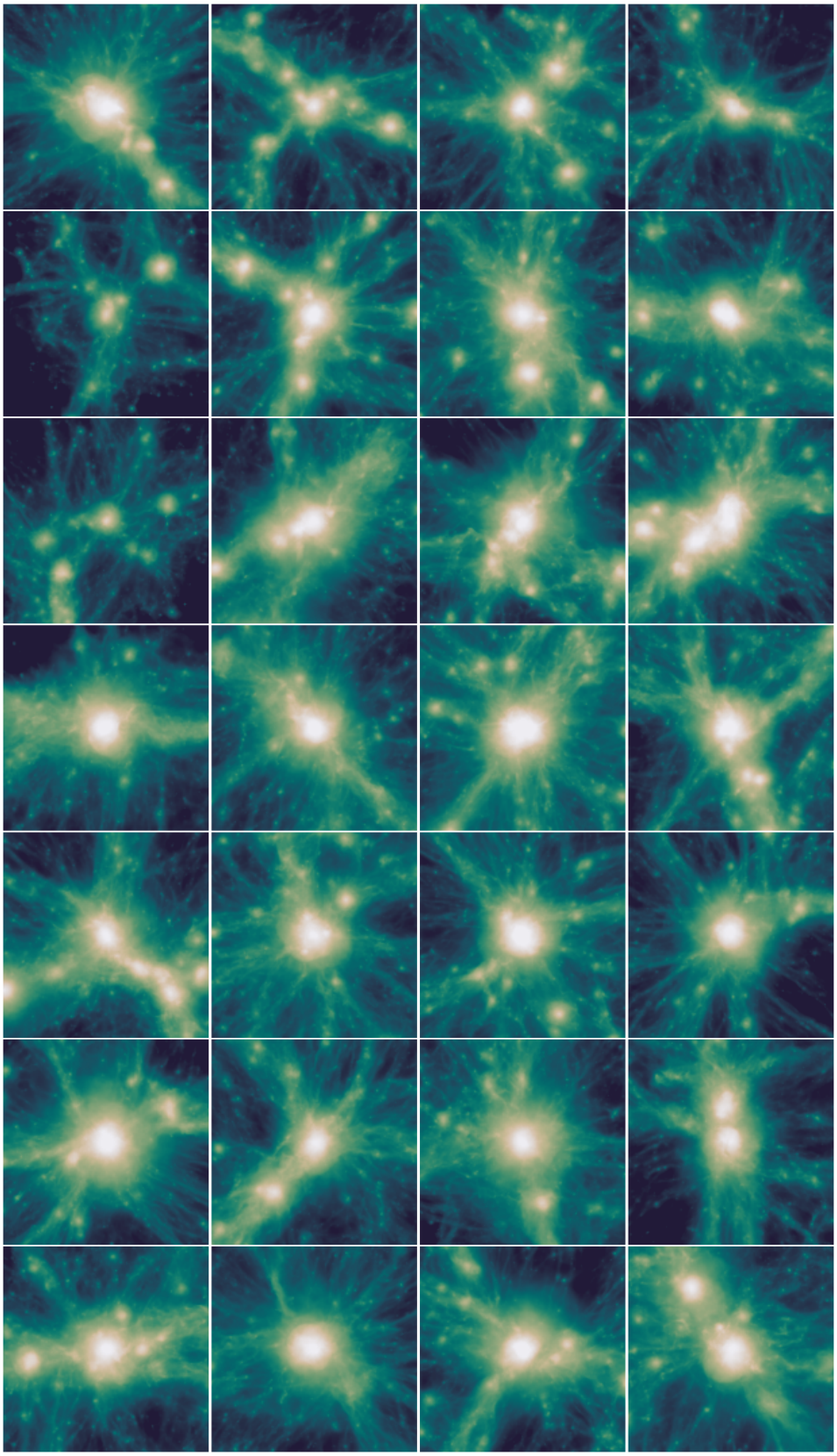

Figure 10.1: *Projected surface density for the 28* DIANOGA *clusters within 15* Mpc/h *of the target halo center in each region. Clusters D1–D29 are shown from top left to bottom right, excluding D12.*

10.2 The $M_{\rm BH} - M_*$ relation at $z = 0$

As a starting point, the BH mass scaling relation with the host galaxy, $M_{\rm BH} - M_*$ (see Sect. 2.2) is presented here illustrating the results and differences arising from the M1 and M2 models (10.2.1) and then outlining the results when comparing different models (Sect.10.2.3).

10.2.1 Results for M1 and M2 models

The BHs included in the analysis were selected based on their spatial association with their host structures. Starting from uncontaminated halos and subhalos with $M_{200} > 1.4 \times 10^{10}\ M_\odot$ (see Table 10.2), the closest BH is associated with each halo [1], and the stellar mass is computed by summing all stars within a physical aperture of 50 pkpc from the halo center. Resolved subhalos of the targeted halos are defined as those containing at least 10^3 DM particles (i.e., with total mass $M_{\rm tot} > 4.7 \times 10^{10}\ M_\odot$). For these subhalos, the BH association is similarly performed by selecting the closest BH within a physical threshold of 10 kpc h^{-1} from the subhalo center. The stellar mass of subhalos is taken as the total stellar mass assigned by SubFind (Dolag et al., 2009).

Figure 10.2 shows the $M_{\rm BH} - M_*$ relation for the **M1** (panel 10.2a) and **M2** (panel 10.2b) models. Diamonds refer to the central galaxies of the main halos, that we identify with the BCGs, color coded according to the distance between the BCG center and the associated BH. Observational data from Gaspari et al. (2019), including error bars, are shown as red dots. To highlight spatial displacements, the top and side panels show 2D histograms of the BH offset from the halo center as a function of (sub-)halo stellar mass (top) and BH mass (side). The grey dashed line in the side panels marks the gravitational softening length for the BH particles. The top right panel displays the PDF of the BH offsets relative to their hosts, comparing BCGs (yellow), their subhalos (teal), and the subhalos identified within the cosmological box (orange). Regarding the $M_{\rm BH} - M_*$ relation, the M1 model reproduces the slope and normalization of the observational data for both subhalos and the box. The M2 model exhibits a higher normalization, as expected from its reduced feedback efficiency. The weaker feedback allows dense gas to accumulate around BHs, increasing accretion rates and leading to larger BH masses compared to M1. Most BCGs populate the high stellar mass end of the relation, following the slope defined by the subhalos. However, a subset of BCGs host overmassive BHs, reaching masses up to $M_{\rm BH} = 3.9 \times 10^{12}\ M_\odot$ in M1 and $10^{12}\ M_\odot$ in M2. These overmassive BHs originate from runaway cold gas accretion, as discussed in Sect. 9.2.1 and Sect. 9.2.2, with the complex environments in these simulations amplifying this effect. Their physical implications are explored in detail in Sect. 10.2.2. Concerning the BH offsets, the overall population of BCGs and subhalos, both in the Dianoga regions and in the cosmological box, is well-centered, with typical offsets around 0.1 kpc, below the BH softening length. Regardless of the model, the 2D histograms indicate that the most massive subhalos tend to host the most centrally located BHs. Accordingly, the top-right histogram shows that BCGs tend to host more centrally located BHs compared to less massive structures. This behavior is expected in the DF model, since more massive structures host more massive BHs, which experience

[1] This differs from the association used in Sect. 7.2.4, where the *most massive* BH within the aperture was selected. We verified that the two approaches yield very similar results, since the DF modelling adopted in these simulations ensures that the most massive BH efficiently sinks to the center of the most massive structures.

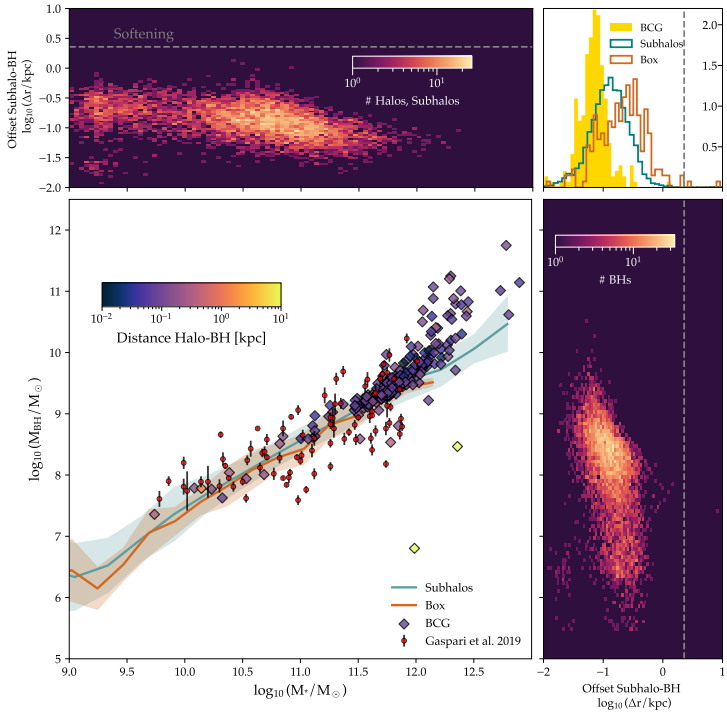

(a) *M1*

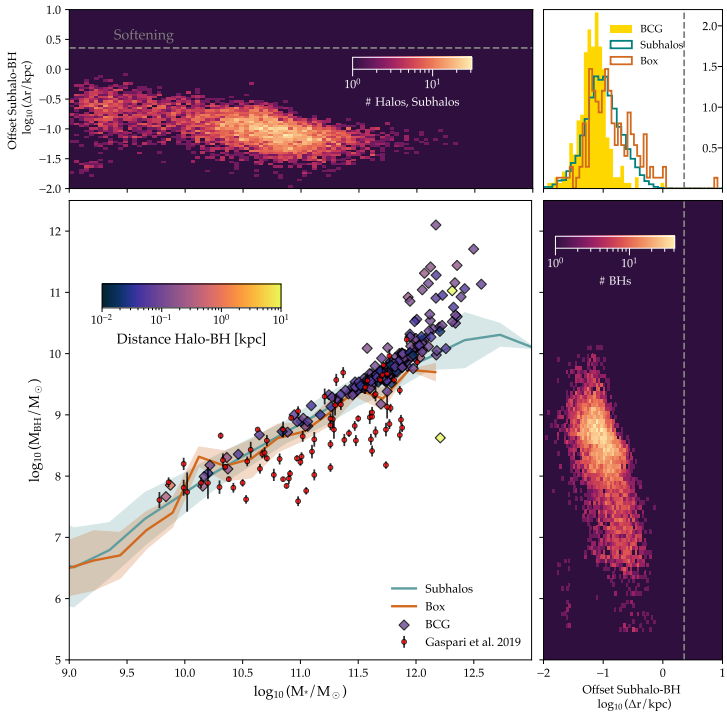

(b) *M2*

Figure 10.2: *$M_{\rm BH} - M_*$ relation for the **M1** (panel 10.2a) and **M2** (panel 10.2b) models. The central panels show data for subhalos identified in the DIANOGA regions (teal) and the cosmological box (orange). Diamonds indicate BCGs with total halo mass $M > 1.5 \times 10^{13}$ $M_\odot$, whose stellar masses are calculated within a 50 pkpc aperture. Red dots represent observational data from Gaspari et al. (2019) with error bars. The top and side panels display 2D histograms of BH offsets from the host halo center as a function of halo mass (top) and BH mass (side), with the grey dashed line marking the BH gravitational softening length. The top right panel reports the PDF of BH offsets for BCGs (yellow), their subhalos (teal), and the subhalos identified in the cosmological box (orange).*

stronger DF.

10.2.2 The origin of the overmassive BHs

In Sect. 9.2.2 we showed that the swallowing of cold gas had a significant impact on the accretion model implemented in OpenGADGET3 (Sect. 5.4.2). In the simulations of the `C113` galaxy group presented in Chapter 9, infalling cold gas during a merger event onto a MBH initially in radio mode could trigger prolonged episodes of cold accretion. This process may eventually drive the BH into a quasar stage, where the lower feedback efficiency hinders the BH's ability to expel cold gas from its surroundings. In such cases, the suppression of cold gas via gas swallowing helps prevent strong, sustained accretion episodes. Based on these results, the gas swallowing implementation has been extensively applied in all the simulations presented in this Chapter.

Nevertheless, Fig. 10.2 shows the emergence of overmassive BHs. Even with the higher feedback efficiency adopted in M1, the enhanced feedback only slightly reduces the masses of these *pathological* BHs and does not fully suppress their growth. To investigate whether such overmassive BHs are due to runaway cold gas accretion triggered by dynamical disturbances of the BCG, the evolutionary history of the BHs undergoing overmassive growth in the M1 simulation is examined here. This BH is the progenitor of the most massive and most centrally located BH in the D20 cluster at $z = 0$. Its evolutionary path is illustrated in Figure 10.3.

The left panel of Figure 10.3 presents, from top to bottom, the SFR [2], the mass of the BH undergoing overgrowth, its Eddington ratio $\dot{M}_{\rm BH}/\dot{M}_{\rm Edd}$, and surrounding gas density contributed by cold (dark orange) and hot (light orange) components. The BH plotted in red is the main progenitor of the BH that will eventually reside at the cluster center at $z = 0$. Its evolutionary track includes two mergers, and the properties of the resulting BHs are shown by the teal and blue curves and dots. For those descendants, the bottom panel reports the total surrounding density.

After an initial star-forming phase with SFR $\sim 10^3, \mathrm{M}_\odot, \mathrm{yr}^{-1}$ sustained until $z = 3$, the BCG gradually enters a quiescent phase, reaching $\sim 10, \mathrm{M}_\odot, \mathrm{yr}^{-1}$ by $z = 1.5$. At $z = 1$, the system undergoes a rejuvenation episode, with sustained star formation lasting roughly 4 Gyr, followed by rapid quenching at lookback times of 2 Gyr. This increase in SFR coincides with rapid growth episodes of the BH, seen as sharp jumps in BH mass accretion history in the second panel. As discussed in Sect. 9.2.2, the third panel reveals that these bursts drive the Eddington ratio above the quasar-mode threshold. Inspection of the bottom panel shows that peaks in accretion coincide with encounters of the BH with cold gas clumps in its surroundings. The periodic appearance of these clumps suggests the BH is passing repeatedly through cold-gas dominated regions. Notably, the red BH is not the central BH during the rejuvenation phase, but instead orbits within the cluster potential. To explore this further, the right panel of Figure 10.3 zooms on the evolution between $z = 1.5$ and $z = 0$, showing, from top to bottom: the BCG SFR, the masses accretion histories of the overgrowing BH (red) and of the BHs residing at the center of the BCG (teal), the distance between them, and their surrounding cold gas density. Notably, from $z = 1$ onward, the presence of cold gas clumps surrounding the BH coincides with pericenter passages of the BH close to the central BH. Therefore, the overgrowth of the BH can be explained by these repeated close approaches to the cold-gas rich core of the main halo. After the overgrowing BH reaches the

[2] The SFR is computed from the stellar ages of star particles within 50 kpc of the BCG at $z = 0$.

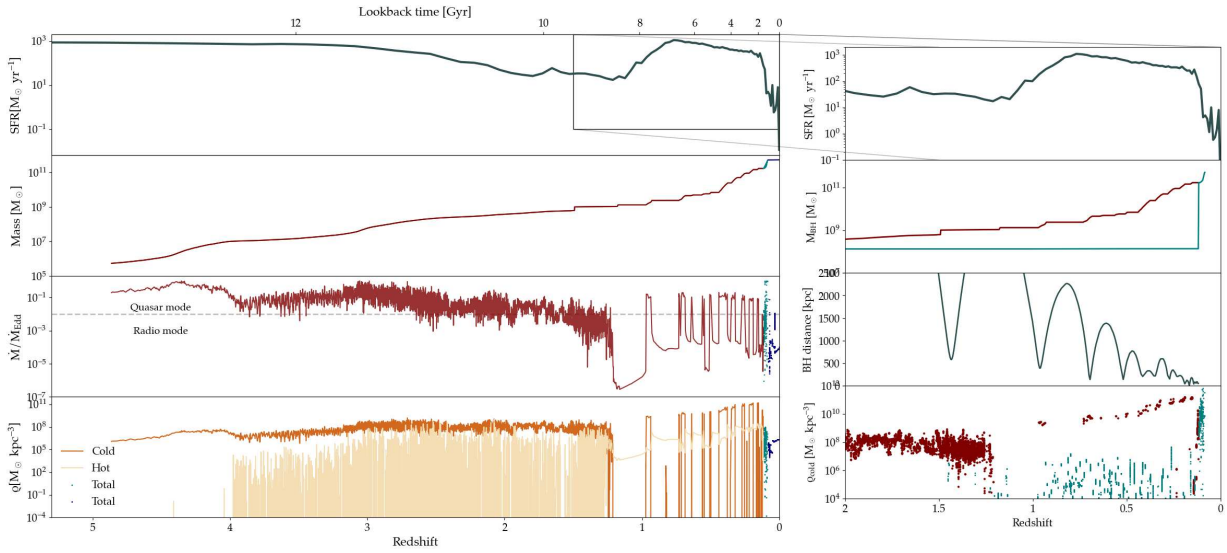

Figure 10.3: *BCG SFR and evolutionary history of the most massive BH undergoing overmassive growth in the M1 simulation of D20. Left panel: from top to bottom we show the SFR, the overgrowing BH mass, the Eddington ratio ($\dot{M}_{\rm BH}/\dot{M}_{\rm Edd}$), and the surrounding gas density separated into cold (dark orange) and hot (light orange) components. The BH tracked in red is the progenitor of the most massive and most centrally located BH in the D20 cluster at $z = 0$. The teal and blue curves represent the properties of its descendant BHs after mergers, and the bottom plot reports their total density. Right panel: the BCG SFR from $z = 1.5$ to $z = 0$, BH masses (red and teal), their relative distance, and their surrounding cold gas density, highlighting the connection between BH passages through cold gas clumps, BH growth, and cluster star formation activity.*

halo center and merges with the central BH, the SFR gets suddenly suppressed.

To complete this picture, Figure 10.4 displays maps of stellar density (top panels) and gas temperature (middle panels) within a 2 Mpc region centered on the most massive halo undergoing SF rejuvenation at redshifts $z = 1.5$, $z = 1$, $z = 0.8$, and $z = 0.5$. The red cross marks the location of the overgrowing BH tracked in Figure 10.3, while the black star in the center marks the position of the central BH in the cluster. The bottom panels show phase diagrams (temperature versus density) of gas particles in the region displayed in the upper panels at the same redshifts. TheThe maps show that during pericenter passages ($z = 1.5$ and $z = 1$), the cluster core is strongly disturbed, with shock fronts and compressed gas developing along the merger axis. By $z = 0.8$, continued compression and feedback activity generate hot gas shells around the center. The phase diagrams reveal that shock-compressed gas reaches densities $\rho \sim 10^2, \mathrm{M}_\odot, \mathrm{kpc}^{-3}$ and temperatures $T \sim 10^8, \mathrm{K}$. At these temperatures the cooling time is short, so compression raises the gas above the star-formation threshold, after which cooling drives it onto the star-forming branch, effectively producing a "rain" of cold gas that fuels sustained star formation.

The maps show that during pericenter passages ($z = 1.5$ and $z = 1$), the cluster core is strongly disturbed, with shock fronts and compressed gas developing along the merger axis. By $z = 0.8$, continued compression and feedback activity generate hot gas shells around the center. The phase diagrams reveal that shock-compressed gas reaches densities $\rho \sim 10^2\,\mathrm{M}_\odot, \mathrm{kpc}^{-3}$ and temperatures $T \sim 10^8\,\mathrm{K}$. At these temperatures the cooling time is short, so compression raises the gas above the SF threshold, after which cooling drives it onto the SF branch, effectively producing a "rain"

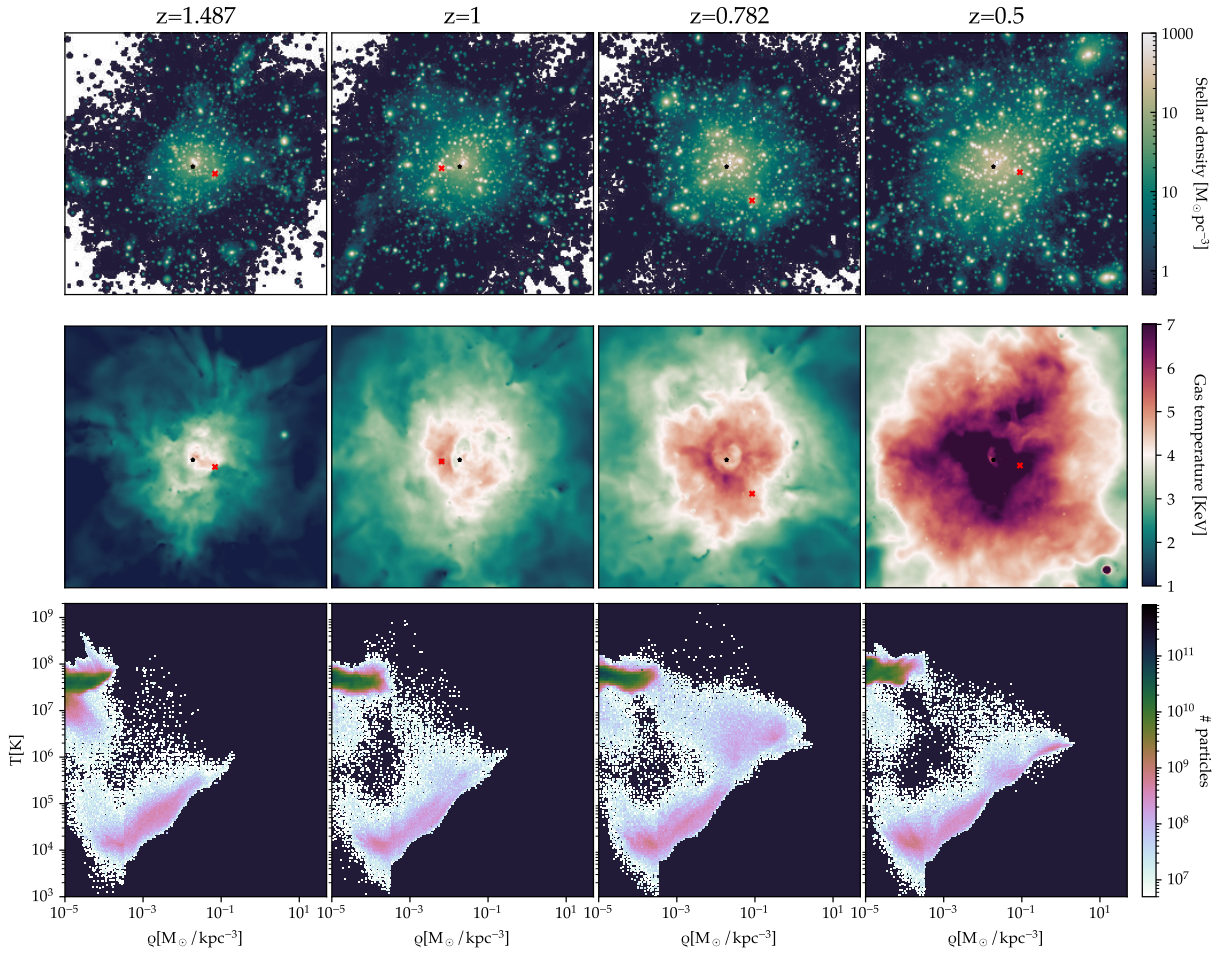

Figure 10.4: *Evolution of the cluster environment around the most massive halo in the M1 simulation during star formation rejuvenation. Top panels display the stellar density maps and middle panels show the gas temperature maps within a 2 Mpc region at redshifts* $z = 1.487$, $z = 1$, $z = 0.782$, *and* $z = 0.5$. *The red crosses mark the position of the overgrowing BH tracked in Figure 10.3. Bottom panels show the corresponding phase diagrams of gas particles displayed in the central panels.*

of cold gas that fuels sustained SF. This is clearly visible in the phase diagram at $z = 0.782$.

Although illustrated here with a single prototypical case, this analysis demonstrates the strong impact of BCG dynamical evolution on BH growth and core ICM thermodynamics. Mergers and the ensuing dynamical disturbances within the cluster environment can simultaneously induce episodes of runaway BH accretion and prolonged periods of renewed SF in the central galaxy. In agreement with the results of Chapter 9, we demonstrated that, according to our BH accretion model, cold gas can induce runaway accretion leading to BH overgrowth, even when the swallowing prescription is adopted.

These findings motivate a systematic exploration of alternative models (M3–M7), designed either to mitigate excessive SF—via cold-cloud evaporation—or to limit runaway BH growth through increased feedback efficiency. These variants of the reference M1 model aim to reduce the availability of dense cold gas that fuels both star formation and BH accretion.

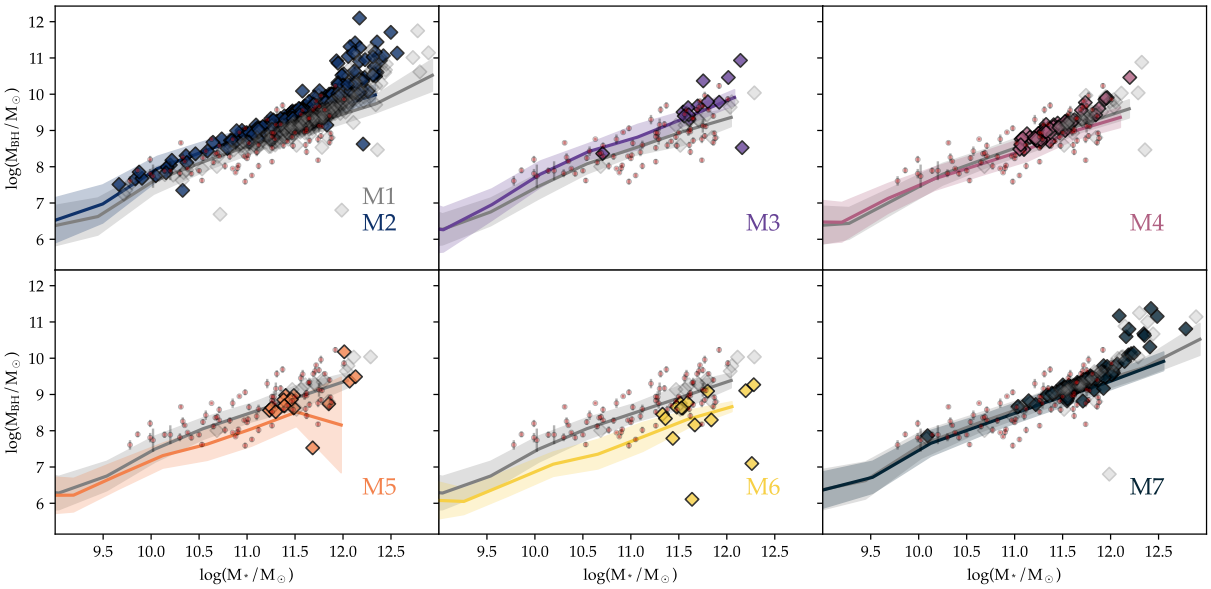

Figure 10.5: *Comparison of the $M_{\rm BH}$–M_* relation for different models, listed in Table 10.1. Each panel compares model M1 (grey) with models M2–M7, as indicated. Solid lines and shaded regions show the mean relation and r.m.s. scatter for subhalos, while diamonds mark BCGs. Only regions simulated with both M1 and the comparison model are included in each panel. Red points show observational data from Gaspari et al. (2019).*

10.2.3 The $M_{\rm BH} - M_*$ relation for different models

Figure 10.5 shows the $M_{\rm BH}$–M_* relation for all models explored in this work. Each panel compares model M1 (shown in grey) with models M2–M7, from top-left to bottom-right, as indicated in each panel. As in the central panel of As in Fig. 10.2, solid lines and shaded regions show the median relation and its r.m.s. scatter for subhalos, while diamonds mark BCGs. Grey diamonds refer to the BCGs in the M1 model. For each panel, the comparison with M1 is restricted to those regions that have been simulated both with M1 and with the model under consideration. The association between BHs and host structures, as well as the computation of stellar masses, follows the procedure described in Sect. 10.2.1. Observational data from Gaspari et al. (2019) are shown as red points.

As previously noted, the higher feedback efficiency in the M1 model lowers the normalization of the relation and overall reduces the masses of overmassive BHs. Model M3 adopts reduced boost factors for cold and hot accretion ($\alpha_{\rm c} = 3$, $\alpha_{\rm h} = 30$), with feedback efficiencies $\eta_f = 0.05$ and 0.2 in quasar and radio mode, respectively. The reduced boost factors act to suppress BH accretion by lowering the effective Bondi rate, while the weaker feedback coupling leads to higher gas densities around the BH and a less efficient suppression of SF. The resulting normalization of the $M_{\rm BH}$–M_* relation is higher than in M1 at $M_* \gtrsim 10^{10} M_\odot$. Overmassive BHs in BCGs still populate the high stellar mass end of the relation in the M3 model, reaching even larger masses than in M1. This indicates that reducing the cold-gas boost alone is insufficient to prevent BH overgrowth, even when the boost factors are lowered by 70%.

In all models adopting the cold clouds evaporation (M4, M5, M6), the slope of the $M_{\rm BH}$–M_* relation is shallower. Even having slightly lower masses compared to M1, the M4 simulations show

evidence for an overmassive BH in the most stellar rich environment, indicating that even the cold clouds evaporation is not able to regulate the cold gas growth in dynamically active environments.

Further increasing the feedback efficiency decreases both the slope and normalization of the relation. When a very strong feedback coupling is adopted in the M6 model ($\eta_f = 0.2$ and 0.8 in quasar and radio mode, respectively), BH masses are significantly underestimated compared to the observational data. Finally, relaxing the Eddington-limit constraint in model M7 yields results broadly consistent with those of M1 and with observational constraints, but it does not suppress BH overgrowth. A more detailed analysis shows that super-Eddington accretion episodes are rare and occur predominantly at high redshift, limiting their impact on the overall BH mass growth down to $z = 0$.

10.3 Mass and luminosity functions of BHs

This Section examines the global properties of the BH population at $z = 0$ through the analysis of their bolometric luminosity and mass functions. By comparing simulations of the DIANOGA clusters and cosmological boxes, possible environment-driven differences are also systematically assessed. The analysis is restricted to BHs associated with resolved gravitational substructures and centrally located within their hosts. Specifically, only the closest BH to the centre of each substructure is considered. Resolved substructures are defined as those containing at least 10^3 dark matter particles. In the cosmological box, the full sample of central BHs in resolved substructures is included, while in the cluster simulations the selection is further restricted to BHs residing within the virial radius of the target region.

10.3.1 The BH luminosity function

As anticipated in Sect. 2.3, the BHLF defined in Eq. (2.6) is a fundamental diagnostic for the population of active BHs. Besides the studies in the X-ray presented in 2.3.1 (see also Miyaji et al. 1999; Barger and Cowie 2005; Aird et al. 2010; Barlow-Hall and Aird 2025; Heather et al. 2025, the latter for more recent results), the BHLF has been obtained by optical, UV and IR observations (Glikman et al. 2011; Giallongo et al. 2015; Ross et al. 2013; Harikane et al. 2022; Yang et al. 2016; Kulkarni et al. 2019; Lacy et al. 2015). In general, these results reveal an increase in the number density of faint quasars at lower redshift compared to bright quasars (Cowie et al. 1996; Cowie et al. 2003; Hasinger et al. 2004; Barger and Cowie 2005), the *cosmic downsizing* (see also Fig. 2.5 and related discussion), and a steepening of the faint-end slope from $z \sim 2$ to $z \sim 0$ (Aird et al. 2015; Kulkarni et al. 2019). In recent years, observations have pushed constraints on the BHLF up to $z \sim 7$ (Bouwens et al. 2025; Matsuoka et al. 2023; Masters et al. 2012; Willott et al. 2010; Shen et al. 2020), although the observations of quasar number densities at $z > 6$ is difficult due to extinction, dust attenuation, and contamination from host galaxies. Following Hopkins et al. (2007), Shen et al. (2020) proposed a new empirical model for the bolometric quasar luminosity function at $z = 0 - 7$, derived from multi-wavelength datasets (optical, UV, IR, X-ray). In the following analysis, we adopt their model as the observational reference for comparison.

In the theoretical context, BHLFs have been produced independently by different cosmological simulations (Covas et al. 2025; Degraf et al. 2010; Ding et al. 2025; Ni et al. 2025; Puerto-Sánchez

et al. 2025; Volonteri et al. 2016b; Sijacki et al. 2015b; Hirschmann et al. 2014). A comparative study by Habouzit et al. (2022) subsequently combined the results from six cosmological simulations (Illustris, TNG100, TNG300, Horizon-AGN, EAGLE and SIMBA) and demonstrated that AGN luminosity functions depend strongly on the adopted accretion and feedback prescription. At $z = 0$, most simulations overpredict BH accretion rates relative to observations. At high redshift, simulations tend to produce too many AGN of all luminosities, although the agreement improves toward lower redshift. However, simulations do not capture rare bright objects in the local Universe, arguably because the simulations cannot resolve the short-timescale AGN variability. Overall, Habouzit et al. (2022) found that current simulations struggle to reproduce a population of AGN simultaneously consistent with observations at both high and low redshift, and across both the faint and bright ends. They also tend to produce a lower AGN fraction in massive galaxies, implying that feedback may quench star formation too efficiently and suppress AGN activity. As in all analyses performed by Habouzit et al. (2022), our simulations are not calibrated on the BHLF; thus the predicted BHLFs are genuine outputs of the models. Within the DIANOGA simulation suite the information about the field objects can be complemented with the cluster properties, allowing us to characterize the relative behaviour and variability of both the BHLF and the BHMF as a function of the environment.

Observational studies of AGN in clusters date back to Cappi et al. (2001); Sun et al. (2002); Molnar et al. (2002), who found an enhanced X-ray surface density of point sources relative to the field. Later works (e.g. Cappelluti et al. 2005; Martini et al. 2006; Eastman et al. 2007) confirmed a significant X-ray source overdensity in clusters, indicative of an overabundance of AGN in overdense environments. However, this issue remained controversial since other works, as Gisler (1978); Hill and Oegerle (1993) reported the opposite trend: a lower AGN fraction in clusters. These apparently conflicting results motivated analyses linking AGN activity to the dynamical state of the cluster, which is especially relevant for this work, as observed in Sect.10.2.2. If AGN activity is (even partly) triggered by galaxy mergers, and mergers are more common in systems with low velocity dispersion, then the AGN fraction should correlate with the dynamical properties of clusters. Indeed, Popesso and Biviano (2006), Martini et al. (2007) and Hwang et al. (2012) found an anticorrelation between cluster velocity dispersion and the AGN fraction. More recently, Koulouridis and Bartalucci (2019) detected a significant excess of low-luminosity X-ray AGN in lower mass clusters, and a decreasing trend in the higher mass ones. This may be due to the increased merging rate in low-mass clusters, whose lower velocity dispersions do not suppress galaxy interactions. This connection between AGN activity and dynamical state also explains why AGN overdensities are frequently observed in protoclusters, where mergers are more frequent. Hudaverdi et al. (2008) reported this in clusters A194 and A1060; Digby-North et al. (2010) found an AGN overdensity at $z > 2$ in protoclusters; and recent works (Traina et al. 2025; Chapman et al. 2025; Shah et al. 2025) found an excess of X-ray and radio-loud sources in the compact core of high-redshift (up to $z \sim 4.3$) clusters.

Within the analysis presented below, the bolometric luminosity of each BH is computed from its accretion rate, $\dot{M}_{\rm BH}$, as

$$L_{\rm bol} = \eta_r \dot{M}_{\rm BH} c^2, \tag{10.1}$$

where η_r is the radiative efficiency (fixed to $\eta_r = 0.1$ for all the simulations) and c is the speed of

light.

To compare cluster and field luminosity functions, cluster number counts must be rescaled to the mean cosmic density. Cluster haloes are defined as regions enclosing an overdensity of $200\,\rho_c(z)$. Assuming central BHs trace the galaxy and dark-matter distribution, their counts reflect the same overdensity. We therefore adopt the normalization of Vulcani et al. (2014), assuming $R_{200} \simeq R_{\rm vir}$. The BH number counts within $R_{\rm vir}$ in each luminosity bin at redshift z are divided by (eq. B1 of Vulcani et al. (2014))

$$200\,\frac{\Omega_0(1+z)^3+\Omega_\Lambda}{\Omega_0}(1+z)^3, \tag{10.2}$$

which converts the intrinsic cluster overdensity to the field-equivalent scale. We stress that this rescaling introduces systematic uncertainties, as it relies on the assumption that BHs trace the underlying overdensity.

Figure 10.6 presents the BHLF for the M1 and M2 models, shown in the left and right panels, respectively. The BHLF is computed for BHs hosted by halos above two total mass thresholds: $M_{\rm tot} > 4.7\times10^{10}M_\odot$ (orange) and $M_{\rm tot} > 1.4\times10^{13}M_\odot$ (teal), the former being the minimum mass threshold to classify resolved substructures. For the Dianoga clusters, solid lines show the mean BHLF over the sample, while shaded regions indicate the corresponding r.m.s. scatter. The darker dash-dotted lines represent the BHLF measured in the cosmological box, applying the same selection on the mass of the host and with the same color-coding. For reference, the observational bolometric luminosity function at $z = 0$ from Shen et al. (2020) is shown as a dashed gray line.

In both the M1 and M2 models, the normalization of the field BHLF (dash-dotted lines) is lower than observed, although the simulated slope agrees well with observations up to $L_{\rm bol} \sim 10^{44}\,{\rm erg\,s^{-1}}$. The decline at higher luminosities in M1 likely reflects the limited simulation volume, which prevents robust sampling of rare, bright AGN. However, this result is in agreement with Habouzit et al. (2022) that showed that many large-scale simulations systematically underproduce the high-luminosity end of the observed AGN population. The contribution at $L_{\rm bol} \simeq 5\times10^{45}\,{\rm erg\,s^{-1}}$ arises from BH undergoing brief overgrowth episodes in the local Universe (Sect. 10.2.2). In cluster environments, the simulated BHLFs reproduce the observational normalization more closely, but exhibit an excess at the bright end. This excess is contributed primarily by BHs residing in massive haloes, and therefore also by the overmassive BHs hosted by BCGs (see Fig. 10.2a). Compared to the field, clusters show a higher BHLF normalization at all luminosities, as well as an excess of bright sources with $L_{\rm bol} > 2\times10^{43}\,{\rm erg\,s^{-1}}$. These findings may indicate an overdensity of AGN in massive clusters. A detailed analysis linking cluster dynamical state to AGN overabundance will be presented in forthcoming work (Damiano et al., in preparation). As expected, the reduced feedback efficiency in the M2 model enhances BH accretion, leading to an overall increase in the normalization of the BHLF relative to M1. Notably, in the M2 model the bright end is not solely contributed by BHs residing in the most massive haloes, suggesting that AGN feedback is relatively more effective at suppressing BH growth in these environments. To further investigate this and assess the impact of the other models, Fig. 10.7 extends the comparison to the full set of Dianoga cluster models, consistently restricting the analysis to regions simulated with both the reference M1 setup and the model shown in each panel. As in Fig. 10.6, solid lines and shaded regions denote the mean BHLF and the corresponding r.m.s. scatter across

clusters simulated with the same physical model. The M1 results are shown in gray in all panels, while the alternative models are color-coded according to the legend. For reference, the dashed grey line corresponds to the data from Shen et al. (2020). The top left panel shows that increasing the feedback coupling efficiency generally raises the normalization of the BHLF in the intermediate luminosity range ($10^{43} \lesssim L_{\rm bol}/[{\rm erg\,s^{-1}}] \lesssim 10^{45}$), while differences remain modest at the faint end, indicating that AGN feedback is less effective in regulating accretion in this regime.

Models including the cold-gas evaporation mechanism systematically exhibit a suppression of the faint end of the luminosity function ($L_{\rm bol} \sim 10^{41} - 10^{42}\,{\rm erg\,s^{-1}}$) and an enhancement at intermediate luminosities. This behaviour is qualitatively consistent with previous findings in large cosmological simulations (e.g. Illustris and Horizon-AGN; Sijacki et al. 2015a; Volonteri et al. 2016b), where it has been attributed to strong stellar- and SN-driven outlflow depleting the gas reservoir in relatively low mass galaxies, thereby decreasing the BH growth (Dubois et al., 2015). However, the striking difference between models with and without the evaporation motivates a deeper investigation. In Appendix E we include the comparison between the cosmic evolution of the BHLF at different redshift for the M5 and the M1 models, that adopt the same feedback factor efficiency with (M1) and without (M5) the evaporation model. We find that suppressing the cold gas reservoir through the evaporation model has a strong effect at high redshift ($z \sim 4-2$), where rapid BH growth is significantly reduced, in agreement with the results of Sect. 9.2.2. At lower redshift ($z \lesssim 1$), using the evaporation model, the accretion becomes inefficient for low- and intermediate-mass BHs, leading to a clear mass segregation in luminosity space and to a faint end increasingly overpopulated by sub-$10^8\,M_\odot$ BHs. Comparing these results with the increased SF activity observed in Sect. 9.2.2, the hypothesis that the quenched BH growth for $M_{\rm BH} < 10^8 M_\odot$ is caused by efficient stellar feedback suggested by Dubois et al. (2015) is plausible, but deserves deeper investigation that will be included in a forthcoming paper. Finally, removing the Eddington limit on accretion (M7 model) does not significantly affect the BHLF at $z = 0$.

10.3.2 The BH mass function

The BHMF provides a census of the mass distribution of SMBHs and encodes their cumulative growth history. While the BHLF provides a snapshot of the instantaneous accretion activity, the BHMF traces the time-integrated accretion (and mergers), making the BHMF a powerful probe of the total SMBH growth over cosmic time. However, observationally constraining the BHMF is considerably more challenging.

As discussed by Kelly and Merloni (2012), the BHMF estimation suffers from two main sources of uncertainties. A first major limitation arises from survey incompleteness. Most surveys are flux-limited and thus select SMBHs based on luminosity rather than mass. Because a broad distribution of BH masses can correspond to a given luminosity, some objects are scattered above and others below the flux threshold, leading to a selection function that is only weakly sensitive to BH mass. As a consequence, the inferred BHMF can be incomplete or biased across all mass bins.

A second major source of uncertainty concerns BH mass estimates themselves. Direct dynamical measurements (see Box 2.1) are available only for a limited number of systems, so BH masses are typically inferred using host-galaxy scaling relations. In particular, BHMFs are commonly

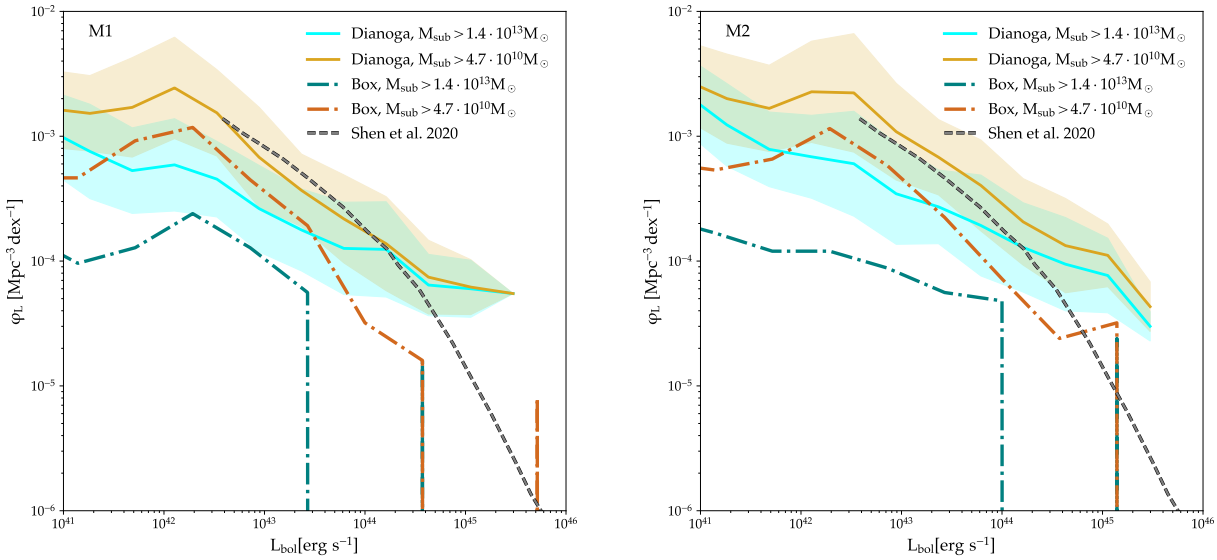

(a) *M1* (b) *M2*

Figure 10.6: *BHLF for the M1 (left panel) and M2 (right panel) models. BHLFs are shown for BHs hosted by halos with total mass above two thresholds:* $M_{\rm tot} > 4.7 \times 10^{10} M_\odot$ *(orange lines) and* $M_{\rm tot} > 1.4 \times 10^{13} M_\odot$ *(lighter orange). Solid lines and shaded regions represent the mean and r.m.s. scatter of the BHLF within the* Dianoga *cluster sample. Darker dash-dotted lines indicate the corresponding BHLFs measured in the cosmological box with matching mass cuts and color coding. The dashed gray line shows the observational bolometric luminosity function fit from Shen et al. (2020) at* $z = 0$.

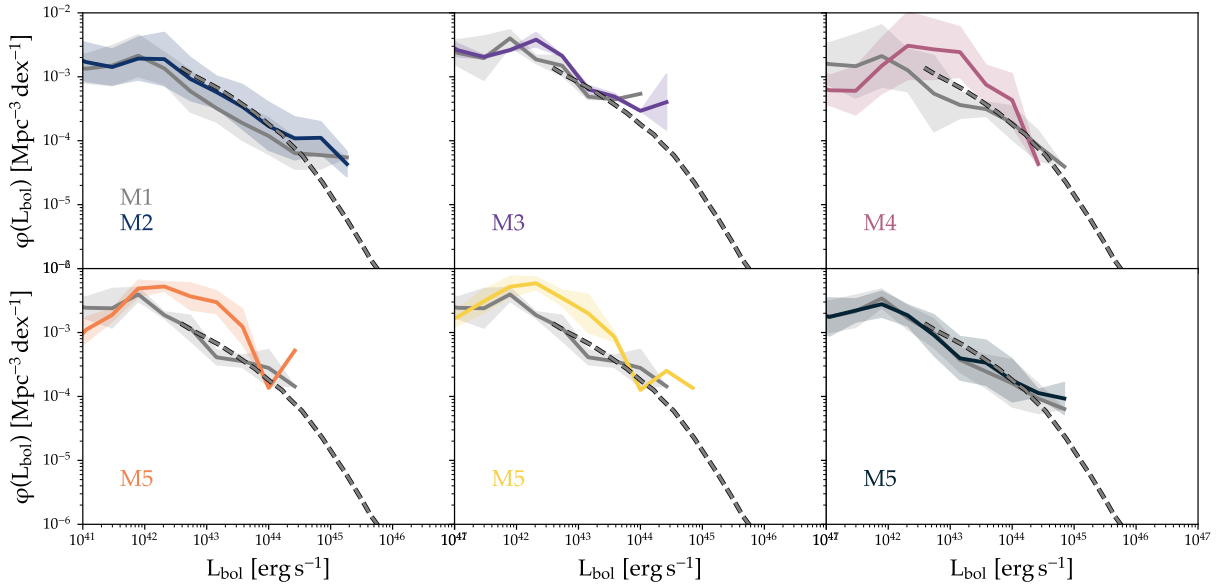

Figure 10.7: *BHLF for the* Dianoga *cluster sample across different physical models. Each panel compares the reference M1 model (gray) with an alternative model, restricting the comparison to clusters simulated with both setups. From top left to bottom right, the M1 results are compared with models M2, M3, M4, M5, M6, and M7. Shaded regions indicate the cluster-to-cluster scatter within the* Dianoga *sample. The dashed line reports the observational fit from Shen et al. (2020).*

inferred using empirical scaling relations between BH mass and host-galaxy properties—such as stellar velocity dispersion or bulge luminosity—combined with the observed galaxy number densities as a function of these same quantities (e.g. Salucci et al., 1999; Yu, 2002; Marconi et al., 2004; Graham et al., 2007; Aller and Richstone, 2002; Lauer et al., 2007; Shankar et al., 2004; Tundo et al., 2007b,a; Mutlu-Pakdil et al., 2016). However, as introduced in Sect. 2.2 these relations are subject to uncertainties. For instance, the $M_{\rm BH} - \sigma_*$ is also sensible to the galactic morphology (e.g. Greene et al., 2008; Graham and Li, 2009), between early- and late-type galaxies, and overall there is no consensus on the validity of the same relation across cosmic epochs (see Sect. 2.2). For observational comparison, in the following analysis we adopt the BHMF presented by Shankar (2013), which assumes that all SMBHs follow the early-type galaxy scaling relations calibrated by McConnell and Ma (2013). We note that adopting alternative prescriptions—such as including contributions from late-type galaxies and pseudobulges—can substantially lower the inferred low-mass end of the BHMF, by up to an order of magnitude at $M_{\rm BH} \sim 10^6\,M_\odot$ (see the discussion in Shankar 2013).

An alternative approach relies on the Soltan argument, which infers the BHMF by integrating the AGN luminosity function over cosmic time (e.g. Yu and Tremaine, 2002; Marconi and Hunt, 2003; Merloni, 2004; Hopkins et al., 2007; Cao and Li, 2008; Cao, 2010). While this method provides a complementary constraint, it requires assumptions about the about AGN light curves, Eddington ratio distributions, duty cycles, radiative efficiencies, and bolometric corrections, all of which introduce additional uncertainties. As a result, different methodologies yield BHMFs with significantly different shapes and normalizations. On the theoretical side, Habouzit et al. (2021) also compiled BHMFs from six cosmological simulation suites (Illustris, TNG100, TNG300, Horizon-AGN, EAGLE, and SIMBA). They found that, at $z = 0$, the overall normalization is broadly consistent with observational estimates based on Merloni and Heinz (2008), with the exception of EAGLE. TNG100, Horizon-AGN, and SIMBA predict an excess of very massive BHs ($M_{\rm BH} \sim 10^{10}\,M_\odot$) and a deficit at the low-mass end. The redshift evolution of the simulated BHMFs shows an increasing normalization toward higher redshift as in Cao (2010). Moreover, simulations generally predict the evolution of a high-mass tail down to $z = 0$, in contrast with models that invoke an anti-hierarchical SMBH build-up. Within this observational and theoretical scenario, we compare in Fig. 10.8 the BHMF for the M1 and M2 models with observational constraints from Shankar (2013), adopting the same selection criteria as in Fig. 10.6. Both models appear to overestimate the BHMF with respect to the data for $M_{\rm BH} > 10^7\,M_\odot$, and underestimate the BH population at lower masses, in agreement with the results of Habouzit et al. (2021). These discrepancies are even more pronounced when analysing the BH population in the DIANOGA sample. The high mass tail of the BHMF in the clusters is contributed by the population of overmassive BHs, lying in more massive structures (teal line). The reduced feedback efficiency in M2 further enhances the discrepancy by increasing BH growth for $M > 10^8\,M_\odot$. The apparent agreement of the BHLF at $z = 0$ with observational data, contrasts with the discrepancy in the BHMF. This indicates that the reference model reproduces present-day accretion rates but fails to capture the full growth history of BHs. While low-luminosity AGN depend primarily on the instantaneous gas supply and late-time feedback regulation, the deficit of low-mass BHs in the BHMF suggests excessive growth at earlier epochs. Indeed, Appendix E shows a pronounced phase of rapid BH growth between $z \simeq 4$ and $z \simeq 2$, which ultimately overpopulates the high-mass

end at $z = 0$.

The results shown in Figs. 10.6 and 10.8 indicate that cluster environments host more luminous and more massive BHs than the field. We stress, however, that this result depends sensitively on the normalization introduced in Eq. (10.2), which assumes that BHs trace the galaxy and dark-matter overdensity within R_{200}, provided that $R_{200} \simeq R_{\rm vir}$. Deviations from these assumptions may introduce systematic uncertainties. A more detailed investigation of environment-driven effects will be presented in future work, where we will compare the AGN fraction in clusters and in the field—following common observational approaches (see Sect. 10.3.1 and references therein)—and relate it to the dynamical state of the host clusters. Since BH growth is sensitive to the specific sub-resolution prescriptions used by each model, it is useful to compare our results on the BHMF for the different models that we simulated. Figure 10.9 shows the BHMF for the different models, adopting the same visualization strategy as Fig. 10.7. The reduced feedback efficiency in the M2 model leads to a more abundant population of BHs with masses $M_{\rm BH} \gtrsim 10^9 M_\odot$. In contrast, at lower masses the BHMFs of M1 and M2 are remarkably similar, indicating that variations in feedback coupling primarily affect the growth of the most massive BHs. This is expected, as stronger feedback is more efficient at regulating accretion in massive halos, as also shown by the agreement on the faint end of the luminosity function in Fig. 10.7 between M1 and M2 models. To disentangle the effects of the feedback efficiency (which differs between M1 and M2) from those of the reduced Bondi boost factor specific to the M3 model, the top–central panel of Fig. 10.9 also includes the BHMF of M2, restricted to clusters simulated with all three models. Relative to M2, the smaller boost factor adopted in M3 suppresses BH growth across the entire mass range. Nevertheless, the higher feedback efficiency in M1 proves substantially more effective in quenching the overabundance of massive BHs, especially at the high-mass end. Models that include cold-gas evaporation (M4, M5, and M6) show a systematic increase in the abundance of low-mass BHs, together with an improved agreement at the massive end of the BHMF with the observational relation. In particular, the comparison between M5 and M1 (top–right panel) suggests that the depletion of low-mass BHs in the other models is primarily linked to excessive early growth driven by cold-gas accretion, as also suggested by the results of Appendix E. By reducing the cold gas reservoir available for both star formation and BH feeding, the evaporation mechanism mitigates this early overgrowth and brings the BHMF closer to the observational constraints of Shankar (2013). Increasing the feedback coupling in M5 and M6 allows the model to reproduce the slope of the BHMF up to $M_{\rm BH} \sim 10^{10} M_\odot$. However, the excess at the high-mass end persists in the M5 model, indicating that overgrowth of the most massive BHs is not fully suppressed even when evaporation is included, in agreement with the discussion of Fig. 10.2.3. When evaporation is combined with very strong feedback, as in M6, BH growth is significantly reduced across the entire mass range, as already noticed in the analysis of the $M_{\rm BH}$–M_* relation. Finally, consistently with the results obtained from other statistical diagnostics, removing the Eddington limit on accretion does not produce a significant change in the BHMF at $z = 0$.

10.4 Multi-BH systems

The growing number of observational detections of dual and binary BHs, reviewed in Chapter 4, strongly motivates a systematic exploration of these populations from a simulation perspective.

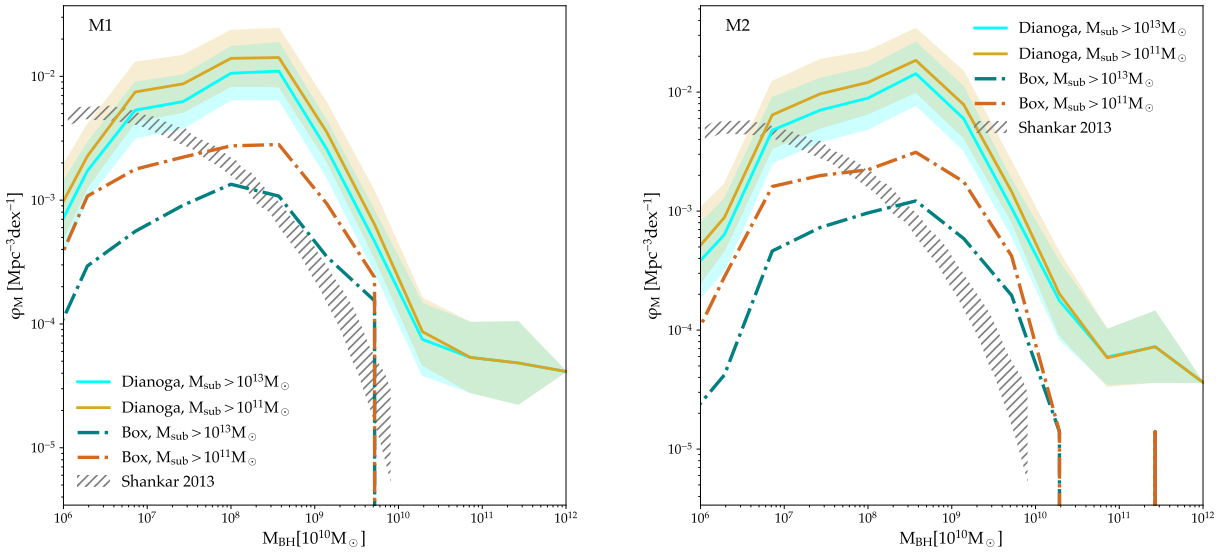

(a) *M1* (b) *M2*

Figure 10.8: *BHMF for the M1 (left) and M2 (right) models in the* DIANOGA *(solid line) and in the cosmological box (dash dotted line). The shaded regions indicate the r.m.s. of scatter across the cluster simulations. The different color coding refers to different mass cuts, as in Fig. 10.6. Observational constraints from Shankar (2013) are shown for comparison.*

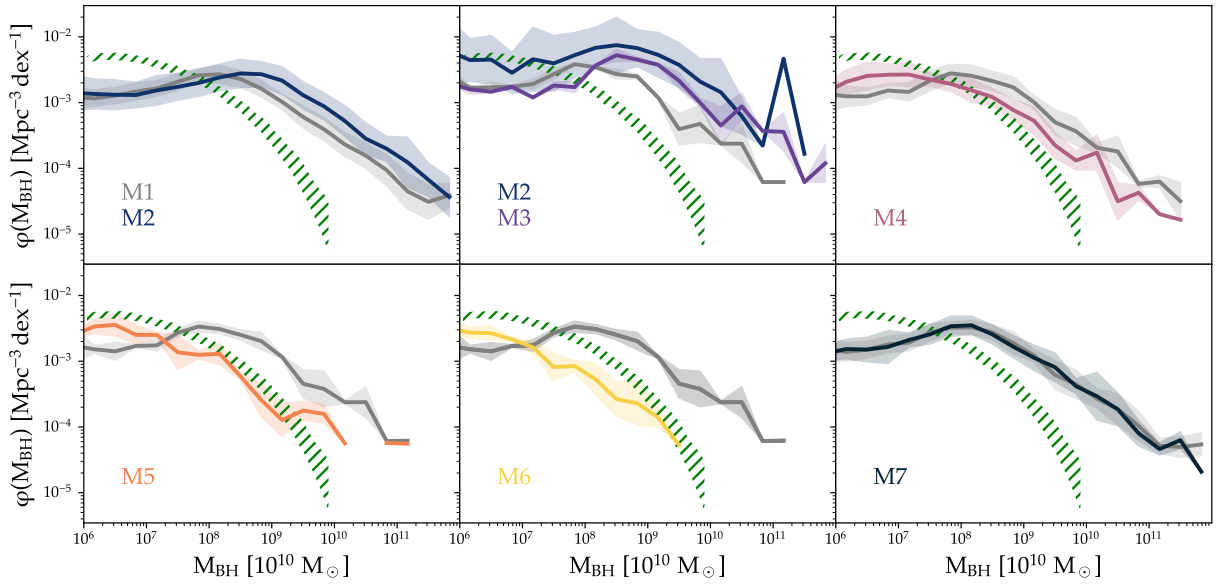

Figure 10.9: *BHMFs for the* DIANOGA *clusters across different models. Each panel compares the reference M1 model (gray) with an alternative model, restricting the comparison to clusters simulated with both setups. From top left to bottom right, M1 is compared with M2, M3, M4, M5, M6, and M7. In the M3 panel, the BHMF for the M2 model is also shown, again restricting the comparison to clusters simulated with all three models, in order to disentangle the effects of the reduced feedback efficiency and the lower Bondi boost factor. Shaded regions indicate the scatter within the* DIANOGA *sample. The diagonal hatched region refers to the BHMF fit from Shankar (2013).*

Several theoretical studies have already addressed the presence and observability of dual and binary BHs in cosmological simulations (Steinborn et al. 2016; Tremmel et al. 2018a; Bellovary et al. 2010; Ricarte et al. 2021; Bellovary et al. 2021; Volonteri et al. 2022; Puerto-Sánchez et al. 2025). These works differ substantially both in their numerical treatment of BH dynamics—particularly whether corrections to DF are included—and in the adopted definitions of dual or binary BH systems. The first study by Steinborn et al. (2016) analyzed BH pairs in the Magneticum Pathfinder simulation. Despite a mass and spatial resolution comparable to that of the simulations presented in this Chapter, the authors argued that no explicit correction to the DF force was required [3] At $z = 2$, Steinborn et al. (2016) found that BHs in pairs lie below the observed $M_{\rm BH} - M_*$ relation. They also reported that dual AGN activity is more prevalent at small BH separations and that galaxy mergers trigger the activity of both BHs in the pair. Tremmel et al. (2018a) studied dual AGN in Milky Way–mass haloes in the ROMULUS25 simulation, adopting the DF correction proposed by Tremmel et al. (2015) (see Sect. 6.1). In their work, BHs were classified as central if located within 0.7 kpc (twice the gravitational softening length) of the halo center. They found that $\sim 30\%$ of the identified SMBHs are off-center, typically within 10 kpc from the halo center. Importantly, $\sim 90\%$ of these wandering BHs had previously reached smaller galactocentric distances, indicating that their displacement is primarily due to orbital stalling. Unlike Steinborn et al. (2016), they found no evidence for enhanced BH growth during merger phases.

Building on this work, Ricarte et al. (2021) compared simulated dual AGN populations with observations from Barrows et al. (2019). They showed that most systems with separations $\geq$ 15 kpc are hosted by distinct galaxies. Notably, at $z \sim 4$, the majority of galaxies hosting an AGN with $L_{\rm bol} \sim 10^{42}$ erg s^{-1} also contain a second AGN of comparable luminosity.

To match the constraints of the observations, Volonteri et al. (2022) classifies the population of dual AGN as those shining above 10^{43} erg s^{-1} and having a relative distance of 30 kpc. The dynamical evolution of massive BHs is corrected for a gaseous DF term, originally proposed by Dubois et al. (2012). They find that at $z = 0$ the brighter BHs of the pairs tend to reside in more massive galaxies compared to the general AGN population and the vast majority of dual AGN can be associated to galaxy mergers. Also, they find that the dual AGN fraction increases with redshift.

More recently, Puerto-Sánchez et al. (2025) analysed dual AGN populations by selecting objects with luminosity $L_{\rm bol} > 10^{43}$erg s^{-1} with separations below 30 kpc, across a wide range of cosmological simulations (Illustris, TNG50, TNG100, TNG300, HorizonAGN, EAGLE, SIMBA, BlueTides, and Astrid), also adopting different prescriptions for BH dynamics. Simulations are discrepant mainly at the cosmic noon ($z \sim 1 - 3$) while they overall underpredict the observed dual AGN abundance at $z = 0$. Contrary to Steinborn et al. (2016), they found that dual AGN at $z = 2$ are, on average, more massive and more luminous than the overall AGN population. Yet, at low redshift, they remain, on average, less massive than the general AGN population. In most pairs, the more massive BH is hosted by the more massive galaxy.

In this context, we investigate the population of systems hosting more than one BH in our simulations, quantifying for the first time the occurrence of BH pairs in the dense enviroment of

[3] However, this conclusion is at odds with the results presented in Sect. 7.3, where we show that no correction or ad-hoc numerical prescription for BH dynamics leads to delayed or suppressed BH mergers, potentially producing an overabundance of systems hosting multiple BHs.

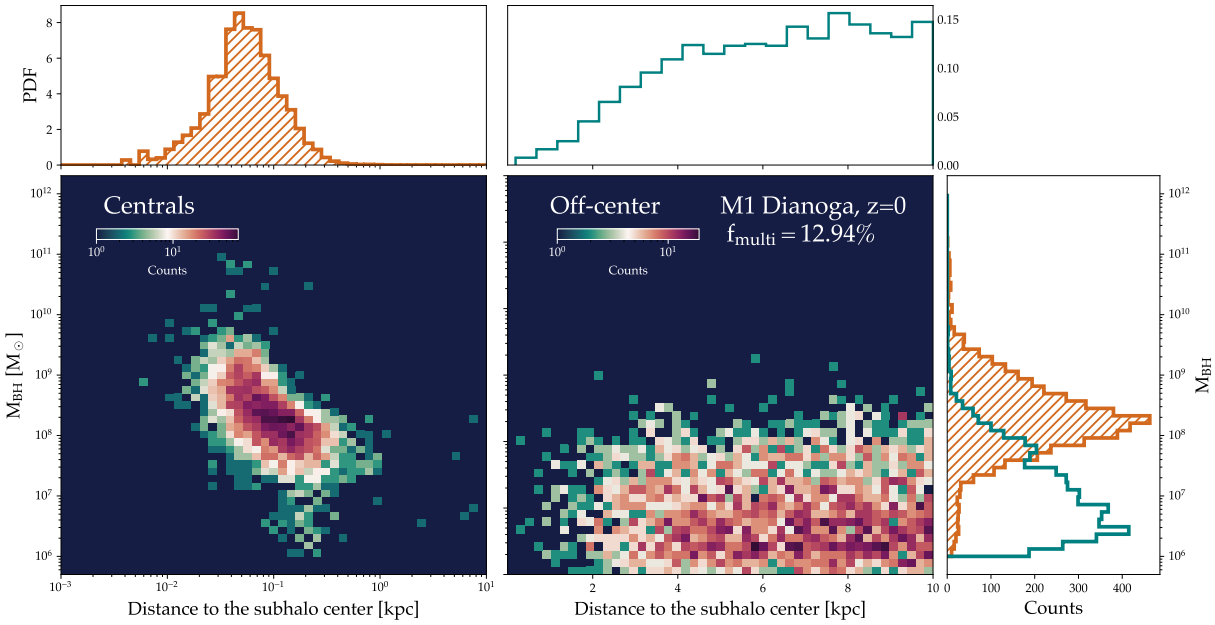

Figure 10.10: *Mass–offset distribution for BHs hosted in resolved (sub-)halos containing multiple BHs in the M1* DIANOGA *clusters. Central panels show two-dimensional histograms of BH mass versus projected distance from the subhalo center for central BHs (left) and satellite BHs (right). Top panels display the PDFs of the offsets, while left panels report number counts as a function of BH mass. In all side plots reporting one-dimensional histograms, central BHs are indicated with orange hatching and satellite BHs with teal lines.*

galaxy clusters. This analysis represents a preliminary yet informative step toward assessing the impact of the enhanced BH orbital evolution enabled by the DF correction adopted in our models.

As an initial study, we restrict the analysis to subhalos hosting more than one BH. We consider only well-resolved subhalos, defined as those containing at least 10^3 DM particles. According to the findings of Tremmel et al. (2018b) and Ricarte et al. (2021), we select systems in which multiple BHs are located within a distance from the subhalo center smaller than $d_{\rm max}$, defined as the minimum between the subhalo half-mass radius and a fixed physical threshold of 10 kpc. At variance with Volonteri et al. (2022) we define the *central* BH as the closest to the subhalo center, while the *satellites* are those confined within $d_{\rm max}$. In this Section, we assess both the abundance of multi-BH substructures and the spatial offsets and luminosities of central and satellite BHs. The analysis is carried out using the M1 model only, and results are presented for both the DIANOGA cluster sample and the corresponding cosmological box.

For the M1 DIANOGA regions, we find that, at $z = 0$, 12.94% of the resolved sub-halos (corresponding to a total of 5064 systems) host more than one BH within their half-mass radius. Most of these systems contain two BHs, while 2.2% host more than two BHs. In the cosmological box simulated with the M1 model, the fraction of multi-BH systems increases to 24.3% (162 structures), with 4.8% of them hosting more than two BHs.

The higher abundance of multi–BH systems in the cosmological box compared to the DIANOGA cluster regions at $z = 0$ can be attributed to the high velocity dispersions characteristic of massive clusters, leading to less frequent galaxy mergers.

Figure 10.10 presents two-dimensional histograms of BH mass versus projected offset from the

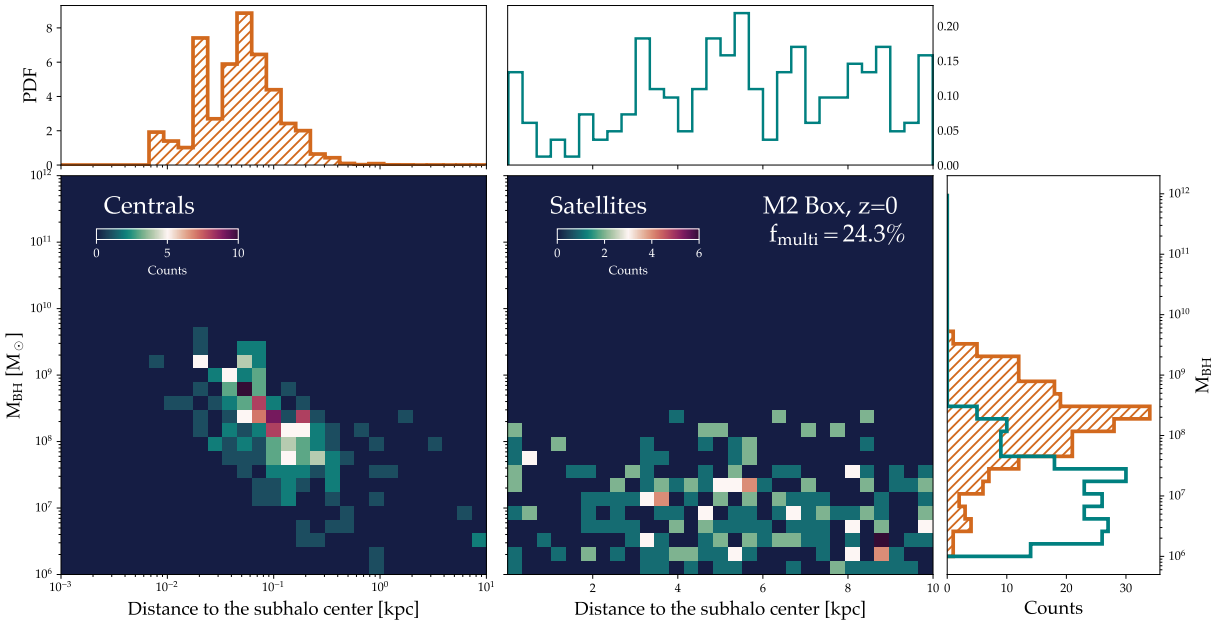

Figure 10.11: *Same as Fig. 10.11 but for the cosmological box simulated with the M1 model.*

subhalo center for central BHs (left panel) and their satellites (right panel) for the M1 DIANOGA simulations. The top panels show the PDFs of the offsets for central and satellite BHs, while the left panel reports the number counts of central and satellite BHs as a function of BH mass. In all one-dimensional histograms, central BHs are indicated by orange hatching, while satellite BHs are shown with teal lines.

The most centered BHs are also the most massive, as expected from the higher efficiency of DF for more massive objects. Central BHs exhibit a mean offset of ~ 0.1 kpc from the subhalo center, consistent with the mean offset found for the central BH population in Figs. 10.2a and 10.2b. This behaviour demonstrates that the DF implementation successfully drives BHs toward the centers of their host substructures, maintaining accurate centering even in complex environments affected by recent mergers or perturbed gravitational potentials due to the presence of additional BHs.

The satellite population shows a gradual decline at small radii: $\sim 10\%$ of satellite BHs are found within 4 kpc of the subhalo center while fewer than 2.5% within 2 kpc. This radial distribution indicates that, within the resolved scales of the simulation, DF efficiently drives satellites inward.

Figure 10.11 presents the same analysis applied to the M1 cosmological box. The results are broadly consistent with those obtained for the DIANOGA clusters: centrally located BHs are more massive and more tightly bound to the centers of their host subhalos. The decline in the abundance of satellite BHs toward smaller galactocentric distances is, however, less pronounced in the cosmological box. This difference likely reflects a combination of reduced statistical significance and the distinct merger histories characterizing field environments. A forthcoming analysis will disentangle the relative contributions of these effects and quantify their impact on the spatial and mass distribution of multi–BH systems.

10.5 Conclusions

In this chapter, we analysed the demographic and dynamical properties of BHs at $z = 0$ in the DIANOGA cosmological simulations of galaxy clusters, examining how different numerical implementations of BH accretion, feedback, and cold-gas regulation affect the resulting BH population. We first considered two sets of 28 cluster zoom-in simulations each, carried out with different choices of the feedback coupling efficiency: $\eta_f = 0.05\,(0.2)$ (M1 model) and $\eta_f = 0.1\,(0.4)$ (M2 model) for the quasar (radio) mode. In addition to the cluster sample, a companion cosmological box was also simulated for both models, allowing a direct comparison between cluster and field environments. Several subsets of simulations were carried out to isolate and study the impact of different sub-resolution prescriptions concerning the AGN sector and behaviour of cold gas. In particular, we explored: (*i*) the effect of a reduced boost factor in the Bondi accretion prescription (model M3); (*ii*) the implementation of a cold-cloud evaporation model (see Sect. 9.1), combined with three different choices of feedback efficiency, $\eta_f = 0.05/0.2$, $0.1/0.4$, and $0.2/0.8$ (models M4, M5, and M6, respectively); and (*iii*) the impact of allowing BHs to accrete above the Eddington limit (model M7).

The analysis presented in this Chapter follows two complementary paths. On the one hand, we examine the statistical properties of the BH population, focusing on the $M_{\rm BH} - M_*$ relation between BHs and their host galaxies, the BHLF and BHMF, assessing both environmental effects and the sensitivity to the adopted sub-resolution prescriptions. On the other hand, we investigate the dynamical evolution of BHs within galaxies, evaluating how the DF correction based on Damiano et al. (2024) performs in tracking BH sinking, centering, and spatial offsets, including systems hosting multiple BHs.

As for the global properties of the BH population, we can draw the following conclusions for the M1 and M2 models:

- The $M_{\rm BH} - M_*$ relation is generally in agreement with observational data for both models. The feedback coupling factor controls the normalization of the relation, which increases for lower values of η_f.

- The simulations exhibit a population of overmassive BHs emerging in the BCGs, with BH masses exceeding $10^{11}\ M_\odot$. We verified that this growth excess is driven by runaway accretion of cold gas, linked to the dynamical activity within the clusters. During merger events, shock-heated gas in the BCG environment can cool, trigger renewed star formation, and sustain enhanced BH growth.

- The BHLF is generally well matched to observations in the DIANOGA clusters, but exhibits a lower normalization in the field. However, the bright end of the BHLF is overpopulated by BHs in massive cluster environments, as a consequence of the massive BH overgrowth.

- The observed BHMF, though affected by stronger observational uncertainties, is not reproduced by the results of our simulations at $z = 0$. In both M1 and M2 models, the low-mass ($10^6 < M/M_\odot < 10^7$) tail underestimates the number of observed BHs, while higher mass bins are overpopulated in our simulations, with a peak at $10^9\ M_\odot$. The similarity of the

results for the M1 and M2 models at the low-mass end indicates the limited effect that feedback has in regulating the early BH growth.

Hence, while the local BHLF is well reproduced and matches observations, the integrated accretion history of the BH population in these simulations is not accurately captured. This motivates the exploration of the BH population when different parameters of our numerical implementation are varied.

- **M3**: the decreased boost factor for cold gas does not prevent the BH overgrowth. The decreased feedback factor with respect to M1 contributes to a further increase the high mass tail of the BHMF.
- **M4-M5-M6**: The evaporation model reduces the slope of the $M_{\rm BH} - M_*$ relation. When combined with the higher feedback coupling factor (M6), it further limits BH growth, thus leading to an underestimate of the observational relation. However, even the evaporation of cold clouds is not able to quench the BH overgrowth. The BHLF exhibits a faint-end peak across all models while the BHMF shows an increased abundance of low-mass BHs in the range $10^6 < M_{\rm BH}/M_\odot < 10^8$ improving the agreement with the observational data. Appendix E reveals that models including the evaporation of cold clouds tend to reduce the growth of BHs at high redshift ($z = 4 - 2$), thus populating lower mass bins of the BHMF at lower redshift. At higher masses, the slope of the BHMF is primarily governed by the feedback efficiency, with stronger feedback (higher η_f) producing fewer massive BHs.
- **M7**: Allowing super-Eddington accretion does not significantly alter the properties of the BH population at present times and the increased accretion does not prevent the BHs from overgrowing.

As for the dynamical evolution of BHs, the implementation of the DF correction in our simulations proves to be effective in tracking the spatial evolution of BHs within their host substructures. The DF model successfully centers the BHs within their subhalos, with typical offsets on the order of ~ 0.1 kpc, below the spatial resolution of the simulations. Subhalos hosting multiple BHs are found to contain a dominant BH which coincides with the most massive in the majority of cases. The distribution of these satellites suggests that DF efficiently drives BHs toward the subhalo centers over time. These results indicate that the DF model captures realistic BH dynamics across a large simulation set, including sinking timescales and multi–BH interactions in dynamically active cluster environments. This analysis represents a preliminary step toward a comprehensive understanding of BH growth and evolution in the Dianoga simulations, naturally preceding a detailed study of their demographics across cosmic times. Relying on a robust and stable DF correction model, the simulations now offer a more reliable framework to track BH dynamics, including the spatial distribution and interaction of multiple BHs within host structures. Despite exploring a wide range of sub-resolution prescriptions – including variations in feedback efficiency, boost factors, cold-gas evaporation, and the removal of the Eddington limit – excessive growth of massive BHs, particularly in BCGs, persists in all models. These challenges point toward the need for novel approaches in modelling BH accretion and feedback, which should capture more accurately the complex interplay between gas thermodynamics and AGN activity, especially in the interaction with the ambient cold gas.

Chapter 11

Conclusions

Motivated by the rapid expansion of observational results – from multi-wavelength surveys of AGN at increasing sensitivity (see Chapter 4) to the opening of the gravitational wave (GW) window on massive black holes (MBHs) mergers – this work contributes to the development of increasingly robust numerical models of the lifecycle of MBHs in cosmological simulations.

Large-scale cosmological hydrodynamical simulations are designed to investigate the processes that govern structure formation across statistically representative volumes of the Universe. However, the need to model such large scales necessarily limits the achievable resolution, preventing a direct treatment of the small-scale physics that governs black hole (BH) accretion, feedback, and dynamical evolution. For instance, BH accretion is regulated by gas reservoirs on sub-parsec scales, while the resulting growth and energy release affect the surrounding medium through thermal and kinetic feedback. Accurately modeling these coupled phenomena remains a major challenge. In this thesis, both the dynamical evolution of MBHs and their growth through sub-resolution prescriptions for accretion and feedback have been systematically investigated.

The first major outcome of this work concerns the dynamical evolution of MBHs. This thesis presents the development and testing of a novel sub-resolution prescription to model dynamical friction (DF) in cosmological simulations. By explicitly accounting for the unresolved gravitational drag experienced by MBHs moving through a collisionless background, the proposed approach alleviates issues such as artificially wandering BHs, numerically induced displacements from the host galaxies, and unrealistic representation of MBH mergers and orbital decay. The novel DF correction has been implemented in the N-body OpenGADGET3 code (Dolag et al., in preparation), adopted for all the simulations presented in this thesis. Through a combination of controlled simulations based on idealized initial conditions and cosmological simulations in a variety of environments, this work has shown that the novel prescription leads to a more stable reconstruction of MBH trajectories across a wide range of environments and resolution regimes.

The second main focus of the thesis concerns the feeding and feedback cycle of MBHs, and its impact on the evolutionary histories of galaxies, galaxy groups and clusters. By systematically analysing different implementations of BH accretion and feedback in the OpenGADGET3 code, this work demonstrates how seemingly minor technical choices in sub-resolution prescriptions and parameter calibration can propagate into substantial differences in MBH growth histories, thermodynamic properties of the surrounding gas and the ensuing evolution of the cosmic structures.

11.1 Summary of the results

The major conclusion from each chapter can be summarised as follows.

11.1.1 Chapter 7

This Chapter presented a validation of the performance of the novel correction for unresolved DF acting on MBHs introduced in Chapter 6 and in Damiano et al. (2024). Through a systematic comparison with commonly adopted numerical techniques – namely BH repositioning and boosted dynamical masses – the proposed model is shown to provide a more physically consistent description of BH dynamics across different environments, from isolated galaxies to group- and cluster-sized haloes. The results demonstrate that the new DF prescription effectively keeps BHs anchored to their host systems without resorting to artificial repositioning (Figure 7.1), thus significantly reducing the formation of spurious WBHs (Figure 7.2), and yields a more realistic description of BH orbital decay during galaxy mergers (Figure 7.10). In doing so, it overcomes key limitations of existing ad hoc approaches, which can either induce unphysical BH displacements or leads to an unrealistic representation of the first stages of merger events. At the same time, global scaling relations between BHs and their host galaxies remain largely unaffected (Figure 7.8), confirming that, within the context of the sub-resolution models for the BH dynamics presented in these simulations, the relations are primarily regulated by accretion and feedback processes rather than by the details of BH dynamics. However, Bahé et al. (2022) showed that if no sub-resolution model for BH dynamics is applied, both the onset of accretion and the effectiveness of AGN feedback are strongly altered.

Overall, this first analysis establishes that the novel method yields promising results in tracking the MBH orbits in cosmological simulations.

11.1.2 Chapter 8

To complement the study of the performance of the model for DF correction, Chapter 8 provided a validation of this model by studying the orbital decay of a MBH within a controlled setup consisting of a dark matter (DM) halo following a Navarro-Frenk-White (NFW) profile, with and without a central stellar component. By comparing N-body simulations against analytical predictions, we established whether the proposed sub-resolution model is capable of reproducing the analytical predictions on the sinking timescales and whether these results converge at progressively increasing numerical resolution.

In the presence of this DF correction, the simulations show that BH sinking timescales are significantly reduced and converge consistently as resolution increases, closely matching analytical predictions (see Figure 8.4). In contrast, simulations without the correction exhibit delayed sinking timescales and a much slower convergence at increasing resolution. The presence of a stellar bulge introduces additional numerical complexity, leading to delayed sinking compared to analytical predictions due to softened forces and numerical heating (Figure 8.7). Nevertheless, the refined version of the DF correction introduced in Chapter 6 (see Damiano et al., 2025) successfully mitigates these effects. Crucially, the refined DF model is quite effective even when the BH mass

is smaller than that of the surrounding particles – a condition commonly encountered in large-scale cosmological simulations (see Figures 8.6, 8.10).

Overall, Chapters 7 and 8 demonstrate that the DF correction introduced in Chapter 6 provides a numerically robust and physically motivated framework for tracking the dynamical evolution of BHs across a wide range of environments and numerical resolutions. Notably, the model does not require any parameter recalibration but naturally adapts to changes in resolution: its contribution increases at low resolution, where unresolved DF is significant, and progressively weakens at higher resolution, when the N-body gravity solver already captures a larger fraction of the DF drag force.

Chapter 9

Resorting to the previously tested DF correction model, Chapter 9 investigates how different numerical choices regarding the sub-resolution implementations for BH feeding and feedback affect BH growth and the evolution of their host systems. By re-simulating the same group-sized halo while varying different prescriptions, it was shown that seemingly minor numerical choices can substantially alter the BH growth history, surrounding gas properties, and star formation activity. Within the models for BH feeding and feedback incorporated in the OpenGADGET3 code, early BH evolution is governed by cold gas accretion and extended quasar-mode phases, while the transition to radio mode limits further growth but remains sensitive to the treatment of cold gas inflows (Figure 9.1). Specific numerical prescriptions, such as stochastic gas swallowing, play a key role in preventing late-time BH overgrowth by removing the cold particles surrounding the BH (Figure 9.2a). Partially removing the cold gas reservoir by introducing a treatment for the evaporation of gas clouds limits the early widespread cold gas-powered BH growth. However, it has the side effect of enhancing the global SFR of the group (Figure 9.2b). Using a different kernel to redistribute AGN feedback energy in radio mode does not significantly alter the BH accretion history, while coupling wind particles with AGN feedback can induce spurious numerical effects (Figure 9.6). Rather than identifying a definitive solution, this analysis underscores the importance of moving toward more realistic feeding and feedback models, particularly those that incorporate more physically motivated models for radiative efficiency and kinetic feedback.

11.1.3 Chapter 10

Chapter 10 presents extended tests of the BH dynamical modelling and of the sub-resolution prescriptions which determine the evolution of MBHs and the ensuing AGN feedback. An extended simulation of galaxy clusters – the so-called Dianoga suite – is here presented with the aim of investigating the demographics and spatial distribution of the BH population at $z = 0$. The suite consists of simulations of 28 zoomed-in Lagrangian regions resolving the evolution of galaxy clusters spanning a mass range of $M_{200} = 10^{14} - 4 \cdot 10^{15}\, M_{\odot}$ at $z = 0$.

By analysing different simulation subsets, designed to explore different sub-resolution parameter choices, this chapter discusses in detail how such choices shape BH growth and their interaction with the host environment. The simulations reproduce observed scaling relations between black hole and host galaxy mass, with feedback efficiency primarily controlling the normalization of the relation. However, an overabundance of overmassive black holes – particularly in brightest central galaxies (BCGs) – emerges due to sporadic episodes of runaway cold gas accretion triggered by

the cluster's dynamical activity (e.g., merger events; Sect. 10.2.2). The demography of MBHs is analysed by comparing the black hole luminosity function (BHLF) and black hole mass function (BHMF) with observations and semi-empirical models by Shen et al. (2020) and Shankar (2013), respectively. The BHLF broadly aligns with the observations, and presents a higher normalization in cluster environment. On the other hand, the BHMF remains largely discrepant, as simulations underpredict low-mass black holes and overpopulate the high-mass end (Figure 10.8). Despite variations in sub-grid modelling – the value of the accretion boost factors, the inclusion of cold cloud evaporation, and allowing super-Eddington accretion – none of these variations has been shown to fully resolve the BH overgrowth problem or to simultaneously reproduce the BHMF and BHLF (Figures 10.7 and 10.9). Quite importantly, the results from such an extended set of high-resolution cosmological simulations further demonstrated that the DF correction introduced is effective at tracking BH sinking and centering, yielding an improved modelling of multiple BH systems within host structures (Figure 10.10). The analysis of the full DIANOGA simulations underscores the inherent challenges in numerically capturing the complex interplay between black holes, gas physics, and feedback processes, particularly in dense cluster environments. Cold gas–triggered accretion is identified as the dominant driver of both black hole overgrowth at $z > 2$ (Appendix E) and the runaway accretion episodes observed at lower redshift. Neither enhanced AGN feedback nor the reduced availability of cold gas introduced by the evaporation model is sufficient to suppress this overgrowth while simultaneously improving agreement with the BHMF and the $M_{\rm BH}$-M_* relation.

The novel DF implementation introduced in this thesis provides a robust method for tracking the dynamical evolution of BHs in cosmological simulations. At the same time, a systematic analysis of the sub-resolution techniques adopted to follow the BH accretion and feedback has revealed both the strengths and the intrinsic limitations of the modeling strategies currently implemented in OPENGADGET3. These results identify clear directions for future developments aimed at further improving the modeling of MBH dynamics and the associated feeding–feedback cycle.

11.2 Future Prospects

11.2.1 Improving the dynamical evolution of MBHs

Within the theoretical framework adopted in this work, the correction for the unresolved DF accounts explicitly for the first-order diffusion coefficient of the Fokker-Planck equation (Eq. 4.9). Higher-order terms (Eq. 4.10), however, remain neglected. In particular, a numerical correction accounting for the second–order diffusion coefficient, associated with stochastic fluctuations of the probability distribution function of particles, has recently been proposed by Genina et al. (2024). They perform controlled simulations, following the same approach as in Chapter 8, demonstrating that the inclusion of this second-order term significantly improves the results, particularly when the BH mass approaches that of the surrounding DM particles. Exploring the impact of this additional term within the same systematic methodology adopted in this thesis – starting from controlled experiments and progressively moving to cosmological environments – could be a natural

extension of this work. Indeed, the results of Chapter 8 showed that, although the DF correction significantly improves the dynamical tracking of BHs, some issues remain. In particular, when a stellar bulge is included, the agreement with analytical predictions worsens, and although the correction successfully reproduces the sinking timescales, it fails to reproduce the orbital ellipticity of the BH. The inclusion of the second-order term is expected to alleviate these issues by reducing numerical noise.

Another aspect to investigate in detail concerns the inclusion of a DF correction term to account for gas drag. Some studies have attempted to model the effect of the DF exerted by the gaseous component on BHs in simulations (Dubois et al., 2016; Chen et al., 2022). While Chen et al. (2022) found that this contribution is subdominant in their simulations, its relative importance is expected to increase at higher resolution and at high redshift, where cold, dense gas becomes more abundant around highly accreting BHs. Assessing the impact of the gas drag under these conditions, and quantifying its interaction with stellar and DM DF contributions, will be crucial to achieve a more complete description of the processes driving MBH orbital decay.

A further direction for improving BH dynamics lies in coupling large-scale cosmological simulations with more advanced numerical techniques to improve the spatial resolution of BH particles. The KETJU algorithm (Mannerkoski et al., 2023), for instance, uses high-accuracy regularization techniques to explicitly integrate small-scale interactions involving BHs and their surrounding stars. KETJU performance improves both in accuracy and computational efficiency when the BH mass exceeds that of surrounding particles, making it particularly attractive for next-generation high-resolution simulations.

Along a similar line, the recently developed RAMCOAL code (Li et al., 2025; Dong-Páez et al., 2025) provides a comprehensive sub-resolution framework for modeling MBH dynamics, incorporating stellar and gaseous dynamical friction, stellar scattering, circumbinary disc interactions, and GW emission. Crucially, RAMCOAL is the first code to enable the on-the-fly tracking of MBH binaries down to the coalescence stage. This approach reduces the uncertainties when predicting key orbital parameters – such as mass ratio and eccentricity – for estimating merger rates and the GW background in cosmological simulations. Embracing this innovative approach would mark a major step forward for OpenGADGET3, making it suitable to deliver robust forecasts for BH mergers for present and upcoming GW detectors, such as LISA (Colpi et al., 2024) and pulsar timing arrays (Antoniadis et al., 2023), in the era of multi-messenger astronomy.

11.2.2 Toward an improved modelling of BH feeding and feedback cycle

The analysis of BH feeding and feedback prescriptions reported in this thesis reveals significant technical challenges, ultimately highlighting the need for a substantial improvement of current numerical sub-resolution approaches.

A recurring issue concerns the role of cold gas. The results of Chapters 9 and 10 demonstrate how delicate the treatment of cold gas is, as it strongly influences several key physical processes. At high redshift, cold gas fuels the early growth of BHs, leaving a clear imprint on the evolution of the bolometric BHLF (Appendix E), which displays a pronounced excess at high luminosities until $z = 2$. This early phase of widespread accretion also leads to an overpopulation of the high-mass end of the BHMF at $z = 0$ (Fig. 10.8).

At $z \leq 1$, cold gas clumps can power phases of very efficient accretion, as shown in Section 10.2.2. These episodes are closely linked to the dynamical activity of galaxy clusters and are difficult to suppress, even when mechanisms such as cold-gas evaporation are included. Moreover, in dynamically active environments, merger-driven shocks can heat and pressurize the ICM while simultaneously enhancing cooling in dense regions, thereby promoting star formation.

Interestingly, evidence for this cold gas transportation by infalling satellites has been very recently seen by JWST in the work by Zhuang et al. (2025) that reported an unambiguous case of direct cold gas transportation onto a Brightest Group Galaxy (BGG) at $z = 0$. The observations reveal a faint satellite, barely detectable at rest-frame optical wavelengths, whose tidal stripping deposits gas and dust onto the central galaxy. The authors complement these findings with an analysis of the TNG50 simulation, identifying similar events in which cold gas is transported during the first apocentric passages of infalling satellites. Consistent with this picture, Staffehl et al. (2025) traced the origin of cold gas in TNG-Clusters (Nelson et al. 2024) and found that, at $z \leq 1$, it predominantly arises from pre-cooled material carried by infalling satellites, with in-situ cooling of the hot intracluster medium contributing primarily in present-day cool-core systems. In the simulations shown in Chapter 10, shock-heated gas not only fuels the BH accretion but also significantly enhances the star formation of the central region of the cluster.

It is rather hard to attribute the emergence of this *cold gas issue* to a single modeling ingredient associated exclusively with either star formation and stellar evolution or AGN feeding and feedback. Instead, it reflects the complex and tightly coupled interplay between these processes, which jointly shape the thermodynamic state of the intracluster and circumgalactic medium in cosmological simulations (Dattathri et al., 2025).

First of all, it is not surprising that similar issues were not reported in earlier low-resolution studies (Bassini et al., 2020; Bassini et al., 2019). The recent work within the GIBLE project (Ramesh and Nelson, 2023) has shown that increasing spatial resolution leads to a higher abundance of small-scale cold gas clumps, even when global gas properties such as total mass, cold fraction, temperature remain comparable. The formation of these small, dense clumps is precisely what triggers the excessive BH growth observed in our simulations.

From the perspective of star formation modeling, the findings of this thesis highlight the limitations of the multiphase model of Springel and Hernquist (2003), which assumes an interstellar medium composed of clouds in hydrostatic equilibrium. In reality, the ISM has a more complex structure, characterized by continuously forming and dispersing filaments and cloud-like structures. When gas undergoes strong compression, particles can populate regions above the star-formation branch (Fig. 10.4), violating the assumed effective equation of state and breaking the model's underlying assumptions. These limitations could be alleviated by adopting a more sophisticated model for star formation that relax the assumption of Springel and Hernquist (2003) (see for instance Burger et al. 2025). Within the OpenGADGET3 collaboration, the MUPPI model (Murante et al. 2015, 2010; Valentini et al. 2017, 2020) does not rely upon an effective equation of state for multiphase particles. Integrating such models into the present simulations suite represents a promising avenue for future work.

On the BH side, both accretion and feedback prescriptions in OpenGADGET3 could be

substantially refined. The assumption of a two-phase medium that allows cold, high-density clumps to coexist around the BH with a hot diffuse medium is intrinsically inconsistent with classical Bondi accretion theory, which requires a homogeneous ambient surrounding the BH. This motivates the development of alternative accretion models capable of capturing the turbulent nature of BH feeding processes. A particularly promising direction is offered by chaotic cold accretion models (Gaspari et al., 2013; Gaspari et al., 2020), which naturally links accretion rates to the thermodynamic and turbulent properties of the surrounding gas. An alternative approach, adopted in the SIMBA simulation (Davé et al., 2019), distinguishes between hot and cold gas accretion, applying Bondi accretion to the hot phase and torque-limited prescriptions (Anglés-Alcázar et al. 2017) to the cold component.

As for the AGN feedback, Chapter 10 highlighted how the enhancement of the feedback coupling factor can lower the normalization of the $M_{\rm BH} - M_*$ relation and that of the BHLF, but also demonstrated that this is not enough to prevent the episodic cold gas accretion at low redshift. Davé et al. (2020) showed that AGN kinetic jet feedback is the primary mechanism responsible for reducing the cold gas content from $z = 1$ to $z = 0$ in massive galaxies $M_* > 10^{10}\,M_\odot$. This is consistent with our findings, which indicate that purely thermal feedback is insufficient to expel the cold gas clumps at low redshift. A more realistic treatment likely requires a transition toward kinetic feedback in the radio mode. Initial implementations of kinetic feedback in OpenGADGET3 have been presented by Barai et al. (2016), but so far tested only in controlled setups. Their integration and systematic calibration in full cosmological simulations remains an important goal for future work. Finally, incorporating spin-dependent radiative efficiencies, as proposed by Sala et al. (2024), offers a natural way to enhance the realism of BH models. Higher radiative efficiencies linked to rapidly spinning massive BHs, along with spin-dependent jet directionality, create a direct connection between the sub-resolution microphysics of accretion and the resulting regulation of BH growth and feedback on the intracluster and intergalactic medium.

In general, the results presented in this thesis underscore the central role played by MBHs in shaping the evolution of galaxies and large-scale structures. By refining the numerical treatment of BH dynamics and critically examining sub-resolution prescriptions for accretion and feedback, this work contributes to the development of the OpenGADGET3 code toward a more accurate treatment of MBHs embedded in complex, evolving environments. Rather than offering definitive solutions, the results emphasize the complexity of the problem and the necessity of continued methodological refinement to keep pace with the continuous advancements in the amount and quality of observational data, in an epoch of fervent discoveries driven by next-generation facilities and multi-messenger astrophysics.

Appendices

Appendix A

Simulation parameters

The set of relevant numerical parameters and the reference resolution adopted for the simulations presented in Chapters 7 and 9 are listed in Table A.1. Those are subdivided into sections, namely:

- **Star formation and stellar evolution**: the star formation model relies upon the definition of the star formation timescale $t_{0,*}$, the fraction of short-lived massive stras β, the energy injection of SN II explosion and the star formation density threshold $\rho_{\rm th}$. Stellar winds with velocity v_w are launched with efficiency ϵ_w. Those particles remain hydrodynamically decoupled once they reach a region having density lower than $f_{\rm dec}\rho_{th}$ or when a delay time δt_w has passed. A Chabrier (2003) IMF is adopted.

- **BH model**: BH are seeded in haloes above a FoF DM mass of $M_{\rm DM,seed}$, provided that halo contains stellar-to-dark-matter and gas-to-stellar ratios above $f_{*,seed}$ and $f_{\rm gas,seed}$. The seed mass of the BH increases with the stellar content of the halo, starting from a minimum value M_0. Accretion onto BHs follows the minimum between the Bondi rate and the Eddington rate. The Bondi prescription includes a boost factor α different for the cold and hot accretion mode. The Eddington limit uses a radiative efficiency η_r. BH–BH mergers occur once the pair reaches separation $d_{\rm merg}$, is gravitationally bound, and has a relative velocity below half the sound speed. AGN feedback is modelled through a pure thermal injection of energy, with the feedback energy rate given depending on the radiative efficiency η_r, the BH accretion $\dot{M}_{\rm BH}$ and the feedback factor η_f which in turn assumes different values for quasar (i.e. $\dot{M}_{\rm BH}/\dot{M}_{\rm Edd} > 1\%$) or radio (i.e. $\dot{M}_{\rm BH}/\dot{M}_{\rm Edd} < 1\%$) mode.

In addition, it is worth mentioning that in the simulations presented in the thesis the PM grid size corresponds to 256^3, the r_s scale used to define the transition between short-range and long-range interactions appearing in Eq. (5.33) and (5.34) is:

$$r_s = a_{\rm SMTH} \cdot \Delta x_{\rm PM}, \tag{A.1}$$

where $\Delta x_{\rm PM}$ is the grid spacing and $a_{SMTH} = 1.25$. Moreover, the Tree algorithm is activated up to a maximum radius $r_{\rm max}$ defined by $r_{\rm max} = r_{\rm CUT} \cdot r_s$, where we adopt $r_{\rm CUT} = 6$.

Table A.1: *Summary of the sub-resolution models adopted for BH physics, AGN feedback, and star formation.*

Label	Meaning	Value
	Resolution (Chapters 7, 9, 10)	
$m_{\rm DM}$	Dark matter particle mass	4.69×10^7 M$_\odot$
$m_{\rm gas}$	Gas particle mass	8.67×10^6 M$_\odot$
m_*	Stellar particle mass	8.7×10^6 M$_\odot$
$\epsilon_{\rm DM}$	DM gravitational softening	4.13 ckpc / 1.38 kpc
$\epsilon_{\rm gas}$	Gas softening	1.38 ckpc
ϵ_*	Stellar softening	0.35 ckpc
$\epsilon_{\rm BH}$	BH softening	0.35 ckpc
	Star Formation and Stellar Evolution	
IMF	Initial mass function	Chabrier (2003)
$t_{0,*}$	Star formation timescale	1.5 Gyr
β	Fraction of massive stars ($> 8\,M_\odot$)	0.1
$e_{\rm SNII}$	SNII energy per explosion	10^{51} erg
$\rho_{\rm th}$	Star formation density threshold	0.1 cm^{-3}
$\eta_{\rm w}$	Wind mass-loading efficiency	2
$v_{\rm w}$	Wind velocity	350 km s^{-1}
δt_w	Wind delay time	0.025 Gyr
$f_{\rm dec}$	Wind decoupling density threshold	$0.5\,\rho_{\rm th}$
	BH Seeding	
$M_{\rm BH,seed}$	Seed BH mass prescription	$M_0 \frac{M_{*,h}}{f_* M_{\rm DM,seed}}$
M_0	Minimum BH seed mass	2.7×10^5 M$_\odot$
$M_{\rm DM,seed}$	Minimum DM halo mass for seeding	6.94×10^{10} M$_\odot$
$f_{*,seed}$	Stellar-to-DM mass ratio	5%
$f_{\rm gas,seed}$	Gas-to-stellar mass ratio	10%
	BH Accretion	
$\dot{M}_{\rm BH}$	BH accretion rate	$\min(\dot{M}_{\rm Bondi}, \dot{M}_{\rm Edd})$
$\dot{M}_{\rm Bondi}$	Bondi accretion rate	$\frac{4\pi G^2 M_{\rm BH}^2 \alpha \rho}{(c_s^2+v^2)^{3/2}}$
$\dot{M}_{\rm Edd}$	Eddington accretion limit	$\frac{4\pi G M_{\rm BH} m_p}{\eta_r \sigma_T c}$
α	Cold/hot accretion boost factor	10/100
η_r	Radiative efficiency	0.1
n_s	Number of gas particle slices for stochastic accretion	4
	BH Merging	
$d_{\rm merg}$	Spatial merging criterion	$5\,\epsilon_{\rm BH}$
$\Delta r_{\rm BH}$	Distance between BHs	$< d_{\rm merg}$
$v_{\rm rel}$	Relative velocity criterion	$< 0.5\,c_s$
$\Phi_{\rm BH1}, \Phi_{\rm BH2}$	Potential-energy binding criterion	$\frac{\lvert\Phi_1-\Phi_2\rvert}{a} < 0.5c_s^2 - v_{\rm rel}^2$
	BH Feedback	
$\dot{E}_{\rm feed}$	AGN energy injection rate	$\eta_r \eta_f \dot{M}_{\rm BH} c^2$
η_f	Coupling efficiency (quasar/radio modes)	0.05/0.2

Appendix B

On the phase-space distribution function surrounding the BHs

One of the hypotheses on which the DF model introduced in Sect. 6.2.1 is based, is that the phase space distribution function in the vicinity of a BH particle can be expressed as in Eq. (6.2).

$$f(v) = \frac{3}{4\pi\epsilon_{BH}^3} \sum_{i}^{N(<\epsilon_{BH})} \delta(v - v_{BH}) \tag{B.1}$$

meaning that the local phase-space distribution is proportional to the PDF within the softening length. The possibility to recover, through this formula, the phase-space distribution surrounding the BH strongly depends on density and resolution. To assess how many particles are required to accurately sample the underlying velocity distribution, an analysis was carried out to determine whether the velocity distribution of particles surrounding the BHs can be reliably recovered when considering only those within the BH softening length. A few representative examples of common conditions encountered in the simulations are presented here. From snapshots of the `D9` and `Cl13` simulations (see Sect. 7.1 and Table 7.1), BHs hosted by galaxies not undergoing mergers or tidal disruptions were identified through visual inspection. For these systems, the velocity distribution of all stellar particles belonging to the host galaxy was found to be well described by a Maxwellian distribution. Subsequently, stellar particles were selected within various distances from each BH, and the distribution of relative velocities between the stars and the BHs was compared. The following limiting radii were considered: 30 kpc, $5, \epsilon_{BH}$, $2, \epsilon_{BH}$, and ϵ_{BH}. Table B.1 lists the BH masses and the stellar masses enclosed within 30 kpc from the halo centre for the examples discussed below.

Table B.1: *Mass of BH and stellar mass of the host sub-halos within 30 kpc whose velocity distribution in shown in Fig. B.1, B.2 and B.3.*

	M_{BH} ($M_\odot$)	M_* (<30kpc) ($M_\odot$)
B.1	7.14×10^7	3.44×10^{10}
B.2	3×10^6	2.14×10^9
B.3	2.57×10^8	6.14×10^{10}

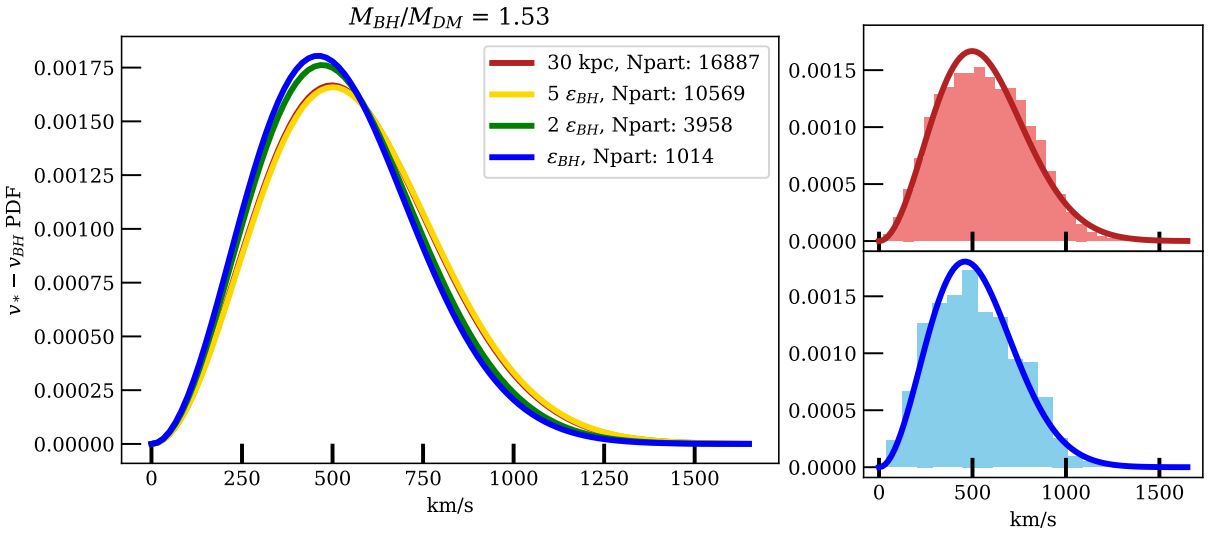

Figure B.1: *Probability distribution functions of the relative velocity between a massive BH (see B.1) in the* `C113` *simulation using DF at redshift* $z = 2.5$*, and the surrounding stars within 30 kpc (enclosing all the stars in the sub-halo) (red line),* $5\ \epsilon_{BH}$ *(yellow line),* $2\ \epsilon_{BH}$ *(green line) and* ϵ_{BH} *(blue line). In the left panel, the best fitting Maxwellian PDFs are compared for these four cases. The right plots superimpose the PDF measured from the simulation with the Maxwellian fit for the 30 kpc case (top) and the* ϵ_{BH} *case (bottom).*

Figure B.1 compares the velocity probability distribution function (PDF) for a selected BH hosted at the centre of a galaxy having more than 16000 star particles. The dynamical BH mass corresponds to 1.53 times the DM particle mass. While less than 10% of the star particles lies within the softening length (see legend), their velocity distribution can be quite accurately described by a Maxwellian distribution, as shown in the left plot. Interestingly, the distributions that best fit in the surroundings of the BH ($2\ \epsilon_{BH}, \epsilon_{BH}$) shift their peaks down to lower relative velocities. Particles with lower relative velocity compared to the BH contribute the most to the computation of the DF correction, according to Eq. (6.8). The same trend can be observed when the host sub-halo is resolved with fewer star particles.

For the case presented in Fig. B.2, the particle number within the entire galaxy is 1265 and only 49 of them are found within ϵ_{BH}, thus contributing to our DF correction. Moreover, the BH mass reaches only 6% of the mass of the DM particles. Even if the system is less resolved than that described in Fig. B.1, the dominant contribution to the PDF of velocity in the vicinity of the BH comes from particles having a velocity relative to the BH smaller than 200 km/s, whose contribution is again dominant in the correction of the DF. Finally, when the BH local velocity distribution deviates from the host galaxy velocity distribution profile, this technique can trace the local velocity distribution. Although the DF force is a *global* effect, whose 'long-range' contribution is already captured by the N-body solver, the added correction should have a *local* nature.

For instance, the velocity distributions in Fig. B.3 describe a peculiar situation. As the BH is displaced from the sub-halo centre of 4 ckpc/h, the velocity distribution in the BH's surroundings differs from that of the sub-halo. Thus, enclosing only particles in the local vicinity of the BH leads to velocity distributions different from the one of the entire system.

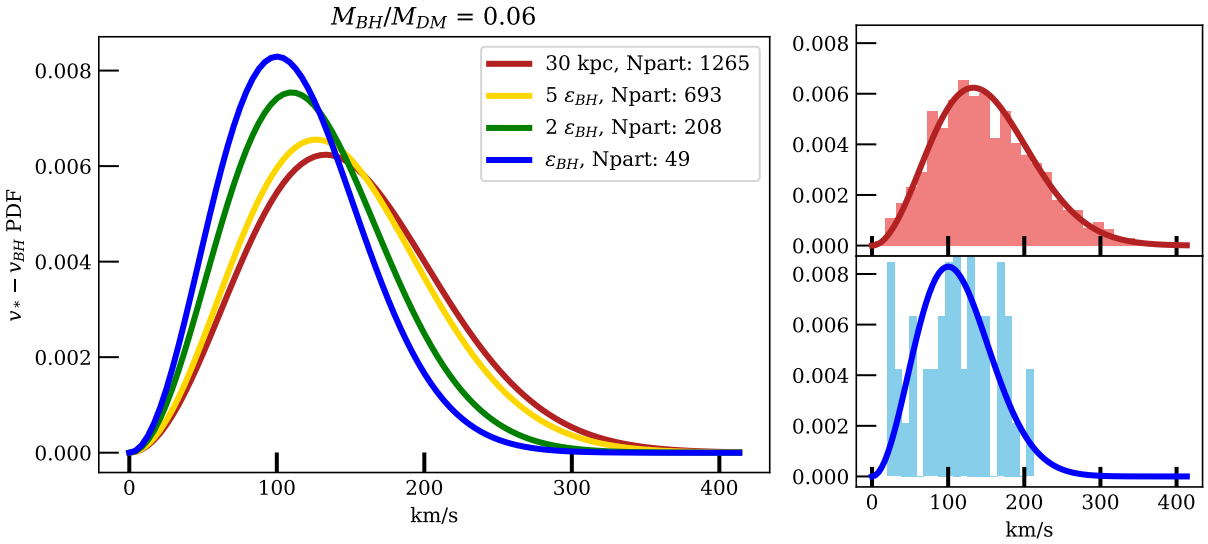

Figure B.2: *PDF fitting of the velocity distribution as Fig. B.1 but for a smaller BH at $z = 2.5$ in the `Cl13` simulation.*

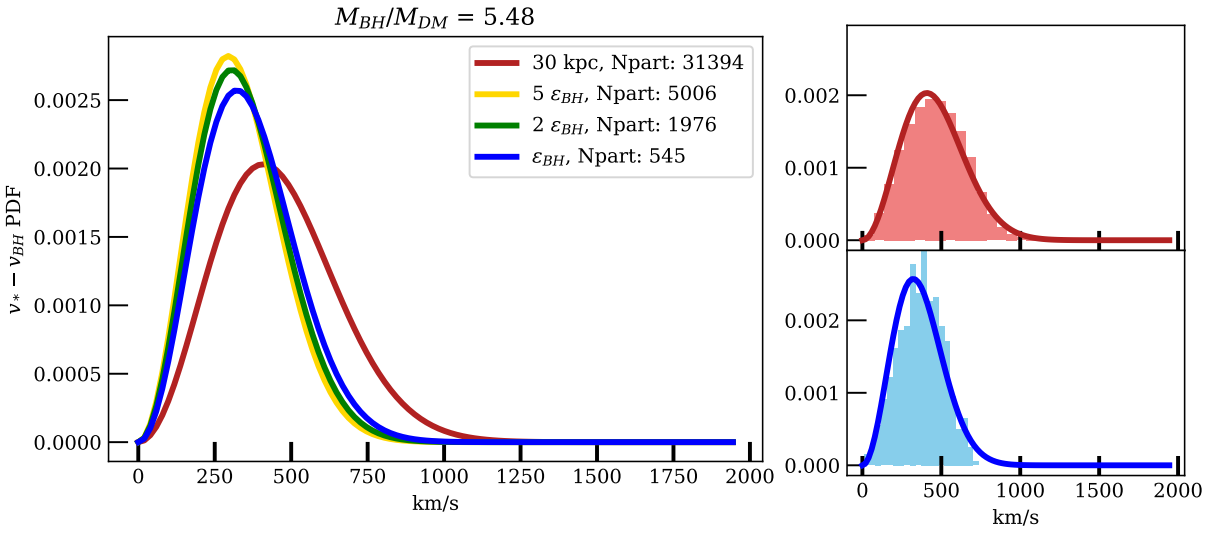

Figure B.3: *PDF fitting of the velocity distribution as in Fig. B.1 for a BH in the `D9` simulation using the DF correction at $z = 2.5$. The relative velocity PDF around the BH is locally different from the global distribution.*

Figures B.2, B.1, and B.3 are only three examples that are representative of the vast majority of the cases obtained when performing tests on the validity of Eq. B.1. Thus, it can be concluded that for well-resolved systems the velocity PDF from particles within the softening length reproduces fairly well the PDF that characterises the BH underlying velocity field. Although for less-resolved systems the velocity dispersion is less constrained, the contribution from particles with low velocity relative to the BH is dominant. These particles are those that provide the main contribution in the DF correction of Eq. 6.4.

Appendix C

OTIS optimization

OTIS uses the `scipy.integrate.solve_ivp` function to integrate the equations of motion. The time-stepping method varies upon the choice of the integration technique, since all those methods employ an adaptive time step that depends on the numerical accuracy. In particular, `Scipy` provides integration techniques for both stiff and non-stiff problems. For instance, Runge-Kutta methods of `R45, R23` use a higher order Runge-Kutta expansion to estimate the solution (5th order for `R45` and 3rd order for `R23`) and a lower-order expansion to estimate the error (4th for `R45` and 2nd for `R23`), and are suitable for non-stiff problems. For either stiff or general problems, other integration technique can be used, such as the implicit Runge-Kutta Radau-IIA method, flagged as `Radau`. In general, for explicit Runge-Kutta methods, the higher the order of the integration is, the lower is the number of timesteps required. On the other hand, integration techniques used for the stiff problems require more timesteps but are more stable against the time-stepping choice.

These considerations are particularly relevant for the integration solved by OTIS. This is not only due to the accuracy of the integration, but also because the acceleration function being integrated is not constant, as it depends on interpolated values of the local Maxwellian distribution function that vary with BH position and velocity. To evaluate the integration performances depending on the timesteps, several tests have been carried out stressing OTIS with the same initial conditions but with different integrators, choosing among the `Scipy` integrators. In addition, the possibility to fix a maximum timestep for the integrations was also explored. The initial conditions adopted for this specific problem imply a BH of $M_{\rm BH} = 10^9$ initially at 20 kpc on a circular orbit around the NFW halo center. The NFW halo has the same characteristics as those specified in the Sect. 8.2.2. Figures C.1 and C.2 reports the results of these tests. Figure C.1 shows the time to solution for the different integrators, using `RK23, Radau, BDLF, LSODA` and `RK45`. Each bar is also color-coded according to the number of times the acceleration is evaluated, as different integrators adopt a different number of function evaluations. The number of timesteps performed by the integrator is written on top of each bar. Different panels correspond to different choices for the maximum allowed timestep, `MaxStep`.

In particular, the left panel corresponds to the default adaptive timestep of the integrator, while in the second and third panels we test the most stringent cases of `MaxStep`=0.05 and 0.01, respectively. Correspondingly, Fig. C.2 shows the results of the integration, in terms of distance of the BH to the halo center as a function of time. Remarkably, the default adaptive timestep choice

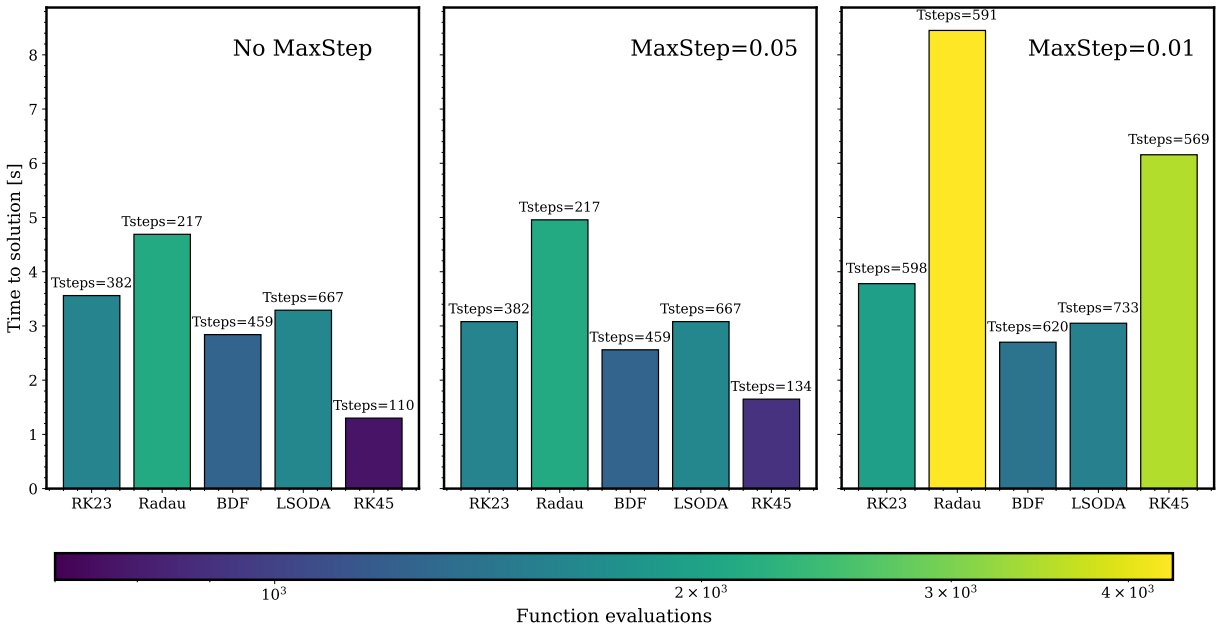

Figure C.1: *Time-to-solution (in seconds) for each integration method, color-coded by the number of function evaluations. Each group of bars corresponds to a different maximum allowed timestep, in Gyr: default (left), 0.05 (middle), and 0.01 (right). The number on top of each bar indicates the number of steps taken.*

of the integrator (left panel) produces a large variation in the results, as demonstrated in the left panel of Fig. C.2. The high-accuracy integrator `RK45`, in particular, predicts a significantly shorter merging timescale (less than 5 Gyr) compared to the other integrators, and reaches this value with the fewer timesteps. When decreasing the maximum timestep choice to 0.05 (central panel) all the integrators but `RK45` remain the same, `RK45` slightly increases the number of required timesteps and correspondingly its sinking timescale also increases. Finally, when further reducing the maximum timescale to 0.01, the integrators converge on the same sinking timescale value. Figure C.1 also shows that the `Radau` integrator is the most computationally expensive, both in terms of time to solution and number of function evaluations. However, the results using the `Radau` integrator remain the same, being suitable for stiff problems and generally stable against the timestep choice. The accurate `RK45` integrator, on the other hand, becomes progressively computationally more expensive as the maximum timestep decreases and is more sensitive to timestep limitations. The main bottleneck of the code is however the distribution function interpolaton rather than the integration itself. For this reason, the `Radau` technique is suggested, given its stability against changing the maximum timestep, at the cost of being computationally more expensive. Indeed, the `Radau` integrator yields already-converged solutions even without imposing a maximum timestep, unlike other methods which require a significant reduction of the maximum step size to achieve convergence, that in case of `RK45` leads to a significant higher time to solution. Anyway, Fig. C.2 shows that the results converge also when using different integrator posing limits on the maximum allowed timestep.

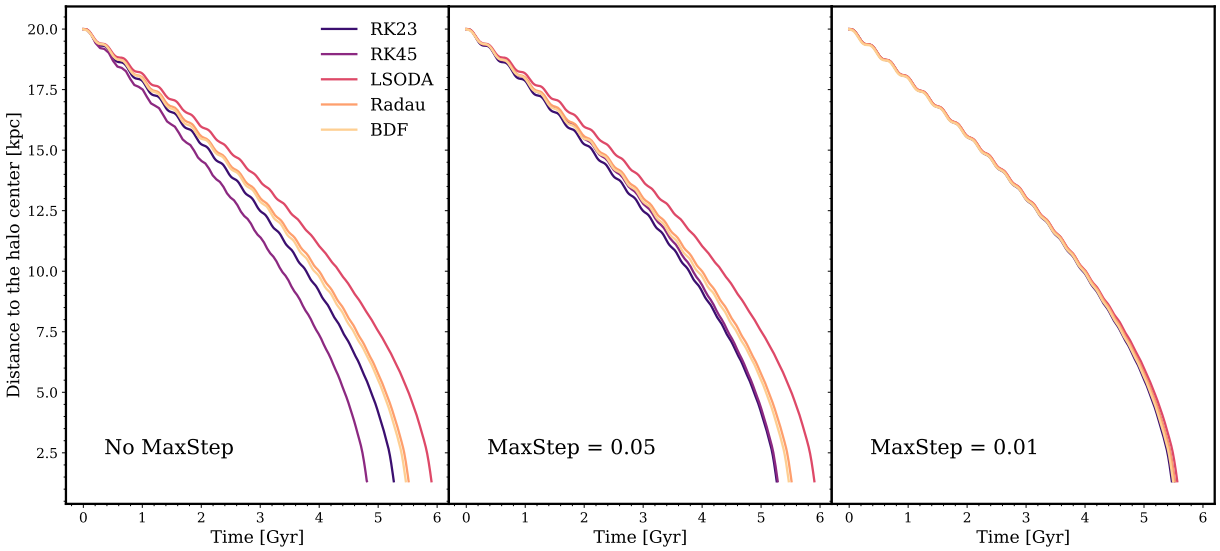

Figure C.2: *Distance of the black hole to the halo center as a function of time, for different integrators and timestep restrictions. From left to right: default adaptive steps, maximum timestep of 0.05 Gyr, maximum timestep of 0.01 Gyr.*

Appendix D

Infalling of a BH on an orbit with initial eccentricity

Section 8.1 demonstrates that for eccentric orbits, the DF has two effects: it circularises the orbit as it approaches the center, and shortens sinking timescales as eccentricity rises. Here, the effectiveness of the DF correction in capturing these effects is examined across different resolution levels.

Figure D.1 shows the BH distance from the halo center for an initial position of 20 kpc with varying orbital eccentricities: $e = 0.3$, $e = 0.5$, $e = 0.8$ in the first, second and third column, respectively. Each row shows the results of simulations with a different sampling of the same NFW halo, where resolution increases from top to bottom: $N_{\rm part} = 10^5$ in the first, 10^6 in the second, 10^7 in the third and $5 \cdot 10^7$ in the fourth row (the same halo realizations discussed in Sect. 8.3.1). Yellow and red lines indicate results from simulations using softening length according to P03 (see Eq.(8.27)) or Z19 (see Eq.(8.28)), respectively. Analytical expectations from OTIS (see Sect. 8.1.4) are shown as blue lines, obtained by setting $b_{\rm max} = r_s = 80$ kpc. Dotted lines represent the softening values of each resolution for P03 (yellow edge) and Z19 (red edge). All simulations incorporate the DF correction from D24 reported in Eq.(8.13). When sampling the halo with 10^5 particles, variations on the BH orbit with the eccentricity are more evident before the BH crosses the softening length value. Within the first 2 Gyrs, the orbits are more eccentric compared to the analytical predictions for $e = 0.3$ and less eccentric for $e = 0.8$. Switching from P03 to Z19 softening further reduces the distance to the halo center due to the lower softening value of Z19. However, at low resolution, distinguishing different orbits according to their eccentricities is not possible; even though the BH is bound within the softening range around the halo center, no clear trend of the sinking timescale with increasing eccentricity is detectable.

At higher resolutions, results from simulations align more closely with theoretical predictions and the sinking timescale becomes more sensitive to the initial orbital eccentricity. For simulations employing $N_{\rm part} = 10^6$ and 10^7 particles, numerical results increasingly approximate analytical expectations as eccentricity rises. Sinking timescales from simulation based on the from P03 softenings are slightly delayed compared to those employing the Z19 softenings.

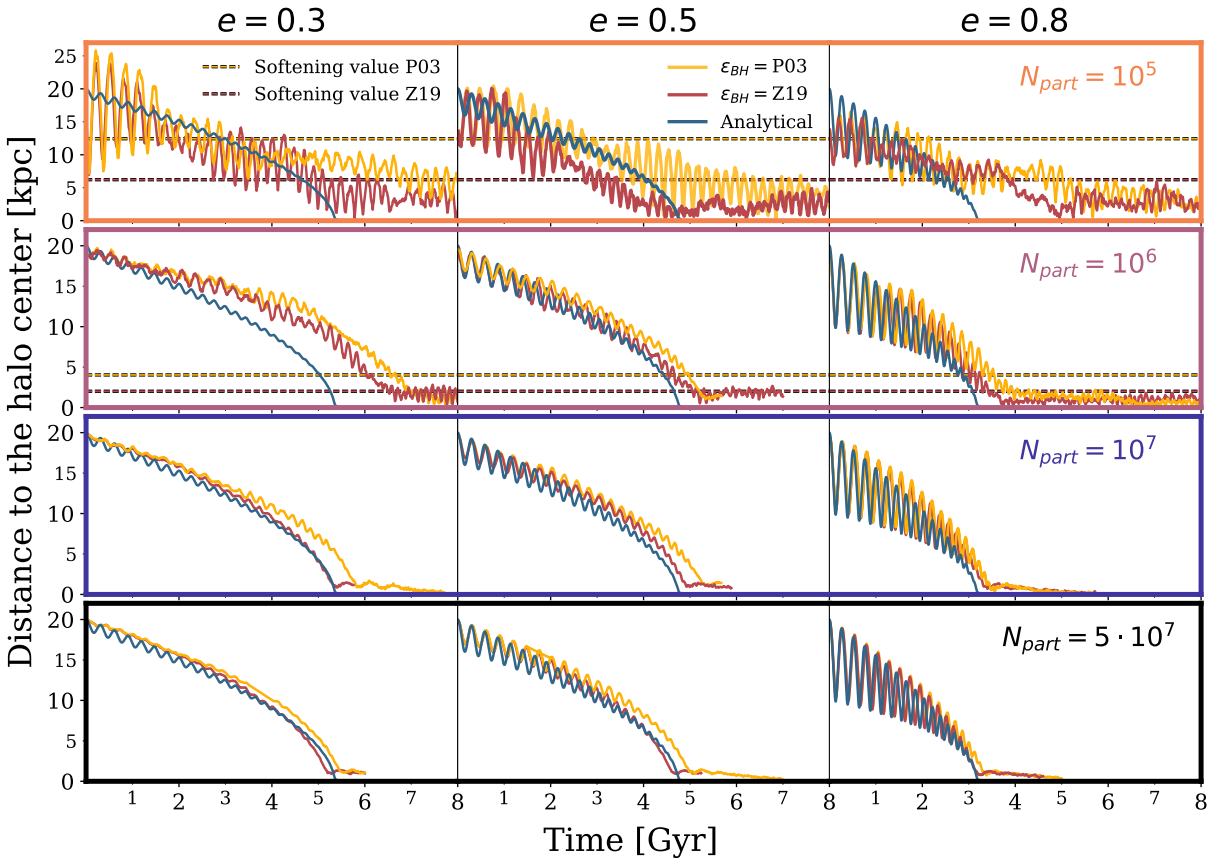

Figure D.1: *BH distance from the halo centre over time, starting from an initial position at 20 kpc, with orbital eccentricities* $e = 0.3, 0.5, 0.8$ *shown in the first, second, and third columns, respectively. Each row represents a different halo resolution:* $\mathrm{N_{part}} = 10^5, 10^6, 10^7, 5 \cdot 10^7$ *from top to bottom. Yellow lines show results for simulations with P03 softening lengths, and red lines indicate Z19 softenings. Analytical predictions for each orbital eccentricity are represented as a blue line. Dotted lines mark softening values for each resolution (yellow edge for P03, red edge for Z19). All simulations apply the DF correction from D24.*

Appendix E

The evolution of the BHLF: impact of the evaporation model

Figure 10.7 highlights a clear distinction between the models with evaporation (M4, M5, M6) and those without it (M1, M2, M3, M7; see Sect. 9.1). In the evaporation prescription, gas particles heated by AGN feedback above their SPH temperature are temporarily removed from the multiphase regime. They can re-enter the multiphase state only once their temperature cools back to the adiabat defined by the multiphase model (Eq. 5.62). As a result, the reservoir of cold gas available for BH accretion is reduced, since these *evaporated* particles no longer participate in the BH fueling and feedback loop.

Throughout Chapters 9 and 10, we have repeatedly emphasized the role of the cold gas reservoir in regulating BH accretion, and how its abundance drives the formation of massive BHs (see Sect. 10.2.2). It is therefore not surprising that the models with and without evaporation exhibit significantly different evolutionary behaviour, both in the BHLF (Fig. 10.7) and on the ingrated BH growth as shown by the BHMF (Fig. 10.9). In this Appendix, we investigate in more detail how these differences arise as a function of redshift and BH mass, with the aim of understanding why the two sets of models produce such distinct BH demographics.

To this end, we compare the time evolution of the BHLF in models M1 and M5. These models share the same feedback coupling factor ($\eta_f = 0.1/0.4$ in quasar/radio mode), and differ only by the inclusion of evaporation the in M5. Figures E.1 and E.2 present the BHLF for M1 and M5, respectively, at redshifts $z = 4, 3.42, 2.16, 1, 0.5$, and 0 (from top to bottom). The green curve shows the outcomes from whole BH population, while the orange, purple and blue curves show the results when including only BHs with $10^5 < M_{\rm BH}/M_\odot < 10^7$, $10^7 < M_{\rm BH}/M_\odot < 10^8$ and $10^8 < M_{\rm BH}/M_\odot < 10^{10}$, respectively. At $z = 0$, we also include the observational BHLF from Shen et al. (2020) (see Sect. 10.3). The comparison is restricted to the DIANOGA clusters simulated with both models.

At first glance, the impact of evaporation is substantial: the BH luminosities, direct tracers of accretion rates, differ significantly between the two models, especially at high redshift. In the M1 model, the BHLF from $z = 4$ to $z = 2$ features a prominent bump at $L_{\rm bol} \sim 10^{44} - 10^{45}\,{\rm erg\,s^{-1}}$, indicating a population of highly accreting BHs, dominated by BH masses below $10^7\,M_\odot$ till $L \simeq 10^{44}\,L_\odot$ and below $10^8\,M_\odot$ for higher luminosities. This feature is much milder in the M5 model, where the faint-end grows steadily from $z = 3.42$ to $z = 2$, and the population of

massive BHs ($M_{\rm BH} > 10^8\,M_\odot$) is less abundant and fainter. The difference thus stems from the strong influence of cold gas availability: without evaporation (M1), the cold gas at high redshift fuels rapid BH growth, producing the bright bump; with evaporation (M5), the reduced cold gas reservoir decreases this rapid BH growth.

Notably, this same bump appears in the local BHMF of all non-evaporation models (Figs. 10.8 and 10.9), confirming its origin in the rapid $z \sim 4$–2 BH growth that shapes the BHLF. Conversely, this bump is suppressed in all the evaporation models (M4, M5, M6 in Fig. 10.9) that also feature an enhanced low mass end, reflecting the more moderate early growth of BHs due to the reduced cold gas supply.

By $z \simeq 2.16$–1, the prominent bright-end bump in the M1 BHLF progressively smooths out. AGN (and possibly stellar) feedback reduces the abundance of luminous sources—predominantly powered by $M_{\rm BH} > 10^8\,M_\odot$ BHs—while simultaneously increasing the number of faint AGN.

Model M5 exhibits a qualitatively similar evolution, with a gradual depletion of the bright-end tail and a growing population of faint sources. However, unlike M1—where BHs of different masses contribute more uniformly to each luminosity bin, particularly at the faint end—M5 displays a clear mass segregation. At $z = 0$, BHs with $M_{\rm BH} < 10^7\,M_\odot$ dominate the faint end for $L_{\rm bol} \lesssim 2 \times 10^{42}\,{\rm erg\,s^{-1}}$, BHs with $10^7 < M_{\rm BH}/M_\odot < 10^8$ dominate the intermediate luminosity range $2 \times 10^{42} \lesssim L_{\rm bol} \lesssim 2 \times 10^{43}\,{\rm erg\,s^{-1}}$, while more massive BHs dominate the brighter bins.

As a consequence, the relatively bright and overpopulated high-luminosity end of the BHLF at $z = 0$ in M5 is primarily contributed by BHs with $M_{\rm BH} < 10^8\,M_\odot$ whose growth becomes inefficient at $z \lesssim 1$. When combined with the results presented in Chapter 9—and in particular Sect. 9.2.2 and Fig. 9.2b, which show enhanced star formation activity in simulations with evaporation—this suggests that the suppressed late-time growth of low-mass BHs may be driven by SN feedback, as proposed by Dubois et al. (2015). Confirming this scenario, however, requires dedicated follow-up analyses.

Overall, the redshift evolution of the BHLF analysed in this Appendix indicates that the overabundance of BHs in the M1 BHMF arises from widespread early overgrowth fueled by cold gas. This growth is significantly mitigated in the evaporation model (M5), leading to a milder evolution and, overall, to better agreement with observational constraints.

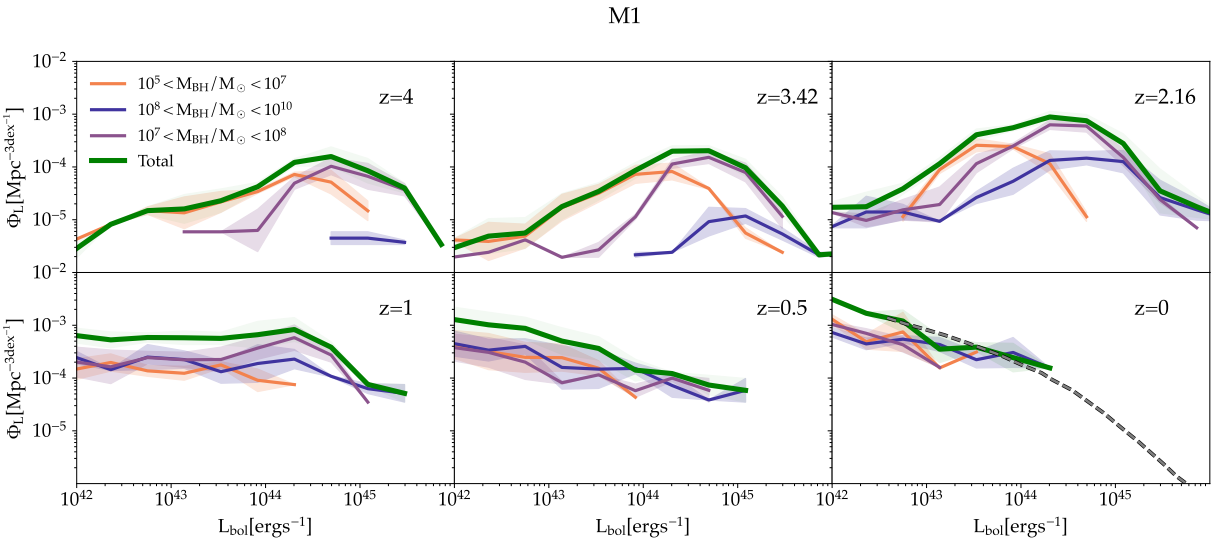

Figure E.1: *Evolution of the BHLF in the M1 model. From top to bottom, panels correspond to redshifts* $z = 4, 3.42, 2.16, 1, 0.5,$ *and* 0. *The green curve shows the BHLF for the full BH population, while the orange, purple, and blue curves show the contributions from BHs with* $10^5 < M_{BH}/M_\odot < 10^7$, $10^7 < M_{BH}/M_\odot < 10^8$, *and* $10^8 < M_{BH}/M_\odot < 10^{10}$, *respectively. At* $z = 0$, *the observational bolometric BHLF from Shen et al. (2020) is also shown.*

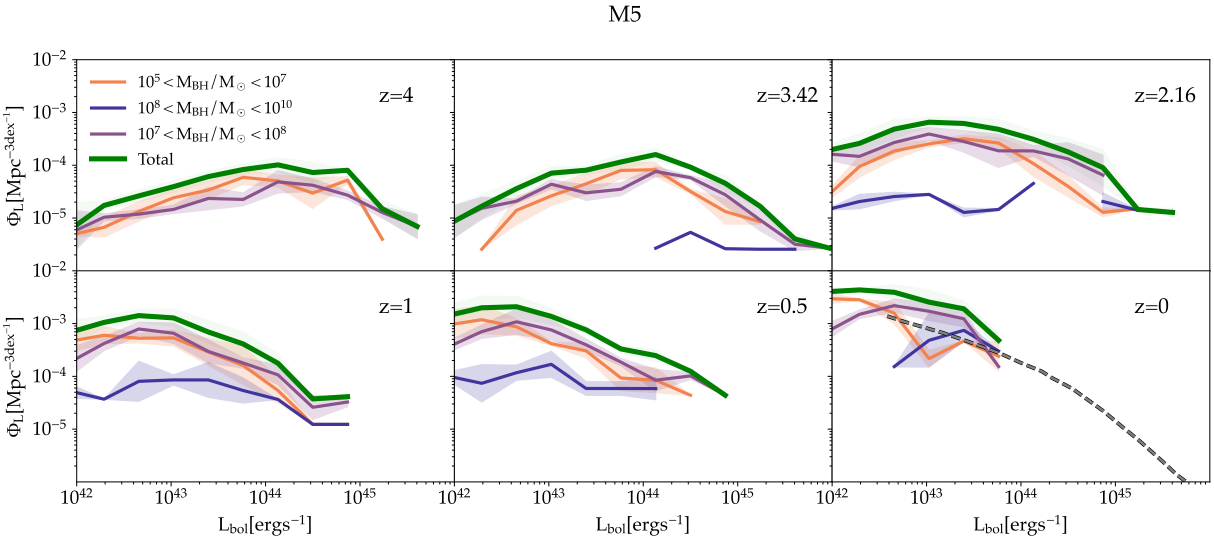

Figure E.2: *Same as Fig. E.1 but for the M5 model.*

Bibliography

B. P. Abbott, R. Abbott, T. D. Abbott, M. R. Abernathy, F. Acernese, K. Ackley, C. Adams, T. Adams, P. Addesso, R. X. Adhikari, V. B. Adya, C. Affeldt, M. Agathos, K. Agatsuma, N. Aggarwal, O. D. Aguiar, L. Aiello, A. Ain, P. Ajith, T. Akutsu, B. Allen, A. Allocca, P. A. Altin, A. Ananyeva, S. B. Anderson, W. G. Anderson, M. Ando, S. Appert, K. Arai, A. Araya, M. C. Araya, J. S. Areeda, N. Arnaud, K. G. Arun, H. Asada, S. Ascenzi, G. Ashton, Y. Aso, M. Ast, S. M. Aston, P. Astone, S. Atsuta, P. Aufmuth, C. Aulbert, A. Avila-Alvarez, K. Awai, S. Babak, P. Bacon, M. K. M. Bader, L. Baiotti, P. T. Baker, F. Baldaccini, G. Ballardin, S. W. Ballmer, J. C. Barayoga, S. E. Barclay, B. C. Barish, D. Barker, F. Barone, B. Barr, L. Barsotti, M. Barsuglia, D. Barta, J. Bartlett, M. A. Barton, I. Bartos, R. Bassiri, A. Basti, J. C. Batch, C. Baune, V. Bavigadda, M. Bazzan, B. Bécsy, C. Beer, M. Bejger, I. Belahcene, M. Belgin, A. S. Bell, B. K. Berger, G. Bergmann, C. P. L. Berry, D. Bersanetti, A. Bertolini, J. Betzwieser, S. Bhagwat, R. Bhandare, I. A. Bilenko, G. Billingsley, C. R. Billman, J. Birch, R. Birney, O. Birnholtz, S. Biscans, A. Bisht, M. Bitossi, C. Biwer, M. A. Bizouard, J. K. Blackburn, J. Blackman, C. D. Blair, D. G. Blair, R. M. Blair, S. Bloemen, O. Bock, M. Boer, G. Bogaert, A. Bohe, F. Bondu, R. Bonnand, B. A. Boom, R. Bork, V. Boschi, S. Bose, Y. Bouffanais, A. Bozzi, C. Bradaschia, P. R. Brady, V. B. Braginsky, M. Branchesi, J. E. Brau, T. Briant, A. Brillet, M. Brinkmann, V. Brisson, P. Brockill, J. E. Broida, A. F. Brooks, D. A. Brown, D. D. Brown, N. M. Brown, S. Brunett, C. C. Buchanan, A. Buikema, T. Bulik, H. J. Bulten, A. Buonanno, D. Buskulic, C. Buy, R. L. Byer, M. Cabero, L. Cadonati, G. Cagnoli, C. Cahillane, J. Calderón Bustillo, T. A. Callister, E. Calloni, J. B. Camp, K. C. Cannon, H. Cao, J. Cao, C. D. Capano, E. Capocasa, F. Carbognani, S. Caride, J. Casanueva Diaz, C. Casentini, S. Caudill, M. Cavaglià, F. Cavalier, R. Cavalieri, G. Cella, C. B. Cepeda, L. Cerboni Baiardi, G. Cerretani, E. Cesarini, S. J. Chamberlin, M. Chan, S. Chao, P. Charlton, E. Chassande-Mottin, B. D. Cheeseboro, H. Y. Chen, Y. Chen, H.-P. Cheng, A. Chincarini, A. Chiummo, T. Chmiel, H. S. Cho, M. Cho, J. H. Chow, N. Christensen, Q. Chu, A. J. K. Chua, S. Chua, S. Chung, G. Ciani, F. Clara, J. A. Clark, F. Cleva, C. Cocchieri, E. Coccia, P.-F. Cohadon, A. Colla, C. G. Collette, L. Cominsky, M. Constancio, L. Conti, S. J. Cooper, T. R. Corbitt, and N. Cornish. Prospects for observing and localizing gravitational-wave transients with Advanced LIGO, Advanced Virgo and KAGRA. *Living Reviews in Relativity*, 21 (1):3, December 2018. doi: 10.1007/s41114-018-0012-9.

Tom Abel, Greg L. Bryan, and Michael L. Norman. The formation and fragmentation of primordial molecular clouds. *The Astrophysical Journal*, 540(1):39–44, September 2000. ISSN 1538-4357. doi: 10.1086/309295. URL http://dx.doi.org/10.1086/309295.

Angela Adamo, Hakim Atek, Micaela B Bagley, Eduardo Bañados, Kirk SS Barrow, Danielle A

Berg, Rachel Bezanson, Maruša Bradač, Gabriel Brammer, Adam C Carnall, et al. The first billion years according to jwst. *Nature Astronomy*, pages 1–14, 2025.

J Aird, K Nandra, ES Laird, A Georgakakis, MLN Ashby, P Barmby, AL Coil, J-S Huang, AM Koekemoer, CC Steidel, et al. The evolution of the hard x-ray luminosity function of agn. *Monthly Notices of the Royal Astronomical Society*, 401(4):2531–2551, 2010.

J. Aird, A. L. Coil, A. Georgakakis, K. Nandra, G. Barro, and P. G. Pérez-González. The evolution of the X-ray luminosity functions of unabsorbed and absorbed AGNs out to z∼ 5. , 451(2): 1892–1927, August 2015. doi: 10.1093/mnras/stv1062.

Hollis B. Akins, Caitlin M. Casey, Erini Lambrides, Natalie Allen, Irham T. Andika, Malte Brinch, Jaclyn B. Champagne, Olivia Cooper, Xuheng Ding, Nicole E. Drakos, Andreas Faisst, Steven L. Finkelstein, Maximilien Franco, Seiji Fujimoto, Fabrizio Gentile, Steven Gillman, Ghassem Gozaliasl, Santosh Harish, Christopher C. Hayward, Michaela Hirschmann, Olivier Ilbert, Jeyhan S. Kartaltepe, Dale D. Kocevski, Anton M. Koekemoer, Vasily Kokorev, Daizhong Liu, Arianna S. Long, Henry Joy McCracken, Jed McKinney, Masafusa Onoue, Louise Paquereau, Alvio Renzini, Jason Rhodes, Brant E. Robertson, Marko Shuntov, John D. Silverman, Takumi S. Tanaka, Sune Toft, Benny Trakhtenbrot, Francesco Valentino, and Jorge Zavala. Cosmos-web: The over-abundance and physical nature of "little red dots"–implications for early galaxy and smbh assembly, 2024. URL https://arxiv.org/abs/2406.10341.

S. W. Allen, R. J. H. Dunn, A. C. Fabian, G. B. Taylor, and C. S. Reynolds. The relation between accretion rate and jet power in x-ray luminous elliptical galaxies. *Monthly Notices of the Royal Astronomical Society*, 372(1):21–30, October 2006. ISSN 1365-2966. doi: 10.1111/j.1365-2966.2006.10778.x. URL http://dx.doi.org/10.1111/j.1365-2966.2006.10778.x.

MC Aller and D Richstone. The cosmic density of massive black holes from galaxy velocitydispersions. *The Astronomical Journal*, 124(6):3035, 2002.

Marcelo A Alvarez, John H Wise, and Tom Abel. Accretion onto the first stellar-mass black holes. *The Astrophysical Journal*, 701(2):L133, 2009.

Pau Amaro-Seoane, Jeff Andrews, Manuel Arca Sedda, Abbas Askar, Quentin Baghi, Razvan Balasov, Imre Bartos, Simone S Bavera, Jillian Bellovary, Christopher PL Berry, et al. Astrophysics with the laser interferometer space antenna. *Living Reviews in Relativity*, 26(1):2, 2023.

A. Amorim, M. Bauböck, M. C. Bentz, W. Brandner, M. Bolzer, Y. Clénet, R. Davies, P. T. de Zeeuw, J. Dexter, A. Drescher, A. Eckart, F. Eisenhauer, N. M. Förster Schreiber, P. J. V. Garcia, R. Genzel, S. Gillessen, D. Gratadour, S. Hönig, D. Kaltenbrunner, M. Kishimoto, S. Lacour, D. Lutz, F. Millour, H. Netzer, C. A. Onken, T. Ott, T. Paumard, K. Perraut, G. Perrin, P. O. Petrucci, O. Pfuhl, M. A. Prieto, D. Rouan, J. Shangguan, T. Shimizu, J. Stadler, A. Sternberg, O. Straub, C. Straubmeier, R. Street, E. Sturm, L. J. Tacconi, K. R. W. Tristram, P. Vermot, S. von Fellenberg, F. Widmann, and J. Woillez. A geometric distance to the supermassive black hole of ngc 3783. *Astronomy amp; Astrophysics*, 654:A85, October 2021. ISSN 1432-0746. doi: 10.1051/0004-6361/202141426. URL http://dx.doi.org/10.1051/0004-6361/202141426.

Felipe Andrade-Santos, Christine Jones, William R. Forman, Lorenzo Lovisari, Alexey Vikhlinin, Reinout J. van Weeren, Stephen S. Murray, Monique Arnaud, Gabriel W. Pratt, Jessica Démoclès, Ralph Kraft, Pasquale Mazzotta, Hans Böhringer, Gayoung Chon, Simona Giacintucci, Tracy E. Clarke, Stefano Borgani, Larry David, Marian Douspis, Etienne Pointecouteau, Håkon Dahle, Shea Brown, Nabila Aghanim, and Elena Rasia. The Fraction of Cool-core Clusters in X-Ray versus SZ Samples Using Chandra Observations. , 843(1):76, July 2017. doi: 10.3847/1538-4357/aa7461.

Daniel Anglés-Alcázar, Romeel Davé, Claude-André Faucher-Giguère, Feryal Özel, and Philip F. Hopkins. Gravitational torque-driven black hole growth and feedback in cosmological simulations. , 464(3):2840–2853, January 2017. doi: 10.1093/mnras/stw2565.

J. Antoniadis, S. Babak, A.-S. Bak Nielsen, C. G. Bassa, A. Berthereau, M. Bonetti, E. Bortolas, P. R. Brook, M. Burgay, R. N. Caballero, A. Chalumeau, D. J. Champion, S. Chianlaridis, S. Chen, I. Cognard, G. Desvignes, M. Falxa, R. D. Ferdman, A. Franchini, J. R. Gair, B. Goncharov, E. Graikou, J.-M. Grießmeier, L. Guillemot, Y. J. Guo, H. Hu, F. Iraci, D. Izquierdo-Villalba, J. Jang, J. Jawor, G. H. Janssen, A. Jessner, R. Karuppusamy, E. F. Keane, M. J. Keith, M. Kramer, M. A. Krishnakumar, K. Lackeos, K. J. Lee, K. Liu, Y. Liu, A. G. Lyne, J. W. McKee, R. A. Main, M. B. Mickaliger, I. C. Niţu, A. Parthasarathy, B. B. P. Perera, D. Perrodin, A. Petiteau, N. K. Porayko, A. Possenti, H. Quelquejay Leclere, A. Samajdar, S. A. Sanidas, A. Sesana, G. Shaifullah, L. Speri, R. Spiewak, B. W. Stappers, S. C. Susarla, G. Theureau, C. Tiburzi, E. van der Wateren, A. Vecchio, V. Venkatraman Krishnan, J. P. W. Verbiest, J. Wang, L. Wang, and Z. Wu. The second data release from the european pulsar timing array: I. the dataset and timing analysis. *Astronomy amp; Astrophysics*, 678:A48, October 2023. ISSN 1432-0746. doi: 10.1051/0004-6361/202346841. URL http://dx.doi.org/10.1051/0004-6361/202346841.

Fabio Antonini and David Merritt. Dynamical friction around supermassive black holes. *ApJ*, 745 (1):83, 2011.

Robert Antonucci. Unified models for active galactic nuclei and quasars. , 31:473–521, January 1993. doi: 10.1146/annurev.aa.31.090193.002353.

Philip J Armitage and Priyamvada Natarajan. Accretion during the merger of supermassive black holes. *The Astrophysical Journal*, 567(1):L9, 2002.

Pawel Artymowicz and Stephen H Lubow. Dynamics of binary-disk interaction. 1: Resonances and disk gap sizes. *Astrophysical Journal, Part 1 (ISSN 0004-637X), vol. 421, no. 2, p. 651-667*, 421:651–667, 1994.

Pawel Artymowicz and Stephen H Lubow. Mass flow through gaps in circumbinary disks. *The Astrophysical Journal*, 467(2):L77, 1996.

D. Asmus, S. F. Hönig, and P. Gandhi. The subarcsecond mid-infrared view of local active galactic nuclei. iii. polar dust emission*. *The Astrophysical Journal*, 822(2):109, May 2016. ISSN 1538-4357. doi: 10.3847/0004-637x/822/2/109. URL http://dx.doi.org/10.3847/0004-637X/822/2/109.

R. J. Assef, D. Stern, C. S. Kochanek, A. W. Blain, M. Brodwin, M. J. I. Brown, E. Donoso, P. R. M. Eisenhardt, B. T. Jannuzi, T. H. Jarrett, S. A. Stanford, C. W. Tsai, J. Wu, and L. Yan. Mid-infrared Selection of Active Galactic Nuclei with the Wide-field Infrared Survey Explorer. II. Properties of WISE-selected Active Galactic Nuclei in the NDWFS Boötes Field. , 772(1):26, July 2013. doi: 10.1088/0004-637X/772/1/26.

A. Audibert, C. Ramos Almeida, S. García-Burillo, F. Combes, M. Bischetti, M. Meenakshi, D. Mukherjee, G. Bicknell, and A. Y. Wagner. Jet-induced molecular gas excitation and turbulence in the Teacup. , 671:L12, March 2023. doi: 10.1051/0004-6361/202345964.

Yannick M Bahé, Joop Schaye, Matthieu Schaller, Richard G Bower, Josh Borrow, Evgenii Chaikin, Roi Kugel, Folkert Nobels, and Sylvia Ploeckinger. The importance of black hole repositioning for galaxy formation simulations. *Monthly Notices of the Royal Astronomical Society*, 516(1):167–184, 2022.

B. Balmaverde, A. Capetti, A. Marconi, G. Venturi, M. Chiaberge, R. D. Baldi, S. Baum, R. Gilli, P. Grandi, E. Meyer, G. Miley, C. O'Dea, W. Sparks, E. Torresi, and G. Tremblay. The murales survey: I. a dual agn in the radio galaxy 3c 459? *Astronomy amp; Astrophysics*, 619:A83, November 2018. ISSN 1432-0746. doi: 10.1051/0004-6361/201833515. URL http://dx.doi.org/10.1051/0004-6361/201833515.

Dinshaw S Balsara. Von neumann stability analysis of smoothed particle hydrodynamics—suggestions for optimal algorithms. *Journal of Computational Physics*, 121(2):357–372, 1995.

Paramita Barai, Giuseppe Murante, Stefano Borgani, Massimo Gaspari, Gian Luigi Granato, Pierluigi Monaco, and Cinthia Ragone-Figueroa. Kinetic agn feedback effects on cluster cool cores simulated using sph. *Monthly Notices of the Royal Astronomical Society*, 461(2):1548–1567, 2016.

AJ Barger and LL Cowie. The number density of intermediate-and high-luminosity active galactic nuclei at z˜ 2-3. *The Astrophysical Journal*, 635(1):115, 2005.

Luis Gabriel C Bariuan, Bradford Snios, Małgosia Sobolewska, Aneta Siemiginowska, and Daniel A Schwartz. The fundamental planes of black hole activity for radio-loud and radio-quiet quasars. *Monthly Notices of the Royal Astronomical Society*, 513(4):4673–4681, April 2022. ISSN 1365-2966. doi: 10.1093/mnras/stac1153. URL http://dx.doi.org/10.1093/mnras/stac1153.

CL Barlow-Hall and J Aird. Measurements of the z= 4-10 x-ray luminosity function: the high space density of moderate-luminosity, obscured agn. *arXiv preprint arXiv:2506.16145*, 2025.

Josh Barnes and Piet Hut. A hierarchical o (n log n) force-calculation algorithm. *nature*, 324 (6096):446–449, 1986.

Joshua E. Barnes. Gravitational softening as a smoothing operation: Softening as smoothing. *Monthly Notices of the Royal Astronomical Society*, 425(2):1104–1120, August 2012. ISSN 0035-8711. doi: 10.1111/j.1365-2966.2012.21462.x. URL http://dx.doi.org/10.1111/j.1365-2966.2012.21462.x.

Joshua E Barnes and Lars Hernquist. Dynamics of interacting galaxies. *In: Annual review of astronomy and astrophysics. Vol. 30 (A93-25826 09-90), p. 705-742.*, 30:705–742, 1992.

Joshua E. Barnes and Lars Hernquist. Transformations of Galaxies. II. Gasdynamics in Merging Disk Galaxies. , 471:115, November 1996. doi: 10.1086/177957.

R Scott Barrows, Mar Mezcua, and Julia M Comerford. A catalog of hyper-luminous x-ray sources and intermediate-mass black hole candidates out to high redshifts. *The Astrophysical Journal*, 882(2):181, 2019.

R. Scott Barrows, Julia M. Comerford, Daniel Stern, and Roberto J. Assef. A census of wise-selected dual and offset agns across the sky: New constraints on merger-driven triggering of obscured agns. *The Astrophysical Journal*, 951(2):92, July 2023. ISSN 1538-4357. doi: 10.3847/1538-4357/acd2d3. URL http://dx.doi.org/10.3847/1538-4357/acd2d3.

R. Scott Barrows, Julia M. Comerford, James Negus, and Francisco Muller-Sanchez. Recoiling Black Hole Candidates from Spatially Offset Broad Emission Lines in MaNGA. , 992(1):38, October 2025. doi: 10.3847/1538-4357/adfbf3.

L. Bassini, E. Rasia, S. Borgani, C. Ragone-Figueroa, V. Biffi, K. Dolag, M. Gaspari, G. L. Granato, G. Murante, G. Taffoni, and L. Tornatore. Black hole mass of central galaxies and cluster mass correlation in cosmological hydro-dynamical simulations. , 630:A144, October 2019. doi: 10.1051/0004-6361/201935383.

L. Bassini, E. Rasia, S. Borgani, G. L. Granato, C. Ragone-Figueroa, V. Biffi, A. Ragagnin, K. Dolag, W. Lin, G. Murante, N. R. Napolitano, G. Taffoni, L. Tornatore, and Y. Wang. The DIANOGA simulations of galaxy clusters: characterising star formation in protoclusters. , 642: A37, October 2020. doi: 10.1051/0004-6361/202038396.

LUIGI Bassini, Elena Rasia, Stefano Borgani, Gian Luigi Granato, C Ragone-Figueroa, V Biffi, A Ragagnin, K Dolag, W Lin, G Murante, et al. The dianoga simulations of galaxy clusters: characterising star formation in protoclusters. *Astronomy & Astrophysics*, 642:A37, 2020.

Andreas Bauer and Volker Springel. Subsonic turbulence in smoothed particle hydrodynamics and moving-mesh simulations. *Monthly Notices of the Royal Astronomical Society*, 423(3): 2558–2578, 2012.

F. E. Bauer, A. C. Fabian, J. S. Sanders, S. W. Allen, and R. M. Johnstone. The prevalence of cooling cores in clusters of galaxies atz 0.15-0.4. *Monthly Notices of the Royal Astronomical Society*, 359(4):1481–1490, June 2005. ISSN 1365-2966. doi: 10.1111/j.1365-2966.2005.08999.x. URL http://dx.doi.org/10.1111/j.1365-2966.2005.08999.x.

A. M. Beck, G. Murante, A. Arth, R. S. Remus, A. F. Teklu, J. M. F. Donnert, S. Planelles, M. C. Beck, P. Foerster, M. Imgrund, K. Dolag, and S. Borgani. An improved sph scheme for cosmological simulations, 2015. URL https://arxiv.org/abs/1502.07358.

M. C. Begelman, R. D. Blandford, and M. J. Rees. Massive black hole binaries in active galactic nuclei. , 287(5780):307–309, September 1980. doi: 10.1038/287307a0.

Mitchell C Begelman and Jason Dexter. Little red dots as late-stage quasi-stars. *arXiv preprint arXiv:2507.09085*, 2025.

Mitchell C Begelman, Roger D Blandford, and Martin J Rees. Theory of extragalactic radio sources. *Reviews of Modern Physics*, 56(2):255, 1984.

Mitchell C Begelman, Marta Volonteri, and Martin J Rees. Formation of supermassive black holes by direct collapse in pre-galactic haloes. *Monthly Notices of the Royal Astronomical Society*, 370(1):289–298, 2006.

Mitchell C. Begelman, Elena M. Rossi, and Philip J. Armitage. Quasi-stars: accreting black holes inside massive envelopes. *Monthly Notices of the Royal Astronomical Society*, 387(4): 1649–1659, July 2008. ISSN 1365-2966. doi: 10.1111/j.1365-2966.2008.13344.x. URL http://dx.doi.org/10.1111/j.1365-2966.2008.13344.x.

Eric C. Bellm, Shrinivas R. Kulkarni, Matthew J. Graham, Richard Dekany, Roger M. Smith, Reed Riddle, Frank J. Masci, George Helou, Thomas A. Prince, Scott M. Adams, C. Barbarino, Tom Barlow, James Bauer, Ron Beck, Justin Belicki, Rahul Biswas, Nadejda Blagorodnova, Dennis Bodewits, Bryce Bolin, Valery Brinnel, Tim Brooke, Brian Bue, Mattia Bulla, Rick Burruss, S. Bradley Cenko, Chan-Kao Chang, Andrew Connolly, Michael Coughlin, John Cromer, Virginia Cunningham, Kishalay De, Alex Delacroix, Vandana Desai, Dmitry A. Duev, Gwendolyn Eadie, Tony L. Farnham, Michael Feeney, Ulrich Feindt, David Flynn, Anna Franckowiak, S. Frederick, C. Fremling, Avishay Gal-Yam, Suvi Gezari, Matteo Giomi, Daniel A. Goldstein, V. Zach Golkhou, Ariel Goobar, Steven Groom, Eugean Hacopians, David Hale, John Henning, Anna Y. Q. Ho, David Hover, Justin Howell, Tiara Hung, Daniela Huppenkothen, David Imel, Wing-Huen Ip, Željko Ivezić, Edward Jackson, Lynne Jones, Mario Juric, Mansi M. Kasliwal, S. Kaspi, Stephen Kaye, Michael S. P. Kelley, Marek Kowalski, Emily Kramer, Thomas Kupfer, Walter Landry, Russ R. Laher, Chien-De Lee, Hsing Wen Lin, Zhong-Yi Lin, Ragnhild Lunnan, Matteo Giomi, Ashish Mahabal, Peter Mao, Adam A. Miller, Serge Monkewitz, Patrick Murphy, Chow-Choong Ngeow, Jakob Nordin, Peter Nugent, Eran Ofek, Maria T. Patterson, Bryan Penprase, Michael Porter, Ludwig Rauch, Umaa Rebbapragada, Dan Reiley, Mickael Rigault, Hector Rodriguez, Jan van Roestel, Ben Rusholme, Jakob van Santen, S. Schulze, David L. Shupe, Leo P. Singer, Maayane T. Soumagnac, Robert Stein, Jason Surace, Jesper Sollerman, Paula Szkody, F. Taddia, Scott Terek, Angela Van Sistine, Sjoert van Velzen, W. Thomas Vestrand, Richard Walters, Charlotte Ward, Quan-Zhi Ye, Po-Chieh Yu, Lin Yan, and Jeffry Zolkower. The Zwicky Transient Facility: System Overview, Performance, and First Results. , 131(995):018002, January 2019. doi: 10.1088/1538-3873/aaecbe.

Jillian M Bellovary, Fabio Governato, Thomas R Quinn, James Wadsley, Sijing Shen, and Marta Volonteri. Wandering black holes in bright disk galaxy halos. *The Astrophysical Journal Letters*, 721(2):L148, 2010.

Jillian M Bellovary, Colleen E Cleary, Ferah Munshi, Michael Tremmel, Charlotte R Christensen, Alyson Brooks, and Thomas R Quinn. Multimessenger signatures of massive black holes in dwarf galaxies. *Monthly Notices of the Royal Astronomical Society*, October 2018. ISSN 1365-2966. doi: 10.1093/mnras/sty2842. URL http://dx.doi.org/10.1093/mnras/sty2842.

Jillian M Bellovary, Sarra Hayoune, Katheryn Chafla, Donovan Vincent, Alyson Brooks, Charlotte R Christensen, Ferah D Munshi, Michael Tremmel, Thomas R Quinn, Jordan Van Nest, Serena K Sligh, and Michelle Luzuriaga. The origins of off-centre massive black holes in dwarf galaxies. *Monthly Notices of the Royal Astronomical Society*, 505(4):5129–5141, June 2021. ISSN 1365-2966. doi: 10.1093/mnras/stab1665. URL http://dx.doi.org/10.1093/mnras/stab1665.

R. Bender and J. L. Nieto. Internal kinematics of low-luminosity ellipsoidal galaxies. , 239:97–112, November 1990.

Vardha N Bennert, Tommaso Treu, Matthew W Auger, Maren Cosens, Daeseong Park, Rebecca Rosen, Chelsea E Harris, Matthew A Malkan, and Jong-Hak Woo. A local baseline of the black hole mass scaling relations for active galaxies. iii. the bh mass-

\

sigma *relation. arXiv preprint arXiv:1409.4428*, 2014.

Vardha N. Bennert, Tommaso Treu, Xuheng Ding, Isak Stomberg, Simon Birrer, Tomas Snyder, Matthew A. Malkan, Andrew W. Stephens, and Matthew W. Auger. A local baseline of the black hole mass scaling relations for active galaxies. iv. correlations between m bh and host galaxy , stellar mass, and luminosity. *The Astrophysical Journal*, 921(1):36, October 2021. ISSN 1538-4357. doi: 10.3847/1538-4357/ac151a. URL http://dx.doi.org/10.3847/1538-4357/ac151a.

Vardha Nicola Bennert, Matthew W Auger, Tommaso Treu, Jong-Hak Woo, and Matthew A Malkan. A local baseline of the black hole mass scaling relations for active galaxies. i. methodology and results of pilot study. *The Astrophysical Journal*, 726(2):59, 2011.

Peter Berczik, David Merritt, Rainer Spurzem, and Hans-Peter Bischof. Efficient merger of binary supermassive black holes in nonaxisymmetric galaxies. *The Astrophysical Journal*, 642(1):L21, 2006.

V. Bharadwaj, T. H. Reiprich, G. Schellenberger, H. J. Eckmiller, R. Mittal, and H. Israel. Intracluster medium cooling, AGN feedback, and brightest cluster galaxy properties of galaxy groups. Five properties where groups differ from clusters. , 572:A46, December 2014. doi: 10.1051/0004-6361/201322684.

Aklant K Bhowmick, Laura Blecha, Paul Torrey, Luke Zoltan Kelley, Mark Vogelsberger, Dylan Nelson, Rainer Weinberger, and Lars Hernquist. Impact of gas spin and lyman–werner flux on black hole seed formation in cosmological simulations: implications for direct collapse. *Monthly Notices of the Royal Astronomical Society*, 510(1):177–196, November 2021. ISSN 1365-2966. doi: 10.1093/mnras/stab3439. URL http://dx.doi.org/10.1093/mnras/stab3439.

Aklant K Bhowmick, Laura Blecha, Paul Torrey, Luke Zoltan Kelley, Rainer Weinberger, Mark Vogelsberger, Lars Hernquist, Rachel S Somerville, and Analis Eolyn Evans. Introducing the brahma simulation suite: signatures of low-mass black hole seeding models in cosmological simulations. *Monthly Notices of the Royal Astronomical Society*, 531(4):4311–4335, 2024.

Stefano Bianchi, Roberto Maiolino, and Guido Risaliti. Agn obscuration and the unified model. *Advances in Astronomy*, 2012:1–17, 2012. ISSN 1687-7977. doi: 10.1155/2012/782030. URL http://dx.doi.org/10.1155/2012/782030.

James Binney and Scott Tremaine. *Galactic Dynamics*. Princeton University Press, 1987. ISBN 978-0-691-08444-2. Google-Books-ID: FtNftAEACAAJ.

James Binney and Scott Tremaine. *Galactic Dynamics: Second Edition*. Princeton University Press, October 2011. ISBN 978-1-4008-2872-2. Google-Books-ID: 6mF4CKxlbLsC.

Simeon Bird, Yueying Ni, Tiziana Di Matteo, Rupert Croft, Yu Feng, and Nianyi Chen. The astrid simulation: galaxy formation and reionization. *Monthly Notices of the Royal Astronomical Society*, 512(3):3703–3716, 2022.

L. Birzan, D. A. Rafferty, P. E. J. Nulsen, B. R. McNamara, H. J. A. Rottgering, M. W. Wise, and R. Mittal. The duty cycle of radio-mode feedback in complete samples of clusters. *Monthly Notices of the Royal Astronomical Society*, 427(4):3468–3488, December 2012. ISSN 1365-2966. doi: 10.1111/j.1365-2966.2012.22083.x. URL http://dx.doi.org/10.1111/j.1365-2966.2012.22083.x.

M. Bischetti, C. Feruglio, E. Piconcelli, F. Duras, M. Pérez-Torres, R. Herrero, G. Venturi, S. Carniani, G. Bruni, I. Gavignaud, V. Testa, A. Bongiorno, M. Brusa, C. Circosta, G. Cresci, V. D'Odorico, R. Maiolino, A. Marconi, M. Mingozzi, C. Pappalardo, M. Perna, E. Traianou, A. Travascio, G. Vietri, L. Zappacosta, and F. Fiore. The WISSH quasars project. IX. Cold gas content and environment of luminous QSOs at z $\sim$ 2.4-4.7. , 645:A33, January 2021. doi: 10.1051/0004-6361/202039057.

R. D. Blandford and M. J. Rees. Extended and compact extragalactic radio sources: interpretation and theory. , 17:265–274, March 1978. doi: 10.1088/0031-8949/17/3/020.

Paul Bode, Jeremiah P Ostriker, and Guohong Xu. The tree particle-mesh n-body gravity solver. *The Astrophysical Journal Supplement Series*, 128(2):561, 2000.

H. Boehringer. ROSAT observations of galaxy clusters and cosmological implications. *Advances in Space Research*, 13(12):181–190, December 1993. doi: 10.1016/0273-1177(93)90110-W.

Benjamin D. Boizelle, Aaron J. Barth, Jonelle L. Walsh, David A. Buote, Andrew J. Baker, Jeremy Darling, and Luis C. Ho. A Precision Measurement of the Mass of the Black Hole in NGC 3258 from High-resolution ALMA Observations of Its Circumnuclear Disk. , 881(1):10, August 2019. doi: 10.3847/1538-4357/ab2a0a.

Mark Bolden and Paul Kervin. Panoramic-Survey Telescope And Rapid Response System: Leveraging Astronomical Technology for Satellite Situational Awareness. In *38th COSPAR Scientific Assembly*, volume 38, page 3, January 2010.

A. Bonafede, K. Dolag, F. Stasyszyn, G. Murante, and S. Borgani. A non-ideal magnetohydrodynamic gadget: simulating massive galaxy clusters. , 418(4):2234–2250, nov 2011. doi: 10.1111/j.1365-2966.2011.19523.x. URL https://doi.org/10.1111%2Fj.1365-2966.2011.19523.x.

H. Bondi. On spherically symmetrical accretion. , 112:195, January 1952. doi: 10.1093/mnras/112.2.195.

Matteo Bonetti, Francesco Haardt, Alberto Sesana, and Enrico Barausse. Post-Newtonian evolution of massive black hole triplets in galactic nuclei - II. Survey of the parameter space. , 477(3): 3910–3926, July 2018. doi: 10.1093/mnras/sty896.

Matteo Bonetti, Elisa Bortolas, Alessandro Lupi, Massimo Dotti, and Sandra I. Raimundo. Dynamical friction-driven orbital circularisation in rotating discs: a semi-analytical description. *MNRAS*, 494(2):3053–3059, May 2020. ISSN 0035-8711, 1365-2966. doi: 10.1093/mnras/staa964. URL http://arxiv.org/abs/2002.04621. arXiv:2002.04621 [astro-ph].

A. Bongiorno, A. Schulze, A. Merloni, G. Zamorani, O. Ilbert, F. La Franca, Y. Peng, E. Piconcelli, V. Mainieri, J. D. Silverman, M. Brusa, F. Fiore, M. Salvato, and N. Scoville. Agn host galaxy mass function in cosmos: Is agn feedback responsible for the mass-quenching of galaxies? *Astronomy amp; Astrophysics*, 588:A78, March 2016. ISSN 1432-0746. doi: 10.1051/0004-6361/201527436. URL http://dx.doi.org/10.1051/0004-6361/201527436.

CM Booth and Joop Schaye. Cosmological simulations of the growth of supermassive black holes and feedback from active galactic nuclei: method and tests. *Monthly Notices of the Royal Astronomical Society*, 398(1):53–74, 2009.

Elisa Bortolas, Pedro R Capelo, Tommaso Zana, Lucio Mayer, Matteo Bonetti, Massimo Dotti, Melvyn B Davies, and Piero Madau. Global torques and stochasticity as the drivers of massive black hole pairing in the young universe. *MNRAS*, 498(3):3601–3615, 2020.

Matteo Boschini, Davide Gerosa, Om Sharan Salafia, and Massimo Dotti. Astrophysical and relativistic modeling of the recoiling black hole candidate in quasar 3C 186. , 686:A245, June 2024. doi: 10.1051/0004-6361/202449596.

Rychard J Bouwens, Eduardo Banados, Roberto Decarli, Joseph Hennawi, Daming Yang, Hiddo Algera, Manuel Aravena, Emanuele Farina, Anniek Gloudemans, Jacqueline Hodge, et al. Beneath the surface:> 85% of z> 5.9 qsos in massive host galaxies are uv-faint. *arXiv preprint arXiv:2506.24128*, 2025.

Dennis B. Bowen, Vassilios Mewes, Manuela Campanelli, Scott C. Noble, Julian H. Krolik, and Miguel Zilhão. Quasi-periodic behavior of mini-disks in binary black holes approaching merger. *The Astrophysical Journal Letters*, 853(1):L17, January 2018. ISSN 2041-8213. doi: 10.3847/2041-8213/aaa756. URL http://dx.doi.org/10.3847/2041-8213/aaa756.

Dennis B. Bowen, Vassilios Mewes, Scott C. Noble, Mark Avara, Manuela Campanelli, and Julian H. Krolik. Quasi-periodicity of supermassive binary black hole accretion approaching merger. *The Astrophysical Journal*, 879(2):76, July 2019. ISSN 1538-4357. doi: 10.3847/1538-4357/ab2453. URL http://dx.doi.org/10.3847/1538-4357/ab2453.

W. N. Brandt and D. M. Alexander. Cosmic x-ray surveys of distant active galaxies: The demographics, physics, and ecology of growing supermassive black holes. *The Astronomy and Astro-*

physics Review, 23(1), January 2015. ISSN 1432-0754. doi: 10.1007/s00159-014-0081-z. URL http://dx.doi.org/10.1007/s00159-014-0081-z.

Volker Bromm, Paolo S. Coppi, and Richard B. Larson. Forming the First Stars in the Universe: The Fragmentation of Primordial Gas. , 527(1):L5–L8, December 1999. doi: 10.1086/312385.

M. Brusa, C. Feruglio, G. Cresci, V. Mainieri, M. T. Sargent, M. Perna, P. Santini, F. Vito, A. Marconi, A. Merloni, D. Lutz, E. Piconcelli, G. Lanzuisi, R. Maiolino, D. Rosario, E. Daddi, A. Bongiorno, F. Fiore, and E. Lusso. Evidence for feedback in action from the molecular gas content in the z ~1.6 outflowing QSO XID2028. , 578:A11, June 2015. doi: 10.1051/0004-6361/201425491.

Greg L Bryan, Michael L Norman, Brian W O'Shea, Tom Abel, John H Wise, Matthew J Turk, Daniel R Reynolds, David C Collins, Peng Wang, Samuel W Skillman, et al. Enzo: An adaptive mesh refinement code for astrophysics. *The Astrophysical Journal Supplement Series*, 211(2):19, 2014.

David A. Buote. On the Origin of Radio Halos in Galaxy Clusters. , 553(1):L15–L18, May 2001. doi: 10.1086/320500.

Jan D Burger, Volker Springel, Eve C Ostriker, Chang-Goo Kim, Sarah MR Jeffreson, Matthew C Smith, Rüdiger Pakmor, Sultan Hassan, Drummond Fielding, Lars Hernquist, et al. Applying a star formation model calibrated on high-resolution interstellar medium simulations to cosmological simulations of galaxy formation. *Monthly Notices of the Royal Astronomical Society*, 544(2):1390–1411, 2025.

Jack O. Burns, Eric J. Hallman, Brennan Gantner, Patrick M. Motl, and Michael L. Norman. Why Do Only Some Galaxy Clusters Have Cool Cores? , 675(2):1125–1140, March 2008. doi: 10.1086/526514.

J.O. Burns, E.J. Hallman, B. Gantner, P.M. Motl, and M. L. Norman. *Beyond the Cool Core: The Formation of Cool Core Galaxy Clusters*, page 349–354. Springer Berlin Heidelberg, 2006. ISBN 9783540734840. doi: 10.1007/978-3-540-73484-0_63. URL http://dx.doi.org/10.1007/978-3-540-73484-0_63.

Stephanie Buttigieg, Debora Sijacki, Christopher J Moore, and Martin A Bourne. Premature supermassive black hole mergers in cosmological simulations of structure formation. *Monthly Notices of the Royal Astronomical Society*, 542(3):2019–2038, 2025.

Turgay Caglar, Leonard Burtscher, Bernhard Brandl, Jarle Brinchmann, Richard I. Davies, Erin K. S. Hicks, Michael Koss, Ming-Yi Lin, Witold Maciejewski, Francisco Müller-Sánchez, Rogemar A. Riffel, Rogério Riffel, David J. Rosario, Marc Schartmann, Allan Schnorr-Müller, T. Taro Shimizu, Thaisa Storchi-Bergmann, Sylvain Veilleux, Gilles Orban de Xivry, and Vardha N. Bennert. LLAMA: The M_{BH}-$\sigma_\star$ relation of the most luminous local AGNs. , 634:A114, February 2020. doi: 10.1051/0004-6361/201936321.

Simone Callegari, Lucio Mayer, Stelios Kazantzidis, Monica Colpi, Fabio Governato, Thomas Quinn, and James Wadsley. Pairing of supermassive black holes in unequal-mass galaxy mergers. *The Astrophysical Journal*, 696(1):L89, 2009.

Simone Callegari, Stelios Kazantzidis, Lucio Mayer, Monica Colpi, Jillian M Bellovary, Thomas Quinn, and James Wadsley. Growing massive black hole pairs in minor mergers of disk galaxies. *The Astrophysical Journal*, 729(2):85, 2011.

Manuela Campanelli, Carlos Lousto, Yosef Zlochower, and David Merritt. Large merger recoils and spin flips from generic black hole binaries. *The Astrophysical Journal*, 659(1):L5–L8, March 2007. ISSN 1538-4357. doi: 10.1086/516712. URL http://dx.doi.org/10.1086/516712.

Maria Giulia Campitiello, Stefano Ettori, Lorenzo Lovisari, Iacopo Bartalucci, Dominique Eckert, Elena Rasia, Mariachiara Rossetti, Fabio Gastaldello, Gabriel W Pratt, Ben Maughan, et al. Chex-mate: Morphological analysis of the sample. *Astronomy & Astrophysics*, 665:A117, 2022.

Xinwu Cao. Cosmological evolution of massive black holes: Effects of eddington ratio distribution and quasar lifetime. *The Astrophysical Journal*, 725(1):388, 2010.

Xinwu Cao and Fan Li. Rapidly spinning massive black holes in active galactic nuclei: evidence from the black hole mass function. *Monthly Notices of the Royal Astronomical Society*, 390(2): 561–566, 2008.

Pedro R Capelo, Marta Volonteri, Massimo Dotti, Jillian M Bellovary, Lucio Mayer, and Fabio Governato. Growth and activity of black holes in galaxy mergers with varying mass ratios. *Monthly Notices of the Royal Astronomical Society*, 447(3):2123–2143, 2015.

M. Cappellari, E. K. Verolme, R. P. van der Marel, G. A. Verdoes Kleijn, G. D. Illingworth, M. Franx, C. M. Carollo, and P. T. de Zeeuw. The Counterrotating Core and the Black Hole Mass of IC 1459. , 578(2):787–805, October 2002. doi: 10.1086/342653.

Nico Cappelluti, M Cappi, M Dadina, G Malaguti, Marica Branchesi, V D'Elia, and GGC Palumbo. X-ray source overdensities in chandra distant cluster fields: a new probe to map the cosmic tapestry? *Astronomy & Astrophysics*, 430(1):39–45, 2005.

M Cappi, P Mazzotta, Martin Elvis, DJ Burke, A Comastri, F Fiore, William Forman, Antonella Fruscione, P Green, D Harris, et al. Chandra study of an overdensity of x-ray sources around two distant (z˜ 0.5) clusters. *The Astrophysical Journal*, 548(2):624, 2001.

CL Carilli, F Walter, R Wang, A Wootten, K Menten, F Bertoldi, E Schinnerer, P Cox, A Beelen, and A Omont. Studying the first galaxies with alma. *Astrophysics and Space Science*, 313(1): 307–311, 2008.

AC Carnall, F Cullen, RJ McLure, DJ McLeod, R Begley, CT Donnan, JS Dunlop, AE Shapley, K Rowlands, O Almaini, et al. The jwst excels survey: too much, too young, too fast? ultra-massive quiescent galaxies at 3< z< 5. *Monthly Notices of the Royal Astronomical Society*, 534 (1):325–348, 2024.

J. Andrew Casey-Clyde, Chiara M. F. Mingarelli, Jenny E. Greene, Andy D. Goulding, Siyuan Chen, and Jonathan R. Trump. Quasars Can Signpost Supermassive Black Hole Binaries. , 987 (2):106, July 2025. doi: 10.3847/1538-4357/adce05.

R. Cassano, S. Ettori, S. Giacintucci, G. Brunetti, M. Markevitch, T. Venturi, and M. Gitti. On the Connection Between Giant Radio Halos and Cluster Mergers. , 721(2):L82–L85, October 2010. doi: 10.1088/2041-8205/721/2/L82.

R. Cassano, S. Ettori, G. Brunetti, S. Giacintucci, G. W. Pratt, T. Venturi, R. Kale, K. Dolag, and M. Markevitch. Revisiting Scaling Relations for Giant Radio Halos in Galaxy Clusters. , 777(2): 141, November 2013. doi: 10.1088/0004-637X/777/2/141.

Kenneth W. Cavagnolo, Megan Donahue, G. Mark Voit, and Ming Sun. An Entropy Threshold for Strong Hα and Radio Emission in the Cores of Galaxy Clusters. , 683(2):L107, August 2008. doi: 10.1086/591665.

Matteo Ceci, Giovanni Cresci, Santiago Arribas, Torsten Böker, AJ Bunker, Stephane Charlot, Katja Fahrion, Isabella Lamperti, Alessandro Marconi, M Perna, et al. The jwst/nirspec view of the nuclear region in the prototypical merging galaxy ngc 6240. *Astronomy & Astrophysics*, 695:A116, 2025.

Gilles Chabrier. Galactic stellar and substellar initial mass function. *Publications of the Astronomical Society of the Pacific*, 115(809):763–795, July 2003. ISSN 1538-3873. doi: 10.1086/376392. URL http://dx.doi.org/10.1086/376392.

Subrahmanyan Chandrasekhar. Dynamical friction. i. general considerations: the coefficient of dynamical friction. *Astrophysical Journal*, 97:255–262, 1943a.

Subrahmanyan Chandrasekhar. Stochastic problems in physics and astronomy. *Reviews of modern physics*, 15(1):1, 1943b.

Scott C. Chapman, Roger P. Deane, Dazhi Zhou, Manuel Aravena, William Rasakanya, Melanie Archipley, James Burgoyne, Jared Cathey, Anthony H. Gonzalez, Ryley Hill, Chayce Hughes, Monica Natalia Isla Llave, Matt Malkan, Kedar A. Phadke, Vismaya Pillai, Ana Posses, Bonnie Slocombe, Manuel Solimano, Justin Spilker, Nikolaus Sulzenauer, Fabio Vito, Joaquin D. Vieira, David Vizgan, George Wang, and Axel Weiss. An Overabundance of Radio-AGN in the SPT2349-56 Protocluster: Preheating the Intra-Cluster Medium. *arXiv e-prints*, art. arXiv:2511.17814, November 2025. doi: 10.48550/arXiv.2511.17814.

Damien Chapon, Lucio Mayer, and Romain Teyssier. Hydrodynamics of galaxy mergers with supermassive black holes: is there a last parsec problem? , 429(4):3114–3122, March 2013. doi: 10.1093/mnras/sts568.

Cheng Chen, Philip J Armitage, and CJ Nixon. On the orbital evolution of binaries with polar circumbinary disks. *The Astrophysical Journal Letters*, 997(2):L31, 2026.

Nianyi Chen, Yueying Ni, A Miguel Holgado, Tiziana Di Matteo, Michael Tremmel, Colin DeGraf, Simeon Bird, Rupert Croft, and Yu Feng. Massive black hole mergers with orbital information: predictions from the astrid simulation. *Monthly Notices of the Royal Astronomical Society*, 514 (2):2220–2238, 2022.

Qihang Chen, Liang Jing, Xingyu Zhu, Yue Fang, Zizhao He, Zhuojun Deng, Cheng Xiang, and Jianghua Wu. Search for quasar pairs with *gaia* astrometric data. i. method and candidates, 2025. URL https://arxiv.org/abs/2504.17777.

XingQian Chen, Peizhen Cheng, Ying Gu, Qi Zheng, MingFeng Liu, and XueGuang Zhang. The orbital kinematics of kpc-scale dual-core systems with double-peaked narrow emission lines. , 539 (1):L24–L30, May 2025. doi: 10.1093/mnrasl/slaf018.

Y. Chen, T. H. Reiprich, H. Böhringer, Y. Ikebe, and Y. Y. Zhang. Statistics of X-ray observables for the cooling-core and non-cooling core galaxy clusters. , 466(3):805–812, May 2007. doi: 10.1051/0004-6361:20066471.

Marco Chiaberge, Grant R. Tremblay, Alessandro Capetti, and Colin Norman. The Recoiling Black Hole Candidate 3C 186: Spatially Resolved Quasar Feedback and Further Evidence of a Blueshifted Broad-line Region. , 861(1):56, July 2018. doi: 10.3847/1538-4357/aac48b.

Sunmyon Chon and Kazuyuki Omukai. Formation of supermassive stars and dense star clusters in metal-poor clouds exposed to strong fuv radiation. *Monthly Notices of the Royal Astronomical Society*, 539(3):2561–2582, 2025.

Charlotte Christensen, Thomas Quinn, Fabio Governato, Adrienne Stilp, Sijing Shen, and James Wadsley. Implementing molecular hydrogen in hydrodynamic simulations of galaxy formation. *Monthly Notices of the Royal Astronomical Society*, 425(4):3058–3076, 2012.

E. Churazov, R. Sunyaev, W. Forman, and H. Böhringer. Cooling flows as a calorimeter of active galactic nucleus mechanical power. , 332(3):729–734, May 2002. doi: 10.1046/j.1365-8711.2002.05332.x.

Mauricio Cisternas, Knud Jahnke, Angela Bongiorno, Katherine J Inskip, Chris D Impey, Anton M Koekemoer, Andrea Merloni, Mara Salvato, and Jonathan R Trump. Secular evolution and a non-evolving black-hole-to-galaxy mass ratio in the last 7 gyr. *The Astrophysical Journal Letters*, 741(1):L11, 2011.

Paul C Clark, Simon CO Glover, Ralf S Klessen, and Volker Bromm. Gravitational fragmentation in turbulent primordial gas and the initial mass function of population iii stars. *The Astrophysical Journal*, 727(2):110, 2011.

L. Coatman, P. C. Hewett, M. Banerji, G. T. Richards, J. F. Hennawi, and J. X. Prochaska. VizieR Online Data Catalog: Correcting CIV-based virial black hole masses (Coatman+, 2017). VizieR On-line Data Catalog: J/MNRAS/465/2120. Originally published in: 2017MNRAS.465.2120C, September 2018.

Fabiola Cocchiararo, Alessia Franchini, Alessandro Lupi, and Alberto Sesana. Radiation pressure role in accreting massive black hole binaries. *arXiv preprint arXiv:2508.18349*, 2025.

M Colpi, S Callegari, M Dotti, and Lucio Mayer. Massive black hole binary evolution in gas-rich mergers. *Classical and quantum gravity*, 26(9):094029, 2009.

Monica Colpi. Massive Binary Black Holes in Galactic Nuclei and Their Path to Coalescence. , 183 (1-4):189–221, September 2014. doi: 10.1007/s11214-014-0067-1.

Monica Colpi, Karsten Danzmann, Martin Hewitson, Kelly Holley-Bockelmann, Philippe Jetzer, Gijs Nelemans, Antoine Petiteau, David Shoemaker, Carlos Sopuerta, Robin Stebbins, et al. Lisa definition study report. *arXiv preprint arXiv:2402.07571*, 2024.

Francoise Combes. Agn feedback and its quenching efficiency. *Frontiers in Astronomy and Space Sciences*, 4:10, 2017.

Julia M Comerford, Kyle Schluns, Jenny E Greene, and Richard J Cool. Dual supermassive black hole candidates in the agn and galaxy evolution survey. *The Astrophysical Journal*, 777(1):64, 2013.

Julia M. Comerford, Rebecca Nevin, Aaron Stemo, Francisco Müller-Sánchez, R. Scott Barrows, Michael C. Cooper, and Jeffrey A. Newman. The origin of double-peaked narrow lines in active galactic nuclei. iv. association with galaxy mergers. *The Astrophysical Journal*, 867(1):66, October 2018. ISSN 1538-4357. doi: 10.3847/1538-4357/aae2b4. URL http://dx.doi.org/10.3847/1538-4357/aae2b4.

Nuno Covas, Israel Matute, Stergios Amarantidis, José Afonso, Giorgio Lanzuisi, Andrea Comastri, Stefano Marchesi, Ciro Pappalardo, Rodrigo Carvajal, and Polychronis Papaderos. Unveiling faint x-ray agn populations in the newathena era: Insights from cosmological simulations. *Monthly Notices of the Royal Astronomical Society*, page staf993, 2025.

L. L. Cowie and J. Binney. Radiative regulation of gas flow within clusters of galaxies: a model for cluster X-ray sources. , 215:723–732, August 1977. doi: 10.1086/155406.

Lennox L. Cowie, Antoinette Songaila, Esther M. Hu, and J. G. Cohen. New Insight on Galaxy Formation and Evolution From Keck Spectroscopy of the Hawaii Deep Fields. , 112:839, September 1996. doi: 10.1086/118058.

LL Cowie, AJ Barger, MW Bautz, WN Brandt, and GP Garmire. The redshift evolution of the 2-8 kev x-ray luminosity function. *The Astrophysical Journal*, 584(2):L57, 2003.

Robert A. Crain, Joop Schaye, Richard G. Bower, Michelle Furlong, Matthieu Schaller, Tom Theuns, Claudio Dalla Vecchia, Carlos S. Frenk, Ian G. McCarthy, John C. Helly, Adrian Jenkins, Yetli M. Rosas-Guevara, Simon D. M. White, and James W. Trayford. The eagle simulations of galaxy formation: calibration of subgrid physics and model variations. *Monthly Notices of the Royal Astronomical Society*, 450(2):1937–1961, April 2015. ISSN 0035-8711. doi: 10.1093/mnras/stv725. URL http://dx.doi.org/10.1093/mnras/stv725.

Jorge Cuadra, PJ Armitage, RD Alexander, and MC Begelman. Massive black hole binary mergers within subparsec scale gas discs. *Monthly Notices of the Royal Astronomical Society*, 393(4): 1423–1432, 2009.

V. Cuciti, R. Cassano, G. Brunetti, D. Dallacasa, R. Kale, S. Ettori, and T. Venturi. Occurrence of radio halos in galaxy clusters. Insight from a mass-selected sample. , 580:A97, August 2015. doi: 10.1051/0004-6361/201526420.

Michael Curtis and Debora Sijacki. Resolving flows around black holes: numerical technique and applications. *MNRAS*, 454(4):3445–3463, October 2015. ISSN 1365-2966. doi: 10.1093/mnras/stv2246. URL http://dx.doi.org/10.1093/mnras/stv2246.

Alice Damiano, Milena Valentini, Stefano Borgani, Luca Tornatore, Giuseppe Murante, Antonio Ragagnin, Cinthia Ragone-Figueroa, and Klaus Dolag. Dynamical friction and the evolution of black holes in cosmological simulations: A new implementation in opengadget3. *Astronomy amp; Astrophysics*, 692:A81, December 2024. ISSN 1432-0746. doi: 10.1051/0004-6361/202450021. URL http://dx.doi.org/10.1051/0004-6361/202450021.

Alice Damiano, Stefano Borgani, Milena Valentini, Giuseppe Murante, Luca Tornatore, Petr Strakos, and Milan Jaros. Dynamical friction and massive black hole orbits: analytical predictions and numerical solutions, 2025. URL https://arxiv.org/abs/2506.20740.

Shashank Dattathri, Priyamvada Natarajan, Antonio J Porras-Valverde, Colin J Burke, Nianyi Chen, Tiziana Di Matteo, and Yueying Ni. The redshift evolution of the mbh–m* scaling relation: New insights from cosmological simulations and semianalytic models. *The Astrophysical Journal*, 984(2):122, 2025.

Romeel Davé, Robert A Crain, Adam RH Stevens, Desika Narayanan, Amelie Saintonge, Barbara Catinella, and Luca Cortese. Galaxy cold gas contents in modern cosmological hydrodynamic simulations. *Monthly Notices of the Royal Astronomical Society*, 497(1):146–166, 2020.

L. P. David, P. E. J. Nulsen, B. R. McNamara, W. Forman, C. Jones, T. Ponman, B. Robertson, and M. Wise. A High-Resolution Study of the Hydra A Cluster with Chandra: Comparison of the Core Mass Distribution with Theoretical Predictions and Evidence for Feedback in the Cooling Flow. , 557(2):546–559, August 2001. doi: 10.1086/322250.

Romeel Davé, Daniel Anglés-Alcázar, Desika Narayanan, Qi Li, Mika H Rafieferantsoa, and Sarah Appleby. simba: Cosmological simulations with black hole growth and feedback. *Monthly Notices of the Royal Astronomical Society*, 486(2):2827–2849, April 2019. ISSN 1365-2966. doi: 10.1093/mnras/stz937. URL http://dx.doi.org/10.1093/mnras/stz937.

Alessandra De Rosa, Cristian Vignali, Bernd Husemann, Stefano Bianchi, Tamara Bogdanović, Matteo Guainazzi, Rubén Herrero-Illana, S. Komossa, Emma Kun, Nora Loiseau, Zsolt Paragi, Miguel Perez-Torres, and Enrico Piconcelli. Disclosing the properties of low-redshift dual AGN through XMM-Newton and SDSS spectroscopy. , 480(2):1639–1655, October 2018. doi: 10.1093/mnras/sty1867.

Jackson DeBuhr, Eliot Quataert, and Chung-Pei Ma. The growth of massive black holes in galaxy merger simulations with feedback by radiation pressure. *Monthly Notices of the Royal Astronomical Society*, 412(2):1341–1360, 2011.

Roberto Decarli, Massimo Dotti, Michele Fumagalli, Paraskevi Tsalmantza, Carmen Montuori, Elisabeta Lusso, David W Hogg, and Jason X Prochaska. The nature of massive black hole binary candidates–i. spectral properties and evolution. *Monthly Notices of the Royal Astronomical Society*, 433(2):1492–1504, 2013.

Colin Degraf, Tiziana Di Matteo, and Volker Springel. Faint-end quasar luminosity functions from cosmological hydrodynamic simulations. *Monthly Notices of the Royal Astronomical Society*, 402 (3):1927–1936, 2010.

Walter Dehnen. Towards optimal softening in three-dimensionaln-body codes - i. minimizing the force error. *Monthly Notices of the Royal Astronomical Society*, 324(2):273–291, June 2001. ISSN 1365-2966. doi: 10.1046/j.1365-8711.2001.04237.x. URL http://dx.doi.org/10.1046/j.1365-8711.2001.04237.x.

I. del Moral-Castro, E. Treister, M. Droguett, C. Riesco, and M. Troncoso. A Multiwavelength Study of Dual AGN in the Nearby Universe. In M. Manteiga, F. González-Galindo, A. Labiano-Ortega, M. J. Martínez-González, N. Rea, M. Romero-Gómez, A. Ulla-Miguel, G. Yepes, C. Rodríguez-López, A. Gómez-García, and C. Dafonte, editors, *Highlights of Spanish Astrophysics XII*, page 79, May 2025.

B. Devecchi and M. Volonteri. Formation of the First Nuclear Clusters and Massive Black Holes at High Redshift. , 694(1):302–313, March 2009. doi: 10.1088/0004-637X/694/1/302.

Arjun Dey, David J. Schlegel, Dustin Lang, Robert Blum, Kaylan Burleigh, Xiaohui Fan, Joseph R. Findlay, Doug Finkbeiner, David Herrera, Stéphanie Juneau, Martin Landriau, Michael Levi, Ian McGreer, Aaron Meisner, Adam D. Myers, John Moustakas, Peter Nugent, Anna Patej, Edward F. Schlafly, Alistair R. Walker, Francisco Valdes, Benjamin A. Weaver, Christophe Yèche, Hu Zou, Xu Zhou, Behzad Abareshi, T. M. C. Abbott, Bela Abolfathi, C. Aguilera, Shadab Alam, Lori Allen, A. Alvarez, James Annis, Behzad Ansarinejad, Marie Aubert, Jacqueline Beechert, Eric F. Bell, Segev Y. BenZvi, Florian Beutler, Richard M. Bielby, Adam S. Bolton, César Briceño, Elizabeth J. Buckley-Geer, Karen Butler, Annalisa Calamida, Raymond G. Carlberg, Paul Carter, Ricard Casas, Francisco J. Castander, Yumi Choi, Johan Comparat, Elena Cukanovaite, Timothée Delubac, Kaitlin DeVries, Sharmila Dey, Govinda Dhungana, Mark Dickinson, Zhejie Ding, John B. Donaldson, Yutong Duan, Christopher J. Duckworth, Sarah Eftekharzadeh, Daniel J. Eisenstein, Thomas Etourneau, Parker A. Fagrelius, Jay Farihi, Mike Fitzpatrick, Andreu Font-Ribera, Leah Fulmer, Boris T. Gänsicke, Enrique Gaztanaga, Koshy George, David W. Gerdes, Satya Gontcho A. Gontcho, Claudio Gorgoni, Gregory Green, Julien Guy, Diane Harmer, M. Hernandez, Klaus Honscheid, Lijuan Wendy Huang, David J. James, Buell T. Jannuzi, Linhua Jiang, Richard Joyce, Armin Karcher, Sonia Karkar, Robert Kehoe, Jean-Paul Kneib, Andrea Kueter-Young, Ting-Wen Lan, Tod R. Lauer, Laurent Le Guillou, Auguste Le Van Suu, Jae Hyeon Lee, Michael Lesser, Laurence Perreault Levasseur, Ting S. Li, Justin L. Mann, Robert Marshall, C. E. Martínez-Vázquez, Paul Martini, Hélion du Mas des Bourboux, Sean McManus, Tobias Gabriel Meier, Brice Ménard, Nigel Metcalfe, Andrea Muñoz-Gutiérrez, Joan Najita, Kevin Napier, Gautham Narayan, Jeffrey A. Newman, Jundan Nie, Brian Nord, Dara J. Norman, Knut A. G. Olsen, Anthony Paat, Nathalie Palanque-Delabrouille, Xiyan Peng, Claire L. Poppett, Megan R. Poremba, Abhishek Prakash, David Rabinowitz, Anand Raichoor, Mehdi Rezaie, A. N. Robertson, Natalie A. Roe, Ashley J. Ross, Nicholas P. Ross, Gregory Rudnick, Sasha Safonova, Abhijit Saha, F. Javier Sánchez, Elodie Savary, Heidi Schweiker, Adam Scott, Hee-Jong Seo, Huanyuan Shan, David R. Silva, Zachary Slepian, Christian Soto, David Sprayberry, Ryan Staten, Coley M. Stillman, Robert J. Stupak, David L. Summers, Suk Sien Tie, H. Tirado, Mariana Vargas-Magaña,

A. Katherina Vivas, Risa H. Wechsler, Doug Williams, Jinyi Yang, Qian Yang, Tolga Yapici, Dennis Zaritsky, A. Zenteno, Kai Zhang, Tianmeng Zhang, Rongpu Zhou, and Zhimin Zhou. Overview of the DESI Legacy Imaging Surveys. , 157(5):168, May 2019. doi: 10.3847/1538-3881/ab089d.

Lankeswar Dey, Achamveedu Gopakumar, Mauri Valtonen, Stanislaw Zola, Abhimanyu Susobhanan, Rene Hudec, Pauli Pihajoki, Tapio Pursimo, Andrei Berdyugin, Vilppu Piirola, et al. The unique blazar oj 287 and its massive binary black hole central engine. *Universe*, 5(5):108, 2019.

Alessandra De Rosa, Cristian Vignali, Paola Severgnini, Stefano Bianchi, Tamara Bogdanović, Maria Charisi, Matteo Guainazzi, Zoltan Haiman, S Komossa, Zsolt Paragi, Miguel Perez-Torres, Enrico Piconcelli, Lorenzo Ducci, Manali Parvatikar, and Roberto Serafinelli. The x-ray view of optically selected dual agn. *Monthly Notices of the Royal Astronomical Society*, 519(4):5149–5160, December 2022. ISSN 1365-2966. doi: 10.1093/mnras/stac3664. URL http://dx.doi.org/10.1093/mnras/stac3664.

Tiziana Di Matteo, Jörg Colberg, Volker Springel, Lars Hernquist, and Debora Sijacki. Direct cosmological simulations of the growth of black holes and galaxies. *The Astrophysical Journal*, 676(1):33, 2008.

JA Digby-North, K Nandra, ES Laird, CC Steidel, A Georgakakis, M Bogosavljević, DK Erb, AE Shapley, NA Reddy, and J Aird. Excess agn activity in the z= 2.30 protocluster in hs 1700+ 64. *Monthly Notices of the Royal Astronomical Society*, 407(2):846–853, 2010.

Boyi Ding, Elia Pizzati, Joop Schaye, Joseph F Hennawi, William McDonald, and Matthieu Schaller. The luminosity function and clustering of bright quasars in the flamingo cosmological simulations. *arXiv preprint arXiv:2510.24283*, 2025.

Xuheng Ding, John Silverman, Tommaso Treu, Andreas Schulze, Malte Schramm, Simon Birrer, Daeseong Park, Knud Jahnke, Vardha N Bennert, Jeyhan S Kartaltepe, et al. The mass relations between supermassive black holes and their host galaxies at 1< z< 2 with hst-wfc3. *The Astrophysical Journal*, 888(1):37, 2020.

Alexander J Dittmann, Adam M Dempsey, and Hui Li. The evolution of inclined binary black holes in the disks of active galactic nuclei. *The Astrophysical Journal*, 964(1):61, 2024.

S. G. Djorgovski, A. J. Drake, A. A. Mahabal, M. J. Graham, C. Donalek, R. Williams, E. C. Beshore, S. M. Larson, J. Prieto, M. Catelan, E. Christensen, and R. H. McNaught. The catalina real-time transient survey (crts), 2011. URL https://arxiv.org/abs/1102.5004.

K Dolag, Stefano Borgani, G Murante, and V Springel. Substructures in hydrodynamical cluster simulations. *Monthly Notices of the Royal Astronomical Society*, 399(2):497–514, 2009.

Klaus Dolag, S. Borgani, S. Schindler, A. Diaferio, and A. Bykov. Simulation techniques for cosmological simulations. *Space Sci. Rev.*, 134, 01 2008. doi: 10.1007/s11214-008-9316-5.

Klaus Dolag, Rhea-Silvia Remus, Lucas M. Valenzuela, Lucas C. Kimmig, Benjamin Seidel, Silvio Fortune, Johannes Stoiber, Anna Ivleva, Tadziu Hoffmann, Veronica Biffi, Ilaria Marini, Paola Popesso, and Stephan Vladutescu-Zopp. Encyclopedia Magneticum: Scaling Relations

from Cosmic Dawn to Present Day. *arXiv e-prints*, art. arXiv:2504.01061, April 2025. doi: 10.48550/arXiv.2504.01061.

Megan Donahue and G. Mark Voit. Baryon cycles in the biggest galaxies. , 973:1–109, August 2022. doi: 10.1016/j.physrep.2022.04.005.

Megan Donahue, Geneviève E. de Messières, Robert W. O'Connell, G. Mark Voit, Aaron Hoffer, Brian R. McNamara, and Paul E. J. Nulsen. Polycyclic Aromatic Hydrocarbons, Ionized Gas, and Molecular Hydrogen in Brightest Cluster Galaxies of Cool-core Clusters of Galaxies. , 732 (1):40, May 2011. doi: 10.1088/0004-637X/732/1/40.

Ai-Jun Dong, Qingwen Wu, and Xiao-Feng Cao. A New Fundamental Plane for Radiatively Efficient Black-hole Sources. , 787(2):L20, June 2014. doi: 10.1088/2041-8205/787/2/L20.

Chi An Dong-Páez, Marta Volonteri, Yohan Dubois, Ricarda S. Beckmann, and Maxime Trebitsch. Wandering and escaping: Recoiling massive black holes in cosmological simulations. , 695:A231, March 2025. doi: 10.1051/0004-6361/202453070.

J. L. Donley, G. H. Rieke, P. G. Pérez-González, J. R. Rigby, and A. Alonso-Herrero. Detecting Obscured AGN in the Distant Universe with Spitzer. In J. Afonso, H. C. Ferguson, B. Mobasher, and R. Norris, editors, *Deepest Astronomical Surveys*, volume 380 of *Astronomical Society of the Pacific Conference Series*, page 119, December 2007. doi: 10.48550/arXiv.astro-ph/0612331.

Martina Donnari, Annalisa Pillepich, Gandhali D Joshi, Dylan Nelson, Shy Genel, Federico Marinacci, Vicente Rodriguez-Gomez, Rüdiger Pakmor, Paul Torrey, Mark Vogelsberger, et al. Quenched fractions in the illustristng simulations: the roles of agn feedback, environment, and pre-processing. *Monthly Notices of the Royal Astronomical Society*, 500(3):4004–4024, 2021.

Daniel J D'Orazio, Zoltán Haiman, and Andrew MacFadyen. Accretion into the central cavity of a circumbinary disc. *Monthly Notices of the Royal Astronomical Society*, 436(4):2997–3020, 2013.

Daniel J. D'Orazio, Zoltán Haiman, and David Schiminovich. Relativistic boost as the cause of periodicity in a massive black-hole binary candidate. , 525(7569):351–353, September 2015. doi: 10.1038/nature15262.

Yohan Dubois, Julien Devriendt, Adrianne Slyz, and Romain Teyssier. Self-regulated growth of supermassive black holes by a dual jet-heating active galactic nucleus feedback mechanism: methods, tests and implications for cosmological simulations. , 420(3):2662–2683, March 2012. doi: 10.1111/j.1365-2966.2011.20236.x.

Yohan Dubois, Marta Volonteri, Joseph Silk, Julien Devriendt, Adrianne Slyz, and Romain Teyssier. Black hole evolution–i. supernova-regulated black hole growth. *Monthly Notices of the Royal Astronomical Society*, 452(2):1502–1518, 2015.

Yohan Dubois, Sébastien Peirani, Christophe Pichon, Julien Devriendt, Raphaël Gavazzi, Charlotte Welker, and Marta Volonteri. The horizon-agn simulation: morphological diversity of galaxies promoted by agn feedback. *Monthly Notices of the Royal Astronomical Society*, 463(4):3948–3964, 2016.

Paul C Duffell, Daniel D'Orazio, Andrea Derdzinski, Zoltan Haiman, Andrew MacFadyen, Anna L Rosen, and Jonathan Zrake. Circumbinary disks: accretion and torque as a function of mass ratio and disk viscosity. *The Astrophysical Journal*, 901(1):25, 2020.

R. J. H. Dunn and A. C. Fabian. Investigating AGN heating in a sample of nearby clusters. , 373 (3):959–971, December 2006. doi: 10.1111/j.1365-2966.2006.11080.x.

RJH Dunn and AC Fabian. Investigating agn heating in a sample of nearby clusters. *Monthly Notices of the Royal Astronomical Society*, 373(3):959–971, 2006.

Charles C Dyer and Peter SS Ip. Softening in n-body simulations of collisionless systems. *Astrophysical Journal, Part 1 (ISSN 0004-637X), vol. 409, no. 1, p. 60-67.*, 409:60–67, 1993.

Jason Eastman, Paul Martini, Gregory Sivakoff, Daniel D Kelson, John S Mulchaey, and Kim-Vy Tran. First measurement of a rapid increase in the agn fraction in high-redshift clusters of galaxies. *The Astrophysical Journal*, 664(1):L9, 2007.

Carl Eckart. Some Transformations of the Hydrodynamic Equations. *Physics of Fluids*, 6(8):1037–1041, August 1963. doi: 10.1063/1.1706859.

D. Eckert, S. Molendi, and S. Paltani. The cool-core bias in X-ray galaxy cluster samples. I. Method and application to HIFLUGCS. , 526:A79, February 2011. doi: 10.1051/0004-6361/201015856.

Dominique Eckert, Massimo Gaspari, Fabio Gastaldello, Amandine M. C. Le Brun, and Ewan O'Sullivan. Feedback from active galactic nuclei in galaxy groups. *Universe*, 7(5):142, May 2021. ISSN 2218-1997. doi: 10.3390/universe7050142. URL http://dx.doi.org/10.3390/universe7050142.

A. C. Edge. The detection of molecular gas in the central galaxies of cooling flow clusters. , 328(3): 762–782, December 2001. doi: 10.1046/j.1365-8711.2001.04802.x.

A. C. Edge, J. B. R. Oonk, R. Mittal, S. W. Allen, S. A. Baum, H. Böhringer, J. N. Bregman, M. N. Bremer, F. Combes, C. S. Crawford, M. Donahue, E. Egami, A. C. Fabian, G. J. Ferland, S. L. Hamer, N. A. Hatch, W. Jaffe, R. M. Johnstone, B. R. McNamara, C. P. O'Dea, P. Popesso, A. C. Quillen, P. Salomé, C. L. Sarazin, G. M. Voit, R. J. Wilman, and M. W. Wise. Herschel photometry of brightest cluster galaxies in cooling flow clusters. , 518:L47, July 2010. doi: 10.1051/0004-6361/201014572.

A. Efstathiou, N. Christopher, A. Verma, and R. Siebenmorgen. Active galactic nucleus torus models and the puzzling infrared spectrum of IRAS F10214+4724. , 436(2):1873–1882, December 2013. doi: 10.1093/mnras/stt1695.

A. Efstathiou, D. Farrah, J. Afonso, D. L. Clements, E. González-Alfonso, M. Lacy, S. Oliver, V. Papadopoulou Lesta, C. Pearson, D. Rigopoulou, M. Rowan-Robinson, H. W. W. Spoon, A. Verma, and L. Wang. A new look at local ultraluminous infrared galaxies: the atlas and radiative transfer models of their complex physics. , 512(4):5183–5213, June 2022. doi: 10.1093/mnras/stab3642.

Vincent R. Eke, Shaun Cole, Carlos S. Frenk, and Julio F. Navarro. Cluster correlation functions in N-body simulations. , 281:703, July 1996. doi: 10.1093/mnras/281.2.703.

David Elbaz, Roger Leiton, Neil Nagar, Koryo Okumura, Maximilien Franco, Corentin Schreiber, Maurilio Pannella, Tao Wang, Mark Dickinson, Tanio Díaz-Santos, et al. Starbursts in and out of the star-formation main sequence. *Astronomy & Astrophysics*, 616:A110, 2018.

Martin Elvis, Belinda J. Wilkes, Jonathan C. McDowell, Richard F. Green, Jill Bechtold, S. P. Willner, M. S. Oey, Elisha Polomski, and Roc Cutri. Atlas of Quasar Energy Distributions. , 95: 1, November 1994. doi: 10.1086/192093.

Ryan Endsley, Daniel P Stark, Jianwei Lyu, Feige Wang, Jinyi Yang, Xiaohui Fan, Renske Smit, Rychard Bouwens, Kevin Hainline, and Sander Schouws. Alma confirmation of an obscured hyperluminous radio-loud agn at z= 6.853 associated with a dusty starburst in the 1.5 deg2 cosmos field. *Monthly Notices of the Royal Astronomical Society*, 520(3):4609–4620, 2023.

Andrés Escala, Richard B. Larson, Paolo S. Coppi, and Diego Mardones. The Role of Gas in the Merging of Massive Black Holes in Galactic Nuclei. I. Black Hole Merging in a Spherical Gas Cloud. , 607(2):765–777, June 2004. doi: 10.1086/386278.

Andrés Escala, Richard B Larson, Paolo S Coppi, and Diego Mardones. The role of gas in the merging of massive black holes in galactic nuclei. ii. black hole merging in a nuclear gas disk. *The Astrophysical Journal*, 630(1):152, 2005.

Michela Esposito, Stefano Borgani, Veronica Strazzullo, Maurilio Pannella, Gian Luigi Granato, Cinthia Ragone-Figueroa, Alex Saro, Mario Nonino, and Milena Valentini. Galaxy populations of protoclusters in cosmological hydrodynamical simulations. *Astronomy & Astrophysics*, 697:A142, 2025.

Event Horizon Telescope Collaboration, Kazunori Akiyama, Antxon Alberdi, Walter Alef, Keiichi Asada, Rebecca Azulay, Anne-Kathrin Baczko, David Ball, Mislav Baloković, John Barrett, Dan Bintley, Lindy Blackburn, Wilfred Boland, Katherine L. Bouman, Geoffrey C. Bower, Michael Bremer, Christiaan D. Brinkerink, Roger Brissenden, Silke Britzen, Avery E. Broderick, Dominique Broguiere, Thomas Bronzwaer, Do-Young Byun, John E. Carlstrom, Andrew Chael, Chi-kwan Chan, Shami Chatterjee, Koushik Chatterjee, Ming-Tang Chen, Yongjun Chen, Ilje Cho, Pierre Christian, John E. Conway, James M. Cordes, Geoffrey B. Crew, Yuzhu Cui, Jordy Davelaar, Mariafelicia De Laurentis, Roger Deane, Jessica Dempsey, Gregory Desvignes, Jason Dexter, Sheperd S. Doeleman, Ralph P. Eatough, Heino Falcke, Vincent L. Fish, Ed Fomalont, Raquel Fraga-Encinas, William T. Freeman, Per Friberg, Christian M. Fromm, José L. Gómez, Peter Galison, Charles F. Gammie, Roberto García, Olivier Gentaz, Boris Georgiev, Ciriaco Goddi, Roman Gold, Minfeng Gu, Mark Gurwell, Kazuhiro Hada, Michael H. Hecht, Ronald Hesper, Luis C. Ho, Paul Ho, Mareki Honma, Chih-Wei L. Huang, Lei Huang, David H. Hughes, Shiro Ikeda, Makoto Inoue, Sara Issaoun, David J. James, Buell T. Jannuzi, Michael Janssen, Britton Jeter, Wu Jiang, Michael D. Johnson, Svetlana Jorstad, Taehyun Jung, Mansour Karami, Ramesh Karuppusamy, Tomohisa Kawashima, Garrett K. Keating, Mark Kettenis, Jae-Young Kim, Junhan Kim, Jongsoo Kim, Motoki Kino, Jun Yi Koay, Patrick M. Koch, Shoko Koyama, Michael

Kramer, Carsten Kramer, Thomas P. Krichbaum, Cheng-Yu Kuo, Tod R. Lauer, Sang-Sung Lee, Yan-Rong Li, Zhiyuan Li, Michael Lindqvist, Kuo Liu, Elisabetta Liuzzo, Wen-Ping Lo, Andrei P. Lobanov, Laurent Loinard, Colin Lonsdale, Ru-Sen Lu, Nicholas R. MacDonald, Jirong Mao, Sera Markoff, Daniel P. Marrone, Alan P. Marscher, Iván Martí-Vidal, Satoki Matsushita, Lynn D. Matthews, Lia Medeiros, Karl M. Menten, Yosuke Mizuno, Izumi Mizuno, James M. Moran, Kotaro Moriyama, Monika Moscibrodzka, Cornelia Müller, Hiroshi Nagai, Neil M. Nagar, Masanori Nakamura, Ramesh Narayan, Gopal Narayanan, Iniyan Natarajan, Roberto Neri, Chunchong Ni, Aristeidis Noutsos, Hiroki Okino, Héctor Olivares, Gisela N. Ortiz-León, Tomoaki Oyama, Feryal Özel, Daniel C. M. Palumbo, Nimesh Patel, Ue-Li Pen, Dominic W. Pesce, Vincent Piétu, Richard Plambeck, Aleksandar PopStefanija, Oliver Porth, Ben Prather, Jorge A. Preciado-López, Dimitrios Psaltis, Hung-Yi Pu, Venkatessh Ramakrishnan, Ramprasad Rao, Mark G. Rawlings, Alexander W. Raymond, Luciano Rezzolla, Bart Ripperda, Freek Roelofs, Alan Rogers, Eduardo Ros, Mel Rose, Arash Roshanineshat, Helge Rottmann, Alan L. Roy, Chet Ruszczyk, Benjamin R. Ryan, Kazi L. J. Rygl, Salvador Sánchez, David Sánchez-Arguelles, Mahito Sasada, Tuomas Savolainen, F. Peter Schloerb, Karl-Friedrich Schuster, Lijing Shao, Zhiqiang Shen, Des Small, Bong Won Sohn, Jason SooHoo, Fumie Tazaki, Paul Tiede, Remo P. J. Tilanus, Michael Titus, Kenji Toma, Pablo Torne, Tyler Trent, Sascha Trippe, Shuichiro Tsuda, Ilse van Bemmel, Huib Jan van Langevelde, Daniel R. van Rossum, Jan Wagner, John Wardle, Jonathan Weintroub, Norbert Wex, Robert Wharton, Maciek Wielgus, George N. Wong, Qingwen Wu, Ken Young, and André Young. First M87 Event Horizon Telescope Results. I. The Shadow of the Supermassive Black Hole. , 875(1):L1, April 2019. doi: 10.3847/2041-8213/ab0ec7.

A. C. Fabian. Cooling Flows in Clusters of Galaxies. , 32:277–318, January 1994. doi: 10.1146/annurev.aa.32.090194.001425.

A. C. Fabian and P. E. J. Nulsen. Subsonic accretion of cooling gas in clusters of galaxies. , 180:479–484, August 1977. doi: 10.1093/mnras/180.3.479.

A. C. Fabian and M. J. Rees. The accretion luminosity of a massive black hole in an elliptical galaxy. , 277(2):L55–L58, November 1995. doi: 10.1093/mnras/277.1.L55.

A. C. Fabian, J. S. Sanders, S. W. Allen, C. S. Crawford, K. Iwasawa, R. M. Johnstone, R. W. Schmidt, and G. B. Taylor. A deep Chandra observation of the Perseus cluster: shocks and ripples. , 344(3):L43–L47, September 2003. doi: 10.1046/j.1365-8711.2003.06902.x.

A. C. Fabian, J. S. Sanders, G. B. Taylor, S. W. Allen, C. S. Crawford, R. M. Johnstone, and K. Iwasawa. A very deep Chandra observation of the Perseus cluster: shocks, ripples and conduction. , 366(2):417–428, February 2006. doi: 10.1111/j.1365-2966.2005.09896.x.

A. C. Fabian, J. S. Sanders, S. W. Allen, R. E. A. Canning, E. Churazov, C. S. Crawford, W. Forman, J. GaBany, J. Hlavacek-Larrondo, R. M. Johnstone, H. R. Russell, C. S. Reynolds, P. Salomé, G. B. Taylor, and A. J. Young. A wide chandra view of the core of the perseus cluster: A wider view of the perseus cluster. *Monthly Notices of the Royal Astronomical Society*, 418(4): 2154–2164, November 2011. ISSN 0035-8711. doi: 10.1111/j.1365-2966.2011.19402.x. URL http://dx.doi.org/10.1111/j.1365-2966.2011.19402.x.

A.C. Fabian. Observational evidence of active galactic nuclei feedback. *Annual Review of Astronomy and Astrophysics*, 50(1):455–489, September 2012. ISSN 1545-4282. doi: 10.1146/annurev-astro-081811-125521. URL http://dx.doi.org/10.1146/annurev-astro-081811-125521.

Andrew C. Fabian. *Cooling Flows in Clusters of Galaxies*, page 24–36. Springer-Verlag, 2002. ISBN 354043769X. doi: 10.1007/10856495_3. URL http://dx.doi.org/10.1007/10856495_3.

D. Fabjan, S. Borgani, L. Tornatore, A. Saro, G. Murante, and K. Dolag. Simulating the effect of active galactic nuclei feedback on the metal enrichment of galaxy clusters. , 401(3):1670–1690, January 2010. doi: 10.1111/j.1365-2966.2009.15794.x.

Jun-Hui Fan, Yi Liu, Bo-Chun Qian, Jun Tao, Zhi-Qiang Shen, Jiang-Shui Zhang, Yong Huang, and Jin Wang. Long-term variation time scales in OJ 287. *Research in Astronomy and Astrophysics*, 10(11):1100–1108, November 2010. doi: 10.1088/1674-4527/10/11/002.

B. L. Fanaroff and J. M. Riley. The morphology of extragalactic radio sources of high and low luminosity. , 167:31P–36P, May 1974. doi: 10.1093/mnras/167.1.31P.

Brian D Farris, Paul Duffell, Andrew I MacFadyen, and Zoltan Haiman. Binary black hole accretion from a circumbinary disk: gas dynamics inside the central cavity. *The Astrophysical Journal*, 783 (2):134, 2014.

Robert Feldmann and Rebekka Bieri. Cosmological simulations of galaxies. *arXiv preprint arXiv:2507.08925*, 2025.

G. J. Ferland, K. T. Korista, D. A. Verner, J. W. Ferguson, J. B. Kingdon, and E. M. Verner. CLOUDY 90: Numerical Simulation of Plasmas and Their Spectra. , 110(749):761–778, July 1998. doi: 10.1086/316190.

G. J. Ferland, M. Chatzikos, F. Guzmán, M. L. Lykins, P. A. M. van Hoof, R. J. R. Williams, N. P. Abel, N. R. Badnell, F. P. Keenan, R. L. Porter, and P. C. Stancil. The 2017 release of cloudy, 2023. URL https://arxiv.org/abs/1705.10877.

Laura Ferrarese and David Merritt. A Fundamental Relation between Supermassive Black Holes and Their Host Galaxies. , 539(1):L9–L12, August 2000. doi: 10.1086/312838.

Laura Ferrarese, Patrick Côté, Elena Dalla Bontà, Eric W. Peng, David Merritt, Andrés Jordán, John P. Blakeslee, Monica Haşegan, Simona Mei, Slawomir Piatek, John L. Tonry, and Michael J. West. A Fundamental Relation between Compact Stellar Nuclei, Supermassive Black Holes, and Their Host Galaxies. , 644(1):L21–L24, June 2006. doi: 10.1086/505388.

C. Ferrari, F. Govoni, S. Schindler, A. M. Bykov, and Y. Rephaeli. Observations of Extended Radio Emission in Clusters. , 134(1-4):93–118, February 2008. doi: 10.1007/s11214-008-9311-x.

C. Feruglio, A. Bongiorno, F. Fiore, M. Krips, M. Brusa, E. Daddi, I. Gavignaud, R. Maiolino, E. Piconcelli, M. Sargent, C. Vignali, and L. Zappacosta. Gas reservoir of a hyper-luminous quasar at z = 2.6. , 565:A91, May 2014. doi: 10.1051/0004-6361/201423719.

C. Feruglio, F. Fiore, S. Carniani, R. Maiolino, V. D'Odorico, A. Luminari, P. Barai, M. Bischetti, A. Bongiorno, S. Cristiani, A. Ferrara, S. Gallerani, A. Marconi, A. Pallottini, E. Piconcelli, and L. Zappacosta. The dense molecular gas in the z $\sim$ 6 QSO SDSS J231038.88+185519.7 resolved by ALMA. , 619:A39, November 2018. doi: 10.1051/0004-6361/201833174.

Alessia Franchini, Alberto Sesana, and Massimo Dotti. Circumbinary disc self-gravity governing supermassive black hole binary mergers. *Monthly Notices of the Royal Astronomical Society*, 507 (1):1458–1467, 2021.

Alessia Franchini, Matteo Bonetti, Alessandro Lupi, and Alberto Sesana. Emission signatures from sub-parsec post-newtonian binaries embedded in circumbinary discs. *Astronomy amp; Astrophysics*, 686:A288, June 2024. ISSN 1432-0746. doi: 10.1051/0004-6361/202449206. URL http://dx.doi.org/10.1051/0004-6361/202449206.

Amelia Fraser-McKelvie, Michael J. I. Brown, and Kevin A. Pimbblet. The rarity of star formation in brightest cluster galaxies as measured by wise. *Monthly Notices of the Royal Astronomical Society: Letters*, 444(1):L63–L67, August 2014. ISSN 1745-3925. doi: 10.1093/mnrasl/slu117. URL http://dx.doi.org/10.1093/mnrasl/slu117.

CS Frenk, Simon DM White, P Bode, JR Bond, GL Bryan, R Cen, HMP Couchman, August E Evrard, N Gnedin, A Jenkins, et al. The santa barbara cluster comparison project: A comparison of cosmological hydrodynamics solutions. *The Astrophysical Journal*, 525(2):554, 1999.

Logan B. Fries, Jonathan R. Trump, Megan C. Davis, C. J. Grier, Yue Shen, Scott F. Anderson, Tom Dwelly, Michael Eracleous, Y. Homayouni, Keith Horne, Mirko Krumpe, Sean Morrison, Jessie C. Runnoe, Benny Trakhtenbrot, Roberto J. Assef, W. N. Brandt, Joel Brownstein, Collin Dabbieri, Alexander Fix, Gloria Fonseca Alvarez, Sara Frederick, P. B. Hall, Anton M. Koekemoer, Jennifer I-Hsiu Li, Xin Liu, Mary Loli Martínez-Aldama, Claudio Ricci, Donald P. Schneider, Hugh W. Sharp, Matthew J. Temple, Qian Yang, Grisha Zeltyn, and Dmitry Bizyaev. The sdss-v black hole mapper reverberation mapping project: Unusual broad-line variability in a luminous quasar. *The Astrophysical Journal*, 948(1):5, April 2023. ISSN 1538-4357. doi: 10.3847/1538-4357/acbfb7. URL http://dx.doi.org/10.3847/1538-4357/acbfb7.

Santiago García-Burillo, Françoise Combes, Antonio Usero, Susanne Aalto, Melanie Krips, Serena Viti, Almudena Alonso-Herrero, LK Hunt, Eva Schinnerer, Andrew J Baker, et al. Molecular line emission in ngc 1068 imaged with alma-i. an agn-driven outflow in the dense molecular gas. *Astronomy & Astrophysics*, 567:A125, 2014.

M. Gaspari, M. Ruszkowski, and S. Peng Oh. Chaotic cold accretion on to black holes. *Monthly Notices of the Royal Astronomical Society*, 432(4):3401–3422, May 2013. ISSN 1365-2966. doi: 10.1093/mnras/stt692. URL http://dx.doi.org/10.1093/mnras/stt692.

M. Gaspari, M. McDonald, S. L. Hamer, F. Brighenti, P. Temi, M. Gendron-Marsolais, J. Hlavacek-Larrondo, A. C. Edge, N. Werner, P. Tozzi, M. Sun, J. M. Stone, G. R. Tremblay, M. T. Hogan, D. Eckert, S. Ettori, H. Yu, V. Biffi, and S. Planelles. Shaken Snow Globes: Kinematic Tracers of the Multiphase Condensation Cascade in Massive Galaxies, Groups, and Clusters. , 854(2):167, February 2018. doi: 10.3847/1538-4357/aaaa1b.

M. Gaspari, D. Eckert, S. Ettori, P. Tozzi, L. Bassini, E. Rasia, F. Brighenti, M. Sun, S. Borgani, S. D. Johnson, G. R. Tremblay, J. M. Stone, P. Temi, H. Y. K. Yang, F. Tombesi, and M. Cappi. The X-Ray Halo Scaling Relations of Supermassive Black Holes. , 884(2):169, October 2019. doi: 10.3847/1538-4357/ab3c5d.

Massimo Gaspari, Francesco Tombesi, and Massimo Cappi. Linking macro-, meso- and microscales in multiphase AGN feeding and feedback. *Nature Astronomy*, 4:10–13, January 2020. doi: 10.1038/s41550-019-0970-1.

Karl Gebhardt, Ralf Bender, Gary Bower, Alan Dressler, S. M. Faber, Alexei V. Filippenko, Richard Green, Carl Grillmair, Luis C. Ho, John Kormendy, Tod R. Lauer, John Magorrian, Jason Pinkney, Douglas Richstone, and Scott Tremaine. A Relationship between Nuclear Black Hole Mass and Galaxy Velocity Dispersion. , 539(1):L13–L16, August 2000. doi: 10.1086/312840.

Anna Genina, Volker Springel, and Antti Rantala. A calibrated model for n-body dynamical friction acting on supermassive black holes. *Monthly Notices of the Royal Astronomical Society*, 534(1): 957–977, 2024.

A. Georgakakis, J. Aird, J. Buchner, M. Salvato, M.-L. Menzel, W. N. Brandt, I. D. McGreer, T. Dwelly, G. Mountrichas, C. Koki, I. Georgantopoulos, L.-T. Hsu, A. Merloni, Z. Liu, K. Nandra, and N. P. Ross. The x-ray luminosity function of active galactic nuclei in the redshift intervalz=3-5. *Monthly Notices of the Royal Astronomical Society*, 453(2):1946–1964, August 2015. ISSN 1365-2966. doi: 10.1093/mnras/stv1703. URL http://dx.doi.org/10.1093/mnras/stv1703.

S. Gezari, J. P. Halpern, and M. Eracleous. Long-Term Profile Variability of Double-peaked Emission Lines in Active Galactic Nuclei. , 169(2):167–212, April 2007. doi: 10.1086/511032.

V. Ghirardini, D. Eckert, S. Ettori, E. Pointecouteau, S. Molendi, M. Gaspari, M. Rossetti, S. De Grandi, M. Roncarelli, H. Bourdin, P. Mazzotta, E. Rasia, and F. Vazza. Universal thermodynamic properties of the intracluster medium over two decades in radius in the x-cop sample. *Astronomy amp; Astrophysics*, 621:A41, January 2019. ISSN 1432-0746. doi: 10.1051/0004-6361/201833325. URL http://dx.doi.org/10.1051/0004-6361/201833325.

Riccardo Giacconi, Andrew Zirm, JunXian Wang, Piero Rosati, Mario Nonino, Paolo Tozzi, Roberto Gilli, Vincenzo Mainieri, Guenther Hasinger, Lisa Kewley, Jacqueline Bergeron, Stefano Borgani, Roberto Gilmozzi, Norman Grogin, Anton Koekemoer, Ethan Schreier, Wei Zheng, and Colin Norman. Chandra deep field south: The 1 ms catalog. *The Astrophysical Journal Supplement Series*, 139(2):369–410, April 2002. ISSN 1538-4365. doi: 10.1086/338927. URL http://dx.doi.org/10.1086/338927.

Emanuele Giallongo, Andrea Grazian, Fabrizio Fiore, Adriano Fontana, Laura Pentericci, Eros Vanzella, M Dickinson, D Kocevski, MARCO Castellano, Stefano Cristiani, et al. Faint agns at z> 4 in the candels goods-s field: looking for contributors to the reionization of the universe. *Astronomy & Astrophysics*, 578:A83, 2015.

R. A. Gingold and J. J. Monaghan. Kernel estimates as a basis for general particle methods in hydrodynamics. *Journal of Computational Physics*, 46:429–453, June 1982. doi: 10.1016/0021-9991(82)90025-0.

Galen R Gisler. Clusters of galaxies and the statistics of emission-line galaxies. *Monthly Notices of the Royal Astronomical Society, vol. 183, June 1978, p. 633-643.*, 183:633–643, 1978.

Myriam Gitti, Fabrizio Brighenti, and Brian R McNamara. Evidence for agn feedback in galaxy clusters and groups. *Advances in Astronomy*, 2012(1):950641, 2012.

Myriam Gitti, Fabrizio Brighenti, and Brian R. McNamara. Evidence for AGN Feedback in Galaxy Clusters and Groups. *Advances in Astronomy*, 2012:950641, January 2012. doi: 10.1155/2012/950641.

Eilat Glikman, SG Djorgovski, Daniel Stern, Arjun Dey, Buell T Jannuzi, and Kyoung-Soo Lee. The faint end of the quasar luminosity function at z 4: implications for ionization of the intergalactic medium and cosmic downsizing. *The Astrophysical Journal Letters*, 728(2):L26, 2011.

Nickolay Y Gnedin, Konstantinos Tassis, and Andrey V Kravtsov. Modeling molecular hydrogen and star formation in cosmological simulations. *The Astrophysical Journal*, 697(1):55, 2009.

Peter Goldreich and Scott Tremaine. The excitation of density waves at the lindblad and corotation resonances by an external potential. *Astrophysical Journal, Part 1, vol. 233, no. 3, Nov. 1, 1979, p. 857-871.*, 233:857–871, 1979.

Justo Antonio González Villalba, Klaus Dolag, and Veronica Biffi. How the cool-core population transitions from galaxy groups to massive clusters: A comparison of the largest Magneticum simulation with eROSITA, XMM-Newton, Chandra and LOFAR observations. , 694:A232, February 2025. doi: 10.1051/0004-6361/202452203.

Gopal-Krishna, Ravi Joshi, Dusmanta Patra, Xiaolong Yang, Luis C. Ho, Paul J. Wiita, and Amitesh Omar. The twin radio galaxy TRG J104454+354055. , 514(1):L36–L40, July 2022. doi: 10.1093/mnrasl/slac055.

Paul H Goubert, Asa FL Bluck, Joanna M Piotrowska, Paul Torrey, Roberto Maiolino, Thomas Pinto Franco, Camilo Casimiro, and Nicolas Cea. Environmental versus intrinsic quenching at cosmic noon: predictions from cosmological hydrodynamical simulations for vlt-moonrise. *Monthly Notices of the Royal Astronomical Society*, 543(3):2006–2034, 2025.

Andrew Gould and Hans-Walter Rix. Binary black hole mergers from planet-likemigrations. *The Astrophysical Journal*, 532(1):L29, 2000.

Alister W Graham and I-hui Li. The mbh–σ diagram and the offset nature of barred active galaxies. *The Astrophysical Journal*, 698(1):812, 2009.

Alister W. Graham, Simon P. Driver, Paul D. Allen, and Jochen Liske. The Millennium Galaxy Catalogue: the local supermassive black hole mass function in early- and late-type galaxies. , 378 (1):198–210, June 2007. doi: 10.1111/j.1365-2966.2007.11770.x.

Matthew J. Graham, S. G. Djorgovski, Daniel Stern, Eilat Glikman, Andrew J. Drake, Ashish A. Mahabal, Ciro Donalek, Steve Larson, and Eric Christensen. A possible close supermassive black-hole binary in a quasar with optical periodicity. , 518(7537):74–76, February 2015. doi: 10.1038/nature14143.

Jenny E. Greene, Luis C. Ho, and Aaron J. Barth. Black holes in pseudobulges and spheroidals: A change in the black hole–bulge scaling relations at low mass. *The Astrophysical Journal*, 688(1): 159–179, November 2008. ISSN 1538-4357. doi: 10.1086/592078. URL http://dx.doi.org/10.1086/592078.

Jenny E. Greene, Luis C. Ho, and Aaron J. Barth. Black Holes in Pseudobulges and Spheroidals: A Change in the Black Hole-Bulge Scaling Relations at Low Mass. , 688(1):159–179, November 2008. doi: 10.1086/592078.

Jesse L Greenstein and Thomas A Matthews. Red-shift of the unusual radio source: 3 c 48. *Nature*, 197(4872):1041–1042, 1963.

Thomas H. Greif, Jarrett L. Johnson, Ralf S. Klessen, and Volker Bromm. The first galaxies: assembly, cooling and the onset of turbulence. *Monthly Notices of the Royal Astronomical Society*, 387(3):1021–1036, July 2008. ISSN 1365-2966. doi: 10.1111/j.1365-2966.2008.13326.x. URL http://dx.doi.org/10.1111/j.1365-2966.2008.13326.x.

Frederick Groth, Ulrich P Steinwandel, Milena Valentini, and Klaus Dolag. The cosmological simulation code <scp>opengadget3</scp> – implementation of meshless finite mass. *Monthly Notices of the Royal Astronomical Society*, 526(1):616–644, September 2023. ISSN 1365-2966. doi: 10.1093/mnras/stad2717. URL http://dx.doi.org/10.1093/mnras/stad2717.

Michael Y Grudić and Philip F Hopkins. A general-purpose time-step criterion for simulations with gravity. *Monthly Notices of the Royal Astronomical Society*, 495(4):4306–4313, 2020.

Alessia Gualandris and David Merritt. Dynamics around supermassive black holes. *arXiv e-prints*, art. arXiv:0708.3083, August 2007. doi: 10.48550/arXiv.0708.3083.

Alessia Gualandris and David Merritt. Long-term evolution of massive black hole binaries. iv. mergers of galaxies with collisionally relaxed nuclei. *The Astrophysical Journal*, 744(1):74, December 2011. ISSN 1538-4357. doi: 10.1088/0004-637x/744/1/74. URL http://dx.doi.org/10.1088/0004-637X/744/1/74.

Alessia Gualandris, Justin I Read, Walter Dehnen, and Elisa Bortolas. Collisionless loss-cone refilling: there is no final parsec problem. *Monthly Notices of the Royal Astronomical Society*, 464(2): 2301–2310, 2017.

Alessia Gualandris, Fazeel Mahmood Khan, Elisa Bortolas, Matteo Bonetti, Alberto Sesana, Peter Berczik, and Kelly Holley-Bockelmann. Eccentricity evolution of massive black hole binaries from formation to coalescence. , 511(4):4753–4765, April 2022. doi: 10.1093/mnras/stac241.

D. Guidetti, M. Murgia, F. Govoni, P. Parma, L. Gregorini, H. R. de Ruiter, R. A. Cameron, and R. Fanti. The intracluster magnetic field power spectrum in Abell 2382. , 483(3):699–713, June 2008. doi: 10.1051/0004-6361:20078576.

Kayhan Gültekin, Douglas O. Richstone, Karl Gebhardt, Tod R. Lauer, Scott Tremaine, M. C. Aller, Ralf Bender, Alan Dressler, S. M. Faber, Alexei V. Filippenko, Richard Green, Luis C. Ho, John Kormendy, John Magorrian, Jason Pinkney, and Christos Siopis. The M-σ and M-L Relations in

Galactic Bulges, and Determinations of Their Intrinsic Scatter. , 698(1):198–221, June 2009. doi: 10.1088/0004-637X/698/1/198.

Kayhan Gültekin, Ashley L. King, Edward M. Cackett, Kristina Nyland, Jon M. Miller, Tiziana Di Matteo, Sera Markoff, and Michael P. Rupen. The Fundamental Plane of Black Hole Accretion and Its Use as a Black Hole-Mass Estimator. , 871(1):80, January 2019. doi: 10.3847/1538-4357/aaf6b9.

Richard Günther and Wilhelm Kley. Circumbinary disk evolution. *Astronomy & Astrophysics*, 387 (2):550–559, 2002.

Hengxiao Guo, Xin Liu, Yue Shen, Abraham Loeb, TalaWanda Monroe, and Jason Xavier Prochaska. Constraining sub-parsec binary supermassive black holes in quasars with multi-epoch spectroscopy - III. Candidates from continued radial velocity tests. , 482(3):3288–3307, January 2019. doi: 10.1093/mnras/sty2920.

F. Haardt and P. Madau. Modelling the UV/X-ray cosmic background with CUBA. In D. M. Neumann and J. T. V. Tran, editors, *Clusters of Galaxies and the High Redshift Universe Observed in X-rays*, page 64, January 2001. doi: 10.48550/arXiv.astro-ph/0106018.

Francesco Haardt and Piero Madau. Radiative transfer in a clumpy universe. ii. the ultraviolet extragalactic background. *The Astrophysical Journal*, 461:20, April 1996. ISSN 1538-4357. doi: 10.1086/177035. URL http://dx.doi.org/10.1086/177035.

Mélanie Habouzit, Yuan Li, Rachel S Somerville, Shy Genel, Annalisa Pillepich, Marta Volonteri, Romeel Davé, Yetli Rosas-Guevara, Stuart McAlpine, Sébastien Peirani, et al. Supermassive black holes in cosmological simulations i: M bh- m relation and black hole mass function. *Monthly Notices of the Royal Astronomical Society*, 503(2):1940–1975, 2021.

Mélanie Habouzit, Marta Volonteri, and Yohan Dubois. Blossoms from black hole seeds: properties and early growth regulated by supernova feedback. *Monthly Notices of the Royal Astronomical Society*, 468(4):3935–3948, March 2017. ISSN 1365-2966. doi: 10.1093/mnras/stx666. URL http://dx.doi.org/10.1093/mnras/stx666.

Mélanie Habouzit, Masafusa Onoue, Eduardo Bañados, Marcel Neeleman, Daniel Anglés-Alcázar, Fabian Walter, Annalisa Pillepich, Romeel Davé, Knud Jahnke, and Yohan Dubois. Co-evolution of massive black holes and their host galaxies at high redshift: discrepancies from six cosmological simulations and the key role of jwst. *Monthly Notices of the Royal Astronomical Society*, 511(3): 3751–3767, January 2022. ISSN 1365-2966. doi: 10.1093/mnras/stac225. URL http://dx.doi.org/10.1093/mnras/stac225.

Martin G. Haehnelt and Martin J. Rees. The formation of nuclei in newly formed galaxies and the evolution of the quasar population. , 263(1):168–178, July 1993. doi: 10.1093/mnras/263.1.168.

M. J. Hardcastle, D. A. Evans, and J. H. Croston. Hot and cold gas accretion and feedback in radio-loud active galaxies. , 376(4):1849–1856, April 2007. doi: 10.1111/j.1365-2966.2007.11572.x.

P. J. Hargrave and M. Ryle. Observations of Cygnus A with the 5-km radio telescope. , 166:305–327, February 1974. doi: 10.1093/mnras/166.2.305.

Yuichi Harikane, Yoshiaki Ono, Masami Ouchi, Chengze Liu, Marcin Sawicki, Takatoshi Shibuya, Peter S Behroozi, Wanqiu He, Kazuhiro Shimasaku, Stephane Arnouts, et al. Goldrush. iv. luminosity functions and clustering revealed with 4,000,000 galaxies at z 2–7: Galaxy–agn transition, star formation efficiency, and implication for evolution at z> 10. *The Astrophysical Journal Supplement Series*, 259(1):20, 2022.

Yuichi Harikane, Yechi Zhang, Kimihiko Nakajima, Masami Ouchi, Yuki Isobe, Yoshiaki Ono, Shun Hatano, Yi Xu, and Hiroya Umeda. A jwst/nirspec first census of broad-line agns at z=4-7: Detection of 10 faint agns with $m_b h$ $10^6 - 10^8 m_s unandtheirhostgalaxyproperties, 2023. URL$.

D. E. Harris and Henric Krawczynski. X-Ray Emission from Extragalactic Jets. , 44(1):463–506, September 2006. 10.1146/annurev.astro.44.051905.092446.

Günther Hasinger, Takamitsu Miyaji, and Maarten Schmidt. Luminosity dependent evolution of soft x-ray selected agn. *Astron. & Astroph*, 2004.

E. Hatziminaoglou, A. Omont, J. A. Stevens, A. Amblard, V. Arumugam, R. Auld, H. Aussel, T. Babbedge, A. Blain, J. Bock, A. Boselli, V. Buat, D. Burgarella, N. Castro-Rodríguez, A. Cava, P. Chanial, D. L. Clements, A. Conley, L. Conversi, A. Cooray, C. D. Dowell, E. Dwek, S. Dye, S. Eales, D. Elbaz, D. Farrah, M. Fox, A. Franceschini, W. Gear, J. Glenn, E. A. González Solares, M. Griffin, M. Halpern, E. Ibar, K. Isaak, R. J. Ivison, G. Lagache, L. Levenson, N. Lu, S. Madden, B. Maffei, G. Mainetti, L. Marchetti, A. M. J. Mortier, H. T. Nguyen, B. O'Halloran, S. J. Oliver, M. J. Page, P. Panuzzo, A. Papageorgiou, C. P. Pearson, I. Pérez-Fournon, M. Pohlen, J. I. Rawlings, D. Rigopoulou, D. Rizzo, I. G. Roseboom, M. Rowan-Robinson, M. Sanchez Portal, B. Schulz, D. Scott, N. Seymour, D. L. Shupe, A. J. Smith, M. Symeonidis, M. Trichas, K. E. Tugwell, M. Vaccari, I. Valtchanov, L. Vigroux, L. Wang, R. Ward, G. Wright, C. K. Xu, and M. Zemcov. HerMES: Far infrared properties of known AGN in the HerMES fields. , 518:L33, July 2010. 10.1051/0004-6361/201014679.

RM Heath and CJ Nixon. On the orbital evolution of binaries with circumbinary discs. *Astronomy & Astrophysics*, 641:A64, 2020.

Cameron Heather, Teeraparb Chantavat, Siri Chongchitnan, and Poemwai Chainakun. The brightest x-ray agns at redshift 3 z 6. *Monthly Notices of the Royal Astronomical Society*, 543(4): 3783–3790, 2025.

Nicholas A Henden, Ewald Puchwein, Sijing Shen, and Debora Sijacki. The fable simulations: a feedback model for galaxies, groups, and clusters. *Monthly Notices of the Royal Astronomical Society*, 479(4):5385–5412, 2018.

Joseph F. Hennawi, Michael A. Strauss, Masamune Oguri, Naohisa Inada, Gordon T. Richards, Bartosz Pindor, Donald P. Schneider, Robert H. Becker, Michael D. Gregg, Patrick B. Hall, David E. Johnston, Xiaohui Fan, Scott Burles, David J. Schlegel, James E. Gunn, Robert H. Lupton, Neta A. Bahcall, Robert J. Brunner, and Jon Brinkmann. Binary Quasars in the Sloan Digital Sky Survey: Evidence for Excess Clustering on Small Scales. , 131(1):1–23, January 2006. 10.1086/498235.

Lars Hernquist. An Analytical Model for Spherical Galaxies and Bulges. *ApJ*, 356:359, June 1990. ISSN 0004-637X. 10.1086/168845. URL https://ui.adsabs.harvard.edu/abs/1990ApJ...356..359H. Publisher: IOP ADS Bibcode: 1990ApJ...356..359H.

John M Hill and William R Oegerle. Dynamics of cd clusters of galaxies. i-redshift data for seven clusters. *Astronomical Journal (ISSN 0004-6256), vol. 106, no. 3, p. 831-847.*, 106:831–847, 1993.

Shingo Hirano and Volker Bromm. Formation and survival of population iii stellar systems. *Monthly Notices of the Royal Astronomical Society*, 470(1):898–914, 2017.

Michaela Hirschmann, Klaus Dolag, Alexandro Saro, Lisa Bachmann, Stefano Borgani, and Andreas Burkert. Cosmological simulations of black hole growth: Agn luminosities and downsizing. *Monthly Notices of the Royal Astronomical Society*, 442(3):2304–2324, 2014.

Luis C. Ho and Minjin Kim. The Black Hole Mass Scale of Classical and Pseudo Bulges in Active Galaxies. , 789(1):17, July 2014. 10.1088/0004-637X/789/1/17.

JA Hodge, Ian Smail, F Walter, Elisabete da Cunha, AM Swinbank, M Rybak, B Venemans, WN Brandt, G Calistro Rivera, Scott C Chapman, et al. Alma reveals potential evidence for spiral arms, bars, and rings in high-redshift submillimeter galaxies. *The Astrophysical Journal*, 876(2):130, 2019.

Loren Hoffman and Abraham Loeb. Dynamics of triple black hole systems in hierarchically merging massive galaxies. , 377(3):957–976, May 2007. 10.1111/j.1365-2966.2007.11694.x.

J. Drew Hogg, Laura Blecha, Christopher S. Reynolds, Krista Lynne Smith, and Lisa M. Winter. 2MASX J00423991 + 3017515: an offset active galactic nucleus in an interacting system. , 503 (2):1688–1702, May 2021. 10.1093/mnras/stab576.

Kelly Holley-Bockelmann, J Christopher Mihos, Steinn Sigurdsson, Lars Hernquist, and Colin Norman. The evolution of cuspy triaxial galaxies harboring central black holes. *The Astrophysical Journal*, 567(2):817, 2002.

S. F. Hönig and M. Kishimoto. The dusty heart of nearby active galaxies. II. From clumpy torus models to physical properties of dust around AGN. , 523:A27, November 2010. 10.1051/0004-6361/200912676.

Philip F. Hopkins. A new class of accurate, mesh-free hydrodynamic simulation methods. *Monthly Notices of the Royal Astronomical Society*, 450(1):53–110, April 2015. ISSN 1365-2966. 10.1093/mnras/stv195. URL http://dx.doi.org/10.1093/mnras/stv195.

Philip F. Hopkins and Eliot Quataert. An analytic model of angular momentum transport by gravitational torques: from galaxies to massive black holes: Angular momentum transport and agn fuelling. *Monthly Notices of the Royal Astronomical Society*, 415(2):1027–1050, July 2011. ISSN 0035-8711. 10.1111/j.1365-2966.2011.18542.x. URL http://dx.doi.org/10.1111/j.1365-2966.2011.18542.x.

Philip F Hopkins, Lars Hernquist, Thomas J Cox, Tiziana Di Matteo, Paul Martini, Brant Robertson, and Volker Springel. Black holes in galaxy mergers: Evolution of quasars. *The Astrophysical Journal*, 630(2):705, 2005.

Philip F. Hopkins, Gordon T. Richards, and Lars Hernquist. An Observational Determination of the Bolometric Quasar Luminosity Function. , 654(2):731–753, January 2007. 10.1086/509629.

Philip F Hopkins, Andrew Wetzel, Coral Wheeler, Robyn Sanderson, Michael Y Grudić, Omid Sameie, Michael Boylan-Kolchin, Matthew Orr, Xiangcheng Ma, Claude-André Faucher-Giguère, Dušan Kereš, Eliot Quataert, Kung-Yi Su, Jorge Moreno, Robert Feldmann, James S Bullock, Sarah R Loebman, Daniel Anglés-Alcázar, Jonathan Stern, Lina Necib, Caleb R Choban, and Christopher C Hayward. Fire-3: updated stellar evolution models, yields, and microphysics and fitting functions for applications in galaxy simulations. *Monthly Notices of the Royal Astronomical Society*, 519(2):3154–3181, December 2022. ISSN 1365-2966. 10.1093/mnras/stac3489. URL http://dx.doi.org/10.1093/mnras/stac3489.

Philip F Hopkins, Ethan O Nadler, Michael Y Grudić, Xuejian Shen, Isabel Sands, and Fangzhou Jiang. Novel conservative methods for adaptive force softening in collisionless and multispecies n-body simulations. *Monthly Notices of the Royal Astronomical Society*, 525(4):5951–5977, 2023.

Meicun Hou, Zhiyuan Li, and Xin Liu. A chandra x-ray survey of optically selected agn pairs. *The Astrophysical Journal*, 900(1):79, September 2020. ISSN 1538-4357. 10.3847/1538-4357/aba4a7. URL http://dx.doi.org/10.3847/1538-4357/aba4a7.

Jian Hu. The black hole mass-stellar velocity dispersion correlation: bulges versus pseudo-bulges. , 386(4):2242–2252, June 2008. 10.1111/j.1365-2966.2008.13195.x.

David A Hubber, Giovanni P Rosotti, and Richard A Booth. Gandalf–graphical astrophysics code for n-body dynamics and lagrangian fluids. *Monthly Notices of the Royal Astronomical Society*, 473(2):1603–1632, 2018.

M. Hudaverdi, E. N. Ercan, A. Mert-Ankar, F. Gok, E. Aktekin, G. I. Gun, B. Ugras, T. Guver, and H. Kunieda. Multi-Band Analysis of Abell 2255. *arXiv e-prints*, art. arXiv:0803.2168, March 2008. 10.48550/arXiv.0803.2168.

D. S. Hudson, R. Mittal, T. H. Reiprich, P. E. J. Nulsen, H. Andernach, and C. L. Sarazin. What is a cool-core cluster? a detailed analysis of the cores of the X-ray flux-limited HIFLUGCS cluster sample. , 513:A37, April 2010. 10.1051/0004-6361/200912377.

Pablo Huijse, Jordy Davelaar, Joris De Ridder, Nicholas Jannsen, and Conny Aerts. Periodic variability in space photometry of 181 new supermassive black hole binary candidates, 2025. URL https://arxiv.org/abs/2505.16884.

H. S. Hwang, C. Park, D. Elbaz, and Y.-Y. Choi. Activity in galactic nuclei of cluster and field galaxies in the local universe. , 538:A15, February 2012. 10.1051/0004-6361/201117351.

Nadine Häring and Hans-Walter Rix. On the black hole mass-bulge mass relation. *The Astrophysical Journal*, 604(2):L89–L92, March 2004. ISSN 1538-4357. 10.1086/383567. URL http://dx.doi.org/10.1086/383567.

Francesca Iannuzzi and Klaus Dolag. Adaptive gravitational softening in gadget: Adaptive softening in gadget. *Monthly Notices of the Royal Astronomical Society*, 417(4):2846–2859, August 2011. ISSN 0035-8711. 10.1111/j.1365-2966.2011.19446.x. URL http://dx.doi.org/10.1111/j.1365-2966.2011.19446.x.

Kohei Inayoshi. Little red dots as the very first activity of black hole growth, 2025. URL https://arxiv.org/abs/2503.05537.

Kohei Inayoshi, Eli Visbal, and Zoltán Haiman. The assembly of the first massive black holes. *Annual Review of Astronomy and Astrophysics*, 58(1):27–97, August 2020. ISSN 1545-4282. 10.1146/annurev-astro-120419-014455. URL http://dx.doi.org/10.1146/annurev-astro-120419-014455.

Shu-ichiro Inutsuka. Reformulation of smoothed particle hydrodynamics with riemann solver. *Journal of Computational Physics*, 179(1):238–267, 2002.

J. R. Ipser. A numerical method for integrating the stellar-dynamical Fokker-Planck equation in a fixed inhomogeneous gravitational background. *ApJ*, 218:846–856, December 1977. ISSN 0004-637X. 10.1086/155740. URL https://ui.adsabs.harvard.edu/abs/1977ApJ...218..846I. Publisher: IOP ADS Bibcode: 1977ApJ...218..846I.

Yuzo Ishikawa, Nadia L Zakamska, Yue Shen, Xin Liu, Yu-Ching Chen, Hsiang-Chih Hwang, Andrey Vayner, David SN Rupke, Sylvain Veilleux, Dominika Wylezalek, et al. Vodka-jwst: Synchronized growth of two supermassive black holes in a massive gas disk? a 3.8 kpc separation dual quasar at cosmic noon with the nirspec integral field unit. *The Astrophysical Journal*, 982 (1):22, 2025.

Željko Ivezić, Kristen Menou, Gillian R. Knapp, Michael A. Strauss, Robert H. Lupton, Daniel E. Vanden Berk, Gordon T. Richards, Christy Tremonti, Michael A. Weinstein, Scott Anderson, Neta A. Bahcall, Robert H. Becker, Mariangela Bernardi, Michael Blanton, Daniel Eisenstein, Xiaohui Fan, Douglas Finkbeiner, Kristian Finlator, Joshua Frieman, James E. Gunn, Pat B. Hall, Rita S. J. Kim, Ali Kinkhabwala, Vijay K. Narayanan, Constance M. Rockosi, David Schlegel, Donald P. Schneider, Iskra Strateva, Mark SubbaRao, Aniruddha R. Thakar, Wolfgang Voges, Richard L. White, Brian Yanny, Jonathan Brinkmann, Mamoru Doi, Masataka Fukugita, Gregory S. Hennessy, Jeffrey A. Munn, Robert C. Nichol, and Donald G. York. Optical and radio properties of extragalactic sources observed by the first survey and the sloan digital sky survey. *The Astronomical Journal*, 124(5):2364–2400, November 2002. ISSN 1538-3881. 10.1086/344069. URL http://dx.doi.org/10.1086/344069.

Yashashree Jadhav, Andrew Robinson, Triana Almeyda, Rachel Curran, and Alessandro Marconi. The spatially offset quasar E1821+643: new evidence for gravitational recoil. , 507(1):484–495, October 2021. 10.1093/mnras/stab2176.

Myoungwon Jeon and Volker Bromm. Signature of the first galaxies in jwst deep field observations. *Monthly Notices of the Royal Astronomical Society*, 485(4):5939–5950, 2019.

Peter H Johansson, Andreas Burkert, and Thorsten Naab. The evolution of black hole scaling relations in galaxy mergers. *The Astrophysical Journal*, 707(2):L184, 2009.

GC Jones, R Maiolino, C Circosta, J Scholtz, S Carniani, and Y Fudamoto. Evidence for extended gaseous reservoirs around agn at cosmic noon from alma co (3- 2) observations. *Monthly Notices of the Royal Astronomical Society*, 518(1):691–708, 2023.

Ignas Juodžbalis, Roberto Maiolino, William M. Baker, Sandro Tacchella, Jan Scholtz, Francesco D'Eugenio, Joris Witstok, Raffaella Schneider, Alessandro Trinca, Rosa Valiante, Christa De-

Coursey, Mirko Curti, Stefano Carniani, Jacopo Chevallard, Anna de Graaff, Santiago Arribas, Jake S. Bennett, Martin A. Bourne, Andrew J. Bunker, Stéphane Charlot, Brian Jiang, Sophie Koudmani, Michele Perna, Brant Robertson, Debora Sijacki, Hannah Übler, Christina C. Williams, and Chris Willott. A dormant overmassive black hole in the early universe. *Nature*, 636(8043):594–597, December 2024. ISSN 1476-4687. 10.1038/s41586-024-08210-5. URL http://dx.doi.org/10.1038/s41586-024-08210-5.

A. Just, F. M. Khan, P. Berczik, A. Ernst, and R. Spurzem. Dynamical friction of massive objects in galactic centres: Dynamical friction of massive objects. *MNRAS*, 411(1):653–674, October 2010. ISSN 0035-8711. 10.1111/j.1365-2966.2010.17711.x. URL http://dx.doi.org/10.1111/j.1365-2966.2010.17711.x.

Kagra Collaboration, T. Akutsu, M. Ando, K. Arai, Y. Arai, S. Araki, A. Araya, N. Aritomi, H. Asada, Y. Aso, S. Atsuta, K. Awai, S. Bae, L. Baiotti, M. A. Barton, K. Cannon, E. Capocasa, C.-S. Chen, T.-W. Chiu, K. Cho, Y.-K. Chu, K. Craig, W. Creus, K. Doi, K. Eda, Y. Enomoto, R. Flaminio, Y. Fujii, M.-K. Fujimoto, M. Fukunaga, M. Fukushima, T. Furuhata, S. Haino, K. Hasegawa, K. Hashino, K. Hayama, S. Hirobayashi, E. Hirose, B. H. Hsieh, C.-Z. Huang, B. Ikenoue, Y. Inoue, K. Ioka, Y. Itoh, K. Izumi, T. Kaji, T. Kajita, M. Kakizaki, M. Kamiizumi, S. Kanbara, N. Kanda, S. Kanemura, M. Kaneyama, G. Kang, J. Kasuya, Y. Kataoka, N. Kawai, S. Kawamura, T. Kawasaki, C. Kim, J. Kim, J. C. Kim, W. S. Kim, Y.-M. Kim, N. Kimura, T. Kinugawa, S. Kirii, Y. Kitaoka, H. Kitazawa, Y. Kojima, K. Kokeyama, K. Komori, A. K. H. Kong, K. Kotake, R. Kozu, R. Kumar, H.-S. Kuo, S. Kuroyanagi, H. K. Lee, H. M. Lee, H. W. Lee, M. Leonardi, C.-Y. Lin, F.-L. Lin, G. C. Liu, Y. Liu, E. Majorana, S. Mano, M. Marchio, T. Matsui, F. Matsushima, Y. Michimura, N. Mio, O. Miyakawa, A. Miyamoto, T. Miyamoto, K. Miyo, S. Miyoki, W. Morii, S. Morisaki, Y. Moriwaki, T. Morozumi, M. Musha, K. Nagano, S. Nagano, K. Nakamura, T. Nakamura, H. Nakano, M. Nakano, K. Nakao, T. Narikawa, L. Naticchioni, L. Nguyen Quynh, W.-T. Ni, A. Nishizawa, Y. Obuchi, T. Ochi, J. J. Oh, S. H. Oh, M. Ohashi, N. Ohishi, M. Ohkawa, K. Okutomi, K. Ono, K. Oohara, C. P. Ooi, S.-S. Pan, J. Park, F. E. Peña Arellano, I. Pinto, N. Sago, M. Saijo, S. Saitou, Y. Saito, K. Sakai, Y. Sakai, Y. Sakai, M. Sasai, M. Sasaki, Y. Sasaki, S. Sato, N. Sato, T. Sato, Y. Sekiguchi, N. Seto, M. Shibata, T. Shimoda, H. Shinkai, T. Shishido, A. Shoda, K. Somiya, E. J. Son, A. Suemasa, T. Suzuki, T. Suzuki, H. Tagoshi, H. Tahara, H. Takahashi, R. Takahashi, A. Takamori, H. Takeda, H. Tanaka, K. Tanaka, T. Tanaka, S. Tanioka, E. N. Tapia San Martin, D. Tatsumi, T. Tomaru, T. Tomura, F. Travasso, K. Tsubono, S. Tsuchida, N. Uchikata, T. Uchiyama, T. Uehara, S. Ueki, K. Ueno, F. Uraguchi, T. Ushiba, M. H. P. M. van Putten, H. Vocca, S. Wada, T. Wakamatsu, Y. Watanabe, W.-R. Xu, T. Yamada, A. Yamamoto, K. Yamamoto, K. Yamamoto, S. Yamamoto, T. Yamamoto, K. Yokogawa, J. Yokoyama, T. Yokozawa, T. H. Yoon, T. Yoshioka, H. Yuzurihara, S. Zeidler, and Z.-H. Zhu. KAGRA: 2.5 generation interferometric gravitational wave detector. *Nature Astronomy*, 3:35–40, January 2019. 10.1038/s41550-018-0658-y.

D Kakkad, V Mainieri, Marcella Brusa, P Padovani, S Carniani, C Feruglio, M Sargent, B Husemann, A Bongiorno, M Bonzini, et al. Alma observations of cold molecular gas in agn hosts at z 1.5–evidence of agn feedback? *Monthly Notices of the Royal Astronomical Society*, 468(4): 4205–4215, 2017.

Wei-Bo Kao, Pedro R Capelo, Elia Cenci, Lucio Mayer, Alessandro Lupi, and Luca Sala. A novel

sub-grid model for super-eddington accretion of spinning black holes in galaxy-scale simulations. *arXiv preprint arXiv:2504.19281*, 2025.

A. I. Karakas. Updated stellar yields from asymptotic giant branch models. , 403(3):1413–1425, April 2010. 10.1111/j.1365-2966.2009.16198.x.

Shai Kaspi, Paul S. Smith, Hagai Netzer, Dan Maoz, Buell T. Jannuzi, and Uriel Giveon. Reverberation Measurements for 17 Quasars and the Size-Mass-Luminosity Relations in Active Galactic Nuclei. , 533(2):631–649, April 2000. 10.1086/308704.

S. Kaviraj, C. Laigle, T. Kimm, J. E. G. Devriendt, Y. Dubois, C. Pichon, A. Slyz, E. Chisari, and S. Peirani. The horizon-agn simulation: evolution of galaxy properties over cosmic time. *Monthly Notices of the Royal Astronomical Society*, page stx126, January 2017. ISSN 1365-2966. 10.1093/mnras/stx126. URL http://dx.doi.org/10.1093/mnras/stx126.

K. I. Kellermann, R. Sramek, M. Schmidt, D. B. Shaffer, and R. Green. VLA Observations of Objects in the Palomar Bright Quasar Survey. , 98:1195, October 1989. 10.1086/115207.

Brandon C. Kelly and Andrea Merloni. Mass Functions of Supermassive Black Holes across Cosmic Time. *Advances in Astronomy*, 2012:970858, January 2012. 10.1155/2012/970858.

Dušan Kereš, Mark Vogelsberger, Debora Sijacki, Volker Springel, and Lars Hernquist. Moving-mesh cosmology: characteristics of galaxies and haloes. *Monthly Notices of the Royal Astronomical Society*, 425(3):2027–2048, 2012.

Roy P. Kerr. Gravitational Field of a Spinning Mass as an Example of Algebraically Special Metrics. , 11(5):237–238, September 1963. 10.1103/PhysRevLett.11.237.

Fazeel Mahmood Khan, Andreas Just, and David Merritt. Efficient merger of binary supermassive black holes in merging galaxies. *The Astrophysical Journal*, 732(2):89, 2011.

Fazeel Mahmood Khan, Ingo Berentzen, Peter Berczik, Andreas Just, Lucio Mayer, Keigo Nitadori, and Simone Callegari. Formation and hardening of supermassive black hole binaries in minor mergers of disk galaxies. *The Astrophysical Journal*, 756(1):30, 2012.

Fazeel Mahmood Khan, Kelly Holley-Bockelmann, Peter Berczik, and Andreas Just. Supermassive black hole binary evolution in axisymmetric galaxies: the final parsec problem is not a problem. *The Astrophysical Journal*, 773(2):100, 2013.

M. Kidger, L. Takalo, and A. Sillanpaa. A new analysis of the 11-year period in OJ 287 : confirmationof its existence. , 264:32–36, October 1992.

M Kidger, L Takalo, and A Sillanpaa. A new analysis of the 11-year period in oj287-confirmation of its existence. *Astronomy and Astrophysics (ISSN 0004-6361), vol. 264, no. 1, p. 32-36.*, 264: 32–36, 1992.

D. C. Kim, Ilsang Yoon, and A. S. Evans. Recoiling Supermassive Black Hole in Changing-look AGN Mrk 1018. , 861(1):51, July 2018. 10.3847/1538-4357/aac77d.

D. C. Kim, Minjin Kim, Ilsang Yoon, E. Momjian, Ji Hoon Kim, J. Letai, and A. S. Evans. Adaptive optics and VLBA imaging observations of recoiling supermassive black hole candidates. , 517(3):4081–4091, December 2022. 10.1093/mnras/stac2774.

Minjin Kim and Luis C. Ho. Evidence for a Young Stellar Population in Nearby Type 1 Active Galaxies. , 876(1):35, May 2019. 10.3847/1538-4357/ab11cf.

Andrew King. Black holes, galaxy formation, and the M-sigma relation. *Astrophysical Journal Letters*, 596:L27–L29, 2003.

Andrew King. The black hole masses of high-redshift qsos. *Monthly Notices of the Royal Astronomical Society*, 531(1):550–553, 2024.

C. C. Kirkpatrick, M. Gitti, K. W. Cavagnolo, B. R. McNamara, L. P. David, P. E. J. Nulsen, and M. W. Wise. Direct Evidence for Outflow of Metal-Enriched Gas Along the Radio Jets of Hydra A. , 707(1):L69–L72, December 2009. 10.1088/0004-637X/707/1/L69.

Ralf S Klessen and Simon CO Glover. The first stars: formation, properties, and impact. *Annual Review of Astronomy and Astrophysics*, 61(1):65–130, 2023.

Dale D. Kocevski, S. M. Faber, Mark Mozena, Anton M. Koekemoer, Kirpal Nandra, Cyprian Rangel, Elise S. Laird, Marcella Brusa, Stijn Wuyts, Jonathan R. Trump, David C. Koo, Rachel S. Somerville, Eric F. Bell, Jennifer M. Lotz, David M. Alexander, Frederic Bournaud, Christopher J. Conselice, Tomas Dahlen, Avishai Dekel, Jennifer L. Donley, James S. Dunlop, Alexis Finoguenov, Antonis Georgakakis, Mauro Giavalisco, Yicheng Guo, Norman A. Grogin, Nimish P. Hathi, Stéphanie Juneau, Jeyhan S. Kartaltepe, Ray A. Lucas, Elizabeth J. McGrath, Daniel H. McIntosh, Bahram Mobasher, Aday R. Robaina, David Rosario, Amber N. Straughn, Arjen van der Wel, and Carolin Villforth. CANDELS: Constraining the AGN-Merger Connection with Host Morphologies at z ~2. , 744(2):148, January 2012. 10.1088/0004-637X/744/2/148.

S. Komossa, D. Xu, H. Zhou, T. Storchi-Bergmann, and L. Binette. On the Nature of Seyfert Galaxies with High [O III] λ5007 Blueshifts. , 680(2):926–938, June 2008. 10.1086/587932.

S. Komossa, S. Ciprini, L. Dey, L. C. Gallo, J. L. Gomez, A. Gonzalez, D. Grupe, A. Kraus, S. J. Laine, M. L. Parker, M. J. Valtonen, S. Chandra, A. Gopakumar, D. Haggard, and M. A. Nowak. Supermassive binary black holes and the case of oj 287, 2021. URL https://arxiv.org/abs/2104.12901.

J. Kormendy and D. B. Fisher. Secular Evolution in Disk Galaxies: Pseudobulge Growth and the Formation of Spheroidal Galaxies. In J. G. Funes and E. M. Corsini, editors, *Formation and Evolution of Galaxy Disks*, volume 396 of *Astronomical Society of the Pacific Conference Series*, page 297, October 2008. 10.48550/arXiv.0810.2534.

John Kormendy and Ralf Bender. Supermassive black holes do not correlate with dark matter haloes of galaxies. *Nature*, 469(7330):377–380, January 2011. ISSN 1476-4687. 10.1038/nature09695. URL http://dx.doi.org/10.1038/nature09695.

John Kormendy and Luis C. Ho. Coevolution (Or Not) of Supermassive Black Holes and Host Galaxies. , 51(1):511–653, August 2013. 10.1146/annurev-astro-082708-101811.

John Kormendy and Douglas Richstone. Evidence for a supermassive black hole in ngc 3115. *Astrophysical Journal, Part 1 (ISSN 0004-637X), vol. 393, no. 2, July 10, 1992, p. 559-578. Research supported by Ambrose-Monell Foundation.*, 393:559–578, 1992.

John Kormendy and Douglas Richstone. Inward Bound—The Search For Supermassive Black Holes In Galactic Nuclei. , 33:581, January 1995. 10.1146/annurev.aa.33.090195.003053.

John Kormendy, David B. Fisher, Mark E. Cornell, and Ralf Bender. Structure and Formation of Elliptical and Spheroidal Galaxies. , 182(1):216–309, May 2009. 10.1088/0067-0049/182/1/216.

Michael Koss, Richard Mushotzky, Ezequiel Treister, Sylvain Veilleux, Ranjan Vasudevan, and Margaret Trippe. Understanding Dual Active Galactic Nucleus Activation in the nearby Universe. , 746(2):L22, February 2012. 10.1088/2041-8205/746/2/L22.

Michael J. Koss, Laura Blecha, Phillip Bernhard, Chao-Ling Hung, Jessica R. Lu, Benny Trakhtenbrot, Ezequiel Treister, Anna Weigel, Lia F. Sartori, Richard Mushotzky, Kevin Schawinski, Claudio Ricci, Sylvain Veilleux, and David B. Sanders. A population of luminous accreting black holes with hidden mergers. , 563(7730):214–216, November 2018. 10.1038/s41586-018-0652-7.

E. Koulouridis and I. Bartalucci. High density of active galactic nuclei in the outskirts of distant galaxy clusters. , 623:L10, March 2019. 10.1051/0004-6361/201935082.

Andrey V Kravtsov and Stefano Borgani. Formation of galaxy clusters. *Annual Review of Astronomy and Astrophysics*, 50(1):353–409, 2012.

Julian H. Krolik and Mitchell C. Begelman. Molecular Tori in Seyfert Galaxies: Feeding the Monster and Hiding It. , 329:702, June 1988. 10.1086/166414.

Mark R Krumholz. The star formation law in molecule-poor galaxies. *Monthly Notices of the Royal Astronomical Society*, 436(3):2747–2762, 2013.

Girish Kulkarni, Gábor Worseck, and Joseph F Hennawi. Evolution of the agn uv luminosity function from redshift 7.5. *Monthly Notices of the Royal Astronomical Society*, 488(1):1035–1065, 2019.

Fabio La Franca, F Fiore, A Comastri, GC Perola, N Sacchi, Marcella Brusa, F Cocchia, C Feruglio, G Matt, Cristian Vignali, et al. The hellas2xmm survey. vii. the hard x-ray luminosity function of agns up to z= 4: More absorbed agns at low luminosities and high redshifts. *The Astrophysical Journal*, 635(2):864, 2005.

Mark Lacy, Susan E Ridgway, Anna Sajina, Andreea O Petric, Elinor L Gates, Tanya Urrutia, and Lisa J Storrie-Lombardi. The spitzer mid-infrared agn survey. ii. the demographics and cosmic evolution of the agn population. *The Astrophysical Journal*, 802(2):102, 2015.

Lev Davidovic Landau. *The Kinetic Equation in the Case of Coulomb Interaction*. Defense Technical Information Center, 1958.

Culbert B. Laney. *Computational Gasdynamics*. Cambridge University Press, 1998.

Muhammad A. Latif and Andrea Ferrara. Formation of supermassive black hole seeds. *Publications of the Astronomical Society of Australia*, 33, 2016. ISSN 1448-6083. 10.1017/pasa.2016.41. URL http://dx.doi.org/10.1017/pasa.2016.41.

Tod R Lauer, SM Faber, Douglas Richstone, Karl Gebhardt, Scott Tremaine, Marc Postman, Alan Dressler, MC Aller, Alexei V Filippenko, Richard Green, et al. The masses of nuclear black holes in luminous elliptical galaxies and implications for the space density of the most massive black holes. *The Astrophysical Journal*, 662(2):808, 2007.

M. Laurenti, E. Piconcelli, L. Zappacosta, F. Tombesi, C. Vignali, S. Bianchi, P. Marziani, F. Vagnetti, A. Bongiorno, M. Bischetti, A. del Olmo, G. Lanzuisi, A. Luminari, R. Middei,

M. Perri, C. Ricci, and G. Vietri. X-ray spectroscopic survey of highly accreting agn. *Astronomy amp; Astrophysics*, 657:A57, January 2022. ISSN 1432-0746. 10.1051/0004-6361/202141829. URL http://dx.doi.org/10.1051/0004-6361/202141829.

Nicholas M. Law, Shrinivas R. Kulkarni, Richard G. Dekany, Eran O. Ofek, Robert M. Quimby, Peter E. Nugent, Jason Surace, Carl C. Grillmair, Joshua S. Bloom, Mansi M. Kasliwal, Lars Bildsten, Tim Brown, S. Bradley Cenko, David Ciardi, Ernest Croner, S. George Djorgovski, Julian van Eyken, Alexei V. Filippenko, Derek B. Fox, Avishay Gal-Yam, David Hale, Nouhad Hamam, George Helou, John Henning, D. Andrew Howell, Janet Jacobsen, Russ Laher, Sean Mattingly, Dan McKenna, Andrew Pickles, Dovi Poznanski, Gustavo Rahmer, Arne Rau, Wayne Rosing, Michael Shara, Roger Smith, Dan Starr, Mark Sullivan, Viswa Velur, Richard Walters, and Jeff Zolkower. The Palomar Transient Factory: System Overview, Performance, and First Results. , 121(886):1395, December 2009. 10.1086/648598.

S. M. Lea and D. S. De Young. The dynamical interaction between galaxies and intracluster gas in clusters of galaxies. , 210:647–665, December 1976. 10.1086/154871.

J. P. Leahy and R. A. Perley. VLA Images of 23 Extragalactic Radio Sources. , 102:537, August 1991. 10.1086/115892.

A. Leccardi, M. Rossetti, and S. Molendi. Thermo-dynamic and chemical properties of the intra-cluster medium. , 510:A82, February 2010. 10.1051/0004-6361/200913094.

Harry J. Lehto and Mauri J. Valtonen. OJ 287 Outburst Structure and a Binary Black Hole Model. , 460:207, March 1996. 10.1086/176962.

S. Lepp and J. M. Shull. Molecules in the early universe. , 280:465–469, May 1984. 10.1086/162013.

Sandrine Lescaudron, Yohan Dubois, Ricarda S Beckmann, and Marta Volonteri. Dynamical friction of a massive black hole in a turbulent gaseous medium. *Astronomy & Astrophysics*, 674: A217, 2023.

Junyao Li, John D. Silverman, Yue Shen, Marta Volonteri, Knud Jahnke, Ming-Yang Zhuang, Matthew T. Scoggins, Xuheng Ding, Yuichi Harikane, Masafusa Onoue, and Takumi S. Tanaka. Tip of the iceberg: overmassive black holes at 4<z<7 found by jwst are not inconsistent with the local $\mathcal{M}_{\rm bh}$-$\mathcal{M}_\star$ relation, 2024. URL https://arxiv.org/abs/2403.00074.

Kunyang Li, Tamara Bogdanović, and David R Ballantyne. Pairing of massive black holes in merger galaxies driven by dynamical friction. *ApJ*, 896(2):113, 2020.

Kunyang Li, Marta Volonteri, Yohan Dubois, Ricarda Beckmann, and Maxime Trebitsch. RAMCOAL: Tracking on-the-fly massive black hole binary evolution and coalescence in galaxy simulations. , 701:A232, September 2025. 10.1051/0004-6361/202452562.

Qiong Li, Christopher J. Conselice, Qiao Duan, Duncan Austin, Tom Harvey, Nathan Adams, George Bendo, Lewi Westcott, Vadim Rusakov, Zheng Cai, Yuanhang Ning, and Shiwu Zhang. A dual agn at z = 5.4 associated with a lyman-alpha nebula in the center of a cosmic filament, 2025. URL https://arxiv.org/abs/2508.09749.

D. N. C. Lin and J. Papaloizou. Tidal torques on accretion discs in binary systems with extreme mass ratios. , 186:799–812, March 1979. 10.1093/mnras/186.4.799.

Boyuan Liu, James Gurian, Kohei Inayoshi, Shingo Hirano, Takashi Hosokawa, Volker Bromm, and Naoki Yoshida. Towards a universal analytical model for population iii star formation: interplay between feedback and fragmentation. *Monthly Notices of the Royal Astronomical Society*, 534(1): 290–312, 2024.

Fu-Kun Liu, Xue-Bing Wu, and SL Cao. Double—double radio galaxies: remnants of merged supermassive binary black holes. *Monthly Notices of the Royal Astronomical Society*, 340(2): 411–416, 2003.

Tingting Liu, Michael Koss, Laura Blecha, Claudio Ricci, Benny Trakhtenbrot, Richard Mushotzky, Fiona Harrison, Kohei Ichikawa, Darshan Kakkad, Kyuseok Oh, Meredith Powell, George C. Privon, Kevin Schawinski, T. Taro Shimizu, Krista Lynne Smith, Daniel Stern, Ezequiel Treister, and C. Megan Urry. The bat agn spectroscopic survey. xviii. searching for supermassive black hole binaries in x-rays. *The Astrophysical Journal*, 896(2):122, June 2020. ISSN 1538-4357. 10.3847/1538-4357/ab952d. URL http://dx.doi.org/10.3847/1538-4357/ab952d.

Yuan Liu. Finding binary active galactic nuclei by the centroid shift in imaging surveys. *Astronomy amp; Astrophysics*, 580:A133, August 2015. ISSN 1432-0746. 10.1051/0004-6361/201526266. URL http://dx.doi.org/10.1051/0004-6361/201526266.

K. Y. Lo. Mega-Masers and Galaxies. , 43(1):625–676, September 2005. 10.1146/annurev.astro.41.011802.094927

Abraham Loeb. Observable signatures of a black hole ejected by gravitational-radiation recoil in a galaxy merger. *Physical Review Letters*, 99(4), July 2007. ISSN 1079-7114. 10.1103/physrevlett.99.041103. URL http://dx.doi.org/10.1103/PhysRevLett.99.041103.

Abraham Loeb and Frederic A Rasio. Collapse of primordial gas clouds and the formation of quasar black holes. *arXiv preprint astro-ph/9401026*, 1994.

Enrique Lopez-Rodriguez, Cristina Ramos Almeida, Miguel Pereira-Santaella, Ismael García-Bernete, Robert Nikutta, Almudena Alonso-Herrero, Enrica Bellocchi, Andrew Bunker, Steph Campbell, Françoise Combes, Richard Davies, Tanio Diaz-Santos, Lindsay Fuller, Poshak Gandhi, Santiago García-Burillo, Omaira González-Martín, Erin K. S. Hicks, Sebastian Hönig, Kohei Ichikawa, Masatoshi Imanishi, Takuma Izumi, Alvaro Labiano, Nancy A. Levenson, Christopher Packham, David Rosario, Dimitra Rigopoulou, Daniel Rouan, Taro Shimizu, Marko Stalevski, Martin Ward, Lulu Zhang, Claudio Ricci, Donaji Esparza-Arredondo, and Begoña García-Lorenzo. Gatos. n. on the physical origin of the extended mir emission in agn, 2025. URL https://arxiv.org/abs/2507.19350.

Aaron D. Ludlow, Joop Schaye, and Richard Bower. Numerical convergence of simulations of galaxy formation: the abundance and internal structure of cold dark matter haloes. , 488(3): 3663–3684, September 2019. 10.1093/mnras/stz1821.

Alessandro Lupi, Alessandro Trinca, Marta Volonteri, Massimo Dotti, and Chiara Mazzucchelli. Size matters: are we witnessing super-eddington accretion in high-redshift black holes from jwst? *Astronomy & Astrophysics*, 689:A128, 2024.

N. López-Gonzaga, L. Burtscher, K. R. W. Tristram, K. Meisenheimer, and M. Schartmann. Mid-infrared interferometry of 23 agn tori: On the significance of polar-elongated emission. *Astronomy*

amp; Astrophysics, 591:A47, June 2016. ISSN 1432-0746. 10.1051/0004-6361/201527590. URL http://dx.doi.org/10.1051/0004-6361/201527590.

Linhao Ma, Philip F Hopkins, Luke Zoltan Kelley, and Claude-André Faucher-Giguère. A new discrete dynamical friction estimator based on n-body simulations. *Monthly Notices of the Royal Astronomical Society*, 519(4):5543–5553, 2023.

Andrew I MacFadyen and Miloš Milosavljević. An eccentric circumbinary accretion disk and the detection of binary massive black holes. *The Astrophysical Journal*, 672(1):83, 2008.

Piero Madau, Francesco Haardt, and Martin J. Rees. Radiative transfer in a clumpy universe. iii. the nature of cosmological ionizing sources. *The Astrophysical Journal*, 514(2):648–659, April 1999. ISSN 1538-4357. 10.1086/306975. URL http://dx.doi.org/10.1086/306975.

John Magorrian, Scott Tremaine, Douglas Richstone, Ralf Bender, Gary Bower, Alan Dressler, S. M. Faber, Karl Gebhardt, Richard Green, Carl Grillmair, John Kormendy, and Tod Lauer. The Demography of Massive Dark Objects in Galaxy Centers. , 115(6):2285–2305, June 1998. 10.1086/300353.

U. Maio, K. Dolag, B. Ciardi, and L. Tornatore. Metal and molecule cooling in simulations of structure formation. *Monthly Notices of the Royal Astronomical Society*, 379(3):963–973, August 2007. ISSN 1365-2966. 10.1111/j.1365-2966.2007.12016.x. URL http://dx.doi.org/10.1111/j.1365-2966.2007.12016.x.

Roberto Maiolino, S Carniani, A Fontana, Livia Vallini, L Pentericci, Andrea Ferrara, E Vanzella, A Grazian, Simona Gallerani, M Castellano, et al. The assembly of 'normal'galaxies at z 7 probed by alma. *Monthly Notices of the Royal Astronomical Society*, 452(1):54–68, 2015.

Roberto Maiolino, Jan Scholtz, Joris Witstok, Stefano Carniani, Francesco D'Eugenio, Anna de Graaff, Hannah Übler, Sandro Tacchella, Emma Curtis-Lake, Santiago Arribas, Andrew Bunker, Stéphane Charlot, Jacopo Chevallard, Mirko Curti, Tobias J. Looser, Michael V. Maseda, Timothy D. Rawle, Bruno Rodríguez del Pino, Chris J. Willott, Eiichi Egami, Daniel J. Eisenstein, Kevin N. Hainline, Brant Robertson, Christina C. Williams, Christopher N. A. Willmer, William M. Baker, Kristan Boyett, Christa DeCoursey, Andrew C. Fabian, Jakob M. Helton, Zhiyuan Ji, Gareth C. Jones, Nimisha Kumari, Nicolas Laporte, Erica J. Nelson, Michele Perna, Lester Sandles, Irene Shivaei, and Fengwu Sun. A small and vigorous black hole in the early Universe. , 627(8002):59–63, March 2024. 10.1038/s41586-024-07052-5.

Junichiro Makino and Yoko Funato. Evolution of massive black hole binaries. *The Astrophysical Journal*, 602(1):93, 2004.

Matias Mannerkoski, Alexander Rawlings, Peter H Johansson, Thorsten Naab, Antti Rantala, Volker Springel, Dimitrios Irodotou, and Shihong Liao. Ketju–resolving small-scale supermassive black hole dynamics in gadget-4. *Monthly Notices of the Royal Astronomical Society*, 524(3):4062–4082, 2023.

F. Mannucci, E. Pancino, F. Belfiore, C. Cicone, A. Ciurlo, G. Cresci, E. Lusso, A. Marasco, A. Marconi, E. Nardini, E. Pinna, P. Severgnini, P. Saracco, G. Tozzi, and S. Yeh. Unveiling the population of dual and lensed active galactic nuclei at sub-arcsec separations. *Nature Astronomy*,

6(10):1185–1192, August 2022. ISSN 2397-3366. 10.1038/s41550-022-01761-5. URL http://dx.doi.org/10.1038/s41550-022-01761-5.

A. Marconi, G. Risaliti, R. Gilli, L. K. Hunt, R. Maiolino, and M. Salvati. Local supermassive black holes, relics of active galactic nuclei and the x-ray background. *Monthly Notices of the Royal Astronomical Society*, 351(1):169–185, 06 2004. ISSN 0035-8711. 10.1111/j.1365-2966.2004.07765.x. URL https://doi.org/10.1111/j.1365-2966.2004.07765.x.

Alessandro Marconi and Leslie K. Hunt. The Relation between Black Hole Mass, Bulge Mass, and Near-Infrared Luminosity. , 589(1):L21–L24, May 2003. 10.1086/375804.

Alessandro Marconi and Marco Salvati. Relic black holes and type 2 quasars. *arXiv preprint astro-ph/0110698*, 2001.

I Marini, A Saro, S Borgani, G Murante, E Rasia, K Dolag, W Lin, N R Napolitano, A Ragagnin, L Tornatore, and Y Wang. On the phase-space structure of galaxy clusters from cosmological simulations. , 500(3):3462–3480, November 2020. ISSN 1365-2966. 10.1093/mnras/staa3486. URL http://dx.doi.org/10.1093/mnras/staa3486.

ILARIA Marini, STEFANO Borgani, ALEXANDRO Saro, Gian Luigi Granato, C Ragone-Figueroa, Barbara Sartoris, K Dolag, Giuseppe Murante, ANTONIO Ragagnin, and Y Wang. Velocity dispersion of brightest cluster galaxies in cosmological simulations. *Monthly Notices of the Royal Astronomical Society*, 507(4):5780–5795, 2021.

Crystal L Martin. Properties of galactic outflows: measurements of the feedback from star formation. *The Astrophysical Journal*, 513(1):156, 1999.

Paul Martini, Daniel D Kelson, Eunhyeuk Kim, John S Mulchaey, and Alex A Athey. Spectroscopic confirmation of a large population of active galactic nuclei in clusters of galaxies. *The Astrophysical Journal*, 644(1):116, 2006.

Paul Martini, John S Mulchaey, and Daniel D Kelson. The distribution of active galactic nuclei in clusters of galaxies. *The Astrophysical Journal*, 664(2):761, 2007.

Mary Loli Martínez–Aldama, Michal Zajaček, Bożena Czerny, and Swayamtrupta Panda. Scatter analysis along the multidimensional radius–luminosity relations for reverberation-mapped mg ii sources. *The Astrophysical Journal*, 903(2):86, November 2020. ISSN 1538-4357. 10.3847/1538-4357/abb6f8. URL http://dx.doi.org/10.3847/1538-4357/abb6f8.

Daniel Maschmann, Anaëlle Halle, Anne-Laure Melchior, Françoise Combes, and Igor V. Chilingarian. The origin of double-peak emission-line galaxies: Rotating discs, bars, or galaxy mergers? *Astronomy amp; Astrophysics*, 670:A46, February 2023. ISSN 1432-0746. 10.1051/0004-6361/202244746. URL http://dx.doi.org/10.1051/0004-6361/202244746.

Daniel Masters, Peter Capak, Mara Salvato, Francesca Civano, Bahram Mobasher, Brian Siana, Guenther Hasinger, CD Impey, Tohru Nagao, JR Trump, et al. Evolution of the quasar luminosity function over 3< z< 5 in the cosmos survey field. *The Astrophysical Journal*, 755(2):169, 2012.

S. Mateos, F. J. Carrera, X. Barcons, A. Alonso-Herrero, A. Hernán-Caballero, M. Page, C. Ramos Almeida, A. Caccianiga, T. Miyaji, and A. Blain. Survival of the Obscuring Torus in the Most Powerful Active Galactic Nuclei. , 841(2):L18, June 2017. 10.3847/2041-8213/aa7268.

Yoshiki Matsuoka, Masafusa Onoue, Kazushi Iwasawa, Michael A Strauss, Nobunari Kashikawa, Takuma Izumi, Tohru Nagao, Masatoshi Imanishi, Masayuki Akiyama, John D Silverman, et al. Quasar luminosity function at z= 7. *The Astrophysical Journal Letters*, 949(2):L42, 2023.

Thomas A Matthews and Allan R Sandage. Optical identification of 3c 48, 3c 196, and 3c 286 with stellar objects. *Astrophysical Journal, vol. 138, p. 30*, 138:30, 1963.

B. J. Maughan, P. A. Giles, S. W. Randall, C. Jones, and W. R. Forman. Self-similar scaling and evolution in the galaxy cluster X-ray luminosity-temperature relation. , 421(2):1583–1602, April 2012. 10.1111/j.1365-2966.2012.20419.x.

L. Mayer, S. Kazantzidis, P. Madau, M. Colpi, T. Quinn, and J. Wadsley. Rapid Formation of Supermassive Black Hole Binaries in Galaxy Mergers with Gas. *Science*, 316(5833):1874, June 2007. 10.1126/science.1141858.

Nicholas J. McConnell and Chung-Pei Ma. Revisiting the Scaling Relations of Black Hole Masses and Host Galaxy Properties. , 764(2):184, February 2013. 10.1088/0004-637X/764/2/184.

M. McDonald, B. A. Benson, A. Vikhlinin, B. Stalder, L. E. Bleem, T. de Haan, H. W. Lin, K. A. Aird, M. L. N. Ashby, M. W. Bautz, M. Bayliss, S. Bocquet, M. Brodwin, J. E. Carlstrom, C. L. Chang, H. M. Cho, A. Clocchiatti, T. M. Crawford, A. T. Crites, S. Desai, M. A. Dobbs, J. P. Dudley, R. J. Foley, W. R. Forman, E. M. George, D. Gettings, M. D. Gladders, A. H. Gonzalez, N. W. Halverson, F. W. High, G. P. Holder, W. L. Holzapfel, S. Hoover, J. D. Hrubes, C. Jones, M. Joy, R. Keisler, L. Knox, A. T. Lee, E. M. Leitch, J. Liu, M. Lueker, D. Luong-Van, A. Mantz, D. P. Marrone, J. J. McMahon, J. Mehl, S. S. Meyer, E. D. Miller, L. Mocanu, J. J. Mohr, T. E. Montroy, S. S. Murray, D. Nurgaliev, S. Padin, T. Plagge, C. Pryke, C. L. Reichardt, A. Rest, J. Ruel, J. E. Ruhl, B. R. Saliwanchik, A. Saro, J. T. Sayre, K. K. Schaffer, E. Shirokoff, J. Song, R. Šuhada, H. G. Spieler, S. A. Stanford, Z. Staniszewski, A. A. Stark, K. Story, A. van Engelen, K. Vanderlinde, J. D. Vieira, R. Williamson, O. Zahn, and A. Zenteno. The Growth of Cool Cores and Evolution of Cooling Properties in a Sample of 83 Galaxy Clusters at $0.3 < z < 1.2$ Selected from the SPT-SZ Survey. , 774(1):23, September 2013. 10.1088/0004-637X/774/1/23.

M. McDonald, S. W. Allen, M. Bayliss, B. A. Benson, L. E. Bleem, M. Brodwin, E. Bulbul, J. E. Carlstrom, W. R. Forman, J. Hlavacek-Larrondo, G. P. Garmire, M. Gaspari, M. D. Gladders, A. B. Mantz, and S. S. Murray. The Remarkable Similarity of Massive Galaxy Clusters from $z \sim 0$ to $z \sim 1.9$. , 843(1):28, July 2017. 10.3847/1538-4357/aa7740.

M. McDonald, M. Gaspari, B. R. McNamara, and G. R. Tremblay. Revisiting the cooling flow problem in galaxies, groups, and clusters of galaxies. *The Astrophysical Journal*, 858(1):45, May 2018. ISSN 1538-4357. 10.3847/1538-4357/aabace. URL http://dx.doi.org/10.3847/1538-4357/aabace.

M. McDonald, S. W. Allen, J. Hlavacek-Larrondo, A. B. Mantz, M. Bayliss, B. A. Benson, M. Brodwin, E. Bulbul, R. E. A. Canning, I. Chiu, W. R. Forman, G. P. Garmire, N. Gupta, G. Khullar, J. J. Mohr, C. L. Reichardt, and T. Schrabback. A detailed study of the most relaxed spt-selected galaxy clusters: Properties of the cool core and central galaxy. *The Astrophysical Journal*, 870(2):85, January 2019. ISSN 1538-4357. 10.3847/1538-4357/aaf394. URL http://dx.doi.org/10.3847/1538-4357/aaf394.

Michael McDonald, Sylvain Veilleux, David S. N. Rupke, and Richard Mushotzky. On the Origin of the Extended Hα Filaments in Cooling Flow Clusters. , 721(2):1262–1283, October 2010. 10.1088/0004-637X/721/2/1262.

R. C. McGurk, C. E. Max, A. M. Medling, G. A. Shields, and J. M. Comerford. Spatially Resolved Imaging and Spectroscopy of Candidate Dual Active Galactic Nuclei. , 811(1):14, September 2015. 10.1088/0004-637X/811/1/14.

B. R. McNamara and P. E. J. Nulsen. Heating Hot Atmospheres with Active Galactic Nuclei. , 45(1):117–175, September 2007. 10.1146/annurev.astro.45.051806.110625.

B. R. McNamara and P. E. J. Nulsen. Mechanical feedback from active galactic nuclei in galaxies, groups and clusters. *New Journal of Physics*, 14(5):055023, May 2012. 10.1088/1367-2630/14/5/055023.

BR McNamara, Mina Rohanizadegan, and PEJ Nulsen. Are radio active galactic nuclei powered by accretion or black hole spin? *The Astrophysical Journal*, 727(1):39, 2010.

Elinor Medezinski, Michael McDonald, Surhud More, Hironao Miyatake, Nicholas Battaglia, Massimo Gaspari, David Spergel, and Renyue Cen. On the assembly bias of cool core clusters traced by h nebulae. *The Astrophysical Journal*, 882(2):166, September 2019. ISSN 1538-4357. 10.3847/1538-4357/ab2da2. URL http://dx.doi.org/10.3847/1538-4357/ab2da2.

Harshitha Menon, Lukasz Wesolowski, Gengbin Zheng, Pritish Jetley, Laxmikant Kale, Thomas Quinn, and Fabio Governato. Adaptive techniques for clustered n-body cosmological simulations, 2014. URL https://arxiv.org/abs/1409.1929.

A. Merloni, S. Heinz, and T. Di Matteo. A fundamental plane of black hole activity. *Monthly Notices of the Royal Astronomical Society*, 345(4):1057–1076, November 2003. ISSN 1365-2966. 10.1046/j.1365-2966.2003.07017.x. URL http://dx.doi.org/10.1046/j.1365-2966.2003.07017.x.

A. Merloni, A. Bongiorno, M. Bolzonella, M. Brusa, F. Civano, A. Comastri, M. Elvis, F. Fiore, R. Gilli, H. Hao, K. Jahnke, A. M. Koekemoer, E. Lusso, V. Mainieri, M. Mignoli, T. Miyaji, A. Renzini, M. Salvato, J. Silverman, J. Trump, C. Vignali, G. Zamorani, P. Capak, S. J. Lilly, D. Sanders, Y. Taniguchi, S. Bardelli, C. M. Carollo, K. Caputi, T. Contini, G. Coppa, O. Cucciati, S. de la Torre, L. de Ravel, P. Franzetti, B. Garilli, G. Hasinger, C. Impey, A. Iovino, K. Iwasawa, P. Kampczyk, J. P. Kneib, C. Knobel, K. Kovač, F. Lamareille, J. F. Le Borgne, V. Le Brun, O. Le Fèvre, C. Maier, R. Pello, Y. Peng, E. Perez Montero, E. Ricciardelli, M. Scodeggio, M. Tanaka, L. A. M. Tasca, L. Tresse, D. Vergani, and E. Zucca. On the Cosmic Evolution of the Scaling Relations Between Black Holes and Their Host Galaxies: Broad-Line Active Galactic Nuclei in the zCOSMOS Survey. , 708(1):137–157, January 2010. 10.1088/0004-637X/708/1/137.

Andrea Merloni. The anti-hierarchical growth of supermassive black holes. *Monthly Notices of the Royal Astronomical Society*, 353(4):1035–1047, 2004.

Andrea Merloni and Sebastian Heinz. A synthesis model for agn evolution: supermassive black holes growth and feedback modes. *Monthly Notices of the Royal Astronomical Society*, 388(3): 1011–1030, 2008.

David Merritt and MY Poon. Chaotic loss cones and black hole fueling. *The Astrophysical Journal*, 606(2):788, 2004.

M. Mezcua and H. Domínguez Sánchez. MaNGA AGN dwarf galaxies (MAD) - I. A new sample of AGNs in dwarf galaxies with spatially-resolved spectroscopy. , 528(3):5252–5268, March 2024. 10.1093/mnras/stae292.

Mar Mezcua and Helena Domínguez Sánchez. Hidden agns in dwarf galaxies revealed by manga: Light echoes, off-nuclear wanderers, and a new broad-line agn. *The Astrophysical Journal Letters*, 898(2):L30, July 2020. ISSN 2041-8213. 10.3847/2041-8213/aba199. URL http://dx.doi.org/10.3847/2041-8213/aba199.

Miroslav Micic, Kelly Holley-Bockelmann, Steinn Sigurdsson, and Tom Abel. Supermassive black hole growth and merger rates from cosmological n-body simulations. *Monthly Notices of the Royal Astronomical Society*, 380(4):1533–1540, 2007.

Chris Mihos and Lars Hernquist. Gasdynamics and starbursts in major mergers. *arXiv preprint astro-ph/9512099*, 1995.

Seppo Mikkola and Mauri J Valtonen. Evolution of binaries in the field of light particles and the problem of two black holes. *Monthly Notices of the Royal Astronomical Society*, 259(1):115–120, 1992.

George Miley and Carlos De Breuck. Distant radio galaxies and their environments. , 15(2): 67–144, February 2008. 10.1007/s00159-007-0008-z.

Miloš Milosavljević and David Merritt. Formation of Galactic Nuclei. , 563(1):34–62, December 2001. 10.1086/323830.

Miloš Milosavljević and David Merritt. The final parsec problem. In *AIP conference proceedings*, volume 686, pages 201–210. American Institute of Physics, 2003.

Miloš Milosavljević and E. S. Phinney. The afterglow of massive black hole coalescence. *The Astrophysical Journal*, 622(2):L93–L96, March 2005. ISSN 1538-4357. 10.1086/429618. URL http://dx.doi.org/10.1086/429618.

T Miyaji, G Hasinger, M Salvato, Marcella Brusa, N Cappelluti, F Civano, S Puccetti, M Elvis, H Brunner, S Fotopoulou, et al. Detailed shape and evolutionary behavior of the x-ray luminosity function of active galactic nuclei. *The Astrophysical Journal*, 804(2):104, 2015.

Takamitsu Miyaji, Günther Hasinger, and Maarten Schmidt. Soft x-ray agn luminosity function from rosat surveys i. cosmological evolution and contribution to the soft x-ray background. *Arxiv preprint astro-ph/9910410*, 1999.

S. Molendi, S. De Grandi, M. Rossetti, I. Bartalucci, F. Gastaldello, S. Ghizzardi, and M. Gaspari. The evolving cluster cores: Putting together the pieces of the puzzle. *Astronomy amp; Astrophysics*, 670:A104, February 2023. ISSN 1432-0746. 10.1051/0004-6361/202243421. URL http://dx.doi.org/10.1051/0004-6361/202243421.

Silvano Molendi and Fabio Pizzolato. Is the gas in cooling flows multiphase? *The Astrophysical Journal*, 560(1):194–200, October 2001. ISSN 1538-4357. 10.1086/322387. URL http://dx.doi.org/10.1086/322387.

Sandor M Molnar, John P Hughes, Megan Donahue, and Marshall Joy. Chandra observations of unresolved x-ray sources around two clusters of galaxies. *The Astrophysical Journal*, 573(2):L91, 2002.

J. J. Monaghan. SPH and Riemann Solvers. *Journal of Computational Physics*, 136(2):298–307, September 1997. 10.1006/jcph.1997.5732.

J. J. Monaghan and J. C. Lattanzio. A refined particle method for astrophysical problems. , 149 (1):135–143, August 1985.

Joseph J Monaghan and Robert A Gingold. Shock simulation by the particle method sph. *Journal of computational physics*, 52(2):374–389, 1983.

Mackenzie SL Moody, Ji-Ming Shi, and James M Stone. Hydrodynamic torques in circumbinary accretion disks. *The Astrophysical Journal*, 875(1):66, 2019.

B. Moore, F. Governato, T. Quinn, J. Stadel, and G. Lake. Resolving the Structure of Cold Dark Matter Halos. , 499(1):L5–L8, May 1998. 10.1086/311333.

Raffaella Morganti and Tom Oosterloo. The interstellar and circumnuclear medium of active nuclei traced by H i 21 cm absorption. , 26(1):4, July 2018. 10.1007/s00159-018-0109-x.

Raffaella Morganti, Suma Murthy, Tom Oosterloo, Jay Blanchard, Claire Cook, Zsolt Paragi, Monica Orienti, Hiroshi Nagai, and Robert Schulz. Cold gas in the heart of Perseus A. , 678: A42, October 2023. 10.1051/0004-6361/202347117.

T. Morishita, M. Chiaberge, B. Hilbert, E. Lambrides, L. Blecha, S. Baum, S. Bianchi, A. Capetti, G. Castignani, F. D. Macchetto, G. K. Miley, C. P. O'Dea, and C. A. Norman. The Host Galaxy of the Recoiling Black Hole Candidate in 3C 186: An Old Major Merger Remnant at the Center of a z = 1 Cluster. , 931(2):165, June 2022. 10.3847/1538-4357/ac6a58.

Robert A Mostoghiu Paun, Darren Croton, Chris Power, Alexander Knebe, Adam J Ussing, and Alan R Duffy. Tidal adaptive softening and artificial fragmentation in cosmological simulations. *Monthly Notices of the Royal Astronomical Society*, 542(2):735–746, July 2025. ISSN 1365-2966. 10.1093/mnras/staf1229. URL http://dx.doi.org/10.1093/mnras/staf1229.

Diego J Muñoz, Ryan Miranda, and Dong Lai. Hydrodynamics of circumbinary accretion: angular momentum transfer and binary orbital evolution. *The Astrophysical Journal*, 871(1):84, 2019.

Diego J Muñoz, Dong Lai, Kaitlin Kratter, and Ryan Miranda. Circumbinary accretion from finite and infinite disks. *The Astrophysical Journal*, 889(2):114, 2020.

L Hermosa Muñoz, Almudena Alonso-Herrero, Alvaro Labiano, Pierre Guillard, Lara Pantoni, Victorine Buiten, Daniel Dicken, Maarten Baes, Torsten Boeker, Luis Colina, et al. Miconic: Dual active galactic nuclei, star formation, and ionised gas outflows in ngc 6240 seen with miri/jwst. *Astronomy & Astrophysics*, 693:A321, 2025.

Giuseppe Murante, Pierluigi Monaco, Martina Giovalli, Stefano Borgani, and Antonaldo Diaferio. A subresolution multiphase interstellar medium model of star formation and supernova energy feedback: A multiphase model of sf and sn feedback. *Monthly Notices of the Royal Astronomical Society*, pages no–no, April 2010. ISSN 1365-2966. 10.1111/j.1365-2966.2010.16567.x. URL http://dx.doi.org/10.1111/j.1365-2966.2010.16567.x.

Giuseppe Murante, Stefano Borgani, Riccardo Brunino, and S-H Cha. Hydrodynamic simulations with the godunov smoothed particle hydrodynamics. *Monthly Notices of the Royal Astronomical Society*, 417(1):136–153, 2011.

Giuseppe Murante, Pierluigi Monaco, Stefano Borgani, Luca Tornatore, Klaus Dolag, and David Goz. Simulating realistic disc galaxies with a novel sub-resolution ism model. *Monthly Notices of the Royal Astronomical Society*, 447(1):178–201, 2015.

Burçin Mutlu-Pakdil, Marc S Seigar, and Benjamin L Davis. The local black hole mass function derived from the mbh–p and the mbh–n relations. *The Astrophysical Journal*, 830(2):117, 2016.

Fumitaka Nakamura and Masayuki Umemura. On the Initial Mass Function of Population III Stars. , 548(1):19–32, February 2001. 10.1086/318663.

Devesh Nandal and Abraham Loeb. Supermassive stars match the spectral signatures of jwst's little red dots, 2025. URL https://arxiv.org/abs/2507.12618.

Julio F. Navarro, Vincent R. Eke, and Carlos S. Frenk. The cores of dwarf galaxy haloes. , 283 (3):L72–L78, December 1996. 10.1093/mnras/283.3.L72.

Julio F. Navarro, Carlos S. Frenk, and Simon D. M. White. The Structure of Cold Dark Matter Halos. *ApJ*, 462:563, May 1996. ISSN 0004-637X. 10.1086/177173. URL https://ui.adsabs.harvard.edu/abs/1996ApJ...462..563N. Publisher: IOP ADS Bibcode: 1996ApJ...462..563N.

Julio F. Navarro, Carlos S. Frenk, and Simon D. M. White. A Universal Density Profile from Hierarchical Clustering. , 490(2):493–508, December 1997. 10.1086/304888.

Julio F. Navarro, Carlos S. Frenk, and Simon D. M. White. A Universal Density Profile from Hierarchical Clustering. *ApJ*, 490:493–508, December 1997. ISSN 0004-637X. 10.1086/304888. URL https://ui.adsabs.harvard.edu/abs/1997ApJ...490..493N. Publisher: IOP ADS Bibcode: 1997ApJ...490..493N.

Charles H. Nelson, Richard F. Green, Gary Bower, Karl Gebhardt, and Donna Weistrop. The relationship between black hole mass and velocity dispersion in seyfert 1 galaxies. *The Astrophysical Journal*, 615(2):652–661, November 2004. ISSN 1538-4357. 10.1086/424657. URL http://dx.doi.org/10.1086/424657.

Dylan Nelson, Mark Vogelsberger, Shy Genel, Debora Sijacki, Dušan Kereš, Volker Springel, and Lars Hernquist. Moving mesh cosmology: tracing cosmological gas accretion. *Monthly Notices of the Royal Astronomical Society*, 429(4):3353–3370, 2013.

Dylan Nelson, Annalisa Pillepich, Mohammadreza Ayromlou, Wonki Lee, Katrin Lehle, Eric Rohr, and Nhut Truong. Introducing the tng-cluster simulation: Overview and the physical properties of the gaseous intracluster medium. *Astronomy & Astrophysics*, 686:A157, 2024.

Maia Nenkova, Matthew M. Sirocky, Željko Ivezić, and Moshe Elitzur. AGN Dusty Tori. I. Handling of Clumpy Media. , 685(1):147–159, September 2008. 10.1086/590482.

FanLam Ng and Shutaro Ueda. The relation between the cool-core radius and the host galaxy clusters: thermodynamic properties and cluster mass, 2024. URL https://arxiv.org/abs/2309.16297.

Yueying Ni, Nianyi Chen, Yihao Zhou, Minjung Park, Yanhui Yang, Tiziana Di Matteo, Simeon Bird, and Rupert Croft. The astrid simulation: Evolution of black holes and galaxies to z= 0.5 and different evolution pathways for galaxy quenching. *The Astrophysical Journal*, 990(2):120, 2025.

CJ Nixon and JE Pringle. Accretion discs with non-zero central torque. *New Astronomy*, 85: 101493, 2021.

Ken'ichi Nomoto and Masa-aki Hashimoto. Presupernova evolution of massive stars. *Physics Reports*, 163(1-3):13–36, 1988.

Ken'ichi Nomoto, Chiaki Kobayashi, and Nozomu Tominaga. Nucleosynthesis in Stars and the Chemical Enrichment of Galaxies. , 51(1):457–509, August 2013. 10.1146/annurev-astro-082812-140956.

V. Olivares, P. Salome, F. Combes, S. Hamer, P. Guillard, M. D. Lehnert, F. L. Polles, R. S. Beckmann, Y. Dubois, M. Donahue, A. Edge, A. C. Fabian, B. McNamara, T. Rose, H. R. Russell, G. Tremblay, A. Vantyghem, R. E. A. Canning, G. Ferland, B. Godard, S. Peirani, and G. Pineau des Forets. Ubiquitous cold and massive filaments in cool core clusters. , 631:A22, November 2019. 10.1051/0004-6361/201935350.

Tom Oosterloo, J. B. Raymond Oonk, Raffaella Morganti, Françoise Combes, Kalliopi Dasyra, Philippe Salomé, Nektarios Vlahakis, and Clive Tadhunter. Properties of the molecular gas in the fast outflow in the Seyfert galaxy IC 5063. , 608:A38, December 2017. 10.1051/0004-6361/201731781.

Eve C Ostriker. Dynamical friction in a gaseous medium. *The Astrophysical Journal*, 513(1):252, 1999.

F. N. Owen, C. P. O'Dea, M. Inoue, and J. A. Eilek. VLA observations of the multiple jet galaxy 3C 75. , 294:L85–L88, July 1985. 10.1086/184514.

Timothy B. O'Hara, Joseph J. Mohr, John J. Bialek, and August E. Evrard. Effects of mergers and core structure on the bulk properties of nearby galaxy clusters. *The Astrophysical Journal*, 639(1):64–80, March 2006. ISSN 1538-4357. 10.1086/499327. URL http://dx.doi.org/10.1086/499327.

Brian W O'shea, Kentaro Nagamine, Volker Springel, Lars Hernquist, and Michael L Norman. Comparing amr and sph cosmological simulations. i. dark matter and adiabatic simulations. *The Astrophysical Journal Supplement Series*, 160(1):1, 2005.

Fabio Pacucci and Ramesh Narayan. Mildly super-eddington accretion onto slowly spinning black holes explains the x-ray weakness of the little red dots. *The Astrophysical Journal*, 976(1):96, 2024.

Fabio Pacucci, Bao Nguyen, Stefano Carniani, Roberto Maiolino, and Xiaohui Fan. JWST CEERS and JADES Active Galaxies at z = 4-7 Violate the Local M -M $_\star$ Relation at $>3\sigma$: Implications for Low-mass Black Holes and Seeding Models. , 957(1):L3, November 2023. 10.3847/2041-8213/ad0158.

J Papaloizou and JE Pringle. Tidal torques on accretion discs in close binary systems. *Monthly Notices of the Royal Astronomical Society*, 181(3):441–454, 1977.

Daeseong Park, Jong-Hak Woo, Vardha N Bennert, Tommaso Treu, Matthew W Auger, and Matthew A Malkan. Cosmic evolution of black holes and spheroids. v. the relation between black hole mass and host galaxy luminosity for a sample of 79 active galaxies. *The Astrophysical Journal*, 799(2):164, 2015.

Jongwon Park, Rory Smith, and K Yi Sukyoung. Star formation of merging disk galaxies with agn feedback effects. *The Astrophysical Journal*, 845(2):128, 2017.

P. Parma, H. R. de Ruiter, and R. A. Cameron. Very Large Array Observations of Radio-Selected Dumbbell Galaxies. , 102:1960, December 1991. 10.1086/116018.

Alice Pasetto, Omaira González-Martín, Donaji Esparza-Arredondo, Natalia Osorio-Clavijo, César Ivan Victoria-Ceballos, and Mariela Martínez-Paredes. Agn torus detectability at submillimeter wavelengths: What to expect from alma continuum data. *The Astrophysical Journal*, 872(1):69, 2019.

Alice Pasetto, Omaira González-Martín, Donaji Esparza-Arredondo, Natalia Osorio-Clavijo, César Ivan Victoria-Ceballos, and Mariela Martínez-Paredes. AGN Torus Detectability at Submillimeter Wavelengths: What to Expect from ALMA Continuum Data. , 872(1):69, February 2019. 10.3847/1538-4357/aafa20.

Riccardo Pavesi, Dominik A Riechers, Peter L Capak, Christopher L Carilli, Chelsea E Sharon, Gordon J Stacey, Alexander Karim, Nicholas Z Scoville, and Vernesa Smolčić. Alma reveals weak [n ii] emission in "typical" galaxies and intense starbursts at z= 5–6. *The Astrophysical Journal*, 832(2):151, 2016.

A. Pedlar, H. S. Ghataure, R. D. Davies, B. A. Harrison, R. Perley, P. C. Crane, and S. W. Unger. The radio structure of NGC 1275. , 246:477, October 1990.

A. Pensabene, S. Carniani, M. Perna, G. Cresci, R. Decarli, R. Maiolino, and A. Marconi. The ALMA view of the high-redshift relation between supermassive black holes and their host galaxies. , 637:A84, May 2020. 10.1051/0004-6361/201936634.

L. Pentericci, J. D. Kurk, H. J. A. Röttgering, G. K. Miley, W. van Breugel, C. L. Carilli, H. Ford, T. Heckman, P. McCarthy, and A. Moorwood. A search for clusters at high redshift. II. A proto cluster around a radio galaxy at z=2.16. , 361:L25–L28, September 2000. 10.48550/arXiv.astro-ph/0008143.

Pablo G Pérez-González, Guillermo Barro, George H Rieke, Jianwei Lyu, Marcia Rieke, Stacey Alberts, Christina C Williams, Kevin Hainline, Fengwu Sun, Dávid Puskás, et al. What is the nature of little red dots and what is not. *The Astrophysical Journal*, 968(1):4, 2024.

R. A. Perley, J. W. Dreher, and J. J. Cowan. The jet and filaments in Cygnus A. , 285:L35–L38, October 1984. 10.1086/184360.

Michele Perna, Santiago Arribas, Isabella Lamperti, Chiara Circosta, Elena Bertola, Pablo G Pérez-González, Francesco d'Eugenio, Hannah Übler, Giovanni Cresci, Marta Volonteri, et al. Ga-nifs: High number of dual active galactic nuclei at z 3. *Astronomy & Astrophysics*, 696:A59, 2025.

J. R. Peterson and A. C. Fabian. X-ray spectroscopy of cooling clusters. , 427(1):1–39, April 2006. 10.1016/j.physrep.2005.12.007.

J. R. Peterson, S. M. Kahn, F. B. S. Paerels, J. S. Kaastra, T. Tamura, J. A. M. Bleeker, C. Ferrigno, and J. G. Jernigan. High-Resolution X-Ray Spectroscopic Constraints on Cooling-Flow Models for Clusters of Galaxies. , 590(1):207–224, June 2003. 10.1086/374830.

Hugo Pfister, Marta Volonteri, Yohan Dubois, Massimo Dotti, and Monica Colpi. The erratic dynamical life of black hole seeds in high-redshift galaxies. *Monthly Notices of the Royal Astronomical Society*, 486(1):101–111, 2019.

Joanna M Piotrowska, Asa FL Bluck, Roberto Maiolino, and Yingjie Peng. On the quenching of star formation in observed and simulated central galaxies: evidence for the role of integrated agn feedback. *Monthly Notices of the Royal Astronomical Society*, 512(1):1052–1090, 2022.

Susana Planelles, Stefano Borgani, Dunja Fabjan, Madhura Killedar, Giuseppe Murante, Gian Luigi Granato, C Ragone-Figueroa, and Klaus Dolag. On the role of agn feedback on the thermal and chemodynamical properties of the hot intracluster medium. *Monthly Notices of the Royal Astronomical Society*, 438(1):195–216, 2014.

Richard M. Plotkin, Sera Markoff, Brandon C. Kelly, Elmar Körding, and Scott F. Anderson. Using the Fundamental Plane of black hole activity to distinguish X-ray processes from weakly accreting black holes. , 419(1):267–286, January 2012. 10.1111/j.1365-2966.2011.19689.x.

P. Popesso and A. Biviano. The AGN fraction-velocity dispersion relation in clusters of galaxies. , 460(2):L23–L26, December 2006. 10.1051/0004-6361:20066269.

Simon F. Portegies Zwart, Holger Baumgardt, Piet Hut, Junichiro Makino, and Stephen L. W. McMillan. Formation of massive black holes through runaway collisions in dense young star clusters. , 428(6984):724–726, April 2004. 10.1038/nature02448.

C. Power, J. F. Navarro, A. Jenkins, C. S. Frenk, S. D. M. White, V. Springel, J. Stadel, and T. Quinn. The inner structure of ΛCDM haloes - I. A numerical convergence study. , 338(1): 14–34, January 2003. 10.1046/j.1365-8711.2003.05925.x.

G. W. Pratt, M. Arnaud, R. Piffaretti, H. Böhringer, T. J. Ponman, J. H. Croston, G. M. Voit, S. Borgani, and R. G. Bower. Gas entropy in a representative sample of nearby x-ray galaxy clusters (rexcess): relationship to gas mass fraction. *Astronomy and Astrophysics*, 511:A85, February 2010. ISSN 1432-0746. 10.1051/0004-6361/200913309. URL http://dx.doi.org/10.1051/0004-6361/200913309.

P. Predehl, R. Andritschke, V. Arefiev, V. Babyshkin, O. Batanov, W. Becker, H. Böhringer, A. Bogomolov, T. Boller, K. Borm, W. Bornemann, H. Bräuninger, M. Brüggen, H. Brunner, M. Brusa, E. Bulbul, M. Buntov, V. Burwitz, W. Burkert, N. Clerc, E. Churazov, D. Coutinho, T. Dauser, K. Dennerl, V. Doroshenko, J. Eder, V. Emberger, T. Eraerds, A. Finoguenov, M. Freyberg, P. Friedrich, S. Friedrich, M. Fürmetz, A. Georgakakis, M. Gilfanov, S. Granato, C. Grossberger, A. Gueguen, P. Gureev, F. Haberl, O. Hälker, G. Hartner, G. Hasinger, H. Huber, L. Ji, A. v. Kienlin, W. Kink, F. Korotkov, I. Kreykenbohm, G. Lamer, I. Lomakin, I. Lapshov, T. Liu, C. Maitra, N. Meidinger, B. Menz, A. Merloni, T. Mernik, B. Mican, J. Mohr, S. Müller, K. Nandra, V. Nazarov, F. Pacaud, M. Pavlinsky, E. Perinati, E. Pfeffermann, D. Pietschner, M. E. Ramos-Ceja, A. Rau, J. Reiffers, T. H. Reiprich, J. Robrade, M. Salvato, J. Sanders, A. Santangelo, M. Sasaki, H. Scheuerle, C. Schmid, J. Schmitt, A. Schwope, A. Shirshakov, M. Steinmetz,

I. Stewart, L. Strüder, R. Sunyaev, C. Tenzer, L. Tiedemann, J. Trümper, V. Voron, P. Weber, J. Wilms, and V. Yaroshenko. The eROSITA X-ray telescope on SRG. , 647:A1, March 2021. 10.1051/0004-6361/202039313.

Miguel Preto, Ingo Berentzen, Peter Berczik, and Rainer Spurzem. Fast coalescence of massive black hole binaries from mergers of galactic nuclei: implications for low-frequency gravitational-wave astrophysics. *The Astrophysical Journal Letters*, 732(2):L26, 2011.

Daniel James Price and Joseph John Monaghan. An energy-conserving formalism for adaptive gravitational force softening in smoothed particle hydrodynamics and n-body codes. *Monthly Notices of the Royal Astronomical Society*, 374(4):1347–1358, 2007.

Raj Prince, Aditi Agarwal, Nayantara Gupta, Pratik Majumdar, Bożena Czerny, Sergio A. Cellone, and I. Andruchow. Multiwavelength analysis and modeling of oj 287 during 2017–2020. *Astronomy amp; Astrophysics*, 654:A38, October 2021. ISSN 1432-0746. 10.1051/0004-6361/202140708. URL http://dx.doi.org/10.1051/0004-6361/202140708.

Lewis R Prole, Paul C Clark, Ralf S Klessen, and Simon CO Glover. Fragmentation-induced starvation in population iii star formation: a resolution study. *Monthly Notices of the Royal Astronomical Society*, 510(3):4019–4030, 2022.

Lewis R Prole, John A Regan, Daxal Mehta, Peter Coles, and Pratika Dayal. Primordial black holes in cosmological simulations: growth prospects for supermassive black holes. *The Open Journal of Astrophysics*, 8, August 2025. ISSN 2565-6120. 10.33232/001c.143643. URL http://dx.doi.org/10.33232/001c.143643.

Clara Puerto-Sánchez, Mélanie Habouzit, Marta Volonteri, Yueying Ni, Adi Foord, Daniel Anglés-Alcázar, Nianyi Chen, Paloma Guetzoyan, Romeel Davé, Tiziana Di Matteo, et al. Large-scale dual agn in large-scale cosmological hydrodynamical simulations. *Monthly Notices of the Royal Astronomical Society*, 536(3):3016–3040, 2025.

D. Puy and M. Signore. Molecules in a gravitational collapse, 1998. URL https://arxiv.org/abs/astro-ph/9812411.

Gerald D. Quinlan. The dynamical evolution of massive black hole binaries I. Hardening in a fixed stellar background. , 1(1):35–56, July 1996. 10.1016/S1384-1076(96)00003-6.

Gerald D. Quinlan and Lars Hernquist. The dynamical evolution of massive black hole binaries — ii. self-consistent n-body integrations. *New Astronomy*, 2(6):533–554, December 1997. ISSN 1384-1076. 10.1016/s1384-1076(97)00039-0. URL http://dx.doi.org/10.1016/S1384-1076(97)00039-0.

D. A. Rafferty, B. R. McNamara, P. E. J. Nulsen, and M. W. Wise. The Feedback-regulated Growth of Black Holes and Bulges through Gas Accretion and Starbursts in Cluster Central Dominant Galaxies. , 652(1):216–231, November 2006a. 10.1086/507672.

D. A. Rafferty, B. R. McNamara, P. E. J. Nulsen, and M. W. Wise. The Feedback-regulated Growth of Black Holes and Bulges through Gas Accretion and Starbursts in Cluster Central Dominant Galaxies. , 652(1):216–231, November 2006b. 10.1086/507672.

C. Ragone-Figueroa, G. L. Granato, M. E. Ferraro, G. Murante, V. Biffi, S. Borgani, S. Planelles, and E. Rasia. BCG mass evolution in cosmological hydro-simulations. , 479(1):1125–1136, September 2018. 10.1093/mnras/sty1639.

Rahul Ramesh and Dylan Nelson. Zooming in on the circumgalactic medium: resolving small-scale gas structure with the gible cosmological simulations, 2023. URL https://arxiv.org/abs/2307.11143.

M. J. Rees. Relativistic jets and beams in radio galaxies. , 275(5680):516–517, October 1978. 10.1038/275516a0.

John Regan and Marta Volonteri. Massive black hole seeds. *The Open Journal of Astrophysics*, 7, September 2024. ISSN 2565-6120. 10.33232/001c.123239. URL http://dx.doi.org/10.33232/001c.123239.

Amy E. Reines and Marta Volonteri. Relations between Central Black Hole Mass and Total Galaxy Stellar Mass in the Local Universe. , 813(2):82, November 2015. 10.1088/0004-637X/813/2/82.

Amy E Reines, James J Condon, Jeremy Darling, and Jenny E Greene. A new sample of (wandering) massive black holes in dwarf galaxies from high-resolution radio observations. *The Astrophysical Journal*, 888(1):36, 2020.

H. Reissner. Über die Eigengravitation des elektrischen Feldes nach der Einsteinschen Theorie. *Annalen der Physik*, 355(9):106–120, January 1916. 10.1002/andp.19163550905.

Omar Ulises Reyes-Amador, Omaira González-Martín, Jacopo Fritz, Maarten Baes, Sundar Srinivasan, Ismael García-Bernete, Donaji Esparza-Arredondo, and Marko Stalevski. Towards an observationally motivated agn dusty torus model – ii. the roles of density distribution and chemical composition of the dust, 2025. URL https://arxiv.org/abs/2505.23981.

C Reynolds. Fluorescent iron lines as a probe of astrophysical black hole systems. *Physics Reports*, 377(6):389–466, April 2003. ISSN 0370-1573. 10.1016/s0370-1573(02)00584-7. URL http://dx.doi.org/10.1016/S0370-1573(02)00584-7.

Christopher S. Reynolds, M. C. David Marsh, Helen R. Russell, Andrew C. Fabian, Robyn Smith, Francesco Tombesi, and Sylvain Veilleux. Astrophysical limits on very light axion-like particles from chandra grating spectroscopy of ngc 1275. *The Astrophysical Journal*, 890(1):59, February 2020. ISSN 1538-4357. 10.3847/1538-4357/ab6a0c. URL http://dx.doi.org/10.3847/1538-4357/ab6a0c.

Angelo Ricarte, Michael Tremmel, Priyamvada Natarajan, and Thomas Quinn. Unveiling the Population of Wandering Black Holes via Electromagnetic Signatures. , 916(2):L18, August 2021. 10.3847/2041-8213/ac1170.

Angelo Ricarte, Michael Tremmel, Priyamvada Natarajan, Charlotte Zimmer, and Thomas Quinn. Origins and demographics of wandering black holes. *Monthly Notices of the Royal Astronomical Society*, 503(4):6098–6111, 2021.

C. Ricci, B. Trakhtenbrot, M. J. Koss, Y. Ueda, I. Delvecchio, E. Treister, K. Schawinski, S. Paltani, K. Oh, I. Lamperti, S. Berney, P. Gandhi, K. Ichikawa, F. E. Bauer, L. C. Ho, D. Asmus, V. Beckmann, S. Soldi, M. Baloković, N. Gehrels, and C. B. Markwardt. BAT AGN Spectroscopic

Survey. V. X-Ray Properties of the Swift/BAT 70-month AGN Catalog. , 233(2):17, December 2017. 10.3847/1538-4365/aa96ad.

Gordon T. Richards, Xiaohui Fan, Heidi Jo Newberg, Michael A. Strauss, Daniel E. Vanden Berk, Donald P. Schneider, Brian Yanny, Adam Boucher, Scott Burles, Joshua A. Frieman, James E. Gunn, Patrick B. Hall, Željko Ivezić, Stephen Kent, Jon Loveday, Robert H. Lupton, Constance M. Rockosi, David J. Schlegel, Chris Stoughton, Mark SubbaRao, and Donald G. York. Spectroscopic Target Selection in the Sloan Digital Sky Survey: The Quasar Sample. , 123(6):2945–2975, June 2002. 10.1086/340187.

Gordon T. Richards, Nicholas E. Kruczek, S. C. Gallagher, Patrick B. Hall, Paul C. Hewett, Karen M. Leighly, Rajesh P. Deo, Rachael M. Kratzer, and Yue Shen. Unification of luminous type 1 quasars through c iv emission. *The Astronomical Journal*, 141(5):167, April 2011. ISSN 1538-3881. 10.1088/0004-6256/141/5/167. URL http://dx.doi.org/10.1088/0004-6256/141/5/167.

Mary Rickel, Emily Moravec, Yjan A. Gordon, Martin J. Hardcastle, Jonathon C. S. Pierce, Lawrence E. Bilton, and Ian D. Roberts. The merging galaxy cluster environment affects the morphology of radio-agn, 2025. URL https://arxiv.org/abs/2502.04198.

E. J. Ridley, M. Nicholl, C. A. Ward, P. K. Blanchard, R. Chornock, M. Fraser, S. Gomez, S. Mattila, S. R. Oates, G. Pratten, J. C. Runnoe, P. Schmidt, K. D. Alexander, M. Gromadzki, A. Lawrence, T. M. Reynolds, K. W. Smith, Ł. Wyrzykowski, A. Aamer, J. P. Anderson, S. Benetti, E. Berger, T. de Boer, K. C. Chambers, T. W. Chen, H. Gao, C. P. Gutiérrez, C. Inserra, T. Kangas, G. Leloudas, E. A. Magnier, L. Makrygianni, T. Moore, T. E. Müller-Bravo, S. J. Smartt, K. V. Sokolovsky, R. Wainscoat, and D. R. Young. Time-varying double-peaked emission lines following the sudden ignition of the dormant galactic nucleus AT2017bcc. , 531(1): 1905–1930, June 2024. 10.1093/mnras/stae1129.

Giacomo Riva, GW Pratt, Mariachiara Rossetti, Iacopo Bartalucci, ST Kay, ELENA Rasia, R Gavazzi, K Umetsu, M Arnaud, M Balboni, et al. Chex-mate: The intracluster medium entropy distribution in the gravity-dominated regime. *Astronomy & Astrophysics*, 691:A340, 2024.

GW Roberts-Borsani, RJ Bouwens, PA Oesch, I Labbe, R Smit, GD Illingworth, P van Dokkum, B Holden, V Gonzalez, M Stefanon, et al. z 7 galaxies with red spitzer/irac [3.6]–[4.5] colors in the full candels data set: the brightest-known galaxies at z 7–9 and a probable spectroscopic confirmation at z= 7.48. *The Astrophysical Journal*, 823(2):143, 2016.

S. A. Rodionov and N. Ya. Sotnikova. Optimal Choice of the Softening Length and Time Step in N-body Simulations. *Astronomy Reports*, 49(6):470–476, June 2005. 10.1134/1.1941489.

Carl L. Rodriguez, Bharath Pattabiraman, Sourav Chatterjee, Alok Choudhary, Wei-keng Liao, Meagan Morscher, and Frederic A. Rasio. A new hybrid technique for modeling dense star clusters. *Computational Astrophysics and Cosmology*, 5(1):5, November 2018. ISSN 2197-7909. 10.1186/s40668-018-0027-3. URL https://doi.org/10.1186/s40668-018-0027-3.

Constanze Roedig, Massimo Dotti, Alberto Sesana, Jorge Cuadra, and Monica Colpi. Limiting eccentricity of subparsec massive black hole binaries surrounded by self-gravitating gas discs. *Monthly Notices of the Royal Astronomical Society*, 415(4):3033–3041, 2011.

N Roos. Galaxy mergers and active galactic nuclei. *Astronomy and Astrophysics, vol. 104, no. 2, Dec. 1981, p. 218-228.*, 104:218–228, 1981.

D. J. Rosario, R. C. McGurk, C. E. Max, G. A. Shields, K. L. Smith, and S. M. Ammons. Adaptive Optics Imaging of Quasi-stellar Objects with Double-peaked Narrow Lines: Are They Dual Active Galactic Nuclei? , 739(1):44, September 2011. 10.1088/0004-637X/739/1/44.

Tom Rose, A. C. Edge, F. Combes, M. Gaspari, S. Hamer, N. Nesvadba, A. B. Peck, C. Sarazin, G. R. Tremblay, S. A. Baum, M. N. Bremer, B. R. McNamara, C. O'Dea, J. B. R. Oonk, H. Russell, P. Salomé, M. Donahue, A. C. Fabian, G. Ferland, R. Mittal, and A. Vantyghem. Constraining cold accretion on to supermassive black holes: molecular gas in the cores of eight brightest cluster galaxies revealed by joint CO and CN absorption. , 489(1):349–365, October 2019. 10.1093/mnras/stz2138.

Tom Rose, B. R. McNamara, F. Combes, A. C. Edge, A. C. Fabian, M. Gaspari, H. Russell, P. Salomé, G. Tremblay, and G. Ferland. Does absorption against AGN reveal supermassive black hole accretion? , 518(1):878–892, January 2023. 10.1093/mnras/stac3194.

Marshall N. Rosenbluth, William M. MacDonald, and David L. Judd. Fokker-Planck Equation for an Inverse-Square Force. *Physical Review*, 107(1):1–6, July 1957. 10.1103/PhysRev.107.1. URL https://link.aps.org/doi/10.1103/PhysRev.107.1. Publisher: American Physical Society.

Nicholas P Ross, Ian D McGreer, Martin White, Gordon T Richards, Adam D Myers, Nathalie Palanque-Delabrouille, Michael A Strauss, Scott F Anderson, Yue Shen, WN Brandt, et al. The sdss-iii baryon oscillation spectroscopic survey: the quasar luminosity function from data release nine. *The Astrophysical Journal*, 773(1):14, 2013.

M. Rossetti and S. Molendi. Cool core remnants in galaxy clusters. *Astronomy and Astrophysics*, 510:A83, February 2010. ISSN 1432-0746. 10.1051/0004-6361/200913156. URL http://dx.doi.org/10.1051/0004-6361/200913156.

M. Rossetti, D. Eckert, B. M. Cavalleri, S. Molendi, F. Gastaldello, and S. Ghizzardi. Back and forth from cool core to non-cool core: clues from radio halos. , 532:A123, August 2011. 10.1051/0004-6361/201117306.

M. Rossetti, F. Gastaldello, G. Ferioli, M. Bersanelli, S. De Grandi, D. Eckert, S. Ghizzardi, D. Maino, and S. Molendi. Measuring the dynamical state of Planck SZ-selected clusters: X-ray peak - BCG offset. , 457(4):4515–4524, April 2016. 10.1093/mnras/stw265.

M. Rossetti, F. Gastaldello, D. Eckert, M. Della Torre, G. Pantiri, P. Cazzoletti, and S. Molendi. The cool-core state of Planck SZ-selected clusters versus X-ray-selected samples: evidence for cool-core bias. , 468(2):1917–1930, June 2017. 10.1093/mnras/stx493.

Ilaria Ruffa, Isabella Prandoni, Robert A Laing, Rosita Paladino, Paola Parma, Hans de Ruiter, Arturo Mignano, Timothy A Davis, Martin Bureau, and Joshua Warren. The agn fuelling/feedback cycle in nearby radio galaxies i. alma observations and early results. *Monthly Notices of the Royal Astronomical Society*, 484(3):4239–4259, 2019.

F. Ruppin, M. McDonald, L. E. Bleem, S. W. Allen, B. A. Benson, M. Calzadilla, G. Khullar, and B. Floyd. Stability of Cool Cores during Galaxy Cluster Growth: A Joint Chandra/SPT

Analysis of 67 Galaxy Clusters along a Common Evolutionary Track Spanning 9 Gyr. , 918(2): 43, September 2021. 10.3847/1538-4357/ac0bba.

H. R. Russell, B. R. McNamara, A. C. Edge, M. T. Hogan, R. A. Main, and A. N. Vantyghem. Radiative efficiency, variability and Bondi accretion on to massive black holes: the transition from radio AGN to quasars in brightest cluster galaxies. , 432(1):530–553, June 2013. 10.1093/mnras/stt490.

H. R. Russell, B. R. McNamara, A. C. Fabian, P. E. J. Nulsen, F. Combes, A. C. Edge, M. Madar, V. Olivares, P. Salomé, and A. N. Vantyghem. Driving massive molecular gas flows in central cluster galaxies with AGN feedback. , 490(3):3025–3045, December 2019. 10.1093/mnras/stz2719.

R. P. Saglia, M. Opitsch, P. Erwin, J. Thomas, A. Beifiori, M. Fabricius, X. Mazzalay, N. Nowak, S. P. Rusli, and R. Bender. The SINFONI Black Hole Survey: The Black Hole Fundamental Plane Revisited and the Paths of (Co)evolution of Supermassive Black Holes and Bulges. , 818 (1):47, February 2016. 10.3847/0004-637X/818/1/47.

Nandini Sahu, Alister W. Graham, and Benjamin L. Davis. Black hole mass scaling relations for early-type galaxies. i. mbh–m*, sph and mbh–m*,gal. *The Astrophysical Journal*, 876(2):155, May 2019. ISSN 1538-4357. 10.3847/1538-4357/ab0f32. URL http://dx.doi.org/10.3847/1538-4357/ab0f32.

Nandini Sahu, Alister W. Graham, and Benjamin L. Davis. Revealing Hidden Substructures in the M $_{BH}$-σ Diagram, and Refining the Bend in the L-σ Relation. , 887(1):10, December 2019. 10.3847/1538-4357/ab50b7.

Luca Sala, Milena Valentini, Veronica Biffi, and Klaus Dolag. Supermassive black hole spin evolution in cosmological simulations with opengadget3. *Astronomy & Astrophysics*, 685:A92, 2024.

Paolo Salucci, Ewa Szuszkiewicz, Pierluigi Monaco, and Luigi Danese. Mass function of dormant black holes and the evolution of active galactic nuclei. *Monthly Notices of the Royal Astronomical Society*, 307(3):637–644, 1999.

S. Salviander, G. A. Shields, K. Gebhardt, and E. W. Bonning. The Black Hole Mass-Galaxy Bulge Relationship for QSOs in the Sloan Digital Sky Survey Data Release 3. , 662(1):131–144, June 2007. 10.1086/513086.

Sarah Salviander, Gregory A Shields, and EW Bonning. The black hole mass–galaxy luminosity relationship for sloan digital sky survey quasars. *The Astrophysical Journal*, 799(2):173, 2015.

Allan Sandage. Intensity variations of 3c 48, 3c 196, and 3c 273 in optical wavelengths. *Astrophysical Journal, vol. 139, p. 416-419*, 139:416–419, 1964.

D. B. Sanders and I. F. Mirabel. Luminous Infrared Galaxies. , 34:749, January 1996. 10.1146/annurev.astro.34.1.749.

D. B. Sanders, E. S. Phinney, G. Neugebauer, B. T. Soifer, and K. Matthews. Continuum Energy Distributions of Quasars: Shapes and Origins. , 347:29, December 1989. 10.1086/168094.

Alastair J. R. Sanderson, Ewan O'Sullivan, and Trevor J. Ponman. A statistically selected-chandrasample of 20 galaxy clusters - ii. gas properties and cool core/non-cool core bimodality. *Monthly Notices of the Royal Astronomical Society*, 395(2):764–776, May 2009. ISSN

1365-2966. 10.1111/j.1365-2966.2009.14613.x. URL http://dx.doi.org/10.1111/j.1365-2966.2009.14613.x.

P Santini, E Merlin, A Fontana, B Magnelli, D Paris, M Castellano, A Grazian, L Pentericci, S Pilo, and M Torelli. Passive galaxies in the early universe: Alma confirmation of z 3- 5 candidates in the candels goods-south field. *Monthly Notices of the Royal Astronomical Society*, 486(1):560–569, 2019.

J. S. Santos, P. Rosati, P. Tozzi, H. Böhringer, S. Ettori, and A. Bignamini. Searching for cool core clusters at high redshift. , 483(1):35–47, May 2008. 10.1051/0004-6361:20078815.

Craig L. Sarazin. X-ray emission from clusters of galaxies. *Reviews of Modern Physics*, 58(1): 1–115, January 1986. 10.1103/RevModPhys.58.1.

S. Satyapal, N. J. Secrest, W. McAlpine, S. L. Ellison, J. Fischer, and J. L. Rosenberg. Discovery of a Population of Bulgeless Galaxies with Extremely Red Mid-IR Colors: Obscured AGN Activity in the Low-mass Regime? , 784(2):113, April 2014a. 10.1088/0004-637X/784/2/113.

Shobita Satyapal, Sara L. Ellison, William McAlpine, Ryan C. Hickox, David R. Patton, and J. Trevor Mendel. Galaxy pairs in the Sloan Digital Sky Survey - IX. Merger-induced AGN activity as traced by the Wide-field Infrared Survey Explorer. , 441(2):1297–1304, June 2014b. 10.1093/mnras/stu650.

Shobita Satyapal, Sara L. Ellison, William McAlpine, Ryan C. Hickox, David R. Patton, and J. Trevor Mendel. Galaxy pairs in the Sloan Digital Sky Survey - IX. Merger-induced AGN activity as traced by the Wide-field Infrared Survey Explorer. , 441(2):1297–1304, June 2014c. 10.1093/mnras/stu650.

G. Savorgnan, A. W. Graham, A. Marconi, E. Sani, L. K. Hunt, M. Vika, and S. P. Driver. The supermassive black hole mass–sérsic index relations for bulges and elliptical galaxies. *Monthly Notices of the Royal Astronomical Society*, 434(1):387–397, July 2013. ISSN 1365-2966. 10.1093/mnras/stt1027. URL http://dx.doi.org/10.1093/mnras/stt1027.

S. Sazonov, M. Revnivtsev, R. Krivonos, E. Churazov, and R. Sunyaev. Hard X-ray luminosity function and absorption distribution of nearby AGN: INTEGRAL all-sky survey. , 462(1):57–66, January 2007. 10.1051/0004-6361:20066277.

Maarten Schmidt. 3c273: a star-like object with large red-shift.". *A Century of Nature, Twenty One Discoveries That Changed Science and the World*, 1963a.

Maarten Schmidt. 3c273: a star-like object with large red-shift.". *A Century of Nature, Twenty One Discoveries That Changed Science and the World*, 1963b.

Emma Schwartzman, Tracy E Clarke, Kristina Nyland, Nathan J Secrest, Ryan W Pfeifle, Henrique Schmitt, Shobita Satyapal, and Barry Rothberg. Vadar: Varstrometry for dual agn using radio interferometry. *The Astrophysical Journal*, 961(2):233, 2024.

K. Schwarzschild. On the gravitational field of a mass point according to einstein's theory, 1916. URL https://arxiv.org/abs/physics/9905030.

M. Schwarzschild. A numerical model for a triaxial stellar system in dynamical equilibrium. , 232:236–247, August 1979. 10.1086/157282.

Roberto Serafinelli, Paola Severgnini, Valentina Braito, Roberto Della Ceca, Cristian Vignali, Filippo Ambrosino, Claudia Cicone, Alessandra Zaino, Massimo Dotti, Alberto Sesana, Vittoria E. Gianolli, Lucia Ballo, Valentina La Parola, and Gabriele A. Matzeu. Unveiling Sub-pc Supermassive Black Hole Binary Candidates in Active Galactic Nuclei. , 902(1):10, October 2020. 10.3847/1538-4357/abb3c3.

P. Severgnini, V. Braito, C. Cicone, P. Saracco, C. Vignali, R. Serafinelli, R. Della Ceca, M. Dotti, F. Cusano, D. Paris, G. Pruto, A. Zaino, L. Ballo, and M. Landoni. A possible sub-kiloparsec dual agn buried behind the galaxy curtain. *Astronomy amp; Astrophysics*, 646:A153, February 2021a. ISSN 1432-0746. 10.1051/0004-6361/202039576. URL http://dx.doi.org/10.1051/0004-6361/202039576.

Paola Severgnini, Valentina Braito, Claudia Cicone, Paolo Saracco, C Vignali, ROBERTO Serafinelli, Roberto Della Ceca, M Dotti, F Cusano, D Paris, et al. A possible sub-kiloparsec dual agn buried behind the galaxy curtain. *Astronomy & Astrophysics*, 646:A153, 2021b.

Ekta A. Shah, Brian C. Lemaux, Ben Forrest, Nimish Hathi, Lu Shen, Olga Cucciati, Denise Hung, Finn Giddings, Derek Sikorski, Lori Lubin, Roy R. Gal, Giovanni Zamorani, Emmet Golden-Marx, Sandro Bardelli, Letizia Pasqua Cassarà, Bianca Garilli, Gayathri Gururajan, Hyewon Suh, Daniela Vergani, and Elena Zucca. Enhanced active galactic nucleus activity in overdense galactic environments at $2 < z < 4$. , 704:A101, December 2025. 10.1051/0004-6361/202452055.

F Shankar, Paolo Salucci, GL Granato, Gianfranco De Zotti, and Luigi Danese. Supermassive black hole demography: the match between the local and accreted mass functions. *Monthly Notices of the Royal Astronomical Society*, 354(4):1020–1030, 2004.

Francesco Shankar. The demography of supermassive black holes: Growing monsters at the heart of galaxies. *New Astronomy Reviews*, 53(4–6):57–77, April 2009. ISSN 1387-6473. 10.1016/j.newar.2009.07.006. URL http://dx.doi.org/10.1016/j.newar.2009.07.006.

Francesco Shankar. Black hole demography: from scaling relations to models. *Classical and Quantum Gravity*, 30(24):244001, 2013.

Francesco Shankar, David H. Weinberg, and Jordi Miralda-Escudé. Self-Consistent Models of the AGN and Black Hole Populations: Duty Cycles, Accretion Rates, and the Mean Radiative Efficiency. , 690(1):20–41, January 2009. 10.1088/0004-637X/690/1/20.

Xuejian Shen, Philip F Hopkins, Claude-André Faucher-Giguère, DM Alexander, Gordon T Richards, Nicholas P Ross, and RC Hickox. The bolometric quasar luminosity function at z= 0–7. *Monthly Notices of the Royal Astronomical Society*, 495(3):3252–3275, 2020.

Yue Shen and Abraham Loeb. Identifying supermassive black hole binaries with broad emission line diagnosis. *The Astrophysical Journal*, 725(1):249–260, November 2010. ISSN 1538-4357. 10.1088/0004-637x/725/1/249. URL http://dx.doi.org/10.1088/0004-637X/725/1/249.

Ji-Ming Shi, Julian H Krolik, Stephen H Lubow, and John F Hawley. Three-dimensional magnetohydrodynamic simulations of circumbinary accretion disks: disk structures and angular momentum transport. *The Astrophysical Journal*, 749(2):118, 2012.

W. Shi and X. Liu. Binary Black Hole Model for the OJ 287 Periodic Optical Outbursts. In L. C. Ho and J. W. Wang, editors, *The Central Engine of Active Galactic Nuclei*, volume 373 of *Astronomical Society of the Pacific Conference Series*, page 245, October 2007.

Debora Sijacki, Volker Springel, Tiziana Di Matteo, and Lars Hernquist. A unified model for agn feedback in cosmological simulations of structure formation. *Monthly Notices of the Royal Astronomical Society*, 380(3):877–900, 2007.

Debora Sijacki, Mark Vogelsberger, Dušan Kereš, Volker Springel, and Lars Hernquist. Moving mesh cosmology: the hydrodynamics of galaxy formation. *Monthly Notices of the Royal Astronomical Society*, 424(4):2999–3027, 2012.

Debora Sijacki, Mark Vogelsberger, Shy Genel, Volker Springel, Paul Torrey, Gregory F. Snyder, Dylan Nelson, and Lars Hernquist. The illustris simulation: the evolving population of black holes across cosmic time. , 452(1):575–596, jul 2015a. 10.1093/mnras/stv1340. URL https://doi.org/10.1093%2Fmnras%2Fstv1340.

Debora Sijacki, Mark Vogelsberger, Shy Genel, Volker Springel, Paul Torrey, Gregory F Snyder, Dylan Nelson, and Lars Hernquist. The illustris simulation: the evolving population of black holes across cosmic time. *Monthly Notices of the Royal Astronomical Society*, 452(1):575–596, 2015b.

Joseph Silk, Mitchell C Begelman, Colin Norman, Adi Nusser, and Rosemary FG Wyse. Which came first: supermassive black holes or galaxies? insights from jwst. *The Astrophysical journal letters*, 961(2):L39, 2024.

A. Sillanpaa, L. O. Takalo, T. Pursimo, H. J. Lehto, K. Nilsson, P. Teerikorpi, P. Heinaemaeki, M. Kidger, J. A. de Diego, J. N. Gonzalez-Perez, J. M. Rodriguez-Espinosa, T. Mahoney, P. Boltwood, D. Dultzin-Hacyan, E. Benitez, G. W. Turner, J. W. Robertson, R. K. Honeycut, Yu. S. Efimov, N. Shakhovskoy, P. A. Charles, K. J. Schramm, U. Borgeest, J. V. Linde, W. Weneit, D. Kuehl, T. Schramm, A. Sadun, R. Grashuis, J. Heidt, S. Wagner, H. Bock, M. Kuemmel, A. Heines, M. Fiorucci, G. Tosti, G. Ghisellini, C. M. Raiteri, M. Villata, G. de Francesco, S. Bosio, and G. Latini. Confirmation of the 12-year optical outburst cycle in blazar OJ 287. , 305: L17, January 1996.

J. D. Silverman, P. J. Green, W. A. Barkhouse, D. W. Kim, M. Kim, B. J. Wilkes, R. A. Cameron, G. Hasinger, B. T. Jannuzi, M. G. Smith, P. S. Smith, and H. Tananbaum. The Luminosity Function of X-Ray-selected Active Galactic Nuclei: Evolution of Supermassive Black Holes at High Redshift. , 679(1):118–139, May 2008. 10.1086/529572.

A. Soltan. Masses of quasars. , 200:115–122, July 1982. 10.1093/mnras/200.1.115.

Rachel S Somerville. The co-evolution of galaxies, black holes, and agn in a hierarchical universe. *arXiv preprint arXiv:0808.1254*, 2008.

Martin W. Sommer and Kaustuv Basu. A comparative study of radio halo occurrence in sz and x-ray selected galaxy cluster samples. *Monthly Notices of the Royal Astronomical Society*, 437(3):2163–2179, November 2013. ISSN 1365-2966. 10.1093/mnras/stt2037. URL http://dx.doi.org/10.1093/mnras/stt2037.

Cristiana Spingola and Anna Barnacka. Constraining VLBI-optical offsets in high redshift galaxies using strong gravitational lensing. , 494(2):2312–2326, May 2020. 10.1093/mnras/staa870.

Randall J. Splinter, Adrian L. Melott, Sergei F. Shandarin, and Yasushi Suto. Fundamental Discreteness Limitations of Cosmological N-Body Clustering Simulations. , 497(1):38–61, April 1998. 10.1086/305450.

Volker Springel. The cosmological simulation code GADGET-2. , 364(4):1105–1134, December 2005. 10.1111/j.1365-2966.2005.09655.x.

Volker Springel. E pur si muove: Galilean-invariant cosmological hydrodynamical simulations on a moving mesh. , 401(2):791–851, January 2010. 10.1111/j.1365-2966.2009.15715.x.

Volker Springel. Smoothed particle hydrodynamics in astrophysics. *Annual Review of Astronomy and Astrophysics*, 48(1):391–430, August 2010. ISSN 1545-4282. 10.1146/annurev-astro-081309-130914. URL http://dx.doi.org/10.1146/annurev-astro-081309-130914.

Volker Springel and Lars Hernquist. Cosmological smoothed particle hydrodynamics simulations: a hybrid multiphase model for star formation. *Monthly Notices of the Royal Astronomical Society*, 339(2):289–311, 2003.

Volker Springel and Simon D. M. White. Tidal tails in cold dark matter cosmologies. , 307(1): 162–178, July 1999. 10.1046/j.1365-8711.1999.02613.x.

Volker Springel, Naoki Yoshida, and Simon D. M. White. GADGET: a code for collisionless and gasdynamical cosmological simulations. , 6(2):79–117, April 2001. 10.1016/S1384-1076(01)00042-2.

Volker Springel, Naoki Yoshida, and Simon D.M. White. Gadget: a code for collisionless and gasdynamical cosmological simulations. *New Astronomy*, 6(2):79–117, April 2001. ISSN 1384-1076. 10.1016/s1384-1076(01)00042-2. URL http://dx.doi.org/10.1016/S1384-1076(01)00042-2.

Volker Springel, Tiziana Di Matteo, and Lars Hernquist. Modelling feedback from stars and black holes in galaxy mergers. *Monthly Notices of the Royal Astronomical Society*, 361(3):776–794, 2005.

Milan Staffehl, Dylan Nelson, Mohammadreza Ayromlou, Eric Rohr, and Annalisa Pillepich. The abundance and origin of cool gas in galaxy clusters in the tng-cluster simulation. *arXiv preprint arXiv:2503.01960*, 2025.

Flora Stanley, CM Harrison, DM Alexander, J Simpson, Kirsten Kraiberg Knudsen, J R Mullaney, DJ Rosario, and J Scholtz. Deep alma photometry of distant x-ray agn: improvements in star formation rate constraints, and agn identification. *Monthly Notices of the Royal Astronomical Society*, 478(3):3721–3739, 2018.

Lisa K Steinborn, Klaus Dolag, Michaela Hirschmann, M Almudena Prieto, and Rhea-Silvia Remus. A refined sub-grid model for black hole accretion and agn feedback in large cosmological simulations. *Monthly Notices of the Royal Astronomical Society*, 448(2):1504–1525, 2015.

Lisa K Steinborn, Klaus Dolag, Julia M Comerford, Michaela Hirschmann, Rhea-Silvia Remus, and Adelheid F Teklu. Origin and properties of dual and offset active galactic nuclei in a cosmological simulation at. *Monthly Notices of the Royal Astronomical Society*, 458(1):1013–1028, 2016.

Megan R Sturm and Amy E Reines. A breakdown of the black hole–bulge mass relation in local active galaxies. *The Astrophysical Journal*, 971(2):173, 2024.

Hyewon Suh, Francesca Civano, Benny Trakhtenbrot, Francesco Shankar, Günther Hasinger, David B Sanders, and Viola Allevato. No significant evolution of relations between black hole mass and galaxy total stellar mass up to z 2.5. *The Astrophysical Journal*, 889(1):32, 2020.

M. Sun. Every BCG with a Strong Radio Agn has an X-Ray Cool Core: Is the Cool Core-Noncool Core Dichotomy Too Simple? , 704(2):1586–1604, October 2009. 10.1088/0004-637X/704/2/1586.

M Sun, SS Murray, M Markevitch, and A Vikhlinin. Chandra observation of a2256: A cluster at the early stage of merging. *The Astrophysical Journal*, 565(2):867, 2002.

R. Sunyaev, V. Arefiev, V. Babyshkin, A. Bogomolov, K. Borisov, M. Buntov, H. Brunner, R. Burenin, E. Churazov, D. Coutinho, J. Eder, N. Eismont, M. Freyberg, M. Gilfanov, P. Gureyev, G. Hasinger, I. Khabibullin, V. Kolmykov, S. Komovkin, R. Krivonos, I. Lapshov, V. Levin, I. Lomakin, A. Lutovinov, P. Medvedev, A. Merloni, T. Mernik, E. Mikhailov, V. Molodtsov, P. Mzhelsky, S. Müller, K. Nandra, V. Nazarov, M. Pavlinsky, A. Poghodin, P. Predehl, J. Robrade, S. Sazonov, H. Scheuerle, A. Shirshakov, A. Tkachenko, and V. Voron. Srg x-ray orbital observatory: Its telescopes and first scientific results. *Astronomy amp; Astrophysics*, 656:A132, December 2021. ISSN 1432-0746. 10.1051/0004-6361/202141179. URL http://dx.doi.org/10.1051/0004-6361/202141179.

R. A. Sunyaev and Ya. B. Zeldovich. Small-Scale Fluctuations of Relic Radiation. , 7(1):3–19, April 1970. 10.1007/BF00653471.

R. A. Sunyaev and Ya. B. Zeldovich. The Observations of Relic Radiation as a Test of the Nature of X-Ray Radiation from the Clusters of Galaxies. *Comments on Astrophysics and Space Physics*, 4:173, November 1972.

G. Tabor and J. Binney. Elliptical galaxy cooling flows without mass drop-out. , 263:323–334, July 1993. 10.1093/mnras/263.2.323.

Linda J. Tacconi, Reinhard Genzel, and Amiel Sternberg. The evolution of the star-forming interstellar medium across cosmic time. *Annual Review of Astronomy and Astrophysics*, 58(1): 157–203, August 2020. ISSN 1545-4282. 10.1146/annurev-astro-082812-141034. URL http://dx.doi.org/10.1146/annurev-astro-082812-141034.

Giuliano Taffoni, Lucio Mayer, Monica Colpi, and Fabio Governato. On the life and death of satellite haloes. *MNRAS*, 341(2):434–448, 2003.

Rosie Y Talbot, Debora Sijacki, and Martin A Bourne. Simulations of spin-driven agn jets in gas-rich galaxy mergers. *Monthly Notices of the Royal Astronomical Society*, 528(3):5432–5451, 2024.

Qing-Hua Tan, Yu Gao, Kotaro Kohno, Xiao-Yang Xia, Alain Omont, Cai-Na Hao, Shu-De Mao, Emanuele Daddi, Yong Shi, Ying-He Zhao, and Pierre Cox. Resolving the Interstellar Medium in Ultraluminous Infrared QSO Hosts with ALMA. , 887(1):24, December 2019. 10.3847/1538-4357/ab50be.

P. Taylor and C. Kobayashi. Seeding black holes in cosmological simulations. *Monthly Notices of the Royal Astronomical Society*, 442(3):2751–2767, June 2014. ISSN 0035-8711. 10.1093/mnras/stu983. URL http://dx.doi.org/10.1093/mnras/stu983.

Romain Teyssier. Ramses: A new n-body and hydrodynamical code. *Astrophysics Source Code Library*, pages ascl–1011, 2010.

Romain Teyssier. Numerical cosmology. *arXiv preprint arXiv:2510.13129*, 2025.

F. K. Thielemann, D. Argast, F. Brachwitz, W. R. Hix, P. Höflich, M. Liebendörfer, G. Martinez-Pinedo, A. Mezzacappa, K. Nomoto, and I. Panov. Supernova Nucleosynthesis and Galactic Evolution. In Wolfgang Hillebrandt and Bruno Leibundgut, editors, *From Twilight to Highlight: The Physics of Supernovae*, page 331, January 2003. 10.1007/10828549_46.

P. A. Thomas, A. C. Fabian, K. A. Arnaud, W. Forman, and C. Jones. The prevalence of cooling flows in early-type galaxies. , 222:655–672, October 1986. 10.1093/mnras/222.4.655.

Christopher Tiede, Jonathan Zrake, Andrew MacFadyen, and Zoltan Haiman. Gas-driven inspiral of binaries in thin accretion disks. *The Astrophysical Journal*, 900(1):43, 2020.

Giuseppe Tormen, Francois R Bouchet, and Simon DM White. The structure and dynamical evolution of dark matter haloes. *Monthly Notices of the Royal Astronomical Society*, 286(4): 865–884, 1997.

L. Tornatore, S. Borgani, K. Dolag, and F. Matteucci. Chemical enrichment of galaxy clusters from hydrodynamical simulations. , 382(3):1050–1072, December 2007. 10.1111/j.1365-2966.2007.12070.x.

A. Traina, F. Vito, F. Arrigoni-Battaia, C. C. Chen, C. Vignali, X. Prochaska, S. Cantalupo, A. Pensabene, P. Tozzi, A. Travascio, R. Gilli, M. N. Isla Llave, S. Marchesi, and G. Mazzolari. The properties of X-ray selected AGN in protoclusters pinpointed by Enormous Lya Nebulae. *arXiv e-prints*, art. arXiv:2507.03078, July 2025. 10.48550/arXiv.2507.03078.

Benny Trakhtenbrot, Paulina Lira, Hagai Netzer, Claudia Cicone, Roberto Maiolino, and Ohad Shemmer. Fast-growing SMBHs in Fast-growing Galaxies, at High Redshifts: the Role of Major Mergers as Revealed by ALMA. *Frontiers in Astronomy and Space Sciences*, 4:49, November 2017. 10.3389/fspas.2017.00049.

Maxime Trebitsch, Yohan Dubois, Marta Volonteri, Hugo Pfister, Corentin Cadiou, Harley Katz, Joakim Rosdahl, Taysun Kimm, Christophe Pichon, Ricarda S. Beckmann, Julien Devriendt, and Adrianne Slyz. The obelisk simulation: Galaxies contribute more than agn to hi reionization of protoclusters. *Astronomy amp; Astrophysics*, 653:A154, September 2021. ISSN 1432-0746. 10.1051/0004-6361/202037698. URL http://dx.doi.org/10.1051/0004-6361/202037698.

Scott Tremaine, Karl Gebhardt, Ralf Bender, Gary Bower, Alan Dressler, S. M. Faber, Alexei V. Filippenko, Richard Green, Carl Grillmair, Luis C. Ho, John Kormendy, Tod R. Lauer, John Magorrian, Jason Pinkney, and Douglas Richstone. The Slope of the Black Hole Mass versus Velocity Dispersion Correlation. , 574(2):740–753, August 2002. 10.1086/341002.

M. Tremmel, M. Karcher, F. Governato, M. Volonteri, T. R. Quinn, A. Pontzen, L. Anderson, and J. Bellovary. The Romulus cosmological simulations: a physical approach to the formation,

dynamics and accretion models of SMBHs. , 470(1):1121–1139, September 2017. 10.1093/mnras/stx1160.

Michael Tremmel, Fabio Governato, Marta Volonteri, and Thomas R Quinn. Off the beaten path: a new approach to realistically model the orbital decay of supermassive black holes in galaxy formation simulations. *Monthly Notices of the Royal Astronomical Society*, 451(2):1868–1874, 2015.

Michael Tremmel, Fabio Governato, Marta Volonteri, Andrew Pontzen, and Thomas R. Quinn. Wandering supermassive black holes in milky-way-mass halos. *The Astrophysical Journal Letters*, 857(2):L22, April 2018a. ISSN 2041-8213. 10.3847/2041-8213/aabc0a. URL http://dx.doi.org/10.3847/2041-8213/aabc0a.

Michael Tremmel, Fabio Governato, Marta Volonteri, Andrew Pontzen, and Thomas R Quinn. Wandering supermassive black holes in milky-way-mass halos. *The Astrophysical journal letters*, 857(2):L22, 2018b.

Tommaso Treu, Jong-Hak Woo, Matthew A Malkan, and Roger D Blandford. Cosmic evolution of black holes and spheroids. ii. scaling relations at z= 0.36. *The Astrophysical Journal*, 667(1): 117, 2007.

K. R. W. Tristram, K. Meisenheimer, W. Jaffe, M. Schartmann, H.-W. Rix, Ch. Leinert, S. Morel, M. Wittkowski, H. Röttgering, G. Perrin, B. Lopez, D. Raban, W. D. Cotton, U. Graser, F. Paresce, and Th. Henning. Resolving the complex structure of the dust torus in the active nucleus of the circinus galaxy. *Astronomy amp; Astrophysics*, 474(3):837–850, October 2007. ISSN 1432-0746. 10.1051/0004-6361:20078369. URL http://dx.doi.org/10.1051/0004-6361:20078369.

I. Trujillo, Peter Erwin, A. Asensio Ramos, and Alister W. Graham. Evidence for a New Elliptical-Galaxy Paradigm: Sérsic and Core Galaxies. , 127(4):1917–1942, April 2004. 10.1086/382712.

P. Tsalmantza, R. Decarli, M. Dotti, and David W. Hogg. A Systematic Search for Massive Black Hole Binaries in the Sloan Digital Sky Survey Spectroscopic Sample. , 738(1):20, September 2011. 10.1088/0004-637X/738/1/20.

Dusán Tubín-Arenas, Mirko Krumpe, David Homan, Alex Markowitz, Meredith Powell, Georg Lamer, Tanya Urrutia, Axel Schwope, Hartmut Winkler, Sabina Bahic, et al. Searching for supermassive black hole binaries within srg/erosita-de-i. properties of the x-ray selected candidates. *Astronomy & Astrophysics*, 698:A192, 2025.

Elena Tundo, M Bernardi, JB Hyde, RK Sheth, and A Pizzella. Scatter in the m (bh)-sigma and m (bh)-l correlations and consequences for the inferred black hole mass function. *Astrophys. J.*, 663(arXiv: astro-ph/0609297):53, 2007a.

Elena Tundo, Mariangela Bernardi, Joseph B Hyde, Ravi K Sheth, and Alessandro Pizzella. On the inconsistency between the black hole mass function inferred from m•-σ and m•-l correlations. *The Astrophysical Journal*, 663(1):53, 2007b.

B. D. Turland. Observations of M87 at 5 GHz with the 5-km telescope. , 170:281–294, February 1975. 10.1093/mnras/170.2.281.

T. J. Turner and L. Miller. X-ray absorption and reflection in active galactic nuclei. *The Astronomy and Astrophysics Review*, 17(1):47–104, March 2009. ISSN 1432-0754. 10.1007/s00159-009-0017-1. URL http://dx.doi.org/10.1007/s00159-009-0017-1.

Hisakazu Uchiyama, Takuji Yamashita, Tohru Nagao, Yoshiaki Ono, Jun Toshikawa, Kohei Ichikawa, Nozomu Kawakatu, Masaru Kajisawa, Yoshiki Toba, Yoshiki Matsuoka, Mariko Kubo, Masatoshi Imanishi, Kei Ito, Toshihiro Kawaguchi, Chien-Hsiu Lee, and Tomoki Saito. A Wide and Deep Exploration of Radio Galaxies with Subaru HSC (WERGS). IX. The most overdense region at z 5 inhabited by a massive radio galaxy. , 74(6):L27–L32, December 2022. 10.1093/pasj/psac075.

Yoshihiro Ueda, Masayuki Akiyama, Kouji Ohta, and Takamitsu Miyaji. Cosmological evolution of the hard x-ray active galactic nucleus luminosity function and the origin of the hard x-ray background. *The Astrophysical Journal*, 598(2):886–908, December 2003. ISSN 1538-4357. 10.1086/378940. URL http://dx.doi.org/10.1086/378940.

Yoshihiro Ueda, Masayuki Akiyama, Günther Hasinger, Takamitsu Miyaji, and Michael G. Watson. Toward the Standard Population Synthesis Model of the X-Ray Background: Evolution of X-Ray Luminosity and Absorption Functions of Active Galactic Nuclei Including Compton-thick Populations. , 786(2):104, May 2014. 10.1088/0004-637X/786/2/104.

Marie-Helene Ulrich. 3c 273: A review of recent results. *Space Science Reviews*, 28(1):89–104, 1981.

C. Megan Urry and Paolo Padovani. Unified Schemes for Radio-Loud Active Galactic Nuclei. , 107:803, September 1995. 10.1086/133630.

Milena Valentini and Klaus Dolag. Hydrodynamic methods and sub-resolution models for cosmological simulations. *arXiv e-prints*, art. arXiv:2502.06954, February 2025. 10.48550/arXiv.2502.06954.

Milena Valentini, Giuseppe Murante, Stefano Borgani, Pierluigi Monaco, Alessandro Bressan, and Alexander M. Beck. On the effect of galactic outflows in cosmological simulations of disc galaxies. , 470(3):3167–3193, September 2017. 10.1093/mnras/stx1352.

Milena Valentini, Giuseppe Murante, Stefano Borgani, Gian Luigi Granato, Pierluigi Monaco, Fabrizio Brighenti, Luca Tornatore, Alessandro Bressan, and Andrea Lapi. Impact of AGN feedback on galaxies and their multiphase ISM across cosmic time. , 491(2):2779–2807, January 2020. 10.1093/mnras/stz3131.

Mauri J Valtonen. Are supermassive black holes confined to galactic nuclei? *Comments Astrophys., Vol. 18, No. 4, p. 191-206*, 18:191–206, 1996.

MJ Valtonen, S Ciprini, and HJ Lehto. On the masses of oj287 black holes. *Monthly Notices of the Royal Astronomical Society*, 427(1):77–83, 2012.

R. C. E. van den Bosch, G. van de Ven, E. K. Verolme, M. Cappellari, and P. T. de Zeeuw. Triaxial orbit based galaxy models with an application to the (apparent) decoupled core galaxy NGC 4365. , 385(2):647–666, April 2008. 10.1111/j.1365-2966.2008.12874.x.

Eugene Vasiliev and Monica Valluri. A New Implementation of the Schwarzchild Method for Constructing Observationally Driven Dynamical Models of Galaxies of All Morphological Types. , 889(1):39, January 2020. 10.3847/1538-4357/ab5fe0.

Eugene Vasiliev, Fabio Antonini, and David Merritt. The final-parsec problem in the collisionless limit. *The Astrophysical Journal*, 810(1):49, 2015.

Alberto Vecchio, Monica Colpi, and A Polnarev. Orbital evolution of a massive black hole pair by dynamical friction. *arXiv preprint astro-ph/9405051*, 1994.

Sylvain Veilleux, Roberto Maiolino, Alberto D. Bolatto, and Susanne Aalto. Cool outflows in galaxies and their implications. , 28(1):2, April 2020. 10.1007/s00159-019-0121-9.

MC Vergara, A Askar, F Flammini Dotti, DRG Schleicher, A Escala, R Spurzem, M Giersz, J Hurley, M Arca Sedda, and N Neumayer. Efficient black hole seed formation in low metallicity and dense stellar clusters with implications for jwst sources. *arXiv preprint arXiv:2508.14260*, 2025.

Marianne Vestergaard and Bradley M. Peterson. Determining Central Black Hole Masses in Distant Active Galaxies and Quasars. II. Improved Optical and UV Scaling Relationships. , 641 (2):689–709, April 2006. 10.1086/500572.

Cristian Vignali, Dave M. Alexander, and Andrea Comastri. Evidence for x-ray obscuration in type ii quasar candidates from the sloan digital sky survey. *Monthly Notices of the Royal Astronomical Society*, 354(3):720–726, November 2004. ISSN 1365-2966. 10.1111/j.1365-2966.2004.08231.x. URL http://dx.doi.org/10.1111/j.1365-2966.2004.08231.x.

A. Vikhlinin, M. Markevitch, S. S. Murray, C. Jones, W. Forman, and L. Van Speybroeck. Chandra Temperature Profiles for a Sample of Nearby Relaxed Galaxy Clusters. , 628(2):655–672, August 2005. 10.1086/431142.

A. Vikhlinin, A. Kravtsov, W. Forman, C. Jones, M. Markevitch, S. S. Murray, and L. Van Speybroeck. Chandra Sample of Nearby Relaxed Galaxy Clusters: Mass, Gas Fraction, and Mass-Temperature Relation. , 640(2):691–709, April 2006. 10.1086/500288.

Pauli Virtanen, Ralf Gommers, Travis E. Oliphant, Matt Haberland, Tyler Reddy, David Cournapeau, Evgeni Burovski, Pearu Peterson, Warren Weckesser, Jonathan Bright, Stéfan J. van der Walt, Matthew Brett, Joshua Wilson, K. Jarrod Millman, Nikolay Mayorov, Andrew R. J. Nelson, Eric Jones, Robert Kern, Eric Larson, C J Carey, İlhan Polat, Yu Feng, Eric W. Moore, Jake VanderPlas, Denis Laxalde, Josef Perktold, Robert Cimrman, Ian Henriksen, E. A. Quintero, Charles R. Harris, Anne M. Archibald, Antônio H. Ribeiro, Fabian Pedregosa, Paul van Mulbregt, and SciPy 1.0 Contributors. SciPy 1.0: Fundamental Algorithms for Scientific Computing in Python. *Nature Methods*, 17:261–272, 2020. 10.1038/s41592-019-0686-2.

Mark Vogelsberger, Shy Genel, Debora Sijacki, Paul Torrey, Volker Springel, and Lars Hernquist. A model for cosmological simulations of galaxy formation physics. *Monthly Notices of the Royal Astronomical Society*, 436(4):3031–3067, 2013.

Mark Vogelsberger, Federico Marinacci, Paul Torrey, and Ewald Puchwein. Cosmological simulations of galaxy formation. *Nature Reviews Physics*, 2(1):42–66, 2020.

Marta Volonteri. Gravitational recoil: Signatures on the massive black hole population. *The Astrophysical Journal*, 663(1):L5–L8, June 2007. ISSN 1538-4357. 10.1086/519525. URL http://dx.doi.org/10.1086/519525.

Marta Volonteri. Formation of supermassive black holes. , 18(3):279–315, July 2010. 10.1007/s00159-010-0029-x.

Marta Volonteri and Amy E Reines. Inferences on the relations between central black hole mass and total galaxy stellar mass in the high-redshift universe. *The Astrophysical journal letters*, 820 (1):L6, 2016.

Marta Volonteri, Francesco Haardt, and Piero Madau. The Assembly and Merging History of Supermassive Black Holes in Hierarchical Models of Galaxy Formation. , 582(2):559–573, January 2003. 10.1086/344675.

Marta Volonteri, Piero Madau, Eliot Quataert, and Martin J. Rees. The Distribution and Cosmic Evolution of Massive Black Hole Spins. , 620(1):69–77, February 2005. 10.1086/426858.

Marta Volonteri, Tamara Bogdanović, Massimo Dotti, and Monica Colpi. Massive black holes in merging galaxies. *Proceedings of the International Astronomical Union*, 11(A29B):285–291, 2015.

Marta Volonteri, Yohan Dubois, Christophe Pichon, and Julien Devriendt. The cosmic evolution of massive black holes in the horizon-agn simulation. *Monthly Notices of the Royal Astronomical Society*, 460(3):2979–2996, 2016a.

Marta Volonteri, Yohan Dubois, Christophe Pichon, and Julien Devriendt. The cosmic evolution of massive black holes in the horizon-agn simulation. *Monthly Notices of the Royal Astronomical Society*, 460(3):2979–2996, 2016b.

Marta Volonteri, Mélanie Habouzit, and Monica Colpi. The origins of massive black holes. *Nature Reviews Physics*, 3(11):732–743, September 2021. ISSN 2522-5820. 10.1038/s42254-021-00364-9. URL http://dx.doi.org/10.1038/s42254-021-00364-9.

Marta Volonteri, Hugo Pfister, Ricarda Beckmann, Massimo Dotti, Yohan Dubois, Warren Massonneau, Gibwa Musoke, and Michael Tremmel. Dual agn in the horizon-agn simulation and their link to galaxy and massive black hole mergers, with an excursus on multiple agn. *Monthly Notices of the Royal Astronomical Society*, 514(1):640–656, 2022.

Marta Volonteri, Mélanie Habouzit, and Monica Colpi. What if young z$>$ 9 jwst galaxies hosted massive black holes? *Monthly Notices of the Royal Astronomical Society*, 521(1):241–250, 2023.

Benedetta Vulcani, Gabriella De Lucia, Bianca M. Poggianti, Kevin Bundy, Surhud More, and Rosa Calvi. What do simulations predict for the galaxy stellar mass function and its evolution in different environments? *The Astrophysical Journal*, 788(1):57, May 2014. ISSN 1538-4357. 10.1088/0004-637x/788/1/57. URL http://dx.doi.org/10.1088/0004-637X/788/1/57.

Liang Wang, Tingfeng Yi, Shun Zhang, Vinit Dhiman, and Liang Dong. Search for quasi-periodic oscillations of AGNs in the Swift BAT 157-month hard X-ray survey. , 77(2):381–388, April 2025. 10.1093/pasj/psaf005.

SX Wang, WN Brandt, B Luo, I Smail, DM Alexander, ALR Danielson, JA Hodge, A Karim, BD Lehmer, JM Simpson, et al. An alma survey of submillimeter galaxies in the extended chandra deep field-south: the agn fraction and x-ray properties of submillimeter galaxies. *The Astrophysical Journal*, 778(2):179, 2013.

Yijun Wang, Tao Wang, Luis C. Ho, Yuxing Zhong, and Bin Luo. The fundamental plane of black hole activity for low-luminosity radio active galactic nuclei across 1<z<4. *Astronomy amp; Astrophysics*, 689:A327, September 2024. ISSN 1432-0746. 10.1051/0004-6361/202449732. URL http://dx.doi.org/10.1051/0004-6361/202449732.

Charlotte Ward, Suvi Gezari, Sara Frederick, Erica Hammerstein, Peter Nugent, Sjoert van Velzen, Andrew Drake, Abigail García-Pérez, Immaculate Oyoo, Eric C. Bellm, Dmitry A. Duev, Matthew J. Graham, Mansi M. Kasliwal, Stephen Kaye, Ashish A. Mahabal, Frank J. Masci, Ben Rusholme, Maayane T. Soumagnac, and Lin Yan. AGNs on the Move: A Search for Off-nuclear AGNs from Recoiling Supermassive Black Holes and Ongoing Galaxy Mergers with the Zwicky Transient Facility. , 913(2):102, June 2021. 10.3847/1538-4357/abf246.

Charlotte Ward, Suvi Gezari, Peter Nugent, Matthew Kerr, Michael Eracleous, Sara Frederick, Erica Hammerstein, Matthew J. Graham, Sjoert van Velzen, Mansi M. Kasliwal, Russ R. Laher, Frank J. Masci, Josiah Purdum, Benjamin Racine, and Roger Smith. Panic at the ISCO: Time-varying Double-peaked Broad Lines from Evolving Accretion Disks Are Common among Optically Variable AGNs. , 961(2):172, February 2024. 10.3847/1538-4357/ad147d.

Michael S. Warren. 2hot: an improved parallel hashed oct-tree n-body algorithm for cosmological simulation. In *Proceedings of the International Conference on High Performance Computing, Networking, Storage and Analysis*, SC13, page 1–12. ACM, November 2013. 10.1145/2503210.2503220. URL http://dx.doi.org/10.1145/2503210.2503220.

Rainer Weinberger, Volker Springel, Rüdiger Pakmor, Dylan Nelson, Shy Genel, Annalisa Pillepich, Mark Vogelsberger, Federico Marinacci, Jill Naiman, Paul Torrey, and Lars Hernquist. Supermassive black holes and their feedback effects in the illustristng simulation. *Monthly Notices of the Royal Astronomical Society*, 479(3):4056–4072, June 2018. ISSN 1365-2966. 10.1093/mnras/sty1733. URL http://dx.doi.org/10.1093/mnras/sty1733.

Z. L. Wen and J. L. Han. Substructure and dynamical state of 2092 rich clusters of galaxies derived from photometric data. , 436(1):275–293, November 2013. 10.1093/mnras/stt1581.

Daniel Whalen, Bob van Veelen, Brian W O'Shea, and Michael L Norman. The destruction of cosmological minihalos by primordial supernovae. *The Astrophysical Journal*, 682(1):49, 2008.

Robert P. C. Wiersma, Joop Schaye, and Britton D. Smith. The effect of photoionization on the cooling rates of enriched, astrophysical plasmas. *Monthly Notices of the Royal Astronomical Society*, 393(1):99–107, February 2009. ISSN 1365-2966. 10.1111/j.1365-2966.2008.14191.x. URL http://dx.doi.org/10.1111/j.1365-2966.2008.14191.x.

Chris J Willott, Philippe Delorme, Céline Reylé, Loic Albert, Jacqueline Bergeron, David Crampton, Xavier Delfosse, Thierry Forveille, John B Hutchings, Ross J McLure, et al. The canada–france high-z quasar survey: nine new quasars and the luminosity function at redshift 6. *The Astronomical Journal*, 139(3):906, 2010.

Nico Winkel, Vardha N. Bennert, Raymond P. Remigio, Tommaso Treu, Knud Jahnke, Vivian U, Aaron J. Barth, Matthew Malkan, Bernd Husemann, Xuheng Ding, and Simon Birrer. Combining Direct Black Hole Mass Measurements and Spatially Resolved Stellar Kinematics to Calibrate the M $_{BH}$–σ $_{\star}$ Relation of Active Galaxies. , 978(1):115, January 2025. 10.3847/1538-4357/ad9272.

Jong-Hak Woo, Tommaso Treu, Matthew A Malkan, and Roger D Blandford. Cosmic evolution of black holes and spheroids. i. the mbh-σ relation at z= 0.36. *The Astrophysical Journal*, 645 (2):900, 2006.

Q. Wu, M. Scialpi, S. Liao, F. Mannucci, and Z. Qi. Dulag: A dual and lensed agn candidate catalog with the gaia multipeak method. *Astronomy amp; Astrophysics*, 692:A154, December 2024. ISSN 1432-0746. 10.1051/0004-6361/202452291. URL http://dx.doi.org/10.1051/0004-6361/202452291.

Lizhi Xie, Gabriella De Lucia, Fabio Fontanot, Michaela Hirschmann, Yannick M Bahé, Michael L Balogh, Adam Muzzin, Benedetta Vulcani, Devontae C Baxter, Ben Forrest, et al. The first quenched galaxies: When and how? *The Astrophysical Journal Letters*, 966(1):L2, 2024.

Guohong Xu. A New Parallel N-Body Gravity Solver: TPM. , 98:355, May 1995. 10.1086/192166.

Zhang XueGuang. More than 60% of double-peaked narrow emission lines not related to dual galaxy systems? *arXiv preprint arXiv:2507.12893*, 2025.

Jinyi Yang, Feige Wang, Xue-Bing Wu, Xiaohui Fan, Ian D McGreer, Fuyan Bian, Weimin Yi, Qian Yang, Yanli Ai, Xiaoyi Dong, et al. A survey of luminous high-redshift quasars with sdss and wise. ii. the bright end of the quasar luminosity function at z 5. *The Astrophysical Journal*, 829(1):33, 2016.

G. Yepes. Cosmological Numerical Simulations. In D. Valls-Gabaud, M. A. Hendry, P. Molaro, and K. Chamcham, editors, *From Quantum Fluctuations to Cosmological Structures*, volume 126 of *Astronomical Society of the Pacific Conference Series*, page 279, September 1997.

Jaiyul Yoo, Jordi Miralda-Escudé, David H. Weinberg, Zheng Zheng, and Christopher W. Morgan. The Most Massive Black Holes in the Universe: Effects of Mergers in Massive Galaxy Clusters. , 667(2):813–825, October 2007. 10.1086/521015.

Qingjuan Yu. Evolution of massive binary black holes. , 331(4):935–958, April 2002. 10.1046/j.1365-8711.2002.05242.x.

Qingjuan Yu. Evolution of massive binary black holes. *Monthly Notices of the Royal Astronomical Society*, 331(4):935–958, 2002.

Qingjuan Yu and Scott Tremaine. Observational constraints on growth of massive black holes. *Monthly Notices of the Royal Astronomical Society*, 335(4):965–976, 2002.

Hu Zhan. Optimal Softening for N-Body Halo Simulations. , 639(2):617–620, March 2006. 10.1086/499763.

Congyao Zhang, Eugene Churazov, and Alexander A Schekochihin. Generation of internal waves by buoyant bubbles in galaxy clusters and heating of intracluster medium. *Monthly Notices of the Royal Astronomical Society*, 478(4):4785–4798, May 2018. ISSN 1365-2966. 10.1093/mnras/sty1269. URL http://dx.doi.org/10.1093/mnras/sty1269.

Hengyue Zhang, Martin Bureau, Ilaria Ruffa, Timothy A. Davis, Pandora Dominiak, Jacob S. Elford, Federico Lelli, and Thomas G. Williams. WISDOM Project–XXV. Improving the CO-dynamical supermassive black hole mass measurement in the galaxy NGC 1574 using high spatial resolution ALMA observations. , 541(3):2540–2552, August 2025. 10.1093/mnras/staf1161.

Tianchi Zhang, Shihong Liao, Ming Li, and Liang Gao. The optimal gravitational softening length for cosmological n-body simulations. *Monthly Notices of the Royal Astronomical Society*, 487(1):1227–1232, May 2019. ISSN 1365-2966. 10.1093/mnras/stz1370. URL http://dx.doi.org/10.1093/mnras/stz1370.

Qi Zheng, XueGuang Zhang, QiRong Yuan, Paola Severgnini, and Cristian Vignali. Sdss j222428.53+261423.2: unique emission lines properties unveil a sub-kiloparsec dual agn candidate. *Monthly Notices of the Royal Astronomical Society: Letters*, 531(1):L76–L81, March 2024. ISSN 1745-3933. 10.1093/mnrasl/slae033. URL http://dx.doi.org/10.1093/mnrasl/slae033.

Qi Zheng, XueGuang Zhang, QiRong Yuan, Paola Severgnini, and Cristian Vignali. SDSS J222428.53+261423.2: unique emission lines properties unveil a sub-kiloparsec dual AGN candidate. , 531(1):L76–L81, June 2024. 10.1093/mnrasl/slae033.

Ming-Yang Zhuang, Jinyi Shangguan, Yuan Bian, Yue Shen, Luis C. Ho, Min Du, Junyao Li, Zhao-Yu Li, and Jing Wang. Cold gas infall onto a brightest group galaxy via a gas-rich minor merger, 2025. URL https://arxiv.org/abs/2512.13932.

Kastytis Zubovas and Andrew King. Clearing Out a Galaxy. , 745(2):L34, February 2012. 10.1088/2041-8205/745/2/L34.

Lorenz Zwick and Lucio Mayer. Relativistic binary-disc dynamics and the timing of oj-287's flares, 2023. URL https://arxiv.org/abs/2305.19149.

Lorenz Zwick, Christopher Tiede, and Lucio Mayer. Little red dots as self-gravitating discs accreting on supermassive stars: Spectral appearance and formation pathway of the progenitors to direct collapse black holes. *arXiv preprint arXiv:2507.22014*, 2025.

Hannah Übler, Roberto Maiolino, Emma Curtis-Lake, Pablo G. Pérez-González, Mirko Curti, Michele Perna, Santiago Arribas, Stéphane Charlot, Madeline A. Marshall, Francesco D'Eugenio, Jan Scholtz, Andrew Bunker, Stefano Carniani, Pierre Ferruit, Peter Jakobsen, Hans-Walter Rix, Bruno Rodríguez Del Pino, Chris J. Willott, Torsten Boeker, Giovanni Cresci, Gareth C. Jones, Nimisha Kumari, and Tim Rawle. Ga-nifs: A massive black hole in a low-metallicity agn atz5.55 revealed by jwst/nirspec ifs. *Astronomy amp; Astrophysics*, 677:A145, September 2023. ISSN 1432-0746. 10.1051/0004-6361/202346137. URL http://dx.doi.org/10.1051/0004-6361/202346137.

UNIVERSITÀ
DEGLI STUDI
DI TRIESTE

La borsa di dottorato è cofinanziata con risorse dell'Unione europea, NextGeneration EU - Piano Nazionale di Ripresa e Resilienza, Missione 4 – Componente 2– Investimento 3.3 CUP J93C22000540006